# Transactions of the ASME

HEAT TRANSFER DIVISION
Chairman, R. J. SIMONEAU
Secretary, F. A. KULACKI
Senior Technical Editor, K. T. YANG
Technical Editor, I. CATTON
Technical Editor, M. EPSTEIN
Technical Editor, G. M. FAETH
Technical Editor, R. GREIF
Technical Editor, P. J. MARTO
Technical Editor, R. H. PLETCHER
Technical Editor, R. K. SHAH
Technical Editor, R. VISKANTA

BOARD ON COMMUNICATIONS
Chairman and Vice President
K. N. REID, JR.

Members-at-Large
J. T. COKONIS
W. G. GOTTENBERG
D. KOENIG
M. KUTZ
F. LANDIS
R. E. NICKELL
J. ORTLOFF
C. PHILLIPS
H. C. REEDER

President, G. KOTNICK
Executive Director,
PAUL ALLMENDINGER
Treasurer,
ROBERT A. BENNETT

PUBLISHING STAFF
Mng. Dir., Publ., J. J. FREY
Dep. Mng. Dir., Pub.,
JOS. SANSONE
Managing Editor,
CORNELIA MONAHAN
Production Editor,
VALERIE WINTERS
Editorial Prod. Asst.
MARISOL ANDINO

**The Journal of Heat Transfer** (ISSN 0022-1481) is published quarterly for $100 per year by The American Society of Mechanical Engineers, 345 East 47th Street, New York, N Y 10017. Second class postage paid at New York, NY and additional mailing offices. POSTMASTER: Send address changes to The Journal of Heat Transfer, c/o THE AMERICAN SOCIETY OF MECHANICAL ENGINEERS, 22 Law Drive, Box 2300, Fairfield, NJ 07007-2300.
**CHANGES OF ADDRESS** must be received at Society headquarters seven weeks before they are to be effective. Please send old label and new address.
**PRICES:** To members, $24.00, annually; to nonmembers, $100.00. Add $6.00 for postage to countries outside the United States and Canada.
**STATEMENT from By-Laws.** The Society shall not be responsible for statements or opinions advanced in papers or . . . printed in its publications (B7.1, para. 3).



**INDEXED** by the Engineering Index, Inc.

# Journal of Heat Transfer

Published Quarterly by The American Society of Mechanical Engineers

VOLUME 107 • NUMBER 2 • MAY 1985


## ANNOUNCEMENTS



## TECHNICAL PAPERS

(Contents continued)



## TECHNICAL NOTES



## DISCUSSION

M. Epstein
Mem. ASME

G. M. Hauser

R. E. Henry

Fauske & Associates, Inc.,
Burr Ridge, Ill. 60521

# Thermophoretic Deposition of Particles in Natural Convection Flow From a Vertical Plate

*An analysis is made for thermophoretic transport of small particles through a free-convection boundary layer adjacent to a cold, vertical deposition surface. The gas–particle, boundary layer equations are solved numerically for both laminar and turbulent flow. The numerical results indicate that, for a fixed set of boundary conditions and physical properties, the particle concentration at the wall in the laminar flow is very close to that in turbulent flow. A simple expression is suggested relating the particle transport rate to the heat transfer coefficient for the laminar and turbulent flow regimes.*

## Introduction

Small particles, such as dust, when suspended in a gas with a temperature gradient, experience a force in the direction opposite to the temperature gradient. This so-called thermophoretic force is utilized in air-cleaning devices to remove submicron- and micron-sized particles from gas streams. The deposition of particulate material on heat exchanger surfaces with the concomitant reduction of exchanger effectiveness has been attributed to therophoresis. The subject of the thermophoretic deposition of radioactive particles is currently one of importance in view of its relevance to postulated accidents in a nuclear reactor.

The initial studies of thermophoretic transport involved simple one-dimensional flows for the measurement of the thermophoretic velocity (see, e.g., Goldsmith and May [1]). Recently, Talbot et al. [2] numerically solved for the velocity and temperature fields in the laminar boundary layer adjacent to a heated plate. Using several available theoretical expressions for the thermophoretic force (or transport coefficient), they calculated the trajectory of a particle entering the boundary layer. Measurements of the thickness of the particle-free layer next to the heated plate were compared with the calculated trajectories and it was found that the theory of Brock [3], modified slightly to fit the data for very small particles, gave the best overall agreement with the measurements. They also found good agreement of the experimental data obtained by others with their modified formula of Brock. For a review of the data and the theoretical expressions for the thermophoretic velocity, Talbot et al. [2] should be consulted.

The first analysis of thermophoretic deposition in a flow geometry of engineering interest appears to be that of Hales et al. [4]. They solved the laminar boundary layer equations for simultaneous aerosol and steam transport to an isothermal vertical surface situated adjacent to a large body of an otherwise quiescent air–steam–aerosol mixture. Their analysis of particle deposition in natural convection flow was complicated by the simultaneous occurrence of diffusiophoresis, which is a transport of particles owing to a vapor concentration gradient. The calculated results reported in [4] were limited to wall-to-bulk fluid temperature ratios $T_w/T_\infty$ only slightly less than unity. In this limiting case, the particle concentration at the wall is essentially equal to that outside the boundary layer and, therefore, the particle deposition rate can readily be calculated from published solutions for the temperature field or correlations of the local heat transfer rate.

Contributed by the Heat Transfer Division for publication in the JOURNAL OF HEAT TRANSFER. Manuscript received by the Heat Transfer Division December 8, 1983.

Thermophoretic deposition in laminar flows has also been studied theoretically by Goren [5] and by Walker et al. [6]. Goren treated the thermophoresis of aerosol particles in the laminar-compressible, boundary layer flow past a flat plate, while Walker et al. studied thermophoretic deposition in laminar flow through a tube.

Consideration is given here to the deposition of aerosol particles on a cold vertical plate in a natural convection boundary layer. The study to be reported includes both laminar flow and the practically important case of turbulent flow. This study involves an important quantitative difference from the problem studied by Hales et al. [4] in that the bulk gas temperature s allowed to exceed the plate temperature by a considerable amount (highly cooled wall). In this case the particle concentration at the wall is unknown and must be determined from the solution of the conservation equation for the particle field before the flux of particles to the wall can be computed.

## Physical Model

Consider a warm gas containing suspended aerosol particles exposed to a cold vertical plate that is maintained at temperature $T_w < T_\infty$. The temperature gradient established in the downward moving free-convection boundary layer between the plate and the quiescent gas–particle mixture drives the particles towards the plate, where they deposit. Here we shall assume that the particle concentration is sufficiently dilute so that the physical properties of the mixture are those of the gas phase. Hence the particle mass per unit volume of gas should be much less than the gas density, or $d^3 N \rho_s/\rho \ll 1$. For most solids and gases at standard conditions, $\rho_s/\rho$ is of order $10^3$. Thus the concentration level of, say, 1-$\mu$m-dia particles necessary to strongly influence mixture properties must exceed about $10^8$ particles per cubic centimeter of gas.

Particles of only a single size are assumed to be present in the gas. This implies that the particulate matter is sufficiently dilute that pairs or groups of particles may be considered noninteracting. This assumption places a more serious restriction on the particle concentration than that mentioned in the foregoing. It is well known that high number density aerosols rapidly coagulate by random thermal (Brownian) motion, and furthermore, experimental evidence indicates that coagulation results from nearly every collision between two particles [7]. As the particles coagulate, the particle concentration decreases and their sizes increase at a rate dependent on the local particle concentration. The coagulation time is defined here to be the time required for the particle field to reduce its concentration by 10 percent, viz, $t \simeq 0.1/(CN)$, where $C$ is the coagulation constant [7] and has

the value of about $2.72 \times 10^{-10}$ cm$^3$ s$^{-1}$ for particles in air at normal temperature and pressure. The importance of Brownian coagulation within the free convection boundary layer can be assessed by examining the ratio of the coagulation time to the time it takes the particles to traverse the thickness of the boundary layer $\delta/v_T$ where $v_T$ is the thermophoretic velocity (see equation (1)). For laminar flow with $Gr_x = 10^9$, 1-$\mu$m particles, and a vertical distance from the leading edge of the plate of $x = 50$ cm, this ratio indicates that the analysis is limited to particle concentrations less than $10^7$ particles per cubic centimeter of gas.

It should be mentioned that particles smaller than about $10^{-2}$ $\mu$m in diameter suspended in gases exhibit a Brownian motion that is sufficiently intense to contribute to the particle deposition rate. However, for particles with a size of 0.1 $\mu$m the particle Brownian diffusion coefficient is of order $10^{-5}$ cm$^2$ s$^{-1}$. Thus for particles of this size or larger the Brownian diffusion sublayer is so thin that it does not alter the thermophoretic particle deposition rate [5, 6]. The only effect of Brownian diffusion is to create a thin particle concentration boundary layer allowing the true wall boundary condition of zero particle concentration to be satisfied. In the analysis that follows, we neglect Brownian diffusion deposition.

Following a common practice in thermophoretic transport analysis, we will assume that in the absence of thermophoresis the particles move with the local gas velocity. This assumption can be appreciated by considering the ratio of the "stopping distance" of an individual particle to the vertical distance from the leading edge of the plate $x$. The stopping distance $\lambda$, a measure of the penetration depth of a particle injected into a quiescent gas, is given by $(\rho_s d^2 u)/(18\ \mu)$. It is in the region $0 < x \lesssim \lambda$ near the leading edge where the particles find it difficult to couple with the gas motion. Further down the plate at distances large with respect to the stopping distance, the particles assume nearly gas velocity. Using the maximum or peak value of the vertical velocity component in natural convection flow, $u \simeq 0.3\ [g\beta(T_\infty - T_w)x]^{1/2}$, the ratio $\lambda/x$ is estimated to be about 0.01 for 10-$\mu$m particles in air, $T_\infty - T_w = 100$°C, and a vertical distance along the plate of only 1 cm.

While the particles may move with the gas in the natural convection boundary layer at large distances from the wall, they may act differently near the wall when the flow is turbulent. It is well known that in forced-convection flow the rate of turbulent deposition can be of the order of or greater than the deposition rates due to Brownian motion, or diffusiophoresis or thermophoresis [8, 9]. The most popular description of turbulent deposition from gases involves $y$-directional penetration of large particles by inertial effects through the laminar sublayer. Indeed, the experimental data on deposition from pipe flows show that the ratio of the stopping distance based on the friction velocity to a distance approximately equivalent to the thickness of the laminar sublayer, $\delta_{lam} = 5\nu/(\tau_w/\rho)^{1/2}$, is the dimensionless group that best characterizes turbulent deposition [8–10]. For forced turbulent pipe flow, the dimensionless stopping distance that has proved most convenient for deposition data correlation is $S = (d^2 u^{*2} \rho_s)/(18\ \rho\nu^2)$, where $u^*$ is the friction velocity calculated using the Fanning friction factor. The experimental data indicate that particles for which $S < 0.15$ follow the gas motion near the wall and do not impinge on the wall by the inertial mechanism [10]. Assuming that in the region close to the wall (plate) in natural convection flow the relation connecting $u^*$ with the peak velocity is the same as that connecting $u^*$ with the free-stream velocity in forced flow, we find $S = (f/400)\,(d/x)^2\,(\rho_s/\rho)\,Gr_x < 0.15$ as the criterion for negligible turbulent deposition in natural convection flow, where $f$ is the Fanning friction factor. If one introduces the typical values $Gr_x = 10^{11}$, $x = 250$ cm, and $f = 0.01$, we estimate $S = 0.04$ for 10-$\mu$m particles. This is small enough to render turbulent (inertial) deposition negligible. In what follows, we neglect the turbulent deposition of particles.

The one significant point to conclude from the foregoing discussion is that particles less than about 10 $\mu$m in diameter follow the streamlines of the turbulent natural convection flow everywhere within the boundary layer. Thus the eddy diffusion of particles suspended in a turbulent natural convection boundary layer should be similar to the eddy diffusion of gas molecules, even near the wall, providing the particles are smaller than the scale of turbulence. The measurements of deposition rates for particles in isothermal, forced-convection turbulent flows are summarized in [10]. Indeed, it has been found that when the dimensionless stopping distance is small, particles deposit in accord with the usual relations for the mass transfer of molecular species in turbulent flow, indicating that the eddy diffusivity of the particles and of the gas are equal throughout the boundary layer. On the basis of the previous discussion, it seems reasonable to assume that

## Nomenclature

$A$ = dimensionless parameter, equation (14)
$C$ = coagulation constant, cm$^3$ s$^{-1}$
$d$ = diameter of the particles
$f$ = Fanning friction factor
$F$ = dimensionless gas flow stream function
$g$ = gravitational acceleration
$Gr_x$ = local Grashof number, $g\beta(T_\infty - T_w)\,x^3/\nu^2$
$j$ = particle deposition flux, particles cm$^{-2}$ s$^{-1}$
$K$ = dimensionless thermophoretic velocity coefficient, equation (1)
$n$ = dimensionless particle concentration, $N/N_\infty$, equation (13)
$N$ = particle concentration, particles cm$^{-3}$
$Nu_x$ = local Nusselt number, $x(\partial T/\partial y)_{y=0}/(T_\infty - T_w)$
Pr = Prandtl number
$S$ = dimensionless particle stopping distance
$Sh_x$ = local Sherwood number for particle deposition, equation (25)
$t$ = time
$T$ = temperature
$u$ = gas velocity parallel to plate
$u^*$ = friction velocity
$v$ = gas velocity normal to plate
$v_T$ = thermophoretic velocity of the particles, equation (1)
$x$ = coordinate along the vertical plate
$y$ = coordinate normal to the plate
$y^+$ = scaling distance normal to the plate for turbulent flow, equation (9)

### Greek Symbols

$\alpha$ = thermal diffusivity of gas
$\beta$ = compressibility of gas, K$^{-1}$
$\delta$ = boundary layer thickness
$\delta_{lam}$ = thickness of the laminar sublayer in turbulent flow
$\epsilon$ = eddy diffusivity for turbulent momentum, energy, and particle transport
$\eta$ = dimensionless similarity coordinate, equation (10)
$\lambda$ = particle stopping distance
$\theta$ = dimensionless gas temperature, equation (13)
$\mu$ = viscosity of gas
$\nu$ = kinematic viscosity of gas
$\rho$ = density of gas
$\rho_s$ = density of particle material
$\tau_w$ = shear stress at wall (plate surface)

### Subscripts

$w$ = at the wall (plate surface)
$\infty$ = outside the free convection boundary layer

this is also the case for turbulent natural convection flow, although it would be desirable to have experimental data for this flow regime.

In addition to the assumptions discussed in the foregoing, gas physical property variations are neglected, except for those density variations necessary to give a buoyancy force. The adhesion force between deposited particles and the plate is assumed strong enough to prevent resuspension of the particles by the natural convection flow. Finally, the local similarity form of the boundary layer equations is assumed to apply for turbulent natural convection (see the following).

## Governing Equations

The thermophoretic velocity $v_T$ is related to the temperature gradient by the equation

$$v_T = -K \frac{\nu}{T} \frac{\partial T}{\partial y} \tag{1}$$

in which $K$ is the dimensionless thermophoretic transport coefficient. As already demonstrated in the previous section, contributions to particle transport by Brownian motion and, in the case of turbulent flow, particle inertia can be neglected in the natural convection boundary layer. The coefficient $K$ in equation (1) depends mainly on the Knudsen number—the molecular mean free path divided by the particle diameter. As mentioned previously, Talbot et al. [2] proposed a semiempirical formula for $K$ that fits the majority of the available data over a wide range of Knudsen numbers. Using their formula, the value of $K$ is found to be about 0.6 for submicron-sized particles and decreases to 0.1 for 10-$\mu$m particles. Note from equation (1) that only the thermophoretic velocity normal to the plate is considered, since the temperature gradient in this direction is very much larger than in the direction parallel to the plate.

The flow, heat transfer, and particle transfer processes obey the basic principles of momentum, energy, and mass conservation. The mathematical statements of these laws take on different forms when specialized to the laminar and turbulent flow regimes under consideration here. For turbulent natural convection flow along a vertical plate, the appropriate boundary layer equations are as follows

$$\frac{\partial u}{\partial x} + \frac{\partial v}{\partial y} = 0 \tag{2}$$

$$u \frac{\partial u}{\partial x} + v \frac{\partial u}{\partial y} = \frac{\partial}{\partial y}\left[(\nu + \epsilon) \frac{\partial u}{\partial y}\right] + g\beta(T - T_\infty) \tag{3}$$

$$u \frac{\partial T}{\partial x} + v \frac{\partial T}{\partial y} = \frac{\partial}{\partial y}\left[(\alpha + \epsilon) \frac{\partial T}{\partial y}\right] \tag{4}$$

$$u \frac{\partial N}{\partial x} + v \frac{\partial N}{\partial y} + \frac{\partial}{\partial y}(N v_T) = \frac{\partial}{\partial y}\left(\epsilon \frac{\partial N}{\partial y}\right) \tag{5}$$

In writing the foregoing expressions, we have made the usual assumption that the eddy diffusivity for gas-phase momentum $\epsilon$ is equal to that for gas-phase energy transport. In addition, as mentioned earlier, the eddy diffusivity of particles is assumed to be equal to the local eddy diffusivity of the gas.

Equations (2–5) are subject to the boundary conditions

$$u = 0, \quad T = T_\infty, \quad N = N_\infty \quad \text{at } y = \infty \tag{6}$$

$$u = v = 0, T = T_w \quad \text{at } y = 0 \tag{7}$$

Recall that in the absence of Brownian particle diffusion we do not have a condition to be satisfied by $N$ at the plate surface ($y = 0$). A nonzero particle concentration at $y = 0$ must be determined from the solution of equations (2–5).[1]

As is usual in the analysis of turbulent natural convection problems, we choose an expression for the eddy diffusivity that has been proposed for forced convection flow. In particular, we choose the form

$$\frac{\epsilon}{\nu} = 0.4\, y^+ [1 - \exp(-0.0017\, y^{+2})] \tag{8}$$

where $y^+$ is the scaling distance for turbulent flow

$$y^+ = \left(\frac{\tau_w}{\rho}\right)^{1/2} \frac{y}{\nu} \tag{9}$$

Equation (8) has been successfully applied to the problem of turbulent free-convection heat transfer by Kato et al. [11] and Noto and Matsumoto [12].

To solve equations (2–4), Noto and Matsumoto [12] have introduced the conventional Pohlhausen similarity transformation for laminar natural convection flow and reduced the equations to ordinary differential equations by exploiting the concept of local similarity. Their predicted temperature profiles and local Nusselt numbers are in good agreement with the theoretical [11, 13, 14] and experimental [15–17] results. Given the close relationship between energy and particle transport, there is good reason to believe that the local similarity concept, when applied to equation (5), will yield numerically correct particle concentration profiles.

In the spirit of [12], we introduce the following transformed variables

$$\eta = A \cdot \frac{y}{x^{1/4}} \tag{10}$$

$$u(x,\eta) = 4\, \nu\, A^2 x^{1/2} \frac{\partial F}{\partial \eta}(x,\eta) \tag{11}$$

$$v(x,\eta) = A\, \nu\, x^{-1/4}\left[\eta \frac{\partial F}{\partial \eta}(x,\eta) - 3\, F(x,\eta)\right] \tag{12}$$

$$\theta(x,\eta) = \frac{T - T_\infty}{T_w - T_\infty}; \quad n(x,\eta) = \frac{N}{N_\infty} \tag{13}$$

where

$$A = \left[\frac{g\beta(T_\infty - T_w)}{4\, \nu^2}\right]^{1/4} \tag{14}$$

In accord with the local similarity concept, we assume that variations of $F$, $\theta$, and $n$ in the $x$-direction are very small compared with those in the $\eta$-direction, and we postulate that

$$\frac{\partial F}{\partial x} = \frac{\partial \theta}{\partial x} = \frac{\partial n}{\partial x} = 0 \tag{15}$$

The reported good agreement with experimental data and with theoretical results obtained with different computational techniques [12] testifies to the utility of the local similarity method when applied to the turbulent natural convection flow problem. However, it should be emphasized that the actual error resulting from the use of equation (15), while presumably small, cannot be obtained in a rigorous way without undertaking the difficult problem of solving equations (2–5) directly. Such a formidable numerical undertaking is well beyond the scope of the present paper.

When equations (10–13) are substituted into (2–5) and the restrictions (15) are applied, the following three ordinary differential equations are obtained

$$\left(1 + \frac{\epsilon}{\nu}\right)F''' + \left[3\, F + \left(\frac{\epsilon}{\nu}\right)'\right]F'' - 2\, F'^2 + \theta = 0 \tag{16}$$

$$\left(\frac{1}{\mathrm{Pr}} + \frac{\epsilon}{\nu}\right)\theta'' + \left[3\, F + \left(\frac{\epsilon}{\nu}\right)'\right]\theta' = 0 \tag{17}$$

$$\frac{\epsilon}{\nu} n'' + \left[3\, F + K\frac{T'}{T} + \left(\frac{\epsilon}{\nu}\right)'\right]n'$$

$$- K\frac{T'}{T}\left\{\frac{T'}{T} + \left[\frac{1}{\mathrm{Pr}} + \frac{\epsilon}{\nu}\right]^{-1}\left[3\, F + \left(\frac{\epsilon}{\nu}\right)'\right]\right\}n = 0 \tag{18}$$

where

[1] Strictly speaking, with respect to the particle field, the location $y = 0$ should be interpreted as designating the outer edge of the very thin Brownian sublayer.

$$\frac{T'}{T} = -\frac{(1-T_w/T_\infty)\theta'}{1-(1-T_w/T_\infty)\theta} \tag{19}$$

and with the boundary conditions

$$F'=0, \quad \theta=0, \quad n=1 \quad \text{at } \eta=\infty \tag{20}$$

$$F=0, \quad F'=0, \quad \theta=1 \quad \text{at } \eta=0 \tag{21}$$

In the foregoing equations, the primes denote differentiation with respect to $\eta$. In similarity variables the scaling distance $y^+$ that appears in equation (8) for the eddy diffusivity becomes

$$y^+ = (64\,\mathrm{Gr}_x)^{1/8}[F''(0)]^{1/2}\eta \tag{22}$$

Since equation (18) is of second order, it requires an additional boundary condition imposed on the dimensionless particle concentration $n$. On physical grounds, the second-order turbulent transport term $(\epsilon/\nu)n'' + (\epsilon/\nu)'n'$ as well as $\epsilon$ itself must vanish at the plate (at $\eta = 0$). Thus, evaluating the particle boundary layer equation (18) at the surface location $\eta = 0$, we find the following relation between the particle concentration and its gradient at the surface (see also equation (19))

$$n(0) = \frac{T(0)}{T'(0)} \cdot n'(0) = -\frac{T_w/T_\infty}{1-T_w/T_\infty} \cdot \frac{n'(0)}{\theta'(0)} \tag{23}$$

This condition and the last of boundary conditions (20) are sufficient for solution of equation (18). Once again, the neglect of Brownian motion prevents us from assigning a value to $n$ at the wall.

The foregoing boundary layer equations and boundary conditions (16–21) have been derived for particle transport within a turbulent natural convection boundary layer. These same equations may be made to apply to laminar flow simply by setting $\epsilon/\nu$ and $(\epsilon/\nu)'$ equal to zero.

In the preceding paragraphs, the governing differential equations for the temperature and particle concentration distributions have been derived. The solution of these equations will now be related to the particle deposition rate. The flux of particles to the wall $j$ readily follows from equation (1) as

$$j = -K\,N(0)\,\frac{\nu}{T_w}\left(\frac{\partial T}{\partial y}\right)_{y=0} \tag{24}$$

In terms of the transformed variables of equations (10) and (13), the expression for $j$ becomes

$$\mathrm{Sh}_x = \frac{(-j)x}{\nu\,K\,N_\infty} = -\left(\frac{1}{4}\,\mathrm{Gr}_x\right)^{1/4}(T_\infty/T_w - 1)\theta'(0)n(0) \tag{25}$$

where $\mathrm{Sh}_x$ is the local Sherwood number for thermophoretic particle transport. It is seen from equation (25) that once the dimensionless temperature slope $\theta'(0)$ and the dimensionless particle concentration $n(0)$ have been supplied by the solutions, then the particle deposition rate is immediately known. Numerical values of the quantity $\theta'(0)$ for both laminar and turbulent natural convection heat transfer along an isothermal vertical surface may be found in a number of heat transfer texts and in the research literature and is usually reported in terms of the local Nusselt number $\mathrm{Nu}_x = -(\mathrm{Gr}_x/4)^{1/4} \cdot \theta'(0)$. Therefore, it is only necessary to present the particle concentration results.

It is interesting to note that if we put $K \cdot \mathrm{Pr} = 1$, a remarkable simplification is possible. Equation (1) becomes

$$v_T = -\frac{\alpha}{T}\frac{\partial T}{\partial y} \tag{26}$$

Substituting (26) into equation (4), it is readily seen that the solutions of equations (4) and (5) for laminar or turbulent flow are related by

$$\frac{N}{N_\infty} = \frac{T}{T_\infty} \tag{27}$$

For this singular case it is not necessary to solve the conservation equations in order to determine the particle concentration at the plate, since $n(0) = T_w/T_\infty$ for both laminar and turbulent flow. This simple result was first reported by Goren [5] for the problem of thermophoretic deposition of particles on a flat plate in laminar forced conviction [5].

## Results

Numerical solutions of equations (16–18) subject to the boundary conditions (20), (21), and (23) were carried out for Prandtl numbers of 0.5, 0.72, 0.73, 1.0, and 1.5 (i.e., gases), for $K$ ranging from essentially zero to unity, and for $T_w/T_\infty$ of 0.25, 0.5, 0.75, and 0.9. These values cover the parameter space of engineering interest. In the case of turbulent flow, the value of the local Grashof number must be specified (see equation (22)); it was varied between $10^{10}$ and $10^{12}$.

A plot of the dimensionless particle concentration at the wall as a function of $K$ for Pr = 0.73 is shown in Fig. 1. The results plotted correspond to laminar flow. The particle concentration at the wall decreases below its value far from the wall, viz., $N_\infty$, with decreasing temperature ratio $T_w/T_\infty$ and increasing $K$. Interestingly enough, to the scale which the graph in Fig. 1 is plotted, the turbulent flow results for Pr = 0.73 are found to be almost indistinguishable from those found for laminar flow. In fact, no matter what values of the parameters Pr, $\mathrm{Gr}_x$, $K$, and $T_w/T_\infty$ are selected, within the ranges of practical interest, the calculated particle concentrations $n(0)$ for laminar flow show less than 4.0 percent deviations from those calculated for turbulent flows. For the case $K \cdot \mathrm{Pr} = 1$, on the basis of the prior discussion, the value of $n(0)$ for turbulent natural convection is identical to that for laminar convection and equal to $T_w/T_\infty$. The numerical calculations indicate that this equivalence of $n(0)$'s for the two natural convection flow regimes is, for all practical purposes, also satisfied when $K \cdot \mathrm{Pr}$ is not equal to 1; it is true even when the departure from $K \cdot \mathrm{Pr} = 1$ is large. From Fig. 2 it is seen that while the particle concentration distribution for laminar flow differs notably in shape from that for turbulent flow, at the wall the two profiles converge to practically the same particle concentration. This behavior is typical of all the cases investigated and may not seem unreasonable when the factors effecting $n(0)$ are discussed.

We note from equation (23) that there is a unique relation between the particle concentration at the surface of the plate and the ratio of slopes $n'(0)/\theta'(0)$ at this location. Now, changing the flow regime from laminar to turbulent (but keeping Pr, $T_w/T_\infty$, and $K$ fixed) increases the heat transfer $-\theta'(0)$. But with the transition to turbulence there also occurs

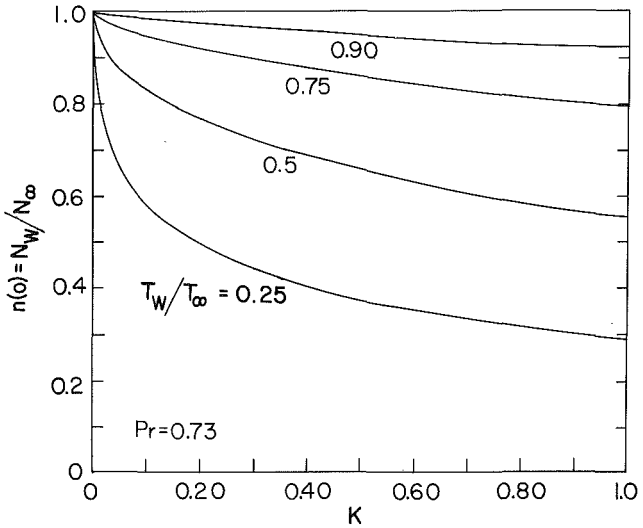


**Fig. 1 Particle concentration at the wall as a function of the thermophoretic velocity coefficient for laminar or turbulent flow; $T_w/T_\infty$ as a parameter**

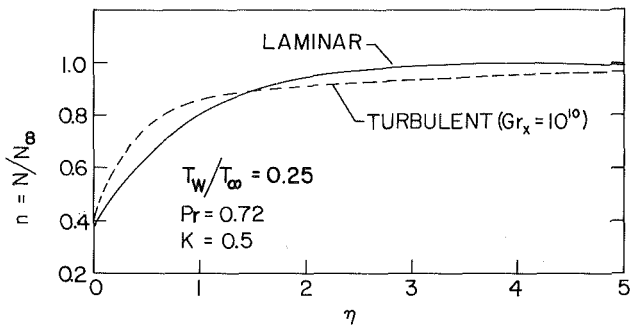


**Fig. 2 Comparison of laminar and turbulent particle concentration profiles**

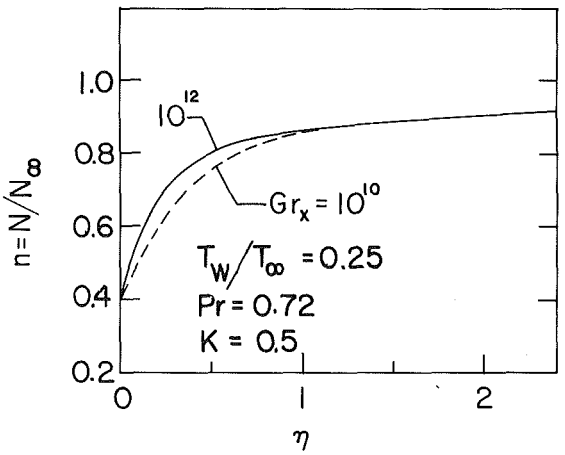


**Fig. 3 Comparison of particle concentration profiles in turbulent flow**

an increase in the particle concentration gradient that, owing to the similarity between particle and heat transport, appears to be almost identical to the increase in $-\theta'(0)$, and thus $n(0)$ remains essentially unchanged. Similarly, imposing major changes in the Grashof number has no significant effect on $n(0)$ as both gradients $n'(0)$ and $\theta'(0)$ undergo an almost identical percent deviation. Figure 3 shows two particle concentration profiles near the wall, in the turbulent boundary layer, for Grashof numbers of $10^{10}$ and $10^{12}$. Again, while some difference in the profile shapes is apparent, the two curves tend to a common particle concentration at the wall.

Since the dimensionless temperature slope $\theta'(0)$ (or local Nusselt number $Nu_x$) in equation (25) for particle transport is readily calculable by hand using available heat transfer correlations, whereas $n(0)$ must be obtained from the simultaneous numerical solution of equations (16-18), one is tempted to inquire if a simple formula can be found to estimate $n(0)$ for cases of Pr, $Gr_x$, $K$, and $T_w/T_\infty$ not explicitly shown in Fig. 1. The simple function

$$n(0) = \frac{1-(K\cdot\mathrm{Pr})^{1.25\ T_w/T_\infty}}{1-(K\cdot\mathrm{Pr})^{1.25}} \tag{28}$$

was found to be very successful in this regard and represents the computed values of $n(0)$ to a relative error of less than 3.0 percent for the values of Pr, $Gr_x$, $K$, and $T_w/T_\infty$ investigated here (see beginning of this section). This empirical fit to the numerical data clearly shows that varying $Gr_x$ from $10^{10}$ to $10^{12}$ for the case of turbulent flow has a negligible effect on the particle concentration $n(0)$. In addition, it is apparent that the two parameters $K$ and Pr can be replaced by the product $K\cdot$Pr. Thus, accurate estimates of $n(0)$ for both laminar and turbulent natural convection can be obtained from a simple "two-parameter correlation," viz., equation (28). Moreover, by replacing the numerical exponent 1.25 by 1.1 in the numerator and denominator of equation (28) the calculated results of Goren [5] for deposition in forced incompressible laminar flow over a cold flat plate can be accurately reproduced. Note that for the singular case $K\cdot\mathrm{Pr} = 1$, equation (28) reduces to the simple result $n(0) = T_w/T_\infty$ discussed previously.

Combining equations (25) and (28) gives the dimensionless form of the local thermophoretic particle flux

$$\mathrm{Sh}_x = \frac{1-(K\cdot\mathrm{Pr})^{1.25\ T_w/T_\infty}}{1-(K\cdot\mathrm{Pr})^{1.25}} \cdot \left(\frac{T_\infty}{T_w} - 1\right) \cdot \mathrm{Nu}_x \tag{29}$$

from which $j$ can be calculated for laminar or turbulent flow by simply inserting the appropriate heat transfer correlation for $Nu_x$.

## Conclusions

We have performed particle deposition rate calculations for the natural convection boundary layer on a vertical flat plate for the cases of laminar and turbulent flows. It was demonstrated by "order-of-magnitude arguments" that thermophoretic deposition is the dominant transport mechanism by which airborne particulates in the size range 0.1–10 $\mu$m are removed under conditions of turbulent natural convection. A simple relation between the nondimensional particle deposition rate and the Nusselt number was found that accurately correlates all the numerical results in terms of only two basic parameters. To the best of the authors' knowledge, there are no experimental data on particle deposition from naturally convected flow. It is hoped that the present treatment will facilitate future comparisons of natural convection deposition theory with laboratory data.

## References


1 Goldsmith, P., and May, F. G., "Diffusiophoresis and Thermophoresis in Water Vapour Systems," *Aerosol Science*, edited by C. N. Davies, Academic Press, London, 1966, pp. 163-194.

2 Talbot, L., Cheng, R. K., Schefer, A. W., and Willis, D. R., "Thermophoresis of Particles in a Heated Boundary Layer," *J. Fluid Mechs.*, Vol. 101, 1980, pp. 737-758.

3 Brock, J. R., "On the Theory of Thermal Forces Acting on Aerosol Particles," *J. Colloid Sci.*, Vol. 17, 1962, pp. 768-770.

4 Hales, J. M., Schwendiman, L. C., and Horst, T. W., "Aerosol Transport in a Naturally-Convected Boundary Layer," *International Journal of Heat and Mass Transfer*, Vol. 15, 1972, pp. 1837-1849.

5 Goren, S. L., "Thermophoresis of Aerosol Particles in the Laminar Boundary Layer on a Flat Plate," *J. Colloid Interface Sci.*, Vol. 61, 1977, pp. 77-85.

6 Walker, K. L., Homsy, G. M., and Geyling, F. T., "Thermophoretic Deposition of Small Particles in Laminar Tube Flow," *J. Colloid Interface Sci.*, Vol. 69, 1979, pp. 138-147.

7 Fuchs, N. A., *The Mechanics of Aerosols*, Pergamon Press, New York, 1964.

8 Friedlander, S. K., and Johnstone, H. F., "Deposition of Suspended Particles from Turbulent Gas Streams," *Ind. Eng. Chem.*, Vol. 49, 1957, pp. 1151-1156.

9 Sehmel, G. A., "Particle Deposition From Turbulent Air Flow," *J. Geophysical Res.*, Vol. 75, 1970, pp. 1766-1781.

10 Hanratty, T. J., and McCoy, D. D., "Rate of Deposition of Droplets in Annular Two-Phase Flow," *Int. J. Multiphase Flow*, Vol. 3, 1977, pp. 319-331.

11 Kato, H., Nishiwaki, N., and Hirata, M., "On the Heat Transfer by Free Convection from a Vertical Plate," *International Journal of Heat and Mass Transfer*, Vol. 11, 1968, pp. 1117-1125.

12 Noto, K., and Matsumoto, R., "Turbulent Heat Transfer by Natural Convection Along an Isothermal Vertical Flat Surface," ASME JOURNAL OF HEAT TRANSFER, Vol. 97, 1975, pp. 621-624.

13 Mason, H. B., and Seban, R. A., "Numerical Predictions for Turbulent Free Convection From Vertical Surfaces," *International Journal of Heat and Mass Transfer*, Vol. 17, 1974, pp. 1329-1336.

14 Oosthuizen, P. H., "A Numerical Study of Turbulent Free Convection from an Isothermal Vertical Plate," Report No. 1170, Thermal and Fluid Sciences Group, Department of Mechanical Engineering, Queen's University, Kingston, Ontario, Canada, 1970.

15 Cheesewright, R., "Turbulent Natural Convection From a Vertical Plane Surface," ASME JOURNAL OF HEAT TRANSFER, Vol. 90, 1968, pp. 1-8.

16 Jakob, M., *Heat Transfer*, Vol. 1, Wiley, New York, 1949.

17 Warner, C. Y., and Arpaci, V. S., "An Experimental Investigation of Turbulent Natural Convection in Air Along a Vertical Heated Flat Plate," *International Journal of Heat and Mass Transfer*, Vol. 11, 1968, pp. 397-406.

# Computation of Forced Laminar Convection in Rotating Cavities

**J. W. Chew**
Theoretical Science Group,
Rolls-Royce Limited,
Derby, England

*Finite difference solutions are presented for forced laminar convection in a rotating cylindrical cavity with radial outflow. This forms a simple model of the cooling flow between two compressor disks in a gas turbine engine. If the fluid enters the cavity from a uniform radial source, it is shown that the local Nusselt number changes from that of a "free disk" near the center of the cavity to that for Ekman layer flow at larger radii. With an axial inlet, the flow, and consequently, the heat transfer, is more complex. If vortex breakdown occurs, then the results are very similar to those for the radial inlet case, but otherwise a wall jet forms on the downstream disk, and the heat transfer from this disk may be several times that for the upstream disk. Variation of mean Nusselt number with rotational speed is qualitatively similar to previously published experimental measurements in turbulent flow. The effect of Prandtl number on heat transfer has also been demonstrated.*

## 1 Introduction

In recent years the problem of heat transfer between two corotating disks, which model the compressor disks of a gas turbine engine, has received considerable attention. A review of this work is given by Owen [1]. In the present contribution, numerical results are given for the heat transfer due to laminar radial outflow between two plane disks. Although the flow in engine conditions will usually be turbulent, these results give a valuable insight into the nature of the problem and aid the interpretation of experimental measurements of the heat transfer due to turbulent flow. The prediction of turbulent flow using the $k$-$\epsilon$ model of turbulence was also attempted, in parallel with the laminar study, and is described in [2]. As the turbulent computations did not agree with experimental measurements, it was considered inappropriate, at this stage, to attempt quantitative predictions closer to engine conditions.

Numerical results for isothermal laminar flow in the cavity between two rotating disks have been given previously by Chew [3] and Chew, Owen, and Pincombe [4]. In the latter reference, the flow structure for the case of radial outflow with either a radial or axial inlet is studied in detail. These two cases are illustrated by the streamline plots in Fig. 1. For the radial inlet case, where the fluid enters the cavity from a central uniform cylindrical source, the flow near the disks can be approximated by two known analytical solutions; the so called 'free disk' solution and an Ekman layer solution. If the radial source is replaced by an axial inlet, the flow becomes more complex, with a wall jet forming on the downstream disk at sufficiently high flow rates. Nevertheless the flow close to the upstream disk could still be approximated by the two analytical solutions, and at the low flow rates, for which vortex breakdown of the central jet occurred, the flow close to both disks was very similar to that for the radial inlet case. These results suggest that it may be possible to build up a model of the heat transfer in the cavity by applying results for simpler flows in the appropriate regions. One aim of the present work is to examine this possibility.

The heat transfer measurements of Owen and Onur [5] are also relevant to the present study. These workers studied heat transfer due to turbulent flow in a rotating cavity with one disk heated and a radial outflow of air. Their results were presented in the form of a mean Nusselt number for heat transfer from the hot disk. Four different heat transfer regimes were identified and correlations were given for each regime. A further objective of the present work is to clarify the relationship between these experimental measurements and the flow structure in the cavity.

The emphasis in this paper is on heat transfer results rather than the flow structure, for details of which the reader is referred to [4]. The same geometry has been assumed here as in [4]. The disk radius is $b = 190$ mm, the inlet radius $a = 19$ mm, and the axial distance between the disks $s = 50.7$ mm. As property variations of the cooling air have been neglected, these results do not include any effects of buoyancy on the convection. As it may be shown that buoyancy forces will affect the flow if there is a temperature difference between the two disks (see [6]), attention here is confined to the case of the two disks having the same radial temperature distribution.

## 2 The Mathematical Model

The primitive variable form of the axisymmetric constant property Navier-Stokes and continuity equations used to calculate the flow and pressure fields are exactly as in [4]. For brevity these are not repeated here. The temperature field was obtained by solution of the laminar energy equation for axisymmetric flow of a perfect gas. This equation is given in

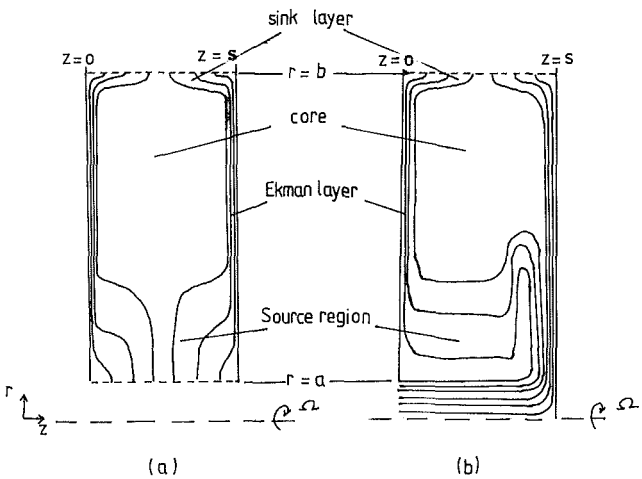


**Fig. 1 Radial outflow through a rotating cavity: (a) radial inlet, (b) axial inlet**

Contributed by the Heat Transfer Division for publication in the JOURNAL OF HEAT TRANSFER. Manuscript received by the Heat Transfer Division December 2, 1983.

full in [6]; neglecting compressive work and energy dissipation terms, it may be written

$$\frac{1}{r}\frac{\partial}{\partial r}(r\rho uh)+\frac{\partial}{\partial z}(\rho wh)=\frac{1}{r}\frac{\partial}{\partial r}\left(\frac{rk}{C_p}\frac{\partial h}{\partial r}\right)+\frac{\partial}{\partial z}\left(\frac{k}{C_p}\frac{\partial h}{\partial z}\right) \quad (1)$$

where $h$ is the stagnation enthalpy defined by

$$h=C_pT+\frac{1}{2}(u^2+v_\phi^2+w^2) \quad (2)$$

Here $u$, $v_\phi$, and $w$ are the radial, tangential, and axial components of velocity in an inertial frame of reference ($r$, $\phi$, $z$); $T$ is the temperature, and $\rho$, $\mu$, $k$ and $C_p$ represent the density, viscosity, thermal conductivity, and specific heat at constant pressure of the fluid. In the derivation of equation (1), the specific heat has been assumed constant.

The temperature boundary condition on the disk surfaces was taken as

$$T=T_I+c\left(\frac{r}{b}\right)^n \quad (3)$$

where $T_I$ is the inlet temperature. The constant $c$ was chosen sufficiently large to ensure that compressive work and energy dissipation were negligible. At the inlet and outlet the following conditions were applied

$$T=T_I \text{ at inlet}$$

$$\frac{\partial T}{\partial r}=0 \text{ at outlet } (r=b) \quad (4)$$

The zero gradient condition at the downstream position $r=b$ assumes an insulating porous surface. Although this is not representative of engine conditions, it provides a convenient closure to the problem for the present study in which attention is focused on the heat transfer from the disks away from the outer cylinder. For the axial inlet case, an additional symmetry condition at $r=0$ was also required.

For all the results given here $\rho$, $\mu$, and $C_p$ were taken as 1.225 kg/m$^3$, 1.78 $\times$ $10^{-5}$ kg/ms, and 1.012 kJ/kgK, respectively. For these conditions the appropriate value of $k$ for air is .0251 W/mK giving a Prandtl number (Pr) of 0.718, but in order to study the effect of varying Pr different values of $k$ were used.

The finite difference technique for solution of the velocity and pressure fields is fully described in [3]. This method, which is based on the well-known TEACH computer code [7], incorporates two novel features. Step changes in grid size are employed to obtain sufficient resolution in the boundary layers and the solution for the pressure field is given special treatment in order to obtain convergence of the iterative method at high rotational speeds. The strategy employed here was first to obtain the solution for the velocity and pressure which, owing to the assumption of constant fluid properties, is independent of temperature, and then solve the finite difference form of the energy equation for the stagnation enthalpy.

The solution grid for the stagnation enthalpy was chosen to coincide with the main variables on the staggered grid defined for the flow calculation, and the finite difference representation of equation (1) was obtained by a similar control volume approach to that for the velocities. These equations were solved using the standard "line-by-line" algorithm employed in the TEACH code. Having obtained the stagnation enthalpies, the temperatures were calculated from equation (2) and the heat flux from the disk was obtained from the second-order backward difference formula

$$q=k(1.5T_o-2T_1+.5T_2)/\delta z \quad (5)$$

where $q$ is the heat flux, and $T_0$, $T_1$, and $T_2$ represent the temperature on the disk and at distances $\delta z$ and $2\delta z$ from the disk.

Step changes in the grid size were used as in [3] and [4]. As the grid had been found to be sufficiently fine to avoid truncation error in the velocity calculations, it follows from the Reynolds analogy between tangential velocity and temperature (Dorfman [8]) that for a Prandtl number of 1 and a quadratic temperature distribution on the disk, the grid was also adequate for the temperature calculation. As no tests were made at other conditions to check that the results were independent of grid size, it is possible that some of the results given contain truncation errors. However, any such effects are probably small and the results are unlikely to be qualitatively incorrect.

## 3 Radial Outflow with a Radial Inlet

The flow structure for this case is illustrated in Fig. 1($a$). Fluid enters the cavity radially through the central source and, owing to centrifugal effects, is entrained into boundary layers on the two disks. When all the fluid has been entrained into these layers, a quiescent core forms and the disk boundary layers are of Ekman layer form. The effect of the cylindrical sink at $r=b$ is confined to a small "sink layer." The flow

## Nomenclature

$a$ = inlet radius
$b$ = outer radius of cavity
$c$ = constant in power law distribution of temperature
$c_n$ = constant in equation (6)
$C_p$ = specific heat at constant pressure
$C_w$ = mass flow parameter = $Q/\nu b$
$h$ = stagnation enthalpy defined by equation (2)
$k$ = thermal conductivity
$n$ = exponent in power law distribution of temperature
Nu = local Nusselt number = $rq/(T_s-T_I)k$
$\overline{\text{Nu}}$ = mean Nusselt number = $b\bar{q}/(\bar{T}_s-T_I)k$
Pr = Prandtl number = $\mu C_p/k$
$q$ = heat flux
$\bar{q}$ = mean heat flux = $\int_a^b rqdr/\int_a^b rdr$
$Q$ = source volumetric flow rate
$r$ = radial distance
$\text{Re}_\phi$ = rotational Reynolds number = $\Omega b^2/\nu$
$s$ = axial distance between the two disks
$T$ = temperature
$\bar{T}_s$ = mean disk temperature = $\int_o^b rT_s dr/\int_o^b rdr$
$u,v_\phi,w$ = radial, tangential, and axial velocity components in a stationary cylindrical coordinate system ($r,\phi,z$)
$z$ = axial distance
$\delta z$ = axial grid spacing
$\epsilon_b$ = radial Rossby number at $r=b$
$\epsilon_r$ = radial Rossby number = $Q/4\pi r^2(\nu\Omega)^{1/2}$ = $b^2C_w/\text{Re}_\phi^{1/2}\,4\pi r^2$
$\mu$ = dynamic viscosity
$\nu$ = kinematic viscosity = $\mu/\rho$
$\rho$ = density
$\phi$ = angular coordinate
$\Phi$ = function of Pr in equation (6)
$\Omega$ = angular velocity of disk

**Subscripts**

$I$ = inlet
$s$ = disk

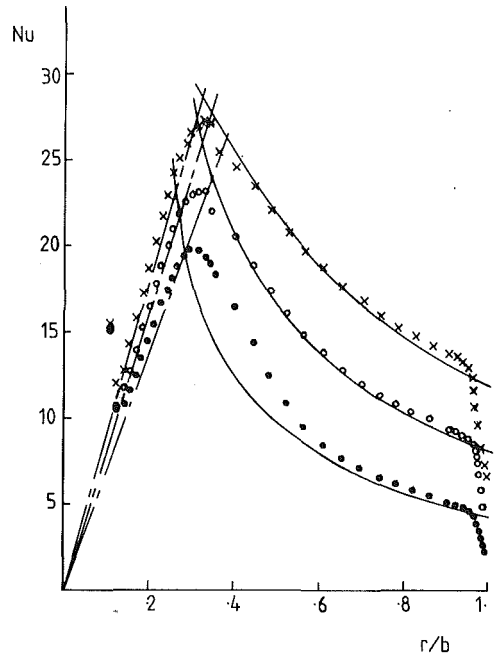


**Fig. 2 Radial variation of Nusselt number for different power law temperature distributions: Radial inlet $Re_\phi = 2.5 \times 10^4$, $C_w = 79$, $Pr = .718$, $T_s - T_I \propto r^n$.**

| n | 1 | 2 | 3 |
|---|---|---|---|
| Numerical results | • | ○ | × |

— — — equation (6) ——— equation (7).

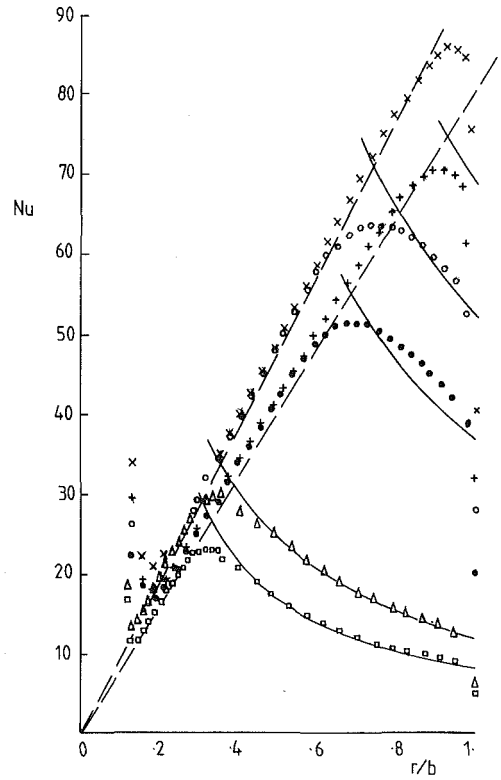


**Fig. 3 Radial variation of local Nusselt number with a quadratic temperature distribution on the disk: Radial inlet, $Re_\phi = 2.5 \times 10^4$.**

| Pr | 1 | 1 | 1 | .718 | .718 | .718 |
|---|---|---|---|---|---|---|
| $C_w$ | 79 | 331 | 605 | 79 | 331 | 605 |
| Numerical results | △ | ○ | × | □ | • | + |

— — — equation (6) ——— equation (7).

conditions are characterized by a nondimensional flow rate, $C_w = Q/\nu b$, and a rotational Reynolds number, $Re = \Omega b^2/\nu$.

Figure 2 shows the local Nusselt number ($Nu = rq/k(T_s - T_I)$) distribution for the case $Re = 2.5 \times 10^4$, $C_w = 79$ and $Pr = .718$ with linear, quadratic, and cubic temperature conditions on the disks. For comparison with the numerical results, the free disk and Ekman layer solutions are also shown. The free disk solution for local and mean Nusselt numbers is taken from Dorfman [8] and may be written

$$Nu = c_n \Phi(Pr) Re_\phi^{1/2} \left(\frac{r}{b}\right); \quad \overline{Nu} = c_n \Phi(Pr) Re_\phi^{1/2} \tag{6}$$

where $c_n$ is a constant depending on the choice of $n$ in (3) and $\Phi$ is a function of Pr only. The Ekman layer solution is given by

$$Nu = \frac{n}{4\pi} Pr C_w \frac{b}{r}\left[1 - \frac{3}{4}(n-2)Pr\epsilon_r\right] - \frac{n^2 s}{2r} \tag{7}$$

where $\epsilon_r$ ($= b^2 C_w / Re_\phi^{1/2} 4\pi r^2$) is a radial Rossby number. This expression is derived from a solution given in [6], with certain second-order terms being neglected. It is apparent that, as might be expected from the flow structure, there are distinct regions where these two solutions apply. The radial position $r/b = 0.3$ corresponds roughly to the extent of the "source region" and for $r/b$ less than this value, the numerical results are close to those of a free disk. Note that the steep rise in the Nusselt number close to the source at $r/b = 0.1$ is due to the imposition of a uniform radial velocity at this position and would probably not be obtained experimentally. For $0.3 < r/b < 0.95$, the flow is dominated by the Ekman layers, and equation (7) is expected to be valid. The results for the quadratic and cubic temperature distributions are in good agreement with this expression, but for the linear case there is a significant department from this solution at the lower values of $r/b$. This deviation could be due to the difference, at $r/b = 0.3$ between the actual temperature of the fluid and that assumed in the similarity solution. At larger radii the effect of the conditions at this point diminishes and the two solutions converge. The region $0.95 < r/b < 1$ corresponds to the "sink layer" of the flow, and the Nusselt number is reduced, in this area, as the fluid flows away from the disk.

The influence of flow rate and Prandtl number on the local Nusselt number is illustrated in Fig. 3. This shows the results for $Pr = 0.718$ and 1 at three different flow rates, given by $C_w = 79$, 331, and 605 with the rotational speed given by $Re_\phi = 2.5 \times 10^4$ and a quadratic temperature distribution assumed on the disk. The free disk and Ekman layer solutions are also plotted for these conditions. The results all show a similar pattern to those for the lower flow rate ($C_w = 79$), described above, with the radial variation of the Nusselt number being consistent with the flow in the cavity. The main effects of increasing the flow rate appear to be the extension of the inner layer leading to a larger region for which the free disk solution is valid, and an increase in the Nusselt number in the Ekman layer region, in agreement with equation (7). Within the source region the Nusselt number does not show any significant variation with flow rate. The variation of Nusselt number with Prandtl number appears to be well predicted by equation (6).

An analytical expression for the mean Nusselt number may be derived from an overall heat balance on the cavity. As the sink boundary layer at $r = b$ is a small region, it is reasonable to suppose that the enthalpy flow out of the cavity can be calculated by assuming that the Ekman solution holds at $r = b$. Neglecting kinetic effects and using the solution given in [6] for the temperature, the following expression may be obtained for the mean Nusselt number

$$\overline{Nu} = \frac{(n+2)Pr C_w}{4\pi}\left[1 - \frac{3n}{4}\epsilon_b Pr\right] - \frac{(n+2)n}{2}\frac{s}{b} \tag{8}$$

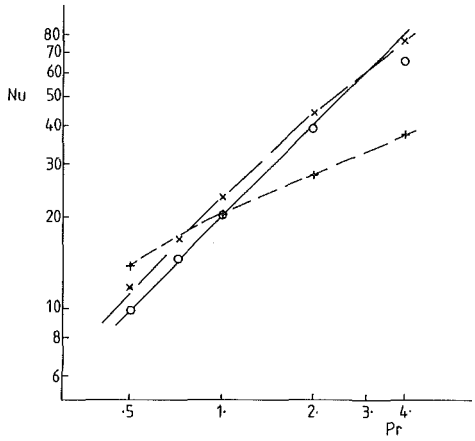


Fig. 4 Effect of Prandtl number on Nusselt number
Radial inlet: $Re_\phi = 2.5 \times 10^4$, $C_w = 79$, $T_s - T_l \propto r^2$

Numerical results { × Mean Nusselt number; + Local Nusselt number at $r/b = .21$; ○ Local Nusselt number at $r/b = .62$

– – – equation (6)
——— equation (7)
— — equation (8)

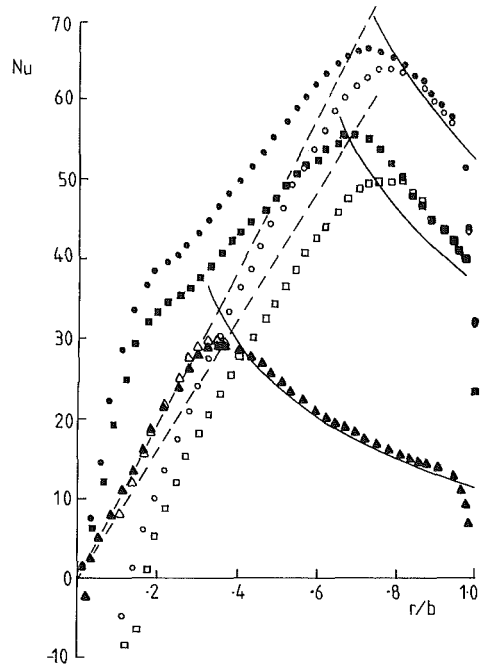


Fig. 5 Radial variation of local Nusselt number with a quadratic temperature distribution on the disk: Axial inlet, $Re_\phi = 2.5 \times 10^4$

| Pr | | 1 | 1 | .718 |
|---|---|---|---|---|
| $C_w$ | | 79 | 331 | 331 |
| Numerical results | upstream disk | △ | ○ | □ |
| | downstream disk | ▲ | ● | ■ |

— — equation (6) ——— equation (7)

where $\epsilon_b$ is the radial Rossby number at $r=b$. In this derivation, terms of second order or higher in $\epsilon_b$, $s/b$, $a/b$, and $Re_\phi^{-1/2}$ have been neglected and the heat flux from each disk is assumed equal.

The variation with Prandtl number of the mean Nusselt number and the local Nusselt numbers at $r/b = 0.21$ and 0.62, for the case $Re_\phi = 2.5 \times 10^4$, $C_w = 79$ with a quadratic temperature distribution is shown in Fig. 4. The radial positions for the local Nusselt numbers are chosen so that one is in the inner layer and the other is in the Ekman layer region. Equation (8) is shown for comparison with the mean Nusselt numbers, and the free disk and Ekman layer solutions are given for comparison with the local Nusselt numbers. In general, the numerical results are in good agreement with the theory, although there is a significant difference at $Pr = 4$ for the Nusselt number at $r/b = 0.62$. This departure is due to fluid temperature taking a longer radial distance to adjust from the conditions at the outer edge of the inner layer to those of the similarity solution.

## 4 Radial Outflow With an Axial Inlet

In this section, the effects of replacing the radial inlet by an axial inlet $0 \le r \le a$, $z = 0$ are discussed. The flow structure for this case is illustrated in Fig. 1(*b*).

Figure 5 gives the local Nusselt number distribution on both the upstream and downstream disks, for $Re_\phi = 2.5 \times 10^4$ and $C_w = 79$ and 331, with a quadratic temperature distribution on the disks. At the higher flow rate results for Prandtl numbers of both 1 and 0.718 are presented, while for $C_w = 79$ only the results for the case $Pr = 1$ are given. For the latter case, in which vortex breakdown occurs in the flow, there is very little difference between the results on the disks, and comparison with Fig. 3 shows that the heat transfer is very similar to the radial inlet case. For $C_w = 331$, however, there is a significant difference between the disks. The formation of a wall jet on the downstream disk leads to the heat transfer being increased on this surface. Although the entrainment of fluid by the upstream disk is similar to that of a free disk, the heat transfer from this disk is reduced below that of a free disk, and may even become negative, due to the convection of heat from the downstream disk.

Assuming a quadratic temperature distribution and $Pr = 1$, results were obtained for a range of different rotational Reynolds numbers at a fixed flow rate ($C_W = 331$). Local Nusselt numbers for these conditions are shown in Fig. 6. In [4] it was shown that, for this $C_w$, the flow for $Re_\phi \le 5000$ was no longer of the form shown in Fig. 1(*b*) but was similar to that expected for a nonrotating cavity. In this case the main flow is from the inlet jet to the wall jet on the downstream disk and then direct to the sink with some recirculation being induced in the rest of the cavity.

Looking first at the results for the upstream disk (Fig. 6(*a*)), it is apparent that the change in flow structure that occurs as the rotation speed is reduced radically affects the heat transfer. At the lower speeds, inflow occurs on this disk and heat is convected to the disk, leading to negative Nusselt numbers over a large part of the surface. At the higher speeds, fluid is pumped radially outwards on the disk, and so the heat transfer is positive over most of its area.

The results for the downstream disk (Fig. 6(*b*)) also reflect the change in flow structure with rotational speeds, but, owing to the dominant influence of the wall jet, the effects are less marked than for the upstream disk. Towards the center of the cavity, the Nusselt numbers change very little with rotational speed, but at the point $r/b = 0.3$, there is a definite divergence of the results. This is evidently due to the temperature conditions within the cavity, as it was shown in [4] that the radial velocity within the wall jet was insensitive to rotational speed at this radius. Toward the outer part of the cavity, the results for the two highest rotational speeds converge again. This confirms the analytical result (equation (7)), that for Ekman layer flow with a quadratic temperature distribution, the Nusselt number is independent of rotational speed. At lower speeds, Ekman layer flow is not attained, and heat transfer is reduced. The main effect of the change in flow structure, mentioned above, is a steep drop in the Nusselt number in the outer part of the cavity.

The variation of mean Nusselt number with rotational Reynolds number is shown in Fig. 7. The results for free disk

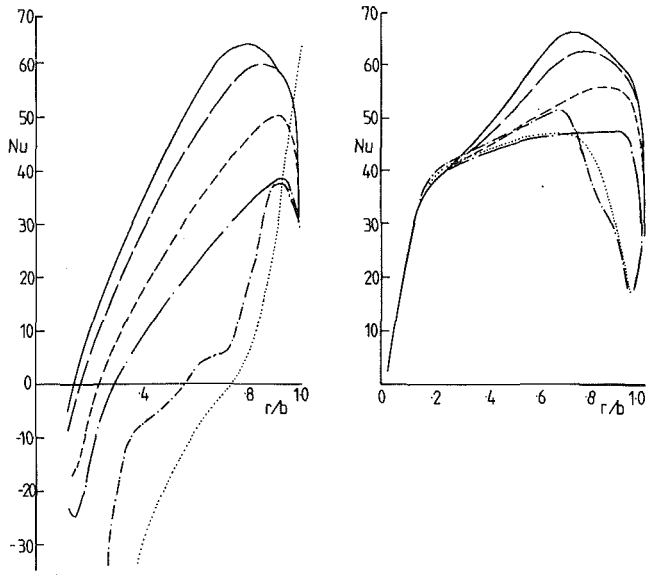


**Fig. 6** *Radial variation of Nusselt number for different values of* $Re_\theta$
Axial inlet, $C_w = 331$, $Pr = 1$, $T_s - T_l \propto r^2$

| $Re_\phi/10^3$ | 2 | 5 | 7.5 | 12.5 | 20 | 25 |
|---|---|---|---|---|---|---|
| Numerical results | .... | -.- | —·— | --- | — — | — |

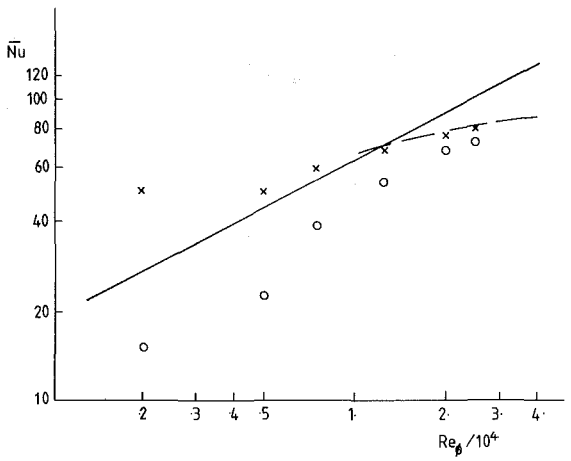


**Fig. 7** *Effect of rotational speed on the mean Nusselt number*
Axial inlet, $C_w = 331$, $Pr = 1.0$, $T_S - T_l \propto r^2$

Numerical results: o upstream disk; × downstream disk

___ equation (6) — — equation (8)

and Ekman layer flow are shown for comparison with the numerical predictions. Qualitatively these results are similar to heat transfer measurements for turbulent flow (Owen and Onur [5]). At high Reynolds numbers the results for both disks converge towards the Ekman layer solution; this corresponds to Owen and Onur's regime III. At low values of $Re_\phi$ the Nusselt numbers for the downstream disk are independent of rotational speed as in regime I. The strongest variation of the Nusselt number occurs at intermediate values of $Re_\phi$, as in regime II.

The effect of varying the Prandtl number has been investigated in detail for the flow case $Re_\phi = 2.5 \times 10^4$, $C_w = 331$ with a quadratic temperature distribution. Figure 8 shows the variation with Prandtl number of the mean Nusselt number

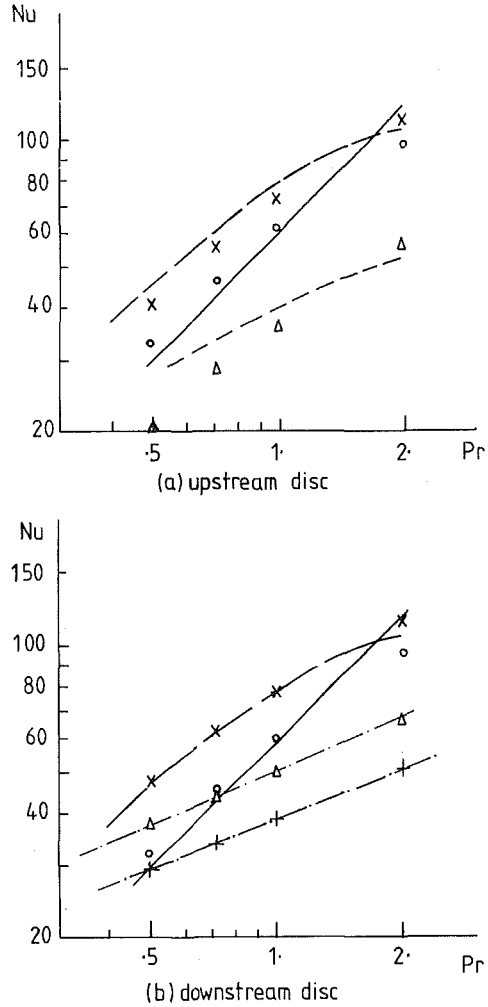


**Fig. 8** *Effect of Prandtl number on Nusselt number:*
Axial inlet, $Re_\phi = 2.5 \times 10^4$, $C_w = 331$, $T_s - T_l \propto r^2$

Numerical results:
× mean Nusselt number
\+ local Nusselt number at $r/b = .2$
△ local Nusselt number at $r/b = .41$
o local Nusselt number at $r/b = .89$

___ equation (6); ___ equation (7); — — equation (8), —·— equation (9)

and the local Nusselt number at certain radial positions for the two disks.

For $0.5 \le Pr < 1$ the influence of Prandtl number on the mean Nusselt number and the local number at $r/b = .89$ is similar to that of the Ekman layer solutions (8) and (7). The results for $Pr = 2$, however, do not fit into this pattern. In the case of the mean Nusselt number, this is possibly due to the neglect of second order terms involving Pr in deriving equation (8). For the local Nusselt number, equation (7) is exact for $n = 2$, and so the departure must be due to the difference between the actual fluid temperature and that assumed by the similarity solution at the start of the Ekman layer regime.

As expected, within the inner layer the results are very different for the two disks. Although the flow close to the upstream disk is similar to that of a free disk, Fig. 8(*a*) shows the Nusselt number at $r/b = 0.41$ is more sensitive to Prandtl number than equation (6). This is presumably due to fluid entrained by this disk being heated to some extent before it reaches this part of the cavity.

The results for the downstream disk at $r/b = 0.2$ and 0.41

(Fig. 8(*b*)) have been found to be well predicted by the formula

$$Nu = Pr^{.4} Nu_1 \tag{9}$$

where $Nu_1$ denotes the value of Nu when $Pr = 1$.

A survey of the literature on heat transfer due to laminar wall jets did not reveal any other results to compare with this expression. However, it is of interest to note, that, for turbulent flow, the factor $Pr^{.4}$ occurs in the empirical correlations of the Nusselt number due to a round jet impinging on a flat surface (Martin [9]).

## 5 Conclusions

The computer program, described in [3], for the prediction of laminar isothermal source-sink flow in a rotating cavity, has been extended to solve the energy equation in addition to the mass and momentum equations. This program has been used to investigate heat transfer in a cavity with radial outflow for the special case when buoyancy forces are negligible and the velocity field is independent of the temperature field.

For the case of a radial inlet, the heat transfer over that part of the disks where fluid is being entrained is very similar to that for a free disk. At larger radii, where the Ekman solution describes the flow, the numerical predictions for the local Nusselt number converge to the results of a similarity solution for the temperature profile. The variation of Nusselt number with Prandtl number is also consistent with free disk and Ekman layer solutions.

With an axial inlet, the flow, and consequently the heat transfer, is more complex. If vortex breakdown occurs then the results are very similar to those for the radial inlet case. For other flow conditions the heat transfer from the downstream disk is greater than that from the upstream disk, owing to the impingement of the inlet jet on the downstream surface and the formation of a wall jet. At sufficiently low rotational speeds the wall jet extends to the outer edge of the cavity and the flow goes directly from this region to the sink. The flow in the rest of the cavity is then a secondary recirculation and as a consequence the heat transfer from the downstream disk is several times that from the upstream disk. At higher speeds, Ekman layer flow occurs in the outer part of the cavity and in this region the flow and heat transfer are the same on each disk. As for the radial inlet case, the effect of Prandtl number on Nusselt number in the Ekman layer regions was consistent with theory. In the wall jet region the Nusselt number was found to be proportional to $Pr^{.4}$.

## Acknowledgments

This work was undertaken during the tenure of a Research Fellowship, funded by Rolls-Royce, at the Thermo-Fluid Mechanics Research Centre, University of Sussex. I would like to thank Dr. J. M. Owen for his interest in this project.

## References

1 Owen, J. M., "Fluid Flow and Heat Transfer in Rotating Disc Systems. Int. Centre for Heat and Mass Transfer Series, Heat and Mass Transfer in Rotating Machinery," edited by D. E. Metgzer, and N. H. Afgan, Hemisphere, Washington, D.C., 1984, pp. 81–103.

2 Chew, J. W., "Prediction of the Flow in Rotating Disc Systems using the k-$\epsilon$ Turbulence Model," Paper No. 84-GT-229, ASME Gas Turbine Conference, Amsterdam, 1984.

3 Chew, J. W., "Development of a Computer Program for the Prediction of Flow in a Rotating Cavity," *Int. J. Num Methods in Fluids*, Vol. 4, 1984, pp. 667–683.

4 Chew, J. W., Owen, J. M., and Pincombe, J. R., "Numerical Predictions for Laminar Source-Sink Flow in a Rotating Cylindrical Cavity," *J. Fluid Mech.*, Vol. 143, 1984, pp. 451–466.

5 Owen, J. M., and Onur, H. S., "Convective Heat Transfer in a Rotating Cylindrical Cavity," ASME *Journal of Engineering for Power*, Vol. 105, 1983, pp. 265–271.

6 Chew, J. W., "Computation of Flow and Heat Transfer in Rotating Cavities," D Phil thesis, School of Engineering and Applied Sciences, University of Sussex, 1982.

7 Gosman, A. D., and Ideriah, F. J. K., TEACH-T: "A General Computer Program for Two Dimensional Turbulent Recirculating Flows," *Calculation of Recirculating Flows*, Department of Mechanical Engineering, Imperial College, London, 1976.

8 Dorfman, L. A., *Hydrodynamic Resistance and Heat Loss of Rotating Solids*, (1st English ed.), Ch. 5, Oliver and Boyd Limited, Edinburgh, 1963, pp. 77–98.

9 Martin, H., "Heat and Mass Transfer between Impinging Gas Jets and Solid Surfaces," *Advances in Heat Transfer*, Vol. 13, 1977, pp. 1–60.

# Effects of Upstream Geometry on Natural Convection of a Darcian Fluid About a Semi-Infinite Inclined Heated Surface

**C. T. Hsu**
Fluids Mechanics Department,
TRW Space and Technology Group,
Redondo Beach, CA 90278

**P. Cheng**
Dept. of Mechanical Engineering,
University of Hawaii at Manoa,
Honolulu, HI 96822
Mem. ASME

*The method of matched asymptotic expansions is applied to the problem of steady natural convection of a Darcian fluid about a semi-infinite inclined heated surface with a power law variation of wall temperature, i.e., $\hat{T}_w \alpha \hat{x}^\lambda$ for $\hat{x} \geq 0$ where $0 \leq \lambda < 1$. The leading edge of the inclined surface intercepts at an angle, $\Lambda_0$, with another impermeable unheated surface extending upstream. The effects of the inclination angle $\alpha_0$ $(0 \leq \alpha_0 < < \pi/2)$ of the heated surface as well as the upstream geometry at $\hat{x} < 0$ (as specified by $\Lambda_0$) on heat transfer and fluid flow characteristics near the heated surface are investigated. At a given inclination angle $\alpha_0$, it is found that heat transfer from an upward-facing heated inclined surface is larger than that of a downward-facing heated surface, and that decreasing the intercepting angle $(\Lambda_0)$ tends to lower the heat transfer rate. These effects become increasingly pronounced as the Rayleigh number is decreased.*

## Introduction

Considerable amount of work has been devoted to the study of higher-order effects in natural convection of a Newtonian fluid during the past decade [1-9]. In particular, higher-order boundary layer theory has been obtained for a flat plate with a finite length by Yang and Jerger [1] as well as by Messiter and Linan [2], and that for a semi-infinite plate by Heiber [3], Riley and Drake [4] as well as by Mahajan and Gebhart [5]. Yang and Jerger's higher-order analysis for a vertical isothermal plate was later extended to an inclined isothermal plate by Kierkus [6] who uses Rich's boundary layer solution [10] as the first-order approximation. Kierkus shows that although higher-order corrections in the temperature distribution and the local surface heat flux are zero, their effects modify the velocity field near the edge of the boundary layer along the inclined heated surface substantially. For the problem of natural convection of a Newtonian fluid above a horizontal line source of heat, higher-order boundary layer theory was obtained by Hieber and Nash [7]. The higher-order effect of a horizontal bounding surface below the line source has been considered by Riley [8] and by Afzal [9].

The related problem of higher-order effects in natural convection of a Darcian fluid about a vertical heated plate has been considered by Cheng and Hsu [11] while that of a horizontal plate has been considered by Chang and Cheng [12]. In this paper, Cheng and Hsu's perturbation analysis for natural convection of a Darcian fluid about a semi-infinite vertical will be extended to that of an inclined heated plate with an inclination angle of $\alpha_0$, and with its leading edge intercepting at an angle $\Lambda_0$ with another semi-infinite unheated plate extending upstream (see Fig. 1). As in the previous paper [11], the heated plate is assumed to have a power law variation of wall temperature, i.e., $\hat{T}_w = \hat{T}_\infty + A\hat{x}^\lambda$, where $\hat{x}$ is measured from the leading edge along the heated surface. It will be shown that the first-order solution of the problem reduces to that given by Cheng and Minkowycz [13] with the gravitational acceleration replaced by its component parallel to the inclined surface. The effect of upstream geometry (as described by the intercepting angle) appears as a matching boundary condition while that of the inclination angle appears as a nonhomogeneous term in the higher-order inner problems. For the case of an isothermal plate ($\lambda = 0$), the second-order corrections in temperature and local surface heat flux will be shown to be identically zero while the third-order solution cannot be determined owing to the leading edge effect. For other temperature distributions $(0 < \lambda < 1)$, a uniformly valid solution is obtained up to the fourth order where the leading edge effect begins to appear. Numerical solutions are carried out for both upward-facing and downward-facing heated plates with different values of $\lambda$, $\alpha_0$, and $\Lambda_0$. At a given inclination angle $\alpha_0$, it was found that heat transfer from an upward-facing heated surface is larger than that of a downward-facing heated surface, and that decreasing the intercepting angle $\Lambda_0$ tends to lower the surface heated flux.

## Analysis

Consider the problem of steady free convection of a Darcian fluid about a semi-infinite inclined heated surface $(\hat{x} \geq 0)$ at a temperature $\hat{T}_w$ as shown in Fig. 1 where $\hat{x}$ is the coordinate along the heated surface and $\hat{y}$ is the coordinate perpendicular to the surface. $\alpha_0$ is the inclination angle of the heated surface relative to the vertical with a positive value indicating an upward-facing plate and a negative value in-

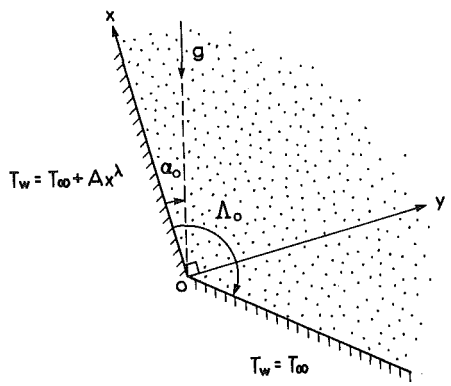


Fig. 1 The coordinate system

*Contributed by the Heat Transfer Division for publication in the* JOURNAL OF HEAT TRANSFER. *Manuscript received by the Heat Transfer Division January 18, 1984.*

dicating a downward-facing plate. $\Lambda_0$ is the angle of the upstream unheated impermeable surface relative to the heated surface. Figure 2 shows a few values of $\alpha_0$ and $\Lambda_0$ for which numerical solutions have been carried out.

If it is assumed that (*a*) the Darcy law is applicable, (*b*) the fluid and the porous medium are in local thermal equilibrium, (*c*) properties of the fluid and the porous medium are constant, and (*d*) the Boussinesq approximations are applicable, the governing equations in terms of the dimensionless stream function ($\psi$) and temperature ($\theta$) are

$$\nabla^2\psi=\theta_y-\tan\alpha_0\theta_x \tag{1}$$

$$\theta_x\psi_y-\theta_y\psi_x=\epsilon^2\nabla^2\theta \tag{2}$$

In equations (1) and (2) the dimensionless variables are

$$\psi=\hat{\psi}\epsilon^2/\alpha,\quad \theta=(\hat{T}-\hat{T}_\infty)/\Delta\hat{T}_r,\quad x=\hat{x}/\hat{l},\quad y=\hat{y}/\hat{l} \tag{3}$$

where $\hat{l}$ is a characteristic length, $\Delta\hat{T}_r = A\hat{l}^{\lambda}$, and $\epsilon = 1/\sqrt{\mathrm{Ra}_\alpha}$ with $\mathrm{Ra}_\alpha = \mathrm{Ra}\cos\alpha_0$ and $\mathrm{Ra} = \rho_\infty K\beta g\Delta\hat{T}_r\hat{l}/\mu\alpha$, where $\rho_\infty$ and $T_\infty$ are the density and temperature of the fluid at infinity; $\mu$ and $\beta$ are the viscosity and the thermal expansion coefficient of the fluid; $K$ and $\alpha$ are the absolute permeability and the equivalent thermal diffusivity of the saturated porous medium; $g$ is the gravitational acceleration. The superscript "$\hat{}$" in equation (3) denotes the corresponding dimensional quantities. It is noted that the small parameter, $\epsilon = \mathrm{Ra}_\alpha^{-1/2}$, that appears in equation (2) is artificial, i.e., it can be eliminated from equations (1) and (2) with a proper rescaling of variables.

If the wall temperature is a power function of distance, the boundary conditions at the heated wall and at infinity are

$$\psi_x(x,0)=0,\qquad \theta(x,0)=x^{\lambda}\quad x\geq 0 \tag{4a,b}$$

$$\psi_y(x,\infty)=0,\qquad \theta(x,\infty)=0\quad x\geq 0 \tag{5a,b}$$

The boundary conditions on the intercepting impermeable unheated surface upstream in a polar coordinate ($r$, $\Lambda$) are

$$\psi(r,\Lambda_0)=0,\quad \theta(r,\Lambda_0)=0\quad x<0 \tag{6a,b}$$

where $r=(x^2+y^2)^{1/2}$ and $\Lambda=\tan^{-1}y/x$; the former is the dimensionless distance from the origin and the latter is the angle measured clockwise from the heated inclined surface.

In this paper, we shall obtain an analytical solution in the limit of $\epsilon\to 0$, i.e., in the limit of $\hat{l}$ being large. Thus, the solution obtained in this paper represents the far field solution of a local corner flow.

**Outer Expansions.** As discussed in our previous paper [11], the outer solution for $\theta$ is

$$\theta(x,y;\epsilon)=0\quad \text{everywhere} \tag{7a}$$

whereas the outer expansion for the stream function can best be expanded in terms of the polar coordinates as

$$\psi(r,\Lambda;\epsilon)=r^{\frac{\lambda+1}{2}}\sum_{m=0}\epsilon^{m+1}r^{-\frac{\lambda+1}{2}m}\psi_m(\Lambda) \tag{7b}$$

Substituting equations (7) into equation (1) and (6*a*) leads to

$$\frac{\partial^2\psi_m}{\partial\Lambda^2}+\left[\frac{\lambda+1}{2}-\frac{\lambda+1}{2}m\right]^2\psi_m=0 \tag{8}$$

subject to the boundary condition

$$\psi_m(\Lambda_0)=0 \tag{9}$$

As $y\to 0$, $\psi_m$ must match with the inner solution.

**Inner Expansions.** Our previous paper [11] suggests that the inner expansion can be written as

$$\psi(x,y;\epsilon)=X^{\frac{\lambda+1}{2}}\sum_{m=0}\epsilon^{(m+1)}X^{-\frac{\lambda+1}{2}m}\Psi_m(\eta) \tag{10a}$$

## Nomenclature

$A$ = wall temperature parameter
$A_1$ = constant defined in equation (27*c*)
$D_1$ = constants defined in equation (17*b*)
$F_1$ = function associated with the particular solution of the second-order inner problem
$f_0, f_1, f_2$ = dimensionless inner perturbation stream functions
$g$ = acceleration due to gravity
$G_1$ = function associated with the particular solution of the second-order inner problem
$g_0, g_1, g_2$ = dimensionless inner perturbation temperature functions
$K$ = permeabillity of the porous medium
$k$ = thermal conductivity of the saturated porous medium
$L$ = a characteristic length
$\overline{\mathrm{Nu}}$ = average Nusselt number
$\mathrm{Nu}_x$ = local Nusslet number
$p$ = pressure
$\hat{Q}$ = total surface heat flux
$r$ = radial distance from the origin
$\mathrm{Ra}_x$ = local Rayleigh number
$\mathrm{Ra}_{x,\alpha}$ = local Rayleigh number based on the component of the gravitational acceleration parallel to the inclined heated surface
$T$ = dimensionless temperature
$u$ = dimensionless Darcian velocity in the $x$-direction
$v$ = dimensionless Darcian velocity in the $y$-direction
$X$ = dimensionless inner coordinate
$x$ = dimensionless coordinate
$Y$ = dimensionless inner coordinate
$y$ = dimensionless coordinate
$\alpha$ = equivalent thermal diffusivity
$\alpha_0$ = inclination angle of the heated surface
$\alpha_m$ = exponent of the perturbation parameter
$\beta$ = coefficient of thermal expansion
$\epsilon$ = perturbation parameter
$\eta$ = similarity variable
$\Theta$ = dimensionless inner temperature
$\theta$ = dimensionless temperature
$\Lambda$ = angle of the polar coordinate
$\Lambda_0$ = angle between the heated inclined surface and the impermeable surface upstream
$\lambda$ = constant defined in equation (4*b*)
$\rho$ = density of the fluid
$\mu$ = viscosity of the fluid
$\Psi$ = dimensionless inner stream function
$\psi$ = dimensionless stream function

**Superscripts**

$\hat{}$ = dimensional variables

**Subscripts**

$\infty$ = condition at infinity
$w$ = condition at the wall

$$\theta(x,y;\epsilon) = X^{\lambda} \sum_{m=0} \epsilon^m X^{-\frac{\lambda+1}{2}m} \Theta_m(\eta) \tag{10b}$$

where the inner variables are $X=x$ and $\eta = X^{\frac{\lambda-1}{2}} Y$ with $Y = y/\epsilon$. Substituting equations (10) into equations (1)–(2) leads to a set of inner problems whose boundary conditions at $Y \to \infty$ can be obtained by matching with the outer solutions to the appropriate order.

### Solutions of the Inner and Outer Problems

*First-Order Inner Solution.* The governing equations and boundary conditions for the first-order inner problem are identical to those considered by Cheng and Minkowycz [13] for the problem of natural convection of a Darcian fluid about a semi-infinite vertical plate in an infinite porous medium based on the boundary layer approximation. In terms of the notation of the present paper, the solution is

$$\Psi_0 = f_0(\eta), \quad \Theta_0 = g_0(\eta) \tag{11a,b}$$

where $f_0(\eta)$ and $g_0(\eta)$ have been determined in [13]. The asymptotic expansions for $\Psi_0$ and $\Theta_0$ are

$$\Psi_0 = f_0(\infty) + \exp, \quad \Theta_0 = \exp \tag{12a,b}$$

where "exp" represents the exponential decay terms. It is worth noting that the effect of inclination angle enters the first-order inner solution through the parameter $\epsilon$ in the similarity variable $\eta$.

*First-Order Outer Solution.* The matching conditions for $\psi_0$ and $\theta_0$ can be determined from equations (12) to give

$$\psi_0(0) = f_0(\infty), \quad \theta_0(0) = 0 \tag{13a,b}$$

Equation (8) for $m=0$ subject to boundary conditions (9) and matching condition (13*a*) has a solution of the form

$$\psi_0(\Lambda) = \frac{f_0(\infty) \sin\left[\frac{\lambda+1}{2}(\Lambda_0 - \Lambda)\right]}{\sin\left(\frac{\lambda+1}{2}\Lambda_0\right)} \tag{14}$$

Therefore, for $y \to 0$, we have

$$\psi(r,\Lambda)\Big|_{\Lambda\to 0} = f_0(\infty) x^{\frac{\lambda+1}{2}} \left[1 - \epsilon \frac{Y}{x}\left(\frac{1+\lambda}{2}\right) \cot\left(\frac{1+\lambda}{2}\right)\Lambda_0 + \epsilon^2 \frac{Y^2}{x^2} \frac{(1-\lambda^2)}{8} + \ldots.\right] \tag{15}$$

and consequently

$$\psi_y\Big|_{\Lambda\to 0} = \epsilon^2 f_0(\infty) x^{\frac{\lambda+1}{2}} \left[-\left(\frac{1+\lambda}{2x}\right) \cot\left(\frac{1+\lambda}{2}\right)\Lambda_0 + \frac{y}{x^2} \frac{(1-\lambda^2)}{4} + \ldots.\right] \tag{16}$$

It is relevant to note that equation (14) is the solution to equation (8) if $\sin(\lambda+1)\Lambda_0/2 \neq 0$, i.e., $\lambda \neq (2n\pi/\Lambda_0 - 1)$ where $n = 0, 1, 2, \ldots$. Because of space limitations, the case of $\sin(\lambda+1)\Lambda_0/2 = 0$ will not be discussed further in this paper.

*Second-Order Inner Solution.* The matching conditions for the second-order inner problem are

$$\Theta_1(\infty) = 0, \quad \Psi_1'(\infty) = D_1 \tag{17a,b}$$

where

$$D_1 = -\left(\frac{1+\lambda}{2}\right) f_0(\infty) \cot\left[\left(\frac{1+\lambda}{2}\right)\Lambda_0\right].$$

Equations (17) are obtained from equations (7*a*) and (16). It is interesting to note that the effect of upstream geometry appears as a matching condition which is associated physically with the entrainment of the fluid at the edge of the thermal boundary layer. The governing equations for $\Psi_1(\eta)$ and $\Theta_1(\eta)$ are

$$\Psi_1'' = \Theta_1' - \tan\alpha_0 \left[\lambda g_0 + \frac{\lambda-1}{2}\eta g_0'\right] \tag{18}$$

$$\Theta_1'' + \frac{\lambda+1}{2} f_0 \Theta_1' - \frac{\lambda-1}{2} f_0' \theta_1 = \lambda g_0 \Psi_1' \tag{19}$$

subject to boundary conditions

$$\Theta_1(0) = \Psi_1(0) = 0 \tag{20a,b}$$

and the matching conditions (17*a*, *b*). To solve the second-order inner problem, it is pertinent to note that the second-order inner problem is linear and that with the exception of the nonhomogeneous term in equation (18), the governing equations and boundary conditions for the second-order problem are similar to those for a vertical plate [11]. Thus, solution to the second-order inner problem can be obtained by superposition which results in

$$\Psi_1(\eta) = D_1 f_1(\eta) - \tan\alpha_0 F_1(\eta) \tag{21}$$

$$\Theta_1(\eta) = D_1 g_1(\eta) - \tan\alpha_0 G_1(\eta) \tag{22}$$

where $f_1(\eta)$ and $g_1(\eta)$ are the homogeneous solutions determined in [11], and $F_1(\eta)$ and $G_1(\eta)$ are the particular solutions which are determined from

$$F_1'' = G_1' + \lambda g_0 + \frac{\lambda-1}{2}\eta g_0' \tag{23}$$

$$G_1'' + \frac{\lambda+1}{2} f_0 G_1' - \frac{\lambda-1}{2} f_0' G_1 = \lambda g_0 F_1' \tag{24}$$

subject to the boundary conditions

$$F_1(0) = G_1(0) = 0 \tag{25a,b}$$

$$F_1'(\infty) = G_1(\infty) = 0 \tag{26a,b}$$

It is relevant to note that (*a*) the perturbation functions $f_1$, $g_1$, $F_1$, and $G_1$ depend only on $\lambda$, and (*b*) $g_1(\eta) = G_1(\eta) = 0$ and $f_1'(\eta) = 1$ for $\lambda = 0$ [11].

From equations (21–26), the asymptotic solutions for $\Psi_1$ and $\Theta_1$ are

$$\Psi_1 \sim A_1 + D_1\eta - \tan\alpha_0 F_1(\eta_\infty) + \exp \tag{27a}$$

$$\Theta_1 \sim \exp \tag{27b}$$

where

$$A_1 = D_1[f_1(\eta_\infty) - \eta_\infty] = -\frac{\lambda+1}{2} f_0(\infty) \cot\left[\left(\frac{\lambda+1}{2}\right)\Lambda_0\right][f_1(\eta_\infty) - \eta_\infty]. \tag{27c}$$

*Second-Order Outer Solution.* It follows from equations (27) that the matching conditions for the second-order outer problem are

$$\psi_1(0) = A_1 - \tan\alpha_0 F_1(\eta_\infty), \; \theta_1(0) = 0 \tag{28a,b}$$

The boundary condition for $\psi_1$ is

$$\psi_1(r,\Lambda_0) = 0 \tag{28c}$$

The solution of equation (8) with $m=1$ subject to the boundary conditions (28*c*) and the matching condition (28*a*) is

$$\psi_1(\Lambda) = [A_1 - \tan\alpha_0 F_1(\eta_\infty)]\left(1 - \frac{\Lambda}{\Lambda_0}\right) \tag{29}$$

which gives

$$\psi_1'(0) = -[A_1 - \tan\alpha_0 F_1(\eta_\infty)]/\Lambda_0 \tag{30}$$

*Third-Order Inner Solution.* The matching conditions for $\Psi_2$ and $\Theta_2$ as obtained from equations (16), (30), and (7*a*) are

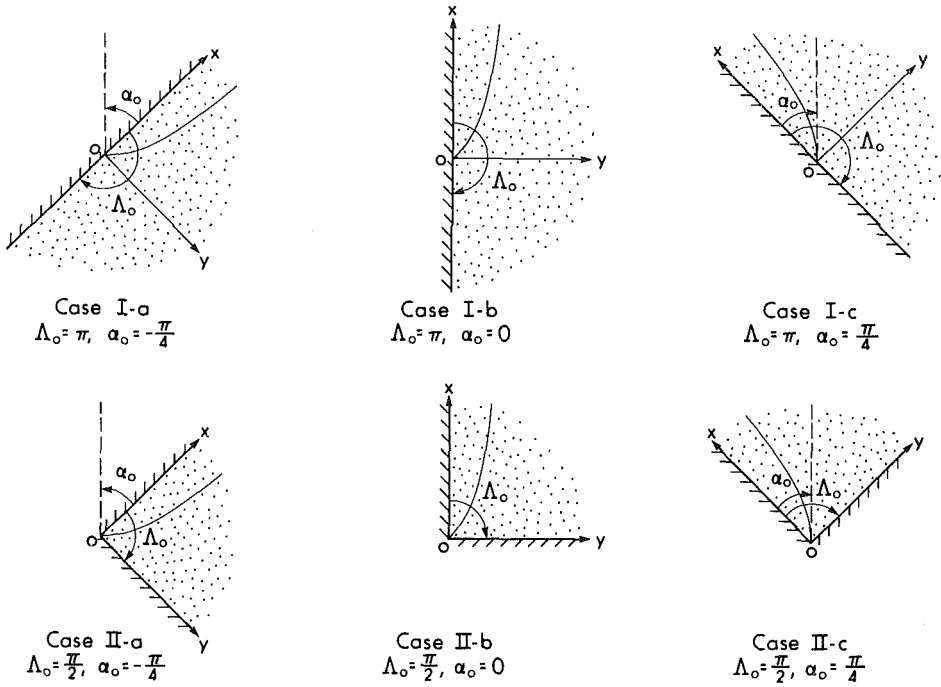


**Fig. 2 An inclined heated plate with different upsteam geometries**

$$\Psi_2'(\infty) = \frac{1-\lambda^2}{4} f_0(\infty)\eta Y - [A_1 - \tan\alpha_0 F_1(\eta_\infty)]/\Lambda_0 \tag{31}$$

$$\Theta_2(\infty) = 0 \tag{32}$$

The governing equations for $\Psi_2(\eta)$ and $\Theta_2(\eta)$ can be obtained by substituting equations (10) into equations (1-2) to give

$$\Psi_2'' - \Theta_2'' = \frac{1-\lambda}{2}\left[\frac{\lambda+1}{2} f_0 + \frac{3\lambda-1}{2}\eta f_0' + \frac{\lambda-1}{2}\eta^2 f_0''\right]$$

$$+ D_1 \tan\alpha_0 \left(\frac{1-\lambda}{2}\right)(g_1 + \eta g_1') - \tan^2\alpha_0 \left(\frac{1-\lambda}{2}\right)(G_1 + \eta G_1') \tag{33}$$

and

$$\Theta_2'' + \frac{\lambda+1}{2} f_0 \Theta_2' + f_0' \Theta_2 = \lambda g_0 \Psi_2' + \frac{\lambda+1}{2}\Psi_2 g_0'$$

$$+ (1-\lambda)\left[\lambda g_0 + \frac{5\lambda-3}{4}\eta g_0' + \frac{\lambda-1}{4}\eta^2 g_0''\right]$$

$$+ \frac{\lambda-1}{2}(D_1 f_1' - \tan\alpha_0 F_1')(D_1 g_1 - \tan\alpha_0 G_1) \tag{34}$$

with boundary conditions given by

$$\Psi_2(0) = \Theta_2(0) = 0 \tag{35a,b}$$

and matching conditions (31). Equations (33-35) show that the perturbation functions $\Psi_2$ and $\Theta_2$ depend on $\lambda$, $\alpha_0$, and $\Lambda_0$. Note that, for $\alpha_0 = 0$ and $\Lambda_0 = \pi$, $\Psi_2(\eta)$ and $\Theta_2(\eta)$ reduce to $f_2(\eta)$ and $g_2(\eta)$ of the vertical flat plate results [11].

**Eigenvalues and Eigenfunctions.** In the previous section on the inner problem it has been shown that the effect of upstream geometry appears as a nonhomogeneous term in the boundary conditions while that of the inclination angle appears as a nonhomogeneous term in the differential equations. Thus, the homogeneous parts of the inner problems considered in this paper are identical to those of a vertical flat plate considered previously by Cheng and Hsu [11]. For this reason the eigenvalues and eigenfunctions of the present problem are identical with the previous paper, which are of the form

$$\Psi_m^e = X^{\left(\frac{1+\lambda}{2}\right)(1-\alpha_m)} f_m(\eta) \tag{36a}$$

$$\Theta_m^e = X^{\lambda - \left(\frac{1+\lambda}{2}\right)\alpha_m} g_m(\eta) \tag{36b}$$

where the functions $f_m(\eta)$ and $g_m(\eta)$ for $0 \le \lambda < 1$ have been determined numerically [11] and $\alpha_m$'s are the eigenvalues having the values of $\alpha_m = 2$ for $\mu = 0$ and $\alpha_m > 2$ for $0 < \lambda < 1$.

## Results and Discussion

**Numerical Integration of Perturbation Functions.** The perturbation functions $f_0$, $g_0$, $f_1$, and $g_1$ were numerically integrated elsewhere [11, 13]. The particular solution of the second-order inner problem, as given by equations (23-26), has been numerically integrated for $\lambda = 0$ and 1/3. Note that for $\lambda = 0$, $G_1(\eta) = G_1'(\eta) = 0$, i.e., second-order correction in temperature and local surface heat flux are zero. The third-order solution as given by equations (33-35) have been numerically integrated for selected values of $\lambda$ for the six cases shown in Fig. 2, where Case I-*b* is the case considered previously by Cheng and Hsu [11].

**Stream Function and Velocity Along the Inclined Plate.** From equations (10*a*), (11*a*), (21), and (36*a*), the inner solution for stream function is given by

$$\Psi = \epsilon\left\{x^{1/2} f_0(\eta) - \epsilon\left[\frac{f_0(\infty)}{2}\cot\left(\frac{\Lambda_0}{2}\right) f_1(\eta) + F_1(\eta)\tan\alpha_0\right] + 0(\epsilon^2)\right\}, \quad \lambda = 0 \tag{37a}$$

$$\Psi = \epsilon\left\{x^{\frac{\lambda+1}{2}} f_0(\eta) - \epsilon\left[\frac{\lambda+1}{2} f_0(\infty)\cot\left(\frac{\lambda+1}{2}\Lambda_0\right) f_1(\eta) + F_1(\eta)\tan\alpha_0\right] + \epsilon^2 x^{-\frac{\lambda+1}{2}}\Psi_2(\eta) + 0(\epsilon^n)\right\}, \quad 0 < \lambda < 1 \tag{37b}$$

where $n \leq \alpha_m$. Theoretically, a term of $0(\epsilon^2 \log \epsilon)$ has to be inserted in equation (37*a*) between $0(\epsilon)$ and $0(\epsilon^2)$ since the eigenfunction for $\lambda=0$ is of $0(\epsilon^2)$ in the postulated inner expansion. As discussed by Stewartson [14] the insertion of these terms is needed so that solution will be consistent at infinity. However, a recent study by Daniels and Simpkins [15] shows that the logarithmic terms does not exist in the type of the flow considered in the present paper.*

It follows from equations (37) that the inner solution for the velocity component along the inclined surface is

$$\frac{\mu \hat{u}}{K\rho_\infty g\beta(\hat{T}_w - \hat{T}_\infty)\cos\alpha_0}$$

$$= \begin{cases} f_0'(\eta) - \dfrac{1}{\sqrt{\mathrm{Ra}_{x,\alpha}}}\left[\dfrac{\lambda+1}{2} f_0(\infty)\cot\left(\dfrac{\Lambda_0}{2}\right) f_1'(\eta) \right. \\ \left. + F_1'(\eta)\tan\alpha_0\right] + 0(\epsilon^2), \quad \lambda = 0 \\ f_0'(\eta) - \dfrac{1}{\sqrt{\mathrm{Ra}_{x,\alpha}}}\left[\dfrac{\lambda+1}{2} f_0(\infty)\cot\left(\dfrac{\lambda+1}{2}\Lambda_0\right) f_1'(\eta) \right. \\ \left. + F_1'(\eta)\tan\alpha_0\right] + \Psi_2'(\eta)/\mathrm{Ra}_{x,\alpha} + 0(\epsilon^n), \quad 0<\lambda<1 \end{cases} \tag{38a}$$

(38*b*)

For the case of $\lambda=0$, equations (37) and (38) show that the second-order terms in the inner solution for velocity vanish only for Case I-*b* where $\Lambda_0=\pi$ and $\alpha_0=0$. For other cases second-order correction for the inner solution for the velocity field do exist. Letting $\eta \to \infty$, equation (38) become

$$\frac{\mu \hat{u}}{K\rho_\infty g\beta(\hat{T}_w - \hat{T}_\infty)\cos\alpha_0}$$

$$= \begin{cases} -\dfrac{1}{\sqrt{\mathrm{Ra}_{x,\alpha}}}\left[\dfrac{\lambda+1}{2} f_0(\infty)\cot\left(\dfrac{\Lambda_0}{2}\right)\right] + 0(\epsilon^2), \lambda = 0 \\ -\dfrac{1}{\sqrt{\mathrm{Ra}_{x,\alpha}}}\left[\dfrac{\lambda+1}{2} f_0(\infty)\cot\left(\dfrac{\lambda+1}{2}\Lambda_0\right)\right] \\ + \dfrac{1}{\mathrm{Ra}_{x,\alpha}}\left\{\dfrac{1-\lambda^2}{4} f_0(\infty)\eta \right. \\ \left. - \dfrac{[A_1 - \tan\alpha_0 F_1(\eta_\infty)]}{\Lambda_0}\right\} + 0(\epsilon^n), \quad 0<\lambda<1 \end{cases} \tag{39a}$$

(39*b*)

which is the matching condition.

It can be shown that the outer solution for the velocity component along the inclined surface is

$$\frac{\mu \hat{u}}{K\rho_\infty g\beta(\hat{T}_w - \hat{T}_\infty)\cos\alpha_0}$$

$$= -\frac{\dfrac{\lambda+1}{2} f_0(\infty)[1+\eta^2/\sqrt{\mathrm{Ra}_{x,\alpha}}]^{\frac{\lambda-1}{4}} \cos\left[\dfrac{\lambda+1}{2}\Lambda_0 - \dfrac{\lambda-1}{2}\Lambda\right]}{\sqrt{\mathrm{Ra}_{x,\alpha}}\sin\left(\dfrac{\lambda+1}{2}\Lambda_0\right)}$$

$$- \frac{[A_1 - \tan\alpha_0 F_1(\eta_\infty)]\cos\Lambda}{\mathrm{Ra}_{x,\alpha}[1+\eta^2/\sqrt{\mathrm{Ra}_{x,\alpha}}]^{1/2}\Lambda_0} + 0(\epsilon^3) \tag{40}$$

where $\Lambda = \tan^{-1}(\eta\sqrt{\mathrm{Ra}_{x,\alpha}})$.

*The authors wish to thank an anonymous reviewer for calling our attention to the recent work by Daniels and Simpkins [15], who considered the case of $\lambda=0$ and $\alpha_0=0$ with an adiabatic lower plate.

A uniformly valid solution for the velocity component parallel to the heated surface can be obtained by adding the inner solution given by equation (38) to the outer solution given by equation (40) and subtracting the matching conditions given by equation (39). The numerical results of the uniformly valid solution for the velocity component parallel to the heated surface for Case I-*a,b,c* and II-*b* with $\lambda=1/3$ and $\mathrm{Ra}_{x,\alpha}=20$ are presented in Fig. 3. In these figures, the solid lines are the first-order theory, i.e., the boundary layer approximation, while the dashed lines are for higher-order theory. The effect of upstream geometry on the vertical velocity component adjacent to the heated vertical surface is shown in Fig. 3(*a*). It is seen that the decrease of the angle $\Lambda_0$ between the heated surface relative to the upstream impermeable surface tends to retard the buoyancy-induced flow. This is owing to the fact that the entrained fluid cannot be drawn from upstream for the case of $\Lambda_0=\pi/2$, i.e., Case II-b. The velocity component parallel to the heated inclined plate for upward-facing plate (Case I-*c*) and the downward-facing plate (Case I-*a*) at the same inclination angle with $\lambda=1/3$ and $\mathrm{Ra}_{x,\alpha}=20$ is shown in Fig. 3(*b*). It is seen that the velocity component parallel to the heated surface is higher for the case of an upward-facing inclined plate than that of a downward-facing inclined plate.

**Temperature and Surface Heat Flux.** Since the outer solutions as well as matching conditions for temperature are zero, the inner solution is uniformly valid for the whole flow field. It follows from equations (10*b*), (11*b*), and (22) that the uniformly valid solution for temperature is

$$\theta = \begin{cases} g_0(\eta) + 0(\epsilon^2), \quad \text{for } \lambda = 0 \\ x^\lambda g_0(\eta) - \epsilon\left[\dfrac{\lambda+1}{2} f_0(\infty)\cot\left(\dfrac{\lambda+1}{2}\Lambda_0\right) g_1(\eta) \right. \\ \left. + G_1(\eta)\tan\alpha_0\right] x^{\frac{\lambda-1}{2}} \\ + \epsilon^2\Theta_2(\eta)/x + 0(\epsilon^n), \text{ for } 0<\lambda<1 \end{cases} \tag{41a}$$

(41*b*)

Equations (41) for Cases I-*a,b,c* and II-*b* at $\lambda=1/3$ and $\mathrm{Ra}_{x,\alpha}=20$ are plotted in Figs. 4 were the solid lines are for the boundary layer theory and the dashed lines are for the third-order theory. Since the second-order theory is very close to the third-order theory, the second-order results are omitted in the graphs. Figure 4(*a*) shows that decreasing the angle $\Lambda_0$ increases the temperature because of the decrease in velocity as shown in Fig. 3(*a*). For the same reason, the temperature near the downward-facing heated plate is higher than that of the upward-facing plate as is shown in Fig. 4(*b*).

Differentiating equations (41) with respect to $y$ gives the following expressions for the local Nusselt number

$$\frac{\mathrm{Nu}_x}{\sqrt{\mathrm{Ra}_{x,\alpha}}} = \begin{cases} g_0'(0) + 0(\epsilon^2), \text{ for } \lambda = 0 \\ g_0'(0) - \dfrac{1}{\sqrt{\mathrm{Ra}_{x,\alpha}}}\left[\dfrac{\lambda+1}{2}\cot\left(\dfrac{\lambda+1}{2}\Lambda_0\right)\right. \\ \left. f_0(\infty) g_1'(0) + G_1'(0)\tan\alpha_0\right] \\ + \dfrac{\Theta_2'(0)}{\mathrm{Ra}_{x,\alpha}} + 0(\epsilon^{\alpha_m}), \text{ for } 0<\lambda<1 \end{cases} \tag{42a}$$

(42*b*)

Equation (42*a*) shows that the second-order effects on the local heat transfer rate are zero for an isothermal plate.

Equation (42*b*) for Cases I-*a,b,c* and II-*b* at $\lambda=1/3$ are plotted as dashed lines in Fig. 5. For comparison, the results given by the boundary layer theory are plotted as solid

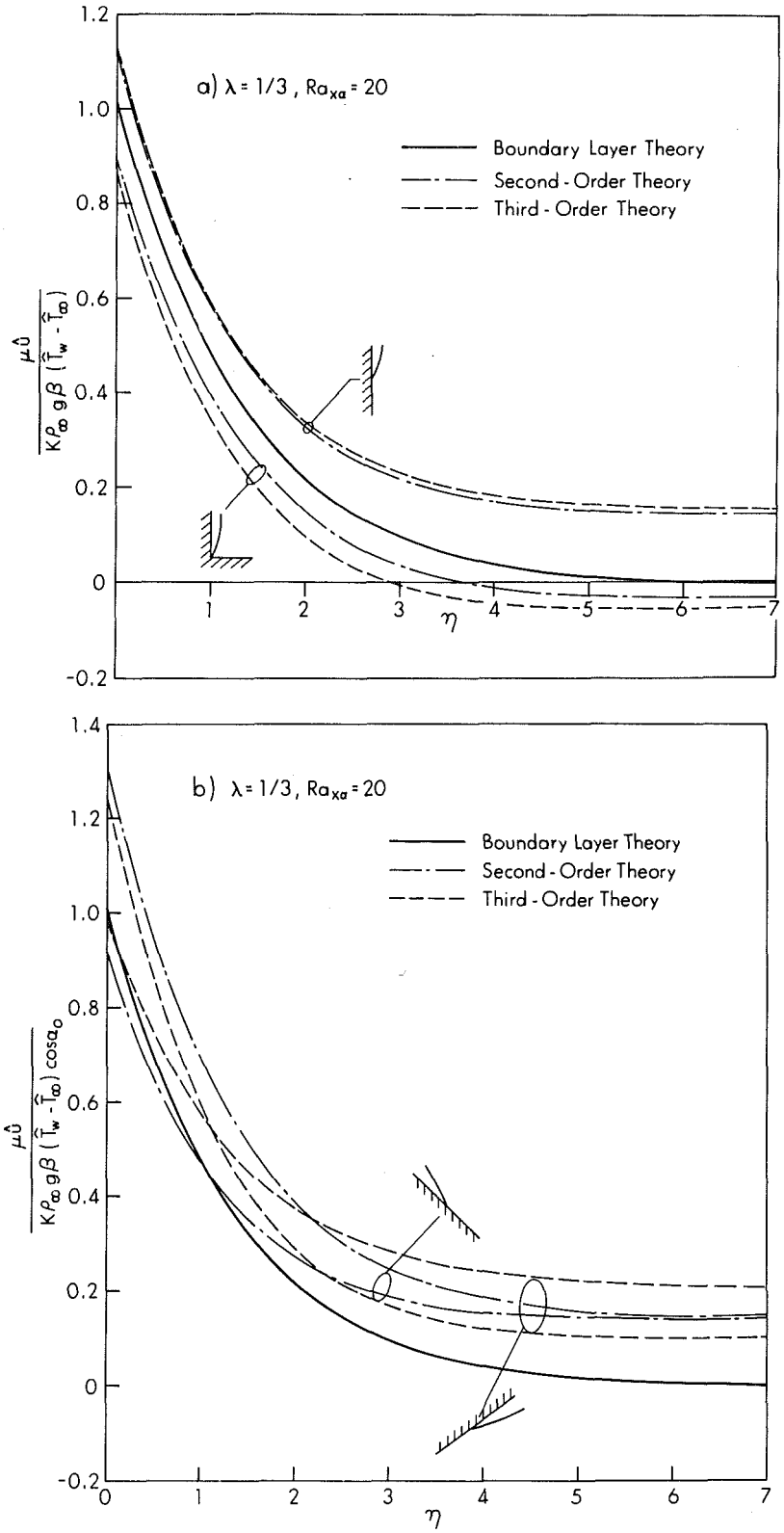


**Fig. 3 Effects of upstream geometry and inclination angle of the heated plate on the buoyancy-induced velocity parallel to the heated plate: (*a*) cases I-*b* and II-*b*, (*b*) cases I-*a* and I-*c***

straight lines. It is seen from Fig. 5(*a*) that the decrease of the angle $\Lambda_0$ retards the heat transfer rate because of the decrease in the velocity of the buoyancy-induced flow. Figure 5(*b*) shows that at the same inclination angle, the local heat transfer rate is higher for the case of an upward-facing plate than that of a downward-facing plate because of the increase in velocity in the former situation. Figure 5 also shows that the higher-order theory converges to the boundary layer theory at high Rayleigh numbers (defined based on the component of the gravitational acceleration parallel to that of the inclined plate) where the higher-order effects become unimportant.

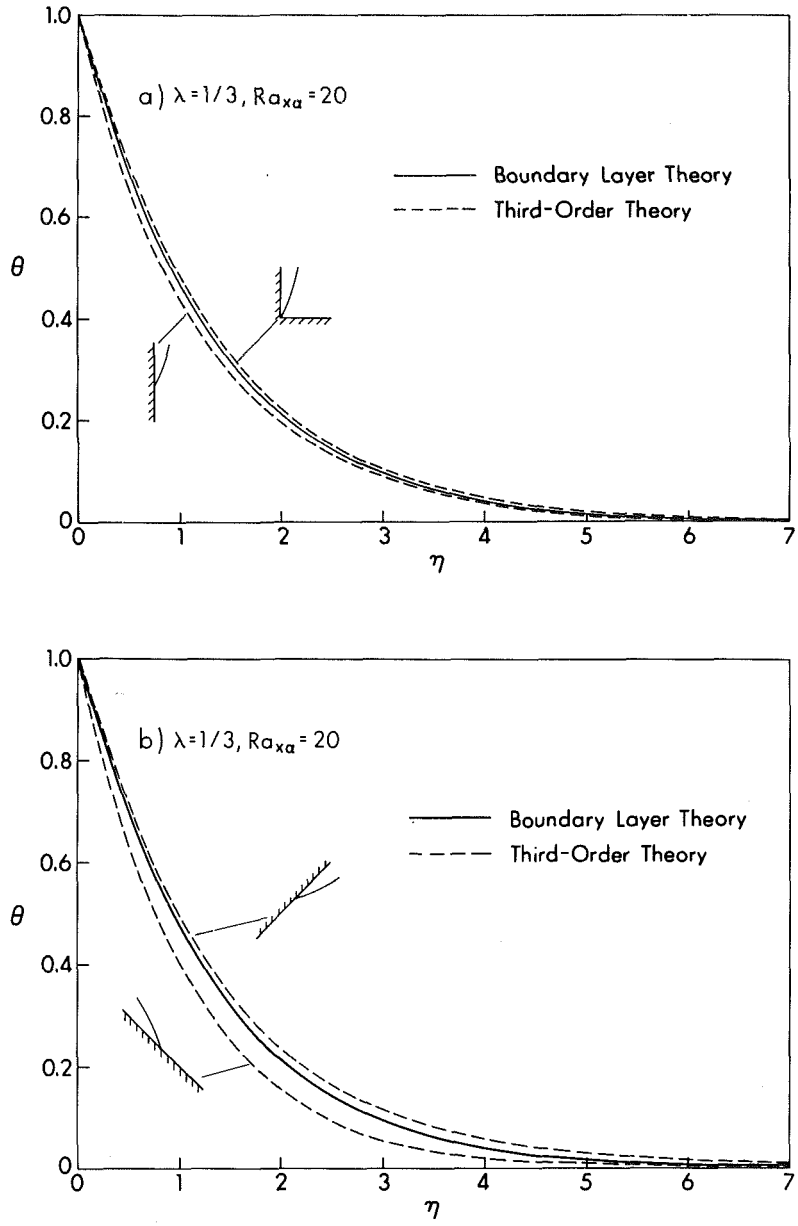


**Fig. 4 Effects of upstream geometry and inclination angles of the heated plate on temperature profiles: (*a*) cases I-*b* and II-*b*, (*b*) cases I-*a* and I-*c***

The total thermal energy $\hat{Q}$ that is convected away at $\hat{x}$ is

$$\hat{Q}=\rho c\int_0^\infty \hat{u}(\hat{T}-\hat{T}_\infty)\,d\hat{y} \tag{43}$$

For a vertical plate with a length $\hat{l}$, the total heat transfer from the plate is equal to the total thermal energy convected away at $\hat{x}=\hat{l}$. Thus, the total heat transfer rate for a vertical plate with a length $\hat{l}$ can be obtained by substituting the leading terms of equations (38–41) into equation (43) and letting $\hat{x}=\hat{l}$ to give

$$\overline{\mathrm{Nu}}=\frac{\hat{Q}}{k(\overline{T_w-T_\infty})}=\sqrt{\mathrm{Ra}_\alpha}\left\{\frac{2[-g_0'(0)]}{3\lambda+1}-\frac{S}{\sqrt{\mathrm{Ra}_\alpha}}+0(\epsilon^2)\right\} \tag{44}$$

where $\overline{\mathrm{Nu}}$ is the average Nusselt number,

$$(\overline{T_w-T_\infty})=\frac{1}{\hat{l}}\int_0^{\hat{l}}(\hat{T}_w-\hat{T}_\infty)\,d\hat{x}=A\hat{l}^\lambda/(1+\lambda),$$

and

$$S(\lambda,\Lambda_0,\alpha_0)=\frac{\lambda+1}{2}f_0(\infty)\cot\left[\left(\frac{1+\lambda}{2}\right)\Lambda_0\right]\int_0^\infty f_1' g_0\,d\eta$$

$$+\tan\alpha_0\int_0^\infty F_1' g_0\,d\eta$$

$$+\frac{\left(\frac{\lambda+1}{2}\right)f_0(\infty)}{\sin\left(\frac{\lambda+1}{2}\Lambda_0\right)}\int_0^\infty\cos\left[\frac{\lambda+1}{2}\Lambda_0-\frac{\lambda-1}{2}\Lambda\right]g_0(\eta)\,d\eta$$

$$-\frac{\lambda+1}{2}f_0(\infty)\cot\left(\frac{1+\lambda}{2}\Lambda_0\right)\int_0^\infty g_0(\eta)\,d\eta$$

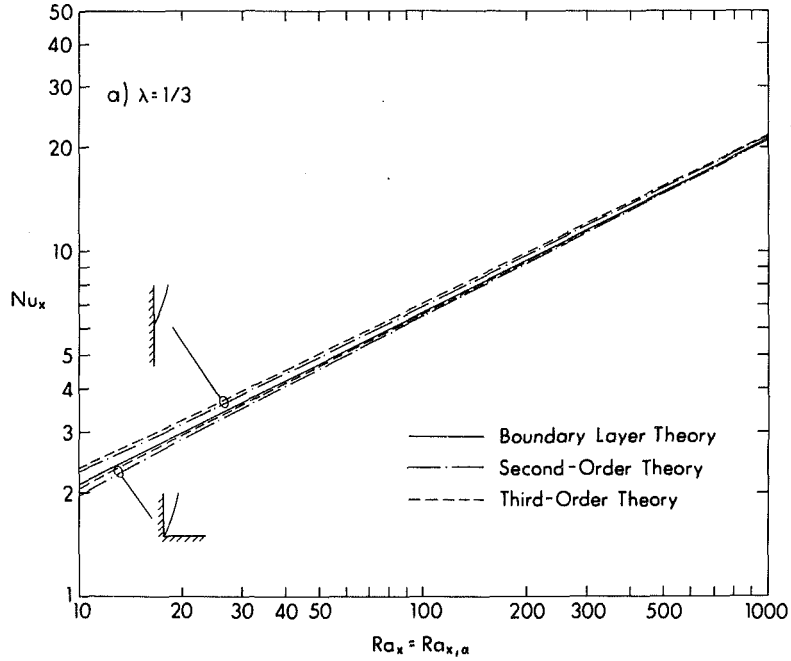


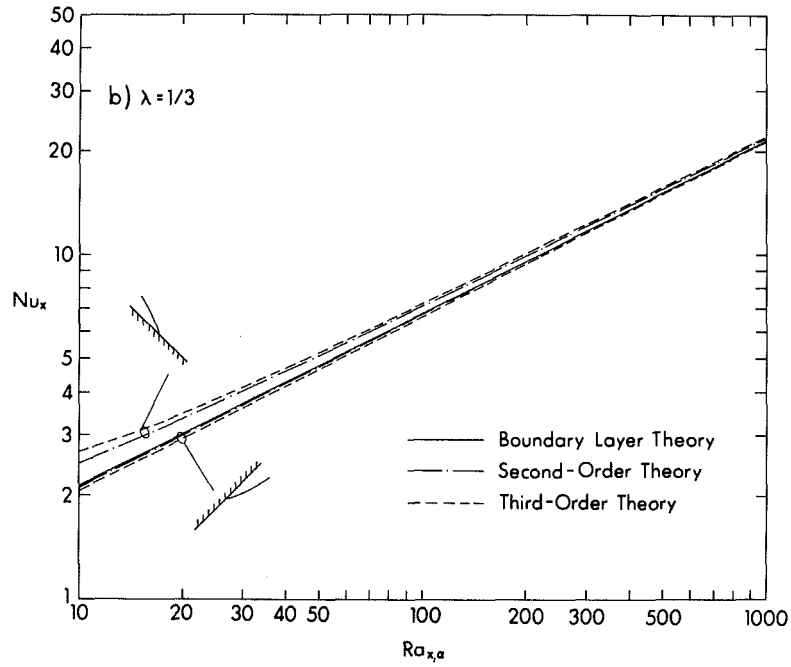


**Fig. 5 Effects of upstream geometry and inclination angle of the heated plate on the local Nusselt number: (*a*) cases I-*b* and II-*b*, (*b*) cases I-a and I-c**

The value of $S$ indicates the second-order effects of upstream geometry ($\Lambda_0$) and inclination angle ($\alpha_0$) on the average Nusselt number.

Equation (44) was computed for the six cases shown in Fig. 2. The effects of the upstream geometry on the average Nusselt number for a vertical heated plate with $\lambda = 0$ and $\lambda = 1/3$ are shown in Figs. 6(*a*) and 6(*b*). For the case of an isothermal plate ($\lambda = 0$), Fig. 6(*a*) shows that the second-order correction on the average Nusselt number is positive because of the fluid entrainment from upstream, although the second-order effect on the local Nusselt number is zero (see equation (42*a*)). Figure 6 also shows that reducing the intercepting angle $\Lambda_0$ decreases the average surface heat flux. The effect of $\Lambda_0$ on the average Nusselt number of an inclined surface is displayed in Fig. 7 which shows that at a given inclination angle $\alpha_0$, the average surface heat flux is higher for an upward-facing plate than that of a downward-facing plate.

## Concluding Remarks

The following conclusions may be drawn from the present analysis:

1. For the case of an isothermal ($\lambda = 0$) surface, the second-order effects of upstream geomety and inclination angle of the heat plate on the temperature distribution and the local surface heat flux are identically zero. The second-order effects, however, do modify the velocity profile near the outer

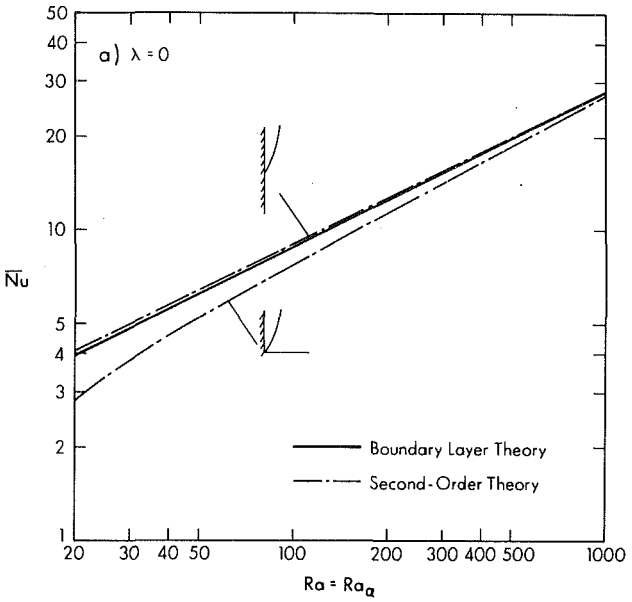


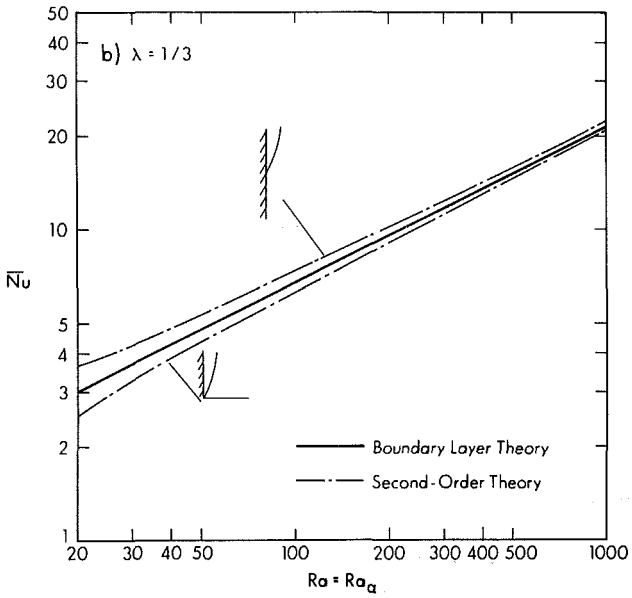


Fig. 6 Effects of upstream geometry on the average Nusselt number of a vertical heated plate: (*a*) $\lambda = 0$, and (*b*) $\lambda = 1/3$

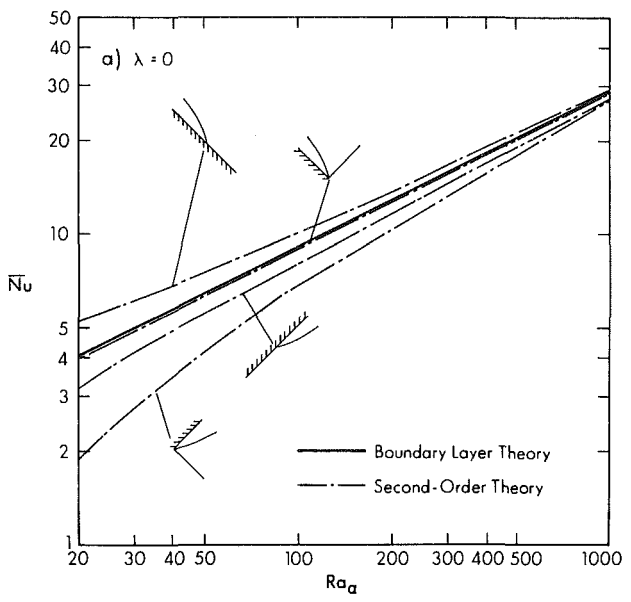


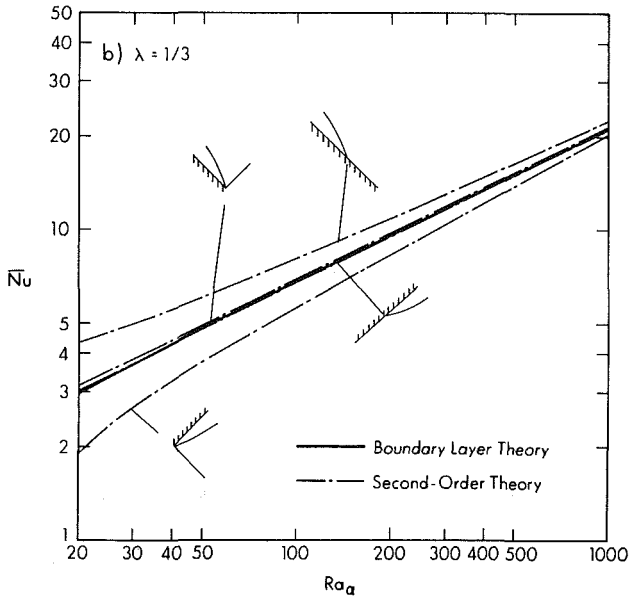


Fig. 7 Effects of upstream geometry on the average Nusselt number of an inclined heated plate: (*a*) $\lambda = 0$, and (*b*) $\lambda = 1/3$

edge of the thermal layer resulting in a change of the average heat flux. The third-order effect cannot be determined without a detailed analysis of the leading edge effect which is beyond the scope of this work.

2. For other values of $\lambda$, a uniformly valid solution has been obtained up to the fourth order where the leading edge effect begins to appear. The second and third-order effects do modify the temperature profile, velocity, and local and average heat flux.

3. At the same inclination angle, the surface heat flux is higher for an upward-facing inclinded plate than that of a downward-facing inclined plate.

4. Reducing the intercepting angle between the heated surface relative to the upstream impermeable surface tends to decrease the amount of entrained fluid, and consequently retards the surface heat flux.

5. The effects of upstream geometry and inclination of the heated plate on the heat transfer characteristics become more prounced as the Rayleigh number is decreased.

## Acknowledgments

The authors gratefully acknowledge the support of the National Science Foundation on this work through Grant No. MEA-8312095. They would like to thank an anonymous reviewer for helpful discussions and suggestions, and T. Le for his assistance in the numerical computations.

## References

1 Yang, K. T., and Jerger, E. W., "First-Order Perturbations of Laminar

Free-Convection Boundary Layers on a Vertical Plate," ASME JOURNAL OF HEAT TRANSFER, Vol. 86, 1964, pp. 107–115.

2 Messiter, A. F., and Linan, A., "A Vertical Plate in Laminar Free Convection: Effects of Leading and Trailing Edges and Discontinuous Temperature," *ZAMP*, Vol. 27, 1976, pp. 633–651.

3 Hieber, C. A., "Natural Convection Around a Semi-Infinite Vertical Plate: Higher-Order Effects," *Int. J. Heat Mass Transfer*, Vol. 17, 1974, pp. 785–790.

4 Riley, D. S., and Drake, D. G., "Higher Approximations to Free Convection Flow from a Heated Vertical Flat Plate," *Applied Sci. Res.*, Vol. 30, 1975, pp. 193–207.

5 Mahajan, R. L., and Gebhart, B., "Higher-Order Approximations to the Natural Convection Flow over a Uniform Flux Vertical Surface," *Int. J. Heat Mass Transfer*, Vol. 21, 1978, pp. 549–556.

6 Kierkus, W. T., "An Analysis of Laminar Free Convection Flow and Heat Transfer about an Inclined Isothermal Plate," *Int. J. Heat Mass Transfer*, Vol. 11, 1968, pp. 241–253.

7 Hieber, C. A., and Nash, E. J., "Natural Convection above a Line Heat Source: Higher-Order Effects and Stability," *Int. J. Heat Mass Transfer*, Vol. 18, 1975, pp. 1473–1479.

8 Riley, N., "Free Convection from a Horizontal Line Source of Heat," *ZAMP*, Vol. 25, 1974.

9 Afzal, N., "Convective Wall Plume: Higher Order Analysis," *Int. J. Heat Mass Transfer*, Vol. 23, 1980, pp. 504–513.

10 Rich, B. R., "An Investigation of Heat Transfer from an Inclined Flat Plate in Free Convection," *ASME Trans.*, Vol. 75, 1953, pp. 489–499.

11 Cheng, P., and Hsu, C. T., "Higher-Order Approximations for Darcian Free Convective Flow about a Semi-Infinite Vertical Flat Plate," ASME JOURNAL OF HEAT TRANSFER, Vol. 106, No. 1, Feb. 1984, pp. 143–151.

12 Chang, I. D., and Cheng, P., "Matched Asymptotic Expansisn for Free Convection about an Impermeable Horizontal Surface in a Porous Medium." *Int. J. Heat Mass Transfer*, Vol. 26, 1984, pp. 163–174.

13 Cheng, P., and Minkowycz, W. J., "Free Convection about a Vertical Flat Plate Embedded in a Porous Medium with Applications to Heat Transfer from a Dike," *J.G.R.*, Vol. 82, 1977, pp. 2040–2044.

14 Stewartson, K., "On Asymptotic Expansions in the Theory of Boundary Layers," *J. Math. Phys.*, Vol. 36, 1957, pp. 173–191.

15 Daniels, P. G., and Simpkins, P. G., "The Flow Induced by a Heated Vertical Wall in a Porous Medium," *Q. J. Mech. Appl. Mech.*, Vol. 37, 1984, pp. 339–354.

# Natural Convection in a Stably Heated Corner Filled With Porous Medium

**S. Kimura**

**A. Bejan**
Assoc. Mem. ASME

Department of Mechanical Engineering
and Materials Science,
Duke University,
Durham, NC 27706

*This is a study of the single-cell natural convection pattern that occurs in a "stably heated" corner in a fluid-saturated porous medium, i.e., in the corner formed between a cold horizontal wall and a hot vertical wall situated above the horizontal wall, or in the corner between a hot horizontal wall and a cold vertical wall situated below the horizontal wall. Numerical simulations show that this type of corner flow is present in porous media heated from the side when a stabilizing vertical temperature gradient is imposed in order to suppress the side-driven convection. Based on numerical solutions and on scale analysis, it is shown that the single cell corner flow becomes increasingly more localized as the Rayleigh number increases. At the same time, the mass flow rate engaged in natural circulation and the conduction-referenced Nusselt number increase. Numerical results for the flow and temperature fields and for the net heat transfer rate are reported in the Darcy-Rayleigh number range 10–6000.*

## Introduction

Ever since its emergence as an important subfield in thermal convection, the topic of natural convection through a fluid-saturated porous medium has been studied primarily in one of the two main configurations in which the phenomenon can exist:

(*i*) Porous layers heated from below
(*ii*) Porous layers heated from the side

Aside from many practical applications that differentiate rather severely between the relevance of one configuration over the relevance of the other (e.g., geophysical applications for configuration (*i*), and building insulation technology for configuration (*ii*)), the flows housed by the two configurations differ in a fundamental sense. Unlike in layers heated from the side, where fluid motion is present as soon as an infinitesimally small temperature difference is applied across the layer, in layers heated from below convection is possible only if the temperature difference exceeds a critical threshold value. Furthermore, as the temperature difference increases, in layers heated from the side the flow remains unicellular (e.g., two-dimensional layers with rectangular cross-section, or the "porous" equivalent of the double-pane window problem), whereas in layers heated from below the flow evolves as a collection of Benard cells whose number increases discretely. The fundamental difference between configurations (*i*) and (*ii*) is amply documented in the literature, for example, [1–3] for layers heated from below and [4–6] for layers heated from the side.

An interesting interaction between the two phenomena (*i*) and (*ii*) is observed in connection with the thermal insulation design problem of suppressing the natural circulation in a layer heated from the side. As illustrated later in this article (Figs. 2, 3), the natural convection driven by heating from the side can be suppressed, at least partially, by the imposition of a stabilizing vertical temperature gradient. In other words, the natural convection flow of type (*ii*) is inhibited rather efficiently through the imposition of a temperature gradient designed to inhibit convection of type (*i*). The same conclusion applies in the case of enclosures filled with fluid (without a porous matrix), as demonstrated earlier by Ostrach and his co-workers [7–9] and by Shiralkar and Tien [10].

As shown in [7–10] and in Fig. 3(*a*) of the present study, the side-driven natural circulation does not disappear completely even when the vertical stabilizing gradient is greater than the destabilizing horizontal gradient. Even under these conditions, natural convection persists in the two opposing corners formed by the cooled bottom wall and the heated lateral wall, and by the heated top wall and the cooled lateral wall. The corner region shown schematically in Fig. 1 is the focus of the present study. The same corner region corresponds to the lower right-hand corner of Fig. 3. One very interesting feature of the corner flow is that it occupies a smaller and smaller space as the temperature difference between the two walls increases. To document and explain this behavior, and to calculate the heat transfer potential of the corner flow is the objective of the present study.

## Mathematical Formulation

We begin with the numerical simulation of the natural convection flow in a layer heated from the side and from above in order to illustrate the persistence of a single-cell flow in a stably heated corner. Next, we conduct numerical experiments in the isolated corner region defined in Fig. 1. Focusing on a square box filled with fluid-saturated porous medium, the conservation equations for mass, momentum, and energy are

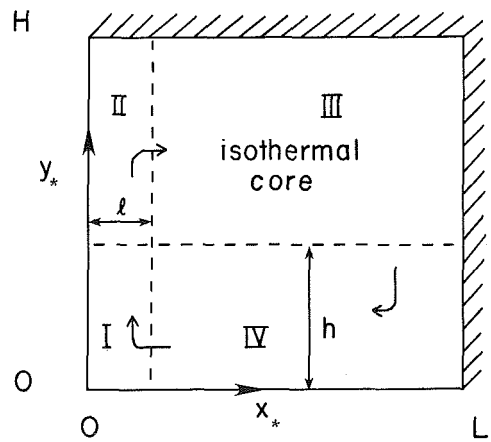


**Fig. 1 Schematic of a stably heated corner in a fluid saturated porous medium**

Contributed by the Heat Transfer Division for publication in the JOURNAL OF HEAT TRANSFER. Manuscript received by the Heat Transfer Division June 14, 1983.

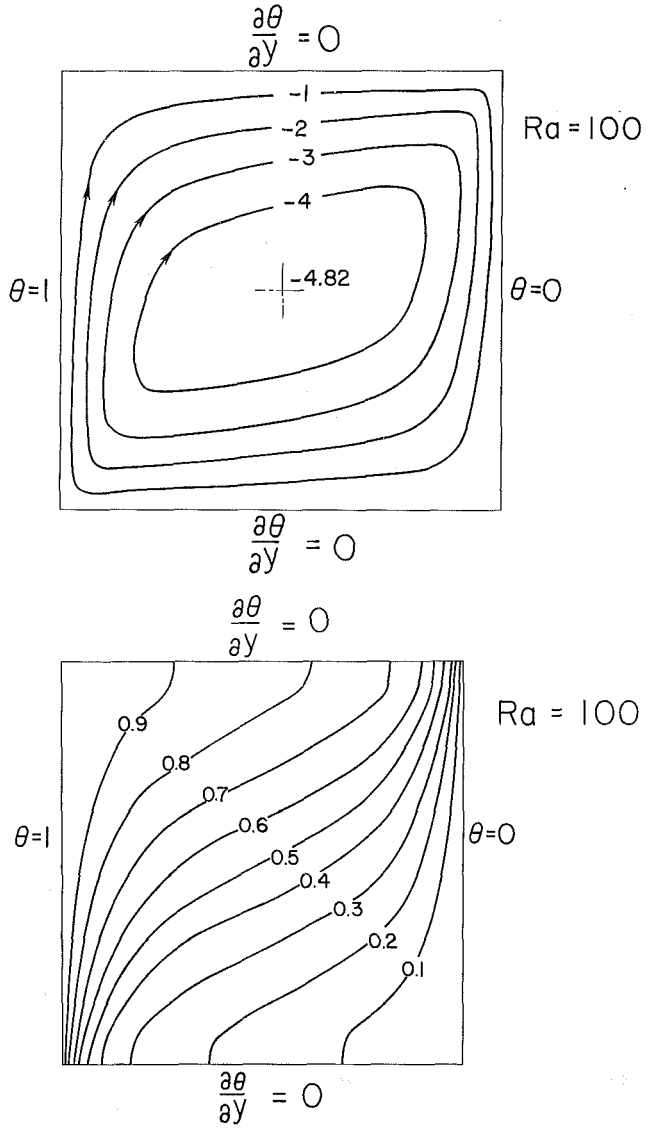


**Fig. 2 Flow and temperature field in a square box bounded by differentially heated side walls and adiabatic top and bottom walls ($L/H = 1$, Ra = 100)**

$$\frac{\partial u_*}{\partial x_*} + \frac{\partial v_*}{\partial y_*} = 0 \tag{1}$$

$$\frac{\partial u_*}{\partial y_*} - \frac{\partial v_*}{\partial x_*} = -\frac{g\beta K}{\nu}\frac{\partial T_*}{\partial x_*} \tag{2}$$

$$u_*\frac{\partial T_*}{\partial x_*} + v_*\frac{\partial T_*}{\partial y_*} = \alpha\left(\frac{\partial^2 T_*}{\partial x_*^2} + \frac{\partial^2 T_*}{\partial y_*^2}\right) \tag{3}$$

These equations are written in a coordinate system with the $y$-axis pointing against gravity, and for a Boussinesq-incompressible fluid that obeys the Darcy flow model [1]. The symbols appearing in equations (1-3) are defined in the Nomenclature and in Fig. 1. For numerical computations, it is necessary to place equations (1-3) in dimensionless form

$$\frac{\partial^2\psi}{\partial x^2} + \frac{\partial^2\psi}{\partial y^2} = -\mathrm{Ra}\frac{\partial\theta}{\partial x} \tag{4}$$

$$\frac{\partial(\theta,\psi)}{\partial(x,y)} = \frac{\partial^2\theta}{\partial x^2} + \frac{\partial^2\theta}{\partial y^2} \tag{5}$$

by introducing the dimensionless stream function $\psi(x,y)$

$$u = \partial\psi/\partial y,\ v = -\partial\psi/\partial x \tag{6}$$

and the dimensionless variables

$$\psi = \psi_*/\alpha,\ \theta = (T_* - T_{c_*})/(T_{H_*} - T_{c_*}),\quad (x,y) = (x_*,y_*)/H \tag{7}$$

Parameter Ra is the Darcy-modified Rayleigh number

$$\mathrm{Ra} = g\beta KH(T_{H_*} - T_{c_*})/\nu\alpha \tag{8}$$

The boundary conditions for the isolated stably heated corner region of Fig. 1 are

$$\begin{aligned} &\theta = 1,\ \psi = 0 \quad \text{at} \quad x = 0\\ &\frac{\partial\theta}{\partial x} = 0,\ \psi = 0 \quad \text{at} \quad x = L/H\\ &\theta = 0,\ \psi = 0 \quad \text{at} \quad y = 0\\ &\frac{\partial\theta}{\partial y} = 0,\ \psi = 0 \quad \text{at} \quad y = 1 \end{aligned} \tag{9}$$

The problem described here as equations (4), (5), and (9) was solved numerically based on an algorithm described in detail in the next section. Before showing the numerical solution for the corner flow, it is instructive to illustrate the effect of a stabilizing vertical temperature gradient on the well-known, single-cell circulation in a layer heated and cooled along the sides. Figure 2 shows the characteristic streamlines and isotherms in a square porous medium with different side temperatures and with adiabatic top and bottom walls. These results were generated numerically using 21 × 21 grid points and a coordinate transformation that increased the density of grid points near the impermeable walls (see the next section).

In Fig. 3, the side-wall temperatures were kept the same as in Fig. 2; however, the top and bottom walls are now isothermal and at different temperatures. The effect of the vertical temperature gradient on the flow and temperature

## Nomenclature

$g$ = gravitational acceleration
$h$ = boundary layer thickness along bottom wall
$H$ = cavity height
$k$ = thermal conductivity of fluid/porous matrix combination
$K$ = permeability of porous matrix
$l$ = vertical boundary layer thickness
$L$ = cavity width
Nu = Nusselt number
$p$ = deformed $x$-coordinate
$q$ = deformed $y$-coordinate
$q''$ = heat flux specified along the bottom wall
$Q$ = rate of heat transfer per unit length
Ra = Rayleigh number
$T$ = temperature
$\Delta T$ = temperature difference, $T_H - T_c$
$u$ = horizontal velocity component
$v$ = vertical velocity component
$x$ = horizontal coordinate
$y$ = vertical coordinate

### Greek Symbols

$\alpha$ = thermal diffusivity
$\beta$ = coefficient of thermal expansion
$\delta$ = residue of numerical error
$\epsilon$ = coordinate deformation parameter
$\nu$ = kinematic viscosity
$\theta$ = dimensionless temperature, $(T_* - T_{c_*})/(T_{H_*} - T_{c_*})$
$\psi$ = stream function

### Superscripts

$k$ = iteration order
$-$ = average value

### Subscripts

$*$ = dimensional quantity
$H$ = indicating hot wall
$c$ = indicating cold wall

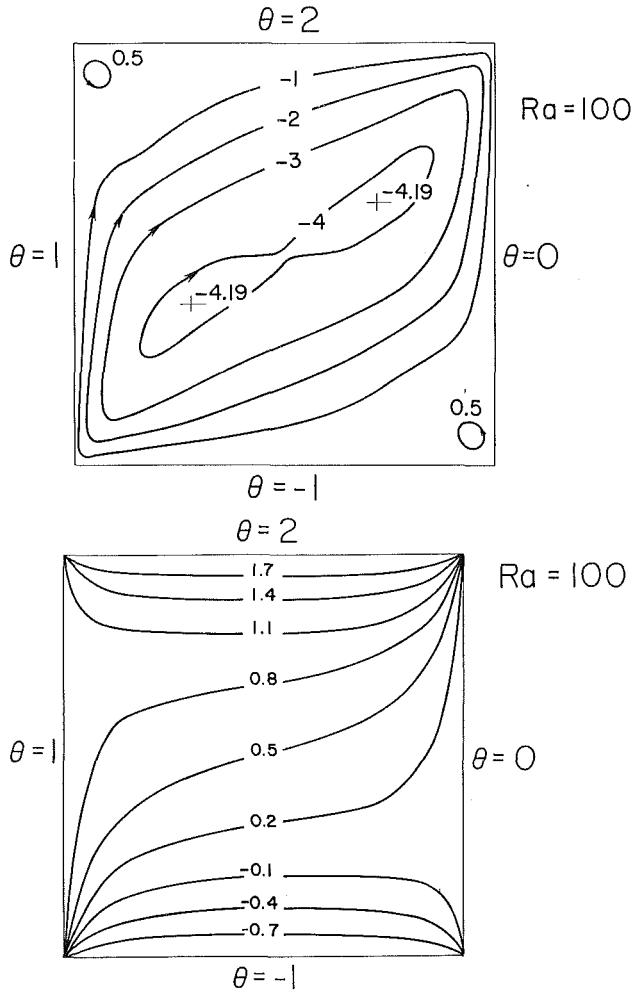


**Fig. 3 Flow and temperature field in a square box bounded by differentially heated side walls, with positive (stabilizing) vertical temperature gradient ($L/H$ = 1, Ra = 100)**

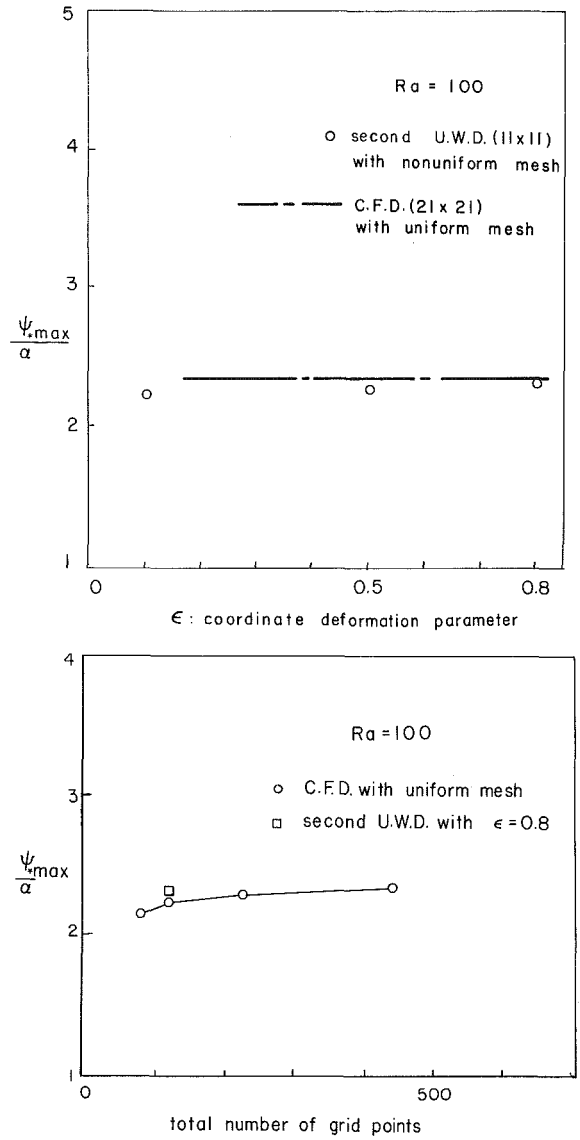


**Fig. 4 The effect of (*a*) coordinate deformation and (*b*) number of grid points, on the accuracy of numerical calculations**

patterns is very similar to the effect found in Newtonian fluids [7–10]. The thermal stratification of the porous medium is evident in Fig. 3(*b*); also visible is the formation of cellular flows in the two stably heated corners of the square enclosure.

## Numerical Experiments

The phenomenon of natural convection in a stably heated corner in a porous medium was simulated numerically. The second upwind method was used for the convection terms in the energy equation (5), and the remaining terms were approximated by centered finite difference. The resulting coupled algebraic equations were solved iteratively. In order to position more grid points near the solid boundaries of the porous medium, we employed the coordinate transformation suggested by Küblbeck et al. [11]

$$p(x) = \frac{1}{2}\left[1+\tan\left[\frac{\pi}{2}(2x-1)\epsilon\right]/\tan\left(\frac{\pi}{2}\epsilon\right)\right]$$

$$q(y) = \frac{1}{2}\left[1+\tan\left[\frac{\pi}{2}(2y-1)\epsilon\right]/\tan\left(\frac{\pi}{2}\epsilon\right)\right] \qquad (10)$$

where $p$ and $q$ serve as new independent variables, and $\epsilon$ indicates the deformation rate of the original $x-y$ coordinate system. The effect of the foregoing coordinate transformation on the numerical result of the total mass flow rate $\psi_{max}$ is shown in Fig. 4. It is known that the centered-finite difference approximation for the advection term gives more accurate results than the upwind approximation in natural convection problems (Chow and Tien [12]), and that it can be subject to numerical instability unless a sufficient number of grid points are employed. In the case of Ra = 100, the centered finite difference scheme with 21 × 21 equidistant grid points converges rapidly; on Figs. 4(*a*) and 4(*b*), the centered finite difference result is compared with the corresponding results obtained based on the scheme employed in the present study (second upwind with coordinate transformation). The comparison shows that the $\psi_{max}$ results obtained with the 11 × 11 nonuniform grid system ($\epsilon$=0.8) and with the upwind method agrees well with that based on the centered difference method. The relative discrepancy between the two calculations is about 3 percent, and it indicates that the coordinate transformation yields a substantial improvement in accuracy.

The steady state was determined by monitoring the convergence of the temperature field, using the following criterion

$$\frac{\sum_{i}^{m}\sum_{j}^{n}|\theta_{ij}^{k+1}-\theta_{ij}^{k}|}{\sum_{i}^{m}\sum_{j}^{n}|\theta_{ij}^{k+1}|} \le \delta \qquad (11)$$

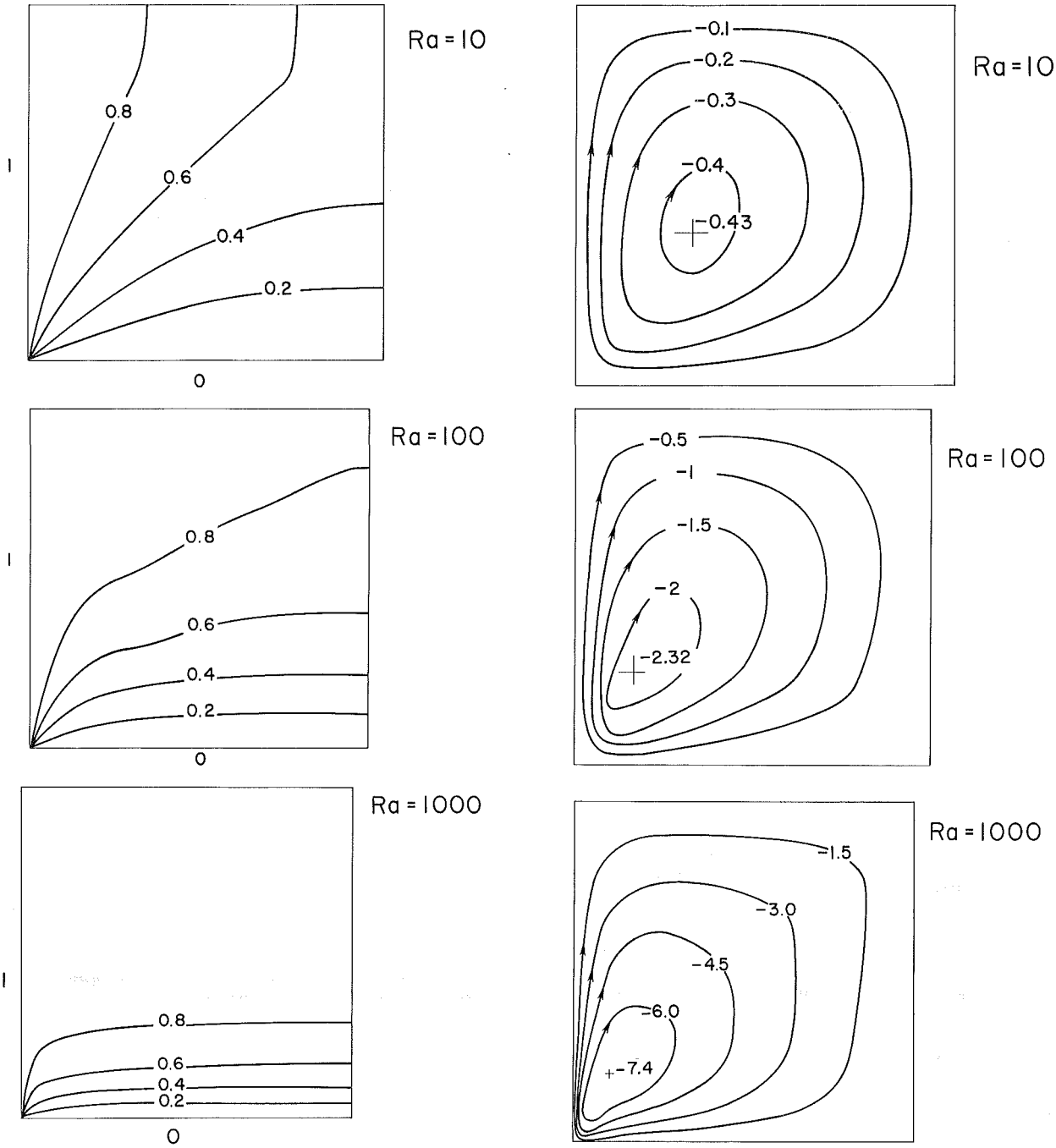


**Fig. 5 Streamlines and isotherms for natural convection in a stably heated corner with isothermal walls ($L/H = 1$): (*a*) Ra = 10; (*b*) Ra = 100; (*c*) Ra = 1000**

where $k$ indicates the iteration order. Once the temperature field has converged, the convergence of the hydrodynamic field is guaranteed, because the stream function equation (4) is linear and the source term (the right-hand side) depends only on the temperature field. The $\delta$ residue was taken as $5 \times 10^{-5}$. The further decrease of $\delta$ does not yield a significant change in the overall Nusselt number and in $\psi_{max}$. For the high Rayleigh number regime (Ra $\geqq$ 1000), we used 41 × 41 grid points in a nonuniform mesh.

Solutions for the flow and temperature patterns are presented in Fig. 5. The isotherms show that the bottom-wall thermal boundary layer becomes visible when Ra exceeds 0(100), and that the boundary layer thickness decreases continuously as Ra increases. The boundary layer along the heated vertical wall also becomes thinner; in fact, its thickness appears to decrease faster than the horizontal boundary layer thickness (this trend is suggested by the migration of the point of $\psi_{max}$ on the streamline patterns of Fig. 5). The streamlines show that the single-cell corner flow becomes more "local" as the Rayleigh number increases.

The numerical results show also that the flow and the heat convected by it intensify as the Rayleigh number increases. The increase in the total flow rate is illustrated in Fig. 6 as $\psi_{*max}/\alpha$ versus Ra: The numerical data suggest asymptotically a proportionality of type $\psi_{*max}/\alpha \sim \mathrm{Ra}^{1/3}$, which, as shown in the next section, is consistent with scale analysis. The overall heat transfer rate is reported in Fig. 7 as the overall Nusselt number

$$\mathrm{Nu} = \frac{Q}{k\Delta T_*} \tag{12}$$

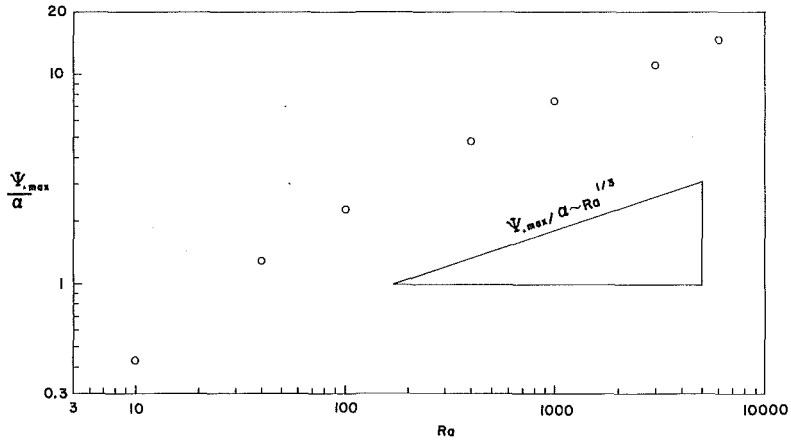


**Fig. 6 The maximum value of the dimensionless stream function $\psi_{*max}/\alpha$, as a function of the Rayleigh number**

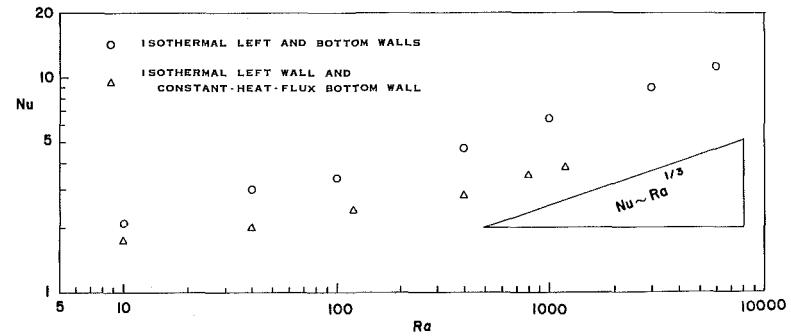


**Fig. 7 The heat transfer rate through a stably heated corner region filled with fluid saturated porous medium**

where $Q$ is the wall-to-wall heat transfer rate per unit length normal to the plane of Fig. 1. The Nusselt number was calculated by integrating along either wall the temperature gradient normal to the wall: these alternative evaluations of Nu agree within 6 percent. The discrepancy in the two alternative Nu calculations may be attributed to the phenomenon of numerical diffusion. This effect is intensive in regions where the velocity vector is inclined with respect to the orthogonal grid, i.e, in the vicinity of the four corners.

Throughout the numerical simulation of convection in the corner between two isothermal walls, the temperature of the corner point was taken as the average temperature $(T_{H_*} + T_{C_*})/2$. This choice is consistent with what happens in a real system where two isothermal walls of similar construction come in direct thermal contact. In order to model the continuous variation of the temperature around the corner of a real system, we also simulated numerically the flow in the corner between an isothermal vertical wall and a horizontal wall with specified uniform heat flux (Fig. 8). In this system, the corner point temperature is equal to the temperature of the hot vertical wall, as the bottom wall temperature decreases monotonically in the positive $x$-direction. The overall structure of the flow and temperature fields closely resembles the one observed in the case of two isothermal walls (see Ra = 1000, in Fig. 5). The heat transfer rate is also similar to the one calculated previously, as shown in Fig. 7. The Nusselt number is now defined as

$$\mathrm{Nu} = \frac{q'' L/k}{T_{H_*} - \bar{T}_{c_*}} \tag{13}$$

where $q''$ is the heat flux specified along the bottom wall, and $\bar{T}_{c_*}$ is the average temperature of the bottom wall

$$\bar{T}_{c_*} = \frac{1}{L}\int_0^L T_{c_*}\, dx \tag{14}$$

## Scale Analysis

The influence exercised by the Rayleigh number on the corner convection phenomenon can be explained qualitatively based on pure scaling arguments. As shown in Fig. 1 and, in greater detail, in Fig. 5 and 8, at high enough Rayleigh numbers the differentially heated corner enters the boundary layer regime. Let $l$ and $h$ be the vertical and, respectively, horizontal boundary layer thickness scales: these length scales divide the corner region into four domains labeled I–IV on Fig. 1. Assuming that region I is a boundary layer region, in other words, assuming that

$$l << h \tag{15}$$

the scaling laws required by equations (1–3) are

$$\frac{u_*}{l} \sim \frac{v_*}{h} \tag{16}$$

$$\frac{v_*}{l} \sim \frac{Kg\beta}{\nu}\frac{\Delta T_*}{l} \tag{17}$$

$$v_* \frac{\Delta T_*}{h} \sim \alpha \frac{\Delta T_*}{l^2} \tag{18}$$

Combining equations (17) and (18), we find a relationship between the two thicknesses

$$\frac{h}{l^2} \sim \frac{Kg\beta\Delta T_*}{\alpha\nu} \tag{19}$$

The other relationship between $h$ and $l$ follows from the constraint that the heat transfer to the vertical boundary layer is eventually released by the horizontal layer to the horizontal (cold) wall

$$Q \sim hk\frac{\Delta T_*}{l} \sim Lk\frac{\Delta T_*}{h} \tag{20}$$

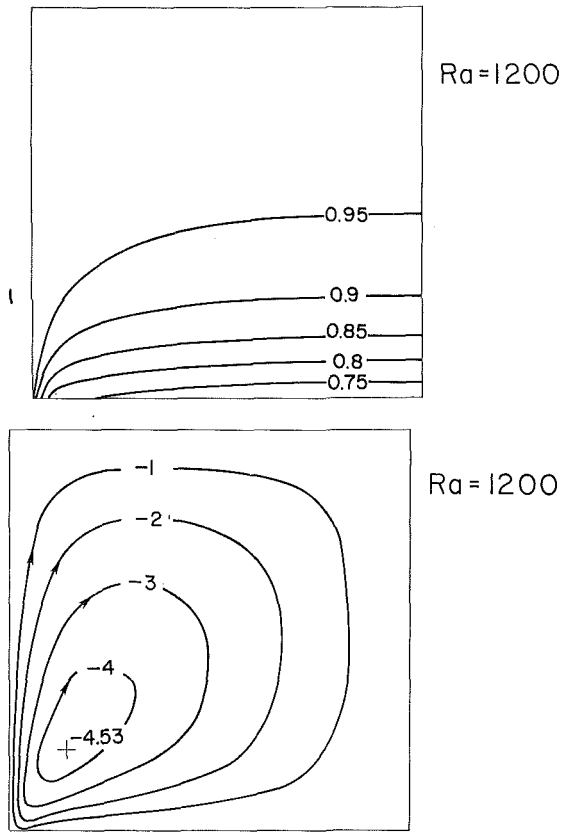


**Fig. 8 Streamlines and isotherms for natural convection in a stably heated corner with isothermal vertical wall and constant-heat-flux along the horizontal wall ($L/H$ = 1, Ra = 1200)**

Equations (19, 20) are sufficient for determining the length scales of high-Ra corner convection. Noting that in this study $H=L$, the sought scales are

$$h \sim H\mathrm{Ra}^{-1/3} \tag{21}$$

$$l \sim H\mathrm{Ra}^{-2/3} \tag{22}$$

Therefore, the slenderness assumption that preceded the scale analysis, equation (15), is valid when $\mathrm{Ra}^{1/3}$ is much greater than 0(1)

$$\frac{h}{l} \sim \mathrm{Ra}^{1/3} >> 1 \tag{23}$$

This high-Ra criterion suggests that only the highest Rayleigh numbers simulated numerically in Figs. 5 and 8 qualify as marginal cases of boundary layer convection. Despite the relatively low $\mathrm{Ra}^{1/3}$ values of the cases documented numerically, the trends, exhibited by the data of Figs. 6 and 7 agree very well with those recommended by the boundary layer scales (21, 22). For example, the stream function scale in the boundary layer regime must be

$$\psi_* \sim v_* l \sim \alpha \mathrm{Ra}^{1/3} \tag{24}$$

which agrees very well with the trend approached asymptotically by the data of Fig. 6. For the Nusselt number, the boundary layer scaling recommends

$$\mathrm{Nu} = \frac{Q}{k\Delta T_*} \sim \frac{L}{h} \sim \mathrm{Ra}^{1/3} >> 1 \tag{25}$$

The validity of this scaling law is confirmed by the high Rayleigh number data of Fig. 7.

## Concluding Remarks

In this study we focused on the heat and fluid flow fundamentals of buoyancy-driven convection in the stably heated corner of a fluid-saturated porous medium (Fig. 1). Based on numerical simulations, we showed that this type of corner flow is a characteristic of porous media heated from the side and, simultaneously, from above (Figs. 2,3): in this manner, the corner phenomenon documented in this study promises to survive in (hence, to plague the insulation value of) side-heated porous layers with stabilizing vertical temperature gradients.

Numerical solutions and scaling arguments suggest that the flow driven by the differentially heated corner becomes increasingly more localized as the Rayleigh number increases. At the same time, the mass flow rate that engages in natural circulation increases (Fig. 6), and so does the conduction-referenced Nusselt number (Fig. 7). Numerical simulations showed also that the flow and temperature patterns in a corner region with uniform heat flux along the bottom wall (Fig. 8) are essentially the same as when the bottom wall is isothermal (Fig. 5).

It is worth keeping in mind that the conclusions of this study rest on the validity of the Darcy flow model, on which the mathematical formulation was based. The Darcy flow model is valid provided the Reynolds number based on local velocity and pore size does not exceed 0(1).

## Acknowledgment

This research was conducted with the partial support of National Science Foundation Grant No. MEA-82-07779.

## References

1 Cheng, P., "Heat Transfer in Geothermal Systems," *Advances in Heat Transfer*, Vol. 14, 1979, pp. 1–105.

2 Lapwood, E. R., "Convection of Fluid in a Porous Medium," *Proc. Cambridge Philos. Soc.*, Vol. 44, 1948, pp. 508–521.

3 Strauss, J. M., "Large Amplitude Convection in Porous Media," *J. Fluid Mech.*, Vol. 64, 1974, pp. 51–63.

4 Weber, J. E., "The Boundary Layer Regime for Convection in a Vertical Porous Layer," *International Journal of Heat and Mass Transfer*, Vol. 18, 1975, pp. 569–573.

5 Bankvall, C. G., "Natural Convection in Vertical Permeable Space," *Wärme- und Stoffübertragung*, Vol. 7, 1974, pp. 22–30.

6 Hickox, C. E., and Gartling, D. K., "A Numerical Study of Natural Convection in a Horizontal Porous Layer Subjected to an End-to-End Temperature Difference," ASME JOURNAL OF HEAT TRANSFER, Vol. 103, 1981, pp. 797–802.

7 Ostrach, S., "Natural Convection Heat Transfer in Cavities and Cells," Keynote paper at the Seventh International Heat Transfer Conference, Munich, 1982.

8 Fu, B. I., and Ostrach, S., "The Effects of Stabilizing Thermal Gradients on Natural Convection Flows in a Square Enclosure," in *Natural Convection*, edited by I. Catton and R. N. Smith, ASME HTD, Vol. 16, 1981.

9 Ostrach, S., and Raghavan, C., "Effect of Stabilizing Thermal Gradients on Natural Convection in Rectangular Closures," ASME JOURNAL OF HEAT TRANSFER, Vol. 101, 1979, pp. 238–243.

10 Shiralkar, G. S., and Tien, C. L., "A Numerical Study of the Effect of a Vertical Temperature Difference Imposed on a Horizontal Enclosure," *Numerical Heat Transfer*, Vol. 5, 1982, pp. 185–197.

11 Küblbeck, K., Merker, G. P., and Straub, J., "Advanced Numerical Computation of Two-Dimensional Time-Dependent Free Convection in Cavities," *Int. J. Heat Mass Transfer*, Vol. 23, 1980, pp. 203–217.

12 Chow, L. C., and Tien, C. L., "An Examination of Four Differencing Schemes for Some Elliptic-Type Convection Equations," *Numerical Heat Transfer*, Vol. 1, 1978, pp. 87–100.

# Liquid Diffusion in Fibrous Insulation

**S. Motakef**

**M. A. El-Masri**

Department of Mechanical Engineering,
Massachusetts Institute of Technology,
Cambridge, Mass. 02139

*Vapor condensation in insulated structures degrades their physical properties as well as thermal performance. Motion of the condensate within the insulation is a crucial factor in analyzing annual moisture retention in building shells. The diffusion of liquid can be caused by several driving potentials. A model for isothermal liquid transport in fibrous insulation is presented. The model relates liquid diffusion to the characteristics of the insulation. These are identified as void-fraction and its spatial distribution, mean fiber radius, directionally index, and tortuousity factor. Due to the anisotropic layered structure of the fiberglass insulation, liquid diffusion along the three principal directions are studied. The diffusion of liquid from one layer to the next is controlled by liquid diffusion along the layers and the tortuosity factor. Diffusion along the layers is caused by the suction potential and retarded by the viscous forces. By balancing the suction and the viscous forces, a model for transient diffusion in terms of the five medium properties is obtained. An electrical resistance probe for in-situ measurement of liquid content in insulation samples of high voidage has been developed. Data on liquid diffusion under isothermal concentration gradients for commercial fiberglass insulations have been acquired. The experimental data show consistent agreement with the model predictions.*

## Introduction

The condensation of water vapor in building structures is a widely observed phenomenon [1]. The presence of condensate in structures is undesirable for it could promote such phenomena as wood decay, corrosion of metals, efflorescence, and a decrease in the structural strength of the shell upon freezing. During the past decade considerable attention has been paid to the increase of thermal efficiency of buildings through added insulation. However, the possible problems associated with moisture condensation in the insulated structures have not been adequately considered. Traditionally, vapor barriers have been used to inhibit moisture migration into the insulated structure. Yet, it has been shown that holes as small as .036 percent of the total area reduce the resistance of the barrier to vapor flow by 92 percent [2]. Futhermore, air infiltration through the building shell contributes substantially to condensation in the insulation. Hence, study of the behavior of the condensate in insulation is crucial to the understanding of the performance of insulated structures. As the condensate accumulates it migrates to other parts of the insulation. The liquid flux in a gravity-free environment is affected by the gradients in two thermodynamic potentials: liquid content and temperature. The migration of liquid in unsaturated porous bodies is caused by the action of capillary forces. The capillary forces cause the liquid to diffuse from regions of higher liquid content to drier regions (i.e., against the liquid content gradient). As the value of the surface tension of water increases with decreasing temperature the liquid migrates towards the colder side under the influence of temperature gradient.

In this paper a study of isothermal liquid diffusion in fibrous insulation in absence of gravitational forces is presented. The movement of liquid in a porous body depends strongly on the structure of the medium. By studying the physical attributes of the fiberglass insulation, a model based on an ordered array of filaments is developed. Liquid diffusion in the insulation is caused by the suction potential of the medium and retarded by the viscous forces. Each of those phenomena is studied individually and their combination used in the development of a diffusion theory. Experimental investigations are performed and the model is corroborated. The fiberglass batts used as thermal insulation in roofs and walls consist of layers of fiberglass filaments that are held together with a phenolic binder. The batts usually have a very high void fraction (95–99 percent), with binder accounting for as much as 20 percent of the weight. The fiberglass filaments have varying diameters with an average value of $3.56 \times 10^{-6}$ m. Each fiberglass layer differs from its adjacent layers in the volume of filaments and binder that it contains; and, hence, a different void fraction. The fiberglass filaments are dispersed randomly in each layer. However, the inspection of insulation under the microscope reveals that the number of fibers along the batt is slightly larger that that across the batt, and the number of fibers that are perpendicular to the batt and run from one layer to the other is very small, Fig. 1(*a*).

In sum, the fiberglass insulation is an inhomogeneous assemblage of fiberglass filaments and phenolic binder. The insulation is characterized by an anisotropic fiber density and a nonuniform void-fraction distribution.

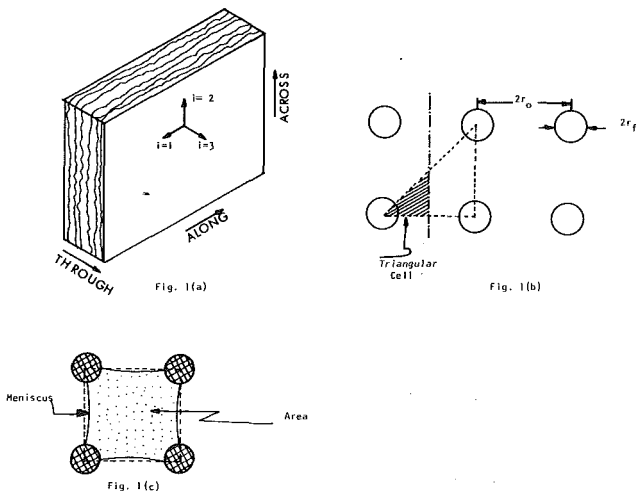


**Fig. 1 Schematic of insulation batts and fiber arrangement**

Contributed by the Heat Transfer Division for publication in the JOURNAL OF HEAT TRANSFER. Manuscript received by the Heat Transfer Division February 17, 1984. Paper No. 83-WA/HT-60.

## Model

The study of liquid diffusion in fiberglass insulation requires a model for the distribution of fibers. It is proposed that each fiberglass layer be considered as the basic element. The overall behavior of the insulation is determined by a large number of such layers.

Each layer is modeled as a matrix of ordered filaments, each with radius $r_f$. If $N$ denotes the total number of filaments in a cube of unit dimension, the void-fraction, $\bar{\epsilon}$, would be

$$\bar{\epsilon} = 1 - N\pi r_f^2 \tag{1}$$

The filaments are distributed, unequally, along the three orthogonal axes. The three axes are numbered 1, 2, 3 for along the layers, across the layers, and perpendicular to the layers, Fig. 1(*a*). The number of filaments in the direction $i$ ($i = 1, 2, 3$) is denoted as $n_i$, hence

$$\sum_{i=1}^{3} n_i/N = 1 \tag{2}$$

The term $n_i/N$ represents the ratio of fibers in direction $i$ to the total number of fibers. It is referred to as the directionality index.

Directional void fraction $\bar{\epsilon}_i$ is defined as the void fraction based only on the number of filaments parallel to direction $i$

$$\bar{\epsilon}_i = 1 - n_i/N.(1 - \bar{\epsilon}) \qquad i = 1,2,3 \tag{3}$$

The filaments are modelled to be arranged in a square array, Fig. 1 (*b*). Hence, the half-distance between adjacent filaments, $r_{oi}$ can be shown to be

$$\frac{r_{oi}}{r_f} = \sqrt{\frac{\pi}{4(1-\bar{\epsilon})}} \qquad i = 1,2,3 \tag{4}$$

**Suction Sites.** Liquid diffuses in the fibrous media by the action of capillary forces at the menisci formed by the placement of fibers relative to each other. The strength of the suction potential at such sites depends on the radius of curvature of the menisci. Hence the pressure drop across the menisci in the insulation can be represented as

$$\Delta P = 2\sigma\cos\theta/r_s \tag{5}$$

where $r_s$ is an equivalent "suction radius." In light of the layered arrangement of the fiberglass insulation, we focus on the fiber arrangement consistent with the square array model, Fig. 1(*c*), with the fibers forming the menisci being parallel and unidirectional. Since the surface tension force acts on one quarter of the perimeter of each fiber, and using equation equation (4), one finds the suction force per unit of the indicated area as

$$\left(\frac{F}{A}\right)_i = \frac{2\sigma\cos\theta(1-\bar{\epsilon}_i)}{r_f} \qquad i = 1,2 \tag{6}$$

Comparing equation (5) with (6) yields the equivalent suction radius

$$r_s = r_f/(1-\bar{\epsilon}_i) \quad i = 1,2 \tag{7}$$

**Viscous Drag.** The flow of liquid in a fibrous medium is retarded by the action of the viscous forces. In the following a model is developed which relates the pressure drop to the characteristics of the fibrous media.

In the square array model of the medium, the filaments are either parallel or perpendicular to the direction of flow. The model considers the flow to be the linear superposition of two flows: flow along an array of filaments, and flow across a bank of filaments. The superposition of the two flows assumes that the effect of one flow field on the other is negligible; the case which is readily encountered at flow through a medium with high void fraction. The total pressure drop is, then, the weighted sum of the pressure drops in the two flows.

In the viscous flow of a fluid along an array of filaments, the pressure drop is related to the velocity field. The velocity field is described by the following equation with the appropriate boundary conditions

$$\frac{dP}{dz} = \frac{-1}{\mu} \cdot \frac{d^2 u}{d^2 r} \tag{8}$$

To obtain the boundary conditions for the foregoing equation, a unit cell must be chosen such that the whole flow field can be reproduced by reflecting the cell on each of its sides. Sparrow [3] used a triangular cell, Fig. 1(*b*), and obtained the following expression for the flow field at high void fractions ($\bar{\epsilon} > .90$)

$$\frac{\bar{u}}{\frac{-1}{\mu}\frac{dP}{dz} r_f^2} = \frac{2\left[\zeta_i^4\left(\frac{1}{2\pi}\{\ln\zeta_i^2 + \ln 2 - 3\} + \frac{1}{6}\right) + \frac{1}{4}\zeta_i^2 - \frac{\pi}{64}\right]}{\zeta_i^4 - \frac{\pi}{4}} \tag{9}$$

where $\zeta_i$ is the nondimensional separation distance

$$\zeta_i = \sqrt{\frac{\pi}{4n_i/N(1-\bar{\epsilon})}} \qquad i = 1,2,3 \tag{10}$$

Happel [4] has shown that the flow across a bank of cylinders can be described as

$$\frac{\bar{u}}{\frac{-1}{\mu}\frac{dP}{dz} r_i^2} = \frac{\xi_i^2\left[\ln\xi_i - \frac{1}{2}\left(\frac{\xi_i^4 - 1}{\xi_i^4 + 1}\right)\right]}{4\pi} \tag{11}$$

where

## Nomenclature

$f$ = frequency distribution
$h$ = layer thickness
$k_i$ = directional permeability
$L_i$ = distance traveled along layer by diffusing liquid
$L_o$ = distance between two interconnections
$n_i$ = number of fibers per unit area in direction $i$
$N$ = total number of fibers in a cube of unit dimension
$p$ = pressure
$r$ = radial coordinate
$r_f$ = fiber radius
$r_o$ = half the distance between two fiber filaments
$r_s$ = equivalent suction radius
$r^*$ = equivalent diffusion radius
$u$ = average velocity
$z$ = coordinate in flow direction

**Greek Symbols**

$\alpha$ = liquid diffusivity
$\bar{\epsilon}$ = void-fraction for a layer of fibers
$\bar{\epsilon}_i$ = directional void fraction
$\epsilon_T$ = macroscopic void fraction
$\zeta$ = nondimensional distance
$\xi$ = nondimensional distance
$\theta$ = contact angle between liquid and medium
$\mu$ = liquid viscosity
$\rho$ = liquid density
$\sigma$ = liquid surface tension
$\tau$ = tortuosity

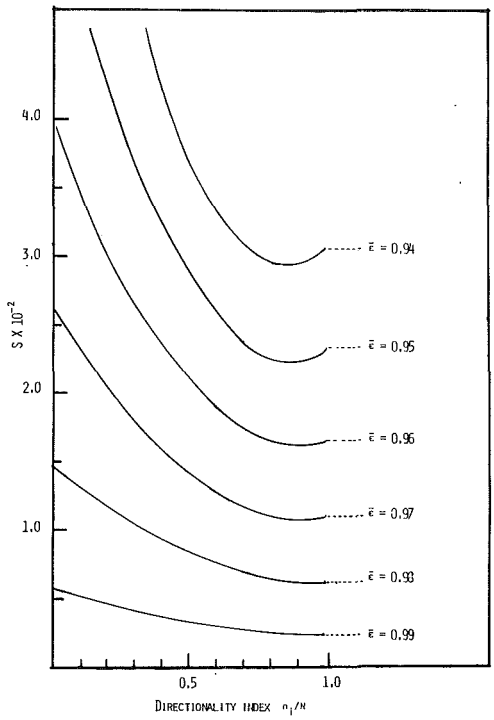


**Fig. 2** $S(n_i/N,\bar{\epsilon})$ **versus** $n_i/N$

$$\xi_i=\sqrt{\frac{\pi}{4[1-(n_i/N)\bar{\epsilon}}} \qquad i=1,2,3 \tag{12}$$

Denoting the drag force per unit length of cylinders parallel and perpendicular to the flow by $(F/L)_{11}$, and $(F/L)_{\perp}$, respectively, the pressure drop can be written as

$$\left(\frac{\Delta P}{L}\right)_i=n_i\left(\frac{E}{L}\right)_{11}+(N-n_i)\left(\frac{F}{L}\right)_{\perp} \qquad i=1,2,3 \tag{13}$$

Using equation (1) we have, in a succinct form

$$\left(\frac{\Delta P}{L}\right)_i=\frac{4\bar{u}\mu_i}{r_f^2}S(n_i/N,\bar{\epsilon}) \qquad i=1,2,3 \tag{14}$$

where $S$ is the parameter denoting the terms that represent the effect of fiber orientation and medium void fraction:

$$\frac{S(n_i/N,\bar{\epsilon})}{(1-\bar{\epsilon})}=\frac{(1-n_i/N)\pi}{\ln\xi_i-\frac{1}{2}\left(\frac{\xi_j^4-1}{\xi_i^4+1}\right)}$$

$$+\frac{(n_i/N)\zeta_i^2\left(\zeta_i^2-\frac{\pi}{4}\right)}{8\left[\zeta_i^4\left(\frac{1}{2\pi}\ln\zeta_i^2+\ln 2-3\{+\frac{1}{6}\right)+\frac{1}{4}\zeta_i^2-\frac{\pi}{64}\right]} \tag{15}$$

In Fig. 2, a plot of $S$ versus $n_i/N$, with $\bar{\epsilon}$ as the parameter is given. As shown, $S$ demonstrates a very strong dependence on $\bar{\epsilon}$. At a given $\bar{\epsilon}$, the value of $S$ decreases as $n_i/H$ increases up to a critical value, beyond this value of $n_i/N$ the value of $S$ increases.

Equation (14) can be written in the more familiar form of Darcy's equation

$$\bar{u}=\frac{-1}{\mu}\cdot\begin{bmatrix}k_1&0&0\\0&k_2&0\\0&0&k_3\end{bmatrix}\cdot\begin{bmatrix}dP/dx_1\\dP/dx_2\\dP/dx_3\end{bmatrix} \tag{16}$$

with the directional permeabilities $k_i$ given by

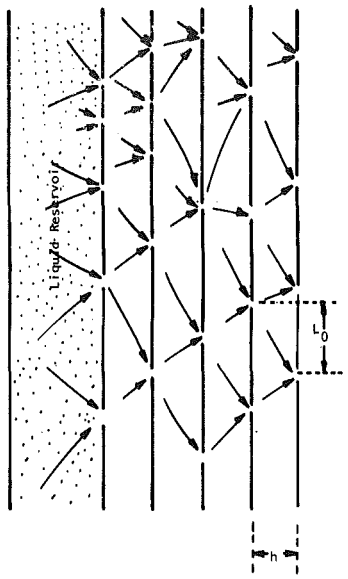


**Fig. 3 Liquid diffusion pattern through the layers**

$$k_i=\frac{r_f^2}{4S(n_i/N,\bar{\epsilon})} \qquad i=1,2,3 \tag{17}$$

**Diffusion In Fibrous Media.** The diffusion process is controlled by the balance of surface tension forces with the viscous forces. In the case of diffusion in layered fibrous-media, diffusion from one layer to the other is more complex than diffusion along the layers. For this reason diffusion in the two directions will be discussed separately.

*Diffusion Along Layers.* Using equations (5) and (14), the balance of viscous forces with surface tension forces yields

$$\frac{4\mu S(n_i/N,\bar{\epsilon})}{r_f^2}\bar{u}_i=\frac{2\sigma\cos\theta}{r_s\ L_i} \qquad i=1,2 \tag{18}$$

where $L_i$ is the length of the diffused front in the $i$-direction. Recognizing that $u_i=dL_i/dt$, then

$$L_i=\sqrt{\frac{\sigma\cos\theta}{\mu}\cdot\frac{r_f^2}{S\,r_s}\cdot t} \qquad i=1,2 \tag{19}$$

Using equation (7), which relates $r_s$ to the properties of the medium, with equation (18), yields

$$L_i=\sqrt{\frac{\sigma\cos\theta}{\mu}\cdot\frac{(1-\bar{\epsilon})n_i/N}{S(n_i/N,\bar{\epsilon})}\cdot r_f\cdot t} \qquad i=1,2 \tag{20}$$

Equation (20) describes liquid diffusion along and across the fiberglass layers, $i=1,2$, where the majority of the menisci are of the type that relate to equation (7).

Equation (20) can be written in a succinct form, first proposed by Washburn [5] for flow of liquids in capillaries:

$$L_i=\sqrt{\alpha r_i^* t} \quad i=1,2 \tag{21}$$

where $\alpha$ is the liquid diffusivity

$$\alpha=\sigma\cos\theta/2\mu \tag{22}$$

and $r_i^*$ is the equivalent "diffusion radius"

$$r_i^*=\frac{2(1-\bar{\epsilon})n_i/N}{S(n_i/N,\bar{\epsilon})}\cdot r_f \quad i=1,2 \tag{23}$$

Equation (23) identifies and isolates the medium properties that control the liquid diffusion in the fibrous media. The three independent variables are the void fraction, directionality index, and the fiber radius.

*Diffusion Through Layers.* Liquid diffuses along the fibrous layers due to the action of capillary forces. However,

there does not exist a well-defined suction site distribution which would promote liquid diffusion from one layer to the adjacent one. The percentage of fibers which pass through adjacent layers is very small, and hence are not capable of forming the necessary suction sites. It is the opinion of the authors that liquid diffuses from one layer to the next, as shown in Fig. 3. Certain points exist that "connect" the two adjacent layers, and the liquid is capable of diffusing from one layer to the other through these interconnections. The liquid has to travel a length $L_o$ along a layer before reaching an "interconnection." Physically, the interconnections are points that certain fibers from a layer deviate and approach or merge into the next layer such that there exists a continuous path for the liquid to diffuse from one layer to the other. It should be borne in mind that in each layer the fibers are so intermingled as to render a differentiation between movement along and across a layer redundant. Hence the liquid diffusion from one interconnection point to the other is characterized by the equivalent diffusion radius $r^*$ as defined in equation (23).

The time that it takes for the liquid to move between two interconnection points is, in view of equation (21),

$$t = \frac{(L_o + h)^2}{\alpha r_i^*} \tag{24}$$

Rearranging equation (24) yields

$$h = \sqrt{\alpha r_i^* \left[ \frac{1}{(L_o/h+1)^2} \right]_t} \tag{25}$$

Equation (25) is of the form of equation (21). The term in the brackets in equation (25) is the square of the ratio of minimum distance through layers to the characteristic distance traveled by a water particle and is defined as the tortuousity factor, $\tau$:

$$\tau = \frac{1}{(L_o/h+1)^2} \tag{26}$$

The tortuosity factor is a property of the medium and is the measure of the extent of the interconnectedness of adjacent layers.

**Effect of the Nonuniformity of Void Fraction.** Equations (7), (12), and (23) show that the equivalent suction radius, pressure drop, and liquid diffusion radius have a parametric dependence on the void fraction $\bar{\epsilon}$. However, $\bar{\epsilon}$ is not uniform in the fiberglass insulation. The variations of void fraction in the medium can be represented by a spatial frequency distribution, with the constraints that

$$\int_0^1 f(\bar{\epsilon}) d\bar{\epsilon} = 1$$

$$\int_0^1 \bar{\epsilon} f(\bar{\epsilon}) d\bar{\epsilon} = \epsilon_T \tag{27}$$

where $\epsilon_T$ is the macroscopic void fraction of the medium. In the one-dimensional model the insulation consists of many layers with different void fractions. Hence, according to equation (7) and (14) there will exist distributions $f(r_s)$ and $f(S)$, which correspond to the void fraction distribution $f(\bar{\epsilon})$.

In considering the pressure drop along a layered fibrous medium it should be recognized that the layers offer varying amounts of resistance to the flow. The layers can be considered to be in parallel with each other. Therefore

$$S_{eq}(n_i/N, \epsilon_T) = \left[ \int_0^1 \frac{f(\bar{\epsilon}) d\bar{\epsilon}}{S(n_i/N, \epsilon)} \right]^{-1} \tag{28}$$

It is well known that when a number of resistances are placed in parallel with each other, the equivalent resistance is smaller than each of the original resistances. Hence the value of $S$, for a given void fraction and directionality index, obtained on the basis of a square array, Fig. 1(*b*), is the maximum value that any fibrous medium, with the same void fraction and $n_i/N$, will have. Any nonuniformity in the spacing in-between the fibers will cause a decrease in the viscous resistance to flow.

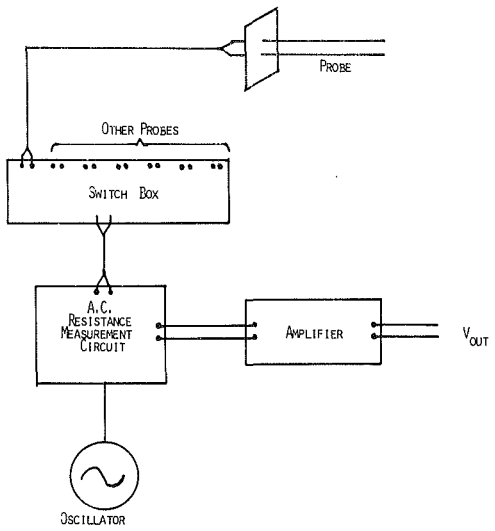


**Fig. 4 Schematic of the probe and associated electronics circuit**

The $r^*$-distribution for a medium of many layers can be calculated from a knowledge of the $\bar{\epsilon}$-distribution and the directionality index. However, such a calculation presumes no coupling between adjacent layers. As liquid diffuses along layers, with different $r^*$'s, it creates a transverse pressure variation in the direction of $i = 3$. Liquid will flow through the layers in such a manner as to decrease the pressure variations. Hence, liquid diffusion in interconnected layers will be characterized by an $r^*$-distribution different from the one calculated by equation (23). It has been shown that when two capillaries of unequal radii are interconnected the rate of liquid diffusion in the two coupled capillaries is different from the diffusion rate in the two otherwise isolated capillaries [6]. However, the behavior of many interconnected capillaries is difficult, if not impossible, to solve analytically and no experiments exist to show any specific trend. It can be surmised that the effect of the coupling will be to cause a general decrease in the strength of the suction potential, which translates to smaller $r^*$ values. Furthermore, the coupling will cause the $r^*$-distribution to become more flat and less peaked, as the decrease in the value of $r^*$ will be more pronounced at its higher values. However, the difference between the $r^*$-distribution, calculated by equation (23) for some $\bar{\epsilon}$-distribution, from the distribution that would have incorporated the effect of coupling should not be so large as to mask the overall behavior predicted by the model.

## Experimental Results and Data Analysis

Experiments were conducted to make quantitative measurements of the behavior of liquid in the insulation. The experiments were conducted on two types of fiberglass insulation: a "heavier" and a "lighter" one with macroscopic void-fraction values of 0.945, and 0.982 respectively. The experiments were conducted to measure the suction-radius distribution, pressure drop-flow rate relationship, and the diffusion-radius distribution. Electronic liquid-content measurement probes were developed and a special liquid prepared for use in the experiments. In the following a description of the probes, the liquid, and the three sets of experiments are given.

**Liquid Content Probes.** Probes have been developed which are capable of making instantaneous insitu measurement of liquid content in fibrous insulation. The probe, Fig. 4, consists of two stainless steel rods of 0.46 mm

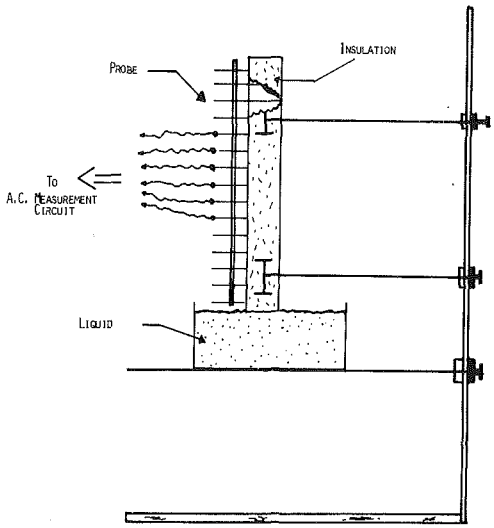


**Fig. 5 Schematic of experiment on measurement of suction-radius in insulation samples**

dia spaced 6.26 mm apart. The electrical resistance across each probe pair is measured by an a-c resistance measurement circuit. As the amount of liquid bridging the two rods changes, the probe resistance and thus the output voltage of the circuit changes. Hence by the proper installation and calibration of the probes instantaneous values of liquid content averaged over the probe measuring volume can be obtained. In any experiment a number of such probes is employed. An electronic switching system scans the set of probes continuously, and the output voltage is recorded on a chart recorder. The probe was found to make very good measurements at higher liquid contents. In the region of lower liquid contents, as the liquid "bridges" begin to break up, (liquid contents up to approximately 10 percent), the measurement errors become appreciable.

**The Liquid.** As mentioned above, the liquid content measurement probes work on the basis of measuring the electrical resistance of the liquid that bridges the probe. This requires that the electrical resistivity of the liquid be constant. However it has been found that the phenolic binder dissoves in water and causes strong changes in its electrical resistivity. To overcome this problem distilled and de-ionized water was mixed with insulation pieces and brought to boil. The liquid was allowed to boil for a period of time so that it would become saturated with the binder. It was then cooled to room temperature and filtered. The liquid was, then, saturated at room temperature and would not accept any more binder as it came in contact with the insulation. The density and the viscosity of the liquid were found to be, within the range of experimental error, identical with those of pure water. The value of the quantity $\sigma\cos\theta$ was measured by capillary rise in a glass tube and found to be 73 dynes/cm at room temperature, an increase of 10 percent over that of pure water.

**Measurement of Suction-Radius Distribution.** In order to measure the suction-radius distribution samples of the fiberglass insulation were allowed to absorb the liquid against gravity, Fig. 5. The experiment was conducted along, across, and through the layers. The steady-state height that the liquid reached reached was recorded with the aid of the probes and by visual observation. The experiments on absorption along and across the layers were carried out on 17 different samples for both insulation types. Six samples were used in experiments on flow through the layers. The observed frequency distributions of the liquid columns in the samples were aggregated to yield a total frequency distribution. This

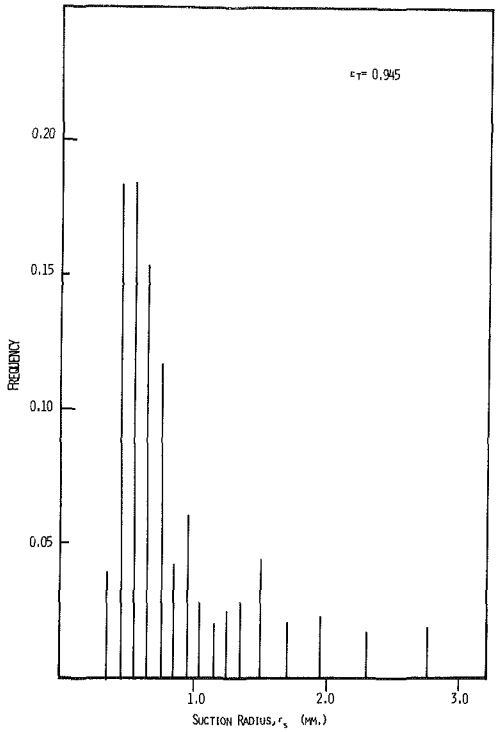


**Fig. 6 Suction-radius distribution**

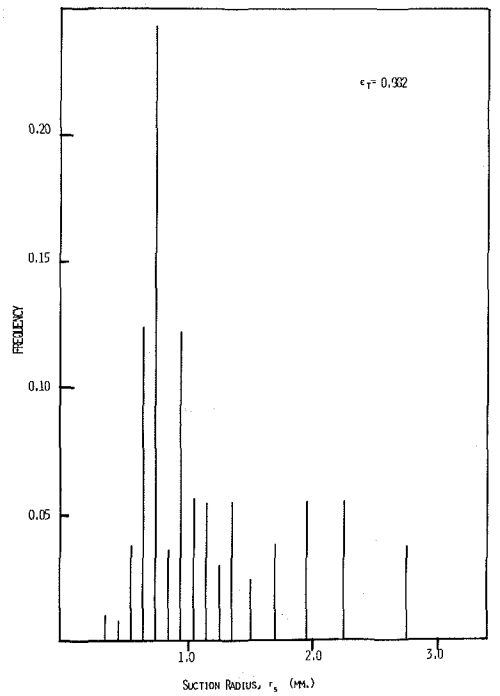


**Fig. 7 Suction-radius distribution**

combined distribution was then translated to a distribution of the suction radius through the following balance

$$\rho g h = 2\sigma\cos\theta / r_s$$

The frequency distribution of the suction-radius in the directions along and across the fiber layers were not observed to be substantially different. The frequency distribution along the fiber layers for the two types of insulation are shown in Figs. 6 and 7. The samples were found to absorb liquid through the layers to a uniform height. The liquid rose *through* the layers to a height of 1.6 cm and 1.3 cm for the heavier and lighter insulation, respectively.

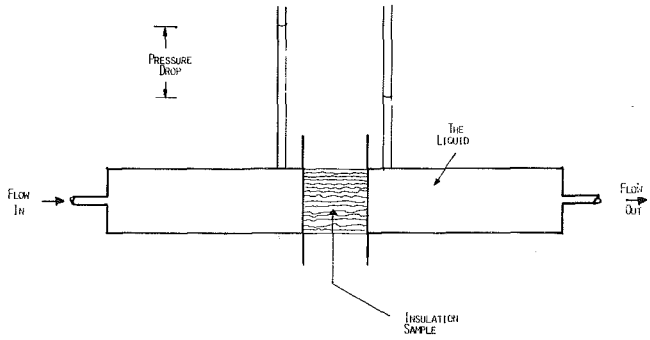


Fig. 8 A schematic of experiment on measurement of pressure drop versus flow rate relationship

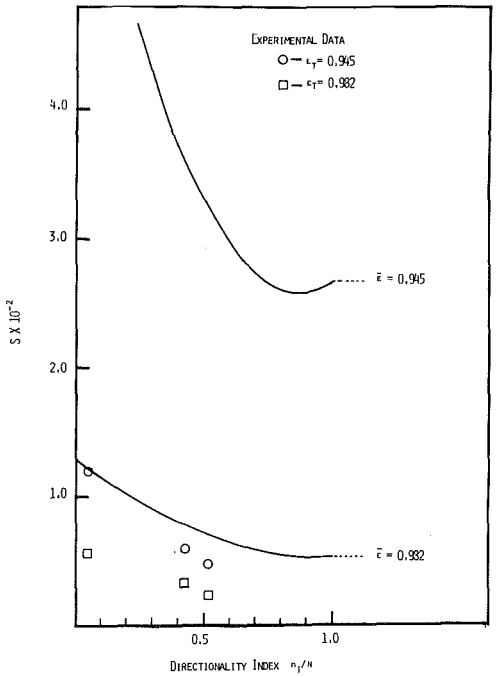


Fig. 9 Comparison of experimental data on $S(n_i/N,\bar{\epsilon})$ with theoretical prediction based on a homogeneous void-fraction distribution

**Measurement of Pressure Drop.** A schematic of the apparatus used to measure the pressure drop associated with the flow of the liquid in the insulation is shown in Fig. 8. The apparatus consists of two chambers that are separated by a piece of insulation. The four sides of the insulation which are not in contact with the two chambers are impermeable to liquid flow. Liquid is pumped through the insulation and the flow rate is measured. Two vertical tubes are connected to the two chambers close to the insulation. The pressure drop across the insulation is measured by the differential rise of liquid in the vertical tubes. Experiments were conducted on the three directions for the two insulation types. In contrast to the $r^*$-distribution, the pressure-drop across and along the layers showed an appreciable difference. The experimental results were reduced to yield values for the $S$ factor of equation (14). The experimental results are shown against the background of the theoretical predictions for *homogeneous* medium in Fig. 9. The directionality index, $n_i/N$, is not easily definable for the samples. However, microscopic observations reveal that the ratios 53, 42, and 5 percent for both insulation types are reasonable. Hence, these values are used when reference is made to the directionality index in either of the three directions.

**Measurement of the Diffusion Phenomenon.** The experiments on diffusion rates were conducted only on one

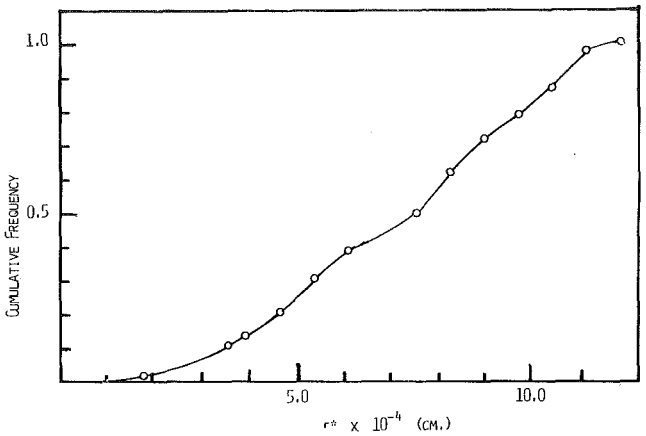


Fig. 10 Cummulative frequency distribution of the diffusion radius, $r^*$

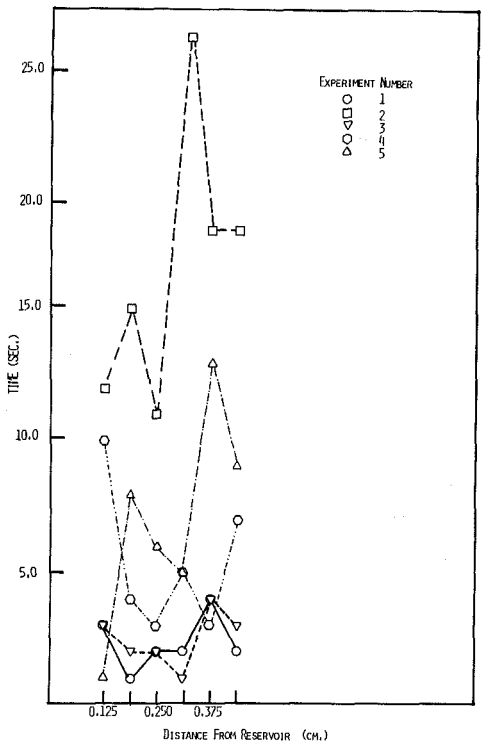


Fig. 11 Travel time between succeeding probes

insulation type, $\epsilon_T = 0.945$. This is because the samples used in this experiment were made as thin as possible so that the effect of the hydrostatic head on the diffusion pattern be negligible. However, as the samples of the lighter insulation were cut into thin sections, they would lose their structural integrity and the layers would separate. Although some data has been taken with this insulation and reported in [7], the experimental results are highly uncertain and are not reported here.

Two different techniques were employed for the experiment across, along, and through the layers. In the experiment of liquid diffusion along the across the layers the samples were held horizontally. The liquid was introduced at one end of the sample and allowed to diffuse along the layers. As the liquid diffused along the layers, photographs of the sample were taken at varying time intervals. The photography technique was used because as the liquid traveled along the layers the color of the sample would change sufficiently to allow an accurate measurement of the diffusion front. Each photograph would yield a frequency distribution for the lengths traveled by the diffusing liquid. Using this frequency

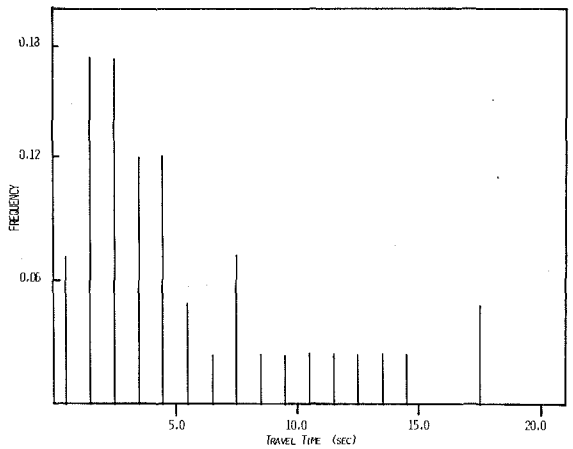


**Fig. 12 Frequency of travel time between succeeding probes (compiled from seven experiments)**

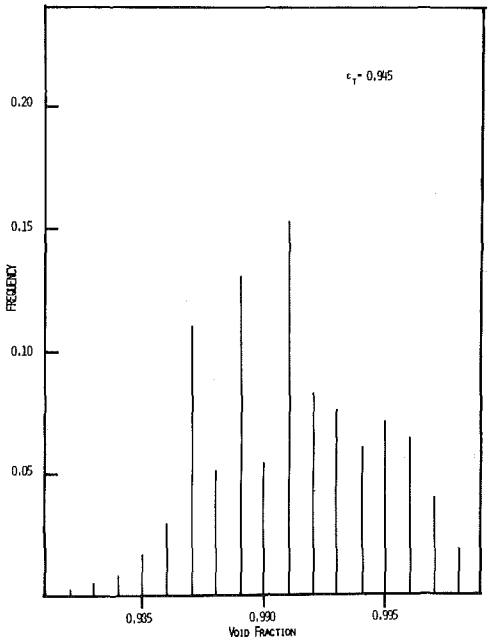


**Fig. 13 Void fraction distribution**

distribution, the time that corresponds to it, and equation (21), the frequency distribution for the diffusion radius $r^*$ can be obtained. The result shown in Fig. 10 is for diffusion along the layers, $n_i/N = 0.52$.

In the study of diffusion from one layer to the other, the liquid-content measurement probes were used. Several probes were put in series and were inserted into the sample, such that the probe series be parallel with the layers. The liquid was introduced to one layer and allowed to diffuse through the layers. The probes would record the amount of liquid that was present at each location as a function of time. In Fig. 11 the times that it would take for the liquid to diffuse from one probe to the next, separated by 6.35 mm, is presented. As it can be seen, for a given experiment the travel time between two succeeding groups of probes not only does not increase uniformly but shows strong irregularity. Were the tortuosity factor of equation (26) uniform the travel time would have increased monotonically as the liquid front traveled a larger distance away from the reservoir. However, the irregular pattern suggests that not only is the tortuosity not constant, but its variations are so strong that they overshadow the effect of increased length as the front moves forward. The travel time between *any* two adjacent groups of probes was recorded for several experiments, Fig. 12. This figure indicates that there exists a noticeable distribution of travel times when a

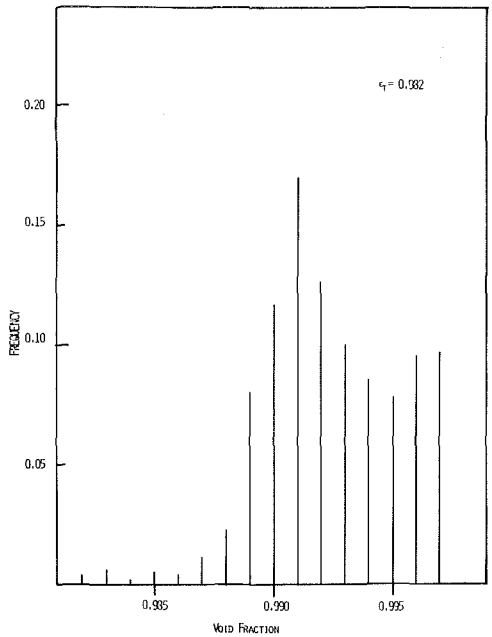


**Fig. 14 Void fraction distribution**

statistically large number of observations are compiled. The data on the travel time can be reduced, using equation (25), to generate a frequency distribution for the product $r^*\tau$. It can be shown that given the frequency distribution of a product $r^*\tau$ and the frequency distribution of one of the terms, namely $r^*$, a unique frequency distribution for the other term $\tau$ cannot be obtained. However, if it is assumed that the two parameters $r^*$ and $\tau$ are statistically independent, then the average of their product equals the product of their averages.

$$\overline{r^*\tau} = \overline{r^*} \cdot \overline{\tau} \tag{29}$$

Using an average value of $7 \times 10^{-4}$ for $\overline{r^*}$, we have

$$\bar{\tau} = 3.45 \times 10^{-2}$$

or

$$L_o/h = 4.38$$

This value of $L_o/h$ is very reasonable. Using an average value of 2 mm for $h$, the number of interconnections between layers is about 1 per cm.

## Discussions

In the development of models for diffusion of liquids in fibrous masses it was noted that there are five independent variables: the void-fraction and its spatial distribution; the directionality index $n_i/N$; the fiber radius $r_f$, and the tortuosity factor, $\tau$. The model is capable of predicting the experimental observations once the five independent variables are defined. The macroscopic void fraction, the directionality indices, and the fiber radius are known within an acceptable accuracy. Hence the model needs as the input the void-fraction distribution and the tortuosity factor to predict the experimental results. Considering the experiments along the layers, one of the three experimental results ($r_s$-distribution, $S$, or $r^*$-distribution) can be used to establish the void-fraction distribution.

Of the three experimental results, the $r_s$-distribution is used to yield the $\bar{\epsilon}$-distribution, and the other two results are predicted.[1]

[1] In [7] the observed values of $S$ and $r^*$-distribution are each used separately to yield the void-fraction distribution, and predict the other two experimental results. The model predicts the experimental results with varying degrees of success.

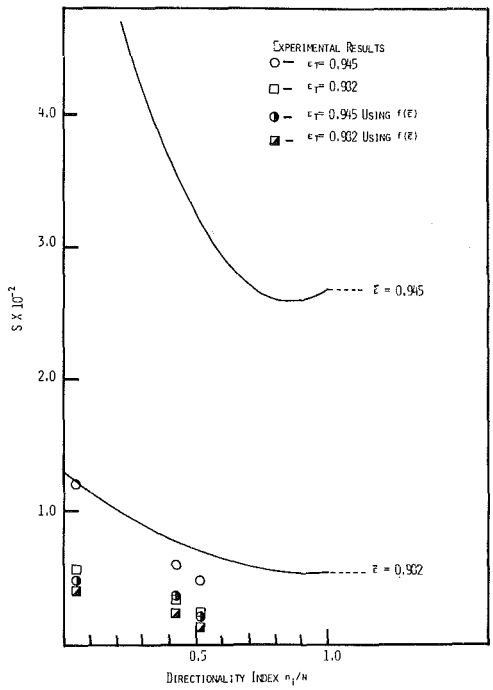


**Fig. 15 Comparison of values of $S(n_i/N, \bar{\epsilon})$ using $f(\bar{\epsilon})$ with experimental observations**

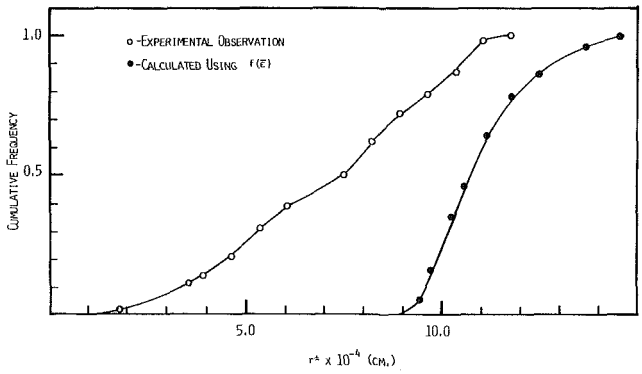


**Fig. 16 Comparison of the diffusion-radius distribution computed using $f(\bar{\epsilon})$ with the experimental observation**

The observed frequency distributions of the suction radius are used to calculate the void-fraction distributions for the two types of insulation, Figs. 13 and 14. The $\bar{\epsilon}$-distributions are then used to generate corresponding distributions for the $S$ term. The total pressure drop along and across the layers is, then, calculated according to equation (14). The value of $S$ corresponding to flow through the layers is generated by placing the resistances in series and obtaining the equivalent resistance. The calculated values of $S$ compare very well with the observed values, Fig. 15. As mentioned before, the effect of parallel layers, each offering a different resistance to flow is to decrease the overall flow resistance. This can be observed by the difference between the values of $S$ calculated on the basis of the $\epsilon$-distributions and the ones based on the macroscopic value of the void fraction. The $r^*$ distribution, for the insulation type with $\epsilon_T = 0.942$ calculated using the void-fraction distribution, is presented on Fig. 16, and compared with the observed distribution. The comparison indicates that although the experimental values of $r^*$ cover a range wider than the calculated ones, the agreement between the two is appreciable. The calculated distribution is based on the assumption that the capillaries are not interconnected. As explained in the section on effects of nonuniformity of void fraction, the coupling between the layers leads to an overall decrease in the value of the diffusion radius and the flattening of its distribution. These effects present themselves in the comparison of experimental and calculated distributions of $r^*$.

In general, the prediction of liquid diffusion in the fibrous insulation based on the proposed model has been successful to a large extent.

## Conclusion

A model for isothermal liquid diffusion in fibrous insulation has been developed and verified with experimental results. The model identifies the insulation properties that control the diffusion dynamics as the void-fraction and its distribution, fiber radius, directionality index, and the tortuosity factor. A method for in situ measurement of liquid content in insulation was used to acquire data on two types of fiberglass insulation. For each type, the macroscopic void fraction, directionality indices, and fiber radius are known. The experimental results yielded the tortuoisty factor and void-fraction distribution.

The predictions based on the model are in satisfactory agreement with the experimental observations.

## References

1 Hutcheon, N. B., "General Report: Influence of Moisture on Thermal Properties of Materials, Building Products, and Building Elements," *First International CIB/RILEM Symposium on Moisture Problems in Buildings*, Paper No. 4-0, Helsinki, 1965, pp. 1-15.

2 Bauer, W., "Influence of Holes on Water-Vapor Permeability of Vapor—Checking Surface Layers," *First International CIB/RILEM Symposium on Moisture Problems in Building*, Paper No. 2-21, Helsinki, 1965, pp. 1-6.

3 Sparrow, E. M., and Loeffler, A. L., Jr., "Longitudinal Laminar Flow Between Cylinders Arranged in Regular Array," *AIChE Journal*, Vol. 5, No. 3, 1959, pp. 325-330.

4 Happel, John, "Viscous Flow Relative to Arrays of Cylinders," *AIChE Journal*, Vol. 5, No. 2, 1959, pp. 174-177.

5 Washburn, E. W., "The Dynamics of Capillary Flow," *Physical Review*, Vol. XVII, Series II, No. 3, 1921, pp. 273-283.

6 Kremnev, O. A., et al., "Flow Through Interconnected Capillaries," *Fluid Mechanics Soviet Research*, Vol. 5, No. 1, 1976, pp. 17-22.

7 Motakef, S., "Simultaneous Heat and Mass Transfer with Phase Change in Insulated Structures," Ph.D. thesis, M.I.T., May 1984.

# Heat Transfer From Rectangular Plates Inclined at Different Angles of Attack and Yaw to an Air Stream

D. G. Motwani

U. N. Gaitonde

S. P. Sukhatme

Department of Mechanical Engineering,
Indian Institute of Technology,
Bombay 400076, India

*Average heat transfer coefficients during forced convection air flow over inclined and yawed rectangular plates have been experimentally determined. Tripping wires at the edges ensured that a turbulent boundary layer prevailed over the plates. The experiments were carried out for a constant surface temperature and covered two plates of different aspect ratios, angles of attack from 0 to 45 deg, angles of yaw from 0 to 30 deg, and Reynolds numbers from $2 \times 10^4$ to $3.5 \times 10^5$. The results show that the average heat transfer coefficient is essentially insensitive to the aspect ratio and angle of yaw. However, it is a function of Reynolds number and the angle of attack. Correlation equations for various angles of attack are suggested.*

## Introduction

The present heat transfer study is concerned with the three-dimensional behavior of a turbulent boundary layer on a flat plate oriented to an oncoming air stream at various angles of attack and yaw. The well-known wedge-flow studies are for a two-dimensional situation and are consequently applicable to plates extending to infinity in the span-wise direction. Experimental studies on laminar two-dimensional flows over inclined plates were conducted by Drake [1], Braud [2], and Test et al. [3]. While Drake [1] and Test et al. [3] have used special side attachments on a finite span plate to obtain a two-dimensional flow, Braud [2] did experimentation in the central portion of an inclined roof where the air flow pattern was essentially two-dimensional.

In contrast to these studies, the only known studies on the three-dimensional flow over an inclined plate are from Sparrow and his co-workers [4, 5]. The motivation behind their work was the need for obtaining suitable correlations for the wind heat transfer coefficient on the cover of a solar flat plate collector. Based on their extensive mass transfer experiments on square and rectangular plates held in a wind tunnel, they suggested a global correlation of the form

$$j = 0.86(\mathrm{Re})^{-0.5}; \quad 2\times10^4 < \mathrm{Re} < 10^5; \qquad (1)$$

$$25 \text{ deg} \le \alpha \le 90 \text{ deg}, \; 0 \text{ deg} \le \Phi \le 45 \text{ deg}$$

The exponent $-0.5$ on Re in equation (1) suggests the presence of a laminar boundary layer in Sparrow's experiments. The purpose of the present investigation is to provide a similar correlation or correlations for a three-dimensional turbulent boundary layer on the plate. The experiments for determining average Nusselt numbers have been conducted for constant surface temperatures over Reynolds numbers ranging from $2 \times 10^4$ to $3.5 \times 10^5$, angles of attack varying from 0 to 45 deg, and angles of yaw from 0 to 30 deg. Aspect ratios of 2/3 (AR I) and 3/2 (AR II) have been used.

## Experimental Work

**Apparatus.** A low-turbulence open-circuit wind tunnel was used for obtaining the experimental data. It had a 61-cm-square cross section. The turbulence intensity was ascertained by a DISA hot-wire anemometer system. The measurements were made with the test apparatus in the wind tunnel at the highest angle of attack of 45 deg, the hot-wire probe being located 90 cm and 45 cm upstream. It was found that the turbulence intensity decreased from about 1% to about 0.3% as the velocity increased from 1 to 24 m/s and that similar values were obtained at both locations. Almost identical values were measured in the unobstructed wind tunnel without the test apparatus.

Figure 1 shows a schematic diagram of the test apparatus. A polished aluminum plate (3 mm thick) having dimensions of 300 × 200 mm was used as the test plate. Nichrome wire (14.4 ohm/m) uniformly and closely wound on a mica sheet was used for heating the plate. A guard heater was used to minimize the heat loss from the bottom. The guard heater was separated from the test plate and its heater by an insulating Bakelite plate, 6 mm thick, sandwiched between two copper sheets (3 mm). Bakelite strips (3 mm thick) were fixed on all the four edges of the test plate. A G.I. sheet (1.5 mm) was fixed all around to give rigidity to the entire assembly. An additional 15-mm-thick "Thermocole" slab, beveled at the top, was used in order to reduce heat losses from the side edges of the plate. The overall dimensions of the assembly were 339 mm × 239 mm × 22.5 mm thick. The test plate assembly was supported on an adjustable aluminum-angle stand within the wind tunnel and the stand adjusted to fix the angle of attack ($\alpha$) at 0, 15, 30, or 45 deg and that of yaw ($\Phi$) at 0, 15, or 30 deg. The orientation angles, i.e., the angles of attack and yaw, are illustrated in Fig. 2. The reference situation of zero attack and zero yaw is shown in Fig. 2(*a*) with dotted lines, the angle of attack being set by rotating the plates PQRS about axis OY. The angle of yaw is now set by

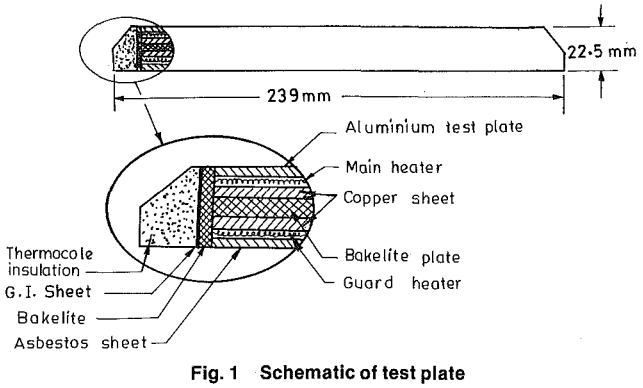


**Fig. 1 Schematic of test plate**

Contributed by the Heat Transfer Division for publication in the JOURNAL OF HEAT TRANSFER. Manuscript received by the Heat Transfer Division September 7, 1983.

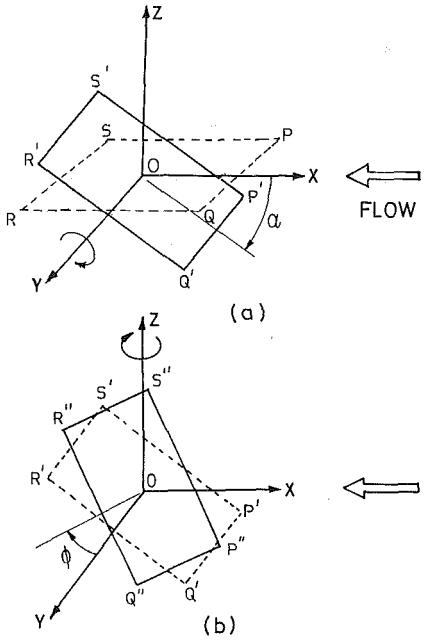


**Fig. 2 Description of plate orientation in terms of angle of attack and yaw, $\alpha$ and $\Phi$**

rotating P′Q′R′S′ ($\alpha$, $\Phi$ = 0) about the axis OZ, Fig. 2($b$). In order to ensure a turbulent boundary layer, tripping wires (0.8 mm dia.) were fixed on all edges having an incoming flow. Thus, for example, for a run having an inclined and yawed plate, tripping wires were placed on the edges PQ and PS.

Temperatures were measured with the help of copper-constantan thermocouples made from 30 gauge wires. Six thermocouples were fixed in thin slots (2 mm deep) cut on the underside of the test plate and were used for measuring its temperature. Thus the temperatures were measured at a depth of about 1 mm from the top surface. Nevertheless these values can be taken to represent the temperatures on the top surface because of the use of an aluminium test plate. It is estimated that the maximum difference between the top surface temperatures and the measured values would be less than 0.01°C. The use of an aluminium test plate coupled with a closely wound heater also ensured that the desired condition of a constant surface temperature was obtained. Measurements in the main series of tests show that the variation in plate surface temperature was almost always less than 3% of the difference between the average plate temperature and the free-stream temperature. A 12-junction thermopile was used to monitor the temperature difference across the Bakelite plate. Three thermocouples were also fixed to the inside surfaces of the wind tunnel duct in order to ascertain the wall temperature, which was required for making the radiation correction. Two thermocouples held in the air stream inside the duct just ahead of the test plate measured the free-stream temperature. A Hewlett-Packard digital multimeter (3465 A), which read up to 0.001 mV was used to measure the thermocouple emf. The thermocouple wire used was calibrated at the steam and ice points.

The velocity was measured at the center of the duct with the help of a Prandtl-Pitot tube and a micromanometer. The accuracy of measurement of the velocity is estimated to be ±1.5%. The uniformity of velocity across the tunnel section was checked. The variation was less than the estimated accurcy of measurement.

The power input to the main heater as well as the guard heater was obtained from two separate regulated power supplies, 0−30 V DC. The power to the main heater was obtained by measuring the voltage drop across the heater, the current through it being ascertained by the voltage drop across a standard resistor placed in series. The Hewlett-Packard multimeter was used for both these measurements.

**Experimental Procedure.** The plate was fixed at a particular angle of attack and yaw, and the velocity set at a desired value. For a fixed main heater input, the guard heater input was regulated so as to maintain as small a temperature difference as possible (<0.1°C) across the Bakelite plate, thereby ensuring that the heat flow from the bottom was negligible.[1] A steady state was usually achieved after about two hours. The average convective heat transfer coefficient was determined from the expression

$$h = \frac{Q_c}{A\,\Delta T} = \frac{Q_{\text{test}} - Q_r - Q_s - Q_b}{A\,(T_p - T_\infty)} \tag{2}$$

**Calibration Tests.** In order to determine the heat lost by radiation ($Q_r$) and the heat lost from the side edges ($Q_s$), it was necessary to conduct two sets of calibration tests. The first set was aimed at determining the emissivity of the test plate surface. The measurements were made on a separate setup available in the laboratory and yielded an average value of emissivity of 0.24 ± 0.02 around a temperature of 320 K. This temperature corresponded approximately with the temperature of the test plate during the main experiment. No significant dependence of emissivity on temperature was observed. As such, the average value was used for determining $Q_r$ in the main series of tests. It is estimated that the

[1] The 12-junction thermopile used for this purpose had six junctions on each side. The junctions were located at the centers of six imaginary equal rectangular areas into which the plate was divided. Thus the average of six local temperature differences was obtained. Typically even when the average temperature difference across the Bakelite plate was less than 0.1°C, some local imbalances occurred with the top side of the Bakelite plate being at a higher temperature in some cases and the reverse occurring in the others. The local imbalances rarely exceeded 0.5°C. The heat flow on account of these temperature differences was negligible. In any case, it was corrected for through the term $Q_b$ in equation (2).

## Nomenclature

$A$ = plate area
AR I = designates span/chord length ratio of 2/3
AR II = designates span/chord length ratio of 3/2
$C$ = circumference of the plate
Gr = Grashof number
$h$ = average heat transfer coefficient
$j$ = $j$-factor, St $\text{Pr}^{2/3}$
$k$ = thermal conductivity
$L$ = chord length
$L^*$ = characteristic length, $4A/C$
Nu = Nusselt number, $hL^*/k$
$\text{Nu}_L$ = Nusselt number, $hL/k$
Pr = Prandtl number
$Q$ = heat loss from the plate
$Q_{\text{test}}$ = power input to test plate
Re = Reynolds number, $u^*L^*/\nu$
$\text{Re}_L$ = Reynolds number, $u^*L/\nu$
St = Stanton number
$T_p$ = average plate temperature
$T_\infty$ = free-stream temperature
$\Delta T$ = temperature difference, $T_p - T_\infty$
$u^*$ = local average free stream velocity
$\alpha$ = angle of attack
$\nu$ = kinematic viscosity
$\Phi$ = angle of yaw

**Subscripts**

$b$ = bottom
$c$ = convective
$r$ = radiative
$s$ = side edges

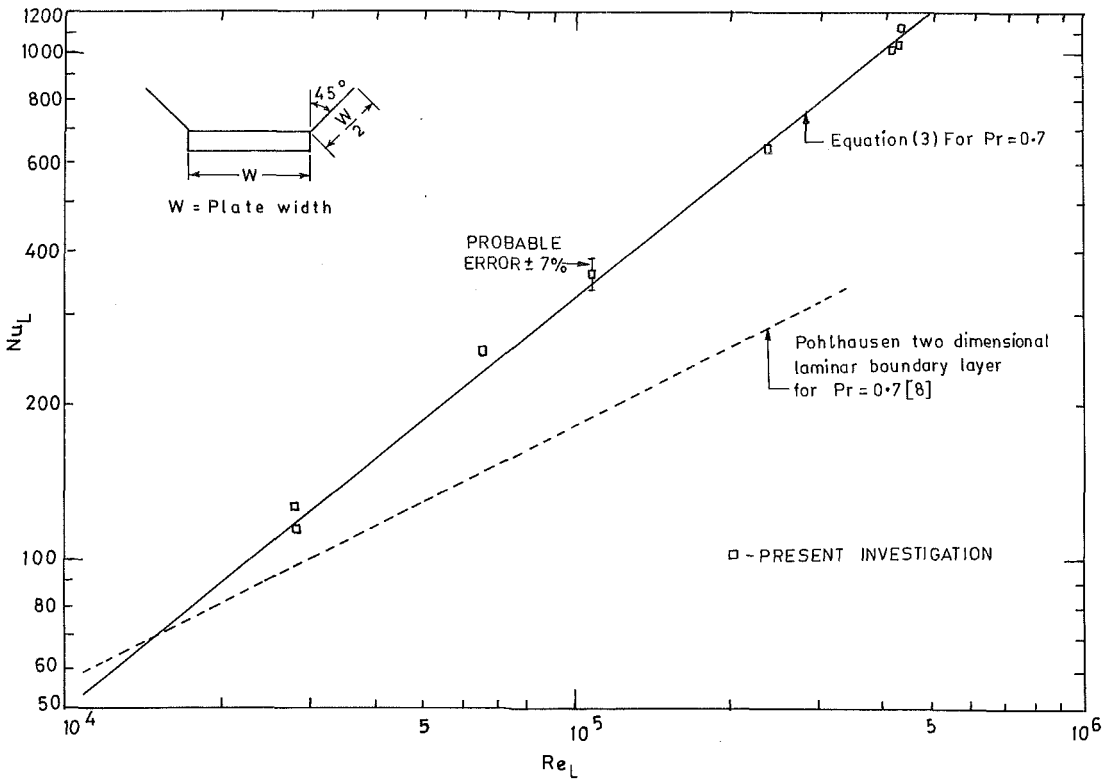


**Fig. 3 Results for two-dimensional boundary layer**

**Table 1 Blockage at different orientations of the test plate (AR II), % area blocked**

| α \ Φ | 0 deg | 15 deg | 30 deg |
|---|---|---|---|
| 0 deg | 3.4 | 5.2 | 5.7 |
| 15 deg | 8.5 | 10.4 | 11.7 |
| 30 deg | 13.7 | 15.4 | 16.3 |
| 45 deg | 17.9 | 19.5 | 19.8 |

Note: Values of blockage for the test plate in AR I mode are slightly less than the above values.

emissivity was obtained to an accuracy of ± 8%. This accuracy of determination was quite adequate, since the value of $Q_r$ generally did not exceed 5% of the total input to the main heater.

The second set of calibration tests was conducted with the objective of determining the side loss $Q_s$. The principle of these tests was to permit the flow of heat from the side edges of the test plate only. In order to ensure this, the top of the test plate was covered with a thick glass-wool slab.[2] The tests were run at different air velocities and temperature differences and for various values of α and Φ. The results showed that the side heat loss was essentially insensitive to values of α and Φ. For this reason, a final calibration plot showing the variation of $Q_s$ with the local average free stream velocity ($u^*$) for various $\Delta T$s was prepared. This was used for determining the side heat loss during the main series of tests. The value of $Q_s$ was, in general, of the order of 10 to 30% of the input to the main heater and the uncertainties in determining $Q_s$ were estimated to be less than ± 10%.

The probable error in determining the average heat transfer coefficient was estimated to be about ± 7%. However, at the lowest values of Re and $\Delta T$, where $Q_s$ was comparatively more, the uncertainties in $h$ may be about ± 10%.[3]

**Effect of Blockage.** Since the area blocked by the test setup was significant at the higher values of α and Φ, the local average free-stream velocity ($u^*$) was ascertained by considering the blockage effect. The free cross section of the tunnel was arrived at by subtracting from the tunnel area the projected area of the setup on a vertical plane perpendicular to the tunnel axis. The values of blockage for different orientations of the plate (AR II) are listed in Table 1. The blockage at higher values of α and Φ does not affect the heat transfer results to some extent. Test and Lessmann [6] have shown that their heat transfer results with and without blockage differ by a maximum of 7%. The maximum blockage in their experiments was also of the order of 20%.

**Preliminary Tests.** Before conducting the main series of tests, it was decided to conduct a few preliminary tests with the object of checking the accuracy of the experimental setup. A logical beginning would perhaps have been to run a few experiments in laminar flow and to check the values obtained against those given in [4, 5]. However, this was not possible because of the insulation fixed along the side edges. As a result, sharp leading edges could not be obtained and the presence of a laminar boundary layer could not be ensured.

It was, therefore, decided to simulate the situation of a two-dimensional turbulent boundary layer on a flat plate at zero yaw and zero attack. Test et al. [3] found 45 deg attachments of half the width of the plate, attached lengthwise, to be best for producing a two-dimensional boundary layer on a three-dimensional model for some situations. Attachments of 45 deg were, therefore, used and the results obtained with such attachments are plotted in Fig. 3. It will be seen that the values obtained are within ± 8% of the well-known two-dimensional correlation equation [7]:

[2] A small amount of heat (estimated to be about 3% of the total heat input) flowed through the glass-wool slab. A suitable correction for this heat flow was applied in calculating the side loss.

[3] This situation occurred in only 13 out of the total 154 data points.

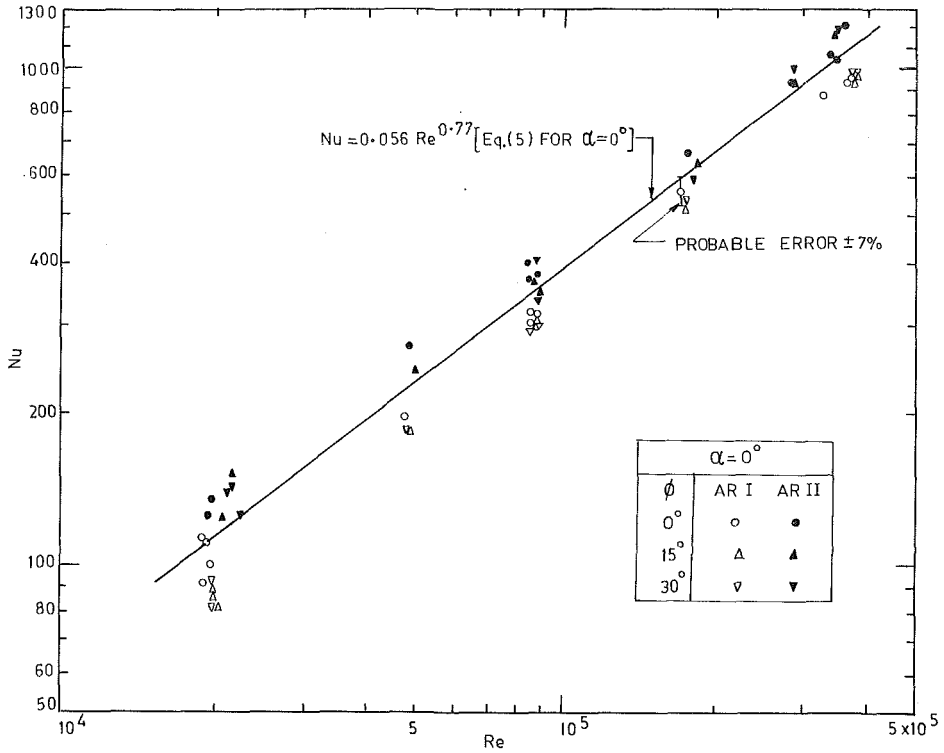


**Fig. 4 Variation of Nusselt number with Reynolds number, angle of attack = 0 deg**

$$Nu_L = 0.0366(Re_L)^{0.8}(Pr)^{1/3} \quad (3)$$

This also confirms the presence of the turbulent boundary layer. The two-dimensional laminar boundary layer equation [8] is also drawn for comparison.

## Results

The parameters varied during the course of experiments included the Reynolds number,[4] the angle of attack, the angle of yaw, the temperature difference $\Delta T$ and the aspect ratio. The Reynolds number was varied from $2 \times 10^4$ to $3.5 \times 10^5$, the angle of attack from 0 to 45 deg, the angle of yaw from 0 to 30 deg, and the temperature difference $\Delta T$ from 6 to 16°C. The two aspect ratios studied were 2/3 (designated as AR I) and 3/2 (designated as AR II). In all, 154 data points were obtained. In addition, a number of experiments were repeated. The scatter among these repeated data points was always found to be less than the estimated uncertainty of ± 7%.

Figures 4–6 show the results in terms of Nu versus Re for $\alpha$ = 0, 15 and 30 and 45 deg respectively for both the aspect ratios and all angles of yaw. The probable error of ± 7% in the determination of Nu is illustrated in each figure with respect to one data point. The solid lines appearing in the figures represent the least squares fit of the data. For comparison, equation (1), which has been developed for higher angles of attack, for the laminar situation is plotted in Fig. 6.

The temperature difference between the plate and the oncoming air ($\Delta T$) was varied form 6 to 16°C at a given Reynolds number. No significant effect was noted, indicating that natural convection effects were negligible. This fact was also confirmed by using the criterion

$$\frac{Gr}{Re^3} < 0.002 \quad (4)$$

[4]The characteristic dimension used in the calculation of the Reynolds number for a three dimensional flow is $L^*$ defined by $L^* = 4A/C$.

proposed by Heiber [9]. Hence the data points are not differentiated on the basis of $\Delta T$ in Figs. 4–6.

**Effect of Yaw.** It will be noted that no specific trend is seen as the angle of yaw varies from 0 to 30 deg over the entire range of the investigation. This is true at all the angles of attack and also for both the aspect ratios. Thus, the heat transfer coefficient seems to be insensitive to the angle of yaw.

**Effect of Aspect Ratio.** To study the effect of aspect ratio, attention is focused again on Figs. 4–6. In Figs. 5 and 6, the two aspect ratios yield essentially the same values of Nusselt numbers. However, the effect of aspect ratio seems to be of some significance at $\alpha$ = 0 deg (Fig. 4). In this case, the Nusselt numbers for the wider span plate (AR II) are higher than those obtained for the narrower plate (AR I). The difference is about 20 to 30%.

**Effect of Angle of Attack.** Next, consideration is given to how the value of Nu responds to changes in the angle of attack. By making comparisons between Figs. 4–6, it is seen that for any given value of Re over the range $2 \times 10^4$ to $3.5 \times 10^5$, the value of Nu decreases as the angle of attack increases from 0 to 15 deg. As the angle of attack increases further to 30 and 45 deg, significant decreases in Nu are observed only for Re > $10^5$.

## Discussion and Comparison

In order to be able to interpret the results, it is useful to visualize the flow field over the plate. Figure 7 shows the general nature of stream lines for the present case. At low angles of attack, a separation bubble is formed just behind the leading edge due to the bluntness of the plate. This is shown in Fig. 7(*a*). However, as the angle of attack is increased the separation bubble decreases in size and eventually disappears [10]. The flow field then corresponds to the situation shown in Fig. 7(*b*) with the boundary layer starting from the leading edge. Further, it is pertinent to point out that as the in-

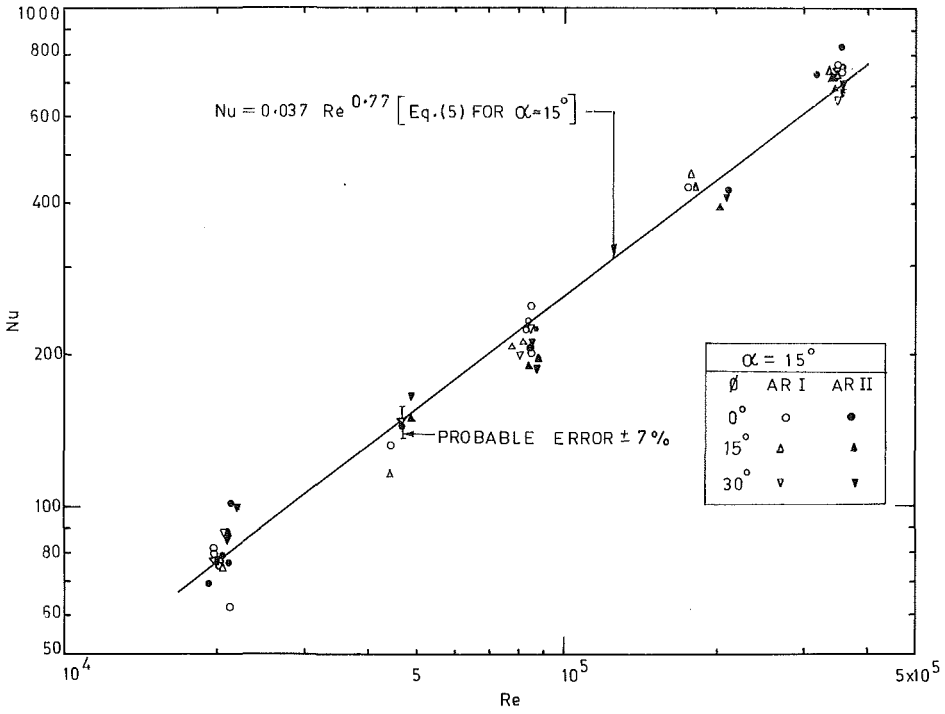


**Fig. 5 Variation of Nusselt number with Reynolds number, angle of attack = 15 deg**

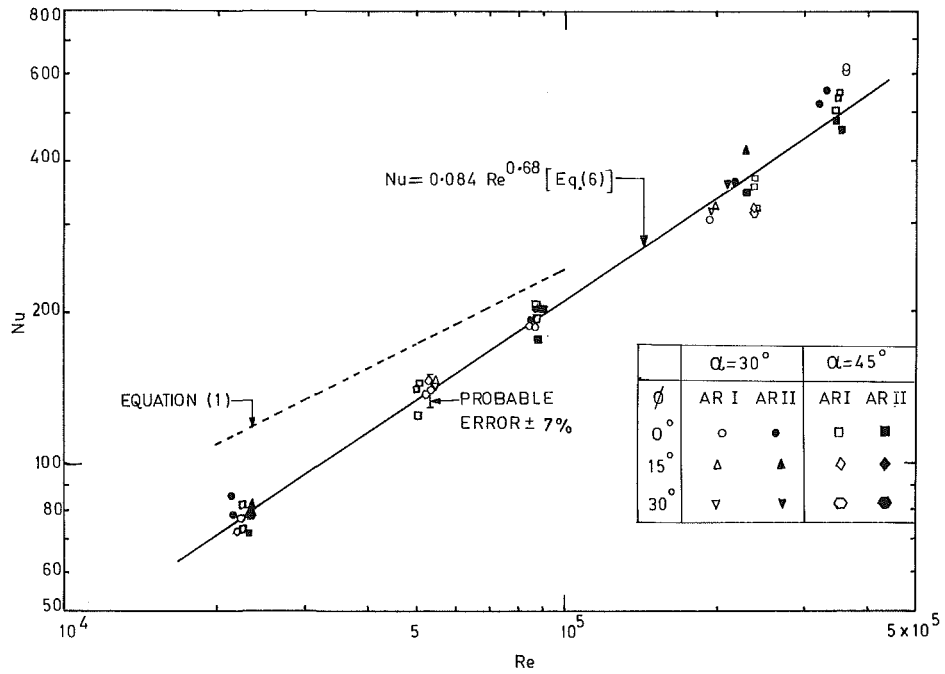


**Fig. 6 Variation of Nusselt number with Reynolds number, angle of attack = 30 and 45 deg**

clination of the plate is increased, a significant portion of the flow escapes over the lateral edges due to the finite size of the plate.

The variation of heat transfer coefficients as seen in Figs. 4–6 will now be discussed. Cases of zero yaw are first considered. It is seen from Fig. 4, which is for $\alpha = 0$ deg, that Nusselt numbers for the wider plate (AR II) are higher compared to those for the narrow plate (AR I). This difference is readily understood if one compares the length of flow path in the two cases. It will be noted that for $\alpha = 0$ deg and $\Phi = 0$ deg, the length of the flow path is shorter in the case of the wider plate (AR II) and hence higher heat transfer coefficients are logical considering the conventional boundary layer theory.

As the angle of attack is increased to 15 deg (Fig. 5), Nusselt numbers are lower than those obtained for $\alpha = 0$ deg. Moreover, the two aspect ratios yield more or less the same values of heat transfer coefficient. Two distinct phenomena seem to be responsible for this behavior. Firstly, as the angle of attack is increased, the escape of flow past the lateral edges reduces the average length of flow path. This effect which is expected to be more pronounced for the narrow plate (AR I)

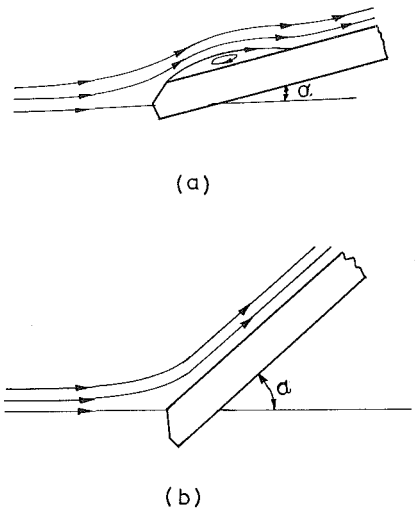


**Fig. 7 Flow patterns on the plate at various angles of attack: *a* small angle of attack; *b* large angle of attack**

more or less nullifies the effect of aspect ratio observed at $\alpha$ = 0 deg. Superimposed on this is the phenomenon of reduction in the size of the separation bubble which reduces the rate of heat transfer from either plate.

With the angle of attack further increased to 30 deg (Fig. 6), it is expected that there is no separation bubble as seen in Fig. 7(*b*). Further, a favorable pressure gradient probably sets in the process of relaminarization. In general, this causes the Nusselt numbers to be lower than those for $\alpha$ = 15 deg. Although the average length of flow path may be shorter for the narrow plate compared to the wider plate, the relaminarization effects are likely to be more pronounced for the narrow plate due to its larger chord length. Thus the Nusselt numbers for the two aspect ratios again do not show any significant difference. The insensitivity of Nusselt numbers to a further increase in angle of attack to 45 deg is also seen in Fig. 6. This stems from the fact that as angle of attack increases, relaminarization effects increase, but at the same time the average length of flow path reduces due to more lateral escape, thus neutralizing the relaminarization effect.

From Figs. 4-6, it may be noted that the effect of yaw is not seen to be significant. This is probably due to the fact that with changes in yaw up to 30 deg, more or less the same average length of flow path is maintained. It is possible that some effect might have been observed with higher values of $\Phi$.

As noted earlier, the only available data for average heat transfer coefficients for a three-dimensional flow over an inclined plate are for the laminar case. It is of interest therefore to compare those results with the present work and to note the remarkably similar trends obtained in both investigations. The insensitivity of Nusselt numbers to the angle of yaw observed in the present investigation has also been reported by Sparrow and Tien [4]. Similarly, the behavior of the data for different aspect ratios is qualitatively in agreement with Sparrow et al. [5]. For angles of attack 0 and 15 deg, there is no data with which the present results could be compared. However, for $\alpha$ = 30 and 45 deg, a comparison is made with the data of Sparrow et al. [5]. It will be seen from Fig. 6 that equation (1) of Sparrow intersects (when extrapolated) with the present data at Re $\approx 2 \times 10^5$. This behavior is analogous to the two-dimensional boundary layer case (Fig. 3). Moreover, the insenstivity to the angle of attack (at $\alpha$ = 30 and 45 deg) observed in the present case is in agreement with Sparrow. It is to be noted that the above similarities in trends have been obtained in spite of the differences in flow patterns between the two situations.

**Correlations.** From the experimental results, correlations relating the Nusselt number to the Reynolds number are developed by making a least-squares fit. The angle of yaw is not included in the correlations because, as noted earlier, its effect is insignificant. The aspect ratio affects the Nusselt number only at $\alpha$ = 0 deg. However, keeping in mind the need for developing as few correlation equations as possible from a design standpoint, it is also not included as a parameter. In Fig. 7, two flow patterns have been suggested for low and high angles of attack. Corresponding to these patterns, the following two equations are develoepd:

$$\mathrm{Nu} = 0.056\left(1 - \frac{\alpha}{44.2}\right)(\mathrm{Re})^{0.77} \quad ; \quad \alpha = 0 \text{ deg}, 15 \text{ deg} \qquad (5)$$

$$\mathrm{Nu} = 0.084(\mathrm{Re})^{0.68} \quad ; \quad \alpha = 30 \text{ deg}, 45 \text{ deg} \qquad (6)$$

where $\alpha$ is in degrees. The above equations predict the values of 85% of the data within $\pm$ 16%.

In equation (5), the exponent of 0.77 on Re clearly suggests the presence of a turbulent boundary layer at low angles of attack. The term $(1 - \alpha/44.2)$ may be attributed to the decreasing size of the separation bubble and the increased lateral outflow as $\alpha$ increases from 0 to 15 deg. On the other hand, in equation (6), the value of the exponent on Re is reduced to 0.68. This indicates relaminarization of the boundary layer because of the favorable pressure gradient at higher angles of attack.

Studies on the measurement of the local heat transfer coefficients and on flow visualization are presently in progress. These should help in clarifying the situation further.

## References

1 Drake, R. M., Jr., "Investigation of the Variation of Point Unit Heat Transfer Coefficient for Laminar Flow Over an Inclined Flat Plate," ASME *Journal of Applied Mechanics*, Vol. 71, 1949, pp. 1-8.

2 Braud, H. J., Jr., "Forced Convective Heat Transfer from an Inclined Shelter Roof Exposed to Solar Radiation," Ph.D. Thesis, Oklahoma State University, 1962.

3 Test, F. L., Lessmann, R. C., and Johary, A., "Heat Transfer During Wind Flow Over Rectangular Bodies in the Natural Environment," ASME JOURNAL OF HEAT TRANSFER, Vol. 103, 1981, pp. 262-267.

4 Sparrow, E. M., and Tien, K. K., "Forced Convective Heat Transfer at an Inclined and Yawed Square Plate—Application to Solar Collectors," ASME JOURNAL OF HEAT TRANSFER, Vol. 99, 1977, pp. 507-512.

5 Sparrow, E. M., Ramsey, J. W., and Mass, E. A., "Effect of Finite Width on Heat Transfer and Fluid Flow about an Inclined Rectangular Plate," ASME JOURNAL OF HEAT TRANSFER, Vol. 101, 1979, pp. 199-204.

6 Test, F. L., and Lessmann, R. C., "An Experimental Study of Heat Transfer During Forced Convection Over a Rectangular Body," ASME JOURNAL OF HEAT TRANSFER, Vol. 102, 1980, pp. 146-151.

7 Colburn, A. P., "A Method of Correlating Forced Convection Heat Transfer Data and a Comparison with Fluid Friction," *Trans. AIChE*, Vol. 29, 1933, pp. 174-210.

8 Pohlhausen, E., *Z.angew Math.u. Mech.*, Vol. 1, 1921, p. 115.

9 Heiber, C. A., "Mixed Convection Above a Heated Horizontal Surface," *International J. Heat and Mass Transfer*, Vol. 16, 1973, pp. 769-785.

10 McCormick, D. C., Lessmann, R. C., and Test, F. L., "Heat Transfer to Separated Flow Regions From a Rectangular Prism in a Cross-Stream," ASME Paper No. 83-HT-28.

# Adiabatic Film Cooling Effectiveness From Heat Transfer Measurements in Compressible, Variable-Property Flow

P. M. Ligrani[1]
C. Camci
Von Karman Institute for Fluid Dynamics,
Chaussée de Waterloo, 72
B-1640 Rhode-St.-
Genese, Belgium

*A variable property correction is given for turbulent boundary layers that are film-cooled using staggered rows of injection holes inclined at 35 deg. With the correction, a relation is provided between the adiabatic film cooling effectiveness for constant property flow and heat transfer coefficients for variable property flow, which are based on the difference between the freestream recovery temperature and wall temperature. The variable property correction was determined from heat transfer measurements for a range of injection parameters at different values of the nondimensional coolant temperature and from results in the literature. Because the flow is compressible, the importance of the injection mass flux ratio, momentum flux ratio, and velocity ratio are considered in the determination of effectiveness.*

## 1 Introduction

Designers of film-cooled components require a detailed knowledge of convective heat transfer processes which occur when a coolant is injected into a boundary layer. Such knowledge is required since film cooling allows a means to protect gas turbine parts, such as turbine blades and combustion chamber linings, from the thermal loading that results from exposure to hot gases. Much information on these processes is available from fundamental studies employing laboratory models having a variety of film cooling injection configurations. Consequently, the relationship between heat transfer in the laboratory studies and that in application require understanding, particularly when constant property results are used to design components exposed to variable-property compressible flows.

In comparison to the large temperature differences that exist between the gas and the surface of turbine blades, the blade surface temperature distribution is relatively isothermal. Thus, in regard to thermal boundary layers developing over a turbine blade surface, a blade designer would naturally be more concerned with data obtained using isothermal wall boundary conditions, rather than data obtained when the wall is exposed to a uniform heat flux. However, adiabatic wall boundary conditions are a subset of the latter type of thermal boundary condition and are advantageous in that they may be used to describe the convection processes that occur during film cooling in an economical way. Such economy is provided because a problem having three temperature potentials, $T_\infty$, $T_c$, and $T_W$, is reduced to a two temperature one. In this case, the heat flux in incompressible flow with film cooling is given by

$$\dot{q}''_w = h_f (T_{AW} - T_W) \tag{1}$$

where $T_{AW}$ may be expressed nondimensionally using adiabatic film cooling effectiveness, $\eta$. The magnitudes of $h_f$ and $T_{AW}$ are generally determined from spanwise averages of local measurements of these two quantities [1-5]. Other investigations [6-7] describe convective film-cooling processes using isothermal wall boundary conditions along with the equation

$$\dot{q}''_w = h (T_{o\infty} - T_w) \tag{2}$$

Here, $h$ is provided with the temperature of the injected fluid, often expressed nondimensionally using $\theta$.

The connection between the two approaches given by equations (1) and (2) began with a study by Metzger et al. [8], who showed the linear dependence of $h/h_o$ on $\theta$ for a variety of injection conditions in constant property flow. In a discussion of this paper, E.R.G. Eckert pointed out that the horizontal and vertical intercepts of such plots gave $1/\eta$ and $h_f/h_o$, respectively. From these two sources, equations (1) and (2) are set equal, and definitions for $\eta$ and $\theta$ are used to give

$$h = h_f (1 - \eta\theta) \tag{3}$$

Dividing by $h_o$ then produces

$$\frac{h}{h_o} = \frac{h_f}{h_o} (1 - \eta\theta) \tag{4}$$

In an investigation involving both slot and discrete hole injection, Metzger and Fletcher [9] then used this approach to obtain $\eta$. Eckert et al. [10] compared $\eta$ determined from these measurements to results from the University of Minnesota and found differences ranging from 0 to 20 percent over a range of conditions. These differences for injection from a single row of holes may have resulted since Metzger and Fletcher's [9] measurements provide a global adiabatic film-cooling effectiveness, instead of a spatial average of effectiveness determined from measurements on a surface which is locally adiabatic. In a more recent paper, Eckert [11] provides additional discussion of the connection between equations (1) and (2). Here, he shows how results from one method can be transformed into parameters used in the other as applied to full-coverage film cooling. Several studies [3-5, 12] have also focused on the effects of density ratio $\rho_c/\rho_\infty$, compressibility, and/or large temperature differences on film-cooled boundary layers; however, none of these have addressed the connection between adiabatic and isothermal boundary conditions when the effects of variable properties are important.

Consideration of the connection between heat transfer measured with isothermal and adiabatic boundary conditions in film-cooled boundary layers with variable properties requires examination of a number of important factors.

1 The $h/h_o$ versus $\theta$ extrapolation procedure used in [8, 9,

[1]Present address: Department of Mechanical Engineering, Naval Postgraduate School, Monterey, Calif. 93943

Contributed by the Heat Transfer Division for publication in the JOURNAL OF HEAT TRANSFER. Manuscript received by the Heat Transfer Division June 6, 1983.

10] is not valid because the energy equation is nonlinear and coupled to the momentum equation. In the present study, a new extrapolation procedure is given for a compressible flow with $M_\infty = 0.64$. In order to account for viscous dissipation, all gas total temperatures in equations (1-4) are replaced by recovery temperatures.

2 The ratio $\rho_c/\rho_\infty$ will change as $h/h_o$ varies with $\theta$ in compressible flow. This leads to the question: Which coolant injection parameter, $m$, $I$, or $U_c/U_\infty$, should be held constant along a collection of $h/h_o$ versus $\theta$ points? Each of these injection parameters is considered in the present extrapolation procedures, and adiabatic film cooling effectiveness is given for constant $m$, $I$, and $U_c/U_\infty$.

3 Determination of $\eta$ from isothermal wall heat transfer measurements requires that

$$\overline{h_f'\,(T_{AW}'-T_W)} = \overline{h_f'(T_{AW}'-T_W)} \tag{5}$$

which is true at a given downstream location only when local $h_f'$ and $\eta'$ are invariant in the spanwise direction and equal to spanwise averaged values, $h_f$ and $\eta$. In the design of the present experiment, two staggered rows of injection holes were chosen instead of say, one row, to give a spanwise uniform flow for $x/d > 20$. Inequality of equation (5) is discussed for results obtained when $x/d < 20$.

With these three points in mind, the primary objective of the present study is to povide a connection between heat transfer in film-cooled boundary layers with variable properties and isothermal wall boundary conditions, and those with constant properties and adiabatic boundary conditions. Empirical variable property correction terms are introduced into equation (4) for this purpose. Thus experimental results are given leading to a relationship between the two types of measurements that are generally made in film-cooled boundary layers: (*i*) $\eta$ and $h_f$, and (*ii*) $h$ at specific values of $\theta$, where the former are for a constant property environment, and the latter are for a variable property environment. The variable property results consist of heat transfer coefficients based on the $(T_{r\infty}-T_w)$ temperature difference which were measured at similar $M_\infty$, Reynolds numbers, and $T_{rc}:T_{r\infty}:T_w$ ratios as exist in the flow near gas turbine blades. The constant property $\eta$ and $h_f$ were measured by Jabbari and Goldstein [1] and Jabbari [2]. The present

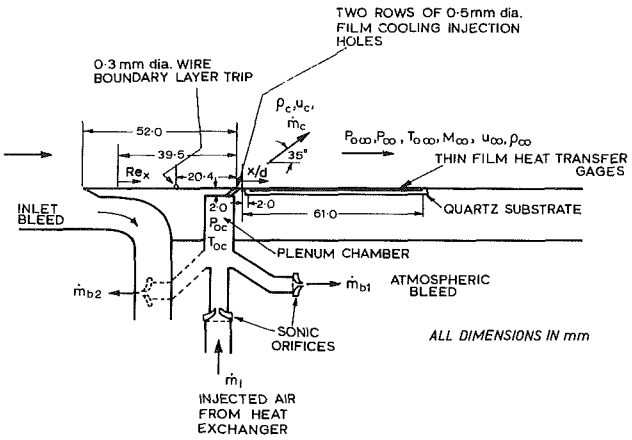


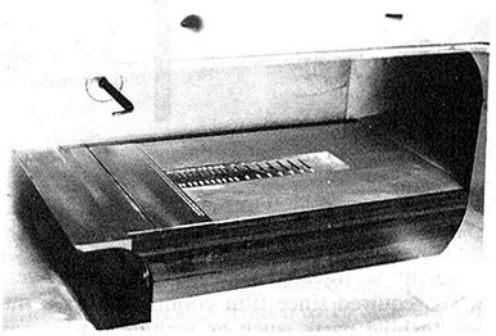

Fig. 1 Test model

model was designed to be geometrically similar to theirs, including the test surface boundary layer and injection geometry.

## 2 Experimental Facility and Measurement Techniques

**(*a*) Model and Test Facility.** The model used for testing is shown in Fig. 1. The photograph shows installation in the CT-2 compression tube facility described by Ligrani et al. [13], Consigny et al. [14] and similar in operation to a facility

## Nomenclature

$A$ = injection hole area
$C_D$ = discharge coefficient
$C_p$ = specific heat at constant pressure
$d$ = injection hole diameter
$h, h_f$ = heat transfer coefficients with film cooling (spanwise averaged), $\dot{q}_w''/(T_{r\infty}-T_w)$, $\dot{q}_w''/(T_{AW}-T_w)$
$h_o$ = heat transfer coefficients without film cooling (spanwise averaged), $\dot{q}_{wo}''/(T_{r\infty}-T_w)$
$I$ = injection momentum flux ratio, $\rho_c U_c^2/\rho_\infty U_\infty^2$
$l$ = length of injection holes
$m$ = injection mass flux ratio, $\rho_c U_c/\rho_\infty U_\infty$
$\dot{m}_c$ = injection mass flow rate, equation (6)
$n,p$ = empirical constants in equation (12)
$P$ = static pressure
Pr = molecular Prandtl number
$\dot{q}_w''$ = wall heat flux with film cooling
$\dot{q}_{wo}''$ = wall heat flux without film cooling
$R$ = gas constant
$\mathrm{Re}_d$ = freestream Reynolds number based on diameter of injection holes, $dU_\infty\rho/\mu$
$\mathrm{Re}_x$ = freestream Reynolds number based on downstream distance measured from effective origin of turbulent boundary layer
St = Stanton number, $h_o/\rho_\infty U_\infty C_p$
$T$ = static temperature
$U$ = mean velocity
$x$ = distance from downstream edge of injection holes
$\delta_1$ = boundary layer displacement thickness at upstream edge of injection holes
$\rho$ = density
$\eta$ = adiabatic film cooling effectiveness (spanwise averaged), $(T_{AW}-T_{r\infty})/(T_{rc}-T_{r\infty})$
$\mu$ = absolute viscosity
$\theta$ = nondimensional coolant temperature, $(T_{rc}-T_{r\infty})/(T_w-T_{r\infty})$

### Subscripts

$AW$ = adiabatic wall
$c$ = coolant
$i$ = isentropic
$o$ = total condition
$r$ = recovery condition
$W$ = wall
$\infty$ = freestream

### Superscripts

$'$ = local value
$\bar{}$ = spanwise average
$\hat{}$ = variable property

described in [15]. CT-2 provides a high-pressure, high-temperature environment for testing by means of an isentropic compression of air by a lightweight piston driven by a high-pressure air supply. When the air in front of the piston reaches the desired pressure level, a fast opening shutter valve is activated allowing flow into the test section. Steady conditions may then be produced for periods as long as several seconds, during which time the same Reynolds numbers, Mach numbers, and $T_{r\infty}:T_{rc}:T_w$ ratios may be produced as exist in the first turbine stage of a gas turbine engine.

For the present tests, the total pressure and temperature in the model free stream were approximately $2.9 \times 10^5$ N/m$^2$ absolute, and 403 K, respectively. The magnitude of $T_w$ was about 290 K. Visualization using a row of surface oil drops showed the flow over the test model to be spanwise uniform. The free-stream Mach number was 0.64 and maintained at this value during test durations using a sonic throat downstream of the test section. The zero pressure gradient was adjusted by means of a valve for the inlet bleed slot, shown in Fig. 1, and measured using a row of static pressure tapings extending from the plate leading edge to the end of the instrumented surface. A zero pressure gradient along the entire length of the test plate also ensured that streamlines approaching the leading edge were parallel to the plate surface.

The model used was geometrically similar to the one described by Jabbari and Goldstein [1] and Jabbari [2]. The magnitude of $\delta_1/d$ in the present study was approximately 0.16, compared to 0.177 for Jabbari's work. This magnitude of $\delta_1/d$ was obtained by placing a 0.3-mm-dia wire trip 20.4 mm upstream of the rows of film-cooling holes, as shown in Fig. 1. The trip was located in order to assure laminar-turbulent transition, as well as to provide the appropriate boundary layer thickness according to correlations presented by Schlichting [16]. From the turbulent boundary layer correlation for boundary layer displacement thickness, the effective origin of the layer was also determined in order to provide the location for measurement of $\mathrm{Re}_x$.

The 0.5-mm-dia injection holes were inclinded at an angle of 35 deg and spaced 3 dia apart in the spanwise direction. A total of 101 injection holes were contained in two rows spaced 2.5 dia apart. The holes in the rows were staggered with respect to each other so that the midspan distance between two holes in the same row located the center line of holes in the adjacent row. For all runs in the present test program, the Reynolds numbers were high enough to ensure that the injectant was turbulent. The magnitude of the mainstream Reynolds number based on hole diameter $\mathrm{Re}_d$ in the present study was $1.1 \times 10^4$ compared to $10^4$ and $2.1 \times 10^4$ for [1]. The temperature of the injected air was varied by means of a regenerative heat exchanger, which provided air for the injectant plenum chamber at rates measured using a sonic orifice. Two atmospheric bleed sonic orifice passages were also connected to the plenum chamber in order to reduce the time required to inject film cooling air over the test surface, and to minimize transient effects in the plenum chamber that may occur at shutter opening when freestream air abruptly moves into the test section. The uniformity of the plenum chamber pressure $P_{oc}$ was found to be satisfactory over a range of injection conditions, after measurement at three different spanwise locations.

Pressures were measured using National Semiconductor and Validyne variable reluctance pressure transducers, connected as near as possible to measurement locations to minimize response time. Temperatures were measured using thermocouples consisting of 0.05-mm-dia chromel-alumel wire with welded junctions. Each pressure and temperature sensor was calibrated individually with respect to a known reference for the range of measurement conditions. Recovery temperatures were calculated using a recovery factor equal to $P_r^{1/3}$ (Kays and Crawford [17]).

Referring to Fig. 1, the mass flow rate of the coolant was calculated using

$$\dot{m}_c = \dot{m}_i - \dot{m}_{b1} - \dot{m}_{b2} \tag{6}$$

Knowing the injection area $A$, the injection mass flux rate then followed from the equation

$$\rho_c U_c = \dot{m}_c / A \tag{7}$$

As injectant properties were desired at the exit of the injection holes, coolant static density and total temperature were given by

$$\rho_c = P_\infty / RT_c \tag{8}$$

and

$$T_{oc} = T_c + U_c^2 / 2C_p \tag{9}$$

respectively. Values of $T_{oc}$, estimated at the exits of the injection holes, were used in equation (9). These values of $T_{oc}$ were based on measured plenum chamber coolant temperatures corrected to account for heat transfer from the coolant to the $l/d = 7$ injection hole surfaces. Injection was started 400–700 ms before the mainstream as experience with the facility showed that less significant injection plenum chamber transients exist than if free stream and injection are started at the same time.

Solution of equations (7-9) thus allowed determination of injectant parameters $U_c$, $\rho_c$, and $T_c$, since all other quantities in these equations were measured or estimated from measurements. From isentropic flow relations, the discharge coefficient could then be calculated using

$$C_d = \rho_c U_c / (\rho_c U_c)_i \tag{10}$$

where

$$(\rho_c U_c)_i = P_\infty \left(\frac{P_{oc}}{P_\infty}\right)^{2/7} \left[\frac{7}{RT_{oc}}\left(1 - \left(\frac{P_{oc}}{P_\infty}\right)^{-2/7}\right)\right]^{1/2} \tag{11}$$

With this procedure, $m$, $I$, $U_c/U_\infty$, $\rho_c/\rho_\infty$, and $C_D$ were obtained for each test run.

**(*b*) Heat Transfer Measurement.** The wall heat flux was measured using thin-film platinum gauges, which may be seen in the photograph of Fig. 1. The gauges had a 1 mm dimension in the $x$-direction and all $x/d$ values were measured to the gauge centerline. The thin films had a spanwise dimension of 12 mm in order to obtain $\dot{q}_w''$ values averaged across the span. The gauges functioned as resistance thermometers. They were connected to operational amplifiers, which maintained constant current across gauges with respect to time. The voltage outputs from these circuits then passed to electrical circuits with resistances and capacitances arranged to produce voltages and currents proportional to temperatures and heat fluxes. These analogue circuits were constructed to simulate one-dimensional heat transfer into a semi-infinite solid, which required mounting of the thin film gauges on low conductivity quartz substrates. Test model parts were designed and constructed to ensure that conduction in metal parts during tests did not affect the temperature in the quartz or the surface thermal boundary condition.

Because of the abrupt flow of hot gas over the test surface at the beginning of the test, the heat flux variation with time has a steplike behavior. Thin film gauge signal traces showed this step, and also indicated fully turbulent flow over the model test surface. Using the $\dot{q}_w''$ versus time traces, the variation of gauge temperature with time may be constructed mathematically using an inverse transformation [18, 19]. The final result for each gauge was a plot of $\dot{q}_w''$ versus surface temperature which may be then be extrapolated to initial condition, at which time the model surface temperature was uniform. Using this procedure, distributions of $\dot{q}_w''$ were obtained equivalent to those on an isothermal surface.

A thorough discussion of thin film gauge construction and

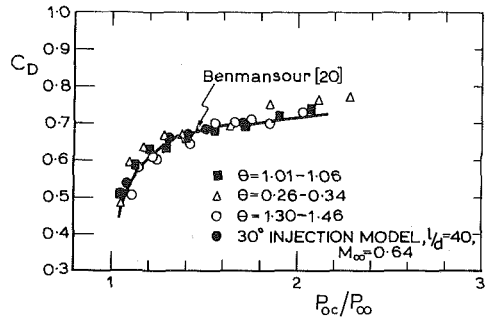


Fig. 2 Film-cooling injection system discharge coefficients

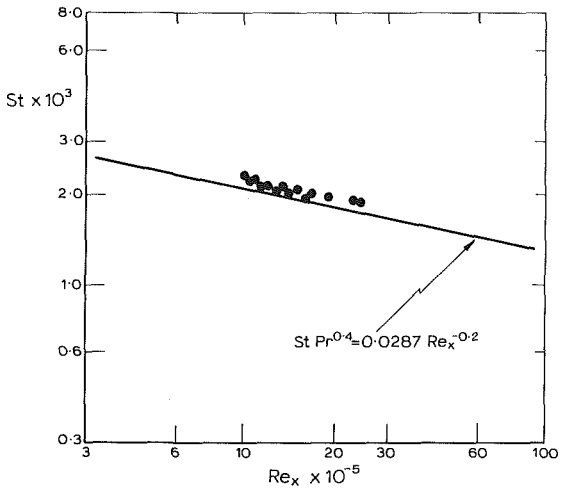


Fig. 3 Baseline heat transfer measurements

measurement details, as applied in the present study, is given in [18].

From the analogue circuits, the signals were sent to amplifier/anti-aliasing filter units which also contained sample and hold devices. The signals were then processed by a multiplexer and analogue-to-digital converter controlled during testing times by a PDP 11/34 computer. The maximum data sampling rate of the system was 500 kHz for the 48 channels, and the signal resolution of the analogue-digital converter was 12 bits. In the present study, a data acquisition rate of 1 kHz, and a sampling time of 512 msec were employed for each channel. In addition to the heat transfer measurements, the system was also used to acquire the output from pressure transducers and thermocouples used to measure various injection and free-stream flow properties during a test run.

## 3 Baseline Experimental Results

**(a) Discharge Coefficients.** The variation of $C_D$ with $P_{oc}/P_\infty$ is shown in Fig. 2. The results indicate satisfactory injection system performance since discharge coefficient values do not show a dependence on nondimensional coolant temperature $\theta$. The measured $C_D$ also agree with results from a model having 30-deg injection holes, $l/d = 40$ and $M_\infty = 0.64$. $C_D$ values are additionally consistent with results at $M_\infty = 0.64$ determined from measurements by Benmansour [20] who employed an injection model having holes inclined at 30 deg with $l/d = 6$.

**(b) Heat Transfer.** Using the procedures described and those given in [18], the baseline results represented in Fig. 3 for zero injection are obtained. The measurements presented in this figure were repeatable within ±3 percent and obtained using the same free-stream conditions described earlier. The data lie just above the flat-plate equation suggested by Kays et al. [17] with maximum differences of about 10 percent. Considering the ±12 percent experimental uncertainty of St (based on a 20:1 confidence level), the results in Fig. 3 provide qualification of heat transfer measurement procedures. These results are also important because they indicate normal boundary layer behavior since the heat transfer is the same as in a normally developing, two-dimensional layer with variable properties. The equation in Fig. 3 is corrected for variable properties using the temperature ratio method of [17]. According to this method, the variable property Stanton number equation is the same as for a constant property environment when $T_w/T_\infty < 1$.

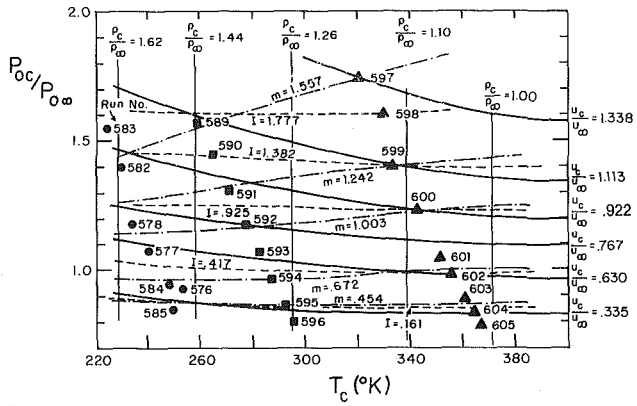


Fig. 4 Experimental operating domain map showing range of injection conditions, ● $\theta$ = 1.30–1.46, ■ $\theta$ = 1.01–1.06, ▲ $\theta$ = 0.26–0.34

## 4 Experimental Results

**(a) Experimental Domain Map.** An experimental operating domain map indicating the range of injection conditions used in the present study is shown in Fig. 4. In the $P_{oc}/P_{o\infty}$ versus $T_c$ coordinates, three sets of data are shown corresponding to cold ($\theta$ = 1.30–1.46), ambient ($\theta$ = 1.01–1.06) and hot ($\theta$ = .26–.34) injection. Lines of constant $m$, $I$, $U_c/U_\infty$, and $\rho_c/\rho_\infty$, determined from measurements at the various data points, show the range of these parameters covered by the present tests. Such results indicate which data runs are required for interpolation in order to obtain information at a constant $m$, $I$, or $U_c/U_\infty$ as the injectant temperature varies. Referring to run number 600, the magnitudes of these three parameters are 1.0, 0.925, and 0.922, respectively. As $T_c$ decreases, the three lines corresponding to these parameter values diverge. Hence, paths followed by injection parameter lines on the domain map differ depending on which injection parameter is held constant. Different injection parameters correspond with different sets of data in variable property flow even though lines representing the injection parameters may intersect at one location on the experimental domain map.

**(b) Heat Transfer Coefficients Based on the $(T_{r_\infty} - T_w)$ Temperature Difference.** In Figs. 5–7, heat transfer coefficients with film cooling, $\hat{h}$ are presented for a wide range of experimental conditions. These $\hat{h}$ values are normalized with respect to heat transfer coefficients without film cooling $\hat{h}_o$, and plotted versus $m$, $I$, and $U_c/U_\infty$. The variation of $\hat{h}/\hat{h}_o$ is presented as it varies linearly with $m$. Magnitudes of $I$ and $U_c/U_\infty$ were determined from injection calculations for individual runs. Run numbers correspond to those presented in Fig. 4. The data in Figs. 5–7 are plotted parametrically with $x/d$, showing the variation of $\hat{h}/\hat{h}_o$ with injection parameters at a given downstream location. These plots allow interpolation along $\hat{h}/\hat{h}_o$ curves at values of $m$, $I$ or $U_c/U_\infty$ between those at measurement points.

The results in Figs. 5, 6, and 7 are presented for $\theta$ values of

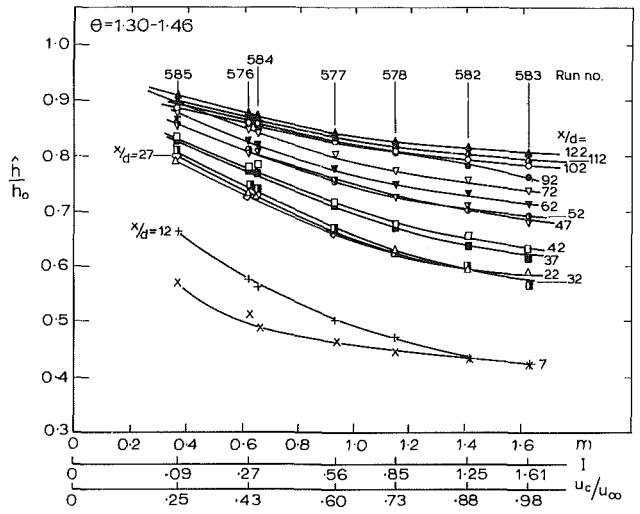


**Fig. 5 Normalized heat transfer coefficients with film cooling at different *x/d* as a function of varying injection parameters**

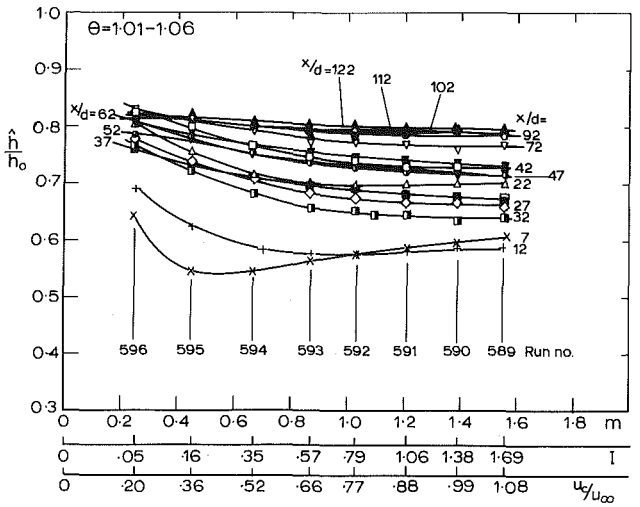


**Fig. 6 Normalized heat transfer coefficients with film cooling at different *x/d* as a function of varying injection parameters**

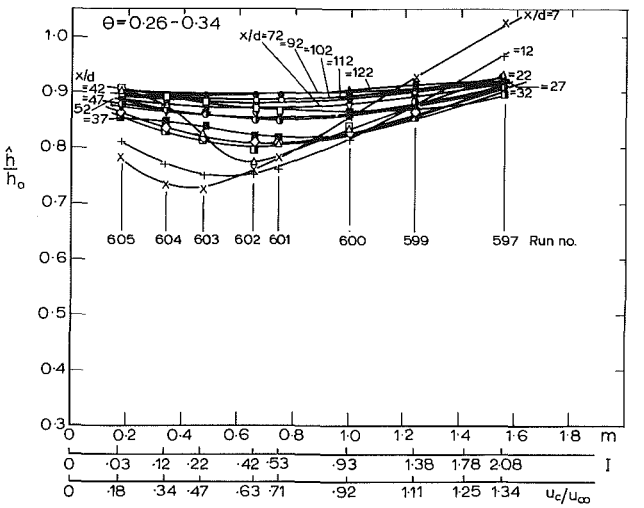


**Fig. 7 Normalized heat transfer coefficients with film cooling at different *x/d* as a function of varying injection parameters**

| x/d | 7 | 12 | 22 | 27 | 32 | 37 | 42 | 47 | 52 | 62 | 72 | 92 | 102 | 112 | 122 |
|---|---|---|---|---|---|---|---|---|---|---|---|---|---|---|---|
| symbol | X | + | Δ | ◇ | ◨ | ■ | □ | ▽ | ◑ | ▼ | ▽ | ● | ○ | ▲ | ▲ |

1.30–1.46, 1.01–1.06, and 0.26–0.34, respectively. From these three figures, the largest variations of $h/\hat{h}_o$ with $m$ occur near the injection location at small $x/d$. At larger $x/d$ locations, farther downstream, the variation of $h/\hat{h}_o$ with $m$ is smaller. Generally, at a given value of $m$, $h/\hat{h}_o$ increases as $x/d$ increases, where the largest variations occur when $\theta$ = 1.30–1.46. Exceptions are evident at high injection rates when $\theta$ = 1.01–1.06.

In Fig. 5, minimum values of $h/\hat{h}_o$ occur for magnitudes of $m$ greater than 1.4. In the two following figures, the $m$ where $h/\hat{h}_o$ curves are minimum have smaller magnitudes. In Fig. 7, the $h/\hat{h}_o$ versus $m$ curves pass through well defined minimum regions only when $x/d < 22$. The magnitudes of the normalized heat transfer coefficients in this figure are also closer to 1.0 than measurements at $\theta$ = 1.0–1.06 and $\theta$ = 1.30–1.46.

**(c) Variable Property Correction.** In order to account for variable properties in equation (4), the left-hand side is multiplied by $(T_{rc}/T_{r\infty})^n (T_{r\infty}/T_w)^p$ to give

$$h/\hat{h}_o (T_{rc}/T_{r\infty})^n (T_{r\infty}/T_w)^p = h_f/h_o(1-\eta\theta) \tag{12}$$

The $(T_{rc}/T_{r\infty})^n (T_{r\infty}/T_w)^p$ term is then an empirical correction for the influence of temperature-dependent fluid properties in film-cooled turbulent boundary layers. With the correction, a relation is provided between constant property $h_f/h_o$, constant property adiabatic film cooling effectiveness, and variable property $h/\hat{h}_o$.

Results which follow show that $(T_{rc}/T_{r\infty})^n$ is included in equation (12) so that adiabatic effectiveness results from the presnt study match those from the University of Minnesota [1, 2]. Determination of $\eta$ is independent of $(T_{r\infty}/T_w)^p$ in equation (12) since $T_{r\infty}$ and $T_w$ are constant regardless of the value of $\theta$. For $m > .65$, empirical constant $n$ is set equal to 1.00, and for $m = .48$, $n$ is set equal to 0.80 in order to obtain: (*i*) data points along straight lines in $h/\hat{h}_o (T_{rc}/T_{r\infty})^n$ versus $\theta$ coordinates, and (*ii*) the best fit to $\eta$ measurements from constant property flows. $n$ is thus dependent on the blowing ratio $m$.

The variable property correction is consistent with results given by Pedersen, Eckert, and Goldstein [3] and Papell and Trout [21], because equation (12) gives $h/\hat{h}_o$, which are dependent on $T_{rc}/T_{r\infty}$. According to [3], in constant property situations, the adiabatic film cooling effectiveness is a function of a number of parameters, including the injection geometry, the turbulence, the Reynolds number in the mainstream, and the mass flux ratio $m$. The authors go on to say that "for variable property flows involving ideal gases with transport properties which can be expressed by a power law, the heat transfer and the film effectivenesses are, in addition, a function of the ratio of the absolute temperatures $T_\infty/T_c$ or of the density ratio $\rho_\infty/\rho_c$."

The $(T_{r\infty}/T_w)^p$ term is required in equation (12) so that corrected $h_f/h_o$ results from the present study match measured results given in [1]. It is applied using

$$h_f/\hat{h}_o = h_f/h_o (T_w/T_{r\infty})^p \tag{13}$$

where $h_f/\hat{h}_o$ is determined from the $\theta = 0$ value extrapolated from measurements of $h/\hat{h}_o$ versus $\theta$, or from measurements of $h/\hat{h}_o (T_{rc}/T_{r\infty})^n$ versus $\theta$. Either way, the same $h_f/\hat{h}_o$ is obtained since $(T_{rc}/T_{r\infty})^n = 1$ at at $\theta = 0$. In equation form

$$h/\hat{h}_o (T_{rc}/T_{r\infty})^n = h_f/\hat{h}_o (1-\eta\theta) \tag{14}$$

Alternatively,

$$h^*/h_o = h_f/\hat{h}_o (1-\eta\theta) \tag{15}$$

where $h^*/h_o$ is partially corrected "artificial" value of $h/\hat{h}_o$, defined for convenience. The value of $p$ in (13) giving the best fit between present results and those from [1] is 0.40. Although valid over a range of injection rates, equation (13) is applied only for the one $(T_w/T_{r\infty})$ ratio of the present study.

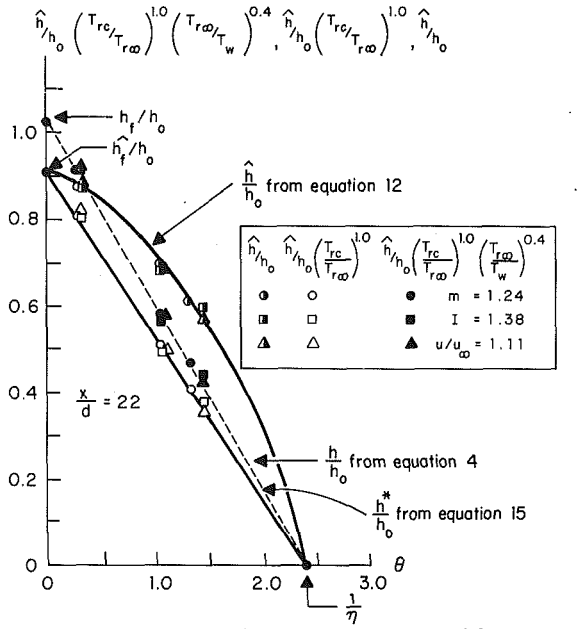


Fig. 8(a) $h\hat{/}h_o$, $h\hat{/}h_o(T_{rc}/T_{r\infty})^{1.0}$, and $h\hat{/}h_o(T_{rc}/T_{r\infty})^{1.0}(T_{r\infty}/T_w)^{0.4}$ versus $\theta$

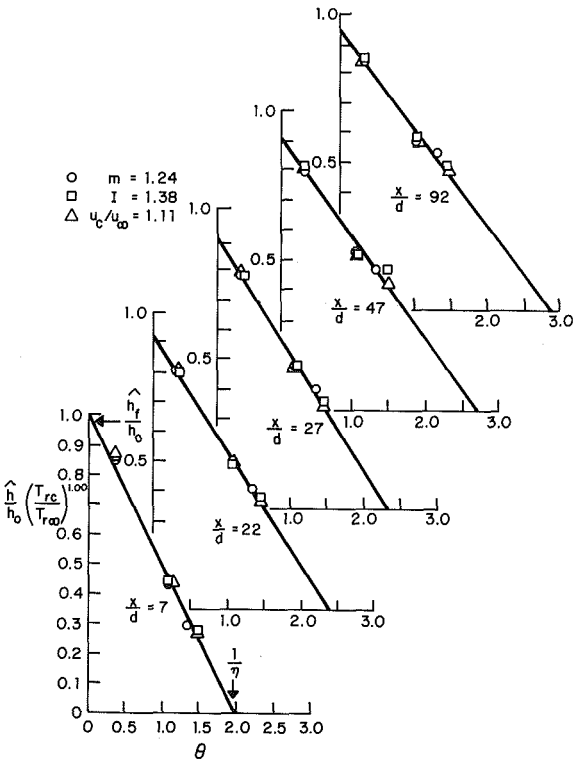


Fig. 8(b) $h\hat{/}h_o(T_{rc}/T_{r\infty})^{1.0}$ versus $\theta$ for different $x/d$

In Fig. 8($a$) are shown: ($a$) variable property $h/\hat{h}_o$ from equation (12), ($b$) $h^*/h_o$ from equation (15), and ($c$) constant property $h/h_o$ from equation (4). These lines correspond to $h/\hat{h}_o$, $h\hat{/}h_o\,(T_{rc}/T_{r\infty})^{1.0}$, and $h\hat{/}h_o\,(T_{rc}/T_{r\infty})^{1.0}\,(T_{r\infty}/T_w)^{0.40}$ data, respectively, where the latter two show a linear variation with $\theta$. The overall effect of variable properties is evident from $h/h_o$ and $h\hat{/}h_o$ results in Fig. 8($a$), and from the equation

$$h\hat{/}h_o\,(T_{rc}/T_{r\infty})^n\,(T_{r\infty}/T_w)^p = h/h_o \qquad (16)$$

The correction term includes the effect of variable density ratio, $\rho_c/\rho_\infty$. It is dependent on nondimensional coolant temperature $\theta$ and should be considered valid only over the nondimensional coolant temperature range of the present measurements: $0 \le \theta < 1.5$.

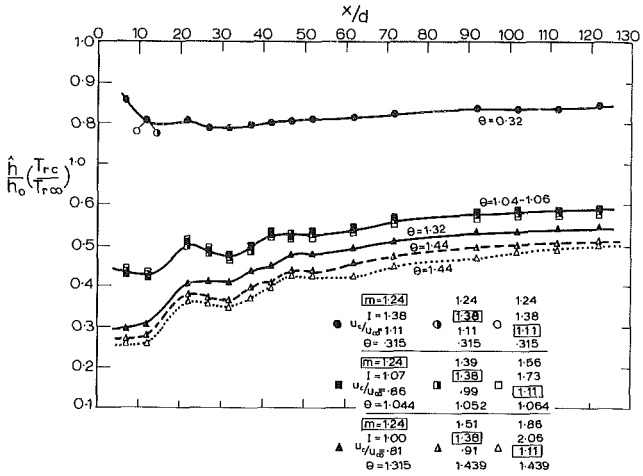


Fig. 9 Variation of $h\hat{/}h_o(T_{rc}/T_{r\infty})^{1.0}$ with $x/d$

(*d*) **Dependence of $h\hat{/}h_o(T_{rc}/T_{r\infty})^n$ on $\theta$ and $x/d$.** In order to show the effect of the portion of the correction term pertaining to adiabatic effectiveness, results in $h\hat{/}h_o\,(T_{rc}/T_{r\infty})^{1.00}$ versus $\theta$ coordinates are given in Fig. 8($b$) for five different values of $x/d$. These results were obtained for $m = 1.24$, $I = 1.38$, and $U_c/U_\infty = 1.11$. Referring to Fig. 4, lines corresponding to these three injection parameters intersect at run number 599. Such intersection points will be referred to as "match points," required in order to provide a suitable basis for comparison of results for the three parameters $m$, $I$, and $U_c/U_\infty$. "Match points" were chosen on the experimental domain map of Fig. 4 at the minimum $\theta$ where measured data were obtained. The smallest $\theta$ was chosen for this purpose in order to obtain the largest differences in the abscissa intercepts of $h\hat{/}h_o\,(T_{rc}/T_{r\infty})^n$ versus $\theta$ lines.

According to Fig. 8($b$), variations of $h\hat{/}h_o\,(T_{rc}/T_{r\infty})^{1.00}$ with $\theta$ obtained for $m = 1.24$, $I = 1.38$, and $U_c/U_\infty = 1.11$ lie along the same line regardless of which parameter is held constant. Such behavior results due to the dependence of $h\hat{/}h_o$ on injection parameters in the film-cooled thermal boundary layer, as evident from results presented in Fig. 5. Here $h\hat{/}h_o$ shows a very weak dependence on all injection parameters for $m > 1.4$. Thus the fact that data for constant $I$, and $U_c/U_\infty$ are along the same line in 8 is not expected for all magnitudes of injection parameters.

The results shown in Fig. 8($b$) are again given in Fig. 9 along with additional data. In this figure, $h\hat{/}h_o\,(T_{rc}/T_{r\infty})^{1.0}$ is given as it varies with $x/d$ for a variety of experimental conditions. The increase of normalized $\hat{h}$ with downstream distance is particularly evident for $\theta = 1.32$–$1.44$. As for Fig. 8, the results in Fig. 9 were determined at measurement points along lines of constant $m$, $I$, and $U_c/U_\infty$ emanating from run number point 599 in Fig. 4. Thus three sets of data each are presented for hot, ambient, and cold injection, where all three data sets for hot injection ($\theta = .315$) are the same since they correspond to the same run number. Even though different data sets were used to determine results for $\theta = 1.04$–$.1.06$, the three curves in Fig. 9 are nearly the same. For $\theta = 1.32$–$1.44$, the $h\hat{/}h_o\,(T_{rc}/T_{r\infty})^{1.0}$ data are slightly different at a given $x/d$, mostly from slightly different $\theta$. Results such as those in Fig. 9 are useful, since they may be used with Fig. 8 type plots in order to determine the variation of the adiabatic film-cooling effectiveness with downstream distance.

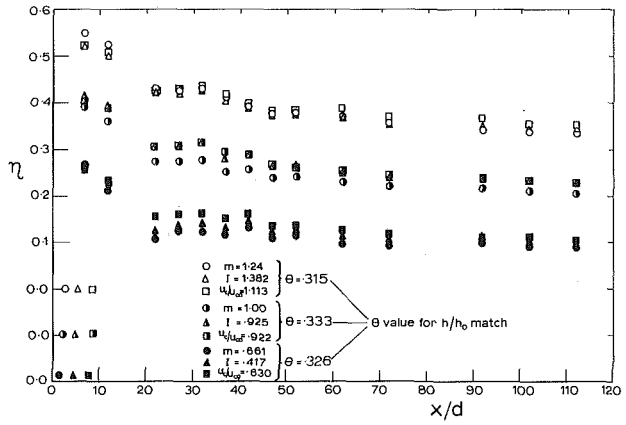


Fig. 10 Adiabatic film cooling effectiveness versus $x/d$ as different injection parameters are held constant

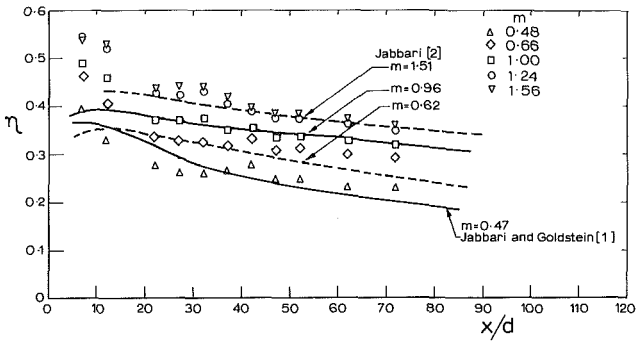


Fig. 11 Comparison of adiabatic film cooling effectiveness with results from [1] and [2]

**(e) Adiabatic Film-Cooling Effectiveness.** The adiabatic film-cooling effectiveness is presented in Fig. 10 at it varies with $x/d$. Results are shown deduced from the same family of data presented in Figs. 8 and 9, along with results from two additional families of data. Values of $\theta$ for the $h/\hat{h}_o$ "match point" are indicated on the figure, and always lie between 0.315 and 0.333. As one expects from results in Figs. 8 and 9, the magnitude of $\eta$ at a given $x/d$ is nearly the same regardless of whether $m = 1.24$, $I = 1.38$, or $U_c/U_\infty = 1.11$. For lower values of these injection parameters, small differences are evident between the $m$, $I$, and $U_c/U_\infty$ results in a given family. Generally, results for constant $U_c/U_\infty$ are several percent higher than the constant $I$ results, which are slightly higher than results at constant $m$. Thus, from Fig. 10, the effect of using constant $m$, $I$, or $U_c/U_\infty$ along a $h/\hat{h}_o\,(T_{rc}/T_{r\infty})^n$ versus $\theta$ line results in effectiveness differences which are no greater than $\pm 10$ percent.

In Fig. 11, $\eta$ results are presented which were deduced by using equation (12) with $n = 1.00$ for $m = .66$, 1.00, 1.24, and 1.56, and $n = 0.80$ for $m = .48$. At a given value of $x/d$, values of $\eta$ increase with $m$, until $m > 1.24$, when further increases in the injection mass flux ratio do not provide higher film cooling effectiveness. At a given mass flux ratio, the effectiveness generally decreases with downstream distance. For $x/d > 20$, Fig. 11 shows that magnitudes of $\eta$ for $m = 1.00$ and $m = 1.56$ agree with Jabbari's [2] measurements at approximately the same injection ratios with a maximum deviation of 10 percent. At $m = 0.66$ and $m = 0.48$ the maximum deviation is about 15 percent. Without the $T_{rc}/T_{r\infty}$ term in equation (12), estimated values of $\eta$ have magnitudes which are one-third to one-half of constant property values at $m = 1.00$. Thus, for $x/d > 20$, the validity of equation (12) is supported by measurements obtained at injection mass flux

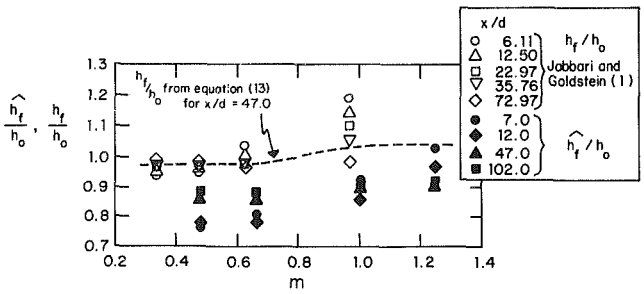


Fig. 12 Normalized film cooling heat transfer coefficients based on the $(T_{AW} - T_W)$ temperature difference

ratios ranging from .48 to 1.56, indicating that the adiabatic film-cooling effectiveness for constant property flow can be deduced from heat transfer measured in a compressible, variable property environment.

The differences between the present results and those from [1] and [2] for $x/d < 20$ are believed to be due to three-dimensional flow near injection holes. According to these sources, $h_f'$ and $\eta'$ are nonuniform in the spanwise direction for $x/d < 20$ with periodic variations dependent on the minimum spanwise distance between injection holes. The local effectiveness $\eta'$ is not equal to the spanwise average effectiveness $\eta$, and equation (5) is not valid. For $x/d > 20$, $n'$ and $h_f'$ become invariant in the cross-stream direction, and equation (5) is valid allowing determination of $\eta$ from variable property heat transfer measurements.

**(f) Heat Transfer Coefficients Based on the $(T_{AW} - T_W)$ Temperature Difference.** The variation of $h_f/\hat{h}_o$ with $m$ is shown in Fig. 12, along with $h_f/h_o$ results from [1]. Magnitudes of $h_f/\hat{h}_o$ were determined from ordinate intercepts of $h/\hat{h}_o\,(T_{rc}/T_{r\infty})^n$ versus $\theta$ lines, as indicated in Fig. 8. Using this procedure, $h_f/\hat{h}_o$ are not dependent on the $(T_{rc}/T_{r\infty})^n$ term in equation (12), because this ratio has the value unity at $\theta = 0$.

The $h_f/\hat{h}_o$ results from the present study are 10–20 percent lower than constant property results from [1]. However, at a given $x/d$, the trends with $m$ from the two sources are similar. At the largest $x/d$ for the two studies (102.0 and 72.97 for [1]), normalized coefficients are nearly constant as $m$ varies. At $x/d \cong 6$–7, $h_f/\hat{h}_o$ and $h_f/h_o$ variations with $m$ are larger than results at all other $x/d$.

Using $p = 0.40$ in equation (13), values of $h_f/h_o$ were calculated from $h_f/\hat{h}_o$ data at $x/d = 47.0$. These corrected $h_f/h_o$ are represented by the dashed line in Fig. 12 and provide a good match with constant property data at about the same $x/d$. Equally good agreement between corrected $h_f/h_o$ and measured values from [1] is also found for other $x/d > 20$.

## 5 Conclusions

An empirical variable property correction for film-cooled turbulent boundary layers is presented. This correction was determined from measurements in a turbulent boundary layer at $M_\infty = 0.64$, $P_{o\infty} = 2.9 \times 10^5$ N/m$^2$, $T_w \cong 290$ K and $T_{o\infty} \cong 403$ K which was film-cooled using two staggered rows of injection holes inclined at 35 deg. The temperature ratio product $(T_{rc}/T_{r\infty})^n (T_{r\infty}/T_w)^p$ is used for the correction as included in the equation

$$h/\hat{h}_o\,(T_{rc}/T_{r\infty})^n (T_{r\infty}/T_w)^p = h_f/h_o(1-\eta\theta) \qquad (12)$$

$n = 1.0$ gives the best fit between $\eta$ values from the present study and those from the University of Minnesota [1, 2] for $.65 < m < 1.6$ and $n = 0.8$ gives the best fit for $m = 0.48$. $p = 0.40$ gives the best fit of $h_f/h_o$ results from the present study to those from [1] for $0.48 < m < 1.00$ and $x/d > 20$.

Equation (12) is useful for $\theta < 1.5$, where it provides a means to determine changes of $\hat{h}/\hat{h}_o$ due to variable properties (including varying density ratio) in film-cooled turbulent boundary layers. All terms on the right-hand side of (12) are for constant properties, whereas $\hat{h}/\hat{h}_o$ is a variable property term.

In order to deduce constant property $\eta$ from variable property $\hat{h}/\hat{h}_o$, plots of $\hat{h}/\hat{h}_o\,(T_{rc}/T_{r\infty})^n$ versus $\theta$ were used. Because $m$, $I$, and $U_c/U_\infty$ all vary with $\theta$ in the compressible environment, the question arises as to which injection parameter to keep constant in the heat transfer plots. Measurements indicate that the $\eta$ in best agreement with constant property measurements is obtained when the injection mass flux ratio $m$ is held constant. However, differences in $\eta$ obtained as $m$, $I$ or $U_c/U_\infty$ are held constant and are never greater than $\pm$ 10 percent, and nearly zero for $1.24 \leq m \leq 1.56$.

Variable property, film-cooled turbulent boundary layers are complex thermal-fluid systems. A complete variable property correction would depend on injection system geometry, injection flow rate parameters, all important temperatures, the fluid mechanics of the flow, the fluid mechanics of the injection jets, the type of fluid, compressibility parameters, and thermal boundary conditions. The variable property equation of the present paper offers a simple correction for a flow with a particular film-cooling geometry over a range of conditions. More experiments are needed to determine the accuracy of proposed corrections over wider ranges of conditions. With the variable property correction terms in equation (12), a means is provided to determine isothermal wall heat transfer coefficients in environments with temperature dependent fluid properties from constant property $h_f$ and $\eta$ data available in the literature. The equation also allows determination of $\hat{h}/\hat{h}_o$ at a given $\theta$ in a variable property environment, provided data are available at two other $\theta$ less than 1.5. As such, the results of the present paper give an indication of the importance of variable properties in film-cooled turbulent boundary layers, and hopefully, will provoke more attention and discussion to this area.

## Acknowledgments

Mr. Rogier Conniasselle is the technical engineer for the von Karman Institute CT-2 facility used for the present study. The authors also acknowledge the helpful comments of three anonymous referees. Mr. M. Pezzani, Professor R. J. Goldstein, and Professor R. J. Moffat are to be thanked for fruitful discussions on the research. Professor P. Bradshaw provided several useful comments after reading the first draft of the manuscript. The support of Professor J. J. Ginoux, Director of the von Karman Institute, is also much appreciated by the authors.

## References

1 Jabbari, M. Y., and Goldstein, R. J., "Adiabatic Wall Temperature and Heat Transfer Downstream of Injection Through Two Rows of Holes," ASME *Journal of Engineering for Power*, Vol. 100, April 1978, pp. 303–307.

2 Jabbari, M. Y., "Film Cooling and Heat Transfer with Air Injection Through a Staggered Row of Holes into an Accelerating Flow," Ph.D. Thesis, University of Minnesota, Minneapolis, Minn., 1973.

3 Pedersen, D. R., Eckert, E. R. G., and Goldstein, R. J., "Film Cooling with Large Density Differences Between the Mainstream and the Secondary Fluid Measured by the Heat Mass Transfer Analogy," ASME JOURNAL OF HEAT TRANSFER, Vol. 99, Nov. 1977, pp. 620–627.

4 Goldstein, R. J., Eckert, E. R. G., and Burggraf, F., "Effects of Hole Geometry and Density on Three-Dimensional Film Cooling," *International Journal of Heat and Mass Transfer*, Vol. 17, 1973, pp. 595–607.

5 Foster N. W., and Lampard, D., "Effects of Density and Velocity Ratio on Discrete Hole Film Cooling," *AIAA Journal*, Vol. 13, No. 8, Aug. 1975, pp. 1112–1114.

6 Choe, H., Kays, W. M., and Moffat, R. J., "The Turbulent Boundary Layer on a Full Coverage Film Cooled Surface. An Experimental Heat Transfer Study with Normal Injection," Report HMT-11, Stanford University, May 1975.

7 Moffat, R. J., "Full-Coverage Film Cooling," Film Cooling and Turbine Blade Heat Transfer, VKI LS 1982-03, von Karman Institute for Fluid Dynamics, Rhode-St-Genese, Feb. 22–26, 1982.

8 Metzger, D. E., Carper, H. J., and Swank, L. R., "Heat Transfer with Film Cooling Near Nontangential Injection Slots," *Journal of Engineering for Power*, Apr. 1968, pp. 157–163.

9 Metzger, D. E., and Fletcher, D. D., "Evaluation of Heat Transfer for Film-Cooled Components," *Journal of Aircraft*, Vol. 8, No. 1, Jan. 1971, pp. 33–38.

10 Eckert, E. R. G., Goldstein, R. J., and Pedersen, D. R., "Comment on 'Evaluation of Heat Transfer for Film-Cooled Turbine Components,' " *Journal of Aircraft*, Vol. 18, No. 1, Jan. 1971, pp. 63–64.

11 Eckert, E. R. G., "Analysis of Film Cooling and Full-Coverage Film Cooling of Gas Turbine Blades," Tokyo International Gas Turbine Congress, 83-TOKYO-IGTC-15, ASME-83-GTJ-2, 1983.

12 Paradis, M. A., "Film Cooling of Gas Turbine Blades: a Study of the Effect of Large Temperature Differences on Film Cooling Effectiveness," ASME *Journal of Engineering for Power*, Vol. 99, No. 1, Jan. 1977, pp. 1–10.

13 Ligrani, P. M., and Breugelmans, F. A. E., "Turbine Blade Cooling Research at the von Karman Institute for Fluid Dynamics," Fifth International Symposium on Air Breathing Engines, Bangalore, India, Feb. 16–21, 1981.

14 Consigny, H., and Richards, B. E., "Short Duration Measurements of Heat Transfer Rate to a Gas Turbine Rotor Blade," ASME *Journal of Engineering for Power*, Vol. 104, No. 3, July, 1982, pp. 542–551.

15 Schultz, D. L., Jones, T. V., Oldfield, M. L. G., and Daniels, L. C., "A New Transient Facility for the Measurement of Heat Transfer Rates," *AGARD Conference Proceedings No. 229, High Temperature Problems in Gas Turbine Engines*, Sept. 1977, pp. 33-1–31-27.

16 Schlichting, H., *Boundary Layer Theory* (6th ed.), McGraw-Hill, New York, 1968.

17 Kays, W. M., and Crawford, M .E., *Convective Heat and Mass Transfer* (2d ed.), McGraw-Hill, New York, 1980.

18 Ligrani, P. M., Camci, C., and Grady, M. S., "Thin Film Heat Transfer Gage Construction and Measurement Details," VKI Technical Memorandum 33, von Karman Institute for Fluid Dynamics, Rhode-St-Genese, Nov. 1982.

19 Oldfield. M. L. G., Jones, T. V., and Schultz, D. L., "On-Line Computer for Transient Turbine Casade Instrumentation," *IEEE Transactions on Aerospace and Electronics Systems*, Vol. AES-14, No. 5, Sept. 1978, pp. 738–749.

20 Benmansour, S., "Discharge Coefficients of Film Cooling Holes," M. Phil. thesis, University of Nottingham, Nottingham, 1981.

21 Papell, S. S., and Trout, A. M., "Experimental Investigation of Air Film Cooling Applied to an Adiabatic Wall by Means of an Axially Discharging Slot," NASA TN D-9, 1959.

# Local and Average Heat Transfer Characteristics for a Disk Situated Perpendicular to a Uniform Flow

**E. M. Sparrow**
Fellow ASME

**G. T. Geiger**

Department of Mechanical Engineering,
University of Minnesota,
Minneapolis, Minn. 55455

*Wind tunnel experiments were performed to determine both the average heat transfer coefficient and the radial distribution of the local heat transfer coefficient for a circular disk facing a uniform oncoming flow. The experiments covered the range of Reynolds numbers Re from 5000 to 50,000 and were performed using the naphthalene sublimation technique. To complement the experiments, an analysis incorporating both potential flow theory and boundary layer theory was used to predict the stagnation point heat transfer. The measured average Nusselt numbers definitively resolved a deep disparity between information from the literature and yielded the correlation* $\overline{Nu} = 1.05\ Pr^{0.36}\ Re^{1/2}$. *The radial distributions of the local heat transfer coefficient were found to be congruent when they were normalized by* $Re^{1/2}$. *Furthermore, the radial profiles showed that the local coefficient takes on its minimum value at the stagnation point and increases with increasing radial distance from the center of the disk. At the outer edge of the disk, the coefficient is more than twice as large as that at the stagnation point. The theoretical predictions of the stagnation point heat transfer exceeded the experimental values by about 6 percent. This overprediction is similar to that which occurs for cylinders and spheres in crossflow.*

## Introduction

This paper is a many-faceted study of heat transfer at a circular disk that is situated perpendicular to a uniform airflow. The experimental portion of the work included independent measurements of the average heat transfer coefficient and of the radial distribution of the local heat transfer coefficient. The measurements were performed over a Reynolds number range spanning an order of magnitude. To attain the desired level of accuracy as well as a high degree of local resolution, the naphthalene sublimation technique, a mass transfer method, was used. The mass transfer coefficients were converted to heat transfer coefficients by means of the analogy between the two processes. In the analytical part of the work, potential flow theory was used in conjunction with boundary layer theory to yield the stagnation point heat transfer coefficient.

To provide perspective for the present work, it is relevant to consider the available literature on heat transfer to a disk facing an oncoming flow. There are, seemingly, two relevant papers, respectively by Sogin [1] (1958) and by Beg [2] (1972). In both cases, the naphthalene sublimation technique was employed to determine the average heat (mass) transfer coefficient. As will be elaborated on shortly, the results obtained by these investigators are at variance, so that one of the objectives of the present research is to provide definitive values of the average heat transfer coefficient in order to settle the issue.

The correlation of the Sogin results yielded a $Re^{1/2}$ dependence for the average Nusselt number, and Beg, seemingly unaware of Sogin's work, sought the same Reynolds number relationship. There are sound reasons for uncertainty about the aptness of a $Re^{1/2}$ dependence for the average Nusselt number. From theory, to be described in detail later in the paper, it can be shown that the stagnation point heat transfer coefficient varies as $Re^{1/2}$. However, away from the stagnation point, the problem does not conform to a similarity solution of the conservation equations. Nonsimilar boundary layers do not, at least in principle, yield power-law relationships between the Nusselt and Reynolds numbers. With this background, another focus of the work is to examine the degree of nonsimilarity which prevails away from the stagnation region.

With regard to the radial distribution of the heat transfer coefficient, the classical, edge-effect-free model would predict a decrease in the coefficient with increasing distance from the center of the disk. On the other hand, the sharp turning of the flow at the outer edge of the disk is expected to give rise to relatively high velocities in that region, with the possibility of locally high heat transfer coefficients – another issue to be examined here.

The final focus of the research is to determine a theoretical prediction of the stagnation point heat transfer coefficient and to compare this result with that found from experiment. In this regard, it may be noted that for other stagnation point flows (for example, a cylinder and a sphere) in a low-turbulence free stream, the measured heat transfer coefficients are somewhat lower than those of the theory.

It is appropriate to briefly elaborate certain relevant factors of the work of Sogin and of Beg. Based on the description given in the paper, the Sogin experiments appear to be carefully performed, but there may be some concern that no provision was made for a pre-data-run equilibration period to enable the naphthalene to attain temperature equality with the airflow. This issue is given relevance by the fact that the vapor pressure of naphthalene is highly sensitive to temperature (10 percent change per °C) and that Sogin measured the air temperature and not the surface temperature of the naphthalene.

Beg's work is characterized by a certain degree of ambiguity in that he gives four separate and conflicting correlations of his experimental results, with that set forth in the abstract and the conclusions being substantially higher than the plotted data (e.g., 30 percent higher at Re = 10,000). Furthermore, the $Nu \sim Re^{1/2}$ type correlation falls well below the data (by about 30 percent at Re = 10,000). No information is given about the critical issue of thermal equilibration and tem-

Contributed by the Heat Transfer Division for publication in the JOURNAL OF HEAT TRANSFER. Manuscript received by the Heat Transfer Division July 3, 1984.

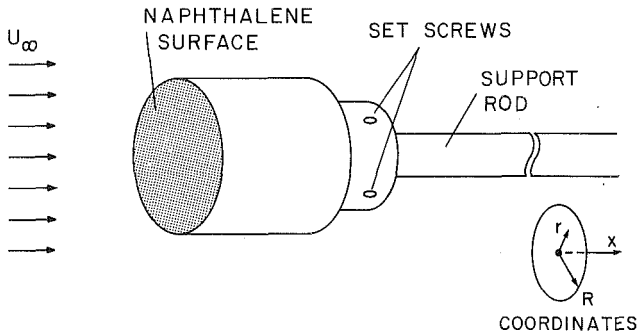


**Fig. 1 The experimental setup**

perature measurement, and Sogin's highly relevant work is not cited.

The data of Beg fall well below those of Sogin. For instance, at Re = 10,000, the respective dimensionless mass transfer coefficients (i.e., average Sherwood numbers) are 103 and 147.

## The Experiments

**Experimental Apparatus.** As was noted in the Introduction, the experiments were performed by making use of the naphthalene sublimation technique. To implement this technique, the disk was made of solid naphthalene implanted in a short cylinder as shown schematically in Fig. 1. The implantation of the naphthalene was accomplished by a casting procedure that will be described shortly.

With respect to the analogy between heat and mass transfer, the naphthalene surface plays a role identical to an isothermal surface in the corresponding heat transfer problem. On the other hand, the host cylinder was of aluminum and did not, therefore, participate in the mass transfer process. In terms of the analogous heat transfer problem, the cylinder corresponds to a perfectly insulated body.

The diameter of the disk and its host cylinder was 3.493 cm, with the cylinder length being approximately equal to the diameter. Integral with the cylinder at its downstream end was a short cylindrical section having a slightly reduced diameter. The shoulder formed by the reduction in diameter helped to position the disk during surface contour measurements made before and after the data runs.

To accommodate the naphthalene layer, whose exposed face constituted the mass transfer surface, a 0.7-cm-deep cavity was machined into the front face of the host cylinder. The cavity was bounded by a thin wall that was steeply sloped so as to be of minimal thickness at the plane of the cavity opening. As a result, the naphthalene-filled cavity was framed by a remarkably thin (0.005 cm) rim of aluminum. To promote adhesion of the naphthalene, the base of the cavity was roughened with grooves.

To facilitate the casting of the naphthalene, a pouring hole was drilled along the axis of the cylinder from one end to the other. Two additional (smaller) holes were provided to enable air to escape from the cavity during the casting process. One of these holes also served as a channel through which thermocouple leads were passed. The thermocouple junction was positioned at the exposed surface of the naphthalene, enabling direct measurement of the surface temperature needed for the evaluation of the naphthalene vapor pressure.

The other component shown in Fig. 1 is the support rod. When the apparatus is in place in the wind tunnel, the rod mates with the cylinder as depicted in the figure, the mating being accomplished by the insertion of the reduced-diameter end of the rod into the axial hole in the cylinder. Recessed screws, also shown in the figure, bear against flats machined into the embedded portion of the rod, thereby holding it in place.

The support rod is the forwardmost member of a system whose function is both to support the disk and to position it perpendicular to the oncoming airflow. The alignment of the disk was facilitated by a universal joint attached to the downstream end of the support rod. In turn, the universal joint was rigidly supported by a stand that was bolted to the floor of the wind tunnel. The crossflow members of the stand were positioned sufficiently far downstream of the disk to preclude any possible interference effects.

Another apparatus component essential to the successful execution of the experiments was a cap that totally suppressed sublimation of naphthalene when it was in place over the disk. Such total suppression was required prior to a data run when the test body, installed in the wind tunnel, was in the process of thermally equilibrating with the airflow; total suppression was also necessary when the body was transported from the wind tunnel laboratory to another laboratory in which the mass measurement instrumentation was situated.

The cap was fabricated from a Teflon rod into which a cylindrical cavity was bored. When in place, the cap covered

## Nomenclature

$A$ = surface area of disk
$C$ = constant in local free-stream velocity representation
$D$ = diameter of disk
$\mathfrak{D}$ = diffusion coefficient
$K_o$ = stagnation point mass transfer coefficient
$K(r)$ = local mass transfer coefficient
$\bar{K}$ = average mass transfer coefficient
$L$ = characteristic length
$\Delta M$ = change of mass
$\dot{m}_o$ = stagnation point mass flux
$\dot{m}(r)$ = local mass flux
$\bar{\dot{m}}$ = average mass flux
Nu = Nusselt number
$\mathrm{Nu}_o$ = stagnation point Nusselt number
$\overline{\mathrm{Nu}}$ = average Nusselt number
Pr = Prandtl number
$R$ = radius of disk
Re = Reynolds number, $U_\infty D/\nu$
$r$ = radial coordinate
Sc = Schmidt number
$\mathrm{Sh}_o$ = stagnation point Sherwood number, $K_o D/\mathfrak{D}$
$\mathrm{Sh}(r)$ = local Sherwood number, $K(r)D/\mathfrak{D}$
$\overline{\mathrm{Sh}}$ = average Sherwood number, $\bar{K}D/\mathfrak{D}$
$s$ = surface coordinate
$U_\infty$ = velocity of uniform oncoming flow
$u_\infty(s)$ = local free-stream velocity at edge of boundary layer
$v$ = radial velocity
$v_\infty(r)$ = radially directed local free-stream velocity
$x$ = axial coordinate
$\beta$ = parameter in boundary layer mass (heat) transfer solution
$\delta_o$ = surface recession at stagnation point
$\delta(r)$ = local surface recession
$\theta'(0)$ = parameter in boundary layer mass (heat) transfer solution
$\nu$ = kinematic viscosity
$\rho_{nw}$ = naphthalene vapor density at disk surface
$\rho_{n\infty}$ = naphthalene vapor density in free stream
$\tau$ = duration of data run
$\phi$ = velocity potential function
$\chi$ = constant which depends on geometry and on Schmidt (Prandtl) number

**Subscripts**

ex = from experiment
th = from theory

the naphthalene disk and most of the host cylinder. The fit was so snug that a small-diameter vent hole had to be provided in the closed end of the cap (the end adjacent to the naphthalene disk) to enable it to be applied to or removed from the test body. Aside from these operations, the vent hole was sealed with pressure-sensitive tape. The closed end of the cap was made thin-walled so as not to greatly elongate the equilibration period.

The wind tunnel used in the experiments was operated over a range of free-stream velocities $U_\infty$ from 2.1 to 21 m/s, corresponding to Reynolds numbers between 5000 and 50,000 based on the diameter of the disk. The cross section of the tunnel test section was a 30.48 by 60.96 cm rectangle (height by width), and the disk was centered in the cross section. Since the ratio of the disk surface area to the tunnel cross-sectional area was about 0.005, blockage effects can be regarded as negligible.

The tunnel was operated in the suction mode, with air being drawn from within the building and discharged out-of-doors, thereby ensuring that the air arriving at the test section was free of naphthalene vapor. To promote the temperature uniformity of the air, the laboratory room was set up as a mixing chamber (e.g., auxiliary fans were used to enhance the mixing), and the windows were masked with aluminum-faced insulation panels.

The velocity in the test section was measured with an impact tube and adjacent wall static tap, both situated slightly upstream and to the side of the disk. The resulting pressure differential was sensed by a Baratron solid-state pressure meter capable of detecting 0.001 Torr, and the same meter was used to measure the difference between the tunnel static pressure and that of the laboratory. Recent measurements had shown the tunnel turbulence level to be about 0.5 percent.

**Experimental Procedure.** A new naphthalene surface was prepared prior to each data run. As a first step, the naphthalene remaining from the preceding data run was removed from the host cylinder by melting and evaporation. Then, the cylinder was placed on a highly polished stainless steel plate so that its axis was vertical and the cavity opening faced downward. The plate surface closed the opening, thereby forming a mold cavity. The thermocouple was then threaded through one of the air vent holes and fixed in place so that the junction contacted the plate. Molten naphthalene was then introduced into the cavity through the axial pour hole, and the displaced air escaped through the vent holes. After the naphthalene had solidified, the cylinder was separated from the plate. The quality of the exposed naphthalene surface was comparable to that of the highly polished plate against which it was cast.

The measurements which were made immediately preceding and immediately following a data run depended on whether average or local mass transfer coefficients were being sought. For the former, the mass of the test body was measured, while for the latter, measurements were made of the surface contour of the disk.

A common feature of all runs was the verification that the disk was oriented perpendicular to the oncoming flow. The original alignment was accomplished by flow visualization using the oil-lampblack technique, with adjustments being made until the stagnation point was situated at the center of the disk. When this condition was achieved, the settings of the universal joint were recorded, and these settings were employed throughout the remainder of the experimental work.

Each run was preceded by an equilibration period during which the capped test body was in place in the wind tunnel and washed by the free-stream velocity of the selected data run. The duration of the equilibration period was chosen to ensure the attainment of steady readings of the thermocouple embedded in the naphthalene surface.

The duration of the data run proper was fixed by the constraint that the mean recession of the naphthalene surface not exceed 0.0025 cm. During the run, the naphthalene surface temperature and the velocity pressure were recorded at uniform and frequent intervals, and averages were computed for use in the data reduction procedure.

The mass of the test body was measured with a Sartorius ultraprecision, electronic analytical balance with a capacity of 166 g and a resolution of $10^{-2}$ mg. Typical mass losses during a data run were in the 15–30 mg range.

Surface contour measurements were made with a stylus-type instrument that senses the elevation of the stylus tip electronically. The measurement system consisted of the stylus, a linear variable differential transformer, signal conditioning electronics, and a printer-equipped digital voltmeter. The nominal resolving power of the instrumentation was 0.000025 cm. For a given data run, surface traverses were made along four radial lines (i.e., two perpendicular diameters), and the measured local surface recessions were averaged to give a single representative radial distribution.

Calibration runs were made to determine the extraneous mass losses during the setup and disassembly of the apparatus, yielding a correction of about 2 percent.

**Data Reduction.** The average mass transfer coefficient $\bar{K}$ for the disk as a whole was evaluated from the defining equation

$$\bar{K} = \bar{\dot{m}}/(\rho_{nw} - \rho_{n\infty}) \tag{1}$$

In this equation, $\bar{\dot{m}}$ is the surface-average rate of mass transfer. It was calculated from the measured change of mass $\Delta M$, the naphthalene mass transfer area $A$, and the duration $\tau$ of the data run, so that $\bar{\dot{m}} = \Delta M/\tau A$. The quantities $\rho_{nw}$ and $\rho_{n\infty}$ are, respectively, the densities of naphthalene vapor at the disk surface and in the free stream. The latter is zero for the present experiments, while the former was evaluated using the vapor pressure/temperature relation for naphthalene [1] (assuming solid-vapor equilibrium at the naphthalene surface), in conjunction with the perfect gas law.

For a dimensionless presentation, $\bar{K}$ was expressed in terms of the average Sherwood number

$$\overline{\mathrm{Sh}} = \bar{K}D/\mathfrak{D} \tag{2}$$

where $D$ is the diameter of the disk, and $\mathfrak{D}$ is the mass diffusion coefficient, which was evaluated using a formula given by Skelland ([3], p. 51). The knowledge of the diffusion coefficient also enabled the Schmidt number Sc ( $= \nu/\mathfrak{D}$) to be calculated, where $\nu$ is the kinematic viscosity of pure air. For all of the operating conditions of the experiments, the Schmidt number was found to be 2.55.

The local mass transfer coefficient $K(r)$ at any radial position $r$ is

$$K(r) = \dot{m}(r)/(\rho_{nw} - \rho_{n\infty}) \tag{3}$$

where $\dot{m}(r)$ is the local mass flux. This coefficient may be normalized by the value of $K$ at the center of the disk (i.e., the stagnation point value)

$$K(r)/K_o = \dot{m}(r)/\dot{m}_o \tag{4}$$

If $\delta(r)$ and $\delta_o$ respectively denote the measured surface recessions at a radial position $r$ and at $r = 0$, it follows that since $\dot{m}(r) = \rho_s\delta(r)$ and $\dot{m}_o = \rho_s\delta_o$ ($\rho_s$ = density of solid naphthalene = 1.146), $\dot{m}(r)/\dot{m}_o = \delta(r)/\delta_o$. Also, since $D/\mathfrak{D}$ is a constant, $K(r)/K_o = \mathrm{Sh}(r)/\mathrm{Sh}_o$. With these,

$$\mathrm{Sh}(r)/\mathrm{Sh}_o = \delta(r)/\delta_o \tag{5}$$

The $\mathrm{Sh}(r)/\mathrm{Sh}_o$ ratio, evaluated from equation (5), will be used to display the radial distribution of the mass transfer coefficient.

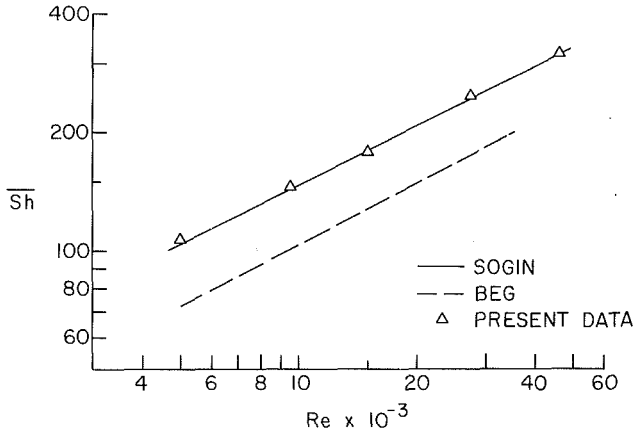

Fig. 2 Average Sherwood numbers

The mass transfer results will be parameterized by the Reynolds number

$$\mathrm{Re} = U_\infty D/\nu \tag{6}$$

where the free-stream velocity was evaluated from the measured velocity pressure.

## Stagnation Point Theory

A prediction of the heat (mass) transfer at the stagnation point of the disk will now be derived by using potential flow theory in conjunction with boundary layer theory. As will be documented shortly, boundary layer theory yields a relationship between the Nusselt (Sherwood) number and the Reynolds number, but the local radially-directed free-stream velocity $v_\infty(r)$, which appears in the Reynolds number, is an unknown. It is the responsibility of potential flow theory to provide $v_\infty(r)$, and that is the first order of business here.

The velocity potential function for a stationary disk situated in a uniform free-stream flow can be written as

$$\phi = \phi_1 + \phi_2 \tag{7}$$

Here, $\phi_1$ is the potential for a disk moving with velocity $U_\infty$ perpendicular to its own plane in an otherwise stationary fluid, and $\phi_2$ is the potential for a uniform flow with free-stream velocity $U_\infty$. The direction of motion of the disk is opposite to that of the free-stream velocity.

With respect to a coordinate system implanted in the disk surface and centered at the stagnation point (see Fig. 1), the radial velocity $v$ is given by $v = \partial\phi/\partial r$. However, $\phi_2 = \phi_2(x)$, where $x$ is the axial coordinate (aligned with $U_\infty$), so that $\partial\phi_2/\partial r = 0$. At the surface of the disk ([4], p. 477)

$$\phi_1 = -(2U_\infty R/\pi)\cos\eta \tag{8}$$

where $R$ is the radius of the disk and $\eta = \sin^{-1}(r/R)$. Therefore, the radial velocity at the surface of the disk follows as

$$v(r) = \partial\phi/\partial r = \partial\phi_1/\partial r = (2U_\infty/\pi)(r/R)(1 - r^2/R^2)^{-1/2} \tag{9}$$

In the neighborhood of the stagnation point, equation (9) reduces to

$$v(r) = (2U_\infty/\pi)(r/R) \tag{10}$$

According to first-order boundary layer theory, the potential-flow-related velocity tangential to the surface is equal to the free-stream velocity for the boundary layer. Thus the radially directed free-stream velocity for the stagnation point boundary layer is

$$v_\infty(r) = (2U_\infty/\pi)(r/R) \tag{11}$$

Next, turning to the boundary layer, it may be noted that axisymmetric stagnation point flow yields a similarity solution. From [5], the stagnation point mass transfer coefficient $K_o$ given by that solution can be expressed as

$$(K_o r/\mathfrak{D})/[v_\infty(r) r/\nu]^{1/2} = \sqrt{3}\theta'(0)/(2-\beta)^{1/2} \tag{12}$$

In this equation, the quantity $\theta'(0)$ depends on the Schmidt number Sc and on the parameter $\beta$, which, for a disk, is equal to 1/2. The numerical value of $\theta'(0)$ was read by interpolation from Table 7.5($d$) of [5] for input values of Sc = 2.55 and $\beta$ = ½, which gave $\theta'(0) = 0.762$.

The substitution of $\theta'(0)$, $\beta$, and $v_\infty(r)$ (from equation (11)) into equation (12) and subsequent rearrangement yields

$$\mathrm{Sh}_o = K_o D/\mathfrak{D} = 1.216\,\mathrm{Re}^{1/2} \tag{13}$$

in which Re is given by equation (6) as before. Note that $\mathrm{Sh}_o$ depends on the half power of the Reynolds number, as expected. The values of $\mathrm{Sh}_o$ from equation (13) will be compared shortly with those from experiment.

## Results and Discussion

**Analogy Between Heat and Mass Transfer.** As a prelude to the presentation of the results, the conversion of the measured mass transfer coefficients to heat transfer coefficients will be discussed. According to the analogy between heat and mass transfer

$$\mathrm{Nu}/f(\mathrm{Pr}) = \mathrm{Sh}/f(\mathrm{Sc}) \tag{14}$$

where the function $f$ is the same for both processes. For most convective heat transfer processes (other than those involving liquid metals), $f(\mathrm{Pr}) = \mathrm{Pr}^m$, $f(\mathrm{Sc}) = \mathrm{Sc}^m$, where $1/3 \le m \le 0.4$.

For heat or mass transfer at an axisymmetric stagnation point, the solutions of [5] can be well correlated using $m$ = 0.36, and this value will be employed here. With this, equation (14) becomes

$$\mathrm{Nu} = (\mathrm{Pr}/\mathrm{Sc})^{0.36}\mathrm{Sh} \tag{15}$$

Since Sc = 2.55 for the present experiments

$$\mathrm{Nu} = 0.714\mathrm{Pr}^{0.36}\mathrm{Sh} \tag{16}$$

which will shortly be used to transform the present Sherwood numbers to Nusselt numbers corresponding to a given Prandtl number.

**Average Sherwood Numbers.** The presentation of results will begin with the average Sherwood number, which is plotted in Fig. 2 as a function of the Reynolds number over the range between 5000 and 50,000. The present $\overline{\mathrm{Sh}}$ values are depicted by the data symbols, while those of Sogin [1] and of Beg [2] are respectively represented by the solid and dashed lines. The Sogin line was plotted from his correlation equation

$$\overline{\mathrm{Sh}} = 1.08\mathrm{Re}^{1/2}\mathrm{Sc}^{1/3} \tag{17}$$

Note that since Sogin used Sc = 2.5 in formulating the correlation, this same value was used here in its evaluation, which gives

$$\overline{\mathrm{Sh}} = 1.47\mathrm{Re}^{1/2} \tag{18}$$

The factor $\mathrm{Sc}^{1/3}$ in equation (17) represents an arbitrary choice. With regard to Beg's results, the line appearing in Fig. 2 was taken from his graphical presentation. Not one of the four correlation equations set forth by Beg matches that line.

Examination of Fig. 2 reveals remarkably good agreement between the present data and the Sogin line. Indeed, the deviations of the data from the line are smaller than the scatter of Sogin's original data. This strong consensus casts doubt on Beg's results and suggests that they be discarded.

In light of the foregoing, the Sogin correlation (18) appears to be the proper representation for the average Sherwood number for naphthalene sublimation at a disk situated perpendicular to an oncoming uniform flow. To generalize this correlation to heat transfer, equation (18) is substituted into equation (16), which gives

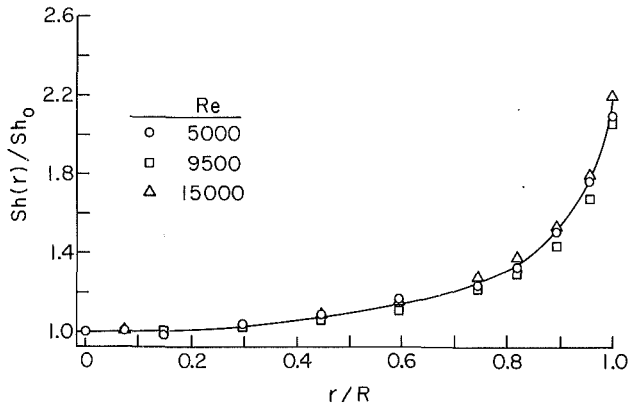


Fig. 3 Radial profiles of the local Sherwood number for the lower Reynolds number range

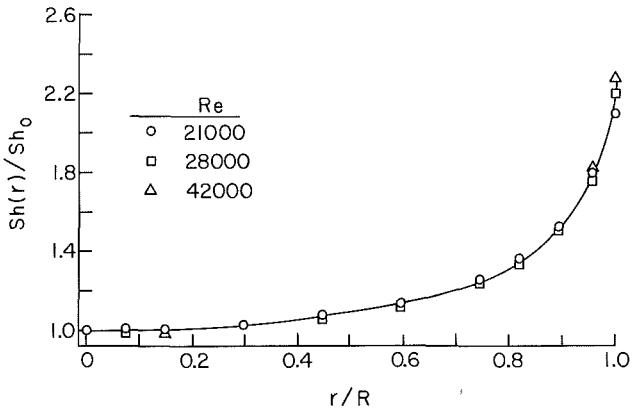


Fig. 5 Stagnation point Sherwood numbers

$$\overline{Nu} = 1.05 Pr^{0.36} Re^{1/2} \quad (19)$$

**Local Sherwood Numbers.** Since the disk is a surface of uniform naphthalene vapor density (analogous to uniform wall temperature), it follows that

$$\overline{Sh} = \int_0^R [Sh(r)] 2\pi r dr / \pi R^2 \quad (20)$$

where Sh($r$) is the local Sherwood number at a radial position $r$. The introduction of the stagnation point Sherwood number Sh$_o$ gives

$$\overline{Sh}/Sh_o = \int_0^R [Sh(r)/Sh_o] 2\pi r dr / \pi R^2 \quad (21)$$

Note that both $\overline{Sh}$ and Sh$_o$ vary as Re$^{1/2}$ (equations (18) and (13), respectively), so that $\overline{Sh}$/Sh$_o$ is independent of the Reynolds number. Because of this, equation (21) suggests the possibility that Sh($r$)/Sh$_o$ is independent of Reynolds number, that is, that the Sh($r$) profiles are similar with respect to Re$^{1/2}$ scaling.

Figures 3 and 4 were prepared to examine this issue. In each figure, Sh($r$)/Sh$_o$ is plotted as a function of the dimensionless radial coordinate $r/R$, where the values of Sh($r$)/Sh$_o$ were determined via equation (5) from the measured surface recessions $\delta(r)$ and $\delta_o$. The first of these figures is for the lower Reynolds numbers of the investigated range, while the second is for the higher Reynolds numbers. The solid line that appears in each figure is one and the same line. It is the average Sh($r$)/Sh$_o$ profile, averaged over all six Reynolds numbers that are represented in the figures.

From Figs. 3 and 4, it is seen that aside from reasonable data scatter, the Sh($r$)/Sh$_o$ profiles are independent of the Reynolds number. The correlation is especially tight in the higher Reynolds number range, where there is considerable data overlap. Since Sh$_o$ ~ Re$^{1/2}$, it follows that the Sh($r$) profiles are similar with respect to Re$^{1/2}$. This finding explains why $\overline{Sh}$ ~ Re$^{1/2}$. It is noteworthy that there are no theoretical or computational results available to either confirm or deny the Re$^{1/2}$ similarity of the Sh($r$) profiles.

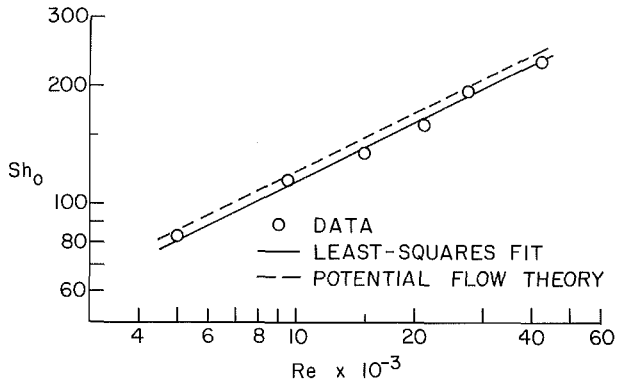


Fig. 4 Radial profiles of the local Sherwood number for the higher Reynolds number range

Another noteworthy feature of Figs. 3 and 4 is the monotonic increasing character of the Sh($r$)/Sh$_o$ profiles. The increase is moderate in the inner half of the disk (i.e., a 10 percent increase in Sh($r$) between $r = 0$ and $r/R = 0.5$) but, thereafter, Sh($r$)/Sh$_o$ increases rapidly, especially between $r/R = 0.9$ and 1.0. At the edge of the disk, Sh($r$)/Sh$_o \simeq 2.2$.

This behavior is to be contrasted with textbook-type, end-effect-free flows which fan out from a stagnation point (or stagnation line). For those flows, the highest value of the transfer coefficient is attained at the stagnation point and decreases with increasing distance from that point. The drop-off of the transfer coefficient is a consequence of the growth of the boundary layer.

Relative to the foregoing, the highly contrasting behavior of Sh($r$) evidenced in Figs. 3 and 4 provides ample testimony to the dominant role played by the finiteness of the disk. The turning of the flow at the edge of the disk requires that the fluid accelerate rapidly in that region. The rapid acceleration causes a thinning of the boundary layer and a consequent increase in the transfer coefficient. What is most remarkable is that the edge effect is felt sufficiently strongly in the neighborhood of the center of the disk to reverse the tendency of Sh($r$) to decrease with radial distance.

**Stagnation Point Results.** It remains to compare the experimentally determined values of the stagnation point Sherwood number with those based on potential flow theory. Such a comparison is shown in Fig. 5, where Sh$_o$ is plotted as a function of the Reynolds number. The figure conveys the experimental data, a least-squares, Re$^{1/2}$ fit of the data given by

$$Sh_o = 1.140 Re^{1/2} \quad (22)$$

and the prediction based on potential flow as expressed by equation (13). The mean scatter of the data about the least-squares line is 3 percent. By comparing equations (22) and (13), it is seen that the theory overpredicts the data by about 6 percent.

To provide perspective for this finding, it is relevant to compare experimental and theoretical results for other stagnation point flows. In general, at a stagnation point (or stagnation line)

$$u_\infty(s)/U_\infty = C(s/L) \quad (23)$$

where $s$ is the distance along the surface measured from the stagnation point, $u_\infty(s)$ is the local free-stream velocity at the edge of the boundary layer, $L$ is the characteristic dimension, and $C$ is a constant specific to the geometry in question.

From boundary layer theory, it is known that, in general

$$K_o s/\mathfrak{D} = \chi[u_\infty(s)s/\nu]^{1/2} \tag{24}$$

in which $\chi$ depends on the geometry and on the Schmidt (or Prandtl) number. Upon elimination of $u_\infty(s)$ from equation (24) with the aid of equation (23), there follows

$$\mathrm{Sh}_o = \chi C^{1/2} \mathrm{Re}^{1/2} \tag{25}$$

where

$$\mathrm{Sh}_o = K_o L/\mathfrak{D},\ \mathrm{Re} = U_\infty L/\nu \tag{26}$$

Suppose that for a given geometry, the constant $C$ has been determined both by experiment and from potential flow theory, yielding respective values $C_{ex}$ and $C_{th}$. Then, the corresponding stagnation point Sherwood numbers can be ratioed to give

$$(\mathrm{Sh}_o)_{ex}/(\mathrm{Sh}_o)_{th} = (C_{ex}/C_{th})^{1/2} \tag{27}$$

or, for the Nusselt number,

$$(\mathrm{Nu}_o)_{ex}/(\mathrm{Nu}_o)_{th} = (C_{ex}/C_{th})^{1/2} \tag{28}$$

The two bluff bodies most often encountered in stagnation flow studies are the cylinder and the sphere. In the case of a cylinder in a uniform crossflow, the result from potential flow theory is that $C_{th} = 4$, while Schmidt and Wenner [6] have found experimentally that $C_{ex} = 3.631$. Hence, the ratio of the stagnation line Nusselt numbers becomes

$$(\mathrm{Nu}_o)_{ex}/(\mathrm{Nu}_o)_{th} = (3.631/4)^{1/2} = 0.953 \tag{29}$$

For a sphere in uniform flow, the potential flow solution yields the result $C_{th} = 3$, while the experiment conducted by Newman and co-workers [7] gives the value $C_{ex} = 2.66$. Thus, for the sphere

$$(\mathrm{Nu}_o)_{ex}/(\mathrm{Nu}_o)_{th} = (2.66/3)^{1/2} = 0.942 \tag{30}$$

The comparison is completed by placing the results of this work in the same form

$$(\mathrm{Sh}_o)_{ex}/(\mathrm{Sh}_o)_{th} = 1.140/1.216 = 0.938 \tag{31}$$

for a disk in uniform axial flow.

Thus it is seen that theory overpredicts the value of the Nusselt (Sherwood) number by 5 to 6 percent. This slight deviation may be rationalized by noting that potential flow theory (the source of the $C_{th}$ values) does not predict the presence of separated regions found in real flows. The presence of these separated regions effectively broadens the body, and thereby reduces the velocity gradient $\partial u_\infty/\partial s$ at the stagnation point.

## Concluding Remarks

The work described here is a many-faceted study of the mass (heat) transfer at a disk of finite diameter situated perpendicular to a uniform free stream. Both average and local mass transfer coefficients were measured using the naphthalene sublimation technique. The analogy between heat and mass transfer was used to convert the measured Sherwood numbers to Nusselt numbers corresponding to any specified Prandtl number. An analysis utilizing both potential flow theory and boundary layer theory was performed to yield predictions of the stagnation point Sherwood number $\mathrm{Sh}_o$ and Nusselt number $\mathrm{Nu}_o$.

The measured average Sherwood numbers definitively resolved a deep disparity between available information from the literature. The recommended correlation for the average Nusselt number is

$$\overline{\mathrm{Nu}} = 1.05\mathrm{Pr}^{0.36}\mathrm{Re}^{1/2}$$

The $\mathrm{Re}^{1/2}$ dependence of the $\overline{\mathrm{Nu}}$ and $\overline{\mathrm{Sh}}$ results, coupled with a similar dependence for $\mathrm{Nu}_o$ and $\mathrm{Sh}_o$, suggested that the radial profiles of the local Sherwood number $\mathrm{Sh}(r)$ (or the local Nusselt number $\mathrm{Nu}(r)$) were similar with respect to $\mathrm{Re}^{1/2}$ scaling. This issue was investigated by a display of $\mathrm{Sh}(r)/\mathrm{Sh}_o$ profiles for six values of the Reynolds number. It was found that within acceptable data scatter, these profiles were independent of the Reynolds number, thereby confirming that $\mathrm{Sh}(r) \sim \mathrm{Re}^{1/2}$.

The radial profiles also showed that the local Sherwood number takes on its minimum value at the stagnation point and increases steadily with increasing radial distance from the center of the disk. The increase is most rapid near the outer edge of the disk, where the local Sherwood number is more than twice as large as that at the stagnation point. This behavior is opposite to the radial decrease of $\mathrm{Sh}(r)$ that is characteristic of textbook-type stagnation flows. It can be attributed to the thinning of the boundary layer associated with the rapid acceleration of the flow induced by the turning which occurs at the outer edge of the disk.

The theoretical predictions of the stagnation point Sherwood number exceeded the experimental values by about 6 percent. It was demonstrated that similar overpredictions occur at the stagnation line of a cylinder in crossflow and at the stagnation point of a sphere in a uniform free stream.

## References


1 Sogin, H. H., "Sublimation from Disks to Air Streams Flowing Normal to Their Surfaces," ASME *Transactions*, Vol. 80, 1958, pp. 61-71.

2 Beg, S. A., "Forced Convective Mass Transfer from Circular Disks," *Warme- und Stoffubertragung*, Vol. 6, 1973, pp. 45-51.

3 Skelland, A. H. P., *Diffusional Mass Transfer*, John Wiley and Sons, New York, 1974.

4 Milne-Thomson, L. M., *Theoretical Hydrodynamics* (4th ed.), Macmillan, New York, 1960.

5 Evans, H. L., *Laminar Boundary Layer Theory*, Addison-Wesley, Reading, Mass., 1968.

6 Schmidt, E., and Wenner, K., "Wärmeabgabe über den Umfang eines angeblasenen geheizten Zylinders," *Forschung auf dem Gebiete der Ingenieurswesens*, Vol. 12, 1941, pp. 65-73.

7 Newman, L. B., Sparrow, E. M., and Eckert, E. R. G., "Free-Stream Turbulence Effects on Local Heat Transfer from a Sphere," ASME JOURNAL OF HEAT TRANSFER, Vol. 94, 1972, pp. 7-14.

# Turbulent Convective Heat Transfer in Forced Cooled Underground Electric Transmission Systems

**R. Ghetzler**[1]

**J. C. Chato**
Fellow ASME

**J. M. Crowley**

Department of Mechanical and Industrial Engineering and Department of Electrical and Computer Engineering, University of Illinois at Urbana-Champaign, Urbana, Ill. 61801

*Heat transfer and friction factors were experimentally determined in a scale model of high-voltage, pipe-type underground transmission systems for Reynolds numbers to 8000. Dielectric insulating oil (Sun No. 4) with a Prandtl number of 120 was utilized for the coolant. Two ratios of cable to enclosure pipe diameters, corresponding to standard and oversize enclosure pipes, were examined for the three-cable system. Helical wire wrap was included to simulate protective skid wires around the cables. Three configurations of cable positioning were considered—open triangular, close triangular, and cradled. A method of generalizing the heat transfer coefficients was developed and tested for rough pipe cables based on extensions of previous work in the literature. The generalized correlation, without correction factors, was found to be applicable only in two cases with appropriate flow pattens and geometries. Heat transfer to the pipe wall could be correlated by standard methods in the high Reynolds number range.*

## Introduction

A majority of the present underground electric power transmission systems that provide power to large urban areas are of the self-cooled, free-convection type. A typical system is shown in Fig. 1. Three cables for the three-phase system are positioned inside of a steel pipe that is filled with dielectric insulating oil. Each cable consists of a segmented copper conductor, wrapped with paper that becomes a good dielectric insulator when permeated with the surrounding dielectric oil. Each cable is wrapped with a metallic sheath and with a skid wire in a helical fashion, which protects the paper insulation when the cable is pulled through long lengths of the enclosure pipe.

Heat generated in the cables by inductive and resistive losses is transferred to the oil via conduction and free convection, and is conducted into the soil. The transmission capacity of such a system is limited by the relatively high thermal resistance presented by free convection to the oil and through the soil.

Recently, the concept of forced convective cooling of such a system has come under increased consideration. At points along the transmission system, cooled oil would be supplied to the pipe and pumped along a portion of the length. The heated oil would be removed, cooled, and returned to the inlet. The length of such a cooling circuit for a subsection of the transmission system would be constrained by thermal and pressure considerations.

Such a scheme with turbulent flow of the cooling oil would reduce the cable to oil thermal resistance and eliminate the soil as a major path for heat transfer.

Several system analysis studies of the engineering and economic aspects of forced cooled power transmission have been made [1–3]. These studies are useful in predicting overall cooling requirements for increased capacity systems. Because of the lack of engineering data related to heat transfer coefficients and pressure drop, general criteria are not derivable from them.

More recently, model experiments have been conducted to determine the friction factor in laminar through turbulent flow. Slutz [4, 5] and Chato et al. [6–14], conducted studies for three configurations. Full-scale tests were conducted by Williams [15] but low ambient temperatures limited the study to laminar and initial transitional flow. Bechenbach et al. [16], developed a theory to predict the friction factor with fully turbulent flow through a pipe cable system as a function of the cable to pipe diameter ratio, skid wire height, spacing, helical angle, and the Reynolds number. The predictions are as much as 30 percent greater than the experimental data for some of the configurations.

Slutz et al. [4], measured the heat transfer coefficients on a short full-scale pipe cable model with only free convection present. Abdulhadi and Chato [6–10] studied free and forced convection in three models. Friction factor correlations were obtained experimentally for two ratios of cable to pipe diameter. Curve fits of heat transfer in the transition and low turbulent regions were made for one configuration. Finite element models have been developed for friction factors and Nusselt numbers in the laminar flow regime [11, 12]. General friction factor and heat transfer correlation as a function of cable diameter/pipe diameter, skid wire roughness, and Prandtl number were not attempted for the transition and turbulent flow regimes.

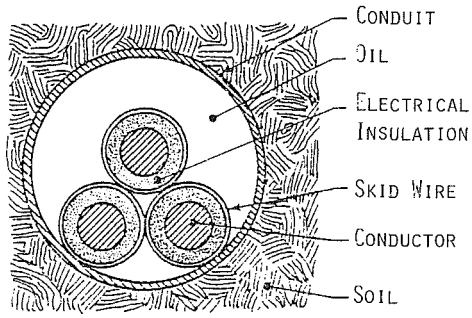


**Fig. 1 Cross section of a typical underground, high-pressure, oil-filled cable system**

[1]Presently with Northrop Defense Systems Division, Rolling Meadows, Ill.

Contributed by the Heat Transfer Division and presented at the ASME Winter Annual Meeting, 1982. Manuscript received by the Heat Transfer Division September 9, 1982. Paper No. 82-WA/HT-56.

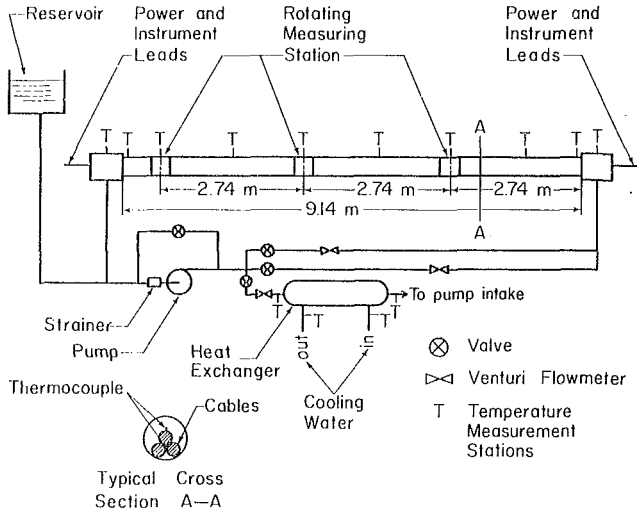


**Fig. 2 Diagram of experimental setup**

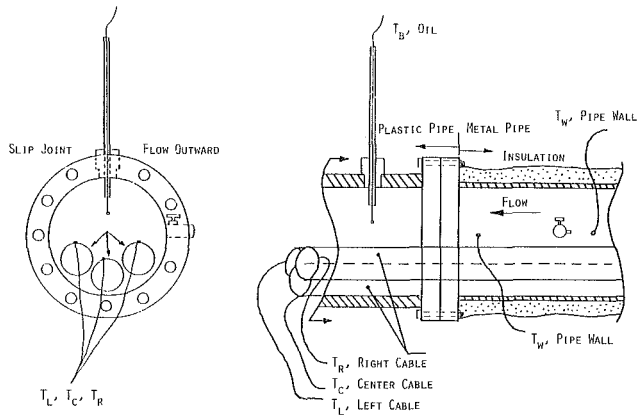


**Fig. 3 Thermocouple locations at the measurement station**

The purpose of the present study was to determine experimentally and to attempt to characterize the heat transfer and friction factors in such a system with turbulent forced convective cooling.

## Experimental Method

The experimental program consisted of flow tests to determine the heat transfer and friction factor characteristics of scale models of pipe-type cable systems in an approximately one-sixth scale model [13].

Standard industrial practice utilizes nominal enclosure pipe sizes of 5 to 14 inches (12.7–35.6 cm). Cable sizes for 69 to 345 kV systems range from 1.8 to 3.9 cm. Skid wire heights vary from 2 to 6 mm. Standard pipe sizes for various voltage cables refer to the pipe sizes usually utilized in existing, self-cooled systems. The oversize pipe indicates the next largest standard pipe size. Thermal/hydraulic characterization of the standard size pipe-cable systems allows performance predictions for forced cooled retrofit of existing self-cooled systems. Characterization of the oversize pipe-cable systems allows determination of the performance advantages that may be obtained for a new forced cooled installation with the larger size. The cable to pipe diameter ratios range from 0.31 for an oversize pipe to 0.39 for a standard pipe size. The diameters of the two selected simulated cables of 12.7 mm (0.5 in.) and 17.4 mm (11/16 in.) with 44.4 mm (1.75 in.) enclosure pipe for the experimental setup give cable to pipe diameter ratios of 0.29 and 0.39, providing a range including the two diameter ratios of interest.

Figure 2 diagrams the basic layout of the experimental setup [13]. The flow loop consists of an 11.2 kW (15 hp) centrifugal pump with a maximum of 0.27 MPa (40 psid) discharge pressure, lines, and valves to supply oil to a bypass heat exchanger and supply the test section through a rotameter for low flow rates or a venturi for higher flow rates. The apparatus utilized in the research is the same as that used in previous forced cooled studies at the University of Illinois at Urbana-Champaign [6–10], with modifications to withstand larger pressure drops needed to extend the studies to higher turbulent Reynolds numbers.

The test section is 9.14 m long and consists of alternating steel and plexiglass pipes of the same 44.4-mm (1.75-in.) i.d. that enclose the three simulated cables. Direct taps are provided at about 0.9-mm (3-ft) intervals along the steel pipe and additional fixed oil temperature measurement stations are positioned as shown. Cable supports are 1.8 m (6 ft) apart.

Electro-wrap heating tape is wrapped around the test section to simulate eddy current heating of the enclosure pipe. It is covered with fiberglass insulation and the heat input is controlled by a Variac and measured by recording the current and voltage across the heating element.

Simulated cables are constructed of three steel tubes with Easy-Heat electric resistance heaters inserted along the axis of the cables, which are controlled by the Variacs. Their power dissipation is measured by precision wattmeters. The simulated skid wires are wrapped around in a helix. Thermocouples are soldered flush to the cable surface at 1.22-m (4-ft) intervals with the thermocouple leads pulled through the inside of the tubes to avoid disturbing the flow.

Figure 3 shows the heat transfer measurement station located near the downstream end of the test section. For wall temperature measurements, thermocouples are mounted on the outside of the pipe wall between the wall and the insulation. The thermocouple measuring oil temperature is mounted in the wall of the plastic pipe to isolate it from the metal pipe, minimizing heat conduction. Temperatures are measured with copper-constantan thermocouples and a Fluke model 2240A datalogger with 0.1°C accuracy and a 2 per second sampling rate. Pressure drop is measured in this region for a length between cable supports.

## Nomenclature

$B$ = defined before Eq. (1)
$D$ = a characteristic dimension of the flow system such as pipe diameter
$D_c$ = cable diameter
$D_H$ = hydraulic diameter
$D_p$ = pipe diameter
$e$ = height of roughness element
$e^+$ = roughness Reynolds number, $= (e/D)\mathrm{Re}(f/2)^{1/2}$
$f$ = friction factor, $= \Delta P D_H / 2LV^2\rho$
$f_e$ = friction factor in a round tube with repeated roughness
$\bar{g}$ = defined by equations (4) and (5)
$L$ = pipe length
Nu = Nusselt number based on $D_H$
$\mathrm{Nu}_{D_c}$ = Nusselt number for the cable based on $D_c$
$p$ = pitch, spacing between the skid wires or between cables
Pr = Prandtl number
Re = Reynolds number based on $D_H$
St = Stanton number
$V$ = mean velocity of flow
$\Delta P$ = pressure drop
$\rho$ = density

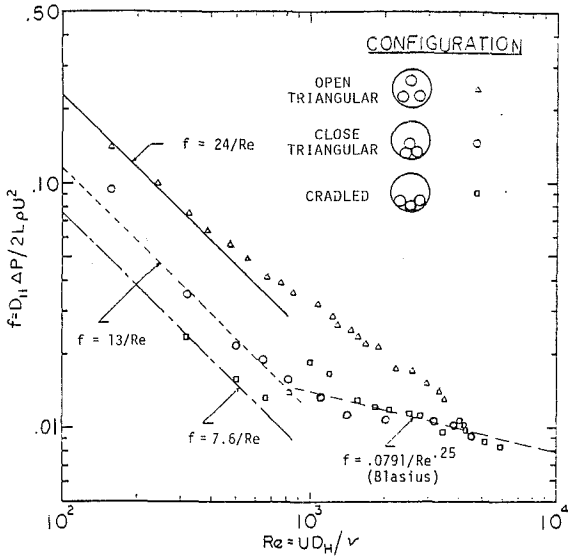


Fig. 4 Friction factors for smooth cable-pipe system: $D_c/D_p = 0.29$, $D_c/D_H = 0.725$, pipe diameter $D_p = 4.44$ cm

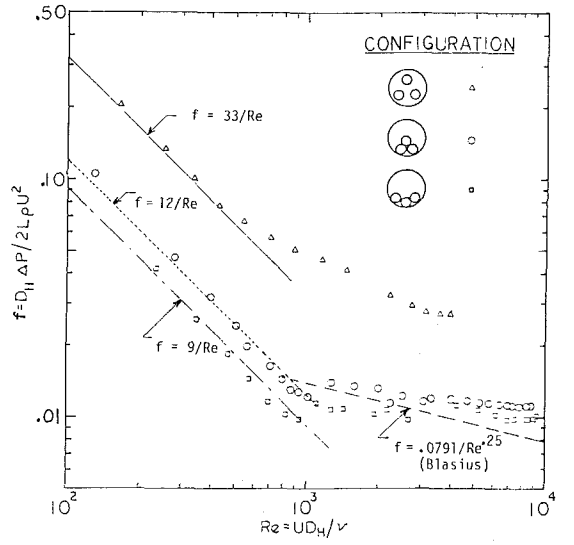


Fig. 5 Friction factors for rough cable-pipe system: $D_c/D_p = 0.29$, $D_c/D_H = 0.725$, skid wire height $e = 0.053$, $e/D_H = 0.03$, pipe diameter $D_p = 4.44$ cm

Chato and Chern [17] analytically modeled the circumferential temperature distribution around a cable. They showed that the outer, metallic shield of the cable, which is used to smooth out the electric field, also smoothes out the circumferential temperature variation caused by nonuniform heat transfer coefficients, i.e., heat fluxes. As will be shown later, these small variations are reflected by the experimental data. The smoothing out effect of the shield makes the average temperature difference between the cable surface and the bulk fluid, and the overall heat transfer coefficient for each cable of interest here, rather than the local values. This concept significantly simplifies the characterization problem. In the experiments the steel tubes simulating the cables were chosen with thick enough walls to provide uniform circumferential temperatures. This fact was verified by rotating the cables to several angular positions and observing less than 5 percent variation in the surface temperatures.

Sun 4 dielectric insulating oil was used for the coolant. A check on total system accuracy, which includes flow meter calibration, oil density, viscosity, and manometer pressure drop measurement, was made by testing the system as a round pipe with the cables removed. The data match $f = 16/\mathrm{Re}$ within 5 percent in the laminar range, $400 < \mathrm{Re} < 1800$. For the turbulent range of $7000 < \mathrm{Re} < 20{,}000$, the friction factor matches the Blasius solution within 7 percent, and the heat transfer is within 11 percent of the McAdams correlation.

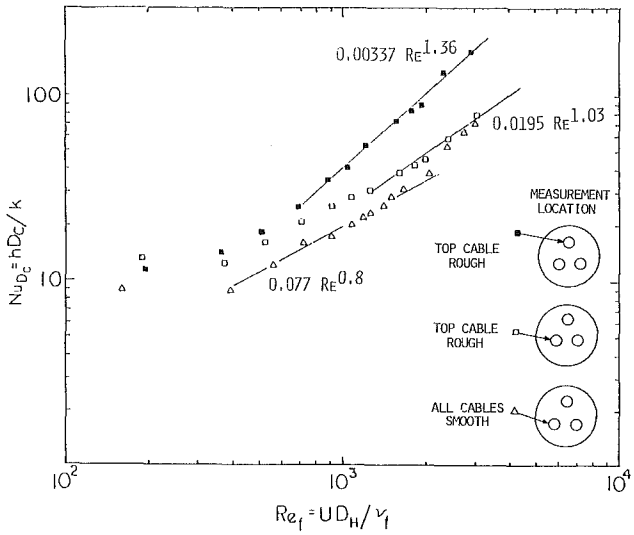


Fig. 6 Heat transfer results for rough and smooth cables in open triangular configuration: $D_c/D_p = 0.29$, $D_c/D_H = 0.725$, skid wire height $e = 0.053$ cm, $e/D_H = 0.03$, pipe diameter $D_p = 4.44$ cm, Pr = 120

## Friction Factor and Heat Transfer Results

Friction factors and heat transfer results for scale-model experiments with $D_c/D_p = 0.29$ corresponding to cable-pipe systems with an oversize pipe are shown in Figs. 4-6. Systems which have cables with or without skid wires will be referred to simply as rough or smooth cable-pipe systems, respectively.

Figure 4 shows the smooth cable-pipe friction factor results for the three cable configurations. The open triangular configuration has the greatest flow resistance. A gradual transition takes place in this case, as indicated by the trend of the divergence of the friction factor from the laminar values of $f = \text{constant}/\mathrm{Re}$, starting at $\mathrm{Re} = 500$. Bechenbach, Glicksman, and Rohsenow [18] attributed the gradual transition starting at this value of Re in their experimental model results, for cables wrapped with simulated skid wires, to turbulence created by the skid wires. However, the smooth, open triangular cable data in Fig. 4 for relative cable spacing, $p/D_c = 1.61$, and in Fig. 7 for $D_c/D_p = 0.39$ and $p/D_c = 1.17$ demonstrate that for these two cases it is a basic characteristic of the interconnected channel flow. Rehme [19] also studied experimentally smooth rod bundle friction factors for 11 values of $p/D_c$ ranging from 2.32 down to 1.025. Examining the results of Rehme for which the transition region was studied indicates a gradual transition for the eight cases of $p/D_c = 1.42$ or less. For the cases greater than 1.86, the transition follows the general behavior similar to that which occurs in one channel. Therefore, considering the present work and the studies of Rehme, it can be concluded that a gradual transition occurs in smooth multiple tube systems with relative cable spacing $p/D_c$ less than about 1.6.

The transition, shown in Fig. 4, for the close triangular and cradled configurations is pronounced and appears at $\mathrm{Re} = 800$, with the general behavior similar to that which occurs in one channel. The Blasius turbulent correlation matches the data for two configurations for $\mathrm{Re} > 1500$ and, therefore, a lower bound on friction factor is provided.

Friction factors for rough cable-pipe systems are shown in Fig. 5. Reconfirming the foregoing conclusion, transition for the open triangular configurations follow the behavior of a

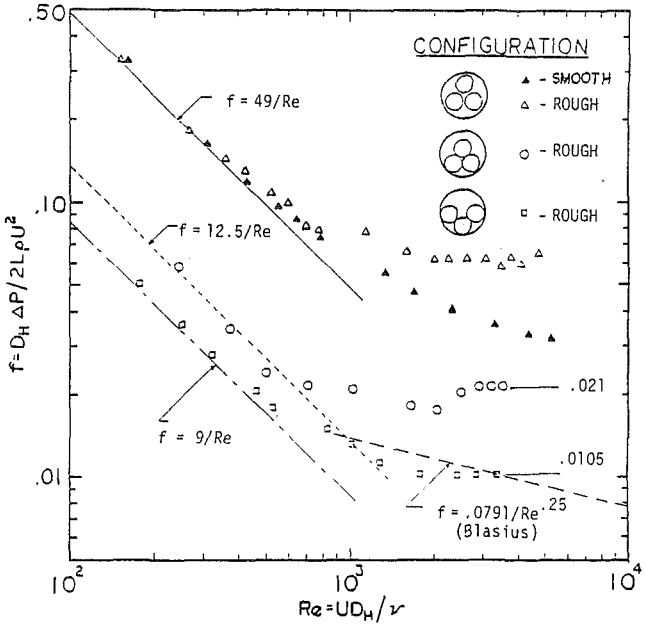


Fig. 7 Friction factors for cable-pipe system: $D_c/D_p = 0.39$, $D_c/D_H = 1.56$, skid wire height $e = 0.088$ cm, $e/D_H = 0.08$, pipe diameter $D_p = 4.44$ cm

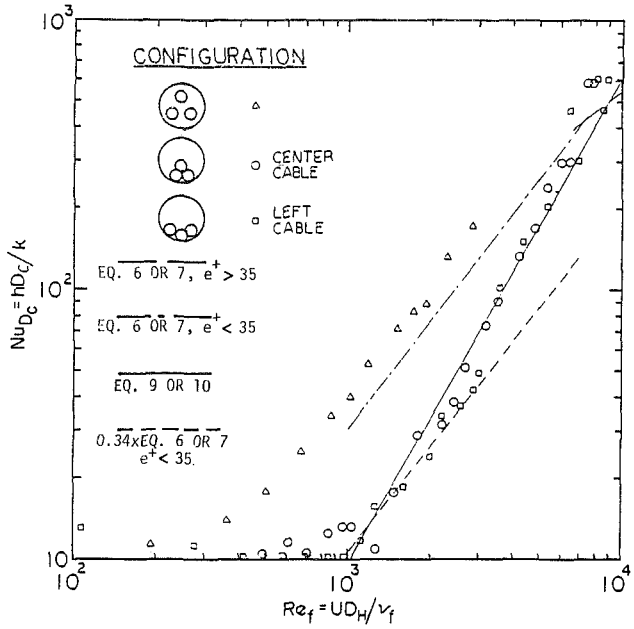


Fig. 9 Comparison of predicted heat transfer correlations with experimental data for oversize rough pipe: $D_c/D_p = 0.29$, $D_c/D_H = 0.725$, skid wire height $e = 0.053$, $e/D_H = 0.03$, pipe diameter $D_p = 4.44$ cm, Pr = 120

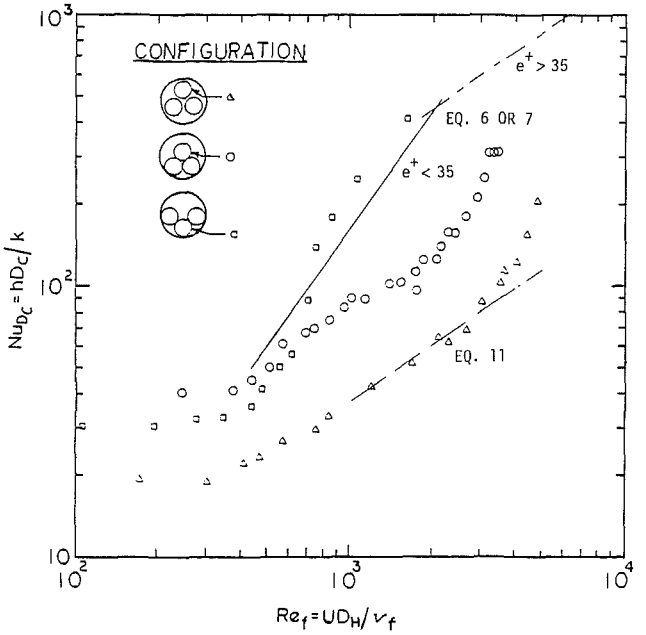


Fig. 8 Comparison of predicted heat transfer correlations with experimental data for standard size rough pipe: $D_c/D_p = 0.39$, $D_c/D_H = 1.56$, skid wire height $e = 0.088$, $e/D_H = 0.08$, pipe diameter $D_p = 4.44$ cm, Pr = 120

system with interacting channels. The turbulent friction factors assume a value of 0.010 for the cradled configuration in the range $1000 < Re < 9000$, and $f$ ranges from 0.014 at $Re = 1000$ to 0.011 at $Re = 9000$ for the close triangular configuration.

Heat transfer in the open triangular configuration is shown in Fig. 6 for a combination of smooth and rough cables. The lowest data of the three cable systems, the system with all smooth cables, shows the Nu becomes a function of $Re^{0.8}$ for $400 < Re < 2000$, which is to be expected for a smooth surface. Above this range, however, these data merge with those of a smooth cable in a system with one rough cable, where the transition is complete around $Re = 1200$ and in the turbulent region Nu is a function of $Re^{1.03}$. The rough cable heat transfer is greater, with Nu proportional to $Re^{1.36}$ and transition completed at $Re = 800$.

Friction factors and heat transfer results for experimental models with $D_c/D_p = 0.39$, corresponding to cable-pipe systems with standard size pipes, are shown in Figs. 7 and 8. As shown in Fig. 7, both the rough and smooth open triangular configurations begin transition at $Re = 500$ with $f$ leveling off to 0.06 for the rough system for $Re > 1500$. The close triangular and cradled configurations have a transition pattern which is between the gradual transition of the open triangular configuration and the sharp one channel transition. Friction factors are 0.021 for close triangular for $Re > 2500$, and 0.0105 for the cradled configuration for $Re > 1800$. Further explanations of the physical mechanisms of these results are given in the following section describing generalized heat transfer and friction factor correlations.

The heat transfer results for $D_c/D_p = 0.39$ are shown in Fig. 8. Comparing the cable heat transfer of the three configurations shows that the heat transfer is greatest in the cradled, less in the close triangular, and least in the open triangular configurations. The results with $D_c/D_p = 0.29$ are shown in Fig. 9. An explanation of these phenomena is given in the following section.

## Generalized Heat Transfer Correlations

The experimental results given in the previous section are for two ratios of cable to pipe diameter, with one skid wire height for each, and for tests with Sun 4 oil. A method is developed and tested here which provides general heat transfer correlations for some of the configurations as a function of skid wire height $e$, pitch $p$, Reynolds and Prandtl numbers. This method extends the work of Webb, Eckert, and Goldstein [20] for heat transfer and friction factors in round pipes with repeated artificial rib roughness to rough cable-pipe systems of interest here. A brief summary of their work and its background is now given.

The earliest significant study of turbulent flow over roughness was made by Nikuradse [21]. He discovered that the universal velocity law he had determined earlier for turbulent flow in smooth tubes [22] could be used for rough sand grain surfaces with only the addition of a variable near

the wall. Further work by Schlichting [23] extended the study of roughness to rectangular channels and flat plates. This work strengthened the argument that Nikuradse's rough surface universal velocity profile is a characteristic of the microscopic geometry of the surface roughness, i.e., height, width, shape, and pitch of transverse rib-type roughness in contrast to the macroscopic geometry, i.e., channel shape, at least to the first approximation. Later works involved studies of basic developments in heat transfer in rough tubes [24]. Dipprey and Sabersky [25] first applied the heat and momentum transfer analogy to flow in a tube with sand-grain roughness to develop general heat transfer correlations. The analogy was applied to artificial roughness with good results by Sheriff and Grumley [26] and Webb, Eckert, and Goldstein [20].

Several basic studies of fluid flow in noncircular channels are of interest here. Eckert and Irvine [27] studied flow in a triangular channel with an apex angle of 12 deg. They found that laminar flow persisted in the corner even as increasing the Reynolds number produced transition and then turbulent flow in the main channel. Maubach [28] developed a method to predict turbulent friction factors for annuli with artificial roughness on the inner tube. Rehme [19] developed a method of predicting the turbulent friction factor from the laminar friction factor in smooth noncircular channels. This method was applied successfully by Chato and Abdulhadi [8] to cable systems, but only with small roughness ratios, i.e., small skid wire height to cable diameter ratios.

In brief summary, Webb et al. [20] measured the friction factors and heat transfer in tubes with repeated roughness of height $e$, and pitch $p$. Utilizing the same method as Nikuradse [21], they were able to correlate a friction factor function

$$[(2/f_e)^{1/2} + 2.5 \ln (2e/D) + 3.75](p/e)^{-0.53} = B(p/e)^{-0.53}$$

versus $e^+ = (e/D)\,\mathrm{Re}\,(f_e/2)^{1/2}$

Their correlations can be approximated as follows

For $e^+ < 35$

$$B(p/e)^{-0.35} = 2.67 - 0.489 \ln(e^+) \tag{1}$$

For $e^+ > 35$

$$B(p/e)^{-0.53} = 0.95 \tag{2}$$

Utilizing the heat-momentum analogy in the same way as [25], they also obtained the heat transfer correlation

$$\mathrm{St} = \frac{f_e/2}{1 + (f_e/2)^{1/2}[\bar{g}(e^+)\mathrm{Pr}^{0.57} - B]} \tag{3}$$

where $\mathrm{St} = \mathrm{Nu}/(\mathrm{Re}\,\mathrm{Pr})$ and

For $e^+ < 35$

$$\bar{g}(e^+) = 12.1 \tag{4}$$

For $e^+ > 35$

$$\bar{g}(e^+) = 4.5(e^+)^{0.28} \tag{5}$$

A method is suggested here which provides general heat transfer correlations for certain cases of rough cables in a pipe-type cable system. The method proposes a physical model and conditions for which the results of Nikuradse [21], Dipprey and Sabersky [25], and Webb et al. [20], would be applicable. The hypotheses which form the basis of the method are:

(*a*) If the geometry of a specific pipe cable system is such that the flow is similar to that in a round pipe or rectangular channel, as studied by the previous investigators, the universal velocity profile should be present. Thus for standard size pipes the cradled configuration (bottom one in Fig. 8) may be correlated in this way because a relatively large portion of the circumference is covered with skid wire. For oversize pipes the open triangular configuration (top one in Fig. 9) qualifies on both counts, but the other two don't have enough "rough" surfaces exposed to turbulent flow below $\mathrm{Re} \simeq 10{,}000$ as discussed below.

(*b*) If the helix angle of the skid wire wrapped around the cable is small, the wire acts in the flow as a two-dimensional repeated rib roughness.

(*c*) If (*a*) and (*b*) are true, the local heat transfer should be a function of the surface roughness only.

(*d*) If laminar flow exists adjacent to a portion of the periphery of a cable, and turbulent flow is adjacent to the rest of the cable, the laminar heat transfer contribution to the total cable heat transfer can be neglected.

Therefore the local heat transfer coefficients, which Webb et al. [20] correlated for the repeated rib roughness in a round pipe, should apply for repeated ribs on the outside of the cables for the same roughness Reynolds number $e^+$.

Points (*a*) and (*c*) merit further discussion. A preliminary judgment may be made based on the flow geometry. Considering the three configurations with $D_c/D_p = 0.29$ as shown in Fig. 5, the large channels above the close triangular and cradled configurations may be expected to characterize the flow of the whole system. The small subchannels may behave similarly to the flow in the acute angles of a triangle duct as studied by Eckert and Irvine [27]. They found that at $\mathrm{Re} = 1000$, the flow remains laminar for 40 percent of the height of the triangle from the apex, coexisting with turbulent flow in the remaining portion. At $\mathrm{Re} = 8000$, the laminar portion of the channel is reduced to about 7 percent of channel height and is further reduced as Re increases. In the same way, the subchannels of the close triangular and cradled system would be expected to be initially laminar, coexisting with the turbulent main flow. As Re is increased, turbulent flow would further penetrate the subchannels with main channel turbulent energy distribution and velocity distribution continued into the subchannel. Thus the correlations of [20] may be considered as the conservative, upper, fully turbulent limit of the mean heat transfer rate that is reached at different high values of the Reynolds number ($>10^4$), depending on the configuration. For some of the configurations, the use of a simple hydraulic diameter $D_H$ may not be entirely justified. In this work we were dealing only with fluids with high Prandtl numbers where the thermal boundary layers were quite thin and each surface (individual cables or pipe walls) acted thermally independently of the others. Thus we have shown [6–14] that the cable Nusselt number could be correlated, based on the cable diameter, as a function of a Reynolds number based on effective, main flow cross-sectional area. Unfortunately, this effective area is difficult to determine, particularly in field practice. Therefore, we retained the use of the conventional hydraulic diameter in the Reynolds number to identify somewhat simplistically the main character of the flow.

Since for cable systems cooled with oil (high Pr) the Nusselt number should be based on cable diameter, the method of calculation suggested is

1 Specify Re, $e$, $p$, and the geometry; calculate $D_H$
2 Determine $f_e$, $e^+$, and $B$ from iterative solution in $f_e$ of equations (1) or (2) using $D_H$
3 Find $\bar{g}(e^+)$ from equations (4) or (5)
4 The Stanton number St is found from equation (3)
5 The Nusselt number is calculated from

$$\mathrm{Nu}_{D_C} = (D_c/D_H)\,\mathrm{St}\,\mathrm{Re}\,\mathrm{Pr} \tag{6}$$

Further simplification may be obtained for fluids with $\mathrm{Pr} > 80$, such as all cable oils, because then in equation (3) the term containing Pr dominates and other terms in the denominator may be neglected. The results are accurate within 7 percent.

Thus, for $\mathrm{Pr} > 80$, steps 4 and 5 above are replaced by

$$\mathrm{Nu}_{D_c} \simeq \frac{(D_c/D_H)(f_e/2)^{1/2}\mathrm{Re}\ \mathrm{Pr}^{0.43}}{\bar{g}(e^+)} \tag{7}$$

The cable heat transfer prediction is first compared with the data for oversized pipe-cable systems, $D_c/D_p = 0.29$, in Fig. 9. In this case, $e/D_H = 0.03$ and $p/e = 14$. The prediction for $e^+ < 35$ is shown by the line labeled "equation (6) or (7), $e^+ < 35$," which provides a good match with the data for the open triangular configuration with practically identical slope and 20 to 25 percent less magnitude.

In the other two configurations, where small subchannels are present, the data matches the prediction only in the range $9000 < \mathrm{Re} < 10{,}000$. We hypothesized that this effect may be due to the opening up of additional effective cable surface to more effective heat transfer as turbulent flow is impressed into the subchannels with increasing Re. To account for this effect and provide a correlation for close triangular and cradled configurations with $D_c/D_p = 0.29$, an experimental effective area factor (EAF) is introduced, which is 0.34 at $\mathrm{Re} = 1000$ and 1.0 at $\mathrm{Re} = 11{,}300$ and which indicates the rather large deviations from the aforementioned theory

$$\mathrm{EAF} = 0.015\ \mathrm{Re}^{0.45}, \quad 1000 < \mathrm{Re} < 11{,}300 \tag{8}$$

For these two configurations

$$\mathrm{Nu}_{D_C} = (D_c/D_H)(f_e/2)^{1/2}\mathrm{Re}\ \mathrm{Pr}^{0.43} \times \mathrm{EAF}/12.1. \tag{9a}$$

or simply

$$\mathrm{Nu}_{D_c} = 1.24 \times 10^{-3}(D_c/D_H)(f_e/2)^{1/2}\mathrm{Re}^{1.45}\mathrm{Pr}^{0.43} \tag{9b}$$

Since this is basically an experimental correlation, it is useable, irrespective of theoretical considerations. Since the curve in the figure is almost a straight line, equation (9*b*) can be approximated by

$$\mathrm{Nu}_{D_c} \simeq 5.897 \times 10^{-6}(D_c/D_H)\mathrm{Re}^{1.814}\mathrm{Pr}^{0.43} \tag{10a}$$

$$\simeq 4.277 \times 10^{-6}\mathrm{Re}^{1.814}\mathrm{Pr}^{0.43} \tag{10b}$$

Similar predictions for $e^+ > 35$ applied to the geometry of Fig. 9 is shown by the line labeled "equations (6) or (7), $e^+ > 35$."

Comparisons of the heat transfer for the three configurations with $D_c/D_p = 0.39$, corresponding to a standard pipe size are shown in Fig. 8. Only the cradled configuration behaves somewhat like one channel and is a possible candidate for the generalized prediction method. The solid line is the predicted value for $e/D_H = 0.08$, $\mathrm{Pr} = 120$ from equations (6) or (7). The close triangular heat transfer is less, and the open triangular is the least, opposite to the trend for $D_c/D_p = 0.29$. An explanation of this result is that in the open triangular and close triangular configurations the interconnecting channels are much larger in relation to the main channel compared to the case where $D_c/D_p = 0.29$. Therefore, exposure of this heat transfer area to turbulent flow takes place only as higher Re numbers are achieved. It can be seen that around $\mathrm{Re} = 3000$, the slope rapidly increases, indicating the opening up of effective area in this range, and it can be hypothesized that full turbulent ($\mathrm{EAF} = 1.00$) will be reached at $\mathrm{Re} \simeq 10{,}000$.

It can be concluded that the parallel slope of the open-triangular data to the generalized correlation for $D_c/D_p = 0.29$ occurred probably because the velocity profile was similar to the general logarithmic law. However, for the Re range of interest, this is probably not true when the cables are much closer together, e.g., $D_c/D_p = 0.39$, resulting in more dramatic modifications in the flow field. An experimental curve fit was made for this case, resulting in

$$\mathrm{Nu}_{D_c} = 0.0353\ \mathrm{Re}^{0.71}\ \mathrm{Pr}^{0.43} \tag{11}$$

The heat transfer to the pipe wall could be correlated in the high Reynolds number range by the standard smooth pipe correlation using $D_H$

$$\mathrm{Nu} = 0.023\ \mathrm{Re}^{0.8}\ \mathrm{Pr}^{1/3} \tag{12}$$

The lower limit of this range varied between $\mathrm{Re} = 1{,}000$ and 4,000, depending on configuration.

## Summary and Conclusions

Heat transfer and friction factors were experimentally determined in a scale model of high voltage, pipe-type underground transmission systems for Reynolds numbers up to 8000. Two ratios of cable-to-enclosure pipe diameters were considered, corresponding to standard and oversize enclosure pipes. Helical wire wrap was included to simulate protective skid wires around the cables. Three configurations of cable positioning were considered, open- and close-triangular, and cradled.

The turbulent friction factor $f$, for oversize pipe systems with rough cables was found to be approximately 0.01 for the cradled configurations: 0.012 for close triangular and 0.03 for open triangular. For standard pipe systems with rough cables, the friction factors were approximately 0.01, 0.02, and 0.06 for the same configurations. For the cradled configuration, which is the most probable position for most of the cable length, the value of $f$ for a smooth cable system was also found to be 0.01. Therefore, for the relative roughness range and pipe-to-cable diameter ratios of interest in applications, $f$ was found to be a constant of 0.01. For the two other configurations, the values of $f$ would be applicable to scaled up systems of the same diameter and roughness ratios present in the scale model. The friction factors were determined from overall pressure drop data and, therefore, included the combined effects of both smooth and rough surfaces which were exposed to the main flow. Thus, no "law of the wall" can be applied to generalize the friction factors.

A method of generalizing the heat transfer coefficients was developed and tested for rough pipe cables, based on extensions of the work by Webb et al. [20] on heat transfer in round pipes with repeated roughness elements. This heat transfer correlation is proposed as the general, upper, fully turbulent limit reached at different values of the Reynolds number, depending on the configuration. For an oversize pipe, open triangular case, the method predicted a correlation of Nu versus Re with the same slope but 20 to 25 percent lower values than the experimental data. For an oversize pipe, close triangular and cradled cases, a correlation was developed to account for roughness and the additional feature of subchannel flow. This correlation matched the data within ±20 percent. For a standard size pipe, cradled configuration, the prediction matches the data within 20 percent. For the other two configurations, the heat transfer is substantially lower than the prediction but tends toward the prediction at the highest Re attained.

Heat transfer to the pipe wall could be correlated by the standard expression for smooth pipes in the high Reynolds number range.

## Acknowledgments

This work was supported in part by Contract No. RP 7853-1-B from the Electric Power Research Institute. Oil was furnished by the Sun Oil Company.

## References

1 Burrell, W. R., "Applications of Oil-Cooling in High Voltage Pipe-Cable Circuits," *IEEE Trans. PAS*, Vol. 84, 1965, pp. 795–805.

2 Notaro, J., and Webster, D. J., "Thermal Analysis of Forced Cooled Cables," *IEEE Trans. PAS*, Vol. 90, 1971, pp. 1225–1231.

3 Stoecker, W. F., Williams, J. L., and Zanona, A., "The Refrigeration of Underground High Voltage Electrical Conductors," *Proc. XIII Congress of Refrigeration*, 1971, and *Progress in Refrigeration Science and Technology*, 1971.

4 Slutz, R. A., et al., "Cooling of Underground Transmission Lines: Heat Transfer Measurements," Part I of IV, MIT Energy Laboratory Report, MIT-EL 74-003, Jan. 1974.

5 Slutz, R. A., Glicksman, L. R., and Rohsenow, W. M., "Measurement of

Fluid Flow Resistance for Forced Cooled Underground Transmission Lines," *IEEE Trans. PAS*, Vol. 94, 1975, pp. 1831–1834.

6 Abdulhadi, R. S., and Chato, J. C., "Natural and Forced Convective Cooling of Underground Electric Cables," Technical Report No. ME-TR-609, UILU-ENG-4003, Department of Mechanical and Industrial Engineering, University of Ill. at U-C, Dec. 1975; also Ph.D. thesis, Abdulhadi, R. S., 1975.

7 Abdulhadi, R. S., and Chato, J. C., "Combined Natural and Forced Convective Cooling of Underground Electric Cables," *IEEE Trans. PAS*, Vol. 96, 1977, pp. 1–8.

8 Chato, J. C., and Abdulhadi, R. S., "Flow and Heat Transfer in Convectively Cooled Underground Electric Cable Systems: Part 1—Velocity Distributions and Pressure Drop Correlations," ASME JOURNAL OF HEAT TRANSFER, Vol. 100, 1978, pp. 30–35.

9 Abdulhadi, R. S., and Chato, J. C., "Flow and Heat Transfer in Convectively Cooled Underground Electric Cable Systems: Part 2—Temperature Distributions and Heat Transfer Correlations," ASME JOURNAL OF HEAT TRANSFER, Vol. 100, 1978, pp. 36–40.

10 Chato, J. C., et. al., "Free and Forced Convective Cooling of Pipe-Type Electric Cables," Final Report, EPRI EL-147, Project 7821, ERDA E(49-18)-1568, 1977.

11 Chern, S. Y., and Chato, J. C., "A Finite-Element Technique to Determine the Friction Factor and Heat Transfer for Laminar Flow in a Pipe with Irregular Cross Sections," *Numerical Heat Transfer*, Vol. 1, 1978, pp. 453–470.

12 Chern, S. Y., and Chato, J. C., "Friction Factors for Forced Cooled, Pipe-Type Electric Cable," *IEEE Trans. Power App. and Sys.*, Vol. PAS-98, 1979, pp. 1560–1565.

13 Ghetzler, R., "The Prediction of the Thermal and Hydraulic Performance of Underground Electric Transmission Systems with Turbulent Forced Convective Cooling," Ph.D. thesis, Department of Mechanical and Industrial Engineering, University of Ill. at U-C, 1981.

14 Chato, J. C., Crowley, J. M., et al., "Free and Forced Convective Cooling of Pipe-Type Electric Cables," *Forced Cooling of Cables*, Vol. 1, Final Report, EPRI EL-1872, Project 7853-1, 1981.

15 Williams, J. L., Eich, A. E. D., and Aibo, T., "Forced Cooling Tests on 230 kV and 345 kV HPOF Cable Systems," *Proceedings IEEE Winter Meeting on PAS*, Jan. 1976.

16 Bechenbach, J. W., Glicksman, L. R., and Rohsenow, W. M., "The Prediction of Friction Factors in Turbulent Flow for an Underground Forced Cooled Pipe-Type Electrical Transmission Cable System," Part III of IV, MIT Energy Laboratory Report MIT-EL 74-005, Sept. 1974.

17 Chato, J. C., and Chern, S. Y., "Effects of Nonuniform Cooling on the Heat Transfer from an Insulated Electric Cable," ASME JOURNAL OF HEAT TRANSFER, Vol. 97, 1975, pp. 424–428.

18 Bechenbach, J. W., Glicksman, L. R., and Rohsenow, W. M., "The Prediction of Friction Factors in Turbulent Flow for an Underground Forced Cooled Pipe-Type Electrical Transmission Cable System," Part III of IV, MIT Energy Laboratory Report MIT-EL 74-005, Sept. 1974.

19 Rehme, K., "Simple Method of Predicting Friction Factors of Turbulent Flow in Non-Circular Channels," *International Journal of Heat and Mass Transfer*, Vol. 6, 1973, pp. 933–950.

20 Webb, R. W., Eckert, E. R. G., and Goldstein, R. J., "Heat Transfer and Friction in Tubes with Repeated-Rib Roughness," *International Journal of Heat and Mass Transfer*, Vol. 14, 1971, pp. 601–617.

21 Nikuradse, S., "Stromungsgesetze in rauhen Rohren," *Forsch. Hft. Ver. Deut. Ing.*, Vol. 361, NACA TM 1292, 1950.

22 Nikuradse, S, "Gesetzmassigkeiten der turbulenten Stromung in glatten Rohren," *Forsch. Hft. Ver. Deut. Ing.*, Vol. 356, 1932.

23 Schlichting, H., "Experimental Investigation of Roughness Problems," NACA TM 823, 1937.

24 Dalle Donne, M., and Meyer, L., "Turbulent Convective Heat Transfer from Rough Surfaces with Two-Dimensional Rectangular Ribs," *International Journal of Heat and Mass Transfer*, Vol. 20, 1977, pp. 583–620.

25 Dipprey, D. F., and Sabersky, R. H., "Heat and Momentum Transfer in Smooth and Rough Tubes at Various Prandtl Numbers," *International Journal of Heat and Mass Transfer*, Vol. 6, 1963, pp. 329–353.

26 Sheriff, N., and Grumley, P., "Heat Transfer and Friction Properties of Surfaces with Discrete Roughness," *International Journal of Heat and Mass Transfer*, Vol. 9, 1966, pp. 1297–1320.

27 Eckert, E. R. G., and Irvine, T. E., "Flow in Corners with Non-Circular Cross-Sections," ASME JOURNAL OF HEAT TRANSFER, Vol. 78, 1956, pp. 709–718.

28 Maubach, K., "Rough Annulus Pressure Drop—Interpretation of Experiments and Recalculations of Square Ribs," *International Journal of Heat and Mass Transfer*, Vol. 15, 1972, pp. 2482–2798.

# Convective Heat Transfer in a Circular Annulus With Various Wall Heat Flux Distributions and Heat Generation

**O. A. Arnas**
Mechanical Engineering Department,
Louisiana State University,
Baton Rouge, La. 70803
Mem. ASME

**M. A. Ebadian**
Mechanical Engineering Department,
Southern University,
Baton Rouge, La. 70813
Mem. ASME

*Convective heat transfer for steady laminar flow between two concentric circular pipes with walls heated and/or cooled independently and subjected to uniform heat generation is presented in analytical closed form utilizing the linearized Navier-Stokes and energy equations. The flow field is hydrodynamically and thermally fully developed. The effect of heat generation is depicted in Fig. 1 where the ratio of the Nusselt number with heat generation to without heat generation is plotted against the radius ratio, the core size $\omega$. It is seen that heat generation may have positive as well as negative effect on the Nusselt number.*

## Introduction

The problem analyzed here, which follows [1-3] very closely, is the convective heat transfer in a steady laminar flow between two concentric circular pipes with walls heated and/or cooled independently and subjected to uniform heat generation. The velocity and temperature distributions, with fully developed profiles, are obtained as the exact solutions of the linearized Navier-Stokes and energy equations and are presented in closed forms. It is shown that the temperature distribution, equation (4), and the heat transfer, equations (35) and (37), through the walls are affected by five independent parameters: the magnitude of heat generation $q_{gen}$, the radius ratio $\omega$, the Reynolds and Prandtl numbers, and the wall temperature gradient $c$. The average Nusselt numbers for the inner and outer walls are obtained explicitly and are calculated for five typical wall heating and/or cooling combinations and for a liquid metal. The numerical results are given in graphical form. No experimental work was done and none is reported in the literature.

The importance of this work is that in the case of a nuclear accident, the coolant will be contaminated and will continue to flow while generating energy. The effect of this energy generation on the heat transfer is necessary information for the designer as well as for the practitioner.

Due to the complexity of the algebra, it is desirable to utilize the tables that have been obtained. Due to limitations of the length of this paper, only one figure is presented. Tabular results may be requested from the authors.

## Viscous Flow in Annular Circular Pipes

The velocity distribution for an incompressible, constant property fluid in laminar flow inside a circular annulus in regions away from the inlet where the velocity profile is considered fully developed is given by [2]

$$w = \mathrm{Re}_L[(1-r^2)-(1-\omega^2)\log r/\log\omega] \tag{1}$$

where

$$w = WL/\nu \tag{2}$$

$$\mathrm{Re}_L = -(1/4)dp/dz \tag{3}$$

and $\omega$ is the radius ratio.

## Temperature Distribution

The temperature distribution in the flow is determined from the solution of the energy equation subject to appropriate boundary conditions. Equation for the temperature distribution inside the annulus of two circular tubes with heat generation is [1]

$$e = e_{in}\log r/\log\omega + q_{gen}(1-r^2+C_1\log r)/4 + G[(C_1+r^2)(1+C_1\log r)-r^2(C_1+r^2/4)]/4 - 3G[1+C_1(1+\omega^2)\log r]/16 \tag{4}$$

where

$$G = c\mathrm{Re}_L\mathrm{Pr} \tag{5}$$

$$C_1 = -(1-\omega^2)/\log\omega \tag{6}$$

$$c = Ck/q \tag{7}$$

where $C$ is the dimensional temperature gradient along the pipe wall.

## Heat Fluxes Through the Walls

The element of heat flux $dU$ measured in the positive direction $r$, through an elemental area $r$ = constant cylindrical surface, is given as

$$dU = -Lqrdrde/dr \tag{8}$$

with

$$e = (Ek)/(Lq) \tag{9}$$

The heat gain rates $U_i$ and $U_o$, per unit length of the inner and outer pipes, are expressed, respectively, as

From inner wall:

$$U_i = -Lq\omega\int_0^{2\pi}\{\partial e/\partial r\}_{r=\omega}d\theta \tag{10}$$

From outer wall:

$$U_o = Lq\int_0^{2\pi}\{\partial e/\partial r\}_{r=1}d\theta \tag{11}$$

The heat gain rates are taken to be positive when heat flows into the fluid.

Taking the derivative of the temperature distribution equation (4) with respect to $r$ and substituting into equations (10) and (11), the inner and outer heat fluxes, respectively, become

$$U_i = -2\pi Lq\{\beta G/\log\omega + q_{gen}(C_1-2\omega^2)/4 + G[(C_1^2-\omega^4)/4 - C_1(3+7\omega^2)/16 + \omega^2(1+C_1\log\omega)/2]\} \tag{12}$$

Contributed by the Heat Transfer Division and presented at the ASME/JSME Joint Thermal Engineering Conference, Honolulu, Hawaii, March 21, 1983. Manuscript received by the Heat Transfer Division April 15, 1983.

$$U_o = 2\pi Lq\{\beta G/\log\omega + q_{gen}(C_1-2)/4 + G[(1+C_1^2)/4 - C_1(7+3\omega^2)/16]\} \quad (13)$$

where

$$e_{in} = \beta G \quad (15)$$

which is an alternate definition for the dimensionless inner wall excess temperature.

Two special values of $\beta$ are given as follows

(*i*) For insulated outer wall, $U_o = 0$.

$$\beta = \beta_i = -\{q_{gen}\log\omega(C_1-2)/4G + \log\omega[(1+C_1^2)/4 - C_1(7+3\omega^2)/16]\} \quad (15)$$

(*ii*) For insulated inner wall, $U_i = 0$.

$$\beta = \beta_o = -\{q_{gen}\log\omega(C_1-2\omega^2)/4G + \log\omega[(C_1^2-\omega^4)/4 - C_1(3+7\omega^2)/16 + \omega^2(1+C_1\log\omega)/2]\} \quad (16)$$

The difference of equations (15) and (16) can be written as

$$\beta_i - \beta_o = q_{gen}\log\omega(1-\omega^2)/2G - \log\omega[(1+\omega^4)/4 - C_1(1-\omega^2)/4 - \omega^2(1+C_1\log\omega)/2] \quad (17)$$

Let the ratio of the heat gain rate from the outer wall to that from both walls per unit length of pipe be denoted by $\lambda$. Then

$$\lambda = (\beta-\beta_i)/(\beta_o-\beta_i) \quad (18)$$

which depends only on the dimensionless inner wall temperature. The value of $\lambda$ for the special case of equal wall temperatures can be defined in terms of the inner wall temperature $T_i$ and the outer wall temperature $T_o$ and

$$E_{in} = (T_i - T_o) \quad \text{at} \quad \beta = 0 \quad (19)$$

Therefore, the value of $\lambda$ from equation (18) becomes

$$\lambda_o = \beta_i/(\beta_i-\beta_o) \quad (20)$$

where $\beta_i$ and $\beta_o$ are defined by equations (15) and (16).

Introducing the ratio $\mu = \lambda/\lambda_o$, an alternative dimensionless inner wall excess temperature $\beta$ can also be expressed as

$$\beta = -(1-\mu)\{q_{gen}\log\omega(C_1-2)/4G + \log\omega[(1+C_1^2)/4 - C_1(7+3\omega^2)/16]\} \quad (21)$$

After substituting the foregoing equation into equations (12) and (13), the inner and outer heat fluxes are reduced to

$$U_i = -2\pi Lq\{q_{gen}(1-\omega^2)/2 + G[C_1(1-\omega^2)/4 - (1+\omega^4)/4 + \omega^2(1+C_1\log\omega)/2] + \mu G[q_{gen}(C_1-2)/4G + (1+C_1^2)/4 - C_1(7+3\omega^2)/16]\} \quad (22)$$

$$U_o = 2\pi Lq\mu\{q_{gen}(C_1-2)/4 + G[(1+C_1^2)/4 - C_1(7+3\omega^2)/16]\} \quad (23)$$

For the special cases considered, the values of $\lambda$, $\beta$, and $\mu$ are

(*i*) For insulated outer wall

$$U_o = 0, \ \lambda = 0, \ \beta = \beta_i, \ \mu = 0$$

(*ii*) For equal wall temperatures

$$T_o = T_i, \ \lambda = \lambda_o, \ \beta = 0, \ \mu = 1$$

For insulated inner wall

$$U_i = 0, \ \lambda = 1, \ \beta = \beta_o, \ \mu = \mu_o = 1/\lambda_o$$

## Heat Transfer

From an energy balance, the mixed mean or bulk temperature $T_m$ at any section $Z$ is defined by

$$T_m = (\rho/Q)\int_S WTdS \quad (24)$$

A mixed mean excess temperature $E_m$ can be defined as

$$E_m = (T_m - T_o) = (\rho/Q)\int_S WEdS \quad (25)$$

or

$$E_m = qLJ/(kI_{oo}) \quad (26)$$

where the values of $J$ and $I_{oo}$ are given in the Appendix.

The mean convective heat transfer coefficients, $h_o$ and $h_i$, for the outer and inner walls, respectively, may be defined as

$$U_o = (T_o - T_m)P_o h_o \quad (27)$$

$$U_i = (T_i - T_m)P_i h_i \quad (28)$$

where

$$P_o = 2\pi L \quad (29)$$

$$P_i = 2\pi\omega L \quad (30)$$

The average Nusselt numbers for the outer and inner walls based on the hydraulic diameter of the pipe are given as

$$\mathrm{Nu}_o = h_o D/k \quad (31)$$

$$\mathrm{Nu}_i = h_i D/k \quad (32)$$

where $D$ is the hydraulic diameter and is given by

$$D = 4S/(P_o+P_i) = 2L(1-\omega) \quad (33)$$

## Nomenclature

$A_{oo}$ = function defined by equation (A6)
$B_{oo}$ = function defined by equation (A7)
$C,c$ = dimensional and dimensionless temperature gradient along the pipe, defined by equation (7)
$C_1$ = function defined by equation (6)
$D$ = hydraulic diameter defined by equation (33)
$(DE)_\omega, (DE)_1$ = functions defined by equations (36) and (38), respectively
$E,e$ = dimensional and dimensionless excess temperature, defined by equation (9)
$E_{in}, e_{in}$ = dimensional and dimensionless excess temperature of the inner pipe, defined by equations (19) and (14), respectively
$E_m$ = mixed mean excess temperature K, defined by equation (25)
$G$ = dimensionless function defined by equation (5), $c\,\mathrm{Re}_L\mathrm{Pr}$
$h_o, h_i$ = outer and inner convective heat transfer coefficients given by equations (27) and (28), $\mathrm{W/(m^2-K)}$
$I_{oo}$ = function defined by equation (A5)
$J$ = function defined by equation (A1)
$J_0, J_2, J_4$ = functions defined by equations (A2), (A3), and (A4)
$k$ = thermal conductivity, W/(m − K)
$L$ = characteristic length, [m]
$\mathrm{Nu}_o, \mathrm{Nu}_i$ = Nusselt numbers on the outer and inner walls, $hD/k$
$\mathrm{Nu}_w/\mathrm{Nu}_{wo}$ = ratio of Nusselt numbers with and without heat generation
$p$ = dimensionless pressure defined by equation (3)
Pe = Peclet number, $\mathrm{Re}_L\mathrm{Pr}$
Pr = Prandtl number, $\nu/\alpha$
$P_o, P_i$ = circumferences of the outer and inner peripheries given by equations (29) and (30)

where $S$ is given by

$$S = \pi L^2(1-\omega^2) \tag{34}$$

Upon substitution of equations (27), (28), and (29) into equations (31) and (32), the inner and outer Nusselt numbers are found to be very complex and require a lot of tedious algebra. After this algebra is performed, the Nusselt numbers become

$$\mathrm{Nu}_i = (DE)_\omega \left[\frac{I_{oo}}{J-\beta G I_{oo}}\right] G\{q_{\mathrm{gen}}(1-\omega^2)/2G + [C_1(1-\omega^2)/4 - (1+\omega^4)/4 + \omega^2(1+C_1\log\omega)/2] + \mu[q_{\mathrm{gen}}(C_1-2)/4G + (1+C_1^2)/4 - C_1(7+3\omega^2)/16]\} \tag{35}$$

where

$$DE_\omega = 2(1-\omega)/\omega \tag{36}$$

and

$$\mathrm{Nu}_o = (DE)_1 \frac{I_{oo}}{J}\mu G[q_{\mathrm{gen}}(2-C_1)/4G + C_1(7+3\omega^2)/16 - (1+C_1^2)/4] \tag{37}$$

where

$$DE_1 = 2(1-\omega) \tag{38}$$

The values of the Nusselt numbers given by equations (35) and (37) are compared with those obtained in [1] and given graphically in Fig. 1 as the ratio of Nusselt number with heat generation to that without heat generation.

## Conclusions

Convective heat transfer in the annulus of two concentric pipes with heat generation is analyzed, and the results are presented graphically that compare the average Nusselt number with heat generation to that without heat generation [1]. This ratio is plotted versus the dimensionless radius ratio, the core size $\omega$. Due to the length of the paper, the tabulated values are not presented but may be obtained from the authors. It is seen in Fig. 1 that the heat generation does affect the Nusselt number considerably, particularly in the case of equal wall temperatures of the two pipes.

The graphical results are only for one value of the heat generation density, which is characteristic of nuclear phenomenon. This nondimensional value is $71.9 \times 10^{-2}$ and was calculated using data given in [4]. It is indeed easy to evaluate equations (35) and (37) numerically for any other heat generation density. The intent in Fig. 1 is to show the effect of heat generation of the fluid in the annulus on heat transfer.

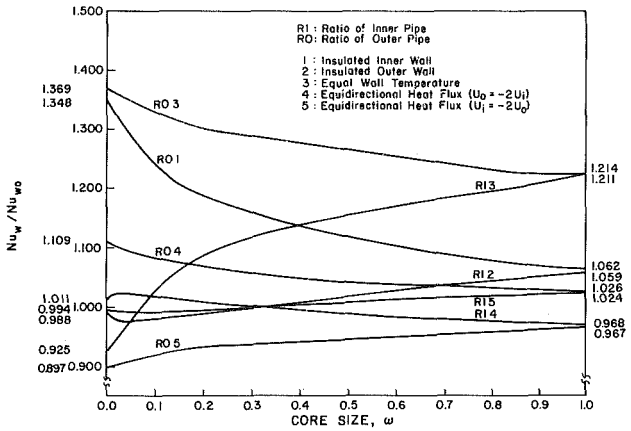


**Fig. 1 Ratio of Nusselt number with heat generation to that without heat generation**

## References


1 Topakoglu, H. C., and Arnas, O. A., "Convective Heat Transfer for Steady Laminar Flow Between Two Confocal Elliptic Pipes With Longitudinal Uniform Wall Temperature Gradient," *International Journal of Heat and Mass Transfer*, Vol. 17, 1974, pp. 1487-1498.

2 Topakoglu, H. C., "Steady Laminar Flows of an Incompressible Viscous Fluid in Curved Pipes," *J. Math. Mech.*, Vol. 16, 1967, pp. 1321-1338.

3 Ebadian, M. A., "Convective Heat Transfer for Steady Laminar Flow Between Two Confocal Elliptic Pipes with Uniform Longitudinal Wall Temperature Gradient and Heat Generation," Ph.D. dissertation, Mechanical Engineering Department, Louisiana State University, Baton Rouge, Dec. 1981.

4 Duderstadt, J. J., and Hamilton, L. J., *Nuclear Reactor Analysis*, Wiley (1st ed.), 1976, Appendix H, pp. 634-635.


## APPENDIX

$$J = (J_o + q_{\mathrm{gen}}J_2 + GJ_4) \tag{A1}$$

where

$$J_0 = \frac{e_{\mathrm{in}}}{\log\omega}\left[-\frac{3}{16} + \frac{7}{16}\omega^4 - \frac{1}{4}\omega^2 - \frac{1}{4}\omega^4\log\omega - \frac{1}{4}\frac{1}{\log\omega}\right.$$

## Nomenclature (cont.)

$q$ = characteristic heat flux defined in equation (8)
$Q$ = mass flow rate through the annulus, kg/s
$Q_{\mathrm{gen}}, q_{\mathrm{gen}}$ = dimensional and dimensionless heat generation densities, defined by $Q_{\mathrm{gen}} = (q/L)q_{\mathrm{gen}}$
$r$ = dimensionless radial coordinate of the annulus, varying between $r = \omega$, the inner pipe, and $r = 1$, the outer pipe
$\mathrm{Re}_L$ = Reynolds number $WL/\nu$
$RI$ = ratio of the Nusselt number with heat generation to that without heat generation, for the inner pipe, Fig. 1
$RO$ = ratio of the Nusselt number with heat generation to that without heat generation, for the outer pipe, Fig. 1
$S, dS$ = full and elemental cross-sectional areas of pipe, $m^2$
$T$ = temperature, equals $CZ + E(x,y)$
$T_o, T_i$ = outer and inner wall temperatures, K
$T_m$ = mixed mean temperature, given by equation (24), K
$U_o, U_i$ = dimensionless heat fluxes from outer and inner walls defined by equations (11) and (10), respectively
$W, w$ = dimensional and dimensionless velocity, defined by equation (2)
$z$ = dimensionless longitudinal coordinate
$\alpha$ = thermal diffusivity, $m^2/s$
$\beta, \beta_i, \beta_o$ = functions defined by equations (14), (15), and (16)
$\lambda, \lambda_o$ = functions defined by equations (18) and (20)
$\mu$ = ratio of $\lambda/\lambda_o$
$\nu$ = kinematic viscosity, $[m^2/s]$
$\rho$ = density
$\omega$ = core size or dimensionless inner radius of the annulus defined as the ratio of the inner radius to the outer radius

$$+\frac{1}{2}\frac{\omega^2}{\log\omega}-\frac{1}{4}\frac{\omega^4}{\log\omega}\Bigg] \tag{A2}$$

$$J_2=\frac{1}{4}\Bigg[\frac{1}{2}(1-\omega^2)-\frac{1}{2}(1-\omega^4)+\frac{1}{6}(1-\omega^6)-C_1\omega^2\log\omega$$
$$+\frac{1}{2}C_1\omega^2+\frac{1}{2}C_1\omega^4\log\omega-\frac{1}{8}C_1\omega^4+\frac{1}{4}C_1^2-\frac{1}{2}C_1^2\omega^2\log^2\omega$$
$$+\frac{1}{2}C_1^2\omega^2\log\omega-\frac{1}{4}C_1^2\omega^2-\frac{3}{8}C_1\Bigg] \tag{A3}$$

$$J_4=-\frac{11}{384}-\frac{7}{64}\omega^4+\frac{5}{96}\omega^6-\frac{5}{64}C_1\omega^4\log\omega+\frac{233}{2304}C_1$$
$$+\frac{31}{236}C_1\omega^4-\frac{1}{128}\omega^8+\frac{1}{192}C_1\omega^6\log\omega-\frac{89}{2304}C_1\omega^6$$
$$+\frac{1}{32}C_1^2\omega^4\log^2\omega-\frac{17}{128}C_1^2+\frac{1}{16}C_1^2\omega^4\log\omega+\frac{1}{128}C_1^2\omega^4$$
$$+\frac{3}{32}\omega^2+\frac{3}{16}C_1\omega^2\log\omega-\frac{47}{256}C_1\omega^2+\frac{3}{32}C_1^2\omega^2\log^2\omega$$
$$-\frac{11}{32}C_1^2\omega^2\log\omega+\frac{1}{8}C_1^2\omega^2-\frac{1}{8}C_1^3\omega^2\log^2\omega+\frac{1}{16}C_1^3$$
$$+\frac{1}{8}C_1^3\omega^2\log\omega-\frac{1}{16}C_1^3\omega^2 \tag{A4}$$

$$I_{oo}=A_{oo}+B_{oo}C_1 \tag{A5}$$

$$A_{oo}=(1-\omega^4)/4 \tag{A6}$$

$$B_{oo}=-(1-\omega^2)/4 \tag{A7}$$

# Analysis of Buoyancy Effect on Fully Developed Laminar Heat Transfer in a Rotating Tube

**R. Siegel**
National Aeronautics and Space Administration,
Lewis Research Center,
Cleveland, Ohio 44135
Fellow ASME

*Laminar heat transfer is analyzed in a tube rotating about an axis perpendicular to the tube axis. The solution applies for flow that is either radially outward from the axis of rotation, or radially inward toward the axis of rotation. The conditions are fully developed, and there is uniform heat addition at the tube wall. The analysis is performed by expanding velocities and temperature in power series using the Taylor number as a perturbation parameter. Coriolis and buoyancy forces caused by tube rotation are included, and the solution is calculated through second-order terms. The secondary flow induced by the Coriolis terms always tends to increase the heat transfer coefficient; this effect can dominate for small wall heating. For radial inflow, buoyancy also tends to improve heat transfer. For radial outflow, however, buoyancy tends to reduce heat transfer; for large wall heating this effect can dominate, and there is a net reduction in heat transfer coefficient.*

## Introduction

The cooling of rotating devices requires that the heat transfer be understood for flow in rotating channels. For channels that are parallel or perpendicular to the axis of rotation, the flow and heat transfer have been extensively reviewed and discussed in the book by W. D. Morris [1]. The paper by Morris and Ayhan [2] specifically addresses the interaction of both Coriolis and rotationally induced buoyancy effects in influencing the heat transfer for a channel rotating about an axis perpendicular to the channel axis (see Fig. 1). The Coriolis acceleration induces a secondary flow, and the resulting increased movement in the fluid region near the wall tends to increase the heat transfer coefficient. Buoyancy, however, can have an opposite effect, as shown experimentally for radial outflow in [2]. For radially outward flow from the rotational axis in a heated tube in perpendicular rotation, the higher temperature region near the wall will create a buoyancy force acting toward the axis of rotation in opposition to the axial pumping pressure. This can reduce the axial velocity near the wall and decrease the heat transfer coefficient. Depending on the magnitudes of the Coriolis and buoyancy effects a net increase or decrease in the heat transfer coefficient will occur relative to that for nonrotating tube flow. The Coriolis and buoyancy forces provide a complex interaction that is not well understood. For radial inflow toward the axis of rotation, experimental results in [1] indicate that the heat transfer will be enhanced by buoyancy effects.

Although some experimental investigations of the combined Coriolis and buoyancy effects have been performed, there is a lack of analytical development. The present paper will analyze the heat transfer for low Reynolds number (a limitation that arises from the use of a perturbation analysis) laminar flow in a tube with uniform heating at the tube wall. The tube is rotating about an axis perpendicular to the tube axis, and the flow is either radially outward from the axis of rotation, or radially inward. The secondary flow in a tube without heat transfer, for perpendicular rotation about an axis, was analyzed by Barua [3] by using a perturbation about Poiseuille flow. The series expansions were in terms of the Taylor number. The velocity distributions in [3] were used in [4] in the energy equation to analyze the heat transfer; hence that analysis did not include buoyancy effects. The authors chose to base the Nusselt number on the average fluid temperature rather than on the usual mixed mean fluid temperature.

The present analysis employs the momentum, continuity, and energy equations in a coupled solution to examine the buoyancy effect. The solution is obtained using series expansions in terms of the Taylor number, so that for zero wall heating the velocity distributions reduce to those in [3]. When buoyancy is reduced to zero, the present solution does not reduce to that in [4] because the mixed mean temperature is used here to compute the temperature difference between wall and fluid. Hence, for zero rotation the Nusselt number reduces to the usual value, 48/11, for laminar flow with uniform wall heat addition [5]. To be able to deal with buoyancy terms, the series expansion method is carried out in a different manner than in [4].

## Analysis

The rotating tube geometry is shown in Fig. 1. A tube of radius $a$ is rotating with angular velocity $\Omega$ about an axis perpendicular to the tube axis. The tube is being uniformly heated at the wall with a heat flux $q_w$, and the velocity

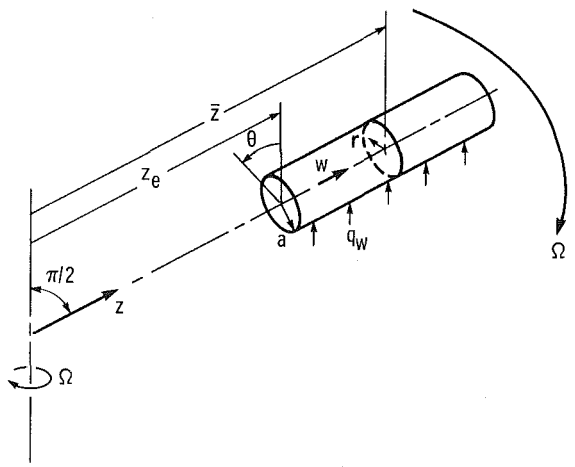


**Fig. 1 Geometry for flow through a heated tube rotating about a perpendicular axis**

Contributed by the Heat Transfer Division for publication in the JOURNAL OF HEAT TRANSFER. Manuscript received by the Heat Transfer Division June 21, 1984.

components in the $r$, $\theta$, $z$ directions are $u$, $v$, $w$. The momentum equation including the buoyancy force is given in [2]. The buoyancy term is expressed in terms of the coefficient of volume expansion as is commonly done in free-convection analyses (Boussinesq approximation). Then a constant reference density can be used throughout the analysis, and the equations are incompressible. Without tube rotation the heat transfer solution is given in [5]. The temperature difference used to express density variations in the buoyancy term is $T - T_b$ where $T_b$ is the mixed mean fluid temperature at axial location $z$. Then the equations of continuity, momentum, and energy are the following, in terms of a coordinate system attached to the tube

$$\nabla \cdot \mathbf{u} = 0 \tag{1}$$

$$\frac{D\mathbf{u}}{D\tau} + 2\omega \times \mathbf{u} = -\frac{1}{\rho_o}\nabla p' - \frac{\Omega^2}{2}\beta(T-T_b)\nabla(r^2\sin^2\theta + z^2) + \frac{\mu}{\rho_o}\nabla^2\mathbf{u} \tag{2}$$

$$\frac{DT}{D\tau} = \frac{k}{\rho_o c_p}\nabla^2 T \tag{3}$$

The $z$-coordinate is measured from the axis of rotation, and $p'(r, \theta, z)$ is the difference between the pressure when there is flow in the rotating tube, and the hydrostatic pressure that exists when the tube is rotating, but there is no flow.

The conditions are now assumed to be fully developed, and the tube is assumed to be at a large enough distance from the axis of rotation so that an average value of $z = \bar{z}$ can be used in the buoyancy term. For fully developed flow there are no variations in the shapes of velocity or temperature profiles with the $z$-direction, and $p'$ must have the form, $p' = b_1 z + f(r, \theta)$. For uniform heating at the tube wall, the entire fully developed temperature distribution must rise linearly with $z$ and hence $\partial^2 T/\partial z^2 = 0$. Applying these conditions, equations (1) to (3) become

$$\frac{\partial}{\partial r}(ru) + \frac{\partial v}{\partial \theta} = 0 \tag{4}$$

$$u\frac{\partial u}{\partial r} + \frac{v}{r}\frac{\partial u}{\partial \theta} - \frac{v^2}{r} - 2\Omega w\sin\theta = -\frac{1}{\rho_o}\frac{\partial f}{\partial r} - \Omega^2\beta(T-T_b)r\sin^2\theta + \frac{\mu}{\rho_o}\left(\nabla^2 u - \frac{u}{r^2} - \frac{2}{r^2}\frac{\partial v}{\partial \theta}\right) \tag{5a}$$

$$u\frac{\partial v}{\partial r} + \frac{v}{r}\frac{\partial v}{\partial \theta} + \frac{uv}{r} - 2\Omega w\cos\theta = -\frac{1}{\rho_o}\frac{1}{r}\frac{\partial f}{\partial \theta} - \Omega^2\beta(T-T_b)r\sin\theta\cos\theta + \frac{\mu}{\rho_o}\left(\nabla^2 v - \frac{v}{r^2} + \frac{2}{r^2}\frac{\partial u}{\partial \theta}\right) \tag{5b}$$

$$u\frac{\partial w}{\partial r} + \frac{v}{r}\frac{\partial w}{\partial \theta} + 2\Omega(u\sin\theta + v\cos\theta) = -\frac{b_1}{\rho_o} - \Omega^2\beta(T-T_b)\bar{z} + \frac{\mu}{\rho_o}\nabla^2 w \tag{5c}$$

## Nomenclature

$a$ = radius of tube
$b_1$ = axial pressure gradient in tube; $\tilde{b}_1 = b_1 a^3/\rho\nu^2$
$b_2$ = axial temperature gradient in tube; $\tilde{b}_2 = a\beta b_2$
$C_4$ = constant in zeroth-order temperature distribution
$C_6$ = constant in second-order temperature distribution
$c_p$ = specific heat of fluid at constant pressure
$f(r,\theta)$ = function in pressure distribution
$G(R)$ = function in second-order temperature distribution
$h$ = heat transfer coefficient in tube
$J$ = Taylor number, $2\Omega a^2/\nu$
$k$ = thermal conductivity of fluid
Nu = Nusselt number, $h2a/k$; $\mathrm{Nu}_p$, value for Poiseuille flow
Pr = Prandtl number, $c_p\mu/k$
$p'$ = difference between local pressure and hydrostatic pressure
$q_w$ = wall heat flux; $\tilde{q}_w = q_w a\beta/k$
$r$ = radial coordinate; $R = r/a$
Re = Reynolds number, $\bar{w}2a/\nu$
$T$ = absolute temperature; $T' = T - T_b$; $\tilde{T}' = \beta(T - T_b)$
$\tilde{T}_0, \tilde{T}_1, \tilde{T}_2$ = functions in series expansion of $\tilde{T}'$
$T_b$ = mixed mean fluid temperature
$T_e$ = fluid temperature at tube entrance
$T_w$ = tube wall temperature
$T_{w,\mathrm{avg}}$ = wall temperature averaged over $\theta$ from 0 to $2\pi$
$\mathbf{u}$ = fluid velocity vector
$u, v, w$ = velocity components in radial, tangential, and axial directions
$W$ = the quantity $wa/\nu$; $\tilde{W} = \bar{w}a/\nu$
$\bar{w}$ = integrated mean value of axial fluid velocity
$w_p$ = axial velocity for Poiseuille flow
$W_0, W_1, W_2$ = functions in series expansion of $W$
$Z$ = dimensionless axial coordinate, $z/a$; $\tilde{Z} = \bar{z}/a$
$z$ = axial coordinate; $\bar{z}$, an average value of $z$; $z_e$, distance from axis of rotation to tube entrance
$\nabla^2$ = Laplacian operator; $\tilde{\nabla}^2 = a^2\nabla^2$
$\nabla^4$ = biharmonic operator; $\tilde{\nabla}^4 = a^4\nabla^4$

### Greek Symbols

$\alpha$ = thermal diffusivity of fluid, $k/\rho_o c_p$
$\beta$ = coefficient of volume expansion
$\theta$ = angular coordinate (see Fig. 1)
$\mu$ = fluid viscosity
$\nu$ = fluid kinematic viscosity, $\mu/\rho_o$
$\rho_o$ = reference density in fluid
$\tau$ = time
$\psi$ = stream function; $\Psi = \psi/\nu$
$\Psi_1, \Psi_2$ = functions in series expansion of $\Psi$
$\omega$ = angular velocity vector
$\Omega$ = angular velocity of tube rotation

$$u\frac{\partial T}{\partial r}+\frac{v}{r}\frac{\partial T}{\partial \theta}+w\frac{\partial T}{\partial z}=\frac{k}{\rho_o c_p}\nabla^2 T \tag{6}$$

where

$$\nabla^2=\partial^2/\partial r^2+(1/r)(\partial/\partial r)+(1/r^2)(\partial^2/\partial\theta^2)$$

A stream function $\psi$ is now defined so that $-\partial\psi/\partial\theta = ru$ and $\partial\psi/\partial r = v$; this satisfies the continuity equation. The $\psi$ is substituted in (5) to eliminate $u$ and $v$. Then (5*a*) is differentiated with respect to $\theta$, and (5*b*) is multiplied by $r$ and differentiated with respect to $r$; the resulting two equations are subtracted to eliminate $f$. Equations (5) are thus reduced to an equation for $\psi$ and one for $w$

$$-2\Omega\left(r\cos\theta\frac{\partial w}{\partial r}-\sin\theta\frac{\partial w}{\partial\theta}\right)+\left(\frac{\partial\psi}{\partial r}\frac{\partial}{\partial\theta}-\frac{\partial\psi}{\partial\theta}\frac{\partial}{\partial r}\right)\nabla^2\psi$$

$$=\beta\Omega^2 r\sin\theta\left(\sin\theta\frac{\partial T'}{\partial\theta}-r\cos\theta\frac{\partial T'}{\partial r}\right)+\nu r\nabla^4\psi \tag{7}$$

where

$$\nabla^4=\frac{\partial^4}{\partial r^4}+\frac{2}{r}\frac{\partial^3}{\partial r^3}-\frac{1}{r^2}\frac{\partial^2}{\partial r^2}+\frac{1}{r^3}\frac{\partial}{\partial r}+\frac{2}{r^2}\frac{\partial^4}{\partial\theta^2\partial r^2}$$

$$-\frac{2}{r^3}\frac{\partial^3}{\partial r\partial\theta^2}+\frac{4}{r^4}\frac{\partial^2}{\partial\theta^2}+\frac{1}{r^4}\frac{\partial^4}{\partial\theta^4}$$

$$\frac{2\Omega}{r}\left(-\frac{\partial\psi}{\partial\theta}\sin\theta+r\frac{\partial\psi}{\partial r}\cos\theta\right)+\frac{1}{r}\left(-\frac{\partial\psi}{\partial\theta}\frac{\partial}{\partial r}+\frac{\partial\psi}{\partial r}\frac{\partial}{\partial\theta}\right)w$$

$$=-\frac{b_1}{\rho_o}-\beta\Omega^2\bar{z}T'+\nu\nabla^2 w \tag{8}$$

where $T' = T - T_b$

For fully developed conditions the shape of the temperature distribution across the tube does not vary with location $z$, and with uniform heat flux $\partial T/\partial z = b_2$ (a constant). The mass flow will be maintained at a fixed value throughout the analysis by suitably adjusting the pressure gradient. Then for the rotating tube, $b_2$ will be the same as for flow in a nonrotating tube, and from an overall heat balance

$$b_2=\frac{2q_w}{\bar{w}a\rho_o c_p} \tag{9}$$

For fully developed conditions, and since the mass flow is being kept constant, the mixed mean temperature obeys, $\partial T_b/\partial z = b_2$. Then by integration (since $T_b = T_e$ at $z = z_e$)

$$T_b=T_e+\frac{2q_w(z-z_e)}{\bar{w}a\rho_o c_p} \tag{10}$$

The energy equation (6) can be written in terms of $T' = T - T_b$, since $\partial T/\partial r = \partial T'/\partial r$, $\partial T/\partial\theta = \partial T'/\partial\theta$, and $\partial T/\partial z = \partial T_b/\partial z = b_2$. Then equation (6) becomes

$$-\frac{1}{r}\frac{\partial\psi}{\partial\theta}\frac{\partial T'}{\partial r}+\frac{1}{r}\frac{\partial\psi}{\partial r}\frac{\partial T'}{\partial\theta}+b_2 w=\alpha\nabla^2 T' \tag{11}$$

Equations (7), (8), and (11) are now put into dimensionless form by using the definitions in the Nomenclature to obtain

$$-J\left(R\cos\theta\frac{\partial W}{\partial R}-\sin\theta\frac{\partial W}{\partial\theta}\right)+\left(\frac{\partial\Psi}{\partial R}\frac{\partial}{\partial\theta}-\frac{\partial\Psi}{\partial\theta}\frac{\partial}{\partial R}\right)\tilde{\nabla}^2\Psi$$

$$=\frac{J^2}{4}R\sin\theta\left(\sin\theta\frac{\partial\tilde{T}'}{\partial\theta}-R\cos\theta\frac{\partial\tilde{T}'}{\partial R}\right)+R\tilde{\nabla}^4\Psi \tag{12}$$

$$J\frac{1}{R}\left(-\frac{\partial\Psi}{\partial\theta}\sin\theta+R\frac{\partial\Psi}{\partial R}\cos\theta\right)+\frac{1}{R}\left(-\frac{\partial\Psi}{\partial\theta}\frac{\partial}{\partial R}+\frac{\partial\Psi}{\partial R}\frac{\partial}{\partial\theta}\right)W$$

$$=-\tilde{b}_1-J^2\frac{\tilde{Z}}{4}\tilde{T}'+\tilde{\nabla}^2 W \tag{13}$$

$$-\frac{1}{R}\frac{\partial\Psi}{\partial\theta}\frac{\partial\tilde{T}'}{\partial R}+\frac{1}{R}\frac{\partial\Psi}{\partial R}\frac{\partial\tilde{T}'}{\partial\theta}+\tilde{b}_2 W=\frac{1}{\mathrm{Pr}}\tilde{\nabla}^2\tilde{T}' \tag{14}$$

To solve these equations, the three unknowns $\Psi$, $W$, and $\tilde{T}'$ are each expanded in a series in powers of $J$

$$\Psi=J\Psi_1(R,\theta)+J^2\Psi_2(R,\theta)+\ldots \tag{15}$$

$$W=W_0(R)+JW_1(R,\theta)+J^2W_2(R,\theta)+\ldots \tag{16}$$

$$\tilde{T}'=\tilde{T}_0(R)+J\tilde{T}_1(R,\theta)+J^2\tilde{T}_2(R,\theta)+\ldots \tag{17}$$

Since for $J = 0$ the flow must reduce to Poiseuille flow, the $\Psi_0 = 0$ and $W_0$ and $\tilde{T}_0$ must be functions only of $R$. Equations (15) to (17) are substituted into (12) to (14) and terms in the same power of $J$ are collected. This yields to second order

*$J^0$ terms:*

$$0=-\tilde{b}_1+\tilde{\nabla}^2 W_0(R) \tag{18a}$$

$$\tilde{b}_2 W_0=\frac{1}{\mathrm{Pr}}\tilde{\nabla}^2\tilde{T}_0 \tag{18b}$$

*$J^1$ terms:*

$$-R\cos\theta\frac{\partial W_0}{\partial R}=R\tilde{\nabla}^4\Psi_1 \tag{19a}$$

$$-\frac{1}{R}\frac{\partial\Psi_1}{\partial\theta}\frac{\partial W_0}{\partial R}=\tilde{\nabla}^2 W_1 \tag{19b}$$

$$-\frac{1}{R}\frac{\partial\Psi_1}{\partial\theta}\frac{\partial\tilde{T}_0}{\partial R}+\tilde{b}_2 W_1=\frac{1}{\mathrm{Pr}}\tilde{\nabla}^2\tilde{T}_1 \tag{19c}$$

*$J^2$ terms:*

$$-R\cos\theta\frac{\partial W_1}{\partial R}+\sin\theta\frac{\partial W_1}{\partial\theta}+\frac{\partial\Psi_1}{\partial R}\frac{\partial}{\partial\theta}(\tilde{\nabla}^2\Psi_1)$$

$$-\frac{\partial\Psi_1}{\partial\theta}\frac{\partial}{\partial R}(\tilde{\nabla}^2\Psi_1)$$

$$=-\frac{R^2}{4}\sin\theta\cos\theta\frac{\partial\tilde{T}_0}{\partial R}+R\tilde{\nabla}^4\Psi_2 \tag{20a}$$

$$-\frac{1}{R}\frac{\partial\Psi_1}{\partial\theta}\sin\theta+\frac{\partial\Psi_1}{\partial R}\cos\theta-\frac{1}{R}\frac{\partial\Psi_1}{\partial\theta}\frac{\partial W_1}{\partial R}-\frac{1}{R}\frac{\partial\Psi_2}{\partial\theta}\frac{\partial W_0}{\partial R}$$

$$+\frac{1}{R}\frac{\partial\Psi_1}{\partial R}\frac{\partial W_1}{\partial\theta}=-\frac{\tilde{Z}}{4}\tilde{T}_0+\tilde{\nabla}^2 W_2 \tag{20b}$$

$$-\frac{1}{R}\frac{\partial\Psi_1}{\partial\theta}\frac{\partial\tilde{T}_1}{\partial R}-\frac{1}{R}\frac{\partial\Psi_2}{\partial\theta}\frac{\partial\tilde{T}_0}{\partial R}+\frac{1}{R}\frac{\partial\Psi_1}{\partial R}\frac{\partial\tilde{T}_1}{\partial\theta}$$

$$+\tilde{b}_2 W_2=\frac{1}{\mathrm{Pr}}\tilde{\nabla}^2\tilde{T}_2 \tag{20c}$$

The solution of (18*a*) is the Poiseuille velocity profile

$$W_0=-\frac{\tilde{b}_1}{4}(1-R^2) \tag{21a}$$

This satisfies the boundary condition of zero velocity at the wall, $W_0 = 0$ at $R = 1$. The integrated mean value of $W_0$ is

$$\bar{W}_0=\frac{1}{\pi}\int_0^{2\pi}\int_0^1 W_0 R\,dR\,d\theta=-\frac{\tilde{b}_1}{8} \tag{21b}$$

Equation (21*a*) is inserted into (18*b*) and the solution for $\tilde{T}_0$ is

$$\tilde{T}_0=\frac{\tilde{q}_w}{\mathrm{Re}}\frac{\tilde{b}_1}{4}\left(\frac{3}{4}-R^2+\frac{R^4}{4}\right)+C_4 \tag{21c}$$

where $\tilde{b}_2 = 4\tilde{q}_w/\mathrm{RePr}$ has been used (from equation (9)). The boundary conditions for the $\tilde{T}$ terms will be treated a little later. For this purpose note that $\partial\tilde{T}_0/\partial R\,|_{R=1} = -\tilde{b}_1\tilde{q}_w/4\mathrm{Re}$.

Equation (21*a*) is substituted into (19*a*) and the solution for $\Psi_1$ is

$$\Psi_1 = -\frac{\tilde{b}_1}{384} R(1-R^2)^2\cos\theta \tag{22a}$$

This satisfies the conditions that $\partial\Psi_1/\partial R = \partial\Psi_1/\partial\theta = 0$ at $R = 1$, so that the velocities $U$ and $V$ will be zero at the wall. Then $W_0$ and $\Psi_1$ are substituted into (19*b*), and the solution for $W_1$ is

$$W_1 = \frac{\tilde{b}_1^2}{768\times 48} R(1-R^2)(R^4-3R^2+3)\sin\theta \tag{22b}$$

This satisfies the boundary condition that $W_1 = 0$ at $R = 1$. The integrated mean value of $W_1$ is

$$\bar{W}_1 = \frac{1}{\pi}\int_0^{2\pi}\int_0^1 W_1 R dR d\theta = 0 \tag{22c}$$

The $\tilde{T}_0$, $\Psi_1$ and $W_1$ are next inserted into (19*c*) and the solution for $\tilde{T}_1$ is

$$\tilde{T}_1 = \frac{\tilde{q}_w}{\mathrm{Re}}\frac{\tilde{b}_1^2}{768}\left[-\left(\frac{1}{6}+\mathrm{Pr}\right)\frac{R^9}{160}+\left(\frac{1}{3}+2\mathrm{Pr}\right)\frac{R^7}{48} -(1+5\mathrm{Pr})\frac{R^5}{48} +\left(\frac{1}{4}+\mathrm{Pr}\right)\frac{R^3}{8}-\left(\frac{83}{6}+43\mathrm{Pr}\right)\frac{R}{480}\right]\sin\theta \tag{22d}$$

It is noted for future use that $\partial T_1/\partial R|_{R=1} = 0$ (this was obtained by using the proper coefficient multiplying the $R$ term).

The second order terms are now calculated. The $\tilde{T}_0$, $\Psi_1$, and $W_1$ are substituted into (20*a*) and the solution for $\Psi_2$ is

$$\Psi_2 = \frac{\tilde{b}_1}{128\times 1920}R^2\left[\frac{\tilde{b}_1}{6\times 48}(17-36R^2+20R^4-R^8) -\frac{4\tilde{q}_w}{\mathrm{Re}}(8-17R^2+10R^4-R^6)\right]\sin 2\theta \tag{23a}$$

This satisfies $\partial\Psi_2/\partial R = \partial\Psi_2/\partial\theta = 0$ at $R = 1$ so that $U$ and $V$ will be zero at the wall. Similarly equation (20*b*) is solved for $W_2$ to yield

$$W_2 = \frac{\tilde{b}_1}{768}\left[\frac{1}{6}(1-3R^2+3R^4-R^6)-\left(\frac{5}{24}R^2-\frac{1}{3}R^4+\frac{R^6}{8}\right)\cos 2\theta\right] +\frac{\tilde{Z}}{16}C_4(R^2-1)+\frac{\tilde{b}_1^3}{768^2\times 48}\left[\left(\frac{37}{120} -\frac{3}{2}R^2+3R^4-\frac{19}{6}R^6+\frac{15}{8}R^8 -\frac{3}{5}R^{10}+\frac{R^{12}}{12}\right)+\frac{1}{5}\left(\frac{923}{840}R^2-\frac{17}{6}R^4+\frac{23}{8}R^6 -\frac{3}{2}R^8+\frac{5}{12}R^{10}-\frac{2}{35}R^{12}\right)\cos 2\theta\right] -\frac{\tilde{b}_1\tilde{b}_2\mathrm{Pr}}{256}\left[\bar{Z}\left(\frac{19}{36}-\frac{3}{4}R^2+\frac{R^4}{4}-\frac{R^6}{36}\right)+\frac{\tilde{b}_1}{64\times 15} \left(\frac{7}{24}R^2-\frac{2}{3}R^4+\frac{17}{32}R^6-\frac{R^8}{6}+\frac{R^{10}}{96}\right)\cos 2\theta\right] \tag{23b}$$

The integrated average value of $W_2$ is

$$\bar{W}_2 = \frac{\tilde{b}_1}{8}\left(\frac{1}{768\times 3}-\frac{\bar{Z}C_4}{4\tilde{b}_1}+\frac{\tilde{b}_1^2}{768^2\times 112} -\frac{11}{768\times 2}\tilde{b}_2\mathrm{Pr}\bar{Z}\right) \tag{23c}$$

Substituting the previously obtained quantities into (20*c*), the solution for $\tilde{T}_2$ can be found as

$$\tilde{T}_2 = \tilde{q}_w\frac{4\tilde{b}_1}{\mathrm{Re}}\left\{\frac{-\tilde{b}_1^2\mathrm{Pr}}{768^2\times 4}\left[-\frac{1}{240}\left(\frac{83}{6}+43\mathrm{Pr}\right)\frac{R^2}{4} +\frac{1}{15}\left(\frac{16}{3}+\frac{73}{4}\mathrm{Pr}\right)\frac{R^4}{16}-\frac{1}{80}\left(\frac{323}{6}+213\mathrm{Pr}\right)\frac{R^6}{36} +\left(\frac{23}{36}+3\mathrm{Pr}\right)\frac{R^8}{64}-\frac{1}{48}\left(\frac{103}{6}+93\mathrm{Pr}\right)\frac{R^{10}}{100} +\frac{13}{20}\left(\frac{1}{6}+\mathrm{Pr}\right)\frac{R^{12}}{144}-\frac{7}{80}\left(\frac{1}{6}+\mathrm{Pr}\right)\frac{R^{14}}{196}\right] +\frac{1}{768\times 24}\left(R^2-\frac{3}{4}R^4-\frac{R^6}{3}-\frac{R^8}{16}\right) -\frac{\tilde{Z}}{64\tilde{b}_1}C_4\left(R^2-\frac{R^4}{4}\right) +\frac{\tilde{b}_1^2}{768^2\times 192}\left(\frac{37}{120}R^2-\frac{3}{8}R^4+\frac{R^6}{3}-\frac{19}{96}R^8 +\frac{3}{40}R^{10}-\frac{R^{12}}{60}+\frac{R^{14}}{588}\right) +\frac{\tilde{q}_w\tilde{Z}}{1024\mathrm{Re}}\left(\frac{19}{9}R^2-\frac{3}{4}R^4+\frac{R^6}{9}-\frac{R^8}{144}\right) +G(R)\cos 2\theta\right\}+C_6 \tag{24}$$

The $G(R)$ is not needed in what follows but it satisfies the condition $\partial G/\partial R|_{R=1} = 0$. For later use note that from (24)

$$\frac{\partial\tilde{T}_2}{\partial R}\bigg|_{R=1} = 4\tilde{q}_w\frac{\tilde{b}_1}{\mathrm{Re}}\left(\frac{1}{768\times 48}-\frac{\bar{Z}C_4}{64\tilde{b}_1} +\frac{\tilde{b}_1^2}{768^2\times 16\times 112}-\frac{11}{768\times 8}\frac{\tilde{q}_w\tilde{Z}}{\mathrm{Re}}\right)$$

In connection with equation (9) and the use of the variable $T'$, the mass flow is kept the same for both the rotating and nonrotating cases. To fulfill this condition, it is first noted that since $\bar{W} = wa/\nu$, for nonrotating flow $\bar{W} = \bar{w}a/\nu = \mathrm{Re}/2$. The $\bar{W}$ is now set equal to $\bar{W}_0 + J\bar{W}_1 + J^2\bar{W}_2$ to yield a condition that $\tilde{b}_1$ must satisfy

$$\frac{\mathrm{Re}}{2} = -\frac{\tilde{b}_1}{8}\left[1-J^2\left(\frac{1}{768\times 3}-\frac{\bar{Z}C_4}{4\tilde{b}_1}+\frac{\tilde{b}_1^2}{768^2\times 112} -\frac{11}{768\times 2}\tilde{b}_2\mathrm{Pr}\bar{Z}\right)\right] \tag{25}$$

This is a preliminary form since the $C_4$ has not yet been obtained.

To obtain $C_4$ and $C_6$, the thermal boundary conditions and an overall heat balance will be examined. The $T(R,\theta)$ can be found from equation (17) since $\tilde{T}' = \beta(T-T_b)$ and $T_b$ is in equation (10). Then using $q_w = k\partial T/\partial r|_{r=a}$ gives in dimensionless form

$$\tilde{q}_w = \frac{\partial\tilde{T}_0(R)}{\partial R}\bigg|_{R=1}+J\frac{\partial\tilde{T}_1(R,\theta)}{\partial R}\bigg|_{R=1}+J^2\frac{\partial\tilde{T}_2(R,\theta)}{\partial R}\bigg|_{R=1}$$

Substituting the previously obtained temperature derivatives gives

$$\tilde{q}_w = -\frac{\tilde{b}_1\tilde{q}_w}{4\mathrm{Re}}+J^2 4\tilde{b}_1\frac{\tilde{q}_w}{\mathrm{Re}}\left(\frac{1}{768\times 48}-\frac{\bar{Z}C_4}{64\tilde{b}_1} +\frac{\tilde{b}_1^2}{768^2\times 16\times 112}-\frac{11}{768\times 8}\frac{\tilde{q}_w\tilde{Z}}{\mathrm{Re}}\right)$$

Noting that $\tilde{b}_2 = 4\tilde{q}_w/\text{RePr}$ it is found that this equation is the same as equation (25); hence the wall heat flux boundary condition is satisfied. Next consider an overall heat balance on the heated tube. This yields for the length of the tube from the entrance at $z_e$ to the location $z$ in the tube,

$$q_w 2\pi a(z-z_e) = \rho_o c_p \int_0^{2\pi}\int_0^a [T(r,\theta,z) - T_e] w(r,\theta) r dr d\theta$$

Eliminate $T_e$ by use of equation (10) and put the result in dimensionless form to yield

$$\int_0^{2\pi}\int_0^1 \tilde{T}' W R dR d\theta = 0 \tag{26}$$

Insert the power series expansions for $\tilde{T}'$ and $W$ and collect terms in $J^0$, $J^1$, and $J^2$. The $J^1$ terms integrate the zero, and the $J^0$ and $J^2$ terms yield expressions for $C_4$ and $C_6$. From the $J^0$ terms

$$\int_0^{2\pi}\int_0^1 W_0 \tilde{T}_0 R dR d\theta = 0$$

Insert $W_0$ and $\tilde{T}_0$ from (21*a*) and (21*c*), and integrate. This yields

$$C_4 = -\frac{11}{96}\tilde{q}_w \frac{\tilde{b}_1}{4\text{Re}} \tag{27}$$

The terms in $J^2$ yield from (26)

$$\int_0^{2\pi}\int_0^1 (\tilde{T}_0 W_2 + \tilde{T}_1 W_1 + \tilde{T}_2 W_0) R dR d\theta = 0$$

This integration requires considerable algebra, as did some of the previous portions of the solution. After elimination of $C_4$ (using equation (27)), and $\tilde{b}_2$ (using $\tilde{b}_2 = 4\tilde{q}_w/\text{RePr}$) there is obtained

$$C_6 = \frac{\tilde{q}_w}{\text{Re}}\left[-\frac{11}{360}\frac{\tilde{b}_1}{768} + \frac{\tilde{Z}\tilde{q}_w}{768}\frac{41}{180}\frac{\tilde{b}_1}{4\text{Re}} - \frac{773}{525}\left(\frac{\tilde{b}_1}{768}\right)^3\left(\frac{16}{21} + \frac{4591}{2319}\text{Pr} + \frac{2944}{773}\text{Pr}^2\right)\right] \tag{28}$$

Similarly by eliminating $C_4$ and $\tilde{b}_2$, the final relation for equation (25), to obtain $\tilde{b}_1$ in terms of the parameters Re and $J$, is

$$-4\text{Re} = \tilde{b}_1\left[1 - \frac{J^2}{768}\left(\frac{1}{3} + \frac{\tilde{b}_1^2}{768 \times 112}\right)\right] \tag{29}$$

The heat transfer quantity of interest is the Nusselt number

$$\text{Nu} = \frac{h2a}{k} = \frac{q_w}{T_{w,\text{avg}} - T_b}\frac{2a}{k} = \frac{2\tilde{q}_w}{\beta(T_{w,\text{avg}} - T_b)}$$

The denominator, $\beta(T_{w,\text{avg}} - T_b)$, is equal to $\tilde{T}'$ evaluated at $R = 1$ and averaged over all $\theta$ from 0 to $2\pi$. The $\theta$ averaged components of $\tilde{T}'$ at the wall are

$$\tilde{T}_0(R=1)_{\text{avg}} = C_4$$

$$J\tilde{T}_1(R=1)_{\text{avg}} = 0$$

$$J^2\tilde{T}_2(R=1)_{\text{avg}} = J^2\left\{\tilde{q}_w\frac{4\tilde{b}_1}{\text{Re}}\left[\frac{\tilde{b}_1^2\text{Pr}}{768^2 \times 320}\left(\frac{4591}{240 \times 63} + \frac{1123}{20 \times 63}\text{Pr}\right) + \frac{50}{768^2 \times 3} - \frac{9C_4\tilde{Z}}{768\tilde{b}_1} + \frac{\tilde{b}_1^2}{768^2 \times 48^2}\frac{3029}{1960} - \frac{\tilde{q}_w\tilde{Z}}{768\,\text{Re}}\frac{211}{192}\right] + C_6\right\}$$

These quantities are inserted into the Nusselt number, the $C_4$ and $C_6$ are eliminated using equations (27) and (28), and the result is rearranged into a convenient form. Then it is divided by the Nusselt number for Poiseuille flow in a nonrotating tube with uniform wall heating, $\text{Nu}_p = 48/11$. This yields the final relation

$$\frac{\text{Nu}}{\text{Nu}_p} = 1\Big/\left\{-\frac{\tilde{b}_1}{4\text{Re}} + \frac{24}{11}\frac{J^2}{\text{Re}}\left[\frac{9}{160}\frac{\tilde{b}_1}{768} - \frac{77}{90}\frac{\tilde{Z}\tilde{q}_w}{768}\frac{\tilde{b}_1}{4\text{Re}} + \left(\frac{\tilde{b}_1}{768}\right)^3\left(\frac{2957}{3150} + \frac{516}{175}\text{Pr}^2\right)\right]\right\} \tag{30}$$

Some results will now be presented and discussed for the velocity profiles in the tube, and for $\text{Nu}/\text{Nu}_p$ as a function of tube rotation and wall heating for both radial outflow and inflow. For radial inflow toward the axis of rotation, the mean axial velocity is in the negative $z$-direction. An examination of the analysis shows that for radial inflow it is only required to use $-\text{Re}$ instead of Re in the final formulas for velocity and Nusselt number. When using the analytical relations, the $J$ must be sufficiently small so that the $J$ and $J^2$ terms are small relative to the zeroth order terms.

## Results and Discussion

The series expansion method used here is a perturbation about Poiseuille flow in a nonrotating tube. Since the expansion is in powers of $J$, and $J$ obviously cannot be too large; how large can be determined by examining the individual terms in the solution. Since the numerical coefficients in the series decrease rapidly (for example, compare 1/384 to 1/(128 × 1920) in equations (22*a*) and (23*a*)), the $J$ does not need to be less than unity. As pointed out by Barua [3], the Reynolds number must also be kept small so that the secondary flows do not become too large for the perturbation solution about Poiseuille flow to be adequate. Hence the results here are for low Reynolds number laminar flow.

Axial velocity distributions are shown in Figs. 2 and 3 in the plane of rotation that contains the leading ($\theta = 3\pi/2$) and trailing ($\theta = \pi/2$) edges of the tube, and in the plane perpendicular to the plane of rotation, $\theta = 0, \pi$. The parameters for the curves are given on each figure. The profiles were calculated using equation (16) with the $W_0$, $W_1$, and $W_2$ from equations (21*a*), (22*b*), and (23*b*). The $C_4$ is in equation (27), and $\tilde{b}_1$ is found from equation (29). For Poiseuille flow $\tilde{b}_1 = -4\text{Re}$, and $W = W_0(R) = \text{Re}(1-R^2)$ (which is the same as $w/\bar{w} = 2[1 - (r/a)^2]$). The profiles have all been normalized relative to the Poiseuille value at the center of the tube. The normalized Poiseuille profile ($J = 0$) is shown in each figure as a curve of short dashes.

Figure 2 shows the effect of tube rotation ($J = 15$) when there is no wall heat transfer and hence there are no buoyancy effects. The velocity distribution is altered by the secondary flows induced by the Coriolis forces. These curves are for radial outflow; radial inflow gives the same results but the Coriolis forces are reversed, and hence the asymmetric curves at $\theta = \pi/2$ and $3\pi/2$ are interchanged. The reversal of the asymmetry is illustrated by comparing the curves for radial outflow with those for radial inflow in Figs. 3(*a*) and 3(*b*). The volume flow in Fig. 2 is the same for the $J = 0$ and $J = 15$ cases; this might not be evident from the few curves shown, since the integration for volume flow includes all $\theta$ values. The secondary flow due to rotation tends to increase the velocity near the wall thereby increasing the Nusselt number as will be shown later. The profile for $\theta = 0$ and $\pi$ is symmetric about the centerline since the secondary flow pattern is in two symmetric cells separated by the plane of rotation which is at $\theta = \pi/2$ and $3\pi/2$. The secondary flow patterns without buoyancy effects are further illustrated by examples in [2] and [3].

Figure 3 shows velocity distributions that result from the

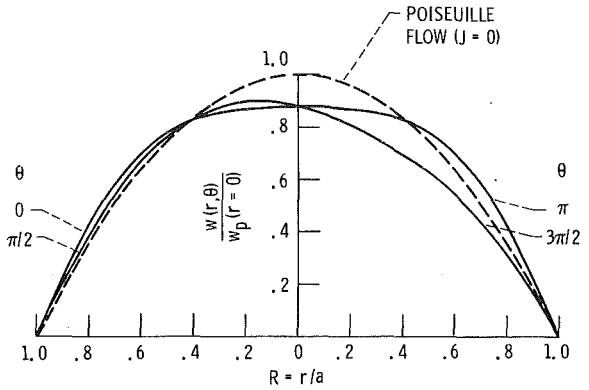


Fig. 2 Effect of rotation on axial velocity profile for radial outflow: Re = 10, $J$ = 15

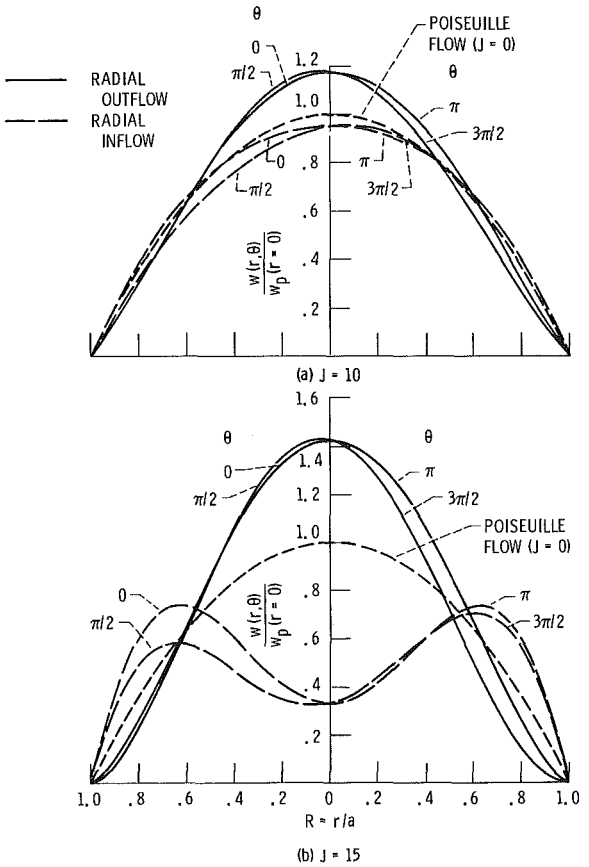


Fig. 3 Effect of rotation and buoyancy on axial velocity profile for radial outflow and inflow: $\tilde{q}_w$ = 0.1, $\bar{z}/a$ = 50, Re = 10

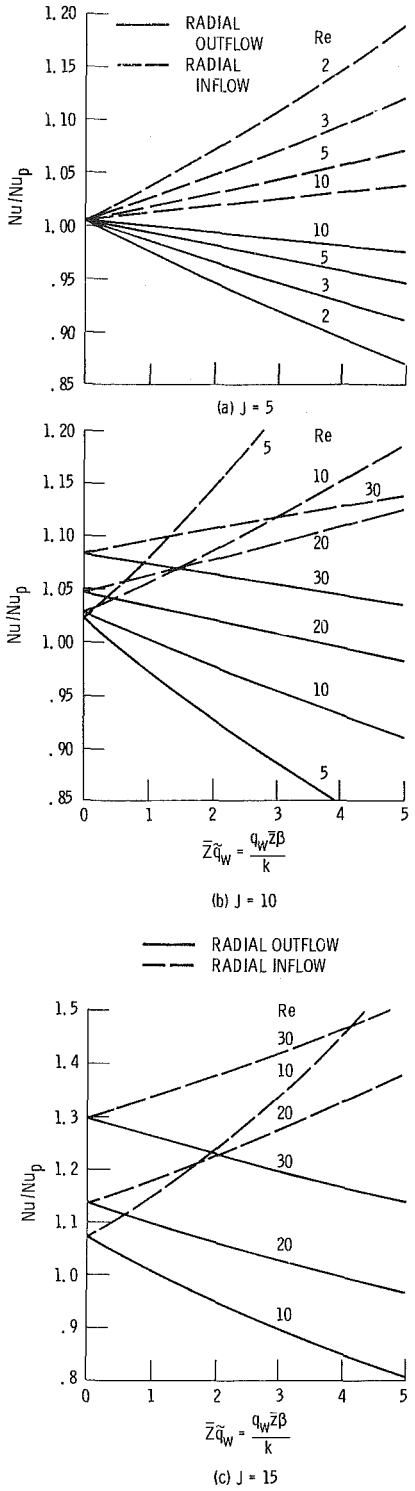


Fig. 4 Effect of rotation and buoyancy on Nusselt number for uniform wall heating: Pr = 0.7

combined effects of Coriolis and buoyancy forces, which is the objective of this study. Figure 3($a$) is for $J$ = 10 and Re = 10. Since the fluid has the highest temperatures near the heated wall, this is the region of highest buoyancy acting in the negative $z$-direction. For radial outflow the axial velocity is reduced in this region, and because total volume flow is preserved (fixed Reynolds number), the velocities increase in the central region of the tube. As will be shown in Fig. 4 for Pr = 0.7, the velocity decrease near the wall is accompanied by a reduction in heat transfer coefficient in opposition to the effect of the secondary velocities induced by the Coriolis forces. For radial inflow the highest buoyancy, which is in the region adjacent to the wall, is acting in the direction of flow, and hence velocities are increased in this region. The velocities are thus decreased in the central region of the tube. The changes in velocity distribution are reflected in an increased Nusselt number as will be shown in Fig. 4.

In Fig. 3($b$), the $J$ has been increased to 15 as compared with $J$ = 10 in Fig. 3($a$); this provides a substantial increase in buoyancy effects. The profiles are again shown for $\theta = 3\pi/2$ and $\pi/2$ (the plane of the leading and trailing edges) and for $\theta$ = 0 and $\pi$ (the plane perpendicular to the plane of rotation). For radial outflow the profiles are similar to those in Fig. 3($a$), but since the buoyancy is more substantial, there is a greater effect on the velocity distribution. The axial velocity is significantly reduced near the wall. For radial inflow the inward buoyancy effect substantially increases the velocity

near the wall to the extent that the peak velocity is no longer near the center of the tube.

Now our attention is turned to the Nusselt number in the tube. This is shown in Fig. 4 in normalized form relative to the Nusselt number for Poiseuille flow. These results are calculated from equation (30) with Pr = 0.7. It is noted that in equation (30) the $\bar{Z}\tilde{q}_w$ appear together, and this parameter along with $J$ is used in Fig. 4 to show the buoyancy effect. Starting with a low value of $J$, Fig. 4($a$) gives results for $J$ = 5. For no heating ($\tilde{q}_w = 0$) the Nusselt number is just slightly above the Poiseuille value as a result of the rotationally induced secondary flow. This effect increases with Reynolds number, but is too small to be evident on the figure. For small Re, on the order of $J$ or less, the Nusselt number is appreciably modified by increases in $\bar{Z}\tilde{q}_w$. For Re = 10 the through flow is sufficiently strong that buoyancy has only a modest effect. As anticipated by the effects on the axial velocity distributions, buoyancy increases the Nusselt number for radial inflow and decreases it for radial outflow.

Figure 4($b$) shows similar results for Pr = 0.7 with a larger rotational velocity, $J$ = 10, and for larger Reynolds numbers. For zero heating the Coriolis induced secondary flow increases the Nusselt number; an effect that increases with Re. For Re = 30 there is about 8 percent increase in Nu over the Poiseuille value. As heating is increased, Nu decreases for radial outflow, and can become less than $Nu_p$; the largest effect is for small Re where buoyancy can have a greater influence. For radial inflow Nu increases with a similar dependence on $\bar{Z}\tilde{q}_w$ and Re.

These effects are further illustrated in Fig. 4($c$) for $J$ = 15. When Re = 30, the secondary flow for $\tilde{q}_w = 0$ increases the heat transfer to about 30 percent over the Poiseuille value. For radial outflow the buoyancy effect gradually reduces the Nu, and for $\bar{Z}\tilde{q}_w = 5$ the heat transfer is only 14 percent above the Poiseuille value. The buoyancy effect is much more substantial for lower values of Reynolds number. These results clearly illustrate how Coriolis and buoyancy interactions with the through flow influence the tube heat transfer. Significant changes in the Nusselt number can be produced by buoyancy effects. The same general effects of buoyancy are described by the experimental results in chapter 6 of [1]. However, since the experimental results are for turbulent flow, it is not possible to make quantitative comparisons with the present laminar theory.

## Concluding Remarks

Heat transfer in a rotating tube has been analyzed for low Reynolds number laminar flow with uniform heat addition at the tube wall, and convenient analytical expressions are given by equations (29) and (30). The coupled equations of momentum and energy were solved by a perturbation method, and the analysis includes the Coriolis and buoyancy terms. The axis of rotation is perpendicular to the tube axis, and the flow can be radially outward or inward. Since buoyancy is acting inward toward the axis of rotation, the heated region near the tube wall produces a buoyancy force that tends to provide inward axial flow in that region. This tends to decrease the Nusselt number for radial outflow, and increase it for inflow. For a fixed Reynolds number the change in Nusselt number is intensified by increases in the Taylor number.

## References


1 Morris, W. D., *Heat Transfer and Fluid Flow in Rotating Coolant Channels*, Research Studies Press, John Wiley and Sons, 1981.

2 Morris, W. D., and Ayhan, T., "Observations on the Influence of Rotation on Heat Transfer in the Coolant Channels of Gas Turbine Rotor Blades," *Institution of Mechanical Engineers. Proceedings,* Vol. 193, 1979, pp. 303–311.

3 Barua, S. N., "Secondary Flow in a Rotating Straight Pipe," *Royal Society of London. Proceedings*, Series A, Vol. 227, 1955, pp. 133–139.

4 Vidyanidhi, V., Suryanarayana, V. V. S., and Chenchu Raju, V. C., "An Analysis of Steady Fully Developed Heat Transfer in a Rotating Straight Pipe," ASME JOURNAL OF HEAT TRANSFER, Vol. 99, Feb. 1977, pp. 148–150.

5 Siegel, R., Sparrow, E. M., and Hallman, T. M., "Steady Laminar Heat Transfer in a Circular Tube with Prescribed Wall Heat Flux," *Applied Scientific Research*, Sec. A, Vol. 7, 1958, pp. 386–392.

# Internal, Shellside Heat Transfer and Pressure Drop Characteristics for a Shell and Tube Heat Exchanger

**E. M. Sparrow**
Fellow ASME

**J. A. Perez**

Department of Mechanical Engineering,
University of Minnesota,
Minneapolis, Minn. 55455

*Per-tube heat transfer coefficients and per-compartment and intracompartment pressure drops were measured on the shell side of a shell and tube heat exchanger. The main focus of the work was to determine the response of these quantities to variations in the size of the baffle window; the Reynolds number was also varied parametrically. The pressure measurements showed that the fluid flow is fully developed downstream of the first compartment of the heat exchanger and that the per-compartment pressure drop is constant in the fully developed regime. Within a compartment, the pressure drop in the upstream half is much larger than that in the downstream half. The per-tube heat transfer coefficients vary substantially within a given compartment (on the order of a factor of two), giving rise to a nonuniform thermal loading of the tubes. Row-average and compartment-average heat transfer coefficients were also evaluated. The lowest row-average coefficients were those for the first and last rows in a compartment, while the highest coefficient is that for the row just upstream of the baffle edge. It was demonstrated that the per-tube heat transfer coefficients are streamwise periodic for a module consisting of two consecutive compartments.*

## Introduction

Shell and tube heat exchangers are employed in a broad range of industrial applications and, in certain fields (e.g., the chemical process industry), they are by far the most-used means of heat exchange. The design of such devices involves a knowledge of the heat transfer and pressure drop characteristics, both for the fluid which flows in the tubes and the fluid which flows outside the tubes. The latter, the shellside flow, is generally more complex than the former because it is forced to sweep back and forth across the tubes by a succession of periodically positioned baffles.

State-of-the-art design recommendations for heat transfer and pressure drop coefficients for the shell side of shell and tube heat exchangers are set forth in the recently published Heat Exchanger Design Handbook [1]. The methodology recommended there is an updated version of that evolved by the multiyear, widely quoted University of Delaware project [2]. Another highly regarded shellside design method is that of Tinker [3, 4], but its inherent complexity has limited its use.

The common focus of the various design methods is to predict the average shellside heat transfer coefficient and pressure drop for a typical compartment of the heat exchanger (a compartment is the space bounded between successive baffle plates). With regard to experimental work, it has, for the most part, averaged over the entire heat exchanger. Indeed, the heat transfer coefficients obtained from such experiments are actually averages over both the tubeside and shellside flows, and simplifying assumptions are needed to infer the exchanger-average, shellside coefficient. The typical pressure drop measurements yield overall inlet-to-exit shellside pressure drops (including inlet and exit losses). This type of heat transfer and pressure drop data do not provide a fully definitive test of the per-compartment predictions furnished by the aforementioned design methods.

In addition to the need for definitive compartment-average experimental results to validate candidate design procedures, more localized heat transfer and pressure drop information is needed to define the path toward improved performance of shell and tube heat exchangers. As a case in point, consideration of the shellside fluid flow pattern in a typical compartment suggests the probability of substantial variations of the heat transfer coefficient among the tubes that pass through the compartment. Correspondingly, within the compartment, there will be a tube to tube variation of the heat transfer between the shell fluid and the tube fluid. Furthermore, because of the repetitive nature of the flow pattern in successive compartments, tubes distinguished by low shellside coefficients in any one compartment will be periodically subjected to the same low coefficients in downstream compartments, and similarly for tubes distinguished by high coefficients.

Therefore, over the length of the exchanger, the heating rates will differ among the various tubes which compose the parallel array. If there is a single-phase flow in the tubes, different inlet-to-exit temperature rises will be sustained in the various tubes. For a two-phase flow in the tubes, the different rates of heating will lead to differences in the vapor fraction. Thus, thermally speaking, the tubes are not equally loaded. The unequal thermal loading represents an inefficiency whose alleviation awaits a knowledge of the individual, per-tube heat transfer coefficients.

The foregoing discussion serves to motivate the experimental research that was performed here. For the experiments, a model heat exchanger was designed to serve as a research tool. It was fabricated to be totally free of leakage paths and, according to the criterion of [2], to have negligible bypass effects. The exchanger encompassed an array of 92 tubes, and shellside heat transfer coefficients were individually measured at each tube in a compartment situated in the fully developed regime. These compartment-related, per-tube results, of interest in their own right, were processed to yield other relevant quantities: (*i*) the per-tube heat transfer coefficient for the periodic fully developed regime (equal to the average of the per-tube coefficients in two successive compartments), (*ii*) the row-average heat transfer coefficient, and (*iii*) the compartment-average heat transfer coefficient.

Contributed by the Heat Transfer Division for publication in the JOURNAL OF HEAT TRANSFER. Manuscript received by the Heat Transfer Division May 3, 1984.

Axial pressure distributions were measured by arrays of pressure taps situated within the exchanger. There were three separate axial arrays of taps, with one tap of each array located in each compartment (making for three taps per compartment). These measurements enabled the determination of the per-compartment pressure drop and provided information about the local pressure drops within the compartment. In addition, the axial pressure distributions served as a means for identifying the hydrodynamic entrance length in a shell and tube heat exchanger.

The main focus of the work was the heat transfer and pressure drop response to changes in the size of the baffle opening (i.e., in the size of the window). Three different heat exchangers were employed during the course of the research, each characterized by a different baffle opening. The range of the investigated openings covered the common range encountered in practice. For each heat exchanger, the Reynolds number was varied from 1350 to 5750.

The measured per-tube heat transfer coefficients are believed to be accurate to 2-3 percent, while the accuracy of the per-compartment pressure drop is about 2 percent. The heat transfer results were actually determined by mass transfer measurements utilizing the naphthalene sublimation technique. Relative to heat transfer experiments, the naphthalene technique affords higher accuracy and greater apparatus flexibility. Relative to other mass transfer techniques, the naphthalene technique has a Schmidt number ($=2.5$) that is closest to the Prandtl numbers of interest in heat transfer applications. Therefore, the transformation of the mass transfer results to heat transfer results via a Schmidt number (or Prandtl number) power law is more accurate than for the high Schmidt number ($\sim 1000$) mass transfer techniques.

Attention will now be turned to the literature and to prior studies in which per-tube measurements were made. The earlier work dealt with systems which deviate significantly from those of practice: a 16-tube array [5, 6] and a rectangular shell [7]. More recently, electrochemical mass transfer techniques (Schmidt number $\sim$ 1000) have been used to accomplish the measurements (e.g., [8-10]), but only compartment-average (rather than per-tube) results are reported.

## The Experiments

**Experimental Apparatus.** The description of the experimental apparatus is facilitated by reference to Fig. 1, in which both a longitudinal section and a cross section are displayed, respectively in diagrams (*a*) and (*b*). In the longitudinal section, a representative set of compartments is illustrated, but the tubes have been omitted in order to preserve clarity. The tubes are shown in the cross-sectional view. To orient the cross-sectional and longitudinal views, it is convenient to match the trio of pressure taps designated as A, B, and C. Note also that although the cross-sectional view does not cut the baffle plates, the edges of the baffles which bound the test section are indicated for orientation purposes (dashed lines).

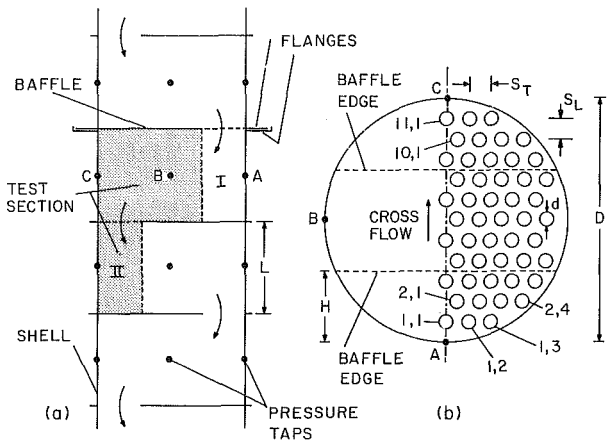


**Fig. 1 Schematic diagrams showing a longitudinal section and a cross section of the experimental apparatus**

As noted earlier, there are 92 tubes in the cross section. However, owing to symmetry, only 49 of the tube positions are unique, and these tubes are displayed in Fig. 1(*b*). The space to the left of the symmetry line is populated with tubes which are mirror images of those shown at the right of the symmetry line. Although Figs. 1(*a*) and (*b*) are useful in describing the geometry and the general constructional features of the apparatus, they do not convey the design nuances and fabrication details that facilitated the efficient collection of local data of high accuracy. That information, copiously illustrated with diagrams, is available in [11].

There are eleven rows of tubes in the cross section. Each tube location is designated by two numbers, as illustrated in Fig. 1(*b*). The first of these is the row number, which increases in the flow direction. The second indicates the tube position in

## Nomenclature

$A_{min}$ = minimum free-flow area in widest part of cross section, equation (8)
$A$ = mass transfer surface area
$A_w$ = free-flow area in window
$D$ = inside diameter of shell
$d$ = tube diameter
$\mathfrak{D}$ = mass diffusion coefficient
$H$ = window opening, Fig. 1
$K$ = baffle cut, $H/D$
$K_m$ = mass transfer coefficient
$K_p$ = per-compartment pressure loss coefficient
$L$ = interbaffle spacing, Fig. 1
$\Delta M$ = change of mass during data run
Nu = Nusselt number
Pr = Prandtl number
$p$ = local pressure in heat exchanger
$p_\infty$ = ambient pressure
$\Delta p$ = per-compartment pressure drop
Re = Reynolds number, $\dot{w}d/\mu A_{min}$
$S_L$ = longitudinal pitch
$S_T$ = transverse pitch
Sc = Schmidt number
Sh = per-tube Sherwood number in a compartment
$Sh_{row}$ = row-average Sherwood number in a compartment
$Sh_{tube/mod}$ = per-tube, per-module Sherwood number
$\overline{Sh}$ = compartment-average Sherwood number
$V^*$ = superficial velocity, $\dot{w}/\rho A_{min}$
$\dot{w}$ = rate of mass flow
$\mu$ = viscosity
$\nu$ = kinematic viscosity
$\rho$ = density
$\rho_{nw}$ = naphthalene vapor density at tube surface
$\rho_{nb}$ = naphthalene vapor density in flow
$\tau$ = duration of data run

each row, with the numeral one denoting the tube nearest the symmetry line and with increasing numbers from left to right.

The tubes are of diameter $d$ and are deployed in an equilateral triangular pattern in which the transverse center-to-center spacing (i.e., the pitch) is $S_T$. The other parameters defining the geometry of the exchanger include the window opening $H$ (which specifies the edge of the baffle), the inside diameter $D$ of the shell, and the interbaffle spacing $L$ (which specifies the axial length of the compartments). These quantities can be expressed in terms of the following dimension ratios

$$S_T/d,\ d/D,\ L/D \tag{1}$$

and the baffle cut

$$K=H/D \tag{2}$$

The dimension ratios of equation (1) were fixed during the course of the experiments at values typical of a broad class of shell and tube heat exchangers, namely, $S_T/d = 1.5$, $d/D = 0.061$, and $L/D = 0.6$ (note that the longitudinal pitch $S_L = (\sqrt{3}/2)S_T$). For the baffle cut, the selected values were

$$K=0.223,\ 0.302,\ \text{and}\ 0.460 \tag{3}$$

The $K = 0.302$ case is illustrated in Fig. 1($b$) (baffle edge between rows 3 and 4). For the $K = 0.223$ case, the baffle edge is positioned between rows 2 and 3, while $K = 0.460$ corresponds to the baffle edge situated between rows 5 and 6. In all cases, the baffle edge was located midway between two adjacent rows of tubes. The tube layout is common to all three cases.

The heat exchanger was assembled as a vertical stack consisting of a succession of sections of the shell, each of length $L$. Each successive pair of shell sections was separated by a baffle plate. As illustrated in Fig. 1($a$), the baffle plates extended slightly beyond the outer surface of the shell, facilitating the application of silicone rubber sealant, which ensured the absence of air leakage at the shell-baffle interfaces. The entire assembly of shell sections and baffle plates was precisely aligned and securely locked together with screws.

The first of the three heat exchangers ($K = 0.302$) was fabricated with nine compartments. The experiments conducted with that exchanger revealed the remarkably rapid attainment of hydrodynamically developed flow, i.e., after only one compartment. Since the research was focused on the fully developed regime, the fabrication task for the second and third heat exchangers ($K = 0.223$ and 0.460) was simplified by the use of fewer compartments, seven rather than nine.

From Fig. 1($b$), it may be seen that the clearance between the shell and the closest shell-adjacent tube is smaller than half the transverse intertube spacing (i.e., smaller than $1/2(S_T - d)$). According to [2], whenever this criterion is fulfilled, bypass effects are negligible. It should also be noted that wherever a tube passed through a hole in a baffle plate, silicone rubber was applied to prevent leakage.

The apparatus was operated in the suction mode, with air drawn from the laboratory into and through the heat exchanger. The air exiting the exchanger was ducted to a flowmeter (a calibrated rotameter), a control valve, and a blower. The blower was situated in a service corridor adjacent to the laboratory, and its discharge was vented outside the building. This outside venting was especially advantageous during the mass transfer data runs because it ensured that the laboratory was free of naphthalene vapor.

The inlet to the heat exchanger was an opening cut into the shell wall of the first compartment. The opening was confined to the part of the wall opposite the window of the first baffle, so that the entering airflow had to traverse all of the tubes of the first compartment before reaching the window. The area of the opening was approximately equal to the free-flow area at the widest part of the exchanger cross section.

**Mass Transfer.** The shaded region labeled *test section* in Fig. 1($a$) indicates where the mass transfer measurements were made. It is readily apparent, however, that zone II in the test section is in every way identical to zone I which immediately precedes the test section. Therefore, in the presentation of the results, the mass transfer coefficients measured in II will be reported as belonging to zone I.

The successful implementation of the naphthalene sublimation technique requires rapid access to the test section in order to enable measurement of the mass of the individual naphthalene coated tubes. The desired rapid access was accomplished by a design that allowed the upper portion of the heat exchanger (i.e., all compartments above the test section) to be separated from the lower portion and to be lifted vertically upward, all in a few seconds. When the upper portion was in its elevated position, the test section was fully exposed. The upper portion was equipped with wheels which rolled in guideways, and the actual lifting was accomplished with the aid of a heavy cord passed over pulleys. When the upper and lower portions were in contact (as in Fig. 1($a$)), they mated via gasket-equipped flanges which were pressed together by quick-acting clamps.

All of the tubes in the test section were made removable to facilitate their use as mass transfer test elements. The other tubes of the exchanger were permanently installed.

During the execution of a data run, mass transfer occurred only in the test section, and there, at only one of the tubes. That is, the surface of only one tube was coated with naphthalene, while the other tubes were metallic. In a sequence of data runs, the position of the mass-transfer-active tube was varied systematically throughout the test section. The practice of using a single active tube is a widely used approach in both heat and mass transfer research studies of crossflow tube banks. Since the mixing of the flow is more vigorous in a shell and tube heat exchanger than in a tube bank, the approach should have even greater merit for the former than for the latter.

Each mass-transfer-active tube was a composite consisting of a metallic core and a naphthalene overcoating. The coating of a tube was accomplished in a multistep process. First, any residual naphthalene remaining from the preceding data run is removed by melting and evaporation. Then the tube is dipped into a bath of molten naphthalene for a sufficient number of times to build up a solid layer whose diameter exceeds the desired diameter $d$. The final step of the process is a machining of the cylindrical surface of the tube on a lathe to yield a finished diameter equal to $d$.

Each mass transfer data run was preceded by an equilibration period during which the heat exchanger (and, in particular, the naphthalene-coated tube) attained temperature equality with the airflow. During this period, sublimation was suppressed by a Teflon sheath which jacketed the coated tube. The mass of the coated tube was measured immediately preceding and immediately after the data run proper. Following the conclusion of the run, a calibration procedure was executed to account for possible extraneous sublimation during the handling of the coated tube. This yielded a correction of about 2 percent. The mass measurements were made using an ultra-precision electronic balance with a resolution of $10^{-5}$ g.

The temperature prevailing in the heat exchanger during a mass transfer data run is a necessary input to the data reduction procedure (the naphthalene vapor pressure is a function of temperature). Temperature measurements were made in the row of tubes immediately upstream of the test section. To this end, in each of two tubes in this row, a precalibrated thermocouple was threaded through the tube

bore and the leads conveyed outside the apparatus. The thermocouple junction was affixed to the inner wall of the tube by a thermally conducting, copper-based epoxy cement. The two thermocouples generally agreed to within the resolving power of the digital millivoltmeter (1 $\mu$V).

**Pressure Drop.** The locations of the pressure taps are shown in both the longitudinal and cross sectional views in Fig. 1. All told, there were 23 taps in the $K = 0.302$ heat exchanger and 17 taps in the $K = 0.223$ and 0.460 heat exchangers.

As seen in Fig. 1, there are three taps in each compartment. Furthermore, the tap locations are the same in all compartments. Because of this, there are three independent combinations of pressure taps that yield the fully developed, per-compartment pressure drop. Thus, referring to Fig. 1(*a*), this quantity can be measured between consecutive center taps, between a left-hand tap in one compartment and the right-hand tap in the next compartment, and between a right-hand tap in one compartment and the left-hand tap in the next compartment.

The pressure measurements were made in a set of data runs separate from the mass transfer runs. The pressure signals were detected by a solid-state capacitance-type pressure meter capable of resolving $10^{-3}$ Torr.

## Data Reduction and Mass/Heat Transfer Analogy

**Data Reduction.** As noted earlier, the mass transfer coefficient was evaluated at each of the individual tubes in the cross section. In dimensionless terms, the per-tube mass transfer coefficient will be expressed by the Sherwood number. In turn, the Sherwood numbers can be transformed to Nusselt numbers, as will be documented shortly.

If $\Delta M$ denotes the net mass loss at a tube during a data run of duration $\tau$, the per-tube mass transfer coefficient $K_m$ may be evaluated from

$$K_m = (\Delta M/\tau A)/(\rho_{nw} - \rho_{nb}) \tag{4}$$

where $A(-\pi dL)$ is the mass transfer surface area (note that $A$ was corrected for the very slight surface recession which occurred during the run). The quantities $\rho_{nw}$ and $\rho_{nb}$ respectively denote the naphthalene vapor densities at the tube surface and in the flow approaching the tube. The latter is zero for the present experiments, while the former was evaluated from the vapor pressure/temperature relation for naphthalene in conjunction with the perfect gas law.

For the Sherwood number $\mathrm{Sh} = K_m d/\mathfrak{D}$, the diffusion coefficient $\mathfrak{D}$ may be eliminated by using the Schmidt number $\mathrm{Sc} = \nu/\mathfrak{D}$, so that

$$\mathrm{Sh} = (K_m d/\nu)\mathrm{Sc} \tag{5}$$

where $\mathrm{Sc} = 2.5$ for naphthalene diffusion in air. The kinematic viscosity appearing in equation (5) was evaluated as that of pure air, with the density corresponding to the mean pressure in the test section.

The Sherwood number results will be parameterized by the Reynolds number

$$\mathrm{Re} = \rho V^* d/\mu \tag{6}$$

The quantity $V^*$ is the superficial velocity at the minimum free-flow area $A_{\min}$ in the row of tubes situated in the widest part of the cross section, i.e., $\rho V^* = \dot{w}/A_{\min}$, where $\dot{w}$ is the rate of mass flow through the heat exchanger. Upon elimination of $\rho V^*$, equation (6) becomes

$$\mathrm{Re} = \dot{w} d/\mu A_{\min} \tag{7}$$

In terms of Fig. 1, $A_{\min}$ can be written as

$$A_{\min} = (D - 10d)L \tag{8}$$

in which the quantity 10 represents the number of tubes in the row in question.

The per-compartment pressure drop $\Delta p$ for the fully developed regime will be represented by the pressure loss coefficient $K_p$

$$K_p = \Delta p/\tfrac{1}{2}\rho V^{*2} \tag{9}$$

To determine $\Delta p$, least-squares straight lines were fitted to the fully developed portion of the individual $p$ versus $x$ distributions that were respectively measured for each of the three sets of pressure taps. The slopes of the three lines, which generally agreed to within one percent, were averaged, and $\Delta p$ was evaluated from the average slope. The density appearing in equation (9) was evaluated at the mean pressure in the fully developed regime.

**Mass/Heat Transfer Analogy.** To convert the mass transfer results to heat transfer results, the analogy between the processes will be employed in the form

$$\mathrm{Nu}/f(\mathrm{Pr}) = \mathrm{Sh}/f(\mathrm{Sc}) \tag{10}$$

where the function $f$ is the same for both heat and mass transfer. For crossflow tube banks and for most other convective heat transfer processes (aside from the liquid metal range), $f(\mathrm{Pr}) = \mathrm{Pr}^m$, $f(\mathrm{Sc}) = \mathrm{Sc}^m$. These relations will be used here along with the tube bank value $m = 0.36$ from [12], so that

$$\mathrm{Nu} = (\mathrm{Pr}/\mathrm{Sc})^{0.36}\mathrm{Sh} \tag{11}$$

Since $\mathrm{Sc} = 2.5$ for the present experiments

$$\mathrm{Nu} = 0.719\mathrm{Pr}^{0.36}\mathrm{Sh}_{2.5} \tag{12}$$

which can be used to convert the present Sherwood numbers to Nusselt numbers corresponding to a given Prandtl number.

## Results and Discussion

**Pressure Drop.** Representative pressure distribution results, typical of the complete collection available in [11], are presented in Fig. 2. On the ordinate, $p$ denotes the pressure at a tap location, while $p_\infty$ is the barometric pressure in the laboratory from which the air was drawn. In addition to the pressure data, the figure contains a schematic diagram showing the numbering scheme for the pressure taps. Based on the periodic nature of the flow field, the taps naturally group into three sets: (*i*) taps 1–8, each of which is situated in the center of a compartment, (*ii*) taps 9–16, each situated at

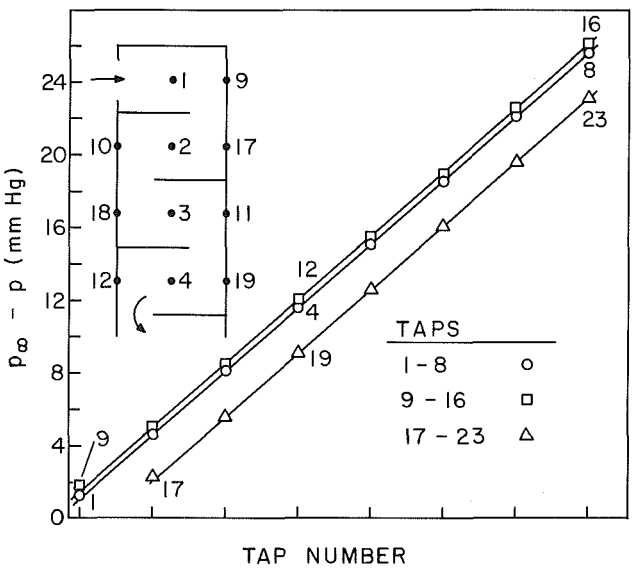


Fig. 2 Representative pressure distribution results ($K = 0.302$, $\mathrm{Re} = 3550$)

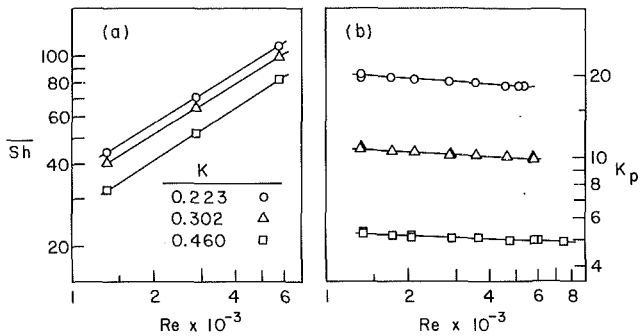


**Fig. 3 Compartment-average Sherwood numbers and dimensionless per-compartment pressure drops**

the downstream end of a compartment, and (*iii*) taps 17–23, each situated at the upstream end of a compartment.

The data corresponding to each set of taps are designated by a common symbol and are interconnected by a least-squares straight line. The three straight lines are virtually parallel. Furthermore, aside from the first point in each set, the data points fall squarely on the lines, with almost no scatter.

Since the successive taps in a given set are separated by the axial length of a compartment, the linearity of the data (aside from the first tap) indicates that the per-compartment pressure drop is the same for all compartments. The uniformity of the per-compartment pressure drop is an indication of the attainment of fully developed flow. Thus the flow is seen to develop very rapidly. Indeed, it appears that the development is completed downstream of the first compartment.

The virtual absence of data scatter and the parallelism of the straight lines is indicative of the geometrical uniformity of the heat exchanger and the precise positioning of the pressure taps.

Of particular note in Fig. 2 is that the spacing between the three parallel straight lines is not uniform. This finding provides insight into the distribution of the pressure drop within a compartment. For concreteness, consider the compartment in which are situated the taps 4, 12, and 19. The figure shows that the pressure drop between taps 19 and 4 is much greater than that between taps 4 and 12, i.e., the pressure drop in the upstream portion of the compartment exceeds the pressure drop in the downstream portion. This finding is plausible because the former reflects the final stages of the turning of the flow around the baffle, while the latter reflects the initial stages of the turning. It is well known from simple systems such as pipe bends that there is greater dissipation in the final stages of the turn than in the initial stages.

The per-compartment pressure drop results, expressed in terms of the pressure loss coefficient $K_p$, are plotted in Fig. 3(*b*) as a function of the Reynolds number (the Sherwood number results of Fig. 3(*a*) will be discussed later). The figure shows that, as expected, the pressure drop is sensitive to the baffle cut $K$, increasing markedly as the baffle cut decreases. It is also seen from the figure that $K_p$ varies only slightly with the Reynolds number. If the losses had been altogether inertial (i.e., $\Delta p \sim \frac{1}{2}\rho V^{*2}$), then $K_p$ would be independent of the Reynolds number, as is the case for turbulent flow in a rough-walled pipe. The slight variation of $K_p$ with Re in Fig. 3(*b*) indicates that skin friction does play a role, albeit small.

A highly accurate and concise representation of all the $K_p$ results was achieved by the correlation

$$K_p = 2.35[K^{-1.027}\exp(0.38A_{\min}/A_w)]\mathrm{Re}^{-0.05} \qquad (13)$$

In this equation, $A_w$ is the free-flow area in the window, which depends on the baffle cut $K$. Equation (13) represents

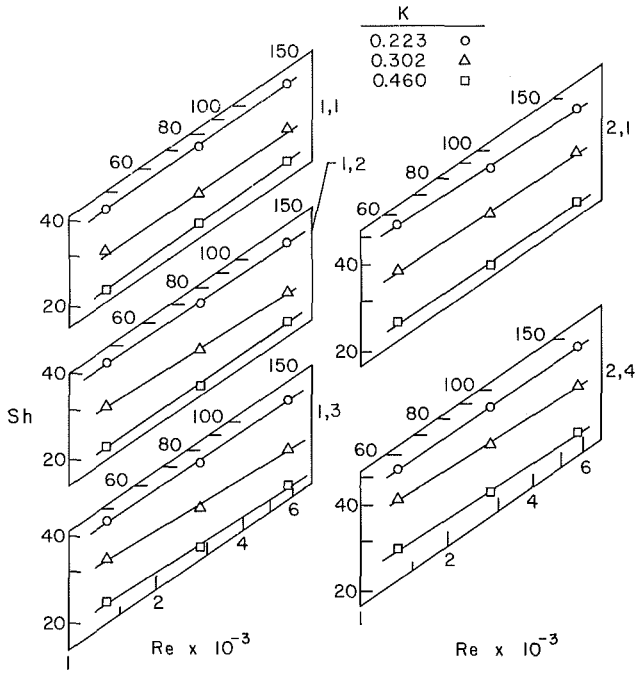


**Fig. 4 Per-tube Sherwood numbers at tubes situated in rows 1 and 2 in a compartment**

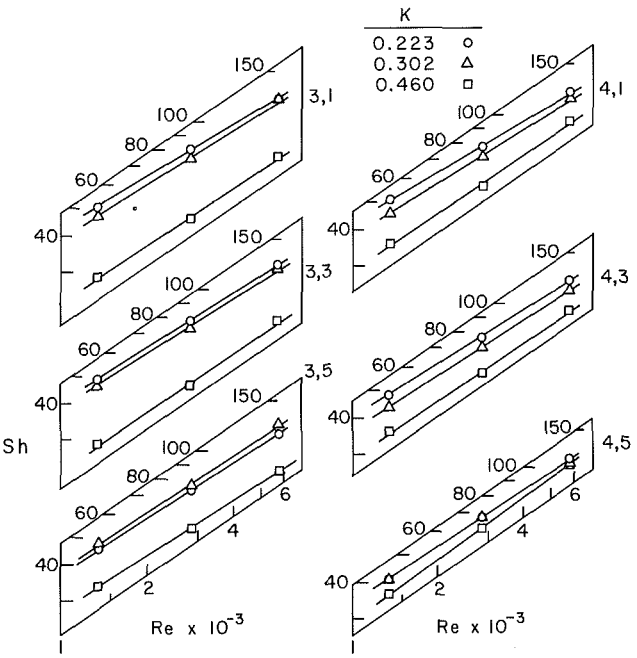


**Fig. 5 Per-tube Sherwood numbers at tubes situated in rows 3 and 4 in a compartment**

80 percent of the data to ± 1 percent, with an extreme deviation of 2 percent.

**Per-Tube Sherwood Numbers.** The per-tube Sherwood numbers at each tube location in a compartment are presented in both graphical and tabular form in [11]. A somewhat condensed version of that presentation is made here in Table 1 and in Figs. 4–8.

The minimum and maximum values of the per-tube Sherwood number in a given compartment are presented in Table 1. The table also shows the tube locations which correspond to the listed $\mathrm{Sh}_{\min}$ and $\mathrm{Sh}_{\max}$ values (the tube locations can be identified in Fig. 1(*b*)).

An overview of the table reveals that there are substantial

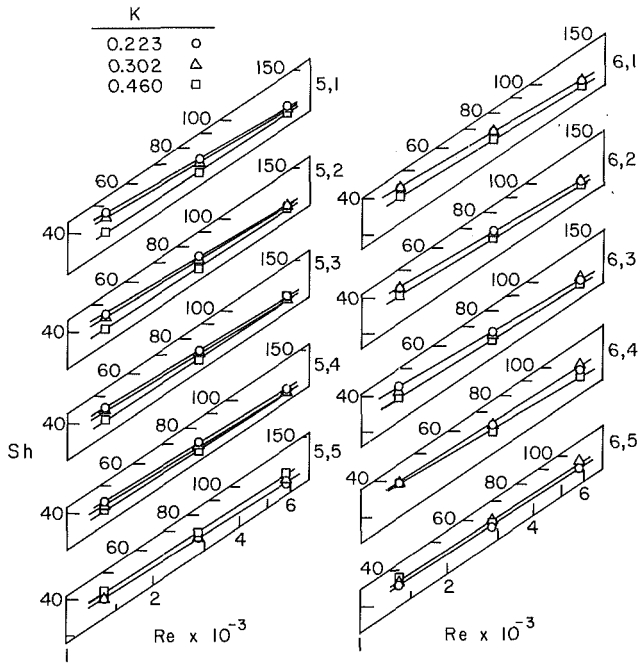


Fig. 6 Per-tube Sherwood numbers at tubes situated in rows 5 and 6 in a compartment

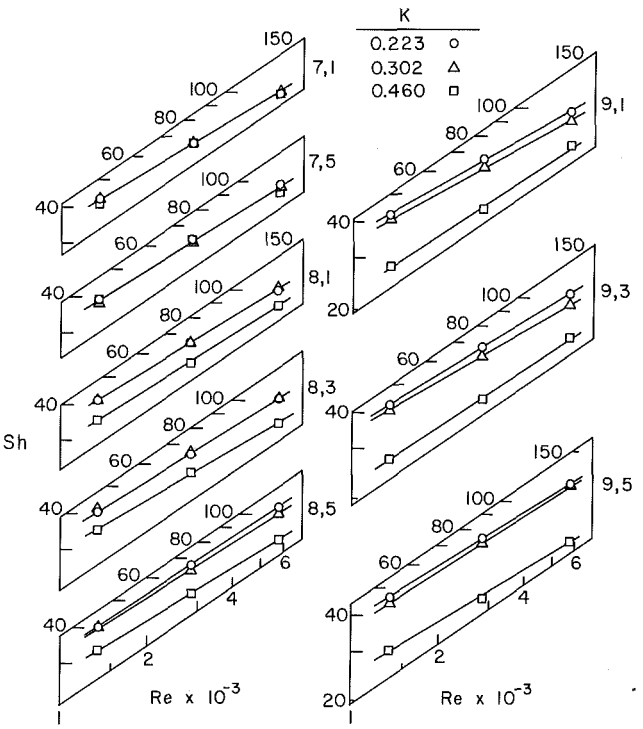


Fig. 7 Per-tube Sherwood numbers at tubes situated in rows 7, 8, and 9 in a compartment

differences in the per-tube Sherwood numbers within a compartment. The $Sh_{max}/Sh_{min}$ ratio varies with the baffle cut, but, for a given baffle cut, is virtually independent of the Reynolds number. For $K$ = 0.223, 0.302, and 0.460, the respective ratios are 1.6, 1.8, and 2.25.

Thus, the larger the baffle cut, the more nonuniform is the per-tube Sherwood number. The practical implications of such nonuniformities have already been discussed in the Introduction.

Table 1 shows that $Sh_{max}$ is attained in the row of tubes just upstream of the baffle edge, at the inlet end of the compartment. On the other hand, $Sh_{min}$ is attained in the most downstream row of the compartment.

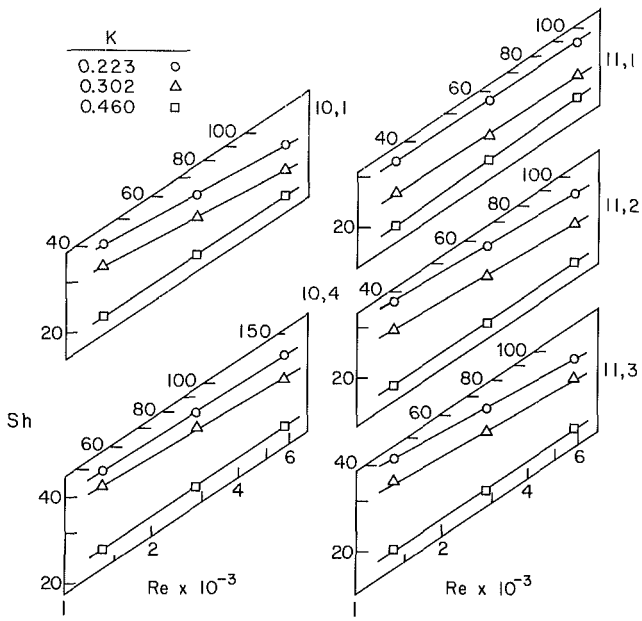


Fig. 8 Per-tube Sherwood numbers at tubes situated in rows 10 and 11 in a compartment

Figures 4–8 convey a more detailed presentation of the per-tube Sherwood number results. Each figure is a two-column mosaic of several strip graphs. The individual strip graphs show the variation of the Sherwood number with the Reynolds number for all three investigated baffle cuts. Each graph pertains to a specific tube location as indicated by the label appearing to the right of the graph. The array of graphs in a given column conveys information about a specific row, starting with row 1 in Fig. 4 and concluding with row 11 in Fig. 8.

In interpreting these figures, it is well to recall from equation (7) that the Reynolds number is, in effect, a dimensionless mass flow rate since $(d/\mu A_{min})$ is a constant for the heat exchangers investigated here. In the crossflow zone, the velocities associated with a given Reynolds number (i.e., with a given mass flow) should not be very different for the different heat exchangers, and the corresponding Sherwood numbers should be nearly equal. However, in the window zone, the velocities will be a function of the baffle cut, so that the Sherwood numbers should vary with the baffle cut. It may also be noted that depending on the location of a particular tube, it may be washed by flows containing crossflow and axial components of different relative strengths. For example, tubes situated in the window zone will experience a stronger axial component than will tubes which are situated between the baffle edges. Since axial flows and crossflows evoke different dependences of Sh on Re (respectively, $Sh \sim Re^{0.8}$ and $Sh \sim Re^{0.6}$), changes of slope of the Sh, Re relation are expected during a row by row traverse of the cross section.

Figure 4 shows results for rows 1 and 2, both of which are situated in the window zone for all three investigated baffle cuts. Since, at a given Reynolds number, the velocity in the window zone is larger for smaller baffle cuts, the Sherwood number results in Fig. 4 are averaged in increasing order with decreasing values of the baffle cut. The data for each tube location and each baffle cut appear to be well described by the power law $Sh \sim Re^n$. The $n$ values, arranged over the three tubes of row 1, are 0.68, 0.64, and 0.68, respectively for $K$ = 0.223, 0.302, and 0.460, while the average $n$ values for the four tubes of row 2 are 0.65, 0.64, and 0.67. The decrease in $n$

**Table 1 Minimum and maximum per-tube Sherwood numbers**

| $K$ | Re | $Sh_{min}$ | Tube no. | $Sh_{max}$ | Tube no. |
|---|---|---|---|---|---|
| 0.223 | 1350 | 34.0 | 11,1 | 55.6 | 2,2 |
| | 2850 | 56.0 | 11,1 | 88.5 | 2,2 |
| | 5750 | 87.9 | 11,2 | 142.3 | 2,3 |
| 0.302 | 1350 | 26.5 | 11,1 | 47.6 | 3,5 |
| | 2850 | 42.3 | 11,1 | 76.0 | 3,5 |
| | 5750 | 68.8 | 11,1 | 123.0 | 3,5 |
| 0.460 | 1350 | 18.9 | 11,2 | 43.2 | 5,5 |
| | 2850 | 31.1 | 11,2 | 68.8 | 5,5 |
| | 5750 | 50.5 | 11,2 | 111.2 | 5,5 |

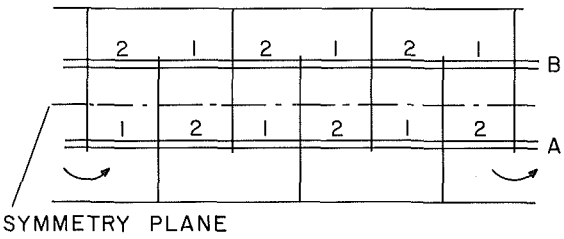


**Fig. 9 Diagram to illustrate two-compartment module**

from 0.68 to 0.65 for the small baffle cut suggests that the velocity field is tending toward more crossflow and less axial flow, which is reasonable since the baffle edge is situated just downstream of row 2 for this case.

Figure 5, left-hand column, shows that for the third row, the Sh values for the small and intermediate baffle cuts (0.223 and 0.302) tend to approach each other. This indicates that the axial velocity component is diminishing and crossflow is taking over (for pure crossflow, Sh would be independent of the baffle cut). For these baffle cuts, the results for row 4 (right-hand column) are similar to those of row 3. The waning of the axial velocity component is also in evidence for the large baffle cut (0.460). The gap between the Sh results for that baffle cut and the others is seen to progressively diminish from the second to the third and from the third to the fourth rows.

An overview of Fig. 6 (rows 5 and 6) shows that the distinction between the small and intermediate baffle cuts has virtually disappeared, while only slight deviations exist for the large baffle cut. For row 6, the average slopes for the three cases are $n = 0.61, 0.62$, and 0.61.

True congruence of the results occurs in row 7, as exemplified in the topmost pair of graphs in the left-hand column of Fig. 7. There, no distinction can be made between the results for the different baffle cuts.

The results displayed in the bottommost trio of graphs in the left column of Fig. 7 suggests that for the large baffle cut case, the flow at row 8 is beginning its turn toward the compartment exit. This inference is based on the departure of the Sh results for this case from those for the other baffle cuts. The latter remain more or less congruent because they continue to be crossflow dominated.

The right column of Fig. 7 (row 9) reflects the heightened turning of the flow for the large baffle cut case, as witnessed by the dropping away of its Sh curve. Evidence of the beginning of turning for the intermediate baffle cut is provided by the separation of its Sherwood numbers from those for the small baffle cut.

The final figure of this set, Fig. 8, displays the Sherwood number results for rows 10 and 11. For both of these rows, the tubes are situated in the window zone for all of the investigated baffle cuts, and the resulting inverse relationship between the baffle cut and the velocity (at a given Reynolds number) gives rise to a significant separation of the respective Sh, Re lines. It is noteworthy that the exponents $n$ ($Sh \sim Re^n$) for the small and intermediate baffle cuts remain in the neighborhood of 0.6, indicating the continuing presence of a strong crossflow component.

The tube-to-tube Sherwood number variations within a given row in a compartment can be extracted from Figs. 4–8, but this information is more easily read from the tabular presentation of [11]. By way of a summary, it may be noted that intrarow Sherwood number variations of 10 percent are not uncommon. Variations as large as 30–40 percent (max divided by min) were encountered in the turning zone at the downstream end of the compartment. In general, smaller intrarow variations existed in the upstream end of the compartment than in the downstream end.

**Per-Tube, Per-Module Sherwood Numbers.** From the standpoint of applications, it is important to note that even in the fully developed regime, the Sherwood number measured at a given tube in a given compartment recurs periodically at that tube in *every other* compartment rather than in every successive compartment. Figure 9 has been prepared to elaborate this and related issues. The figure displays a representative set of compartments and, for illustrative purposes, only a pair of tubes designated as A and B are shown. These tubes are symmetrically positioned with respect to the symmetry plane that passes transversely through the widest part of the cross section.

The tube sections labeled 1 are washed by identical flow fields and, therefore, have the same per-tube Sherwood number $Sh_1$. The tube sections 2 also see identical flow fields (different from that for the tube sections 1) and also have a common Sherwood number $Sh_2$ (in general, $Sh_2 \neq Sh_1$). For tube A, the Sherwood numbers in successive compartments are $Sh_1, Sh_2, Sh_1, \ldots$, while for tube B, the sequence is $Sh_2, Sh_1, Sh_2, \ldots$. Thus the foregoing assertion about alternate-compartment periodicity is affirmed.

To achieve true periodicity, it is appropriate to employ two consecutive compartments as the representative module of the heat exchanger rather than a single compartment. The per-tube, per-module Sherwood numbers are truly representative of the fully developed regime. For such a module, the Sherwood number for tube A is $\frac{1}{2}(Sh_1 + Sh_2)$, and this value repeats for all successive modules; this same value is also appropriate for tube B. Thus, the per-tube, per-module Sherwood numbers are symmetric with respect to the plane which passes transversely through the widest part of the cross section.

Per-tube, per-module Sherwood numbers, to be denoted by $Sh_{tube/mod}$, have been evaluated from the measured per-tube, per-compartment Sherwood numbers for all tube locations and all of the operating conditions of the experiments. The $Sh_{tube/mod}$ values have been normalized by $\overline{Sh}$, where

$$\overline{Sh} = \overline{Sh}_{comp} = \overline{Sh}_{mod} \tag{14}$$

The quantity $\overline{Sh}_{comp}$ is the Sherwood number averaged over all the tubes of a given compartment, while $\overline{Sh}_{mod}$ is the cor-

**Table 2 Values of $Sh_{tube/mod}/\overline{Sh}$ for Re = 2850**

(*a*) $K = 0.223$

| Row | Tube 1 | 2 | 3 | 4 | 5 | Row |
|---|---|---|---|---|---|---|
| 6 | 0.97 | 0.97 | 0.95 | 0.90 | 0.81 | 6 |
| 5 | 0.99 | 0.99 | 0.98 | 0.96 | 0.92 | 7 |
| 4 | 1.01 | 1.01 | 1.00 | 1.00 | 0.94 | 8 |
| 3 | 1.04 | 1.03 | 1.03 | 1.03 | 1.04 | 9 |
| 2 | 1.04 | 1.09 | 1.11 | 1.18 | | 10 |
| 1 | 0.91 | 0.91 | 0.96 | | | 11 |

(*b*) $K = 0.302$

| Row | Tube 1 | 2 | 3 | 4 | 5 | Row |
|---|---|---|---|---|---|---|
| 6 | 1.07 | 1.05 | 1.04 | 0.99 | 0.93 | 6 |
| 5 | 1.08 | 1.07 | 1.05 | 1.02 | 0.99 | 7 |
| 4 | 1.07 | 1.06 | 1.05 | 1.06 | 1.02 | 8 |
| 3 | 1.06 | 1.07 | 1.06 | 1.09 | 1.14 | 9 |
| 2 | 0.86 | 0.88 | 0.94 | 1.04 | | 10 |
| 1 | 0.72 | 0.73 | 0.80 | | | 11 |

(*c*) $K = 0.460$

| Row | Tube 1 | 2 | 3 | 4 | 5 | Row |
|---|---|---|---|---|---|---|
| 6 | 1.25 | 1.26 | 1.22 | 1.16 | 1.14 | 6 |
| 5 | 1.27 | 1.27 | 1.27 | 1.25 | 1.26 | 7 |
| 4 | 1.09 | 1.10 | 1.10 | 1.11 | 1.11 | 8 |
| 3 | 0.88 | 0.89 | 0.88 | 0.87 | 0.97 | 9 |
| 2 | 0.75 | 0.74 | 0.72 | 0.85 | | 10 |
| 1 | 0.71 | 0.65 | 0.67 | | | 11 |

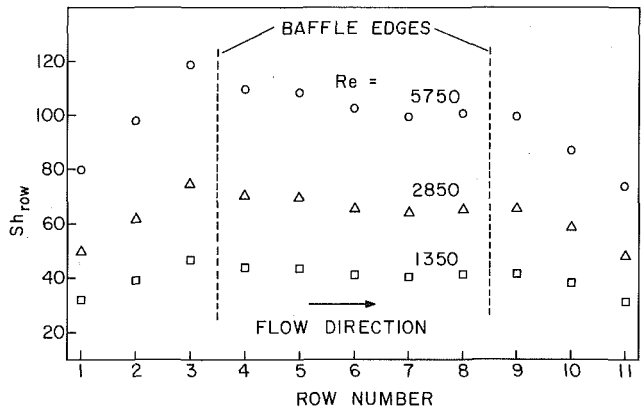


**Fig. 10 Row-average Sherwood numbers in a compartment ($K$ = 0.302)**

responding average for a module. It is readily seen that the two averages are equal in the fully developed regime.

The $Sh_{tube/mod}/\overline{Sh}$ ratios for the intermediate Reynolds number of 2850 are presented in Table 2 for each of the baffle cuts. Similar results for the other Reynolds numbers are available in [11] but, because of the ratio format, the results for the three Reynolds numbers do not differ appreciably.

The table is subdivided into parts (*a–c*) to accommodate the three baffle cuts. The horizontal line which runs through each part of the table indicates the location of the baffle edge.

Table 2 sets forth the variations among the per-tube, per-module Sherwood numbers. For the small baffle cut, the ratio of the maximum to the minimum Sherwood number is about 1.45, but aside from certain isolated tube locations, the variations are moderate. The max–min ratio for the intermediate baffle cut is 1.58. Of particular note are the low Sherwood numbers in the extremities of the windows and the relative uniformity in the crossflow zone. For the largest baffle cut, the max–min ratio is 1.95. Again, relatively low Sherwood numbers occur in the extremities of the windows.

Since $Sh_{tube/mod}$ is a true representation of the fully developed Sherwood number, Table 2 provides an indication of the potential nonuniformities in the thermal loading of the individual tubes. The net extent of the nonuniform loading will depend both on the shellside coefficients of Table 2 and the tubeside coefficients.

**Row-Average Sherwood Numbers.** The per-tube Sherwood numbers were also employed to evaluate row-average Sherwood numbers, and the resulting row-by-row distributions are illustrated in Fig. 10 for the intermediate baffle cut. These results pertain to a compartment. Corresponding results for a module can be deduced from Fig. 10 by averaging the $Sh_{row}$ values for rows 1 and 11, for rows 2 and 10, etc. The vertical dashed lines in the figure indicate the positions of the baffle edges.

The figure shows that the most marked variations in the per-row Sherwood number occur in the window zones, while only modest variations are encountered in the crossflow zone (i.e., between the baffle edges). The lowest Sherwood numbers occur at the extremities of the compartment, i.e., in the first and last rows. The highest value is that for the row just upstream of the first baffle edge.

Figures similar to Fig. 10 are available in [11] for the other baffle cuts. The distributions for the small baffle cut are more uniform than those of Fig. 10, while those for the large baffle cut display larger variations.

**Average Sherwood Numbers.** For conventional design practice, compartment-average Sherwood (Nusselt) numbers

are needed. As already indicated in equation (13), the compartment-average and the module-average Sherwood numbers are identical and are denoted by $\overline{Sh}$. The $\overline{Sh}$ values deduced by averaging the measured per-tube Sherwood numbers are plotted as a function of the Reynolds number in Fig. 3(*a*) for parametric values of the baffle cut.

As seen there, the results are very well described by a power law of the form $\overline{Sh} \sim Re^n$. A compact presentation of the $\overline{Sh}$ results which represent the data within an accuracy of 2 percent or better is

$$\overline{Sh} = 0.630[\exp(-1.29K)]Re^{0.63} \quad (15)$$

The 0.63 exponent reflects the strong influence of crossflow.

By making use of equation (12), equation (15) can be transformed to a Nusselt number relation

$$\overline{Nu} = 0.453[\exp(-1.29K)]Pr^{0.36}Re^{0.63} \quad (16)$$

This equation can serve as a standard against which to compare the per-compartment Nusselt numbers predicted by standard design methods.

## Concluding Remarks

The per-tube heat transfer coefficients and the per-compartment and intracompartment pressure drops reported here are, seemingly, the first open-literature information of this type for the shell side of shell and tube heat exchangers. The main focus of the work was to determine the response of these quantities to systematic variations of the baffle cut. Three model heat exchangers, each with a different baffle cut, were employed in the experiments. For each baffle cut, the Reynolds number was varied parametrically.

The experiments involved mass transfer measurements performed by means of the naphthalene sublimation technique. The Sherwood numbers (dimensionless mass transfer coefficients) determined from these measurements were converted to Nusselt numbers with the aid of the analogy between heat and mass transfer.

The basic measurements provided the distribution of the per-tube Sherwood number within a compartment in the fully developed regime. Among the tubes, large variations of the Sherwood number were encountered (on the order of a factor of two). The extent of the variations increased with increasing baffle cut. These tube to tube variations provide an indication of the potential nonuniformities in the thermal loading of the individual tubes.

It was demonstrated that to obtain per-tube transfer coefficients that recur periodically in the streamwise direction (in step with the periodic nature of the fluid flow), the representative module of the heat exchanger is a cluster of two consecutive compartments rather than a single compartment. Per-tube Sherwood numbers corresponding to such a module were evaluated. Compared with those for a single compartment, the intertube variations were slightly smaller for the former than for the latter.

The per-tube Sherwood numbers were also employed to evaluate row-average results. The lowest row-average Sherwood numbers occur at the extremities of the compartment, i.e., at the first and last rows, while the largest Sherwood number is that for the row just upstream of the baffle edge.

Compartment-average and module-average Sherwood numbers were also evaluated. When rephrased in terms of the Nusselt number, these results were tightly correlated as a function of the Reynolds number and the baffle cut by equation (16). The 0.63 exponent of the Reynolds number in the correlation reflects the strong influence of crossflow.

The pressure distribution measurements provided strong testimony about the rapid development of the fluid flow. Fully developed conditions were found to prevail downstream of the first compartment of the exchanger. The per-compartment pressure drop was shown to be a constant in the fully developed regime. In dimensionless form, the pressure drop was well correlated by equation (13). It was also found that the pressure drop is much greater in the upstream half of a compartment than in the downstream half.

## Acknowledgment

Scholarship support accorded to J. A. Perez by the IIE-CONACYT Program of Mexico is gratefully acknowledged.

## References

1 Schlünder, E. U. (Editor-in-Chief), *Heat Exchanger Design Handbook*, Vol. 3, Hemisphere Publishing Corporation, Washington, D.C., 1983.

2 Bell, K. J., "Final Report of the Cooperative Program on Shell and Tube Heat Exchangers," University of Delaware Engineering Experiment Station, Bulletin No. 5, Newark, Del., 1963.

3 Tinker, T., "Shell Side Characteristics of Shell and Tube Heat Exchangers," General Discussion of Heat Transfer, *Proceedings of the Institution of Mechanical Engineers*, London, 1951, pp. 89–116.

4 Tinker, T., "Tube Heat Exchangers, a Simplified Rating System for Commercial Heat Exchangers," ASME *Transactions*, Vol. 80, 1958, pp. 36–52.

5 Ambrose, T. W., and Knudsen, J. G., "Local Shell Side Heat Transfer Coefficients in Baffled Tubular Heat Exchangers," *AIChE Journal*, Vol. 4, 1958, pp. 332–337.

6 Gurushankariah, M. S., and Knudsen, J. G., "Local Shell Side Heat Transfer Coefficients in the Vicinity of Segmental Baffles in Tubular Heat Exchangers," *Chemical Engineering Progress Symposium Series*, Vol. 55, No. 29, 1959, pp. 29–36.

7 Stanchiewicz, J. W., and Short, B., "Local Shell Side Heat Transfer Coefficients in a Leak-Proof Heat Exchanger," *International Developments in Heat Transfer*, American Society of Mechanical Engineers, New York, 1961, pp. 959–966.

8 Gay, B., Mackley, N. V., and Jenkins, J. D., "Shell-Side Heat Transfer in Baffled Cylindrical Shell-and-Tube Heat Exchangers. An Electrochemical Mass-Transfer Technique," *International Journal of Heat and Mass Transfer*, Vol. 19, 1976, pp. 995–1002.

9 Macbeth, R. V., "Shell-and-Tube Heat Exchanger Data Produced by an Electrochemical Mass Modelling Technique," Paper HX7, *Proceedings Sixth International Heat Transfer Conference*, Vol. 4, 1978, pp. 225–230.

10 Macbeth, R. V., "Heat Exchanger Design and Practices," in *Heat Exchangers: Theory and Practice*, edited by J. Taborek, G. F. Hewitt and N. H. Afgan, Hemisphere, Washington, D.C., 1983, pp. 615–629.

11 Perez Galindo, J. A., "Internal Heat Transfer and Pressure Drop Measurements in a Variously Baffled Shell and Tube Heat Exchanger," Ph.D. thesis, Department of Mechanical Engineering, University of Minnesota, Minneapolis, Minn., 1984.

12 Zukauskas, A., "Heat Transfer from Tube Bundles in Cross Flow," *Advances in Heat Transfer*, Vol. 8, 1972, pp. 93–160.

**G. H. Junkhan**
Professor.
Mem. ASME

**A. E. Bergles**
Professor.
Fellow ASME

**V. Nirmalan**
Research Assistant.

**T. Ravigururajan**
Research Assistant.

Heat Transfer Laboratory,
Department of Mechanical Engineering,
Iowa State University,
Ames, Iowa 50011

# Investigation of Turbulators for Fire Tube Boilers

*This paper summarizes an experimental study of three popular "turbulator" inserts for fire tube boilers. An electrically heated flow facility was developed to deliver hot air to a water-cooled steel tube instrumented to derive sectional average heat transfer coefficients for four regions of the tube. Reference data for the empty tube are in excellent agreement with the accepted correlation. Two commercial turbulators, consisting of narrow, thin metal strips bent and twisted in zig-zag fashion to allow periodic contact with the tube wall, displayed 135 and 175 percent increases in heat transfer coefficient at a Reynolds number of 10,000. A third commercial turbulator, consisting of a twisted strip with width slightly less than tube diameter, provided a 65 percent increase in heat transfer coefficient. The friction factor increases accompanying these heat transfer coefficient increases were 1110, 1000, and 160 percent, respectively, for the same Reynolds number. These data should be useful in assessing overall performance gains to be expected when turbulators are used in actual boilers.*

## Introduction

**Background.** Fire tube boilers frequently provide steam for process applications and for heating of commercial or large residential buildings. In all of these applications, improved boiler efficiency and reduced energy consumption are continuing goals.

A popular modification is the introduction of "turbulators" into the boiler tubes to reduce fuel consumption and improve boiler efficiency. A typical turbulator configuration is a narrow, thin metal strip bent and twisted in zig-zag fashion to allow periodic contact with the tube wall. Other inserts are twisted strips of tube diameter width and wire coils similar to springs. Inserts increase the gas-side heat transfer coefficients, thereby increasing heat recovery from flue gases. Assuming that the equipment is properly operated and adjusted, higher boiler efficiency will result. Of course, boiler performance will reflect the increased flow friction of the turbulators.

To estimate the improvement in fire tube boiler performance due to turbulator inserts, a simulation study can be performed. Here input information includes the gas-side thermal-hydraulic performance of the proposed inserts. Few data on the heat transfer and fluid flow characteristics of turbulators inserts have been reported in the open literature.

This paper describes experiments conducted in the Iowa State University Heat Transfer Laboratory to determine the thermal-hydraulic performance of three commercial turbulators. The measurements were carried out for a smooth tube and for the same tube with the various inserts while cooling a hot gas at flow rates representative of actual boilers. The results can provide a basis for determining tube wall heat fluxes in boiler simulation programs and for boiler design.

**Turbulators Tested.** The somewhat complex geometries of the inserts tested are given in Figs. 1–3, where the nomenclature used is noted on each figure and a letter symbol is used to identify each insert. The manufacturers or distributors of the inserts are given in Appendix A. Numerical values of the various geometric dimensions are given in Table 1. In order to establish a uniform basis for comparison with the various references cited, this paper defines pitch as the length along the tube axis for one full twist (360 deg) of a twisted tape or one full cycle of a bent strip turbulator.

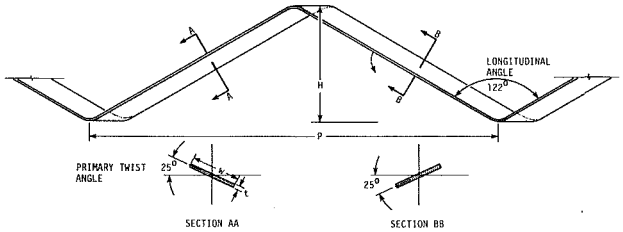


Fig. 1 Geometry of Type A turbulator (not to scale)

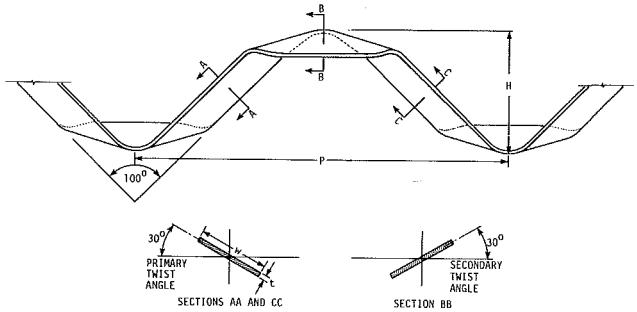


Fig. 2 Geometry of Type B turbulator (not to scale)

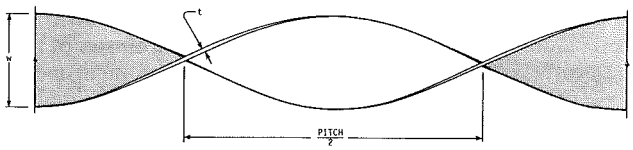


Fig. 3 Geometry of Type C turbulator (not to scale)

**Table 1 Insert characteristics for test tube of 0.0679 m inside diameter**

| Geometry | Insert Type A Fig. 1 | Insert Type B Fig. 2 | Insert Type C Fig. 3 |
|---|---|---|---|
| Overall length, m | 1.842 | 1.854 | 1.892 |
| Height, $H$, m | 0.067 | 0.065 | – |
| Pitch, $P$, m | 0.248 | 0.187 | 0.712 |
| Width, $w$, m | 0.022 | 0.019 | 0.066 |
| Thickness, t, m | 0.0019 | 0.0022 | 0.0014 |
| Longitudinal angle, deg | 122° | 100° | – |
| Primary twist angle, deg | ±25° | 30° | – |
| Secondary twist angle, deg | – | −30° | – |

Contributed by the Heat Transfer Division for publication in the JOURNAL OF HEAT TRANSFER. Manuscript received by the Heat Transfer Division May 18, 1983. Paper No. 83-HT-44.

## Literature Review

A literature search on the effects of turbulators of various types suitable for augmentation of gas heat transfer coefficients in fire tube boilers was conducted using the computerized "Bibliography on Augmentation of Convective Heat and Mass Transfer" [1].

Whitham [2] in 1896 inserted "loosely fitting" and gently twisted ($P$ = 3 m) "retarders" in the forty-four 0.102-m horizontal tubes of a 100-hp boiler. The saving of fuel with turbulators was as much as 8 percent, with the improvements being observed only when "the boiler plant is pushed and the draught is strong." These general conclusions were reinforced over 50 years later by Kirov [3], who fitted an Economic Boiler having seventy-six 0.070-m i.d. tubes with 0.064 m width twisted tapes of $P$ = 0.357 m or 0.710 m. With full-length tapes, the increase in boiler efficiency[1] was 5 to 7 percentage points,[2] equivalent to a fuel saving of 7 to 10 percent. The increase in fan power was negligible for the forced draft system under test; however, use of the turbulators in a natural draft system was not advised.

In a recent study conducted for DOE at Brookhaven National Laboratory, it was found that the addition of turbulators to residential oil-fired boilers resulted in fuel savings of 2–8 percent [4]. Details are not given in the report.

An early but comprehensive study of twisted-tape turbulators with cooling of air was reported by Royds [5]. Electrically heated air was allowed to flow through a tube of 0.059 m i.d. and 0.167 m length. A large number of tests were made with inlet air temperatures varying from 249°C to 605°C. Nine different twisted tapes, sooted to simulate actual boiler conditions, of 0.049 m width were tested with pitches varying from 0.23 m to 1.89 m. The results obtained show that pitches larger than about 0.51 m had very little influence on the heat transfer. Data are reported as curves of heat transfer coefficient as a function of mass velocity. The pressure drop data are also given as a function of mass velocity.

Colburn and King [6] also investigated enhancement effects of twisted tapes. Two full length, apparently snug fitting tapes were tested; however, data were tabulated for only one of these tapes. Data were taken for inlet air temperatures ranging from 109°C to 392°C and inlet tube wall temperatures from 9.3°C to 12.3°C. The results were presented both graphically and tabularly as $\bar{h}_a/c_{pa}$ and frictional pressure drop as functions of mass velocity through the test section.

Studies on twisted-tape enhancement were also conducted by Evans and Sarjant [7] using electrically heated air in an apparatus somewhat similar to that of Colburn and King. Tapes of 0.064 m width, with pitches of 0.177, 0.228, 0.304, and 0.355 m, were tested in a 2.438 m long by 0.076 m i.d. test section. Inlet air temperature was approximately 418°C, while inlet Reynolds numbers varied from about 3000 to 13,000. Results are presented as curves of convective heat transfer coefficient and pressure drop as functions of Reynolds number for different twisted tapes.

Evans and Sarjant attempted to separate the effects of radiation and convection in twisted tape enhancement. While noting that their analysis was not conclusive in this respect, they estimated the maximum contribution of radiation as 25 percent of the measured heat transfer coefficient when gas temperatures above about 605°C were encountered. The contribution of radiation drops rapidly as gas temperature is reduced.

More recent tests of the effects of twisted tapes on cooled air flows were reported by Thorsen and Landis [8]. Air was supplied at temperatures up to 277°C to a 0.0254-m i.d. water cooled tube. Pitches were 0.8, 0.131, and 0.203 m, and the tube-tape gap was about 0.076 mm. A major concern of this work was assessment of the effects of variable properties. A temperature-ratio correction factor was determined primarily from heating data due to the limited values of $(T_s/T_b)$ that could be attained in cooling. Best correlation of the cooling data was achieved by ignoring the temperature-ratio correction. No reference to data for bent strip turbulators similar to those of Figs. 1 and 2 were found.

[1] Boiler efficiency is defined as the heat transferred to the water divided by the heat available from the fuel consumed.

[2] Based on higher heat of combustion of the coal, as fired

## Nomenclature

$A_x$ = cross-sectional flow area of calorimeter section, $m^2$
$c_{pa}$ = specific heat at constant pressure of air, J/kg °C
$c_{pw}$ = specific heat at constant pressure of water, J/kg °C
$D$ = inside diameter of calorimeter pipe, m
$D_t$ = diameter of location of thermocouples in calorimeter pipe wall, m
$f$ = Fanning friction factor, defined in equation (3)
Gr = Grashof number
$\bar{h}_a$ = average heat transfer coefficient for air, $W/m^2$ °C
$H$ = height of turbulator strip, m
$k_s$ = thermal conductivity of calorimeter wall, W/m °C
$L$ = overall length of calorimeter (distance between pressure taps), m
$L_c$ = heat transfer length of a calorimeter section, m
$\dot{m}_a$ = mass flow rate of air, kg/s
$\dot{m}_w$ = mass flow rate of water, kg/s
$\mathrm{Nu}_D$ = Nusselt number based on inside pipe diameter
$\mathrm{Nu}_{D_H}$ = Nusselt number based on hydraulic diameter
$\Delta p$ = measured pressure drop over calorimeter length, Pa
$P$ = pitch of turbulator, m
Pr = Prandtl number
$q_a$ = energy given up by air, W
$q_c$ = energy loss by conduction in calorimeter, W
$q_w$ = energy gain by water, W
$\mathrm{Re}_D$ = Reynolds number based on inside pipe diameter
$\mathrm{Re}_{D_H}$ = Reynolds number based on hydraulic diameter
$t$ = thickness of turbulator strip, m
$T_{a1}$ = inlet air temperature to a calorimeter section (mixed mean), °C
$T_{a2}$ = outlet air temperature from a calorimeter section (mixed mean), °C
$T_b$ = mixed mean of bulk temperature of hot gas, °C
$T_s$ = wall (surface) temperature, °C
$\bar{T}_t$ = average wall temperature in a calorimeter section, °C
$T_{w1}$ = inlet water temperature to a calorimeter section, °C
$T_{w2}$ = outlet water temperature from a calorimeter section, °C
$u_m$ = mean velocity in pipe, m/s
$w$ = width of turbulator strip, m

### Greek Symbols

$\bar{\rho}_a$ = average density of air, $kg/m^3$
$\rho_{a2}$ = outlet density of air, $kg/m^3$
$\rho_{a_1}$ = inlet density of air, $kg/m^3$
$\phi$ = mathematical function

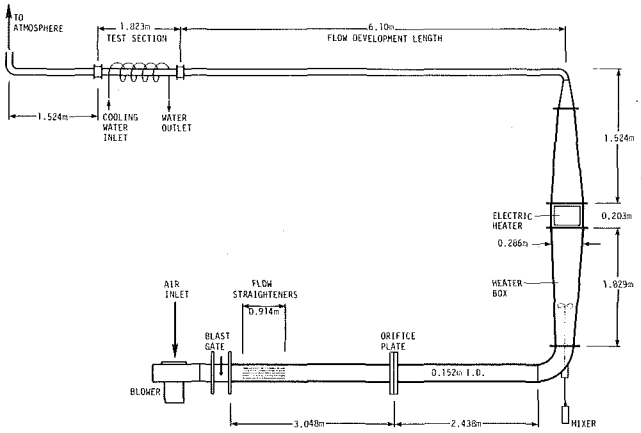


Fig. 4 Flow system (not to scale)

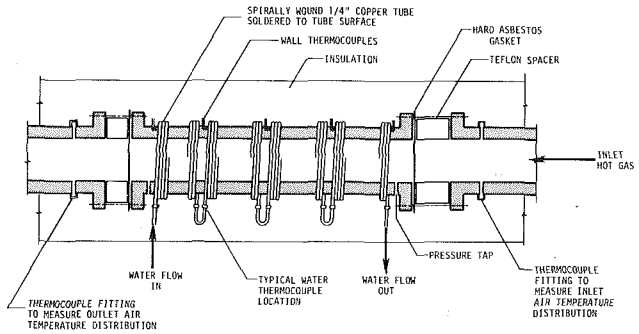


Fig. 5 Test section schematic (not to scale)

## Experimental Program

The test rig consists basically of a blower suitable to produce Reynolds numbers of order 10,000, a heater box to heat the air to about 170°C, and the actual test section where the performance of the turbulators is to be evaluated. The cooling water jacket of the test section simulates fire-tube boiler conditions while serving as a calorimeter.

**Flow System.** The U-shaped flow system to provide hot air to the test section is depicted in Fig. 4. Airflow is provided by a centrifugal blower that delivers 0.283 $m^3/s$ at a head of 0.152 m of water. After leaving the fan, the air passes through flow straighteners and a flow development length of 3.05 m before entering an orifice meter and through an elbow 2.44 m downstream from the orifice meter before entering the heater box.

The heater box was fabricated from sheet steel in three parts: an inlet rectangular diffuser section varying in cross section from 0.152 m × 0.152 m at the entrance to 0.533 m × 0.286 m over a length of 1.829 m. The flow is at low velocity as it enters the 0.203 m long section containing a Chromalox Process Air Duct Heater rated at 10 kW, 240 V, three phase. The box cross section is reduced from 0.533 m × 0.286 m back to 0.152 m × 0.152 m over length of 1.270 m downstream of the heater.

Three autotransformers connected in a 208 V delta circuit provide the electrical input to the heater. High-temperature insulating gasket material prevents direct contact between the heater and the duct. An over-temperature protector in the electrical circuit will cut off electrical power to the heater at a predetermined temperature. A motorized mixer minimizes thermal stratification within the heater section of the duct.

Following the heater box the hot air passes through a bend into a developing length of 6.10 m prior to the test section. After the test section, the air is exhausted into a 1.524-m-long pipe section for discharge outside the building. The heater box and piping leading into and out of the test section are insulated with calcium silicate blocks, suitable for temperatures of more than 918°C. These blocks are covered with an additional layer of glass fiber to reduce the heat loss to a minimum.

The test section was insulated with glass fiber since the outside temperature of the calorimeter is less than 20°C. Precautions were also taken to insulate the hypodermic tubing carrying thermocouple leads for measuring temperatures.

**Test Section.** The test section shown in Fig. 5 is based on a 0.0762 m o.d. carbon, drawn-on-mandrel steel boiler tube with i.d. of 0.0679 m to provide a snug fit with the turbulators tested. The tube is 1.823 m long and is flanged at the ends to facilitate installation and removal of inserts. Each end of the tube is fitted with three pressure taps spaced equally around the circumference. Tube wall temperatures are measured with chromel/alumel thermocouples fitted into axial slots milled part way through the tube wall. Five axial locations for these thermocouples were chosen to correspond with the water calorimeter cooling segments described below. Three thermocouples were installed at each axial location, spaced equally around the tube circumference. The thermocouples were made of welded junctions and were inserted into the slots through small tubes passing under the calorimeter cooling tubing.

The water calorimeter for cooling the gas and conducting energy balances is made of 6.35 mm i.d. copper tubing wound around the tube and soldered to the outside. The tube was installed in a lathe and the copper tubing was soldered to the steel tube as it was being tightly wound.

The calorimeter tubing was connected as four separate segments in series, with water temperature measured at the inlet and outlet of each segment. This feature, together with the wall thermocouples installed as described above, permitted the determination of four separate sectional-average gas side heat transfer coefficients.

**Instrumentation.** The basic measurements needed are the air and water mass flow rates and the various air and water bulk temperatures. Wall temperatures are also required for calculation of the heat transfer coefficients. Additionally, the pressure drop is required to calculate the friction factor.

The air flow, controlled by a blast gate at the blower outlet, passes through flow straighteners before entering the section upstream of an ASME orifice. The orifice pressure drop is monitored by a differential pressure transducer, which is connected via a Scanivalve to a piezometer ring attached to mulitiple pressure taps. The same system was used to measure static pressure. The mass flow rate was found using standard ASME procedures and equations [9]. Static pressure at the test section inlet and pressure drop across the test section were measured by the same technique.

Temperatures measured are the wall temperatures along the test section, inlet and outlet air temperatures, water temperatures at the inlet and outlet of each segment of calorimeter tubing, and the room temperature. Thermocouples are made of 0.33-mm-dia chromel/alumel wire, referenced to a 74°C reference junction. Both temperature and pressure signals were recorded digitally by the Heat Transfer Laboratory Data Acquisition System as described in [10], with the exception of the digital voltmeter, which was a more recent model. Finally, the water flow rate was measured directly using a container on a sensitive balance and stopwatch.

Some of the problems anticipated in the apparatus were air leaks, axial conduction of heat to the test section, and radiation errors in temperature measurements. The absence of air leaks was confirmed by comparing air flow measured by the orifice downstream of the blower with flow measured at

the exhaust (past the test section) taking a pitot tube velocity profile. The difference was less than 1 percent.

To minimize the axial conduction from the test section, Telfon spacers were placed at the inlet and outlet of the test section. Four thermocouples were inserted on either side to measure the temperature drop across the spacers so that the axial conduction from the duct upstream of the test section to the calorimeter water could be estimated. Calculations showed that radiation errors in the temperatures were very small and well within the experimental error margin.

## Procedure

*Testing and Data Acquisition.* After starting the blower and the water pump, the electrical heater was switched on. The flow rate was then adjusted for the run requirements, and when steady state was reached, the temperature drop from the heater box to the test section was less than 15.6°C. The water flow rate was set at about $1.262 \times 10^{-5}$ m$^3$/s, which represented a good compromise between an accurately measurable temperature rise of 8°C across each segment and a nearly isothermal tube wall.

Once steady state was reached, readings of various temperatures and pressures could be taken in about one minute with the data acquisition system.

*Data Reduction.* The computer scanned inlet air and outlet water temperatures for steady state. At steady state, all thermocouple and pressure transducer outputs were read and the overall heat balance for the calorimeter was checked:

$$q_w - q_c = q_a \tag{1}$$

where the conduction gain $q_c$ is for the entire calorimeter, not a portion of it. Agreement to within 5 percent was required to validate a run. (Most energy balances agreed to within 2–3 percent.)

Average heat transfer coefficients were determined for each calorimeter segment. For the first segment the energy added to the water is obtained from $q_w - q_c = \dot{m}_w c_{pw}(T_{w2} - T_{w1})$, where $q_c$ is the estimated heat gain by the water due to conduction from the upstream ducting. This conduction was estimated from the measured axial temperature difference across the teflon spacers, the properties of the teflon, and the geometry of the spacers. Assuming that $q_w - q_c = q_a = \dot{m}_a c_{pa}(T_{a1} - T_{a2})$ for the section, $T_{a2}$ can be calculated. The average wall temperature for a segment $\bar{T}_t$ is found by taking the average of the readings of the three circumferentially located thermocouples at each of the two measuring stations in each segment; that is, $\bar{T}_t$ is the linear average of six readings. The heat transfer coefficient $\bar{h}_a$ is then obtained from the usual expression

$$q_a = \left[\frac{1}{\bar{h}_a \pi D L_c} + \frac{1}{2\pi k_s L_c}\ln\left(\frac{D_t}{D}\right)\right]^{-1} \left[\frac{(\bar{T}_t - T_{a1}) - (\bar{T}_t - T_{a2})}{\ln\left(\frac{\bar{T}_t - T_{a1}}{\bar{T}_t - T_{a2}}\right)}\right] \tag{2}$$

The process is repeated using the outlet air temperature at one segment as the inlet temperature for the next segment. The second and third segments have no conduction correction applied; however, there is conduction heat gain by the coolant in the fourth segment because the uncooled outlet pipe wall is hotter than the calorimeter, requiring a conduction correction similar to that used for the first segment.

In calculating the Reynolds number, no allowance was made for the blockage of turbulators. The average Fanning friction factor is given by

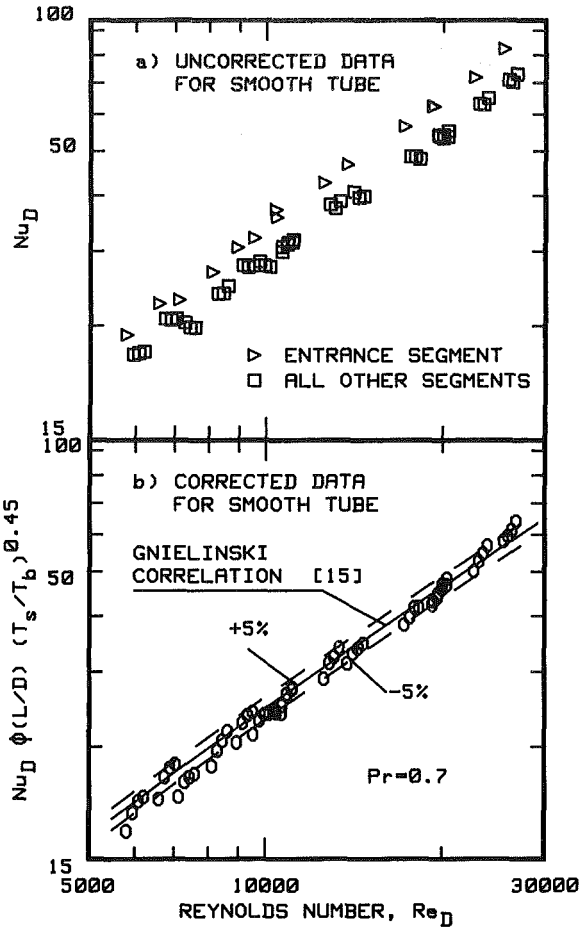


Fig. 6 Heat transfer data for smooth tube

$$f = \frac{\left[\Delta p - \left(\frac{\dot{m}_a}{A_x}\right)^2\left(\frac{1}{\rho_{a2}} - \frac{1}{\rho_{a1}}\right)\right]}{\frac{4L}{D}\frac{\bar{\rho}_a u_m^2}{2}} = \frac{\left[\Delta p - \left(\frac{\dot{m}_a}{A_x}\right)^2\left(\frac{1}{\rho_{a2}} - \frac{1}{\rho_{a1}}\right)\right] D\bar{\rho}_a A_x^2}{2\dot{m}_a^2 L} \tag{3}$$

where the measured pressure drop is corrected for the momentum change.

Uncertainties in Nusselt number, Prandtl number, Reynolds number, and friction factor were estimated from a typical run at Re = 12,500, according to the method of Kline and McClintock [11], using odds of 20 to 1. The following uncertainties are typical of the uncertainties that can be expected in other test runs: $Nu_D$: ±5 percent, $Re_D$: ±3 percent, Pr: ±3.5 percent, and $f$: ±5.3 percent.

Further details of the experiments and data reduction are given in [12].

## Results and Discussion

**Results.** The presentation of the measured data and the enhancement obtained by use of the inserts follow the format suggested in [13].

Before starting to evaluate the characteristics of the turbulators, the apparatus was tested for its plain tube performance at Reynolds numbers from 6000 to 25,000 with nominal inlet air temperature of 186°C.

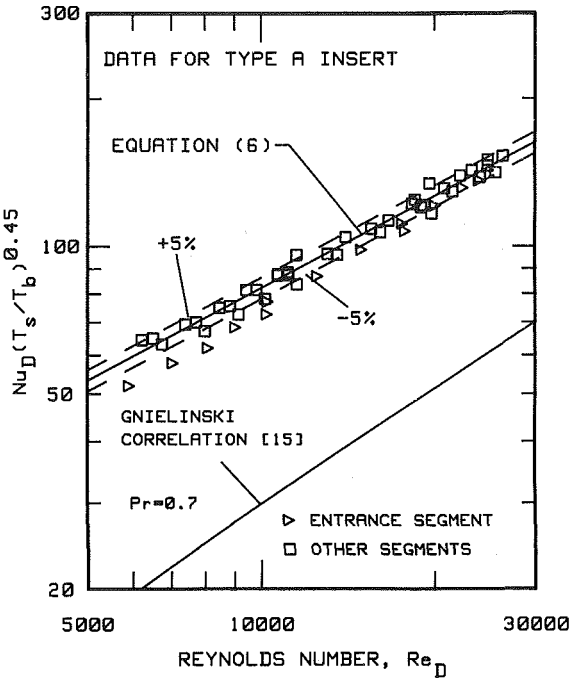


Fig. 7 Heat transfer data for Type A turbulator

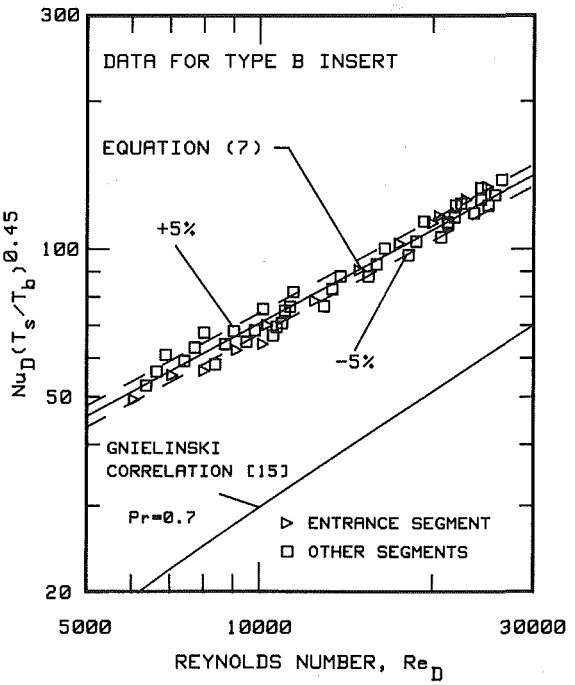


Fig. 8 Heat transfer data for Type B turbulator

The conditions just upstream of the test section approximate an essentially uniform temperature gas with a fully developed velocity profile. At the cooled test section, a temperature profile develops and the heat transfer coefficient in the first section should be that for a developing flow. Further downstream, the temperature profile should become fully developed. This behavior is shown in Fig. 6(*a*) where the Nusselt numbers for the first section all lie above those for the second, third, and fourth sections.

Equations and curves for Nusselt numbers as a function of Reynolds number and $L/D$ for the entrance condition in a smooth tube have been published [14]. Data corrected according to [14] are shown in Fig. 6(*b*) together with lines

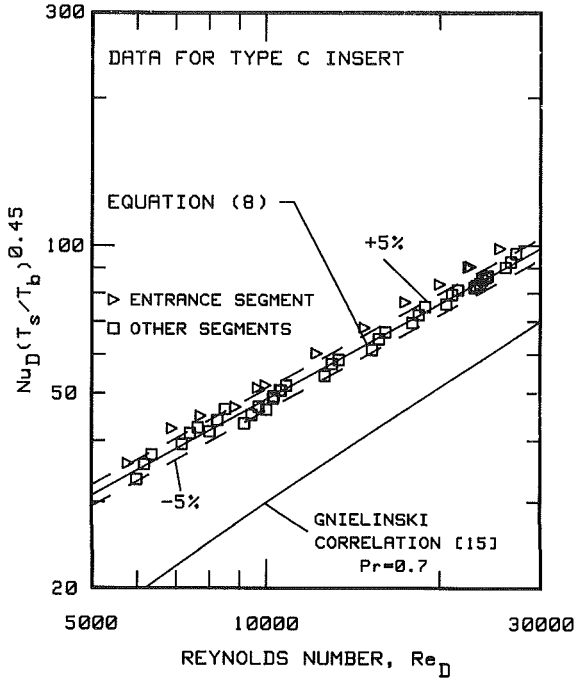


Fig. 9 Heat transfer data for Type C turbulator

representing the Gnielinski [15] correlation for cooling expressed as

$$\mathrm{Nu}_D\left(\frac{T_s}{T_b}\right)^{0.45} = \frac{(f/2)(\mathrm{Re}_D - 1000)\mathrm{Pr}}{1 + 12.7(f/2)^{1/2}(\mathrm{Pr}^{2/3} - 1)} \tag{4}$$

Equation (4) uses the Filonenko friction factor correlation

$$f = (1.58 \ln \mathrm{Re}_D - 3.28)^{-2} \tag{5}$$

as given by Webb [16]. The corrected data generally fall within the ±5 percent lines for Reynolds numbers above 10,000. Below that value, some points fall just below the −5 percent line.

The reduced heat transfer data for the turbulators were plotted over a range of Reynolds numbers and fitted with least squares curves for the data for the second, third, and fourth segments of the calorimeter, based on the evidence of an entrance condition shown by the smooth tube and Pr = 0.7. These equations are

$$\mathrm{Nu}_D\left(\frac{T_s}{T_b}\right)^{0.45} = 0.258\ \mathrm{Re}_D^{0.626} \quad \text{(Type A insert)} \tag{6}$$

$$\mathrm{Nu}_D\left(\frac{T_s}{T_b}\right)^{0.45} = 0.208\ \mathrm{Re}_D^{0.633} \quad \text{(Type B insert)} \tag{7}$$

$$\mathrm{Nu}_D\left(\frac{T_s}{T_b}\right)^{0.45} = 0.122\ \mathrm{Re}_D^{0.649} \quad \text{(Type C insert)} \tag{8}$$

The curves of equations 6, 7, and 8 together with all segmental data, are shown respectively in Figs. 7, 8, and 9 for each insert tested. Large increases over the Gnielinski relation occur for inserts A and B, with a lesser amount for insert C. The data indicate that the first segment contains some sort of entrance effect, especially evident for insert C. No corrections for this effect were made due to the unknown nature of the mixing involved.

Friction data are shown in Fig. 10, where large increases in friction factor over the Filonenko correlation are evident for the Type A and Type B turbulators, with a smaller increase for the Type C turbulator.

Experiments were performed for horizontal and vertical orientations of the Type A and Type B turbulators; all data

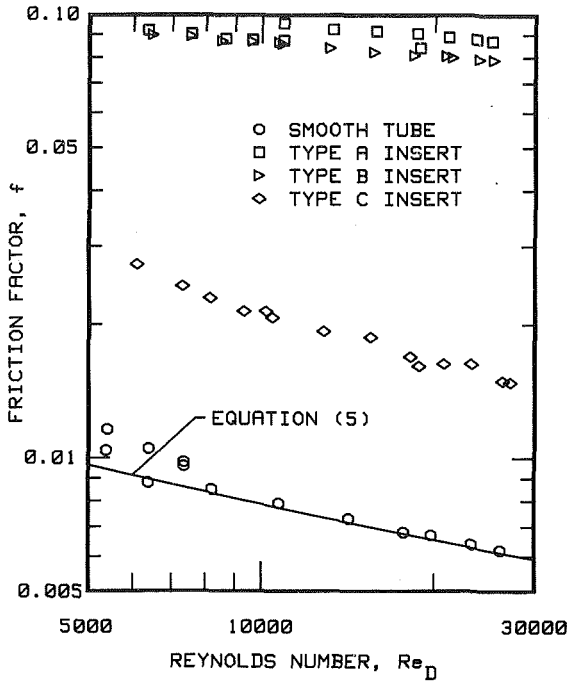


Fig. 10 Data for friction factor as defined in equation (3) for smooth tube and turbulator Types A, B, and C

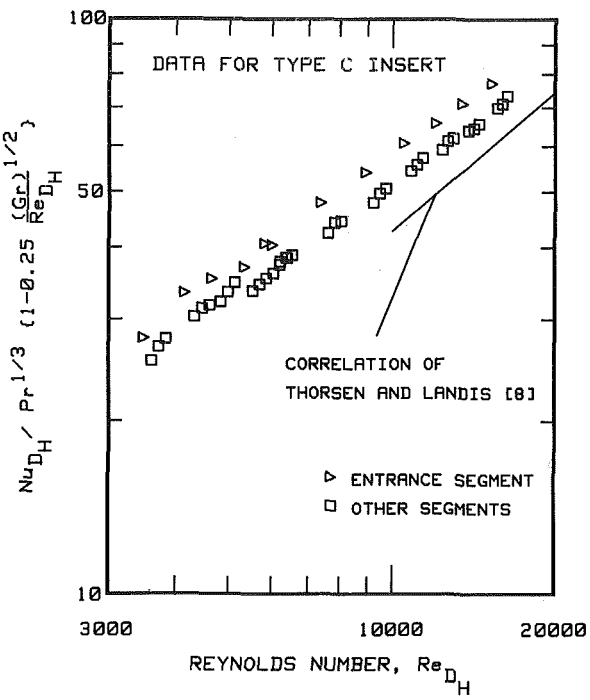


Fig. 12 Comparison of Type C turbulator data with the correlation of Thorsen and Landis [8]

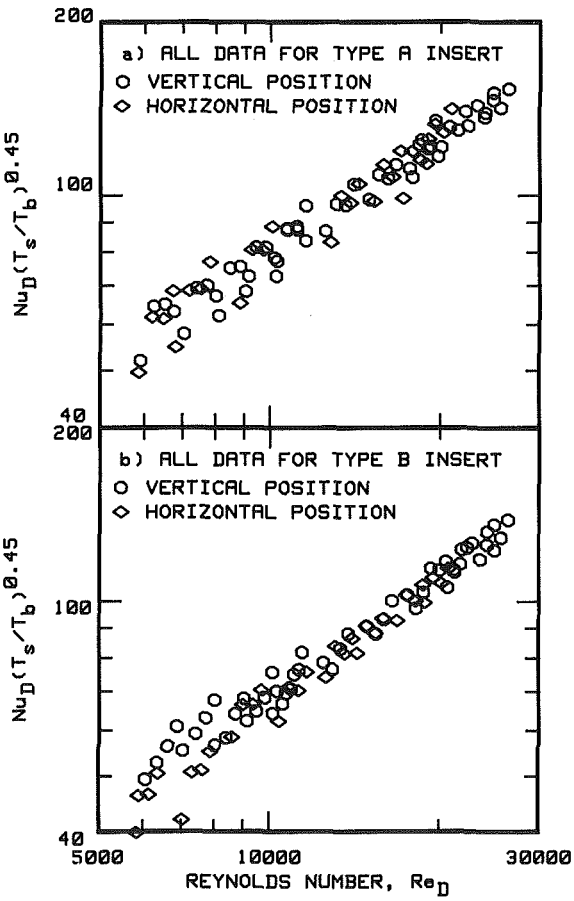


Fig. 11 Comparison of heat transfer data for vertical and horizontal orientation of turbulators

are compared for both turbulators in Fig. 11. Performance differences for the two orientations are small except for the Type B turbulator at low Reynolds numbers where a slight decrease is found for the horizontal orientation.

**Discussion.** The Type A turbulator produced about 175 percent increase in Nusselt parameter over a plain tube, the Type B turbulator an increase of about 135 percent, and the Type C turbulator an increase of about 65 percent.

A few visual observations were made by replacing the calorimeter tube with a plexiglass section and allowing a smoke filament tracer to enter the air flow just upstream of each of the turbulators tested. These visual tests qualitatively indicated that mixing was better with the Type A and B turbulators than with the Type C turbulator.

It is clear from Fig. 9 that the Type C turbulator has an entrance length effect. While the other turbulators also may have an entrance effect, it is different in nature. Types A and B, due to their similar geometry, should have mixing more similar to each other than to Type C.

Turbulator orientation does not materially affect performance. When the Type A and Type B turbulators were positioned horizontally, the Nusselt parameter agreed over the range of the Reynolds number tested within experimental error except for the Type B turbulator. Here the difference was between 15 and 8 percent up to a Reynolds number of 10,000 and negligible at higher Reynolds numbers. It may be that in the horizontal orientation, mixing is not complete at lower Reynolds numbers and the hotter air travels along the upper part of the tube in a partially stratified flow. However, no detailed data were taken to confirm this speculation.

The friction factor for the Type A turbulator is 11.8 times that of a plain tube at a Reynolds number of 10,000; the multiplier is 13.8 at a Reynolds number of 25,000. The Type B turbulator has a friction factor increase of 11.0 and 12.4 times that of the plain tube for the same Reynolds numbers, while the friction factor for the Type C turbulator has increases of 2.7 and 2.5 times, respectively, for these Reynolds numbers. The friction and heat transfer characteristics of the Type C turbulator are both comparable to data noted in the Literature Review.

When evaluating the relative merits of pressure loss cost for a particular heat transfer coefficient increase, it should be borne in mind that heat transfer can be enhanced considerably by merely increasing the air velocity with a concomitant in-

crease in pressure loss. This alternative to enhancement by use of turbulators was noted many years ago by Colburn and King [6]. Said differently, if a given increase in pressure loss is acceptable, it is possible to obtain the same augmentation by increasing the velocity (and the Reynolds number) to obtain a higher convective coefficient. However, this option is generally not available in a fire tube boiler where air/fuel ratios must be maintained. Comparisons should then be made at equal mass flow rates.

A "fine scale" variation of Nusselt number as a function of Reynolds number may be discerned for each subsection of the test section, even though the data fall within the confidence bounds given. Sufficiently detailed tests to investigate the second-order phenomenon have not been carried out. The temperature-dependent property correction $(T_s/T_b)^n$ did not significantly reduce the data scatter for any of the turbulators. This is in accordance with the experience of Thorsen and Landis [8] for twisted-tape turbulators and cooling of gases. However, the temperature-ratio correction was used to correlate the smooth tube data and is recommended by many investigators when turbulators are used for heating of gases.

Finally, a comparison of the data for the Type C turbulator was made with the correlation proposed by Thorsen and Landis [8], as shown in Fig. 12. The original equation, proposed for Reynolds numbers greater than 10,000, includes a temperature ratio correction so as to be compatible with heating data; however, Thorsen and Landis do not recommend this correction for cooling. The present data, with the exception of the inlet developing section, are within about 10 percent of the correlation.

## Concluding Remarks

The present results show that the commercial turbulator inserts tested provide considerable enhancement of gas-side convective coefficients for cooling. Design equations are presented for two bent strip turbulators, and an existing correlation for the twisted strip turbulator is confirmed in fire tube boilers. Although it may be possible to reduce fuel consumption through the use of turbulators, improvement in gas-side convection coefficients does not result in a one-to-one improvement in boiler efficiency. Rather, enhancement of gas side coefficients is only one factor among many items such as fuel/air ratio adjustment, tube cleanliness, and air/gas system flow resistance that lead to reduced fuel consumption and improved boiler efficiency. The calculation of boiler efficiency with turbulators should consider also changes in the water side flow distribution (and heat transfer coefficient) due to the large increase in gas-side heat transfer coefficient.

## Acknowledgments

This study was sponsored by the U.S. Army Facilities Engineering Support Agency (USAFESA) under contract DAAK70-81-C-0219.

## References

1 Bergles, A. E., Webb, R. L., Junkhan, G. H., and Jensen, M. K., "Bibliography on Augmentation of Convective Heat and Mass Transfer," Heat Transfer Laboratory Report HTL-19, ISU-ERI-Ames-79206, COO-4649-6, Iowa State University, Ames, Iowa, May 1979.

2 Whitham, J. M., "The Effect of Retarders in Fire Tubes of Steam Boilers," *Street Railway Journal*, Vol. 12, 1896, p. 374.

3 Kirov, N. Y., "Turbulence Promoters in Boiler Smoke Tubes," *Journal of the Institute of Fuel*, Vol. 22, 1949, pp. 192–196.

4 McDonald, R. J., Batey, J. E., Allen, T. W., and Hoppe, R. J., "Direct Efficiency Measurement and Analysis of Residential Oil-Fired Boiler Systems," Brookhaven National Laboratory, BNL 51171, Nov. 1979.

5 Royds, R., *Heat Transmission by Radiation, Conduction, and Convection* (1st ed.), Constable and Company, London, 1921, pp. 191–201.

6 Colburn, A. P., and King, W. J., "Heat Transfer and Pressure Drop in Empty, Baffled, and Packed Tubes, III Relationship Between Heat Transfer and Pressure Drop," *Industrial and Engineering Chemistry*, Vol. 23, 1931, pp. 919–923.

7 Evans, S. I., and Sarjant, R. J., "Heat Transfer and Turbulence in Gases Flowing Inside Tubes," *Journal of the Institute of Fuel*, Vol. 24, 1951, pp. 216–227.

8 Thorsen, R., and Landis, F., "Friction and Heat Transfer Characteristics in Turbulent Swirl Flow Subjected to Large Transverse Temperature Gradients," ASME JOURNAL OF HEAT TRANSFER, Vol. 90, 1968, pp. 87–97.

9 Bean, H. S. (ed.), "Fluid Meters, Their Theory and Application," Report on the ASME Research Committee on Fluid Meters (6th ed.), ASME, New York, 1971.

10 Junkhan, G. H., and Bergles, A. E., "Heat Transfer Laboratory Data Acquisition System," Heat Transfer Laboratory Report HTL-12, ISU-ERI-Ames-77178, Iowa State University, Ames, Iowa, Dec. 1976.

11 Kline, S. J., and McClintock, F. A., "Describing Uncertainties in Single-Sample Experiments," *Mechanical Engineering*, Vol. 75, pp. 3–8.

12 Junkhan, G. H., Bergles, A. E., Nirmalan, V., and Ravigururajan, T., "Tests of Turbulators for Fire-Tube Boilers," HTL-29, ISU-ERI-Ames-83130, FESA-82023, Iowa State University, Oct. 1982.

13 Marner, W. J., Bergles, A. E., and Chenoweth, J. M., "On the Presentation of Performance Data for Enhanced Tubes Used in Shell-and-Tube Heat Exchangers," ASME JOURNAL OF HEAT TRANSFER, Vol. 105, 1983, pp. 358–365.

14 Mills, A. F., "Experimental Investigation of Turbulent Heat Transfer in the Entrance Region of a Circular Conduit," *Journal of Mechanical Engineering Science*, Vol. 4, 1962, pp. 63–77.

15 Gnielinski, V., "New Equations for Heat and Mass Transfer in Turbulent Pipe and Channel Flow," *International Chemical Engineering*, Vol. 16, 1976, pp. 359–368.

16 Webb, R. L., "A Critical Evaluation of Analytical Solutions and Reynolds Analogy Equations for Turbulent Heat and Mass Transfer in Smooth Tubes," *Wärme- und Stoffübertragung*, Vol. 4, 1971, pp. 197–204.

## APPENDIX A

### Insert Manufacturers or Distributors

| Insert | Manufacturer/Distributor |
|---|---|
| A | Brock "Fuel Saver" Turbulators, Fuel Efficiency, Inc., 131 Stuart Avenue, P.O. Box 48, Newark, N. Y. 14513<br>(Manufacturer) |
| B | Smick Turbulator, American Fuel Economy, Inc., Rt. 1 Canal Rd. E., Ottawa, Ill. 61350<br>(Manufacturer. Direct sales to boiler manufacturers)<br>AEI Fire Tube Turbulator, Allied Energy International, 8601 Wilshire Blvd., Suite 1002, Beverly Hills, Calif. 90211<br>(Retrofit distributor) |
| C | Powermaster Turbulator, Powermaster Corp., P.O. Box 231, Middletown, Pa. 17057<br>(Manufacturer) |

# An Analytical Model to Predict Condensate Retention on Horizontal Integral-Fin Tubes

**T. M. Rudy**
Exxon Research and Engineering Company,
Florham Park, N.J. 07932
Member ASME

**R. L. Webb**
Professor.
Mechanical Engineering Department,
The Pennsylvania State University,
University Park, Pa. 16802
Fellow ASME

*In this paper, the authors develop a general analytical model to predict the amount of surface that is flooded during condensation on a horizontal, integral-fin tube. The model is based on capillary equations that predict the amount of liquid rise on a vertical u-shaped channel. The space between adjacent integral fins forms such a channel. The authors compare the model to test data taken during condensation on three integral-fin tubes (748-to-1378 fpm) and a range of fluid properties. The analytical model predicts the amount of liquid retention on a horizontal, integral-fin tube within ± 10 percent over most of the data. The analysis is performed for the case of negligible vapor shear.*

## Introduction

Since the first commercial development of integral-fin tubes in the late 1940s, designers have used such tubes for single-phase convection, boiling, and condensation heat transfer. An example of a 1024 fpm (26 fpi) integral-fin tube is shown in Fig. 1. This paper deals with shellside condensation in horizontal tube condensers when shear forces are not important.

In 1947, Beatty and Katz [1] developed a model to predict the condensation coefficient on horizontal, integral-fin tubes. Their model assumes that gravity is the dominant force that drains condensate from the condensing surface. Simply stated, the Beatty-Katz model is based on Nusselt's equations [2] for a vertical plate (for the sides of the fin), and a horizontal tube (represents the base tube area between adjacent fins). Equation (1) gives their final resulting equation, which has an empirically adjusted leading coefficient; it predicts their test data for six low surface tension fluids within ± 10 percent.

$$h_{BK} = 0.689F^{0.25}\left(\frac{A_r}{A_{ef}}\frac{1}{D_r^{0.25}} + 1.3\frac{\eta A_f}{A_{ef}}\frac{1}{L^{0.25}}\right) \quad (1)$$

where

$$F = \left(\frac{k^3\lambda\rho^2 g}{\mu\Delta T_{vs}}\right)$$

The empirically determined parameter (0.689) is only 5 percent less than the theoretical value (0.725) derived from the adapted Nusselt equations. The data span fin densities from 422 to 630 fpm.

In 1948, Katz, Hope, and Datsko [3] made static liquid retention measurements of the amount of liquid that is held between the fins on an integral-fin tube. They performed their tests on tubes with several different fin densities and fin heights (276 < fpm < 984 and 1.2 mm < fin height < 5.7 mm). They found that as much as 100 percent of the surface was flooded by retained liquid under their static condition (no condensation occurring on the test surface). However, Katz and Geist [4] rationalized that retention would not occur under dynamic conditions (condensation occurring on the test surface), since the Beatty-Katz model [1] predicted the results so well with the assumption that all of the surface was active (no condensate retention). They did no experiments to verify this assumption.

Karkhu and Borovkov [6], Rifert et al. [7], and Rudy and Webb [5] have proposed that surface tension forces drain the condensate from the fins of the integral-fin tube. Karkhu and Borovkov [6] develop a surface tension-drained model that accounts for condensate retention. However, their model assumes that the flooded zone is constant and independent of fin geometry and fluid properties.

Rifert et al. [7] propose a modification to the Karkhu and Borovkov [6] model to account for the change of liquid retention with tube geometry and surface tension. Their final results produce an equation similar to the form we develop in this paper, but the documentation of their results leaves unanswered questions concerning the basis of their model and the actual agreement between their predicted and test results.

Recent work by Honda et al. [8] is an independent development of an equation similar to that of Rifert et al. [7] and the model developed in this paper.

The purpose of this paper is to:

1) Present data on condensate retention

2) Develop an analytical model to predict the portion of the tube circumference that is covered by retained condensate.

## Experimental Program

This section describes our experimental program and the analysis of the test data that led to the development of our analytical model for condensate retention.

Figure 2 shows a drawing of the test apparatus. Condensation occurs inside a glass bell jar, that is flanged to a flat brass backplate. This provides a test cell that can be pressurized to 207 kPa. The test sections of integral-finned

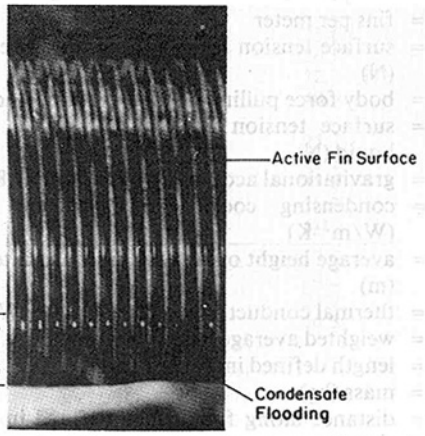


**Fig. 1 Photograph of R-11 condensation on a 1024 fpm, integral-fin tube; 26 percent of the circumference is flooded**

Contributed by the Heat Transfer Division for publication in the JOURNAL OF HEAT TRANSFER. *Manuscript received by the Heat Transfer Division February 3, 1983.*

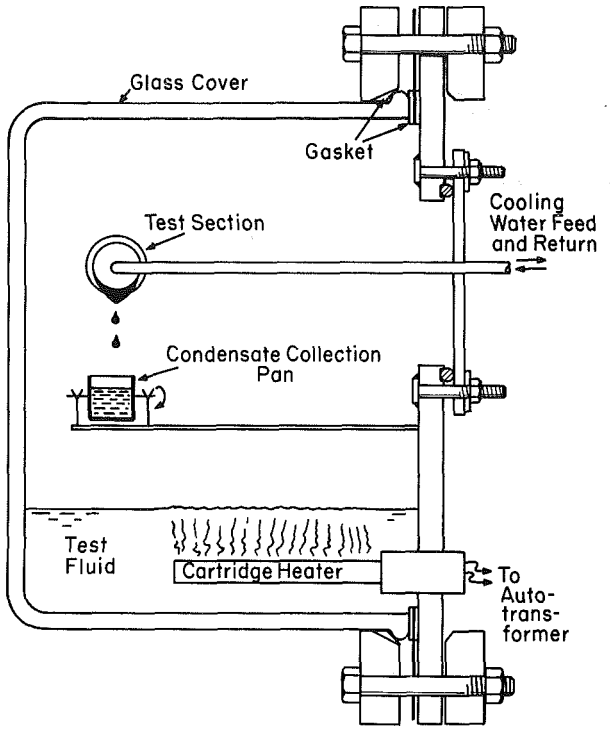


Fig. 2 Cross-sectional view of condensate retention test apparatus

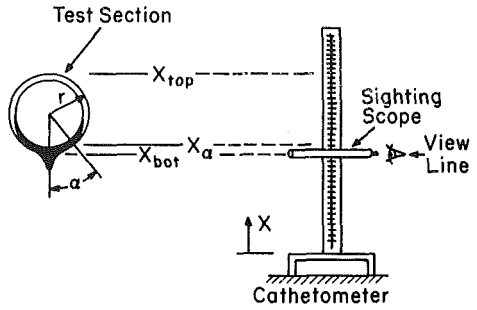


Fig. 3 Apparatus used to measure retention angles $\alpha_1$ and $\alpha_2$

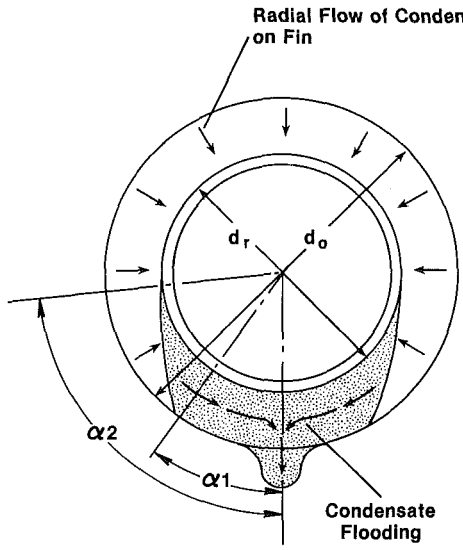


Fig. 4 Cross-section of integral-fin tube showing condensate drainage pattern and retention angles $\alpha_1$ and $\alpha_2$

tube are approximately 51 mm long. A solid plug insert fits inside each test tube. This plug produces an annular channel for high-velocity cooling water and results in uniform cooling of the surface. Insulated 3.2-mm copper tubing carries the cooling water through the backplate to and from the test tube. A pan, positioned under the test tube, collects the condensate to allow calculation of the liquid loading and heat flux. The

## Nomenclature

$a$ = acceleration (m/s$^2$)
$A_{ef}$ = effective surface area $A_{ef} = \eta_s A_o$ (m$^2$)
$A_f$ = fin surface area (m$^2$)
$A_o$ = total outside surface area of tube (m$^2$)
$A_p$ = fin cross-sectional area defined in Fig. 10 (m$^2$)
$A_r$ = tube surface area at base of fins (m$^2$)
$d_o$ = outside diameter of tube (m)
$D_r$ = tube diameter at base of fins (m)
$e$ = fin height (m)
fpi = fins per inch
fpm = fins per meter
$F_1$ = surface tension force pulling up on retained liquid (N)
$F_g$ = body force pulling down on retained liquid (N)
$F_2$ = surface tension force pulling down on retained liquid (N)
$g$ = gravitational acceleration constant (9.81 m/s$^2$)
$h_{BK}$ = condensing coefficient based on equation 1 (W/m$^2$-K)
$H_{avg}$ = average height of retained liquid in interfin channel (m)
$k$ = thermal conductivity of condensate (W/m-K)
$L$ = weighted average height of vertical fin (m)
$L_x$ = length defined in Table 2 (m)
$m$ = mass (kg)
$P$ = distance along fin surface defined in equation (8) (m)
$P_f$ = fin pitch $t_b + s_b$ (m)
$P_L$ = length along fin surface in general case (m)
Re = condensate Reynolds number defined in Table 2 (dimensionless)
$r_o$ = outside radius of integral-fin tube (m)
$s_b$ = space between adjacent fins (m)
$t$ = thickness of fin; $t_t$ at tip; $t_b$ at base (m)
$\Delta T_{vs}$ = temperature difference between condensing temperature and tube wall temperature (K)
$X_{bot}$ = defined in Fig. 3 (m)
$X_{top}$ = defined in Fig. 3 (m)
$X_\alpha$ = defined in Fig. 3 (m)
$\alpha_1$ = condensate retention half-angle of incipient fin exposure (deg)
$\alpha_2$ = maximum half-angle of condensate retention at base of fins (deg)
$\alpha_{avg}$ = average condensate retention angle $\frac{\alpha_1 + \alpha_2}{2}$ (deg)
$\lambda$ = latent heat of vaporization of condensate (J/kg)
$\mu$ = dynamic viscosity of condensate (kg/m-s)
$\eta$ = fin efficiency (dimensionless)
$\eta_s$ = surface efficiency (dimensionless)
$\theta$ = contact angle between liquid condensate and fin surface (deg)
$\phi$ = angle of sides of fin defined in Fig. 12 (deg)
$\rho$ = density of condensate (kg/m$^3$)
$\sigma$ = surface tension of condensate (N/m)

**Table 1 Tube geometries**

| Tube type | | Root diameter (mm) | Fin or spine fin density (fpm) | (fpi) | Height (mm) |
|---|---|---|---|---|---|
| Integral- | fin | 15.88 | 630 | 16 | 1.47 |
| 〃 | 〃 | 15.82 | 748 | 19 | 1.42 |
| 〃 | 〃 | 15.67 | 984 | 25 | 1.30 |
| 〃 | 〃 | 15.82 | 1024 | 26 | 1.42 |
| 〃 | 〃 | 22.46 | 1024 | 26 | 1.42 |
| 〃 | 〃 | 16.26 | 1063 | 27 | 1.32 |
| 〃 | 〃 | 17.09 | 1378 | 35 | 0.89 |
| 〃 | 〃 | 17.17 | 1614 | 41 | 0.91 |
| Spine-fin | | 17.09 | 1378[a] | 35[a] | 0.89 |
| Thermoexcel-C | | 17.0 | 1429 | 36 | 1.20 |

[a] Manufactured at Penn State by Modifying 1378 fpm tube.
Spine geometry: 0.305mm × 0.305mm × 0.89mm
Spine density: $1.627 \times 10^6$ spine/$m^2$

pan holds approximately 9.5 mL of liquid when full. Moving a magnet along the outside of the glass surface causes the cantilivered pan to be dumped and then reset. Several measurements of the time-to-fill give an average value of the rate of condensation. The boiling occurs on a cartridge heater in the lower portion of the test cell. An auto-transformer controls power to the cartridge heater. Copper-constantan thermocouples measure the cooling water inlet, outlet, and test liquid temperatures with direct temperature readout on an electronic datalogger. An absolute-reading mercury manometer measures the test cell pressure. Electrical resistance heating tape keeps the temperature of the manometer and its interconnecting tubing constant and above the vapor saturation temperature.

The liquid retention angles are measured by sighting through the cathetometer, as indicated in Fig. 3.

**Table 2 Summarized data for condensate retention tests**

| Condensing fluid | Geometry fpm(fpi) | Condensate loading (kg/s) | Re[b] | $\alpha_1$ (deg) | $\alpha_2$ (deg) | Saturation $\alpha_{avg}$ (deg) | Temp. (°C) |
|---|---|---|---|---|---|---|---|
| R-11 | 748(19) | 0.0 | 0 | 28.3 | 44.6 | 36.5 | 21.3 |
| | | $4.8 \times 10^{-4}$ | 86 | 25.0 | 42.6 | 33.8 32.4[a] | 20.6 |
| | | 7.7 | 144 | 22.4 | 40.5 | 31.5 | 25.1 |
| | | 10.5 | 211 | 23.4 | 40.1 | 31.8 | 32.8 |
| | 1024(26) | 0.0 | 0 | 37.7 | 71.7 | 54.7 | 19.4 |
| | | 4.8 | 86 | 30.8 | 61.5 | 46.2 46.4[a] | 20.3 |
| | | 9.1 | 170 | 33.7 | 60.0 | 46.9 | 24.5 |
| | | 13.4 | 256 | 31.2 | 60.9 | 46.1 | 28.3 |
| | 1378(35) | 0.0 | 0 | 37.7 | 71.7 | 54.7 | 19.4 |
| | | 4.9 | 86 | 40.0 | 72.4 | 56.2 55.7[a] | 19.1 |
| | | 7.9 | 148 | 39.0 | 72.3 | 55.6 | 24.7 |
| | | 12.9 | 244 | 39.2 | 71.0 | 55.1 | 28.8 |
| | 1378(35) spine | 0.0 | 0 | 22.3 | 38.8 | 30.5 | 17.2 |
| | | 5.2 | 97 | 21.3 | 41.2 | 31.3 33.4[a] | 23.7 |
| | | 6.9 | 130 | 23.6 | 42.2 | 32.9 | 27.4 |
| | | 6.8 | 130 | 23.9 | 43.9 | 33.9 | 28.2 |
| | | 6.7 | 129 | 23.3 | 42.0 | 32.7 | 28.4 |
| | | 8.1 | 151 | 23.8 | 43.9 | 33.9 | 23.4 |
| | | 9.5 | 191 | 23.2 | 46.1 | 34.7 | 34.1 |
| | | 13.0 | 246 | 22.6 | 46.1 | 34.4 | 28.2 |
| | 1417(36) Thermoexcel-C | 0.0 | 0 | 39.4 | 67.3 | 53.4 | 21.9 |
| | | 4.9 | 87 | 32.7 | 69.8 | 51.3 51.2[a] | 20.7 |
| | | 7.1 | 134 | 30.5 | 69.6 | 50.1 | 27.7 |
| R-11 | | 10.5 | 211 | 35.0 | 70.1 | 52.3 | 34.1 |
| n-pentane | 748(19) | 0.0 | 0 | 48.1 | 72.8 | 60.5 | 24.5 |
| | | 1.9 | 65 | 46.6 | 79.1 | 62.9 61.8[a] | 26.2 |
| | | 2.9 | 106 | 47.5 | 75.3 | 61.4 | 32.2 |
| | | 4.4 | 173 | 49.5 | 72.5 | 61.0 | 39.8 |
| | 1024(26) | 0.0 | 0 | 53.6 | 95.2 | 74.4 | 25.1 |
| | | 1.4 | 48 | 51.9 | 99.4 | 75.7 75.9[a] | 26.8 |
| | | 2.8 | 102 | 49.6 | 100.8 | 75.2 | 32.8 |
| | | 4.2 | 165 | 51.1 | 102.3 | 76.7 | 40.8 |
| | 1378(35) | 0.0 | 0 | 60.6 | 111.6 | 86.1 | 23.6 |
| | | 1.6 | 55 | 61.8 | 117.4 | 89.6 90.6[a] | 26.3 |
| | | 2.6 | 95 | 67.2 | 117.7 | 92.5 | 32.3 |
| | | 3.5 | 137 | 61.7 | 117.6 | 89.7 | 40.9 |
| | 1378(35) spine | 0.0 | 0 | 43.7 | 61.8 | 52.8 | 25.7 |
| | | 1.1 | 38 | 44.1 | 77.0 | 60.6 59.1[a] | 28.2 |
| | | 2.1 | 78 | 38.0 | 74.5 | 56.3 | 35.8 |
| | | 2.5 | 93 | 42.1 | 76.2 | 59.2 | 35.7 |
| n-pentane | | 3.3 | 129 | 44.1 | 76.7 | 60.4 | 41.1 |
| Water | 748(19) | 0.0 | 0 | 94.9 | 113.3 | 104.1 | 17.8 |
| | 1024(26) | 0.0 | 0 | 180 | 180 | 180 | 24.2 |
| | 1378(35) | 0.0 | 0 | 180 | 180 | 180 | 23.9 |
| Water | 1378(35) spine | 0.0 | 0 | 88.2 | 132.7 | 110.5 | 16.3 |

[a] Average value of the condensate retention angles ($\alpha_{avg}$) during condensation

[b] $\mathrm{Re} = \dfrac{4\dot{m}}{L_x \mu}$ where $L_x$ = length of test section (m)
$\dot{m}$ = condensate loading (kg/s)
$\mu$ = liquid viscosity (kg/m-s)

The test apparatus measures the horizontal projection of the liquid meniscus. Substitution of the measured fraction of tube radius that is flooded into equation (2) gives the retention angle.

$$\alpha = \cos^{-1}\left[\frac{\left(\frac{X_{top}-X_{bot}}{2}\right)-(X_{\alpha}-X_{bot})}{\left(\frac{X_{top}-X_{bot}}{2}\right)}\right]$$

$$= \cos^{-1}\begin{bmatrix}\text{fraction of tube}\\ \text{radius that is}\\ \text{flooded}\end{bmatrix} \quad (2)$$

We checked the accuracy of this method by drawing several known angles on a piece of paper the size of the test tube and then measuring these angles with the cathetometer. The results agreed within ±5 deg of the correct angle. To check the repeatability of the system, some of the first tests were repeated at the end of the test program and the results were within the accuracy of the apparatus. Figure 4 shows the two retention angles measured. Angle $\alpha_1$ is the angle at which the fins appear to be fully flooded, and $\alpha_2$ is the maximum angle that the retained liquid affects the surface. A transition region from full flooding to zero retention exists between $\alpha_1$ and $\alpha_2$.

Table 1 shows the pertinent geometry of both the tubes tested and other tubes for which data are reported. They include 748, 1024, 1378 fpm integral-finned tubes, the 1429 fpm "Thermoexcel-C" tube [9], and a 1378 fpm "spine-fin" tube. All of the test sections are made of copper.

We tested each tube in three different fluids (water, R-11, and n-pentane) under static (noncondensing) conditions, and only the last two fluids with condensation. The following list gives the test procedure used for each test tube after installing it in the test apparatus:

1 Clean the condensing surface in a solution of acidified thiourea, detergent, and corrosion inhibitors. Then throughly rinse it with water and dry it with a paper towel and heat lamp. Wash the surface with clean R-11.

2 Install the glass cover and evacuate the test shell to 2 mm of mercury.

3 Fill the system with commercial grade R-11 until about 15 mm of liquid covers the cartridge heater.

4 Set the power input to 200 W. After obtaining steady conditions, measure retention angles, condensate collection rate, temperature, and pressure.

5 Repeat step 4 at 300 W, 100 W, and then the static condition with the power off and condensate no longer dripping from the tube.

6 Drain the test fluid and dry out the system.

7 Repeat steps 2 to 6 with n-pentane.

8 Finally, brush water onto the tube surface until it is thoroughly wetted. Measure the static retention angles.

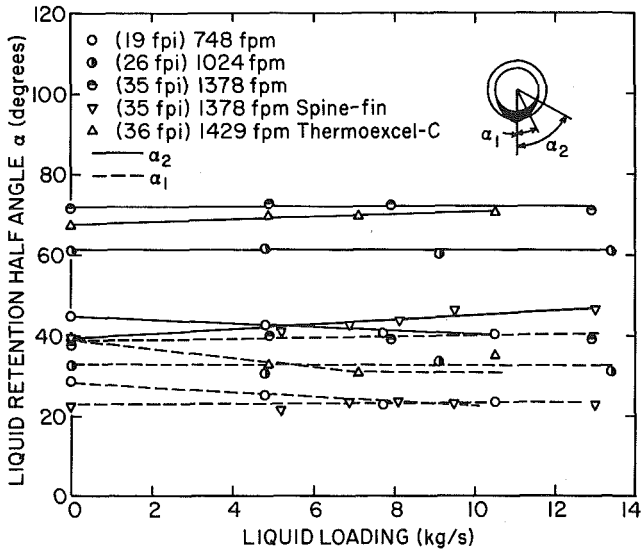


**Fig. 5 Measured condensate retention angles versus R-11 liquid loading**

## Experimental Results and Discussion

Table 2 and Figs. 5–7 show the test results. In Table 2, we consider $\alpha_1$ to be sightly subjective, because it is difficult to fix the point at which the retained liquid begins to expose the fin surface and recede in a continuous manner. We define $\alpha_1$ as the angle of incipient fin exposure. We were able to observe $\alpha_2$ much more distinctly than $\alpha_1$ on all of the tubes. Since between $\alpha_1$ and $\alpha_2$ the fin surface is not completely flooded, $\alpha_{avg} = (\alpha_1 + \alpha_2)/2$ gives an estimate of the amount of surface totally flooded if we assume a linear recession of the retained liquid. The $\alpha_{avg}$ is more properly related to the extent of fin surface flooded, while $\alpha_2$ represents the amount of base surface flooded.

Figure 5 shows the variation in $\alpha_1$ and $\alpha_2$ for R-11 at the static condition and at several dynamic conditions. Notably, the dynamic retention angle does not decrease or approach a negligible value as assumed in the Beatty–Katz model [1]. The 1378 fpm spine-fin tube results show that it has roughly the same condensate retention characteristics as the 748 fpm tube, but more than 35 percent less retention than the 1378 fpm integral-finned tube. The retention angle of the 1429 fpm

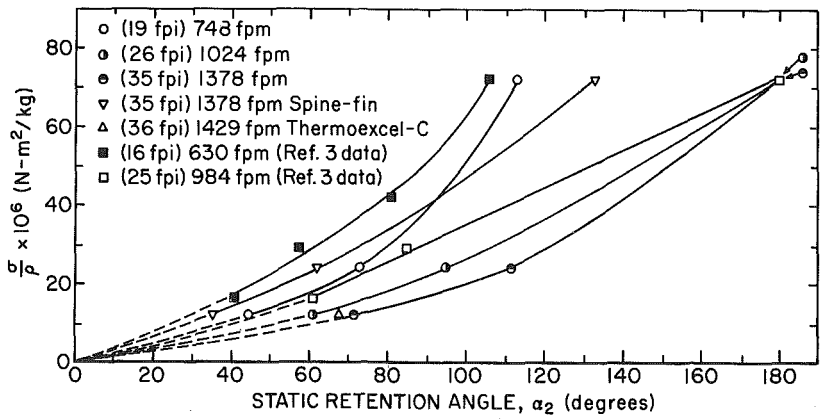


**Fig. 6 Surface tension-to-density ratio of condensate versus condensate retention angle $\alpha_2$**

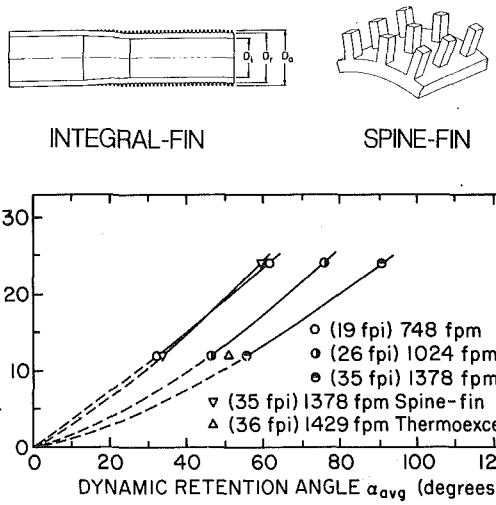


**Fig. 7 Surface tension-to-density ratio of condensate versus average condensate retention angle $\alpha_{avg}$**

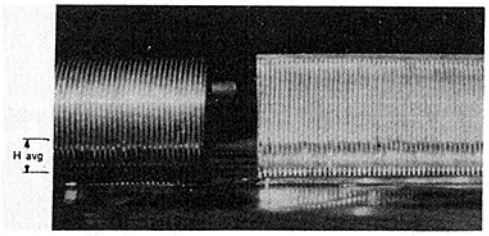


**Fig. 8 Photograph of condensate retention on 1024 fpm integral-fin tube side by side with 1024 fpm vertical fin plate (in liquid pool)**

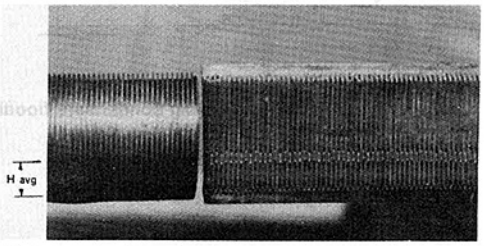


**Fig. 9 Photograph of condensate retention on 1024 fpm integral-fin tube side by side with 1024 fpm vertical fin plate (out of liquid pool)**

Thermoexcel-C (notched-fin) tube is approximately 50 percent higher than that of the 1378 fpm spine-fin tube. This may be due to the fact that the notch depth is only 40 percent of the fin height.

Figure 6 shows the variation of the static retention angle ($\alpha_2$) as a function of the $\sigma/\rho$ parameter for several different tube geometries. In all cases, the retention angle increases with increasing $\sigma/\rho$. For example, at the lowest value of $\sigma/\rho$ tested, the amount of surface flooding (based on $\alpha_2$) ranges from 20 percent for the 1378 fpm spine-fin tube, to 40 percent for the 1378 fpm integral-finned tube. At the $\sigma/\rho$ for water (high value of $\sigma/\rho$), the amount of surface flooding has significantly increased and ranges from 60 percent for the 748 fpm tube to 100 percent for the integral-fin tubes having 1024 fpm or greater. Also, the spine-fin tube has approximately 70 percent of its surface flooded with water.

Figure 6 also includes the data of Katz et al. [3] for 630 and 984 fpm tubes. The Katz et al. data [3] agree fairly well with our data. Their 630 fpm data have retention angles less than our 748 fpm tube, and their 984 fpm tube falls between our 748 and 1024 fpm tube data. The angles shown in Fig. 6 ($\alpha_2$) are our maximum retention angles.

Therefore, while the percentage of flooded area indicated is correct for the base surface, most of these values would be reduced 5 to 10 percent when based on $\alpha_{avg}$, e.g., $(\alpha_1 + \alpha_2)/2$. The overall results in this figure show that a significant portion of the surface is covered by retained condensate.

The amount of condensate retained under dynamic conditions is shown in Fig. 7. The value of the average retention angle ($\alpha_{avg}$) increases with the increase of both $\sigma/\rho$ and fpm. Notice that the flooding on the 1378 fpm spine-fin tube is approximately equal to that of the 748 fpm tube.

Under dynamic conditions, we observed a significant difference in the mode of condensate drainage from the bottom of the test sections. For example, the condensate drained as periodic droplets from the integral-fin tubes, with some continuous streaming occurring only at the highest liquid loading. For the 1378 fpm spine-fin tube, the condensate drained in continuous streams over the entire range of liquid loading. This continuous stream drainage is a very likely factor in reducing its liquid retention angle compared to the other high fpm tubes.

## Development of Condensate Retention Model

Figure 1 shows a 1024 fpm integral-fin tube on which R-11 is condensing at 35°C. Notice that the lower portion of the tube (angle $< \alpha_{avg} = 47$) is fully flooded by condensate as measured by procedures just described.

Based on the experiments, the authors found that the vertical rise height of the condensate ($H_{avg}$) is the same for the two finned test sections shown in Fig. 8. The only difference between these two finned sections is that one is in tubular form and the other is made by slitting a tube section and carefully unrolling the tube into a flat base surface. In Fig. 8, the two finned sections are each touching the surface of the liquid pool (R-11 at ambient conditions in this case). When the two test sections are removed from contact with the liquid pool, both continue to have equal rise height of retained liquid as shown in the photograph in Fig. 9. Also this rise height remains at approximately the same value shown in Fig. 8. The same type of test was performed with other fin spacings and test fluids. The resulting observations were the same. This equality between the flat-base finned section and the round tube suggests that the model to predict the rise height ($H_{avg}$) may be formulated for the less complex geometry of the flat-base test section. This is the approach taken in the following model development, which assumes negligible vapor shear.

Figure 10 shows an arbitrary fin cross-sectional shape and the appropriate surface tension and gravity forces. Bressler [10–12] proposed a similar set of forces acting on the liquid surface in a capillary-rise evaporation model. In the general case, the upward force on the retained liquid is equal to the surface tension ($\sigma$) acting over the length along the fin surface ($P_L$).

$$F_1 = \sigma P_L \tag{3}$$

The downward forces are the body force based on the volume of retained liquid.

$$F_g = \rho g \mathrm{Vol} = \rho g (P_f e - A_p) H_{avg} \tag{4}$$

and the surface tension force based on the surface tension ($\sigma$) acting over the repeating tube dimension (fin pitch $P_f$).

$$F_2 = \sigma P_f \tag{5}$$

Then a summation of the forces in the general case gives

$$\Sigma F = F_1 - F_g - F_2 = 0$$

$$\sigma P_L - \rho g (P_f e - A_P) H_{avg} - \sigma P_f = 0 \tag{6}$$

Solving equation (6) for $H_{avg}$ in the general case gives

$$H_{avg} = \frac{\sigma (P_L - P_f)}{\rho g (P_f e - A_P)} \tag{7}$$

Figure 11 shows photomicrographs (50 X enlargements) of

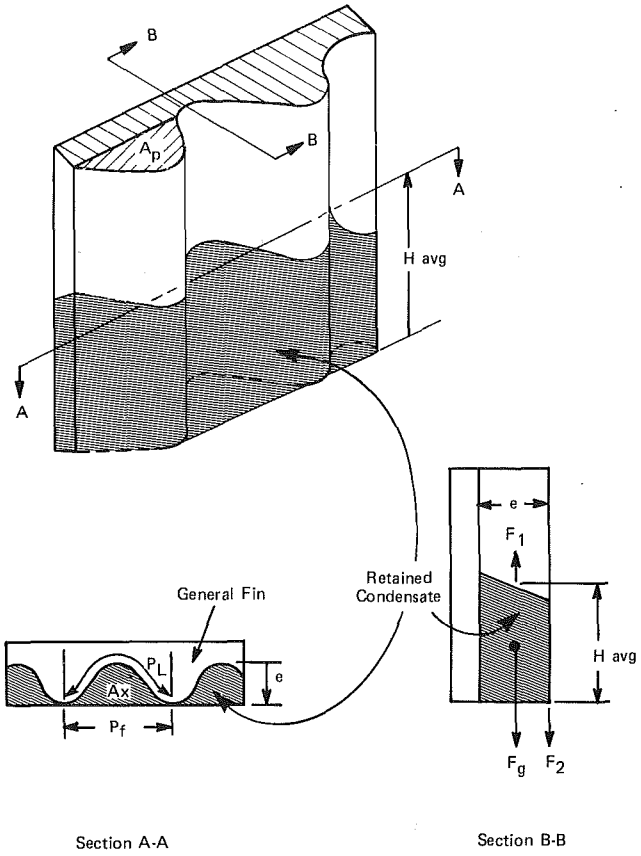


**Fig. 10 Fin geometry for development of generalized retention equation**

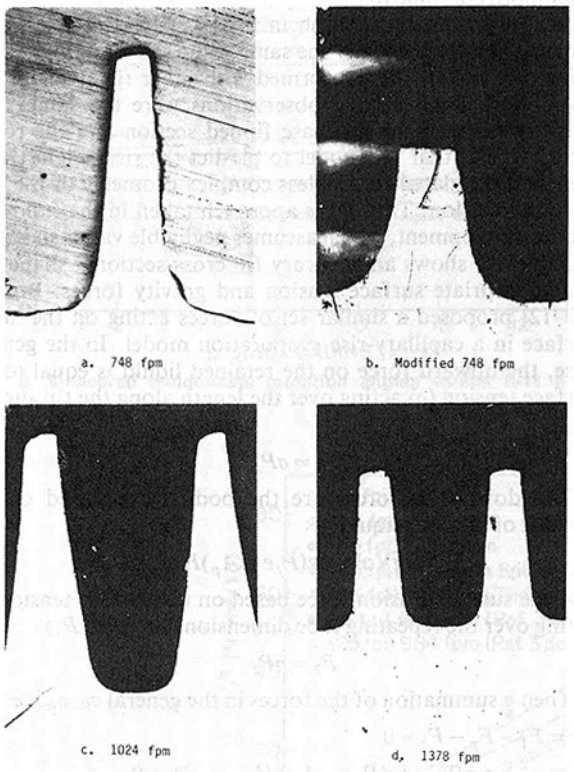


**Fig. 11 Photomicrographs of integral-fin geometries tested**

the integral-fin tubes used in our experimental work. Figure 12 is a cross-sectional drawing defining the specific integral-fin geometry used to make retention calculations in this work.

Substitution of equations (8), (9), and (10)

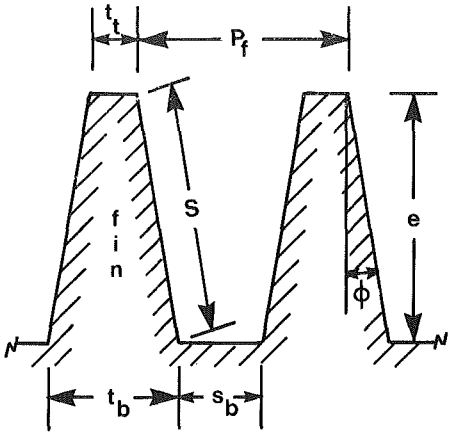


**Fig. 12 Fin geometry definitions for application of generalized condensate retention equation to specific case of trapezoidal-shaped integral fins**

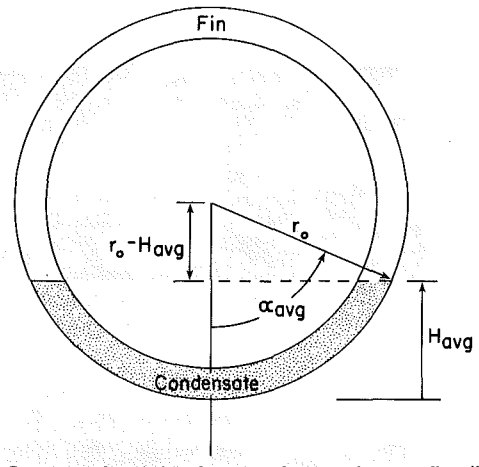


**Fig. 13 Cross-sectional drawing showing condensate flooding angle $\alpha_{avg}$ on integral-fin tube**

$$P = t_t + 2\frac{e}{\cos\phi} \tag{8}$$

$$P_L = P + s_b = t_t + 2\frac{e}{\cos\phi} + s_b \tag{9}$$

$$P_f = t_t + 2S\sin\phi + s_b = t_b + s_b \tag{10}$$

into the generalized equation (7) results in the following equation to predict $H_{avg}$ for trapezoidal-shaped integral-fin tubes.

$$H_{avg} = \frac{\sigma(P + s_b) - \sigma P_f}{\rho g(P_f e - A_P)} = \frac{\sigma(P - t_b)}{\rho g(P_f e - A_P)} \tag{11}$$

where

$$A_p = e(t_t + S\sin\phi) \tag{12}$$

Because of the observed equality in liquid rise for the flat base fin section and round tube fin section (Figs. 8 and 9), the geometry relationships shown in Fig. 13 can be used to develop the final form of the predictive model for retention on the integral-fin tube given in equation (13).

$$\alpha_{avg} = \cos^{-1}\left(1 - \frac{H_{avg}}{r_o}\right) \tag{13}$$

When the definition of $H_{avg}$ from equation (11) is substituted in equation (13), and the diameter ($d_o$) substituted for 2 $r_o$ the equation for the average retention angle is defined by equation (14).

$$\alpha_{avg} = \cos^{-1}\left(1 - \frac{2\sigma(P - t_b)}{d_o \rho g(P_f e - A_P)}\right) \tag{14}$$

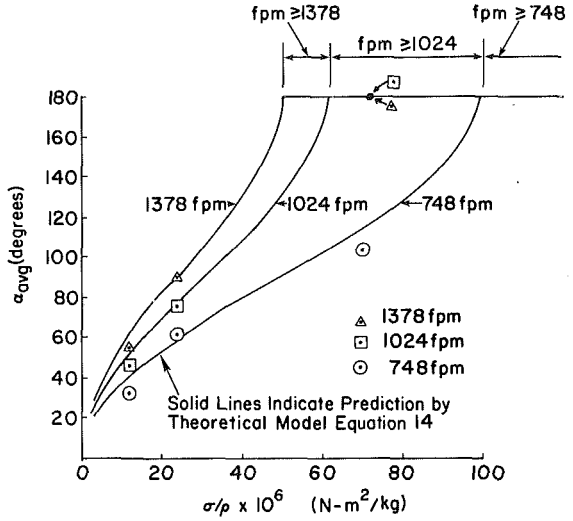


**Fig. 14 Predicted and measured average retention angle $\alpha_{avg}$ versus $\sigma/\rho$ for tubes tested**

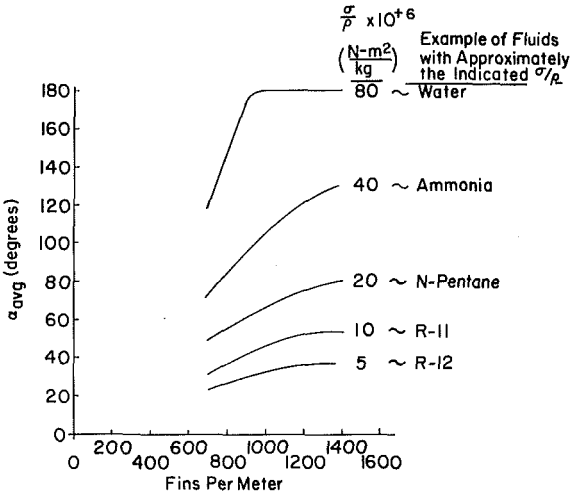


**Fig. 15 Predicted average retention angle $\alpha_{avg}$ versus fin spacing for several values of $\sigma/\rho$ at $d_o$ = 19 mm**

Substituting the following values for the case of a rectangular-integral-fin ($\phi = 0$)

$$P = t_t + 2e = t_b + 2e$$

$$P_f = t_t + s_b$$

$$A_P = et_t = et_b$$

gives

$$\alpha_{avg} = \cos^{-1}\left(1 - \frac{2\sigma(t_b + 2e - t_b)}{d_o \rho g(t_t e + s_b e - et_b)}\right)$$

with the resulting form of equation (14) for the case of a rectangular fin being

$$\alpha_{avg} = \cos^{-1}\left(1 - \frac{4\sigma}{d_o \rho g s_b}\right) \tag{15}$$

For a rectangular-shaped fin, equation (15) demonstrates the relationship between the retention angle ($\alpha_{avg}$) and the dimensionless parameter ($4\sigma/d_o\rho g s_b$). For a given fluid ($\sigma/\rho$), the flooding angle increases with increasing fin density (decreased $s_b$) at a constant tube diameter. However, the retention angle should be smaller on a larger diameter tube for the same fluid and fin density. This last statement evolves from the fact that equation (7) predicts the same liquid rise height ($H_{avg}$), independent of tube diameter, for constant fluid properties and fin density. However, equal liquid rise height ($H_{avg}$) and different tube diameters translates into different flooding angles ($\alpha_{avg}$). Static retention tests conducted on 19 mm and 25 mm 1024 fpm test pieces side by side in acetone showed equal $H_{avg}$. Therefore, as predicted by equation (15), the larger diameter tube will have a smaller flooding angle.

Another observation on equation (15) is that the flooding angle approaches full flooding ($\alpha_{avg}$ = 180 deg) as the property group ($\sigma/\rho g$) becomes equal to twice the geometry parameter group ($s_b d_o/4$). This last condition should be avoided and is investigated as described later in the Application to Design section of this paper.

## Predicted Versus Experimental Results

Figure 14 shows the test results compared to predictions made with our analytical model. The solid lines in this figure show the calculated results using the predictive model (equation (14)). These results show an increase in flooding angle ($\alpha_{avg}$) for increases in either the fin density (fpm) or the surface tension-to-density ratio ($\sigma/\rho$). The test data for the 748, 1024, and 1378 fpm fin densities are indicated by the symbols in Fig. 14. Over most of the test range ($10 \times 10^{-6} < \sigma/\rho < 80 \times 10^{-6}$ N-m²/kg and 748 < fpm < 1378) the predictive model and test results agree within ± 10 percent. The data deviation from the predictive line occurs partly because of the sensitivity of measuring angles at the minimum (little flooding) and maximum (nearly full flooding) retention angles. The maximum error (22 percent overprediction by the model) occurs for the minimum fin density and $\sigma/\rho$ values tested. At that test condition with 748 fpm and R-11, the retention angles are the smallest of all the geometry/fluid combinations tested. The error is smaller over the rest of the range. The generality of the model is emphasized by the fact that the actual fins tested had different fin heights and the fluid property parameter $\sigma/\rho$ was tested for several fluids. The fin height as indicated by both the model and test results is not an important parameter.

## Application to Design

Figure 15 shows the effect of changing fin density on the average retention angle for increasing values of surface tension-to-density ratio ($\sigma/\rho$). Many fluorocarbon refrigerants have $\sigma/\rho$ values less than $12 \times 10^{-6}$ N-m²/kg. Thus the retention angle is a small value for these fluids, and it is understandable why integral-fin tubes perform well in refrigeration applications. Water, however ($\sigma/\rho = 70 \times 10^{-6}$ N-m²/kg) is in the region where the retention angle has maximum values for the range of fin densities tested. There may be good reason to use integral-fin tubes, having low fin densities (large fin spacing) with fluids having high $\sigma/\rho$ if the surface tension effects on the draining condensate film significantly improve the condensing coefficient.

Figure 15 may also be used to define the permissible fin density for a specific $\alpha_{avg}$. For example, if one wishes to limit flooding to 25 percent of the tube surface, one can read the permissible fins per meter. These fpm are listed in Table 3 for 19-mm-dia tubes. As equation (11) indicates, the retention height ($H_{avg}$) is not a function of tube diameter. Therefore, a larger diameter tube should have less of its surface flooded than a smaller diameter tube with the same fin density. This conclusion was verified by static retention tests using a 19 mm and a 25 mm tube with the same 1024 fpm fin density. Both had the same $H_{avg}$.

The analysis just made provides the amount of heat transfer surface area that is relatively ineffective compared to the "active," unflooded condensing surface. The analytical

**Table 3 Permissible fin densities that limit flooding to 25 percent of surface for $d_o$ = 19 mm**

| $\sigma/\rho$ N-m$^2$/kg | Maximum fin density (fpm) | (fpi) |
|---|---|---|
| $6\times10^{-6}$ | 1575 | 40 |
| $12\times10^{-6}$ | 984 | 25 |
| $24\times10^{-6}$ | 630 | 16 |

model developed in this paper provides important information for the calculation of the condensation heat transfer as described by Webb et al. [15]. In [15], a model is developed that combines the beneficial contribution of surface tension forces in draining liquid from the active condensing surface with the deleterious effects of condensate retention on the flooded portion of the surface predicted by the model developed in this paper.

## Limitation of Results

Other parameters, not tested in this work, that may affect the validity of the retention model, are vapor shear and very high liquid loading. Depending on its direction and magnitude, vapor shear may either increase or decrease the actual retention angle. For example, when vapor shear and gravity are acting in the same direction, the actual retention angle should be less than the value predicted by the model.

Our tests were performed over a limited range of liquid loading ($0 < \mathrm{Re} < 260$) and showed little or no effect of liquid loading changes. A factor of 10 increase in the liquid loading caused less than 3 deg change in the average retention angle. However, if the liquid loading is increased by a factor of 100 or more, additional dynamic forces should be included in the model. Other than these limitations just described, the comparison of the predictive model and the test data shows excellent results.

## Conclusions

1 Condensate retention can significantly reduce the amount of active condensing area on an integral-fin tube.

2 The analytical model developed in this paper predicts the amount of flooding on an integral-fin tube and shows the key parameters affecting flooding. Equation (15) shows that, for a rectangular fin, $\alpha_{avg}$ increases as $(4\sigma/\rho g\, s_b d_o)$ increases. At $(4\sigma/\rho g\, s_b d_o) = 2$ the tube is fully flooded. Equation (15) also shows that the important geometry variables are $s_b$ and $d_o$. The flooding angle ($\alpha_{avg}$) increases as $s_b$ or $d_o$ decrease. Fin height is shown not to be a significant parameter.

3 The analytical model (equation (14)) predicts most of the test data for water, n-pentane, and R-11 on 19-mm-dia integral-fin tubes within ±10 percent.

4 A new predictive model is needed that accounts for the positive effects of surface tension induced drainage to be combined with the predictive model developed for condensate retention. Equation (14) for predicting the total amount of flooded surface is a fundamental "building block" for an analytical model to predict the condensing coefficient on integral-fin tubes. The paper by Webb et al. [15] develops this combined model.

## Acknowledgment

The majority of the work reported in this paper was performed by the authors under National Science Foundation Grant Number 79-73-Eng-78-16890.

## References

1 Beatty, K. O. Jr., and Katz, D. L., "Condensation of Vapors on Outside of Finned Tubes," *Chemical Engineering Progress*, Vol. 44, No. 1 Jan. 1948, pp. 55–70.

2 Holman, J. P., *Heat Transfer* (4th ed), McGraw-Hill, New York, 1976, p. 358.

3 Katz, D. L., Hope, R. C., and Datsko, S. C., "Liquid Retention on Integral-Finned Tubes," Department of Engineering Research, University of Michigan, Ann Arbor, Mich., Project M592, Wolverine Tube Div., Calumet and Hecla Consolidated Copper Co., written Aug. 1946, reproduced Apr. 1947.

4 Katz, D. L., and Geist, J. M., "Condensation of Six Finned Tubes in a Vertical Row," ASME *Transactions*, Nov. 1948, pp. 908–914.

5 Rudy, T. M., and Webb, R. L., "Condensate Retention on Horizontal, Integral-Fin Tubing," *Advances in Enhanced Heat Transfer-1981, HTD-Vol 18*, presented at 20th National Heat Transfer Conference, Milwaukee, Wis., Aug. 1981.

6 Karkhu, V. A., and Borovkov, V. P., "Film Condensation of Vapor at Finely-Finned Horizontal Tubes," *Heat Transfer—Soviet Research*, Vol. 3, No. 2, 1971, pp. 183–191.

7 Rifert, V. G., Barabash, P. A., Golubev, A. B., Leont'yev, G. G., and Chaplinskey, S. I., "Investigation of Film Condensation Enhanced by Surface Forces," *Heat Transfer—Soviet Research*, Vol. 9, No. 2, 1977, pp. 23–27.

8 Honda, H., Nozu, S., and Mitsumori, K., "Augmentation of Condensation on Horizontal Finned Tubes by Attaching a Porous Drainage Plate," presented at ASME-JSME Joint Thermal Engineering Conference, Honolulu, Hawaii, Mar. 20–24, 1983.

9 Nakayama, W., et al., "High-Flux Heat Transfer Surface Thermoexcel," *Hitachi Review*, Vol. 24, No. 8, 1975, pp. 329–334.

10 Bressler, R. G., "On the Contour of Liquid-Vapor Interfaces in Capillary Grooves," ASME *Journal of Basic Engineering*, Mar. 1971, pp. 87–89.

11 Bressler, R. G., and Wyatt, P. W., "Surface Wetting Through Capillary Grooves," presented at the Eleventh National Heat Transfer Conference AIChE/ASME, Minneapolis, Minn., Aug. 3–6, 1969.

12 Bressler, R. G., "Forced-Convection Mass Transfer From Wetted Grooves," ASME Paper No. 72-FE-32, 1972.

13 Rudy, T. M., "A Theoretical and Experimental Study of Condensation on Single, Integral-Fin Tubes," Ph.D. thesis, Mechanical Engineering Department, The Pennsylvania State University, University Park, Pa., May, 1982.

14 Rudy, T. M., and Webb, R. L., "An Analytical Model to Predict Condensate Retention on Horizontal, Integral-Fin Tubes," presented at ASME-JSME Joint Thermal Engineering Conference, Honolulu, Hawaii, Mar. 20–24, 1983.

15 Webb, R. L., Rudy, T. M., and Kedzierski, M. A., "Film Condensation on Finned Plates and Horizontal Finned Tubes," ASME JOURNAL OF HEAT TRANSFER, Vol. 107, 1985.

**R. L. Webb**
Department of Mechanical Engineering,
Pennsylvania State University,
University Park, Pa. 16802

**T. M. Rudy**
Exxon Research and Engineering Company,
Florham Park, N.J. 07932

**M. A. Kedzierski**
Department of Mechanical Engineering,
Pennsylvania State University,
University Park, Pa. 16802

# Prediction of the Condensation Coefficient on Horizontal Integral-Fin Tubes

*A theoretical model is developed for prediction of the condensation coefficient on horizontal integral-fin tubes for both high and low surface tension fluids. The model includes the effects of surface tension on film drainage and on condensate retention between the fins. First, the fraction of the tube circumference that is flooded with condensate is calculated. Typically, the condensation coefficient in the flooded region is negligible compared to that of the unflooded region. Then the condensation coefficient on the unflooded portion is calculated, assuming that surface tension force drains the condensate from the fins. The model is used to predict the R-11 condensation coefficient on horizontal, integral-fin tubes having 748, 1024, and 1378 fpm. The predicted values are within* ±20 percent of the experimental values.

## Introduction

Figure 1 illustrates an integral-fin tube, typical of that commercially used for condensation of low surface tension fluids. Such tubes are not used for high surface tension fluids because of the belief that excessive condensate bridging will render them ineffective. However, a theoretical understanding does not exist to predict when condensate bridging will occur, nor its effect on the condensation coefficient. In 1947, Beatty and Katz [1] developed a theoretical equation to predict the condensation coefficient on integral-fin tubes. Their equation has been commonly used for prediction of the condensation coefficient with low surface tension fluids. A disturbing feature of the Beatty and Katz theory is that it assumes no condensate bridging between the fins, and does not contain surface tension as a variable.

The authors have performed an experimental and theoretical study of condensation on integral-fin surfaces in an attempt to understand the effect of surface tension on the condensation performance of integral-fin tubes. The key elements of this work were divided into two areas:

1 The effect of surface tension and geometry on condensate retention between the fins.

2 The development of an analytical model to predict the condensation coefficient accounting for the effects of surface tension on film drainage and condensate retention.

The work relating to item 1 of the investigation is reported in [2]; this reference provides an analytical model to predict the fraction of the tube circumference that is condensate flooded, as a function of the fin geometry and fluid properties. A very small condensation heat flux will occur in this flooded zone.

The present study incorporates the analytical model of [2] in the development of a theoretical model for prediction of the condensation coefficient on integral-fin tubes. The model is applicable to both high and low surface tension fluids, but does not account for vapor shear and inundation effects.

## The Beatty and Katz Model

The condensation coefficient on a horizontal integral-fin tube may be written as the area-weighted average condensation coefficient on the finned surface ($h_f$) and on the tube surface between the fins ($h_h$). Equation (1) defines this relation in algebraic form. It is necessary to establish predictive equations for $h_h$ and $h_f$.

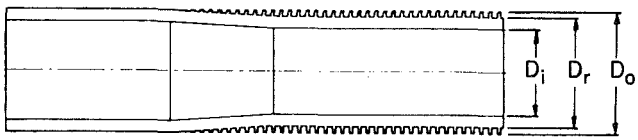


Fig. 1 Typical integral-fin tube

$$h\eta = h_h \frac{A_r}{A} + h_f \eta_f \frac{A_f}{A} \tag{1}$$

The Beatty and Katz model [1] to predict $h_h$ and $h_f$ assumes:

1 Gravity forces drain the condensate from the vertical fins, and from the base tube between the fins

2 No condensate is retained between the fins because of surface tension forces

They used the Nusselt equations [3] for laminar film condensation on horizontal tubes (equation (2)) and vertical plates (equation (3)) to predict $h_h$ and $h_f$, respectively.

$$h_h = 0.725\left(\frac{k^3\rho^2 g\lambda}{\mu\,\Delta T_{vs} D}\right)^{\frac{1}{4}} \tag{2}$$

$$h_v = 0.943\left(\frac{k^3\rho^2 g\lambda}{\mu\,\Delta T_{vs} L}\right)^{\frac{1}{4}} \tag{3}$$

Substitution of equations (2) and (3) in equation (1) gives

$$h\eta = 0.725\left(\frac{k^3\rho^2 g\lambda}{\mu\,\Delta T_{vs}}\right)^{\frac{1}{4}}\left[\frac{A_r}{A} D_r^{-\frac{1}{4}} + 1.3\frac{\eta_f A_f}{A} L_f^{-\frac{1}{4}}\right]. \tag{4}$$

Beatty and Katz assumed that the characteristic length ($L_f$) of the vertical fin may be calculated by equation (5); this is the average vertical fin height over the diameter $D_o$ (diameter over the fins)

$$L_f = \pi(D_o^2 - D_r^2)/4D_o. \tag{5}$$

Their test data for six low surface tension fluids condensing on several finned tube geometries (433 to 630 fpm) was predicted within ±10 percent by equation (4), when the coefficient was decreased 5 percent (from 0.725 to 0.689).

Recent work by the authors [4] have shown that the two key assumptions of the Beatty and Katz model are incorrect. Thus surface tension, rather than gravity force, controls condensate drainage from the fin surface. And condensate bridging of the interfin region may exist around a significant fraction of the

Contributed by the Heat Transfer Division for publication in the JOURNAL OF HEAT TRANSFER. Manuscript received by the Heat Transfer Division November 22, 1983.

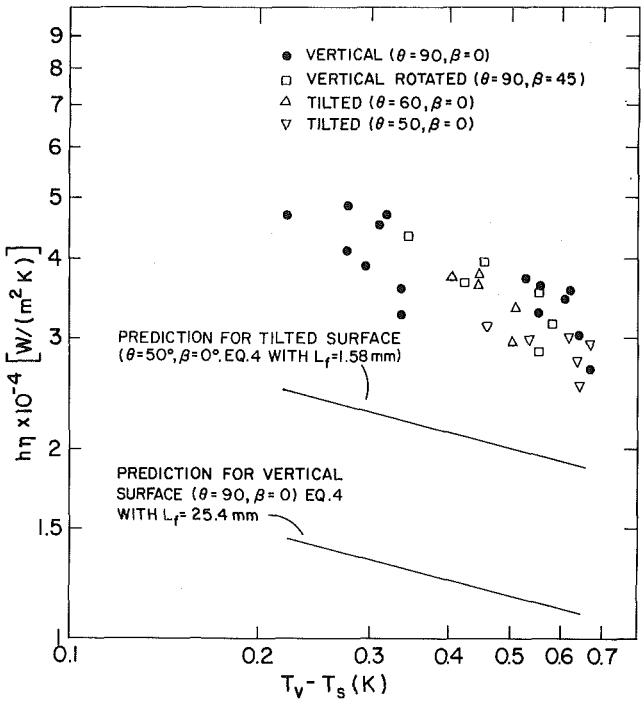


**Fig. 2 Finned plate test results with R-12 condensing at 27°C**

tube circumference. The success of equation (4) in predicting the condensation coefficient for low surface tension fluids is apparently because of compensating errors; the model underpredicts the condensation coefficient on the fins, and neglect of the flooded zone results in overprediction of the "active" surface area. The Beatty and Katz model will yield increasing error (overprediction) as the fin density and/or surface tension is increased.

The authors' experiments provide the basis for a new theoretical understanding of condensation on horizontal integral-fin tubes. The resulting model provides a basis for proposing fin shapes that will yield higher performance than those presently used, and for defining finned-tube geometries that may be used with high surface tension fluids.

**Table 1 Summary of tests conducted**

| Angle (deg) θ | β | $L_f$ (mm) |
|---|---|---|
| 90 | 0 | 25.4 |
| 90 | 45 | 25.4 |
| 50, 60 | 0 | 1.58, 1.60 |

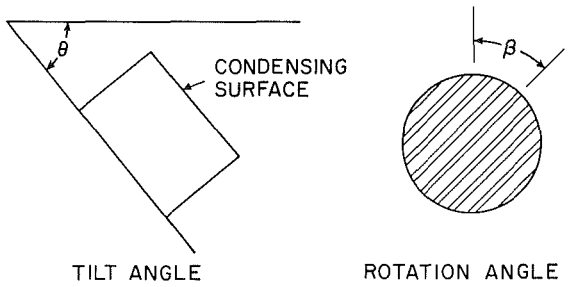


## Experiments on Finned Plates

Webb et al. [5] condensed R-12 on the face of a 51-mm-dia cylinder having fins on one face. The fins were 1 mm high, 0.30 mm thick with 0.84 mm pitch. This finned surface was tested in the three geometric orientations described in Table 1. Figure 2 shows the test results, and the predicted condensation coefficient using equation (4). The different tilt and rotation angles change the characteristic length ($L_f$). The characteristic length associated with the fins is listed in Table 1. Figure 2 shows:

1 The experimental condensation coefficient is essentially independent of geometric orientation.

2 The data are 70 percent underpredicted by equation (4), as applied to a finned plate.

These test results suggest that condensate drainage from the fin surface is not gravity controlled. Thus the first assumption of the Beatty and Katz model appears to be invalid.

## Experiments on Condensate Retention

Rudy and Webb [2, 4] measured the circumferential angle of condensate flooding for several integral-fin tube geometries (748 to 1378 fpm) using R-11, n-pentane and

## Nomenclature

$A$ = heat transfer surface area, $\pi D_o L$ ($m^2$)
$A_f$ = fin surface area ($m^2$)
$A_o$ = outside surface area of tube ($m^2$)
$A_p$ = profile area of fin over fin cross section ($m^2$)
$A_r$ = surface area of tube at base of fins ($m^2$)
Bo = bond number, $\rho g/(dp/ds)$ (dimensionless)
$c_b$ = fraction of tube circumference flooded
$D$ = diameter of plain tube (m)
$D_i$ = internal tube diameter (m)
$D_o$ = diameter of tube over fins (m)
$D_r$ = root diameter of tube (m)
$e$ = fin height (m)
$F_g$ = force due to gravity (N)
$F_s$ = force due to surface tension (N)
fpm = fins per meter
$g$ = gravitational acceleration (9.806 $m/s^2$)
$h$ = condensing coefficient based on $A = \pi D_o L$ ($W/m^2$-K)
$h_b$ = condensing coefficient in flooded region based on $A_r$ ($W/m^2$-K)
$h_f$ = condensing coefficient on fin surface, based on $A_f$ ($W/m^2$-K)
$h_h$ = condensing coefficient for horizontal plain tube ($W/m^2$-K)
$h_i$ = heat transfer coefficient inside tube ($W/m^2$-K)
$h_o$ = condensing coefficient based on total surface area ($W/m^2$-K)
$h_v$ = condensing coefficient for a vertical surface ($W/m^2$-K)
$k$ = thermal conductivity of condensate (W/m-K)
$k_t$ = thermal conductivity of fin metal (W/m-K)
$L$ = length of vertical condensing surface or tube length (m)
$L_f$ = characteristic length (m)
$m$ = defined as $(2h_f/k_t t)^{1/2}$, (1/m)
$\dot{m}$ = condensate flow rate on fin (kg/s)
$\dot{m}_r$ = condensate flow rate leaving $A_r$ (kg/s)
$p$ = pressure (Pa)
$p_f$ = fin pitch (m)
$P$ = wetted perimeter of fin cross section (m)
$q_{b1}$ = heat transfer defined in equation (16$a$) (W)

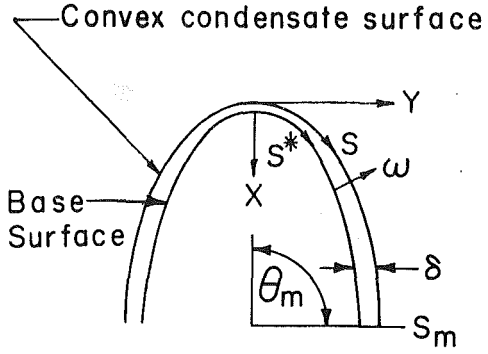


Fig. 3 Coordinate system for condensation in a convex fin surface profile

water. They found that the interfin region was condensate flooded over a significant fraction of the tube circumference. For example, 26 percent of the circumference was flooded with R-11 condensing on a tube having 1,024 fpm. When n-pentane was condensed on the same tube, 42 percent of the circumference was flooded. The effect of condensation rate on the flooding angle was also measured. The tests showed that the flooded zone was essentially independent of condensation heat flux. These tests clearly showed that the second assumption of the Beatty and Katz model (zero condensate retention) is incorrect.

Rudy and Webb [2] provide a detailed description of their condensate retention tests and develop an analytical model to predict the fraction of the tube circumference that is flooded.

As shown in [2], the fraction of the tube circumference that is condensate flooded is

$$c_b = \frac{1}{\pi}\cos^{-1}\left[1 - \frac{2\sigma(P - t_b)}{\rho g D_o (p_f e - A_p)}\right] \tag{6}$$

## Proposed Condensation Model

Equation (1) assumes that there is no condensate bridged zone on the integral-fin tube. The proposed model assumes that equation (1) applies only to the fraction of the tube circumference that is not condensate flooded, $(1 - c_b)$. The proposed model is given by equation (7), in which the first term applies to the unflooded fraction of the tube circumference, and the second term applies to the condensate bridged fraction.

$$h\eta = (1 - c_b)\left(h_h \frac{A_r}{A} + h_f \eta_f \frac{A_f}{A}\right) + c_b h_b \tag{7}$$

Equations must be established to predict $h_f$ (for the fins in the unflooded zone) and $h_h$ (on the unflooded root surface of the tube between fins), and for $h_b$ (in the condensate flooded zone).

**Prediction of $h_f$.** Based on the test results of Fig. 2, it does not appear that gravity force controls condensate drainage from the fin surface. The authors propose that surface tension force is the dominant force affecting condensate drainage from the fin surface.

Prior work dealing with condensation on *vertical* "fluted" tubes has shown that surface tension forces control drainage from the convex portion of the flute, if a special convex surface shape is used. With a proper convex surface shape, surface tension forces drain the condensate in the horizontal plane to the concave channel, where gravity force drains the condensate vertically downward. Gregorig [6] defined the geometric shape of the convex surface that yields a constant condensate film thickness ($\delta$) by virtue of the surface tension force. Zener and Lavi [7] proposed an alternate convex shape that maintains a constant pressure gradient along the convex surface; this geometry yields a 15 percent higher condensation coefficient on the convex surface than predicted for Gregorig's geometric shape. Adamek [8] shows that "thinner" convex flutes yield higher condensation coefficients than the shape proposed by Zener and Lavi.

Mori et al. [9] have shown that the sophisticated shapes analyzed in [6–8] are not necessary to establish significant enhancement. They predicted and measured high condensation coefficients on fluted surfaces of triangular and sine wave shapes and a parabolic convex shape with a flat base region.

Therefore, it is not surprising that surface tension forces may dominate condensate drainage from the rectangular fins tested by Webb, Keswani, and Rudy. Recent theoretical and experimental work by Hirasawa et al. [10] on vertical finned channels directly supports this proposition.

If the local thickness of a laminar condensate film ($\delta$) is known, the local condensation coefficient is given by $k/\delta$. Consider the fin profile and the coordinate system shown by Fig. 3. If the gravity force is small compared to the surface tension induced pressure gradient ($dp/ds$), the momentum equation on the convex surface is

## Nomenclature (cont.)

$q_{b2}$ = heat transfer to tubeside coolant (W)
$q_f$ = condensation rate on one fin (W)
$q_h$ = condensation rate on $A_r$ (W)
$q_t$ = condensation rate on fin tip (W)
$r$ = radius of curvature of convex surface (m)
$R_B$ = radius of curvature of condensate film at fin base (m)
$R_T$ = radius of curvature of condensate film at fin tip (m)
Re = Reynolds number defined by equation (15)
$s$ = coordinate along condensate film (Fig. 3), (m)
$s^*$ = coordinate along base surface (Fig. 3), (m)
$S_m$ = length of convex surface over $0 < \theta < \theta_m$ (m)
$t$ = thickness of fin, $t_t$ (at tip), $t_b$ (at base), (m)
$t_w$ = tube wall thickness (m)
$T_i$ = bulk temperature of tubeside coolant (°C)
$T_t$ = temperature of fin tip (°C)
$T_v$ = vapor temperature (°C)
$T_s$ = wall temperature (°C)
$\Delta T_{vs}$ = $T_v - T_s$ (°C or K)
$u$ = velocity of condensate film; $\bar{u}$ (average velocity) (m/s)
$v$ = volume ($m^3$)
$w$ = spacing between fins (m)
$X$ = coordinate direction (Fig. 3)
$Y$ = coordinate direction (Fig. 3)

### Greek Symbols

$\delta$ = thickness of condensate film on fin surface (m)
$\delta_r$ = thickness of condensate film on $A_r$ (m)
$\zeta$ = parameter in equation (20)
$\eta_f$ = fin efficiency
$\eta$ = surface efficiency (equation (17))
$\theta_m$ = rotation angle of normal to fin surface for $0 \leqq s \leqq S_m$ (rad)
$\lambda$ = latent heat of vaporization of condensate (J/kg)
$\mu$ = dynamic viscosity of condensate (Pa-s)
$\nu$ = kinematic viscosity ($m^2/s$)
$\pi$ = geometric constant 3.14159
$\rho$ = density of condensate ($kg/m^3$)
$\sigma$ = surface tension of condensate (N/m)
$\omega$ = coordinate normal to convex base surface (Fig. 3), (m)

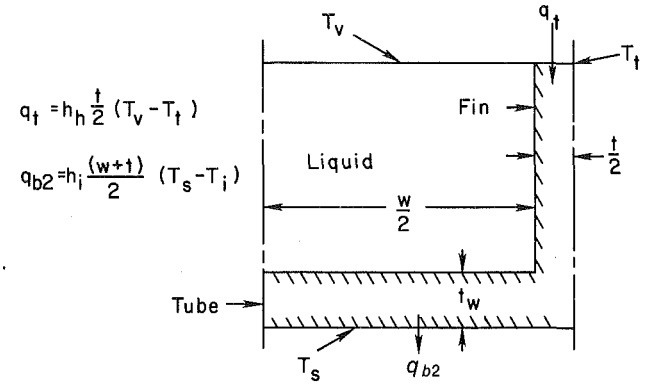


**Fig. 4 Model used to estimate condensation rate in condensate bridged region**

$$\frac{dp}{ds^*} = \mu \frac{d^2u}{d\omega^2} \tag{8}$$

If the condensate film thickness is small, $dp/ds^* = dp/ds$. The $dp/ds$ is defined by equtaion (9), where $r$ is the local radius of curvature of the convex liquid-vapor interface.

$$\frac{dp}{ds} = \sigma \frac{d(1/r)}{ds} \tag{9}$$

Solving equations (8) and (9), one obtains

$$\bar{u} = -\frac{\delta^2 \sigma}{3\mu} \frac{d(1/r)}{ds} \tag{10}$$

A heat balance on the condensate surface gives

$$\frac{d\dot{m}}{ds} = \frac{k\Delta T_{vs}}{\lambda \delta} = \rho \frac{d(\bar{u}\delta)}{ds} \tag{11}$$

Adamek [9] shows that solution of equation (11), with $\bar{u}$ from equation (10) yields

$$\delta^4 = \frac{-4k\mu\Delta T_{vs}}{\sigma\rho\lambda} \left[\frac{d(1/r)}{ds}\right]^{-4/3} \int_o^s \left[\frac{d(1/r)}{ds}\right]^{1/3} ds \tag{12}$$

The average heat transfer coefficient on the convex surface is given by equation (13), with $\delta$ from equation (12)

$$\frac{h_f S_m}{k} = \int_o^{S_m} \frac{ds}{\delta} \tag{13}$$

If the shape of the condensate film is known, the equation for $r(s)$ is known, and the integrations of equations (12) and (13) are easily accomplished.

Webb et al. [5] used an approximate (linear) surface tension drained model to predict the condensation coefficient on the rectangular fin surface of Table 1 finned disk. For the finned plate tested, $c_b \cong 0$ in equation (7). The value of $h_h$ was calculated by equation (2), using the iterative procedure defined in the next section. Less than 2 percent of the total condensation rate occurred on the base surface between the fins. The predicted condensation coefficient was 10 percent below the curve fit of the experimental values.

The authors do not propose the linear surface tension model as an acceptable predictive method. However, it does support the contention that surface tension force is the dominant drainage force on the finned plates. And one would expect the same conclusion for horizontal integral-fin tubes.

**Calculation of $h_h$.** The coefficient $h_h$ is calculated from the Nusselt equation for horizontal tubes taking account of the additional condensate film thickness because of condensate drainage from the fins. Equation (2) may be written in terms of the condensate Reynolds number [3] as

$$h_h = 1.514 \left(\frac{\mu^2}{k^3 \rho^2 g} \mathrm{Re}\right)^{-1/3} \tag{14}$$

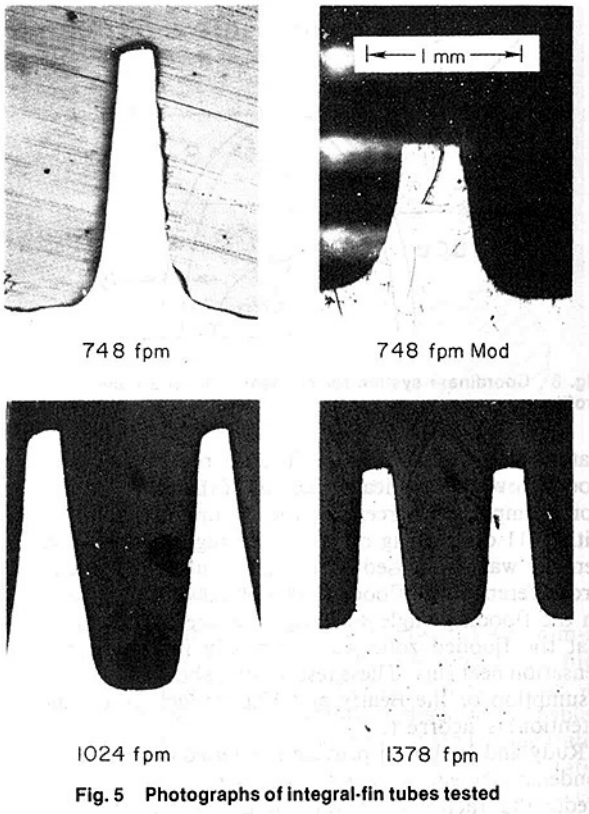


**Fig. 5 Photographs of integral-fin tubes tested**

where

$$\mathrm{Re} = \frac{4\dot{m}_r}{\mu(p_f - t_b)} \tag{15}$$

A rigorous calculation for $h_h$ would employ the iterative method given below

1 Calculate the condensation rate on the fin $\dot{m} = \eta_f h_f A_f \Delta T_{vs}/\lambda$
2 Assume $\dot{m}_r = \dot{m}$
3 Calculate Re from equation (15)
4 Calculate $h_h$ from equation (14)
5 Calculate $q_h = h_h A_r \Delta T_{vs}$
6 $\dot{m}_r = \dot{m} + q_h/\lambda$
7 Repeat steps 3 through 6 until $\dot{m}_r$ converges.

**Calculation of $h_b$.** The term $h_b$ is the heat transfer coefficient for the condensate bridged fraction of the finned tube. For the limiting case of zero fin thickness, $h_b = k/e$. The presence of fins of finite thickness having $k_t/k >> 1$ provides a parallel, high thermal conductivity path to transfer heat from the liquid-vapor interface to the tube surface. Calculation of the heat flux requires analysis of the two-dimensional conduction problem illustrated in Fig. 4. The figure shows that the interfin region is filled with condensate, and the condensate-vapor interface temperature is equal to the vapor saturation temperature ($T_v$). Condensation occurs on the tip of the fin, where $h_h$ is given by equation (2). Heat is convected from the base surface by the tube-side coolant, whose convection coefficient is $h_i$. Using a two-dimensional heat conduction computer code, it is possible to solve for the heat flux to the base surface ($q_{b2}$). For zero fin thickness, and negligible temperature drop across the tube wall, the heat flux is one-dimensional, and is given by

$$q_{b1} = kA \frac{(T_v - T_s)}{e}. \tag{16a}$$

**Table 2 Test tube geometry**

| | | | | |
|---|---|---|---|---|
| Fins/meter (fpm) | 748 | 748 | 1024 | 1378 |
| Geometry code | Std. | Mod. | Std. | Std. |
| Outside diameter $D_o$ (mm) | 19.0 | 17.7 | 19.0 | 19.0 |
| Outside area ($m^2/m$) | 0.162 | 0.099 | 0.195 | 0.172 |
| Area ratio $A_o/\pi D_o L$ | 2.91 | 2.04 | 3.60 | 3.18 |
| Fin height $e$ (mm) | 1.53 | 0.85 | 1.53 | 0.89 |
| Fin Thk. at tip $t_t$ (mm) | 0.20 | 0.28 | 0.20 | 0.20 |
| Fin Thk. at base $t_b$ (mm) | 0.42 | 0.42 | 0.52 | 0.29 |

Letting $q_{b2}/q_{b1} = \phi$, the heat transfer to the coolant in the condensate bridged zone is

$$q_{b2} = \phi k A \frac{(T_v - T_s)}{e} = h_b A (T_v - T_s) \qquad (16b)$$

or

$$h_b = \frac{\phi k}{e}$$

We have solved the two-dimensional conduction problem of Fig. 4 for the case of R-11 condensing on copper tubes having 1,024 fpm with $e = 1.5$ mm and found that $\phi \simeq 5$. For this case, $c_b \simeq 0.29$. This calculation showed that the heat transfer rate across the condensate bridged zone is approximately 0.2 percent of the experimentally determined total heat transfer rate (11). If a higher conductivity fluid, such as water, is condensed on the finned tube it would be necessary to use a larger fin spacing to limit $c_b$ to an acceptable value, e.g., 0.3. The value of $\phi$ will decrease as the fin spacing is increased. For steam condensing on a 19-mm-dia tube having 203 fpm, analytical estimates predict that only 1.6 percent of the heat transfer rate would occur in the condensate bridged zone.

It appears that the second term of equation (7) will be negligible for most practical cases of interest.

## Condensation on Integral-Fin Tubes

**Test Program.** R-11 condensation data were taken on four horizontal integral-fin tubes [11]. Table 2 lists the geometric details of the copper tubes. All except the second tube are commercially available designs. The second tube, 748 modified (mod.), is the same as the standard (std.) 748 fpm tube, except it was machined to reduce the fin height from 1.53 to 0.85 mm. Figure 5 shows crosssection photographs of the fins.

The test apparatus consisted of an electric heated R-11 boiler, the test cell and a post-condenser. The test cell was 95 mm wide, 460 mm high, and 180 mm long. A single 180-mm-long horizontal tube was mounted in the center of the cell. High velocity water flowing inside the test tube was the coolant.

The test section heat load was calculated using the flow rate and temperature rise of the coolant. The flow rate was measured by the weight-time method. The water temperature rise was directly measured using two 10 element, calibrated thermocouples. A typical coolant temperature rise was 1.0°C.

Local heat transfer coefficients were determined at several circumferential locations for three axial positions (center of tube and one each 50 mm from the center of the tube). The test section was designed to allow 180 deg rotation of the tube about its axis. Thus by rotating the tube, the wall temperatures could be measured at the desired number of circumferential locations. Typically, three circumferential locations (top, side, bottom) were used. The wall thermocouples, made of 0.13-mm-dia copper-constantan wire, were implanted in holes drilled into the tube wall between adjacent fins. The fin was bent to provide tight contact between the thermocouple junction and the tube wall. The insulated thermocouple wires were wrapped one-half tube diameter around the tube before routing the wire from the tube.

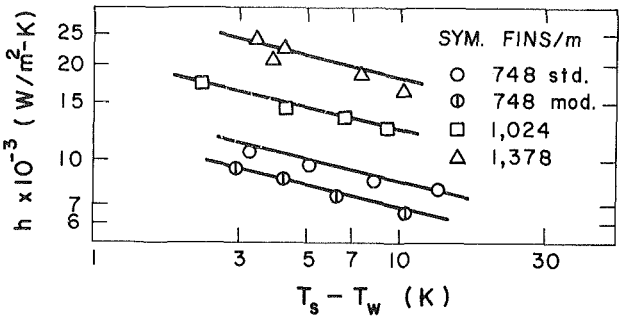


**Fig. 6 Measured condensing coefficients of integral-fin tubes**

Noncondensibles were purged from the apparatus by several cycles of charging with refrigerant followed by evacuation. A post condenser, downstream from the test section, acted to remove any remaining noncondensible gas from the test section. The R-11 condensing temperature ($T_v$) was taken as its saturation temperature at its pressure. The condenser pressure was measured by a mercury filled absolute manometer. The indicated saturation temperature typically agreed within 0.3°C of the measured vapor temperature.

Using the measured circumferential wall temperatures, the average wall temperature ($T_s$) was determined. The condensation coefficient is defined in terms of the envelope area over the fins ($\pi D_o L$).

The data were reduced to the $\eta = 1$ condition as described below. From the data

$$h\eta A = \frac{q}{T_v - T_w} \qquad (17)$$

Using equations (7) and (17), one obtains

$$\eta_f h_f = \frac{q}{T_v - T_w} \frac{1}{(1 - c_b)A_f} - h_h \frac{A_r}{A} \qquad (18)$$

The $h_h$ is calculated using equations (14) and (15). The fin efficiency $\eta_f$ is given by

$$\eta_f = \frac{\tanh [m(e + t/2)]}{m(e + t/2)} \qquad (19)$$

Equations (18) and (19) were iteratively solved for $\eta_f$ and $h_f$. The $h$, based on $A = \pi D_o L$, was calculated by equation (7) using $\eta = \eta_f = 1$, assuming $c_b h_b = 0$.

**Test Results.** The experimental condensation coefficients are shown by the plotted points on Fig. 6. The condensation coefficient ($h$) is based on the "envelope" area over the finned tube, $A = \pi D_o L$.

The 1378 fpm tube provides the highest $h$; its $h$ is 103 and 37 percent higher than that of the 748 and 1024 fpm tubes, respectively. If the $h$ values are recomputed on the basis of the total surface area ($A_o$), the 1378 fpm tube still shows the highest $h_o$. For this definition, $h_o$ of the 1378 fpm tube is 71 percent greater than that of the 748 fpm tube, and 49 percent greater than that of the 1024 fpm tube. Carnavos [12] also tested the 748 fpm geometry with R-11. The Fig. 6 data are 15 percent higher than that of Carnavos.

## Theoretical Predictions

**Linear Surface Tension Model.** The condensation coefficient is predicted using equation (7), with $h_f$ predicted by the approximate linear surface tension model described in [5]. The term $c_b$ in equation (7) is predicted by equation (6). Table 3 compares the predicted $h$ with the measured values.

Table 3 shows that the approximate model predicts the condensation coefficient within −8 to +30 percent for the 0.9-mm fin heights. One would expect the linear approximation to the surface tension pressure gradient to show

Table 3 Ratio of predicted to measured condensation coefficient for $T_{sat} = 35°C$ and $T_v - T_w = 17°C$. $h \sim W/m^2\text{-}K$.

| Geometry | $e$ (mm) | $R_T$ (mm) | $R_B$ (mm) | $h/h_{exp}$ | $h_{exp}$ |
|---|---|---|---|---|---|
| 748 std. | 1.5 | 0.10 | 0.52 | 1.60 | 3,355 |
| 748 mod. | 0.9 | 0.16 | 0.52 | 1.30 | 7,310 |
| 1024 | 1.5 | 0.10 | 0.26 | 1.25 | 3,810 |
| 1378 | 0.9 | 0.10 | 0.23 | 0.92 | 5,685 |

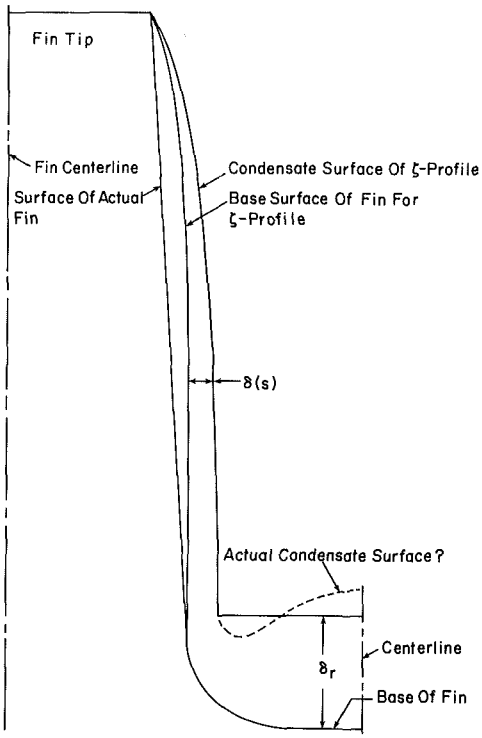


Fig. 7 Condensate film profiles used for analytical prediction of the condensing coefficient (1,378 fpm fin illustrated)

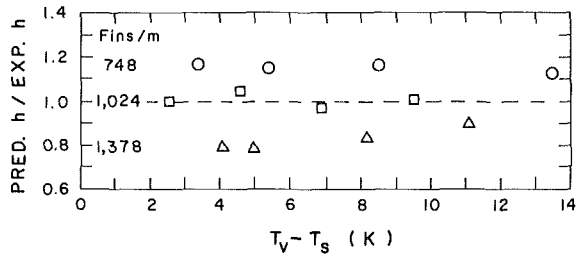


Fig. 8 Comparison of predicted and experimental condensing coefficients

increasing error as the fin height is increased; this expectation is verified for the high fin data of the 748 std. tube.

Although this model is not recommended for design purposes, it does predict the correct qualitative trends for changes of the fin geometry. For example, it predicts:

1 $h$ increases as the fin height decreases
2 $h$ increases as the fin spacing decreases

**Prediction for the Adamek Fin Profiles.** The flat-sided fin geometries of Fig. 5 were not intentionally designed to use surface tension force for condensate drainage. Therefore, it is of interest to predict $h_f$ using equation (13). In a theoretical study of condensation on vertical fluted surfaces, Adamek [8] defined a family of condensate surface profiles, whose curvature is given by equation (20).

$$\frac{1}{r} = \frac{\theta_m}{S_m}\frac{\zeta+1}{\zeta}\left[1-\left(\frac{s}{S_m}\right)^{\zeta}\right] \quad \text{for } -1 \leqq \zeta < \infty \tag{20}$$

The parameter $\zeta$ characterizes the aspect ratio of the fin cross section (height/thickness). The aspect ratio increases as $\zeta$ decreases. The $S_m$ is the length of the convex surface over which the condensate film flows. The $\theta_m$ is the angle through which the convex surface turns from its origin to $S_m$. For the integral-fins of interest here, $\theta_m \simeq 85$ deg. Using equation (20) in equations (12) and (13), one obtains

$$\frac{h_f S_m}{k} = 2.149\left[\frac{\sigma\lambda\theta_m S_m}{\nu k \Delta T_{vs}}\frac{\zeta+1}{(\zeta+2)^3}\right]^{1/4} \tag{21}$$

Integration of equation (12) with equation (20) yields

$$\delta(s) = 1.86\left[\frac{k\nu\Delta T_{vs}}{\sigma\lambda\theta_m}\frac{S_m{}^{\zeta+1}s^{2-\zeta}}{(\zeta+1)(\zeta+2)}\right]^{1/4} \tag{22}$$

We have predicted the condensation coefficient ($h_f$) for fins having the same height ($e$), base thickness ($t_b$), and tip thickness ($t_t$) as the standard geometries shown on Fig. 6. The experimental values for $\Delta T_{vs} = 9.5°C$ are interpolated from Fig. 6. The $h_f$ is predicted for $\Delta T_{vs} = 9.5°C$ using equation (21). The condensation coefficient for the integral-fin tube is then predicted using equation (7). The present prediction uses dimensions scaled from Fig. 5 for the actual trapezoid fin shape. The calculation results are presented in Table 4.

The $\zeta$-values for each fin geometry are listed on line 1 of Table 4. The profile for the 1378 fpm tube, described by equation (20), is shown on Fig. 7. This profile starts with $s = 0$ at the edge of the fin tip, and terminates at the fin base where $s = S_m$. The value of $\theta_m$ is set at 1.484 (85 deg), which closely agrees with the Fig. 5 fin profiles. Because equation (20) describes the shape of the condensate surface, an iterative procedure was used to establish the $\zeta$-value that yields the correct fin thickness at the fin base. Thus the base thickness of the correct $\zeta$-profile is equal to $t_b - t_t + 2\delta(S_m)$, where $\delta(S_m)$ is the condensate film thickness at the fin base, and is calculated by equation (22). The values of $\delta(S_m)$ are listed on line 2 of Table 4. The value of $\delta$ is so small that there is little difference between the geometry of the base surface and the condensate film. Line 4 gives the condensation coefficient on the fin surface ($h_f$), calculated from equation (21) with $\theta_m = 1.484$ and $S_m$ from line 3. The value of $c_b$ is calculated by equation (6), and is given on line 5. The $h_h$ is calculated following the procedure outlined in the "Calculation of $h_h$" section of this paper. Because $\dot{m}/\dot{m}_r \simeq 1$, negligible error would occur if steps 5–7 of the iterative procedure were omitted. The calculated values of $h_h$ are given on line 6. The condensing coefficient, calculated by equation (7) is given on line 7.

The predicted value on line 7 does not account for condensation on the fin tip. Nor does it account for the relatively thick condensate film at the base of the fin, which renders a fraction of $S_m$ ineffective. Therefore, corrections to the condensation coefficient calculation are necessary.

The average condensate thickness associated with $h_h$ is calculated as $\delta_r = k/h_h$; this value is given on line 8. The corrected $S_m$ is $S_m + t_c/2 - \delta_r$. Line 9 shows the ratio of the corrected to line 3 value of $S_m$. The correction results in negligible change of $h_f$. The final prediction for $h$ is given on line 10. Line 11 shows the ratio of the predicted and experimental condensation coefficients. The predicted values are approximately within ±15 percent of the experimental values.

Table 4 Predicted condensation coefficients for tubes having the same fin height and tip/base thickness as the Fig. 6 fins ($T_v = 35°C$, $\Delta T_{vs} = 9.5°C$, $h \sim W/m^2\text{-K}$)

| Line | Item | 748 fpm | 1024 fpm | 1378 fpm |
|---|---|---|---|---|
| 1 | $\zeta$ (eq. 20a) | −0.857 | −0.771 | −0.843 |
| 2 | $\delta$ ($S_m$) mm | 0.0621 | 0.0542 | 0.0391 |
| 3 | $S_m$ (mm) | 1.5936 | 1.5936 | 0.8923 |
| 4 | $h_f$ (eq. 21) | 4,848 | 5,164 | 7,596 |
| 5 | $c_b$ (eq. 6) | 0.223 | 0.287 | 0.338 |
| 6 | $h_h$ | 836 | 648 | 673 |
| 7 | 1st calc. for $h$ | 9,236 | 12,041 | 13,458 |
| 8 | $\delta_r$ (mm) | 0.103 | 0.133 | 0.128 |
| 9 | Corr. $S_m$/Line 3 $S_m$ | 0.991 | 0.982 | 0.970 |
| 10 | Corrected $h$ | 9,197 | 11,963 | 13,552 |
| 11 | Pred. $h$/exp. $h$ | 1.14 | 1.00 | 0.84 |
| 12 | $s/S_m$ at which Bo = 1 | 0.29 | 0.36 | 0.57 |

The same prediction method was applied to all of the data points of Fig. 6. The results are shown in Fig. 8. All of the data points are predicted within ±20 percent. Uncertainty analysis of the experiment indicates ±9 percent uncertainty of the condensation coefficient, assuming no uncertainty of the fluid properties.

The possible sources of error, and their effect on the predicted $h$ are:

1 Violation of the assumption that gravity force is negligible compared to the surface tension force for condensate drainage from the fin. Violation of this assumption would cause overprediction of $h_f$.

2 Concave curvature of the fin surface on the portion of the fin, upstream from the condensate film on the root diameter of the tube ($\delta_r$)

3. Concave curvature of the condensate film ($\delta_r$) on the root diameter of the tube

4. The equation (20) profiles have a small convex curvature, as compared to the flat sided fins shown by Fig. 5.

The analysis assumes gravity force is small compared to surface tension force. The ratio of gravity-to-surface tension is $\rho g/(dp/ds) \equiv$ Bo (the Bond number). The $dp/ds$ is given by equation (20) in equation (9). Line 12 of Table 4 shows the value of $s/S_m$ at which Bo = 1. Because Bo = 1 at $s/S_m$ = 1/3 for the 748 and 1024 fpm geometries ($e$ = 1.59 mm) one would expect overprediction of $h_f$, which does occur. For the 1378 fpm tube ($e$ = 0.9 mm), Bo = 1 at $s/S_m$ = 0.6, and $h$ is not overpredicted.

Figure 7 shows the calculated average condensate thickness ($\delta_r$) at the base of the fins. Except for the 748 fpm tube, the concave curvature of the fin occurs within the condensate region, $\delta_r$. Fin curvature within the liquid region has no effect on $h$. Hirasawa et al. [10] have visually studied gravity drained films in narrow, rectangular channels that have a free liquid surface. They report that the meniscus in the corners causes a thicker film at the center of the channel than near the sides. Thinning of the $\delta_r$ film near the fin base would increase $h_h$. However, since $h_h A_h/\eta_f h_f A_f < 0.05$, a modest increase of $h_h$ would have little effect on the composite $h$ for the tube. It is also possible that thinning of $\delta_r$ near the base of the fin would offer a positive contribution to $h_f$.

Figure 7 shows the condensate film and base surface profile on the 1378 fpm $\zeta$-profiles used for the analytical predictions. Superimposed is the profile of the flat-sided Fig. 5 fins. There is little difference between the two base surface profiles, except near the fin tip. Both profiles share a common mathematical feature, which explains their approximately equal condensation coefficients; both have a very large curvature change, $d(1/r)/ds$, near the fin tip, and quite small curvature change after the tip region. For example, the $dp/ds$ of a $\zeta = -0.8$ profile at $s/S_m$ = 0.1 is only 1.6 percent of the $dp/ds$ value at $s/S_m$ = 0.01; hence nearly all of the potential for curvature change to affect the pressure gradient ($dp/ds$), is dissipated over the initial 10 percent of the surface length. For this example, $dp/ds$ at $s/S_m$ = 0.1 is nine times the gravity force. As the value of $\zeta$ becomes more negative, e.g., −0.9, the fin profile is more "flat-sided" over a larger fraction of its length. Assuming this more "flat-sided" profile, the predicted $h_f$ would decrease by 6, 12, and 7 percent for the 748, 1,024 and 1,378 fpm geometries, respectively. These considerations suggest a conclusion of major importance that is supported by the test data: If the Fig. 5 fin geometries were constructed to have the precise $\zeta$-profiles listed on line 1 of Table 4, significant increase of $h_f$ would not result.

The foregoing discussion of possible errors has identified possible second-order effects that suggest reasons for the relatively small overprediction of the 748 and 1,024 fpm geometries. A possible factor causing underprediction of the 1,378 fpm geometry is the surface tension force on the free liquid surface at the base of the fin ($\delta_r$). This could thin the film on the concave surface at the base of the fins; this effect may be more important for the 1024 and 1378 fpm geometries because of the small channel width.

## Conclusions

1 This work proposes a new theoretical model for prediction of the condensation coefficient on horizontal, integral-fin tubes designed for surface tension drainage from the fins.

2 The model accounts for the effect of condensate bridging between the fins. An analytic equation is provided to predict the fraction of the tube circumference that is condensate bridged.

3 The predicted condensation coefficients using the analytical model are within ±20 percent of experimental values for R-11 condensing on tubes having 748 to 1,378 fins/m. The model suggests that a special, precisely defined curvature on the fin sides is not necessary.

4 The model clearly establishes that surface tension forces control condensate drainage from the fins (for the geometries tested), and that surface tension is responsible for condensate bridging on the lower side of the tube.

5 The condensation rate on the condensate bridged zone is negligible for R-11 condensing on the tubes tested.

6 The model does not account for vapor shear or inundation effects.

## Acknowledgment

The majority of this work was performed under National Science Foundation Grant (79-73-Eng.-78-16980).

## References

1 Beatty, K. O., Jr., and Katz, D. L., "Condensation of Vapors on Outside

of Finned Tubes," *Chemical Engineering Progress*, Vol. 44, No. 1, 1948, pp. 55–70.

2 Rudy, T. M., and Webb, R. L., "Condensate Retention on Horizontal Integral-Fin Tubes," ASME JOURNAL OF HEAT TRANSFER, Vol. 107, No. 2, May 1985, pp. 361–368.

3 Collier, J. G., *Convective Boiling and Condensation* (2d ed.), McGraw-Hill, New York, 1981, pp. 328–332.

4 Rudy, T. M., and Webb, R. L., "Condensate Retention of Horizontal Integral-Fin Tubing," *Advances in Enhanced Heat Transfer—1981*, edited by R. L. Webb, T. C. Carnavos, E. F. Park, Jr., and K. M. Hostetler, ASME Symp. Vol. HTD-Vol. 18, 1981, pp. 35–42.

5 Webb, R. L., Keswani, S. T., and Rudy, T. M., "Investigation of Surface Tension and Gravity Effects in Film Condensation," *Proceedings of 7th International Heat Transfer Conference*, Vol. 5, Munich, Fed. Rep. of Germany, Sept. 6–10, 1982, Hemisphere Publishing Co., Washington, D.C., pp. 175–180.

6 Gregorig, R., "Hautkondensation an feingewellten Oberflachen bei Berucksichtigung der Oberflachenspannugen," *Zeitschrift fur angewandte Mathematik and Physik*, Vol. V, 1954, pp. 36–49.

7 Zener, C., and Lavi, A., "Drainage Systems for Condensation," ASME *Journal of Engineering for Power*, Vol. 96, 1974, pp. 209–215.

8 Adamek, T., "Bestimmung der Kondensationgrossen auf feingewellten Oberflachen zur Auslegung optimaler Wandprofile," *Warme-und-Stoffubertragung*, Vol. 15, 1981, pp. 255–270.

9 Mori, V., Hijikata, K., Hirasawa, S., and Nakayama, W., "Optimized Performance of Condensers with Outside Condensing Surfaces," ASME *Journal of Heat Transfer*, Vol. 103, 1981, pp. 96–102.

10 Hirasawa, S., Hijikata, K., Mori, Y., and Nakayama, W., "Effect of Surface Tension on Condensate Motion in Laminar Film Condensation (Study of Liquid Film in a Small Trough)," *International Journal of Heat and Mass Transfer*, Vol. 23, 1980, pp. 1471–1478.

11 Rudy, T. M., "A Theoretical and Experimental Study of Condensation on Single, Integral-Fin Tubes," Ph.D. thesis, Mechanical Engineering Department, The Pennsylvania State University, University Park, Pa., May 1982.

12 Carnavos, T. C., "An Experimental Study: Condensing R-11 on Augmented Tubes," ASME Paper 80-HT-54, 1980.

# Effect of Fin Spacing on the Performance of Horizontal Integral-Fin Condenser Tubes

K. K. Yau

J. R. Cooper

J. W. Rose

Department of Mechanical Engineering,
Queen Mary College,
London, England E1 4NS

*The dependence of heat transfer performance on fin spacing has been investigated for condensation of steam on horizontal integral-fin tubes. Thirteen tubes have been used with rectangular section fins having the same width and height (0.5 mm and 1.6 mm) and with fin pitch varying from 1.0 mm to 20.5 mm. For comparison, tests were made using a plain tube having the same inside diameter and an outside diameter equal to that at the root of the fins for the finned tubes. All tests were made at near-atmospheric pressure with vapor flowing vertically downward with velocities between 0.5 m/s and 1.1 m/s. The observed heat transfer enhancement for the finned tubes significantly exceeded that to be expected on grounds of increased area. Plots of enhancement against fin density were repeatable and showed local maxima and minima. The dependence of enhancement on fin density did not depend appreciably on vapor velocity or condensation rate for the ranges used. The maximum vapor-side enhancement (i.e., vapor-side heat transfer coefficient of finned tube/vapor-side coefficient for plain tube) was found to be around 3.6 for the tube with a fin spacing of 1.5 mm.*

## Introduction

Experimental studies of condensation on horizontal finned tubes have shown that vapor-side heat transfer coefficient enhancement, by factors up to around five, may be realized. In circumstances where the vapor side dominates, this clearly leads to improvements in the overall performance of the tube. Even for the case of steam, where the vapor-side resistance might typically be around a third to a half of the overall vapor-to-coolant resistance, significant improvement, and consequent reduction in condenser size for given duty, can be achieved.

Despite considerable effort in recent years, the mechanism of condensation on finned surfaces is still imperfectly understood. An early simple model [1] took account of the increase in surface area obtained with fins. Later studies, following Gregorig [2], have demonstrated the important role of surface tension in modifying the shape of the condensate film. More recently, attention has been drawn to the effect of surface tension in relation to the phenomenon of "flooding" or condensate "retention" between fins on the lower parts of horizontal finned tubes [3–7].

In view of the complexity of the three-dimensional condensate flow for which surface tension forces play an important role, it has been found necessary, in theoretical models, to invoke simplifying assumptions for which there is as yet inadequate experimental backing. Moreover, certain parameters affect the heat transfer performance of a tube in opposite ways. For example, increase in fin density tends to improve heat transfer by increasing the effective surface area, but has an adverse effect by increasing condensate retention. Similarly, high surface tension is beneficial in reducing the condensate film thickness over parts of the surface but also increases condensate retention.

Reliable experimental data, from investigations in which the important variables are systematically studied, are of vital importance to the development of a successful model. The present study was directed towards establishing the effect of a single variable, i.e., fin spacing. Following the report [8, 9] that, for a vertical surface, fitted with vertical ribs, the highest enhancement was found when the fraction of surface covered by fins was only 0.1, the present investigation was extended to much lower fin densities than have normally been used in practice. For comparison purposes tests were also made using a plain tube.

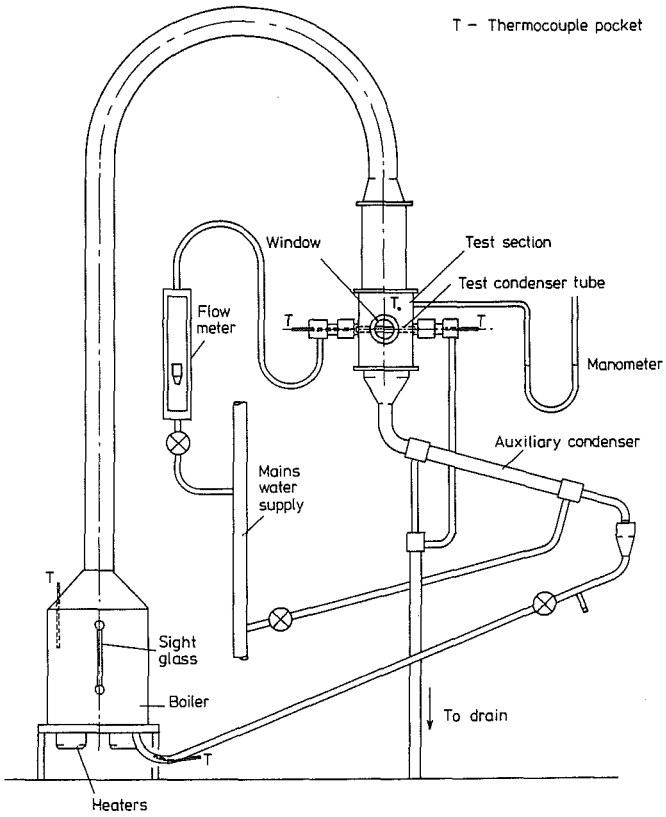


Fig. 1 Apparatus

## Apparatus

Referring to Fig. 1, steam was generated from distilled water in a stainless steel boiler fitted with electric immersion heaters that provided a total power of 16 kW. The steam

Contributed by the Heat Transfer Division for publication in the JOURNAL OF HEAT TRANSFER. Manuscript received by the Heat Transfer Division June 10, 1983.

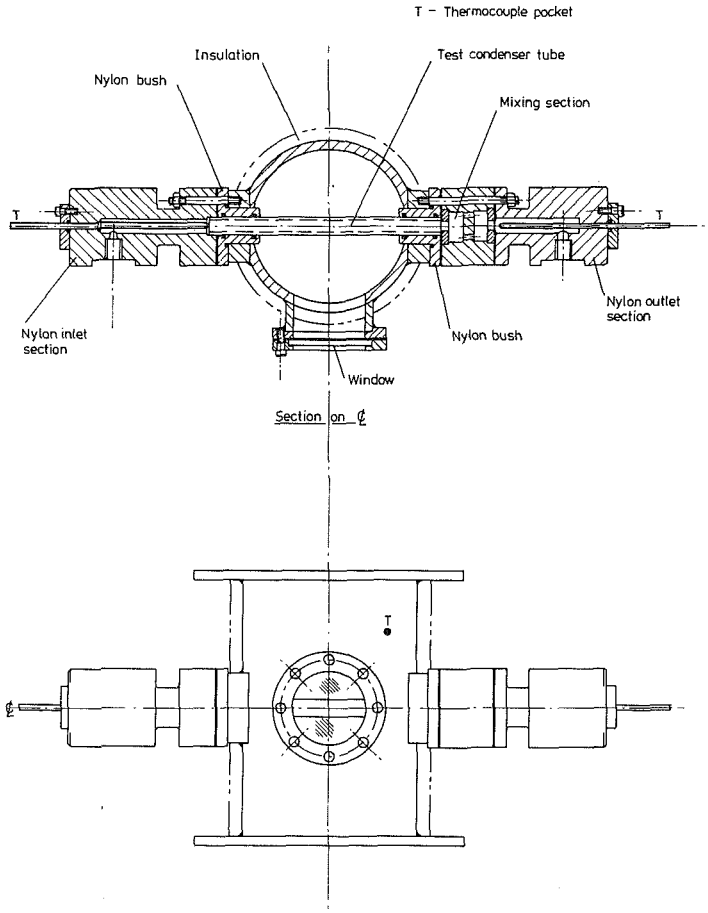


**Fig. 2 Test section**

passed to the test section where it flowed vertically downward over the condenser tube. The condenser tube could be viewed through a window to confirm that film condensation conditions prevailed. Excess steam and condensate were directed to an auxiliary condenser. The condensate from both test tube and auxiliary condenser was returned by gravity to the boiler. The temperature and pressure of the steam just upstream of the test condenser tube were observed by a thermocouple and water manometer. A thermocouple was also used to measure the temperature of the condensate returning to the boiler. The boiler, vapor supply duct, and test section were thermally well insulated. All tests were carried out at near atmospheric pressure.

Details of the test section are shown in Fig. 2. The test

## Nomenclature

$b$ = spacing between fins
$d$ = outside diameter of plain tube, diameter at fin root
$F$ = $gd\mu h_{fg}/u_v^2 k\Delta T$
$G$ = $(\Delta Tk/\mu h_{fg})\,(\rho\mu/\rho_v\mu_v)^{1/2}$
$g$ = specific force of gravity
$h_{fg}$ = specific enthalpy of evaporation
$k$ = thermal conductivity of condensate
$l$ = effective length of condenser tube
Nu = vapor-side Nusselt number, $Qd/k\Delta T$
$\mathrm{Nu}_c$ = coolant Nusselt number
$\mathrm{Pr}_c$ = coolant Prandtl number
$p$ = pitch of fins
$Q$ = heat flux $Q_T/(\pi dl)$
$Q_T$ = heat transfer rate to coolant
$R$ = radius at fin tip
$\mathrm{Re}_c$ = coolant Reynolds number
$\tilde{\mathrm{R}}\mathrm{e}$ = two-phase Reynolds number, $u_v\rho d/\mu$
$T_{\mathrm{in}}$ = coolant inlet temperature
$T_{\mathrm{out}}$ = coolant outlet temperature
$T_o$ = outside surface temperature of plain tube, temperature at base of fins for finned tube
$T_v$ = vapor temperature
$U$ = overall heat transfer coefficient for finned tube referred to surface at diameter $d$, $Q/\Delta T_{\mathrm{lm}}$
$U_p$ = overall heat transfer coefficient for plain tube referred to outside surface
$u_c$ = coolant velocity
$u_v$ = vapor velocity
$\alpha$ = vapor-side heat transfer coefficient, $Q/\Delta T$
$\alpha_p$ = vapor-side heat transfer coefficient for plain tube
$\Delta T$ = $T_v - T_o$
$\Delta T_{\mathrm{lm}}$ = vapor-to-coolant logarithmic mean temperature difference, $(T_{\mathrm{out}} - T_{\mathrm{in}})/\ln[(T_v - T_{\mathrm{in}})/(T_v - T_{\mathrm{out}})]$
$\theta$ = half angle at fin tip, i.e. inclination of fin surface to plane perpendicular to tube axis
$\mu$ = viscosity of condensate
$\mu_c$ = viscosity of coolant at $(T_{\mathrm{in}} + T_{\mathrm{out}})/2$
$\mu_{cw}$ = viscosity of coolant at inside wall temperature
$\mu_v$ = viscosity of vapor
$\rho$ = density of condensate
$\rho_v$ = density of vapor
$\sigma$ = surface tension
$\phi$ = circumferential angle from upper edge of tube to position at which interfin space becomes full of condensate

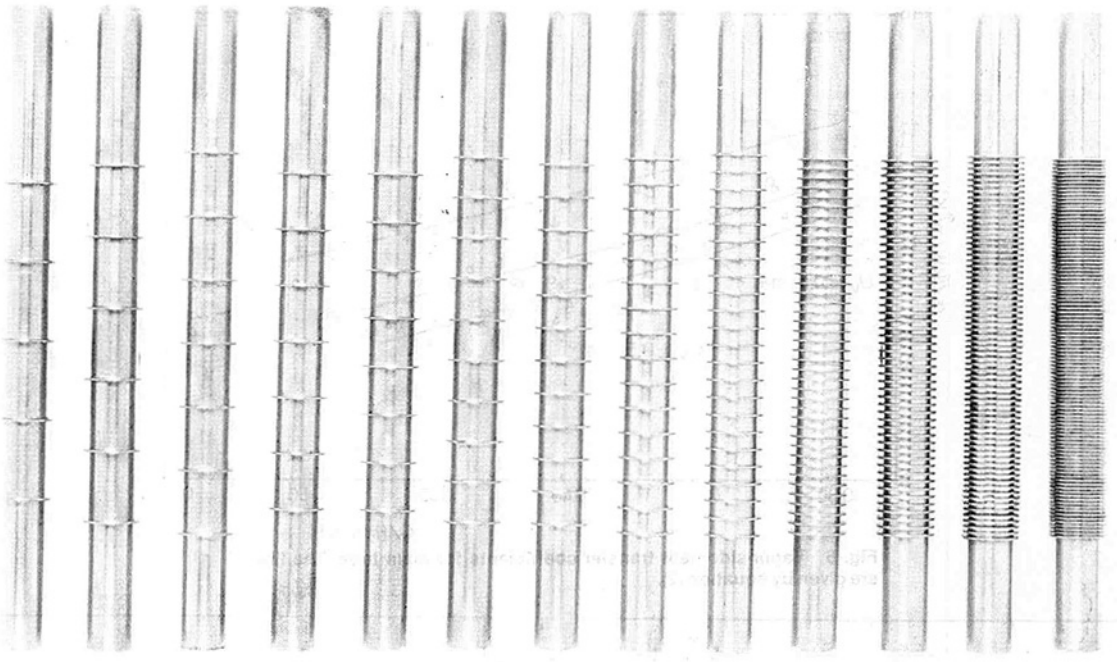

Fig. 3 Condenser tubes

condenser tube and coolant inlet and exit ducts were well insulated from the body of the test section and from the environment by nylon components as shown. The coolant temperature was observed at inlet and exit by thermocouples in closed-ended closely fitting copper tubes, the exit thermocouple being located after a nylon mixing section.[1] All thermo-emfs were observed with a digital voltmeter reading to 1 $\mu$V. That the isothermal immersion of the thermocouples was adequate was checked by withdrawing the junctions by 1 or 2 cm. No change in the thermo-emf was found.

The test condenser tubes, shown in Fig. 3, were of copper with internal diameter 9.78 mm and effective length, i.e., length exposed to steam, of 102 mm. The outside diameter of the plain tube was 12.7 mm. The diameter at the root of the fins was also 12.7 mm, and the fin height and thickness were 1.6 mm and 0.5 mm, respectively. Fin spacings of 0.5, 1, 1.5, 2, 4, 6, 8, 10, 12, 14, 16, 18, and 20 mm were used.

To ensure film condensation, the tubes and ptfe bushes were first thoroughly cleaned with hot detergent solution using a clean cloth and bristle brush. After rinsing with distilled water, they were again cleaned using ethyl alcohol and sodium hydroxide in water at about 80°C (as in [11]). The solution was prepared by mixing equal volumes of ethyl alcohol and an aqueous solution of sodium hydroxide. The concentration of the latter was that required to saturate the alcohol at 80°C. The tubes and bushes were finally rinsed with distilled water and assembled in the test section. This procedure always gave film condensation which persisted throughout the 3- to 4-hr period of testing.

The heat transfer rate to the condenser tube was calculated from the mass flow rate, obtained by a float-type flow meter, and temperature rise of the coolant. The vapor mass flow rate and hence velocity at the test section was obtained from the input power to the boiler by applying a steady flow energy balance between the boiler inlet and the test section. A correction for the relatively small thermal losses from the apparatus was incorporated. The losses were established in preliminary tests in which the minimum power required to provide vapor at the test section was determined. The mass fraction of noncondensing gas (taken to be air) as estimated from pressure and temperature measurements, was $\pm 0.005$, i.e., zero to within the precision of the determination. The accuracy with which the coolant mass flow rate, temperature rise, and the temperature of the vapor were measured indicates an accuracy in the overall heat transfer coefficient better than 5 percent.

[1] The thermocouple calibration procedure and precautions taken to ensure accurate temperature measurements were the same as those described in [10].

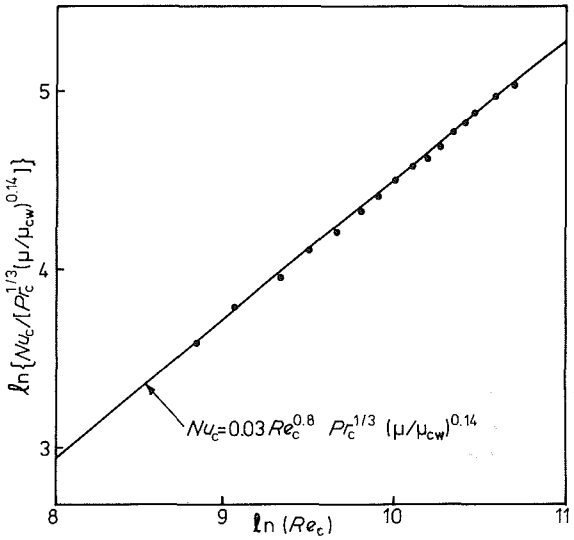


Fig. 4 Coolant-side correlation [12]

## Results

For all tubes, sets of measurements were made at atmospheric pressure and three different boiler heater power inputs. Apart from small variations due to changes in supply voltage, atmospheric pressure, and condensate return temperature, this gave essentially three vapor velocities at the test section, nominally 0.5 m/s, 0.7 m/s, and 1.1 m/s. For each boiler input power, tests were carried out for several coolant flow rates, giving a range of coolant velocities of 1 to 4.5 m/s.

**Coolant-Side Heat Transfer Coefficient.** Figure 4 shows coolant-side data taken in an earlier investigation [12], using essentially the same apparatus but with thermocouples em-

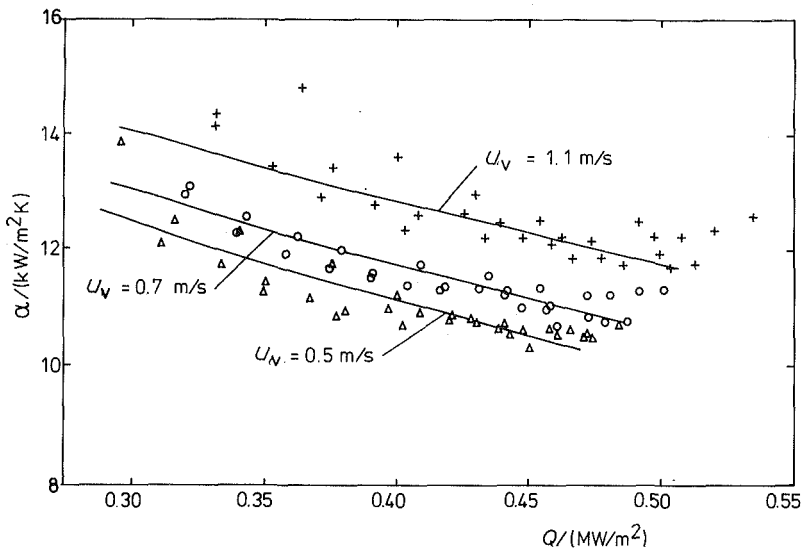


**Fig. 5 Vapor-side heat transfer coefficients for plain tube. The lines are given by equation (2).**

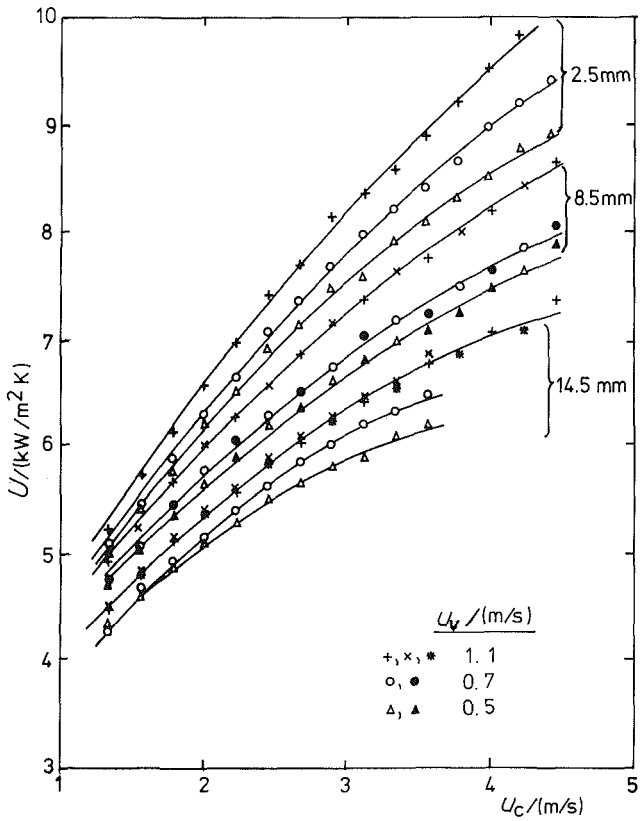


**Fig. 6 Overall heat transfer coefficients for three finned tubes. The fin pitch is indicated on the curves. Different symbols denote tests performed on different occasions.**

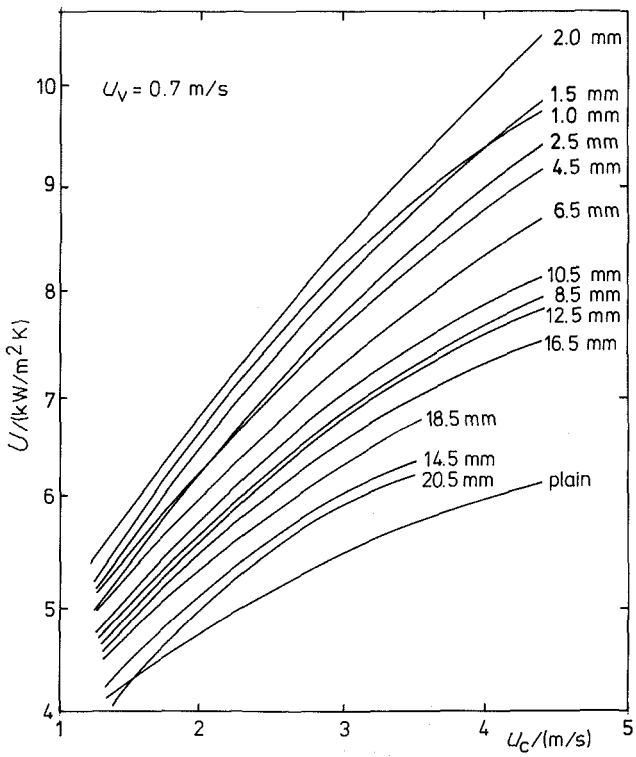


**Fig. 7 Overall heat transfer coefficients for all finned tubes. The fin pitch is indicated on the curves. The lines are quadratic fits to the data.**

bedded in the wall of a plain condenser tube. It may be seen that these data, which cover the same range of coolant conditions as used in the present work, are very well correlated by

$$\mathrm{Nu}_c = 0.03\mathrm{Re}_c^{0.8}\mathrm{Pr}_c^{1/3}(\mu_c/\mu_{cw})^{0.14} \quad (1)$$

Equation (1) was used in the present investigation to determine coolant-side coefficients for all tubes.

**Plain Tube.** In Fig. 5, vapor-side coefficients found by subtracting the wall and coolant-side resistances from the measured overall resistance are compared with the theoretical results of Shekriladze and Gomelauri [13]

$$\mathrm{Nu}\tilde{\mathrm{R}}\mathrm{e}^{-1/2} = 0.64[1+(1+1.69F)^{1/2}]^{1/2} \quad (2)$$

It is evident from Fig. 5 that the present data are in satisfactory agreement with equation (2). (There are significant uncertainties regarding the problem of forced-convection condensation but, for the present ranges of the parameters $F$ (3.2–21.2) and $G$(4.4–7.9), good agreement with equation (2) has been found by other workers (see [14]).

**Finned Tubes.** Overall coefficients for three of the finned tubes are given in Fig. 6. It may be seen that the data are smooth and consistent. It is clear that fin pitch has a strong effect on the overall heat transfer coefficient. The effect of vapor velocity is also evident for each tube. The lines shown in Fig. 6 are quadratic least-squares fits. Similar sets of data were obtained for all of the finned tubes. In Fig. 7 the fitted

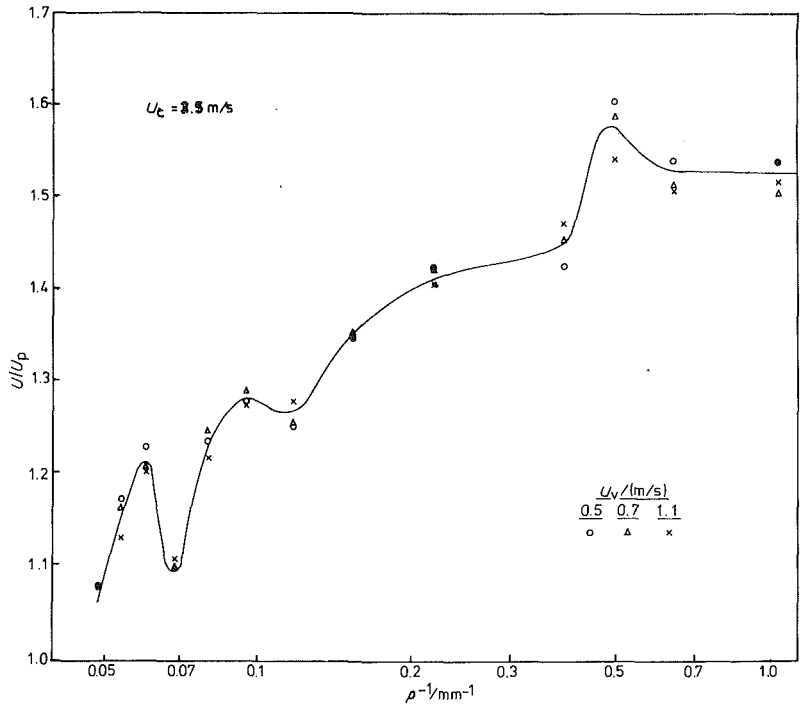


**Fig. 8 Dependence of overall coefficient enhancement ratio on fin density**

lines are shown for all tubes for a vapor velocity of 0.7 m/s. Similar results were obtained for the other vapor velocities. Somewhat lower coefficients were found at a vapor velocity of 0.5 m/s, and somewhat higher values were obtained at 1.1 m/s. Examination of Fig. 7 shows that while there is a general trend towards higher overall heat transfer coefficients with increasing fin density (smaller pitch), the dependence of coefficient on pitch is not monotonic. At lower fin density it may be seen that the coefficient for a pitch of 14.5 mm is significantly less than that for a pitch 16.5 mm. At high fin density, the tube with a fin pitch of 2 mm gave a higher overall coefficient than for the 1.5 mm and 1.0 mm pitch tubes. The general features indicated above are illustrated in Fig. 8, which shows, for a coolant velocity of 3.5 m/s, the dependence on fin density (reciprocal pitch) of the ratio of overall heat transfer coefficient to the plain tube value. Since the coolant and vapor conditions were not precisely the same in all cases, the values of $U_p$ used in the enhancement ratio were not measured values but rather were calculated, for the same vapor temperatures and coolant flow rate and inlet temperature as obtained with a finned tube, on the basis of equations (1) and (2). As noted earlier, this procedure gave excellent agreement with plain tube measurements.

For the low fin densities, the overall coefficients appeared to be related to the mode of drainage of the condensate from the tube, relatively high values being found when the condensate droplets departed from the fins and relatively low values when the departing droplets formed between the fins. Since the enhancement at low fin density was relatively small, detailed visual studies were not made. At the higher fin densities, the lower part of the tube was flooded and the condensate departure pattern was apparently as for the plain tube. At the highest fin densities much or all of the interfin space was filled with condensate. This is thought to be the reason for the falloff on overall coefficient enhancement for fin spacing less than 1.5 mm (fin densities greater than 0.5 mm$^{-1}$).

It is evident from the observed enhancement of the overall coefficient (by factors exceeding 1.5) that the finned tubes gave substantial vapor-side enhancement. For the plain tube

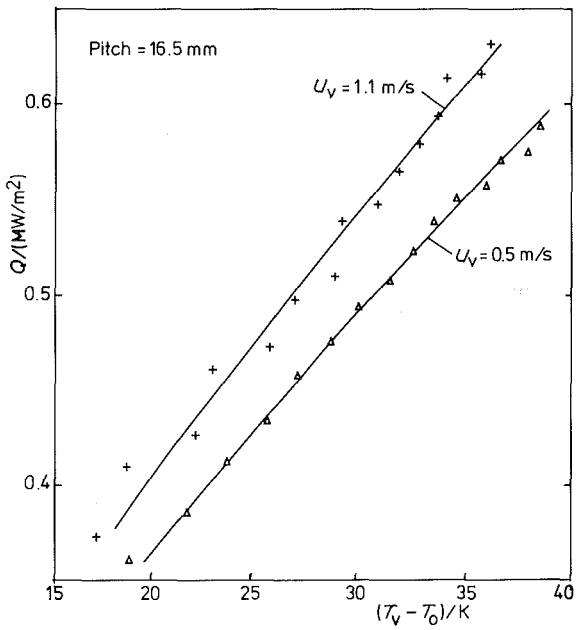


**Fig. 9 Dependence of vapor-side temperature difference on heat flux for finned tube. The lines are fits of the form $Q = a(T_V - T_O)^{0.72}$.**

the proportion of the vapor-to-coolant resistance on the vapor side varied between 30 percent at low coolant velocity, to about 55 percent at high coolant velocity.

Vapor-side heat transfer coefficients for the finned tubes were calculated by subtracting the coolant-side (using equation (1)) and wall resistances from the measured overall resistance. The tube wall was regarded as extending to the root of the fins so that the effects of the fins and condensate are lumped together in the vapor-side heat transfer coefficient. Figure 9 shows the relation between the vapor-side temperature difference and the heat flux for one of the finned tubes at two vapor velocities. Similar smooth curves were found for all tubes and for all vapor velocities. In order to

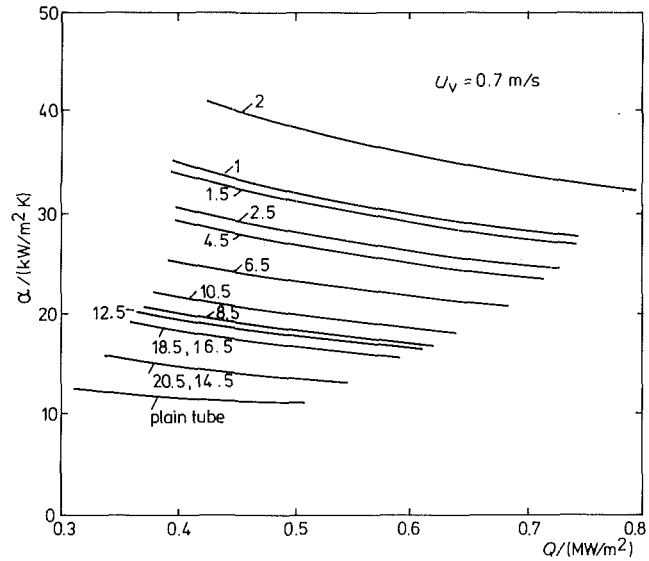


Fig. 10 Dependence of vapor-side heat transfer coefficient on heat flux for all finned tubes. The lines are curve fits to the experimental data (see text). Fin pitch/mm is indicated on the curves.

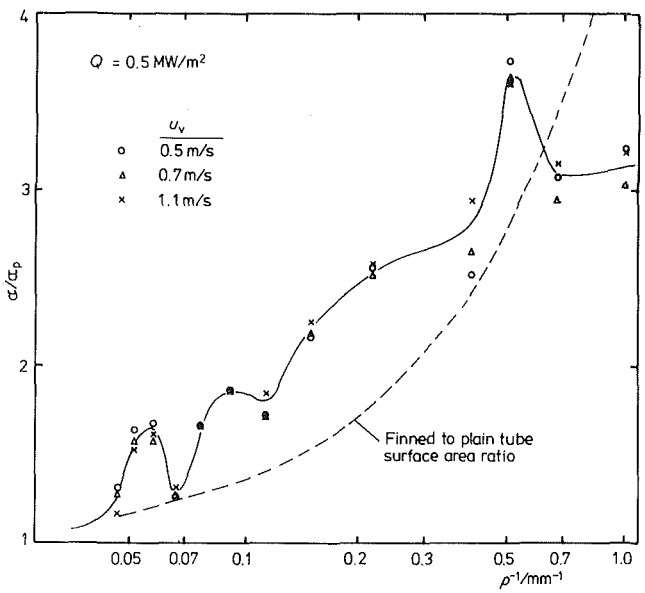


Fig. 11 Dependence of vapor-side enhancement ratio on fin density

make comparisons between the tubes for the same heat flux (condensation rate), the $Q - \Delta T$ curves were fitted[2] by least-squares to equations of the form $Q = a\Delta T^n$ (Nusselt theory would give $n = 0.75$). Extremely good fits were obtained with values of $n$ varying in the range 0.64 to 0.86 with no systematic dependence on fin pitch. It was found that the fits were only marginally less good when adopting a mean value for $n$ of 0.72 for all tubes and redetermining the values of $a$. The lines shown in Fig. 9 are typical of the fits thus found. Similar results were found for all tubes and all three vapor velocities.

The fitted lines for all tubes, for a vapor velocity of 0.7 m/s, are shown in Fig. 10 on an $\alpha$–$Q$ basis, i.e., the lines are given by $\alpha = a^{1/n}Q^{(n-1)/n}$ where $n = 0.72$, and the values of $a$ are those from the $Q - \Delta T$ least-squares fits. Similar results were found for the other vapor velocities.

Figure 11 shows the dependence of vapor-side enhancement (vapor-side coefficient divided by the plain tube value) on fin density for a heat flux of 0.5 MW/m$^2$ (which falls within the experimental range of all tubes). The same general trends as those exhibited by the overall enhancement, given in Fig. 8, may be seen. Note that in Fig. 8 the overall enhancement is calculated for a given coolant flow rate while the vapor-side enhancement (Fig. 11) is for given heat flux. It may be seen from Fig. 11 that the vapor-side enhancement generally increases with increase in fin density but, as in Fig. 8, peaks and troughs are evident at low fin density and a relatively sharp peak occurs at a fin density of 0.5 mm$^{-1}$ (pitch 2 mm, interfin space 1.5 mm) where the vapor-side enhancement was around 3.7. It may be seen from Fig. 10 that the vapor-side enhancement decreases somewhat with increasing heat flux. Extrapolation outside the experimental heat flux ranges for the 2.0 mm pitch tube and the plain tube suggests vapor-side enhancements of around 4 and 3 for heat fluxes of 0.3 MW/m$^2$ and 0.8 MW/m$^2$, respectively.

A detailed analysis of a static liquid film on a finned surface has been given by Honda et al. [4]. The extent of retained condensate in the interfin space is given by

$$\phi = \cos^{-1}\left(\frac{2\sigma\cos\theta}{\rho g b R} - 1\right) \tag{3}$$

[2]Note that $Q$–$\Delta T$ curve fits are used rather than $\alpha$–$Q$ or $\alpha$–$\Delta T$, since the absolute error in $\Delta T$ is presumed approximately uniform whereas the error in $\alpha$ increases with decreasing $\Delta T$.

where $\phi$ is the angle measured circumferentially from the upper edge of the tube to the position at which the interfin space becomes full of condensate. Equation (3) is valid provided the fin height is greater than or equal to $b(1 - \sin\theta)/2\cos\theta$.

For plane-sided fins $\theta = 0$, and equation (3) becomes

$$\phi = \cos^{-1}\left(\frac{2\sigma}{\rho g b R} - 1\right) \tag{4}$$

Equation (4) has also been obtained independently by Owen et al. [7]. The simple argument used in [7] however appears to be based on an incorrect model of the condensate drainage at the lower edge of the tube. An approximate model used by Rudy and Webb [5] also leads to equation (4) when the fin height is large compared with the fin width.

For the best-performing tube in the present work ($b = 1.5$ mm), equation (4) gives $\phi = 82$ deg. This is roughly in line with the appearance of the tube noted during the heat transfer measurements. For the tube diameter and fin section used in the present work, equation (4) indicates that the whole of the interfin space just becomes filled with liquid ($\phi = 0$) for a fin density of 0.74 mm$^{-1}$. As may be seen in Fig. 11, the vapor-side enhancement at this fin density is appreciably less than the maximum enhancement which occurred at the smaller fin density of 0.5 mm$^{-1}$.

## Concluding Remarks

For the finned tubes, significant improvement, exceeding that to be expected on grounds of area increase, in overall coefficient has been obtained, even for low fin densities.

At low fin density, the enhancement was lower than might have been expected in the light of vertical tube data [8, 9]. The sensitivity of the enhancement ratio to pitch at low fin density may be associated with the fact that the fin pitch was of similar magnitude to the Taylor instability wavelength, the appropriate value of which would appear to be $\pi(8\sigma/\rho g)^{1/2}$ [15]. For water at 75°C, this quantity is equal to 23 mm.

At higher fin densities the heat transfer enhancement generally increased with increasing fin density, apparently reaching a maximum for a fin density of 0.5 mm$^{-1}$. For the highest fin densities used (0.7 mm$^{-1}$ and 1.0 mm$^{-1}$) the enhancement obtained was roughly in line with, or perhaps somewhat lower, than that expected on grounds of area increase only, suggesting that most or all of the interfin space

was filled with condensate as would be predicted by equation (4).

A general procedure for calculating the vapor-side heat transfer coefficient would seem to be:

(*a*) Use the approach of Honda et al. [4], to determine $\phi$.

(*b*) For the lower portion of the tube (angles $> \phi$) use an approach along the lines of single-phase flow over finned tubes.

(*c*) For the upper part of the tube (angles $< \phi$), the analysis must include the effect of surface tension on the condensate film flow on and between the fins.

It is considered that (*b*) should not pose too great a problem and theoretical results could be validated by experiments using tube geometries and fluids so that the whole of the interfin space was flooded, i.e., so that $\sigma/\rho gbR > 1.0$ as for the present steam data for the tube with the highest fin density ($1.0\ \text{mm}^{-1}$).

The procedure outlined in (*c*) presents an extremely complex problem, where pressure gradients, due to surface tension and varying surface curvature, play an important role in the three-dimensional flow of the condensate film. Aproaches to this problem have been made in recent years [16–21].

It is considered that more data are required for different fin widths and heights, different tube diameters, and different fluids before useful comparisons with proposed theoretical results can be made. The present data, for one geometry and fluid, suggest that vapor velocity does not have a strong effect on enhancement for the limited velocity range used, i.e., vapor velocity has roughly proportionately the same effect on finned and plain tubes. The effect of condensation rate (heat flux) on enhancement was also rather weak, although in the present case it must be noted that the vapor-side coefficients are increasingly less accurate at lower heat flux since the coolant side increasingly dominates the overall heat transfer coefficient (from which the vapor-side coefficient is determined) with decreasing coolant flow rate.

## References


1 Beaty, K. O., and Katz, D. L., "Condensation of Vapors on Outside of Finned Tubes," *Chem. Eng. Prog.*, Vol. 44, No. 1, 1948, pp. 55–70.

2 Gregorig, R., "Hautkondensation on feingewellten Oberflächen bei Berücksichtigung der Oberflächenspannungen," *Z. Angew. Math. Phys.*, Vol. 5, 1954, pp. 36–49.

3 Rudy, T., and Webb, R. L., "Condensate Retention on Horizontal Integral-Fin Tubing," *Advances in Heat Transfer*, Vol. HTD-IS, ASME, New York, 1981, pp. 35–41.

4 Honda, H., Nozu, S., and Mitsumori, K., "Augmentation of Condensation on Horizontal Finned Tubes by Attaching a Porous Drainage Plate," *Proc. ASME-JSME Thermal Engineering Joint Conference*, Honolulu, Vol. 3, 1983, pp. 289–296.

5 Rudy, T. M., and Webb, R. L., "An Analytical Model to Predict Condensate Retention on Horizontal, Integral-Fin Tubes," *Proc. ASME-JSME Thermal Engineering Joint Conference*, Honolulu, Vol. 1, 1983, pp. 373–378.

6 Rudy, T. M., and Webb, R. L., "Theoretical Model for Condensation on Horizontal Integral-Fin Tubes," *AIChE Symp. Ser. No. 225*, Vol. 79, 1983, pp. 11–18.

7 Owen, R. G., Sardesai, R. G., Smith, R. A., and Lee, W. C., "Gravity-Controlled Condensation on a Horizontal Low-Fin Tube," *Condensers: Theory and Practice*, Inst. Chem. Engrs. Symp. Series 75, 1983, pp. 415–428.

8 Thomas, D. G., "Enhancement of Film Condensation Rates on Vertical Tubes by Vertical Wires," *Ind. Eng. Chem. Fund.*, Feb. 1967, pp. 97–102.

9 Thomas, D. G., "Enhancement of Film Condensation Rate on Vertical Tubes by Longitudinal Fins," *AIChE Journal*, July 1968, pp. 644–649.

10 Le Fevre, E. J., and Rose, J. W., "An Experimental Study of Heat Transfer by Dropwise Condensation," *International Journal of Heat and Mass Transfer*, Vol. 8, 1965, pp. 1117–1133.

11 Marto, P., private communication.

12 Stylianou, S. A., "Laminar Film Condensation of Flowing Vapour on a Horizontal Tube," Project Report, Department of Mechanical Engineering, Queen Mary College, London, 1975.

13 Shekriladze, I. G., and Gomelauri, V. I., "Theoretical Study of Laminar Film Condensation of a Flowing Vapour," *International Journal of Heat and Mass Transfer*, Vol. 9, 1966, pp. 581–591.

14 Lee, W. C., "Filmwise Condensation on a Horizontal Tube in the Presence of Forced Convection and Noncondensing Gas," Ph.D. thesis, University of London, 1982.

15 Yung, D., Lorenz, J. J., and Ganic, E. N., "Vapor/Liquid Interaction and Entrainment in Falling Film Evaporators," ASME JOURNAL OF HEAT TRANSFER, Vol. 102, 1980, pp. 20–25.

16 Hirasawa, S., Hijikata, K., Mori, Y., and Nakayama, W., "Effect of Surface Tension on Laminar Film Condensation (Study of Condensate Film in a Small Groove)," JSME *Transactions*, Vol. 44, 1978, pp. 2041–2048.

17 Hirasawa, S., Hijikata, K., Mori, Y., and Nakayama, W., "Effect of Surface Tension on Laminar Film Condensation Along a Vertical Plate With Small Leading Radius," *Proc. 6th Int. Heat Transfer Conf.*, Vol. 2, 1978, pp. 413–418.

18 Fujii, T., and Honda, H., "Laminar Filmwise Condensation on a Vertical Single-Fluted Plate," *Proc. 6th Int. Heat Transfer Conf.*, Vol. 2, 1978, pp. 419–424.

19 Mori, Y., Hijikata, K., Hirasawa, S., and Nakayama, W., "Optimised Performance of Condensers With Outside Condensing Surface," *Condensation Heat Transfer*, ASME, New York, 1979, pp. 55–62.

20 Panchel, C. B., and Bell, K. J., "Analysis of Nusselt-Type Condensation on a Vertical Fluted Surface," *Condensation Heat Transfer*, ASME, New York, 1979, pp. 45–54.

21 Hirasawa, S., Hijikata, K., Mori, Y., and Nakayama, W., "Effect of Surface Tension on Condensate Motion in Laminar Film Condensation (Study of Liquid in a Small Trough)," *International Journal of Heat and Mass Transfer*, Vol. 23, 1980, pp. 1471–1478.

**T. Nosoko**
Graduate Student.

**Y. H. Mori**
Associate Professor.

Department of Mechanical Engineering,
Keio University,
3-14-1 Hiyoshi, Kohoku-ku,
Yokohama 223, Japan

# Vaporization of Drops of a Denser, Volatile Liquid Dropped Onto a Surface of Another Liquid

*Experiments were performed with single R 113 ($C_2CI_3F_3$) drops dropped onto the surface of immiscible ethylene glycol or water, or miscible n-tridecane in contact with the common vapors of the two liquids. Five different vaporization modes were distinguished in the immiscible systems: film boiling on the surface, film boiling in the bulk (only in R 113/ethylene glycol system), and three other modes in which the two liquids make direct contact. The latter three were replaced, in the miscible system, by an immediate dissolving of drops into the medium. The details of dynamic process in each mode have been revealed with the aid of high-speed cinephotography. Operational conditions required for the occurrence of respective modes and heat transfer characteristics in those modes have also been discussed.*

## Introduction

Thermal interaction between two liquids resulting in the evaporation of the more volatile one has an importance in relation to the development of direct contact evaporators for, for example, water desalination systems, geothermal power plants, industrial waste heat recovery systems, etc., and to vapor explosion in the event of possible accident in some industries. Various configurations are possible in supplying the two liquids in contact with each other. One configuration, which shows promise for some applications, involves spraying drops of a volatile liquid over the surface of another hotter, less-volatile liquid. The volatile liquid may be a lower hydrocarbon or a fluorocarbon refrigerant while the hot liquid is a geothermal brine. It may also be seawater which is to be sprayed onto a hot mineral oil. Thus, the drops may either be lighter or denser than the hot substrate liquid. The case of denser drops is of particular interest in the present study.

The mode of vaporization of the drops after their impingement on the surface will depend on many factors: the properties of the two liquids, temperature excess of the substrate liquid over the saturation temperature of the volatile liquid, initial drop temperature, drop size, velocity of impingement, etc. The most favorable mode for geothermal and other applications may be one which we call "lens evaporation" in which a drop evaporates taking the form of a lens floating on the surface. This is the mode that some researchers [1–4] have exclusively studied, with *n*-pentane or isopentane drops dropped onto water surface, considering such applications. Waldram et al. [5] found, with drops of several kinds of liquids dropped onto a silicone oil surface, that drops could make a direct contact with the surface only when the drop release height was higher than a critical height which was particular to each liquid combination. When the release height was lower, there occurred invariably another mode in which drops evaporated slowly, being separated from the substrate liquid by a vapor film. This mode has been called by some researchers "Leidenfrost boiling," "film boiling," or "Leidenfrost film boiling" based on an analogy with the Leidenfrost phenomenon on a solid surface. We call it hereafter "surface film boiling," however, for the sake of contrast with another type of film boiling. Observations of this kind were then performed by Ochiai and Bankoff [6, 7].

Iida and Takashima [8, 9] observed vaporization processes of single drops of *n*-pentane, dichloromethane, acetone, and methylalcohol dropped onto a silicone oil surface. They gave a rather complicated scheme for vaporization modes involved in those processes. Of particular interest in their results may be the photographic demonstration [8] of a phenomenon which we call hereafter "submerged film boiling"; that is, a drop (particularly a drop of dense dichloromethane) evaporates, being enveloped with a vapor shell in the bulk of the substrate liquid. To our knowledge, this was the first revelation to us of the existence of submerged film boiling though it has been frequently assumed, with little physical justification, in literature dealing with vapor explosion (e.g., [10, 11]) or direct contact evaporation operation (e.g., [12, 13]). The finding by Iida and Takashima may be somewhat confusing in view of another fact: As has been demonstrated clearly by some researchers [14–16], liquid drops suspended in an immiscible, less-volatile liquid never exhibit film boiling even if they are heated up to their superheat limit. This seeming contradiction will be accounted for with the aid of our experimental results.

Similar experiments were carried out by Akiyama [17] with drops of fluorocarbon refrigerant R 113 ($C_2Cl_3F_3$) dropped onto a surface of glycerol maintained at a fairly large temperature excess (60 to 190 K) above the boiling point of R 113. He mentioned seven vaporization modes that he classified. Some of them seem to correspond to the ones reported by Iida and Takashima [8, 9].

In the present work, we attempted to recognize the dynamic process of vaporization of each isolated drop with the aid of high-speed cinephotography. We employed R 113 as the volatile liquid for drops, and ethylene glycol, water, and *n*-tridecane alternately as the hot substrate liquid. The R 113/water system is one of the promising systems for practical applications [18]. Ethylene glycol has a lower surface tension than water, and thus drops more easily penetrate into the bulk breaking through the free surface; this is favorable for detailed observation of various vaporization modes. *n*-Tridecane, which is well miscible with R 113, has such an advantage that we can recognize any liquid–liquid contact in the vaporization process by the consequent mutual dissolving. The temperature difference between the two liquid phases was limited to moderate levels ($\lesssim$ 30 K) considering the most probable operating conditions of direct contact evaporators.

## Experimental

In order to ensure detailed observation of each drop vaporizing in an environment simulating that in direct contact evaporators, experiments were so designed that single isolated

Contributed by the Heat Transfer Division for publication in the JOURNAL OF HEAT TRANSFER. Manuscript received by the Heat Transfer Division January 5, 1984.

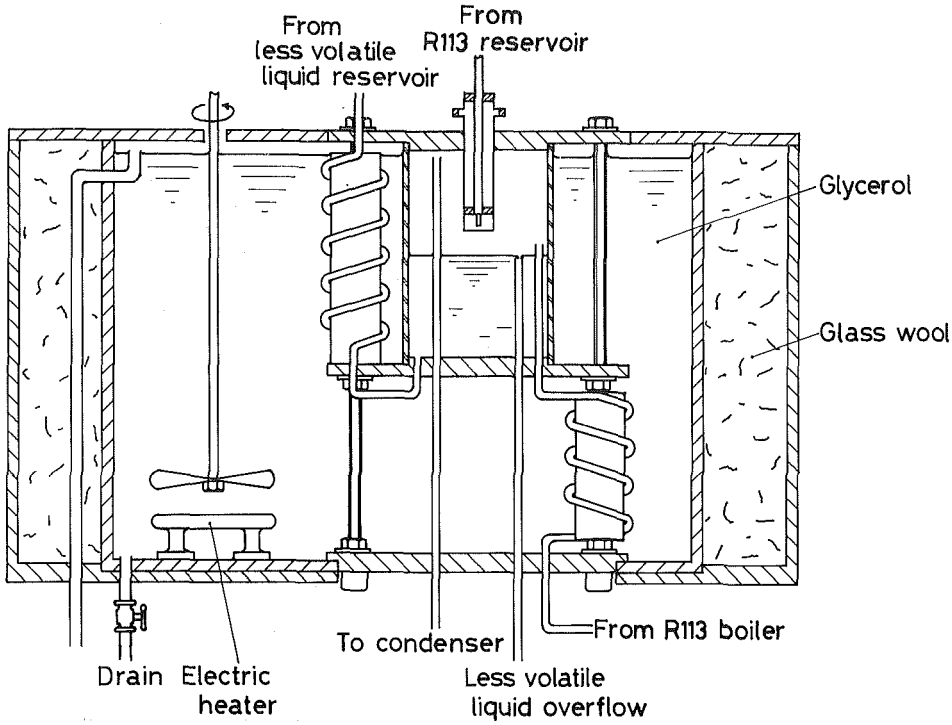


**Fig. 1 Schematic of experimental apparatus**

drops of saturated liquid R 113 were dropped onto the surface of a stagnant, or at least approximately stagnant, substrate liquid through a space filled with common vapors of R 113 and the substrate-liquid substance. In this aspect, our experimental scheme bears some similarity to that of Bentwich et al. [1] and is distinguished from those of others [2–9, 17] in which drops were released in the air held over a substrate liquid and thus they were permitted to evaporate not only by heat supply from the substrate liquid but also due to a vapor pressure gradient in the air unless drops were submerged completely beneath the surface of the substrate liquid.

The main portion of the experimental apparatus is illustrated schematically in Fig. 1. The test vessel was fabricated of a circular pipe of Pyrex glass, 55 mm i.d. and 200 mm in height, and two Bakelite plates closing respectively the top and bottom ends of the pipe. Inserted into the vessel from outside were a nozzle for producing R 113 drops and four Pyrex glass tubes for supplying and draining the substrate liquid and R 113 vapor. The vessel was perfectly sealed from the surrounding glycerol bath as well as from the ambient air by use of Viton O-rings at all junctions. The lower half of the space in the vessel was filled with the substrate liquid, while the other half was filled with common vapors of R 113 and the substrate-liquid substance. The R 113 vapor was supplied into the vessel, at a flow rate of 0.1 to 1 $cm^3/s$, from an all-Pyrex-glass boiler situated outside through a Pyrex glass spiral tube immersed in the glycerol bath to be superheated to some extent. Only when *n*-tridecane was used as the substrate liquid, fresh liquid was continuously supplied to the vessel at a flow rate of 0.01 to 0.1 $cm^3/s$ to prevent a change in properties of the substrate liquid in the vessel due to dissolving of R 113 vapor and, to much lesser extent, of drops dropped onto the liquid surface. The concentration of dissolved R 113 in the substrate liquid was found to vary between 10 and 45 wt. % depending on the sysem temperature.

The nozzle for producing drops had a special structure as illustrated in Fig. 2. The Pyrex glass capillary tube through which R 113 liquid was to be fed was prepared in triplicate with different tip diameters for alternate use; this enabled producing drops with three levels of diameter ranging from 1.2 to 2.8 mm. Outside the capillary tube was a bath of boiling R 113 liquid to control the liquid temperature in the capillary tube to the saturation temperature of R 113. The R 113 vapor generated in the bath was fed down through Teflon tubes immersed in the bath into the bottom chamber enclosing the capillary tip. This device prevented condensation of the vapor of the substrate-liquid substance on the nozzle tip as well as on drops during their formation. The distance between the substrate liquid surface and the nozzle tip, which is simply called drop release height in this paper, was varied in a range between 5 and 60 mm.

Before every experiment R 113 vapor was supplied to the test vessel over 5 h to minimize the amount, if any, of residual air. The interval of drop release onto the surface was regulated to three minutes or more to minimize the trace of thermal and hydrodynamic disturbances caused by former drops to the substrate liquid.

The temperature in the substrate liquid was always the lowest at the surface. Its deviation from the bulk temperature $T_\infty$ was less than 2 K in every run, while $T_\infty$ was kept constant with fluctuation less than $\pm$ 0.5 K. For convenience $T_\infty$ was employed as the reference temperature of the substrate liquid. The temperature in the vapor phase was not uniform particularly because of continuous flooding of nearly saturated vapor of R 113 from the bottom chamber of the nozzle. There was a vertical temperature distribution in the vapor phase, the highest temperature being on the substrate liquid surface.

## Nomenclature

$D_0$ = initial value of equivalent spherical diameter of drop

$h$ = drop release height above the surface of substrate liquid

$T_\infty$ = bulk temperature in substrate liquid

$t_v$ = time required for complete evaporation of drop

Liquid samples used in addition to water were R 113, ethylene glycol and *n*-tridecane of certified purities of 99.9, 95.0, and 99.0 wt. %, respectively. Water was taken from a commercial deionization-distillation apparatus. Listed in Table 1 for reference are densities, saturation temperatures under atmospheric pressure, and vapor pressures at 47.6°C (saturation temperature of R 113 under atmospheric pressure) of the above liquids.

## Results and Discussion

**Vaporization Modes in R 113/Ethylene Glycol System.** We have identified five different vaporization modes based on observations with the naked eye and with high-speed cinephotography. In general, each drop of R 113 released onto the ethylene glycol surface is expected to show any of these modes with the probability depending on the drop diameter $D_0$, drop release height $h$, and the temperature of ethylene glycol. Typical sequences in respective modes are schematically illustrated in Fig. 3 for brief description of their primary features. Some additional explanations are given below.

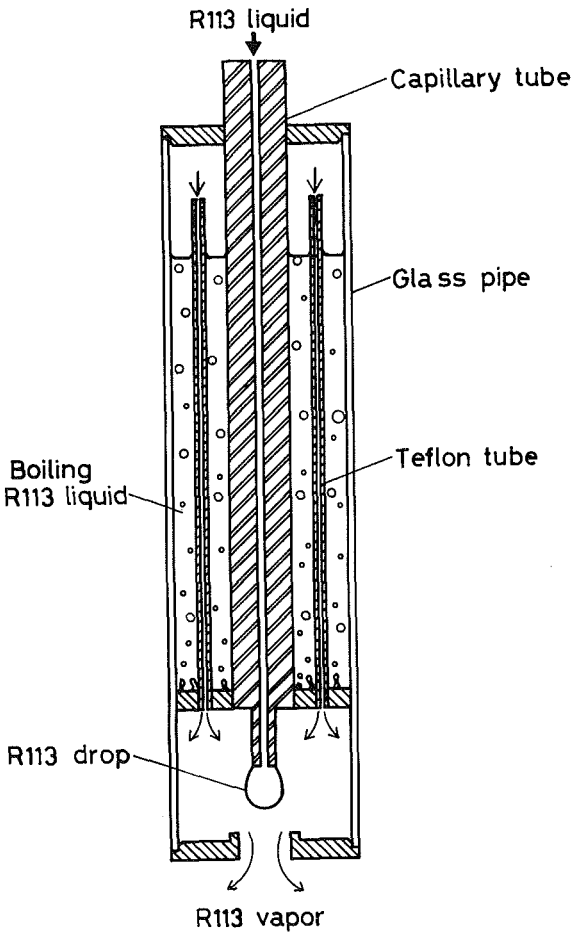


Fig. 2 Structure of the nozzle for producing R 113 drops

*Mode a.* This mode is characterized by the surface film boiling which is in general not new. However, we have noticed a peculiar behavior of drops in the surface film boiling state. Each drop was gradually opalized while exhibiting a small shape oscillation, and as its diameter reduced approximately to 1/4 of its initial value, it suddenly disappeared leaving on the surface a tiny spherical droplet (~ 0.1 mm diameter) or a lens which vanished within another several seconds.[1] We present here a hypothetical explanation on the above observation. Because of the drop surface temperature being lower than the surface temperature of the substrate liquid, some ethylene glycol molecules in the vapor phase presumably condense on the drop surface; this would change the clear R 113 drop to an opaline ethylene glycol-in-R 113 emulsion drop.[2] As the fraction of ethylene glycol in the drop increases to a certain level, the emulsion would break resulting in an immediate coalescence of the ethylene glycol with the substrate liquid and a release of a tiny droplet of residual R 113.

*Mode b.* This mode is primarily characterized by the submerged film boiling state (stages 5 and 6 in Fig. 3). The whole process of the submerged film boiling from its formation to its breakup is demonstrated in a series of photographs given in Fig. 4. Following the impingement on the surface, a drop penetrates into the substrate liquid dragging on itself a vapor film (recognized on photographs as a bold black bordering between the drop and the surrounding) and forming a funnel-shaped cavity behind. In this process the drop elongates in a vertical direction and, in most cases, disintegrates into two parts (stage 4 in Fig. 3). This is succeeded by a closure of the cavity throat, which leaves the lower one of disintegrated drops in the bulk of liquid in the state of submerged film boiling and the other drop on the free surface in the state of surface film boiling. As the former drop rises to the free surface and then bursts there, there appears one of the following states: ($\alpha$) surface film boiling just the same as that in mode *a*, ($\beta$) lens evaporation just as observed in mode *e*, ($\gamma$) disintegration of the drop into two parts, one in the form of a lens and the other in a free fall through the substrate liquid, and ($\delta$) fragmentation of the drop into several parts in various forms. Our observations as described above suggest that the formation of a submerged film boiling state, which was first demonstrated by Iida and Takashima [8], essentially depends on the vapor phase being present in advance between a drop and the substrate liquid and on the relatively low rate of drainage of the vapor while the two liquid phases approach each other. In other words, submerged film boiling is a phenomenon particular to such a configuration of supplying the two liquids in the state of mutual interaction as employed in the present work as well as in Iida and Takashima's work [8, 9]. Once the two liquids make a direct contact to each other, there will never appear

[1] Iida and Takashima [19] discovered that drops suddenly disappeared in the course of surface film boiling. They attributed this phenomenon to a direct contact of drops with the substrate liquid, which would make the drops evaporate away in quite a short time.

[2] Henry et al. [20] reported on a similar phenomenon: A drop of R 11, R 22, or ethanol placed on a mercury surface at temperature above 200°C turns black. They considered this fact to be a result of mercury vapor condensing on the drop.

Table 1 Density and volatility data on liquids used

| | Density at 47.6°C and 101.3 kPa kg/m$^3$ | Saturation temperature at 101.3 kPa °C | Vapor pressure at 47.6°C kPa |
|---|---|---|---|
| R 113 | 1509 | 47.6 | 101.3 |
| Water | 989 | 100.0 | 10.9 |
| Ethylene glycol | 1098 | 197.5 | < 0.1 |
| *n*-Tridecane | 737 | 235.4 | < 0.1 |

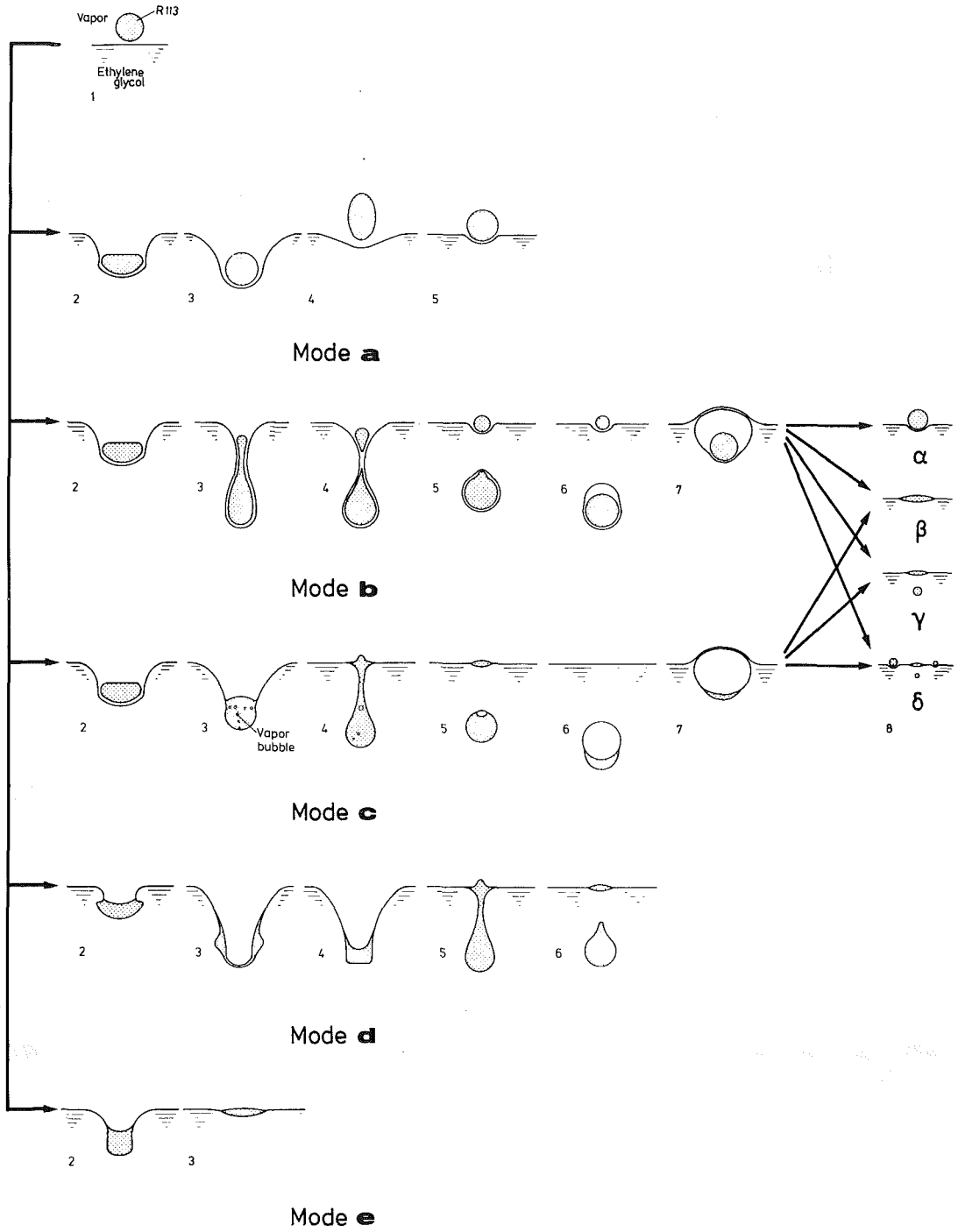


**Fig. 3 Sketches of typical sequences in respective vaporization modes observed in the R 113/ethylene glycol system**

the state of submerged film boiling as has been demonstrated in [14–16].

*Mode c.* This mode is a new finding in our observatrions. A typical sequence is presented in Fig. 5. The difference of this mode from mode *b* is caused by the breaking of the vapor film on the drop surface while the drop penetrates into the substrate liquid (frame 6 in Fig. 5). The vapor film draining along the drop surface after the breaking leaves tiny bubbles there (frame 7 in Fig. 5; stage 3 in Fig. 3). These bubbles are then encapsulated in the drop and coalesce with each other into a single bubble. When the drop disintegrates into a larger part which falls into the substrate liquid and a smaller part which is left on the surface in the form of a lens, the bubble is captured in the former. The succeeding process is characterized by the bubble growth in the drop which is essentially the same as is observable when we simply form a drop (containing one or more vapor nuclei) in the bulk of an immiscible liquid [21]. As the "two-phase bubble" consisting of a vapor phase and a small volume of unvaporized liquid of R 113 bursts at the free surface, one of the three states, $\beta$, $\gamma$, and $\delta$, follows.

*Mode d.* When a drop comes into direct contact with the substrate liquid in an early stage and, at the same time, makes a deep cavity in the substrate liquid, the drop disintegrates into two parts just the same as in mode *c*. The larger part falls through the substrate liquid being superheated, rests on the bottom plate of the test vessel, and with a long and erratic time delay vaporizes explosively. The other part forms a lens

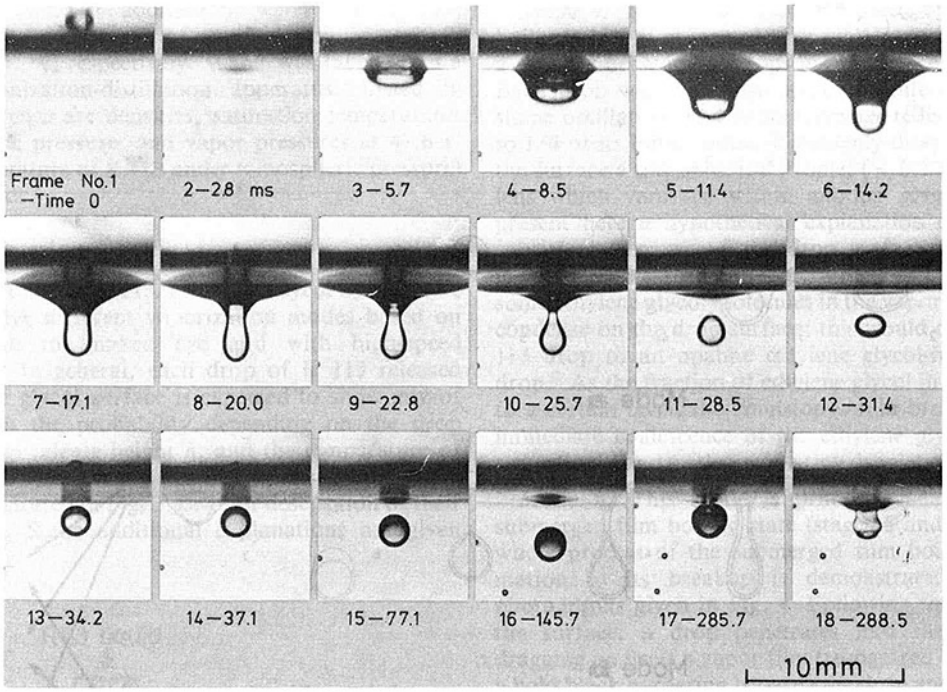


Fig. 4 Photographs showing a sequence of submerged film boiling in a vaporization process of mode *b*: R 113/ethylene glycol system, $D_0$ = 2.0 mm, $T_\infty$ = 74.4°C

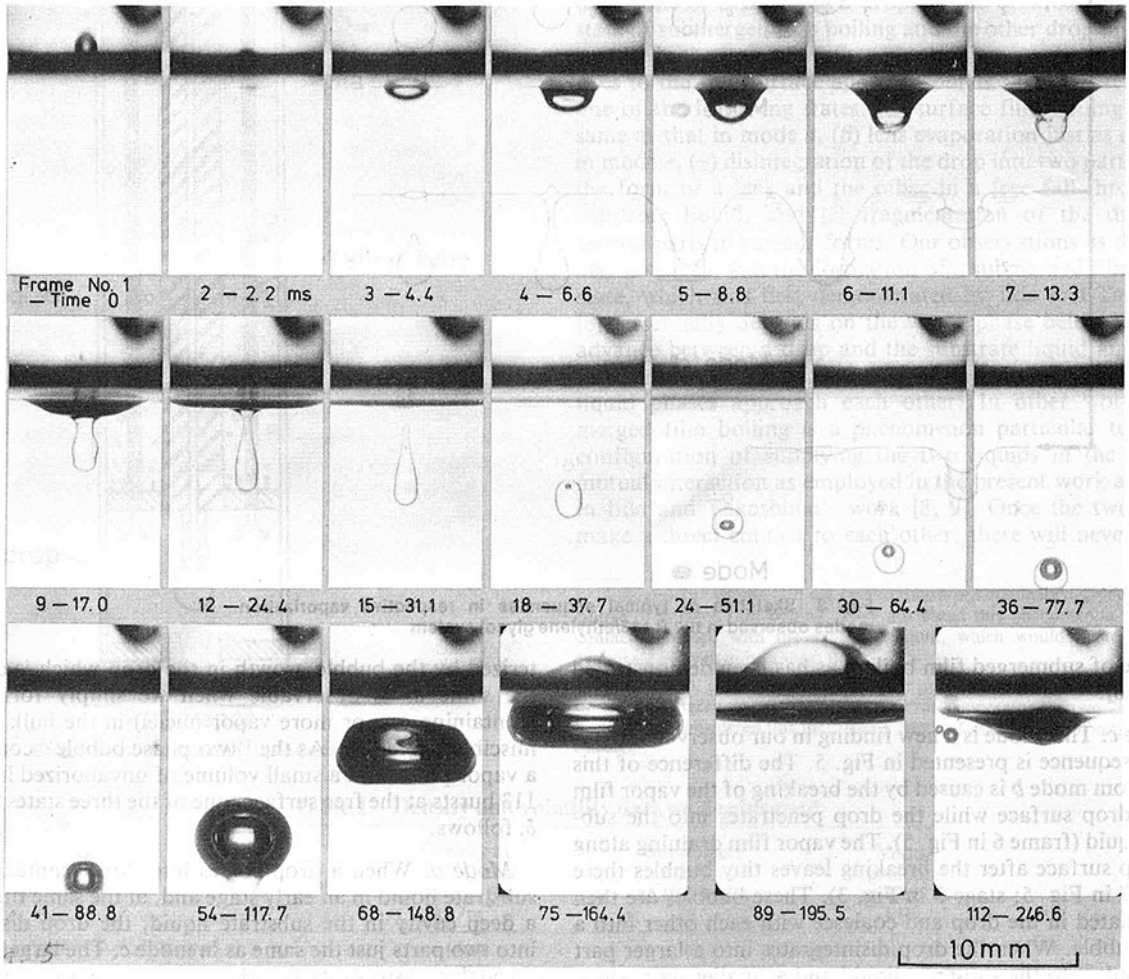


Fig. 5 Photographs of successive steps of formation, growth, and burst of a two-phase bubble in a process of mode *c*: R 113/ethylene glycol system, $D_0$ = 2.0 mm, $T_\infty$ = 76.4°C

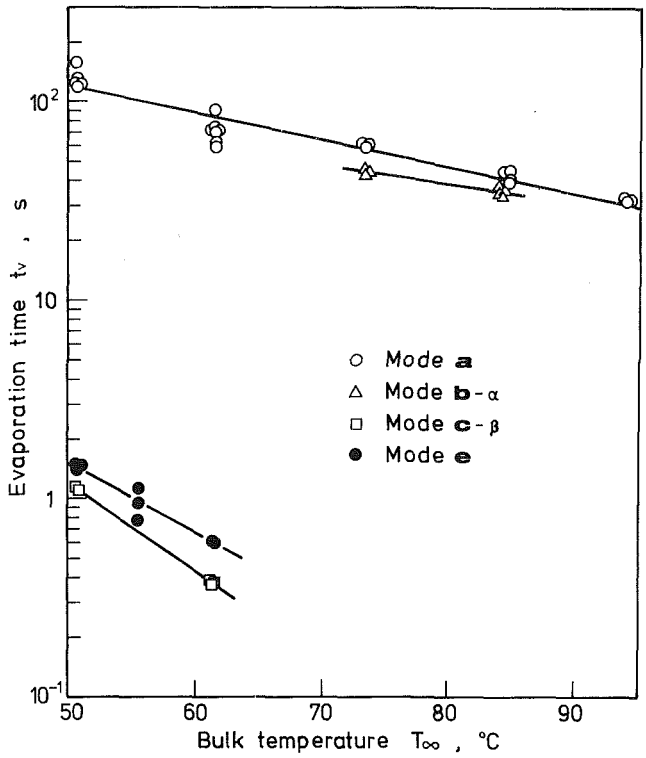


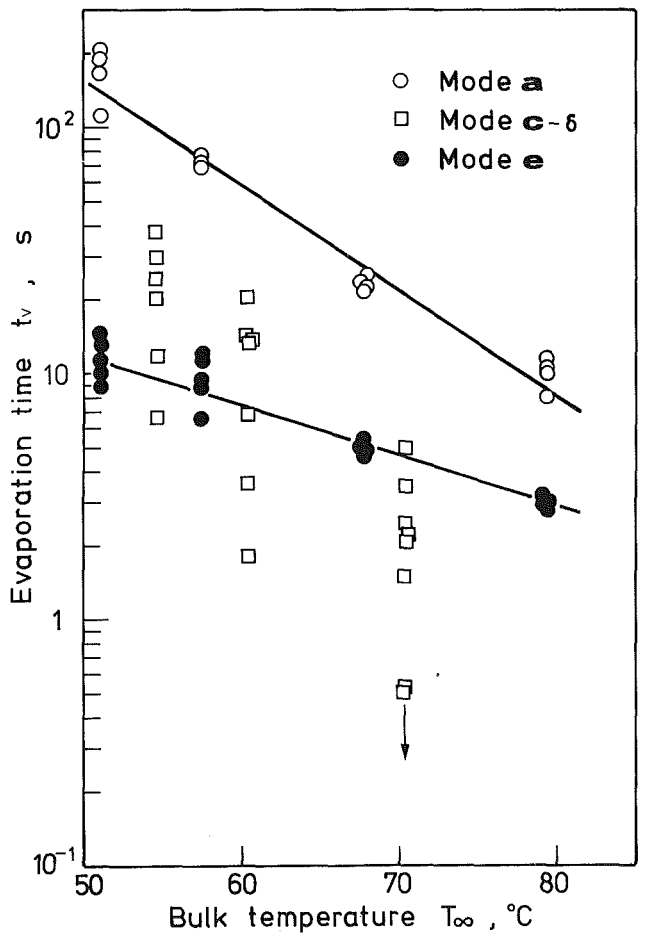


**Fig. 6** Total evaporation time $t_v$ of drops of 2.0 mm initial diameter versus the bulk temperature of the substrate liquid, $T_\infty$: (*a*) R 113/ethylene glycol system; (*b*) R 113/water system; the arrow in (*b*) means that the nearest two symbols indicate longer $t_v$ than true values (but not by how much)

on the free surface and vanishes by evaporation in a short time.

*Mode e.* When a drop comes into direct contact with the substrate liquid in an early stage but makes only a shallow cavity, it simply turns into a single lens floating on the free surface and maintains this form until it vanishes by evaporation.

**Vaporization Modes in R 113/Water System.** Vaporization modes observed in this system were essentially the same as have been identified in R 113/ethylene glycol system except that mode *b* was absent in this system. The absence of mode *b* may be ascribed to the surface tension of water being higher than that of ethylene glycol and thus preventing each drop from penetrating into the water dragging a vapor film on it.

Mode *a* in this system exhibited a difference from that in R 113/ethylene glycol system in that the surface film boiling state always broke before the drop diameter reduced to a half of its initial value and turned into the lens evaporation state. No opalescence was found in drops in the surface film boiling state.

**Vaporization Modes in R 113/*n*-Tridecane System.** We have distinguished two modes characterized by film boiling, i.e., modes *a* and *b*, and an immediate dissolving of drops into the substrate liquid following their impingement onto the surface. (Plumes of R 113 dissolving into the substrate liquid were observed occasionally to discharge vapor bubbles.) It is considered that the other three modes *c*, *d*, and *e*, which were intrinsically related to direct liquid–liquid contact, were exclusively replaced by the abovementioned dissolving process. This fact indicates, on the contrary, that throughout the formation process of either of the surface and submerged film boiling states drops never experienced any direct contact with the substrate liquid.

The surface film boiling state in this system was particularly characterized by lively, erratic movement of drops over the surface. The state was interrupted, in most cases, by each drop accidentally colliding with the side wall of the test vessel or falling into the overflow pipe installed in the substrate liquid layer. The submerged film boiling state broke, when a drop with a vapor blanket on it burst at the surface, followed by either the surface film boiling state (state $\alpha$ at stage 8 in Fig. 3) or an immediate dissolving of the drop into the substrate liquid.

**Evaporation Time.** Figure 6 compares time lengths $t_v$ required for complete evaporation of drops of 2.0 mm initial diameter in various vaporization modes in both R 113/ethylene glycol and R 113/water systems. (In the R 113/*n*-tridecane system $t_v$ could not be specified because of either the dissolving of drops or the aforementioned behavior of drops in the surface film boiling state.) Either of modes *b* an *c* yielded a variation in $t_v$ depending on the variation in state at later stages (see Fig. 3). In Fig. 6, only $t_v$ corresponding to the state dominant in each mode and in each system is presented. (Note that in mode $c-\delta$ in the R 113/water system we define $t_v$ as the time to a complete evaporation of drops dispersed on the surface by the burst of a two-phase bubble taking no account of a couple of minute drops sedimented into the substrate liquid.) In R 113/ethylene glycol system, $t_v$ for modes $c-\beta$ and *e* in which direct liquid–liquid contact is continuously available are lower by two orders of magnitude than those for modes *a* and $b-\alpha$ in which direct liquid–liquid contact is utterly unavailable. In the R 113/water system, the difference in $t_v$ between mode $c-\delta$ or *e* and mode *a* is rather smaller and not much more than one order of magnitude. The temperature dependence of $t_v$ for mode *a* being stronger in the R 113/water system is probably ascribable to an earlier transition from surface film boiling to lens evaporation with an increasing temperature. The wide scatter of data for mode $c-\delta$ in the same system resulted from a wide variation in size of the largest one of drops dispersed

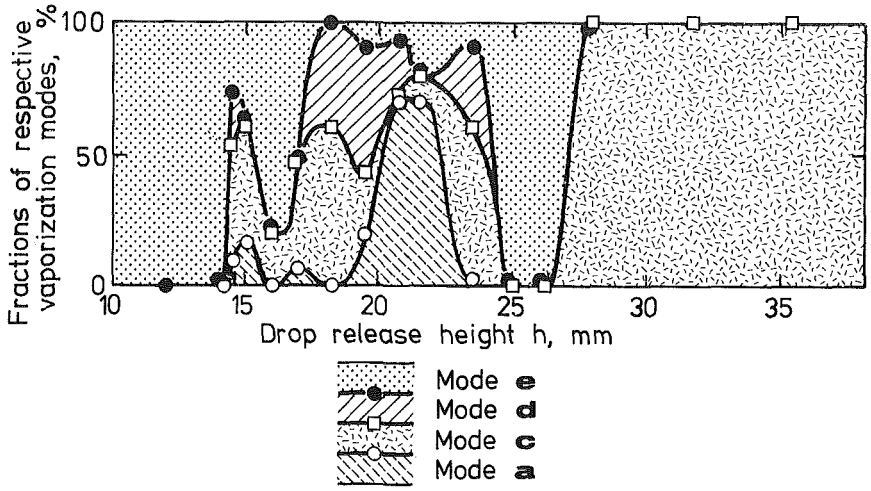


**Fig. 7 Variation of fractions of respective vaporization modes with the drop release height $h$: R 113/ethylene glycol system, $D_0$ = 2.0 mm, $T_\infty$ = 60.0°C**

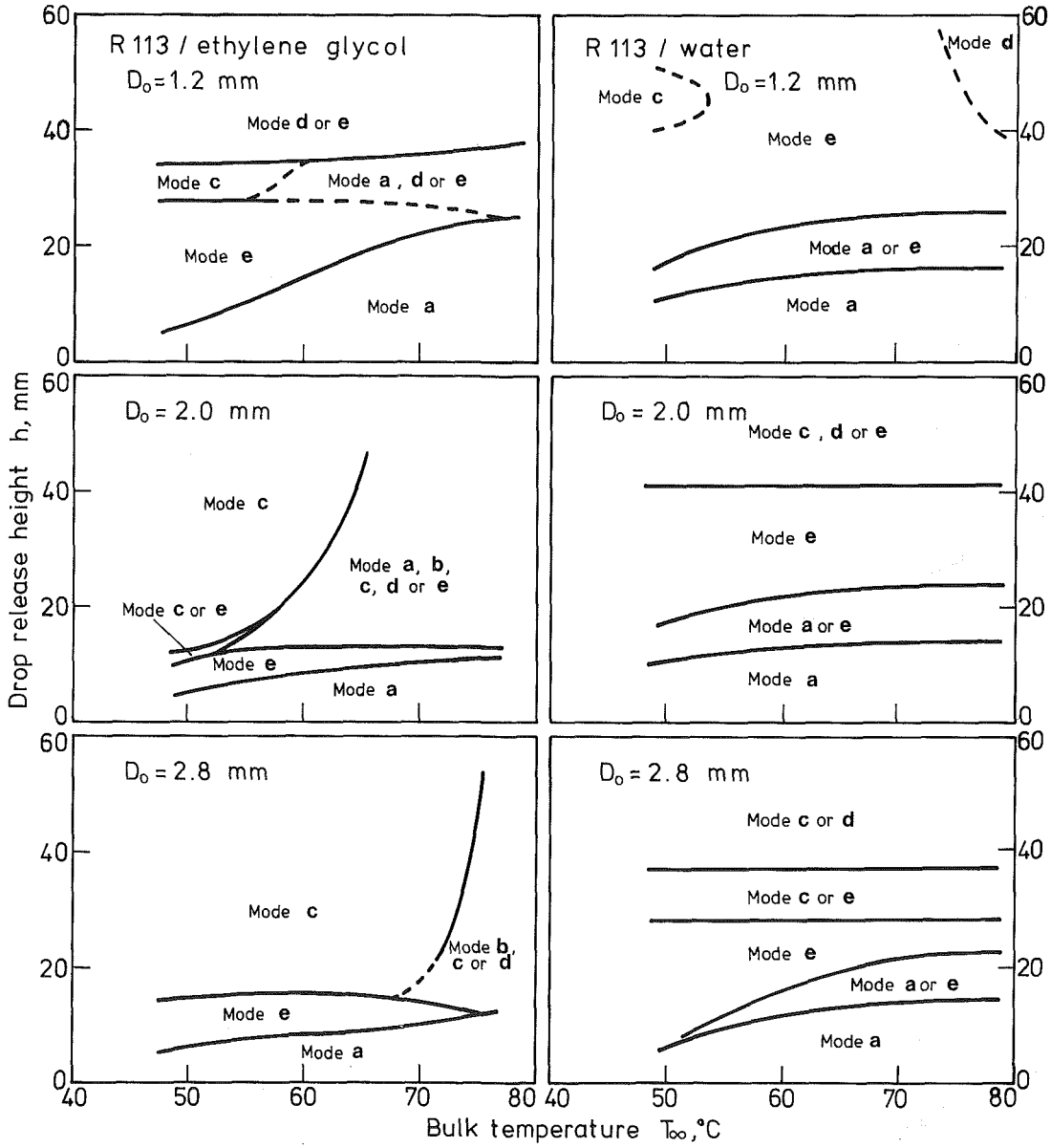


**Fig. 8 Vaporization mode maps: broken curves represent borders less reliable because of insufficient data**

on the surface in the state of surface film boiling when a two-phase bubble burst at the surface; the larger the largest drop the longer the total evaporation time.

Comparing $t_v$ for mode *e* between the two systems we notice an anomalous fact. The R 113/water system gives much longer $t_v$ than the R 113/ethylene glycol system in spite of higher thermal conductivity, higher heat capacity per unit volume, and lower viscosity of the substrate liquid. Further, the former system presumably yields thinner lenses because of higher surface tension of the substrate liquid, which is also a favorable factor for evaporation. Thus, we consider that the above fact may be ascribed to a sort of interfacial instability induced on the lens surface by some capillary or physicochemical effect. Much more intensive research on mode *e* will be required to settle this problem.

**Conditions for Respective Vaporization Modes.** Variable factors that could be controlled in our experiments to determine an operational condition in each system were initial drop diameter $D_0$, drop release height $h$, and the substrate liquid temperature $T_\infty$. Our reasonably precise control of these three factors was sometimes not enough, however, to reproduce, under nominally the same condition, a unique vaporization mode but yielded alternately two or more vaporization modes each of which bore a statistically specified fraction. Figure 7 exemplifies a typical set of data on fractions of respective modes obtained under constant $T_\infty$ and $D_0$. The fraction of each mode shows a fluctuation with a change of the drop release height $h$ over a certain range of $h$. This fluctuation seems to be ascribed to the fact that the phase of shape oscillation of drops at their impingement on the surface changes periodically with the duration of their free fall which in turn depends on $h$. All the results for the R 113/ethylene glycol and R 113/water systems are summarized in Fig. 8 in the form of maps with coordinates of $h$ and $T_\infty$. On each of these maps one can specify a range of either of $h$ and $T_\infty$ wherein a desirable vaporization mode is expected to occur invariably. This is of practical importance because evaporators should be so operated that only modes with shorter evaporation times (i.e., modes *c* and *e*) appear. (Mode *e* may be preferable to mode *c*, because the latter sometimes yields tiny superheated droplets in the bulk of the substrate liquid; see stage 8 in Fig. 3.) In general, dominant mode changes from *a* to *e* and then to *c* with an increase of $h$ under a constant $T_\infty$. These mode transitions generally occur at higher $h$ in the R 113/water system than in the R 113/ethylene glycol system. The transition between modes *a* and *e* may be of particular importance from the aforementioned viewpoint, and thus we would seek, if possible, an adequate criterion for this transition. One may think of a simple criterion, proposed by Ochiai and Bankoff [6], which gives the minimum value required for direct liquid–liquid contact of Weber number based solely on drop properties. However, this criterion could not be successfully applied to correlate our results for $a-e$ transition for different $D_0$ even in a particular system, though the range of Weber numbers corresponding to the transition agreed, only in the gross, with that reported by Ochiai and Bankoff with the R 113/glycerol system. Establishment of a more appropriate criterion is a task left for future consideration.

## Conclusions

Vaporization processes of fluorocarbon drops dripped onto the surface of another hotter liquid were studied with the aid of cinephotography. Particular accomplishments of the work may be listed as follows:

1 Five vaporization modes were identified as sketched in Fig. 3.

2 The whole process of submerged film boiling, whose existence was first noted by Iida and Takashima [8], was revealed (Figs. 3 and 4).

3 The vaporization mode *c* was for the first time recognized, and its whole process was revealed (Figs. 3 and 5).

4 The five vaporization modes were found to fall into two classes, with evaporation rates being largely different from each other (Fig. 6), depending on whether the two liquids make a direct contact.

5 A vaporization mode map was constructed defining domains on a drop release height versus temperature plane for each drop size and each liquid combination (Fig. 8).

## Acknowledgments

We extend sincere thanks to Y. Kohda for his assistance in carrying out major part of the experimental work. We are also indebted to Dr. S. Matsumura who kindly measured concentrations of R 113 dissolved in a number of our *n*-tridecane samples by use of gas chromatography. This work was subsidized by Kajima Foundation's Research Grant and by Kawakami Foundation's Research Grant.

## References

1 Bentwich, M., Landau, U., and Sideman, S., "Direct Contact Heat Transfer With Change of Phase: Evaporation of Discrete Volatile Films from the Surface of a Stagnant Immiscible Liquid," *International Journal of Heat and Mass Transfer*, Vol. 13, 1970, pp. 945–956.

2 Kodres, C. A., Jacobs, H. R., and Boehm, R. F., "Heat Transfer to an Evaporating, Floating, *n*-Pentane Lens," ASME Paper No. 79-HT-13, 1979.

3 Kodres, C. A., Jacobs, H. R., and Boehm, R. F., "A Numerical Method for Determining Direct-Contact Heat Transfer Rates to a Superheated Evaporating Floating Droplet," *Numerical Heat Transfer*, Vol. 3, 1980, pp. 21–34.

4 Kodres, C. A., Jacobs, H. R., and Boehm, R. F., "Design and Evaluation of Evaporating Lens Direct Contact Heat Exchangers," *ASME Journal of Energy Resources Technology*, Vol. 103, 1981, pp. 128–132.

5 Waldram, K. L., Fauske, H. K., and Bankoff, S. G., "Impaction of Volatile Liquid Droplets onto a Hot Liquid Surface," *The Canadian Journal of Chemical Engineering*, Vol. 54, 1976, pp. 456–458.

6 Ochiai, M., and Bankoff, S. G., "A Local Propagation Theory of Vapor Explosions," *Proceedings of the Third Specialists Meeting on Fuel Interactions*, Tokyo, 1976, Vol. 1, pp. 129–152.

7 Ochiai, M., and Bankoff, S. G., "Liquid–Liquid Contact in Vapor Explosions," *Proceedings of the International Meeting on Fast Reactor Safety and Related Physics*, Chicago, Ill., 1976, pp. 1843–1851.

8 Iida, Y., and Takashima, T., "Evaporation of a Liquid Drop on a Hot Liquid Surface (1st Report, Evaporation Configuration and Evaporation Time Curve)" (in Japanese), *Transactions of the Japan Society of Mechanical Engineers*, Vol. 46, Ser. B, 1980, pp. 725–733.

9 Iida, Y., and Takashima, T., "Direct-Contact Heat Transfer Characteristics: Evaporation of a Drop Dropped onto a Hot Liquid-Surface," *International Journal of Heat and Mass Transfer*, Vol. 23, 1980, pp. 1263–1271.

10 Witte, L. C., and Cox, J. E., "Nonchemical Explosive Interaction of LNG and Water," ASME Paper No. 71-WA/HT-31, 1971.

11 Newlands, A. G., and Halstead, W. D., "The Reaction Between Water Droplets and Molten Sodium" *International Journal of Heat and Mass Transfer*, Vol. 21, 1978, pp. 897–903.

12 Umano, S., "Fundamental Studies on Sea Water Refrigeration Concentration and Effective Use of Raw Materials from Sea Water" (in Japanese), Dr. Eng. thesis, Keio University, Tokyo, 1959.

13 Akiyama, M., and Takayama, S., "Fundamental Study of Heat Transfer Characteristics of Direct Contact Evaporator (1)—Experiments with R 113 and Glycerol" (in Japanese), *18th National Heat Transfer Symposium of Japan*, Sendai, 1981, Paper C201.

14 Mori, Y. H., and Komotori, K., "Boiling of Single Superheated Drops in an Immiscible Liquid," *Heat Transfer—Japanese Research*, Vol. 5, 1976, pp. 75–95.

15 Avedisian, C. T., and Glassman, I., "Superheating and Boiling of Water in Hydrocarbons at High Pressures," *International Journal of Heat and Mass Transfer*, Vol. 24, 1981, pp. 695–706.

16 Shepherd, J. E., and Sturtevant, B., "Rapid Evaporation at the Superheat Limit," *Journal of Fluid Mechanics*, Vol. 121, 1982, pp. 379–402.

17 Akiyama, M., "Leidenfrost Temperature of a Liquid Drop with Impurities" (in Japanese), *17th National Heat Transfer Symposium of Japan*, Kanazawa, 1980, Paper B117.

18 Jacobs, H. R., Deeds, R. S., and Boehm, R. F., "Heat Transfer Characteristics of a Surface Type Direct Contact Boiler," ASME Paper No. 76-HT-26, 1976.

19 Iida, Y., and Takashima, T., "Evaporation of a Drop on a Hot Liquid Surface (2nd Report, Experiment and Analysis of Leidenfrost Film Boiling on a Liquid Surface)" (in Japanese), *Transactions of the Japan Society of Mechanical Engineers*, Vol. 48, Ser. B, 1982, pp. 1128–1136.

20 Henry, R. E., Quinn, D. J., and Spleha, E. A., *Proceedings of the Fifth International Heat Transfer Conference*, Tokyo, 1974, Vol. 4, pp. 101–104.

21 Tochitani, Y., Mori, Y. H., and Komotori, K., "Vaporization of Single Liquid Drops in an Immiscible Liquid. Part I: Forms and Motions of Vaporizing Drops," *Warme- und Stoffubertragung*, Vol. 10, 1977, pp. 51–59.

**A. Sharan**
Graduate Assistant.

**J. H. Lienhard**
Professor.
Fellow ASME

**R. Kaul**
Graduate Assistant.

Heat Transfer and
Phase Change Laboratory,
Mechanical Engineering Department,
University of Houston,
Houston, Texas 77004

# Corresponding States Correlations for Pool and Flow Boiling Burnout

*The peak pool boiling heat flux can be nondimensionalized so the dimensionless peak heat flux is a function of a Bond or Laplace number that characterizes the system geometry. The dimensionless peak heat flux can be interpreted as the product of a geometrical function (given by previous investigations), universal functions of the reduced saturation pressure, and the Pitzer acentric factor. The latter universal functions are constructed by correlation. These are combined to give a single prediction of the peak heat flux that applies to all the common geometrical heater configurations. The probable error of the prediction, when it is compared with the available peak heat flux data, is 6.1 percent for substances whose dipole moment is not high. The method is also extended to create a comparable correlation for flow boiling burnout during crossflows over cylinders. There is a lack of data with which to check this correlation fully.*

## Introduction

The first corresponding states correlations of the peak boiling heat flux $q_{\max}$ appeared in the Western literature [1, 2] during the early 1960s, although Borishansky's [1] formulation had been published earlier in Russian [3]. At the time, it was unclear that predictions of $q_{\max}$ would eventually be made, and such correlations seemed to be the court of next resort. When predictions finally were made (see, e.g., [4, 5, 6] or the summary in [7]), interest in corresponding states correlations waned.

There are, however, several reasons to resurrect an interest in corresponding states. For pool boiling, all the predictions involve a fairly simple dependence of $q_{\max}$ on surface tension $\sigma$, the liquid and vapor densities $\rho_f$ and $\rho_g$, and the latent heat $h_{fg}$. All take the form

$$\frac{q_{\max}}{\rho_g^{1/2} h_{fg} \sqrt[4]{g\sigma(\rho_f-\rho_g)}} = f(L'); L' \equiv \frac{L}{\sqrt{\dfrac{\sigma}{g(\rho_f-\rho_g)}}} \tag{1}$$

The functions $f(L')$ are all fairly simple. For example (see details in [6] or [7])

$$\left.\begin{aligned} f(L') &\simeq 0.115 \text{ for large submerged bodies } (L' > 1.2 \text{ to } 4.3) \\ f(L') &= 0.149 \text{ for infinite flat plates } (L' \to \infty) \\ f(L') &= 0.123/(R')^{1/4} \text{ for horizontal cylinders } (0.15 \le R' \le 1.2) \\ f(L') &= 0.227/(R')^{1/2} \text{ for spheres } (0.15 \le R' \le 4.26) \end{aligned}\right\} \tag{2}$$

Thus equation (1) with (2), although it is accurate within about ±15 percent, represents a good deal of smoothing and simplification of complicated phenomena. If the process of correlation can be sufficiently perfected, it might reveal details of the functional dependence of $q_{\max}$ that cannot be brought out by the simplified theories.

The second reason for such correlations is that they circumvent the need for $\sigma$, $\rho_f$, $\rho_g$, and $h_{fg}$ data, which can often be quite hard to find.

We shall therefore develop a more complete correlation based upon the more recent things we have learned both about corresponding states correlations and about $q_{\max}$ predictions.

Contributed by the Heat Transfer Division for publication in the JOURNAL OF HEAT TRANSFER. Manuscript received by the Heat Transfer Division January 5, 1984.

## The Law of Corresponding States for $q_{\max}$ in Pool Boiling

The law of corresponding states says that there exists a universal function

$$g(T_r, p_r, v_r, \omega) = 0 \tag{3}$$

where $T_r$, $p_r$, and $v_r$ are the reduced temperature, pressure, and volume, respectively. The function $\omega$ is a parameter that characterizes the molecular structure of the fluid. It might be a critical compressibility factor, a Riedel factor, or a Pitzer acentric factor. We use the Pitzer factor, since it has proven to be the most effective of the three.

$$\omega \equiv -1 - \log_{10} p_{r_{\text{sat}}} (T_r = 0.7) \tag{4}$$

Lienhard and Schrock [2] noted that the variable $h_{fg}$ could be expressed as function of $p$, $v$, and $T$ through the Clausius–Clapeyron equation, and $\sigma$ is determined with good accuracy by

$$\sigma \simeq (\rho_f - \rho_g)^4 (P/M)^4 \tag{5}$$

where $P/M$ is the Parachor (see, e.g. [8]) divided by the molecular weight. Thus equation (1) takes the form

$$\frac{q_{\max}}{\lambda f(L')} = h(p_{r_{\text{sat}}}, \omega) \tag{6}$$

where $\lambda$ is the appropriate characteristic heat flux

$$\lambda \equiv g^{1/4} p_c \frac{P}{M} \left(\frac{8 p_c}{3 \Re T_c}\right)^{3/4} \tag{7}$$

We note the following three features of equations (6) and (7):

1 The functions $L'$ and $\omega$ were omitted in [2]. Although their influence is secondary, this still hurt the accuracy of the resulting correlations.

2 The function $\lambda$ was developed in [2]. It includes the system variable, gravity $g$. It also includes the unnecessary numerical factor of 8/3, which (being harmless) is retained here.

3 Since $\rho_f$, $\rho_g$, $\sigma$, and $h_{fg}$ are determined by the reduced saturation pressure alone, $T_r$ and $v_r$ do not appear in equation (6).

## The Present Correlation

The function $h(p_{r_{\text{sat}}}, \omega)$ is the dimensionless peak heat flux for an infinite flat plate, $q_{\max_F}$

$$h(p_{r_{\text{sat}}}, \omega) = q_{\max_F}/0.149\lambda \tag{8}$$

In [6], $q_{\max_F}$ is given as

$$q_{\max_F} = 0.149 \rho_g^{1/2} h_{fg} \sqrt[4]{\sigma g(\rho_f - \rho_g)} \tag{9}$$

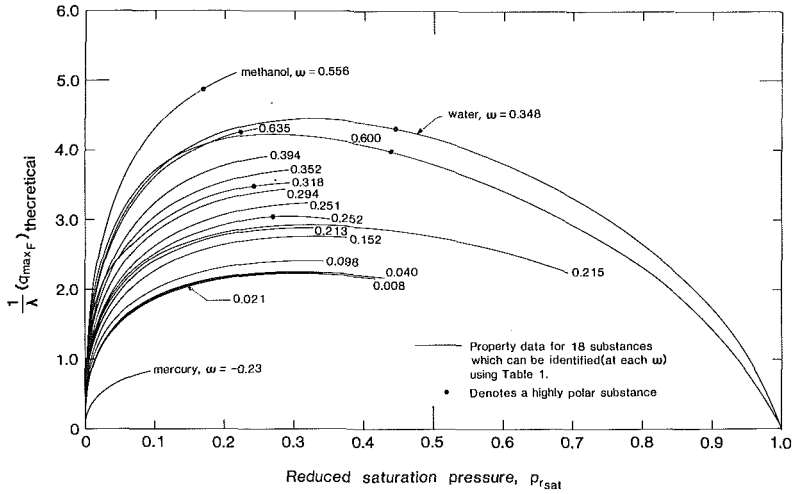


**Fig. 1 The reduced peak heat flux for 18 highly polar, and slightly polar or nonpolar, substances**

We use this expression to ascertain the form of $h$ in the following way:

First we propose that $h(p_{r_{sat}}, \omega)$ can be expressed as

$$h(p_{r_{sat}},\omega) = a(p_{r_{sat}})b(\omega) \tag{10}$$

because previous experience with corresponding states (see, e.g., [9]) suggests that a product law is typical. Then, since the function $a(p_{r_{sat}})$ should be the same for all substances

$$\frac{q_{\max_F}/\lambda}{(q_{\max_F}/\lambda)_{H_2O}} = \frac{a(p_{r_{sat}})b(\omega)}{\{a(p_{r_{sat}})b(\omega)\}_{H_2O}} = g(\omega) \tag{11}$$

We use water as the standard of comparison to normalize these data, only because it is the best documented fluid we have.

The function $g(\omega)$ is evaluated with the help of Fig. 1. Figure 1 is a plot of $q_{\max_F}/\lambda$ as a function of reduced saturation pressure. The curves for most substances are terminated short of $p_{r_{sat}} = 1$, owing to the shortage of property data at high pressures, which was a major motivation for creating a correlation in the first place. (The fluids that we have considered, along with their relevant critical data, Pitzer factors, Parachors, molecular dipole moments, and the sources of these data, are listed in Table 1.) Then in accordance with equation (11), the group

$$\frac{q_{\max_F}/\lambda}{(q_{\max_F}/\lambda)_{H_2O}}$$

is evaluated at many different values of $p_{r_{sat}}$ in the expectation that it will be the same at any $p_{r_{sat}}$ for a given $\omega$.

This ratio is plotted against $\omega$ in Figs. 2 and 3. Figure 2 includes all the fluids that we considered, at six reduced pressures. While there is a definite central tendency among the data, many do not correlate well.

However, it is well known that highly polar molecules can exhibit inconsistencies with the law of corresponding states (see, e.g., [10]). It is also true that molecules with a high

## Nomenclature

$a,b$ = arbitrary functions of $p_{r_{sat}}$ and $\omega$
$a_1,a_2;b_1,b_2$ = arbitrary functions of $p_{r_{sat}}$ and $\omega$ in the flow boiling correlation
$f(L')$ = function of $L'$ in the final correlation for pool boiling
$f_1, f_2$ = functions of $p_{r_{sat}}$ and $\omega$ in the flow boiling correlation
$g$ = the acceleration resulting from gravity or any other body force
$g(\omega)$ = function of $\omega$ in the final correlation for pool boiling
$h(p_{r_{sat}},\omega)$ = function of $p_{r_{sat}}$ and $\omega$
$h_{fg}$ = latent heat of vaporization
$k(p_{r_{sat}})$ = universal function of $p_{r_{sat}}$ in the final correlation for pool boiling
$L$ = any characteristic length
$M$ = molecular weight
$p$ = pressure at the heater surface during boiling
$P$ = the Parachor, explained in equation (5) and context
$q_{\max}$ = the peak boiling heat flux
$R$ = radius of a spherical or cylindrical heater
$\Re$ = the gas constant
$T$ = temperature
$u_\infty$ = velocity of liquid normal of a cylindrical heater
$v$ = specific volume
$W$ = dimensionless quantity defined in equation (19)
We = Weber number, $2\rho_f u_\infty{}^2 R/\sigma$
$\lambda$ = a characteristic heat flux defined in equation (7)
$\rho_f,\rho_g$ = saturated liquid and vapor densities, respectively
$\sigma$ = surface tension
$\phi$ = dimensionless peak heat flux, $\pi q_{\max}/\rho_g h_{fg} u_\infty$
$\omega$ = the Pitzer acentric factor defined in equation (4)

**Subscripts**

$c$ = property evaluated at the thermodynamic critical point
$F$ = quantity for an infinite horizontal heater (or flat plate)
$r$ = reduced property; it is a property divided by its critical value, except in the cases of $h_{fg}$ and $\rho$ as defined by equations (22) and (23)
sat = property evaluated on the saturated liquid/vapor line

**Superscript**

$'$ = length divided by $\sqrt{\sigma/g(\rho_f-\rho_g)}$

Table 1 Fluids used in this study and their physical properties

| | Substance | Dipole Moment (debyes) | Pitzer factor, $\omega$ | Critical Data $T_c$ (°K) | Critical Data $p_c$ (MPa) | $\lambda$** (kW/m$^2$) | P/M $\left(\sqrt[4]{\frac{\text{dyne}}{\text{cm}}}\,\frac{\text{cm}^3}{\text{gm}}\right)$ | Data Source* |
|---|---|---|---|---|---|---|---|---|
| Non-polar fluids and fluids with low dipole moments | Benzene, $C_6H_6$ | 0.0 | 0.215 | 562.1 | 4.894 | 227.72 | 206.2/78.114 | [13,14] |
| | Cyclohexane, $C_6H_{12}$ | 0.3 | 0.213 | 553.4 | 4.073 | 191.45 | 240.3/84.162 | [13,14] |
| | Ethane, $C_2H_6$ | 0.0 | 0.098 | 305.4 | 4.884 | 259.29 | 111.0/30.070 | [13,16] |
| | n-Heptane, $C_6H_{16}$ | 0.0 | 0.352 | 540.2 | 2.736 | 113.28 | 311.0/100.205 | [13,16] |
| | n-Hexane, $C_6H_{14}$ | 0.0 | 0.290 | 507.4 | 2.969 | 129.47 | 269.5/86.178 | [13,16] |
| | Mercury, Hg | 0.0 | -0.230 | 1763. | 153. | 10900. | 70.3/200.6 | [16] |
| | Methane, $CH_4$ | 0.0 | 0.008 | 190.6 | 4.600 | 238.25 | 71.0/16.043 | [13,16] |
| | Nitrogen, $N_2$ | 0.0 | 0.040 | 126.2 | 3.394 | 141.10 | 60.2/28.013 | [13,16] |
| | n-Octane, $C_8H_{18}$ | 0.0 | 0.394 | 568.8 | 2.482 | 101.62 | 350.0/114.232 | [13,16] |
| | Oxygen, $O_2$ | 0.0 | 0.021 | 154.6 | 5.043 | 208.07 | 53.6/31.999 | [13,16] |
| | n-Pentane, $C_5H_{12}$ | 0.0 | 0.251 | 469.6 | 3.374 | 149.63 | 229.1/72.151 | [13,16] |
| | Propane, $C_3H_8$ | 0.0 | 0.152 | 369.8 | 4.246 | 204.38 | 151.3/44.097 | [13,16] |
| Highly polar fluids | Acetone, $C_3H_6O$ | 2.9 | 0.318 | 508.1 | 4.702 | 193.02 | 160.3/58.080 | [13,14] |
| | Ethanol, $C_2H_6O$ | 1.7 | 0.635 | 516.2 | 6.383 | 270.30 | 127.2/46.069 | [13,14] |
| | Freon 113, $C_2Cl_3F_3$ | $\mathcal{O}(1)$ | 0.252 | 487.2 | 3.415 | 130.10 | 244.0/187.380 | [13,17] |
| | Methanol, $CH_4O$ | 1.7 | 0.556 | 512.6 | 8.096 | 302.78 | 88.1/32.042 | [13,14] |
| | 1-Propanol, $C_3H_8O$ | 1.7 | 0.600 | 536.7 | 5.168 | 218.36 | 165.7/60.096 | [13,14] |
| | Water, $H_2O$ | 1.8 | 0.348 | 647.3 | 22.05 | 1037.35 | 52.1/18.015 | [13,16] |

*All $\sigma$ data are from [23]. $\omega_{Hg}$ was calculated from $p_{sat}$ data. Dipole moments are from [13].

**These $\lambda$'s are all based on g = earth-normal gravity.

"deBoer parameter" (see, e.g., [11]) do not obey the law. These are generally such very low boiling point liquids as He and $H_2$. The lowest boiling point liquids included here are $O_2$, $N_2$, and methane. We repeat Fig. 2, omitting those fluids with high dipole moments, in Fig. 3.

Figure 3 reveals that the influence of $p_{r_{sat}}$ is small enough to ignore, and that the low and zero dipole moment fluids define a smooth and uncomplicated $g(\omega)$. It also reveals that the $\omega$-dependence of $q_{max_F}$ is almost linear. This is consistent with previous experience with the Pitzer factor (see, e.g., [9], [12] and [13]). The data can be represented within $\pm 7$ percent by

$$g(\omega) = 0.46 + 1.07\omega \tag{12}$$

Equation (12) is included in Figs. 2 and 3. In Fig. 2, with the highly polar substances included, the error of equation (12) rises to $\pm 16$ percent. The highest deviation of nonpolar and low dipole moment data from a straight line in Fig. 3 is among the low boiling-point fluids: $N_2$, $O_2$, and methane. It is possible that they exhibit some minor failure to conform to the law of corresponding states.

Figure 4 reverses the process of obtaining $g(\omega)$ from Fig. 1 and, in so doing, provides the universal function $k(p_{r_{sat}})$

$$\frac{q_{max}/\lambda}{f(L')g(\omega)} \equiv k(p_{r_{sat}}) \simeq b(\omega)_{H_2O} a(p_{r_{sat}})_{H_2O} \tag{13}$$

It is important to note that the right-hand side only approximates $k$, since $g(\omega)$ was obtained by fairing a line through many points, each of which satisfied equation (11) individually. The faired line, however, does not exactly satisfy equation (11) anywhere. Therefore, $k$ is not wed to the properties of the highly polar fluid, water, as equation (13) would suggest if it were precise.

The data in Fig. 4 can be represented by the equation

$$k(p_{r_{sat}}) = 59p_{r_{sat}}^{0.355} - 52.8p_{r_{sat}}^{1.517} - 6.2p_{r_{sat}}^{10} \tag{14}$$

This expression is well within the data scatter above $p_{r_{sat}} = 0.06$, and it is less than 4 percent high at lower pressures. The data can be represented better at low pressure by the first term alone

$$k(p_{r_{sat}}) = 59p_{r_{sat}}^{0.355} \quad \text{for} \quad p_{r_{sat}} \le 0.06 \tag{15}$$

Finally, if we return to equation (6) with the functions $g$ and $k$, we expect to find

$$\frac{q_{max}}{\lambda f(L')k(p_{r_{sat}})g(\omega)} = 1 \tag{16}$$

The available $q_{max}$ data for fluids with zero, or low, dipole moments are reduced in accordance with the left-hand side of equation (16) and plotted against $p_{r_{sat}}$ in Fig. 5. They have an average value of 0.973, which is almost equal to unity, and a standard deviation of $\pm 0.061$.

## Illustration of the Extension of the Method to Flow Boiling

What is done in the preceding section, can be done any time we have a prediction for burnout that is free of transport properties. Let us repeat the process for a flow boiling configuration.

Hasan, Hasan, Eichhorn, and Lienhard [24] showed that, for the relatively high-speed flow of a saturated liquid normal to a cylinder of diameter, $2R$:

$$\phi \equiv \frac{\pi q_{max}}{\rho_g h_{fg} u_\infty} = 0.000919 \frac{\rho_f}{\rho_g}\left[1 + \frac{16.3}{\text{We}^{1/3}}\right] \tag{17}$$

where $u_\infty$ is the liquid speed and the Weber number, $\text{We} \equiv 2\rho_f u_\infty{}^2 R/\sigma$. Equation (17) takes the reduced form

$$\frac{q_{max}}{p_c u_\infty} = f_1 + \frac{f_2}{W^{1/3}} \tag{18}$$

where the new dimensionless quantities are

$$W \equiv \frac{2u_\infty^2 R}{(p_c/\Re T_c)^3 (P/M)^4} \tag{19}$$

$$f_1 \equiv 0.0002925 \rho_{r_f} h_{r_{fg}} \tag{20}$$

$$f_2 \equiv 0.00477(1 - \rho_g/\rho_f)^{4/3} \rho_{r_f}{}^2 h_{r_{fg}} \tag{21}$$

$$h_{r_{fg}} \equiv h_{fg}/T_c \tag{22}$$

$$\rho_r \equiv \rho/(p_c/\Re T_c) \tag{23}$$

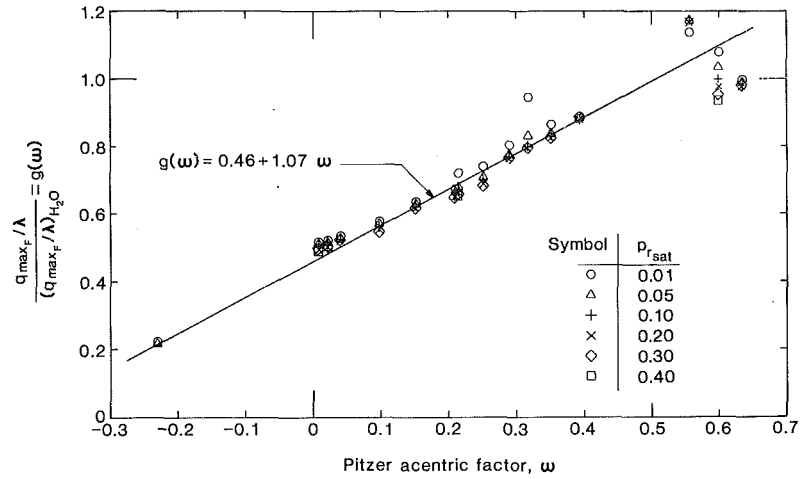


**Fig. 2 An attempt to establish the function $g(\omega)$ using data for fluids of *all dipole moments***

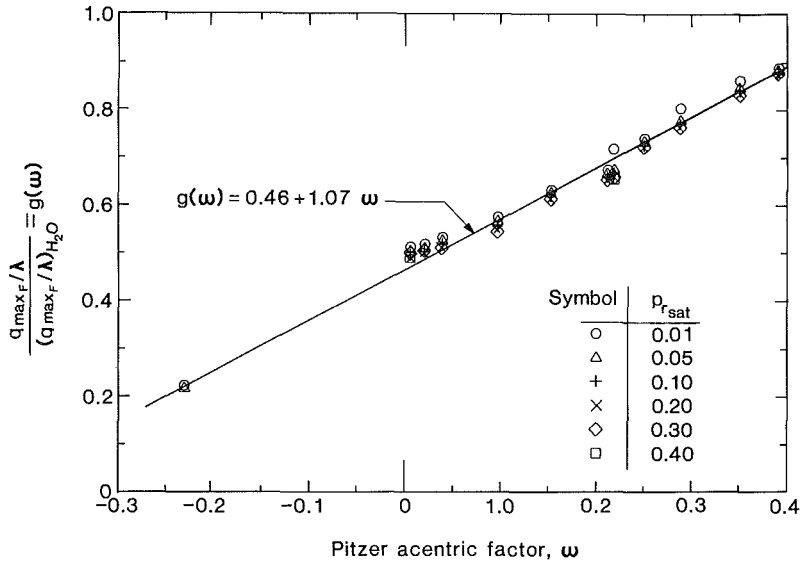


**Fig. 3 The function $g(\omega)$ based on data for slightly polar and nonpolar substances**

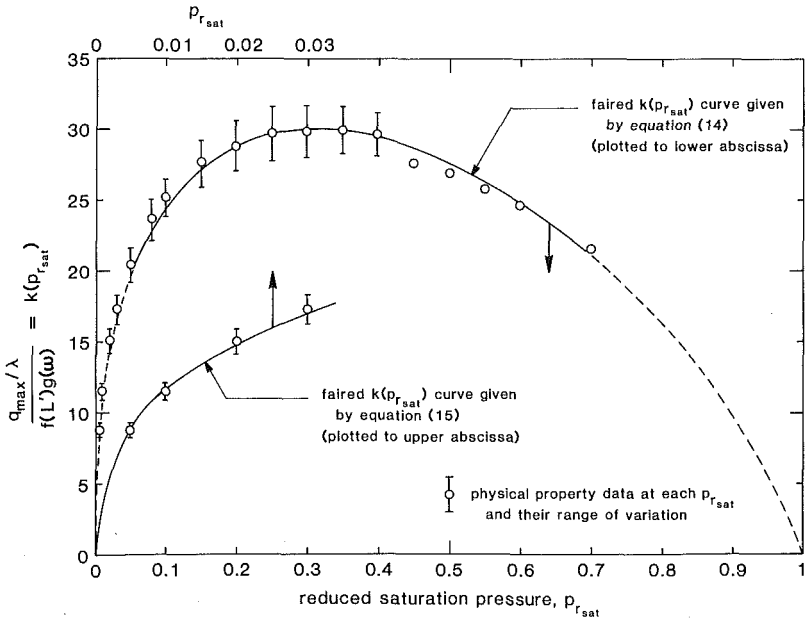


**Fig. 4 Formation of the universal pressure function, $k(p_{r_{sat}})$, based on slightly polar and nonpolar substances**

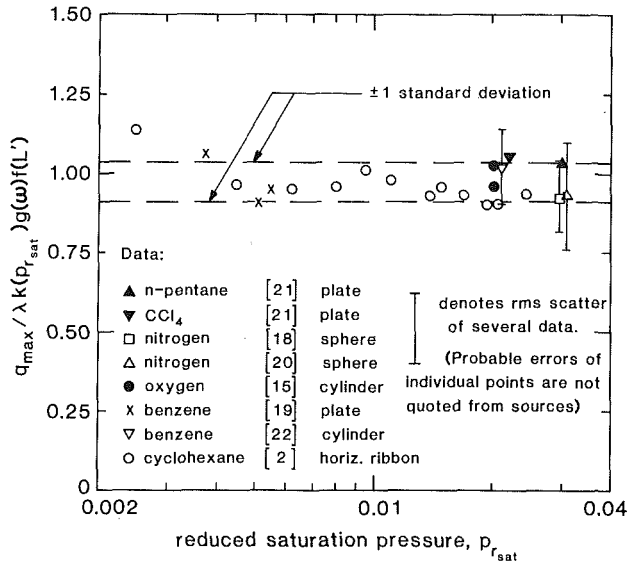


Fig. 5 Comparison of the present prediction (equation (16) or (29)) with $q_{max}$ data for slightly polar and nonpolar substances

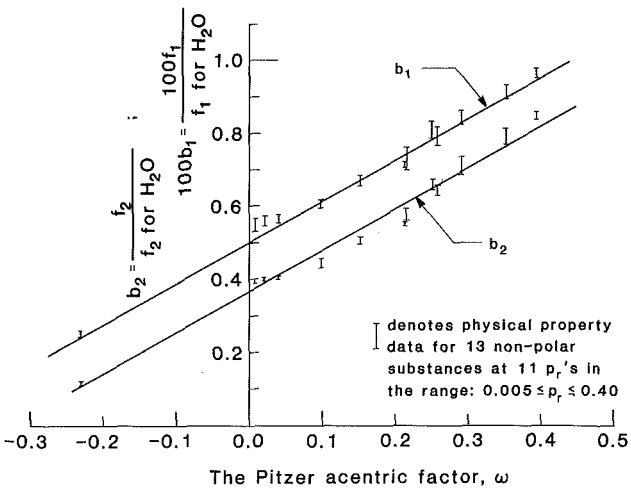


Fig. 6 The functions $b_1(\omega)$ and $b_2(\omega)$ based on data for nonpolar and slightly polar substances

Taking our cue from the pool boiling problem, we again assume that

$$\left.\begin{aligned} f_1 &= a_1(p_{r_{sat}})b_1(\omega) \\ f_2 &= a_2(p_{r_{sat}})b_2(\omega) \end{aligned}\right\} \tag{24}$$

Then, proceeding exactly as we did for pool boiling, we first evaluate the functions $b_1$ and $b_2$. These are shown in Fig. 6 (where we have omitted data for the highly polar fluids). The $\omega$-dependence is again linear, and it is given within $\pm 10$ percent by

$$\left.\begin{aligned} b_1(\omega) &= 0.01135\omega + 0.005 \\ b_2(\omega) &= 1.125\omega + 0.365 \end{aligned}\right\} \tag{25}$$

Figure 7 reverses the process of obtaining $b_1(\omega)$ and $b_2(\omega)$ and provides the pressure functions $a_1(p_{r_{sat}})$ and $a_2(p_{r_{sat}})$:

$$\frac{f_1}{b_1(\omega)} \equiv a_1(p_{r_{sat}}) \quad \text{and} \quad \frac{f_2}{b_2(\omega)} \equiv a_2(p_{r_{sat}}) \tag{26}$$

The data in Fig. 7 can be represented by the equations

$$\left.\begin{aligned} a_1(p_{r_{sat}}) &= 3.0(1 - p_{r_{sat}}{}^{0.58}) \\ a_2(p_{r_{sat}}) &= 7.4(1 - p_{r_{sat}}{}^{0.31}) \end{aligned}\right\} \tag{27}$$

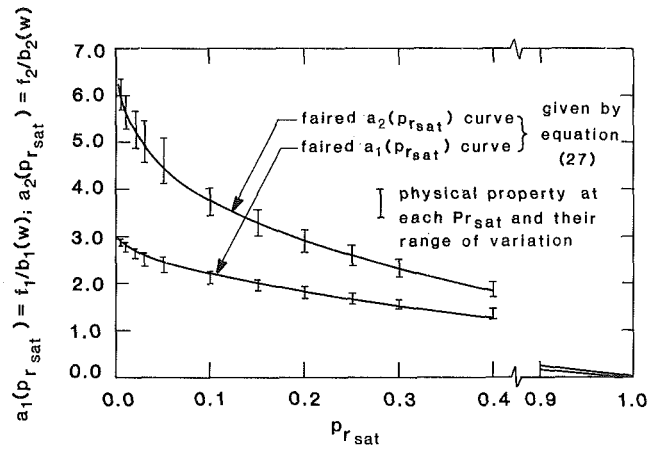


Fig. 7 Formation of the pressure functions, $a_1(p_{r_{sat}})$ and $a_2(p_{r_{sat}})$ based on slightly polar and nonpolar substances

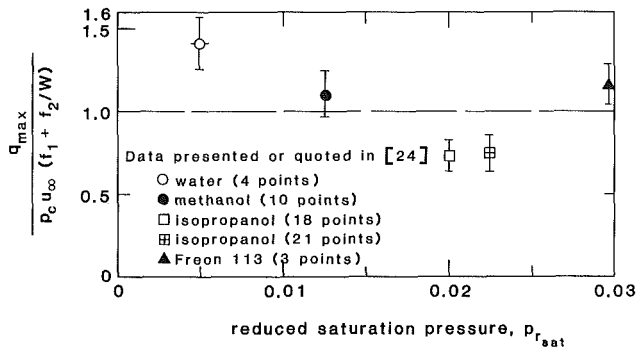


Fig. 8 Comparison of prediction, equation (18), based on equation (17), with data for polar substances only. Deviations might either be the result of the limitations of equation (17), or of the noncomformity of polar substances.

Finally, if we return to equation (18) with the functions $a_1$, $a_2$, $b_1$, and $b_2$, we expect to find

$$\frac{q_{max}}{p_c u_\infty (f_1 + f_2/W^{1/3})} = 1 \tag{28}$$

Unfortunately, we have no nonpolar $q_{max}$ data (that are free of systematic problems) for comparison with equation (28). The available *polar* data (free of end effects, gravity influences, etc.) that are quoted or presented in [24] are reduced according to equation (28) and plotted in Fig. 8. Of course, we do not expect polar substances to show good conformity, but the deviations we see here might be systematic in $p_{r_{sat}}$. It is possible that the linear dependence of $q_{max}$ on $\rho_f/\rho_g$, expressed in equation (17), is not entirely correct, and that Fig. 8 calls attention to this weakness.

Figure 8 strongly calls for flow boiling burnout data in nonpolar liquids. But even without such data, Fig. 8 shows how the use of corresponding states correlations might suggest relatively minor corrections to $q_{max}$ predictions.

It is interesting to recall that in 1941 Cichelli and Bonilla [25] noted that pool boiling burnout maximized, for a given fluid, when $p_{r_{sat}}$ was close to 1/3. The present pressure functions are such that $q_{max}$ is greatest at $p_{r_{sat}} = 0.316$ for pool boiling. However, in flow boiling $q_{max}$ decreases monotonically with $p_{r_{sat}}$, showing no local maximum.

## Conclusions

The peak pool boiling heat flux can be predicted at any pressure, and in any geometry for which $f(L')$ has been established, using

$$q_{max} = \lambda f(L') k(p_{r_{sat}}) g(\omega) \tag{29}$$

The only physical properties of the fluid that need be known are $p_c$, $T_c$, $\omega$, and $P/M$. The functions $k$ and $g$ can be read from Figs. 4 and 3, or calculated from equations (14) or (15) and (12).

This prediction should be accurate within a standard error of $\pm 6.1$ percent for nonpolar and slightly polar fluids. The error for the highly polar fluids can rise to about twice this value. The prediction can be expected to fail if it is applied to such low boiling-point fluids as He or $H_2$.

Corresponding states correlations can be created for burnout *whenever* $q_{max}$ depends only on thermodynamic properties, with no transport properties involved. We have developed another example of such a correlation for flow boiling on a horizontal cylinder. Both the pool and flow boiling correlations suggest that the method has potential value as a means for diagnosing minor weaknesses in $q_{max}$ predictions.

## Acknowledgment

We are grateful to the DOE for contributing support to this work under Contract DE-AC03-815F11557.

## References

1 Borishansky, V. M., Novikov, I. I., and Kutateladze, S. S., "Use of Thermodynamic Similarity in Generalizing Experimental Data of Heat Transfer," Paper No. 56, *Int. Heat Transfer Conf., University of Colorado*, Boulder, Aug. 1961; *Int. Dev. in Heat Transfer*, ASME, N.Y., 1963, pp. 475–482.

2 Lienhard, J. H., and Schrock, V. E., "The Effect of Pressure, Geometry, and the Equation of State upon the Peak and Minimum Boiling Heat Fluxes," ASME JOURNAL OF HEAT TRANSFER, Vol. 85, No. 3, 1963, pp. 261–272.

3 Novikov, I. I., "The Generalized Relation for the Critical Thermal Load," *Zh. Atomnaya Energiya*, Vol. 7, No. 3, Sept. 1959.

4 Lienhard, J. H., and Dhir, V. K., "Extended Hydrodynamic Theory of the Peak and Minimum Heat Fluxes," NASA CR-2270, July 1973.

5 Sun, K. H., and Lienhard, J. H., "The Peak Pool Boiling Heat Flux on Horizontal Cylinders," *International Journal of Heat and Mass Transfer*, Vol. 13, 1970, pp. 1425–1439.

6 Lienhard, J. H., and Dhir, V. K., "Hydrodynamic Prediction of Peak Pool-Boiling Heat Fluxes from Finite Bodies," ASME JOURNAL OF HEAT TRANSFER, Vol. 95, 1973, pp. 152–158.

7 Lienhard, J. H., *A Heat Transfer Textbook*, ch. 10, Prentice Hall, Englewood Cliffs, N.J., 1981.

8 Partington, J. R., *The Properties of Liquids* in *An Advanced Treatise on Physical Chemistry*, Vol. 11, Longmans, Green and Co., New York, 1951, p. 144.

9 Lienhard, J. H., "Corresponding States Correlations of the Spinodal and Homogeneous Nucleation Limits," ASME JOURNAL OF HEAT TRANSFER, Vol. 104, No. 2, 1982, pp. 379–381.

10 Brock, J. R., and Bird, R. B., "Surface Tension and the Principle of Corresponding States," *AIChE Journal*, Vol. 1, 1955, pp. 174–177.

11 Watkinson, A. P., and Lielmezs, J., "Corresponding-States Principle and Surface Tension," *J. Chem. Phys.*, Vol. 47, 1967, pp. 1558–1559.

12 Peck, R. E., "The Assimilation of van der Waals' Fluid in an Extended Law of Corresponding States," *Canadian J. Chem. Engr.*, Vol. 60, June 1982, pp. 446–449.

13 Reid, R. C., Prausnitz, J. M., and Sherwood, T. K., *The Properties of Gases and Liquids*, Appendix A, McGraw-Hill, New York, 1977.

14 Washburn, E. W., ed., *International Critical Tables*, McGraw-Hill, New York, 1928.

15 Lyon, D. N., "Peak Nucleate-Boiling Heat Fluxes and Nucleate-Boiling Heat-Transfer Coefficients for Liquid $N_2$, Liquid $O_2$ and Their Mixtures in Pool Boiling at Atmospheric Pressure," *International Journal of Heat and Mass Transfer*, Vol. 7, 1964, pp. 1097–1116.

16 Reynolds, W. C., *Thermodynamic Properties in SI*, Department of Mechanical Engineering, Stanford University, Calif., 1979.

17 Perry, R. H., and Chilton, C. H., *Chemical Engineers Handbook* (5th ed.), McGraw-Hill, New York, pp. 3–196.

18 Ded, J. S., and Lienhard, J. H., "The Peak Pool Boiling Heat Flux from a Sphere," *AIChE Journal*, Vol. 18, No. 2, 1972, pp. 337–342.

19 Lienhard, J. H., Dhir, V. K., and Riherd, D. M., "Peak Pool Boiling Heat Flux Measurements on Finite Horizontal Flat Plates," ASME JOURNAL OF HEAT TRANSFER, Vol. 95, No. 2, 1973, pp. 477–482.

20 Hendricks, R. C., "Film Boiling from Submerged Spheres," *NASA TND-5124*, June 1969.

21 Berenson, P. J., "Transition Boiling Heat Transfer from a Horizontal Surface," M.I.T. Heat Transfer Laboratory Technical Report No. 17, 1960.

22 Sun, K. H., and Lienhard, J. H., "The Peak Pool Boiling Heat Flux on Horizontal Cylinders," College of Engineering Bull. 88, University of Kentucky, May 1969.

23 Jasper, J. J., "The Surface Tension of Pure Liquid Compounds," *J. Physical and Chemical Reference Data*, Vol. 1, No. 4, 1972, pp. 841–1010.

24 Hasan, M. Z., Hasan, M. M., Eichhorn, R., and Lienhard, J. H., "Boiling Burnout During Crossflow over Cylinders, beyond the Influence of Gravity," ASME JOURNAL OF HEAT TRANSFER, Vol. 103, No. 3, 1981, pp. 478–484.

25 Cichelli, M. T., and Bonilla, C. C., "Heat Transfer to Liquids Boiling Under Pressure," *Transactions AIChE*, Vol. 41, 1945, p. 755.

**A. Sharan**[1]
Research Assistant
Student Mem. ASME

**J. H. Lienhard**
Professor
Fellow ASME

Heat Transfer/Phase-Change Laboratory,
Mechanical Engineering Department,
University of Houston,
Houston, Texas 77004

# On Predicting Burnout in the Jet-Disk Configuration

*The prediction of boiling burnout in the jet-disk configuration by Lienhard and Eichhorn (based on the mechanical energy stability criterion) is used to recorrelate the data of Katto, Monde, and others. This new correlation includes the identification of the ranges of influence of viscosity (of a Reynolds number) and of gravity (of a Froude number.) The correlation brings the data together within a standard deviation of ±8.66 percent in the range in which viscosity and gravity exert no influence.*

## Introduction

Liquid jets impinging on heated plates cool them very effectively when boiling occurs. Most of the measurements of the peak heat flux $q_{max}$ in this configuration have been made by Monde, Katto, Ishii, and Shimizu (see, e.g., [1-5].) They have measured $q_{max}$ as high as 18.26 MW/m$^2$ [1], on water-cooled disks. This arrangement thus offers a way of meeting many current demands for extremely high cooling rates. Our own interest in this process related to its potential use in removing heat from the inside of solar receivers.

In 1979, Lienhard and Eichhorn applied the Mechanical Energy Stability Criterion [6] to the prediction of $q_{max}$ for this configuration, depicted in Fig. 1. Their interest was restricted to the case for which the incoming liquid is saturated, although Katto et al. also provided data for subcooled jets. They pointed out that burnout must then occur when the kinetic energy of the vapor leaving the surface equals or exceeds the mechanical energy carried away as surface energy of the liquid droplets created by boiling. They obtained the following equation for the burnout heat flux

$$\phi \equiv \frac{q_{max}}{\rho_g h_{fg} u} = r^{1/3}\alpha^{1/3}\left[\frac{d}{\eta}\frac{1}{\beta \mathrm{We}}\right]^{1/3} \tag{1}$$

where $r \equiv \rho_f/\rho_g$, $\mathrm{We} \equiv \rho_f u^2 D/\sigma$, $\beta \equiv D/d$, $D$ is the diameter of the disk, $d$ is the jet diameter, $\alpha$ is the fraction of the incoming liquid converted to a droplet spray by the boiling process (see Fig. 1), and $\eta$ is an appropriate mean diameter of the droplets.

The most serious problem involved with equation (1) is that of representing the unknown droplet diameter. Lienhard and Eichhorn used dimensional analysis to express $d/\eta$ as

$$d/\eta\beta = fn(\mathrm{We}\phi^2/\beta, r) \tag{2}$$

where $\beta$ on the right should have been squared—an error that has hitherto gone unnoticed. They looked at the inviscid term from the classical Nukiyama-Tanasawa (see, e.g., [7]) expression for the droplet diameters formed by the aerodynamic breakup of jets

$$\eta \sim \sigma^{1/2}/\rho_f^{1/2} u \tag{3a}$$

and noted that it was dimensional. Adding the missing dimension $d$ and arguing that $u$ should be replaced with $u_g = q/\rho_g/h_{fg}$, the average velocity of vapor normal to the disk, they recast equation (3$a$) in the form suggested by equation (2) they got

$$(d/\eta)^{1/3} = fn(r)\beta^{1/3}\mathrm{We}^a \phi^{2a}\beta^{-a} \tag{3b}$$

where $\beta^{-a}$ should have been $\beta^{-2a}$, and where Nukiyama's result suggests that $a = 1/6$. Assuming that $\alpha$ depended only on $r$, Lienhard and Eichhorn substituted equation (3$b$) in (1) and obtained

$$\phi = \frac{f(r)}{\beta}\left[\frac{\beta^3}{\mathrm{We}}\right]^A \tag{4}$$

They showed that equation (4) correlated the data of Monde and Katto [1, 2], and that $A$ varied from 1/3 to 1/2 as $r$ decreased.

Lienhard and Hasan [8] subsequently expanded the correlation based on equation (4), adding the new results of Katto and Shimizu [4]. These data, obtained with F-12 and F-113, greatly extended the range of $r$ and helped to clarify the variation of $A(r)$. However, Monde [9] recently pointed out to us an error in [4] that reflected the mishandling of $\beta$ in equation (4). He also showed us unpublished data for higher pressures that exposed this error. We must therefore reformulate the correlation.

We shall develop the recorrelation here, considering two previously ignored limitations and continuing to restrict consideration to saturated jets. The two new considerations are the influences of viscosity and of gravity.

## Reformulation of the Correlation

We propose to make two changes in the adaptation of equation (3$a$) to the jet-disk system: We shall take $u$, rather than $u_g$, to be the characteristic velocity because $u_g << u$ in the ranges of interest. Then we enter equation (3$b$) with $\beta^{-2a}$ and $a = 1/6$, and obtain

$$(d/\eta)^{1/3} = fn(r)\,\mathrm{We}^{1/6} \tag{5}$$

We also grant that $\alpha = \alpha(r$ as well as We), which can probably be written as $\alpha = fn(r)fn(\mathrm{We})$. Then equation (1) becomes

$$\phi = \frac{fn(r)}{(\beta\mathrm{We})^{1/3}}\mathrm{We}^{a(r)} \tag{6a}$$

which can be written, for our subsequent convenience, in the form

$$\phi\beta^{1/3} = f_2(r)\left[\frac{1000}{\mathrm{We}}\right]^{A(r)} \tag{6b}$$

## Viscous Retaration of the Liquid Sheet

An inviscid spreading sheet formed by the impinging jet (see Fig. 1) will thin out inversely with radial position. Viscosity has the effect of slowing the sheet so it thins out less rapidly. Indeed, the sheet will even start to thicken as its speed diminishes far enough. (This thickening should not be confused with a hydraulic jump, which can also occur.) Previous experimental studies have shown [1] that burnout occurs at the edge of the disk, where the sheet should be thinnest. Any correlation that ignores viscosity must therefore fail when viscous drag significantly influences the sheet thickness near the edge.

[1]Presently Assembly Engineer, Integrated Device Technology, Santa Clara, CA

Contributed by the Heat Transfer Division for publication in the JOURNAL OF HEAT TRANSFER. Manuscript received by the Heat Transfer Division January 5, 1984.

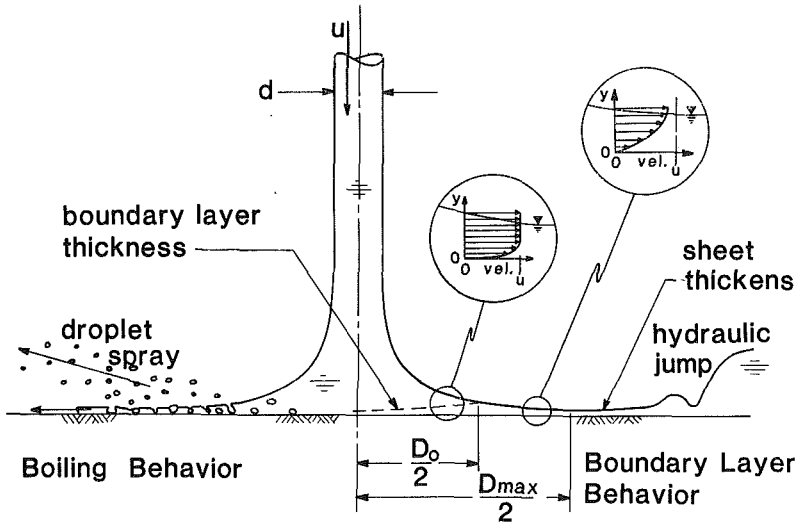


Fig. 1 The jet-disk boiling heat removal configuration (left), and the viscous drag process (right)

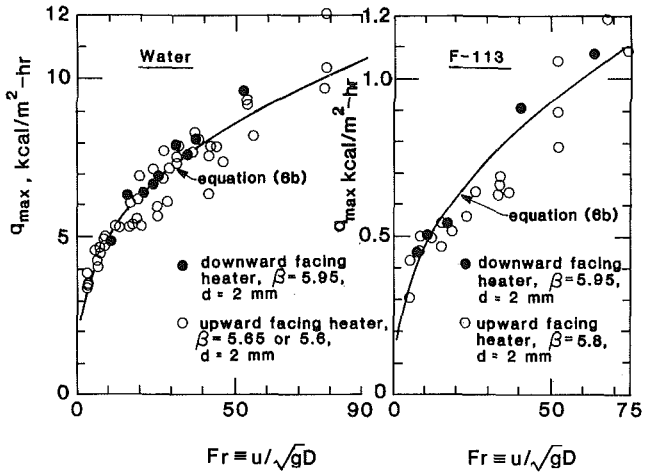


Fig. 2 Experimental demonstration that gravity does not influence burnout when Fr > 10, based on the data of Monde and Katto [1]

Watson [10] calculated the drag using the model shown on the RHS in Fig. 1. He considered drag to occur in a Blasius boundary layer (b.l.) profile, up to a diameter, $D = D_o$, where the b.l. reached the edge of the liquid. Beyond $D_o$, he used a simple parabolic Nusselt profile. His calculation showed that the sheet was thinnest where $D = D_{max}$, defined by

$$\beta_{max} \equiv D_{max}/d = 0.5245\mathrm{Re}^{1/3} \tag{7}$$

where $\mathrm{Re} \equiv ud/\nu$, and where we denote the diameter as a "maximum" because a correlation that does not involve Re, can hardly have any validity beyond this limit. Watson also showed how to predict the actual thickness of the sheet subject to viscosity. His results give the basis for expressing the sheet thickness $\delta$ as

$$\frac{\delta_{actual}}{\delta_{inviscid}} = 1 + 2.816\beta^{3/2}/\sqrt{\mathrm{Re}}; \qquad D < D_o \tag{8a}$$

$$= 4.838\beta^3/\mathrm{Re} + 1.385; \qquad D \geq D_o \tag{8b}$$

*We subsequently identify a maximum permissible increase* of $\delta$ over its inviscid value, beyond which there should be a viscous influence on burnout. We do not know where that limit lies, so we shall have to determine it subsequently, by correlation.

## The Influence of Gravity

The dimensional functional equation for $q_{max}$ takes the following form when we include viscosity and gravity in it

## Nomenclature

$a,b$ = undetermined exponents
$A(r)$ = exponent in equation (4) or (6*b*); a function of $r$
b.l. = boundary layer
$D, D_0, D_{max}$ = diameter of disk heater, diameter of spreading liquid sheet where b.l. first penetrates to outer interface, diameter of spreading liquid sheet where its thickness is least.
$d$ = diameter of incoming jet
Fr = Froude number, $u/\sqrt{gD}$
$f(r), f_2(r)$ = functions of $r$ in equations (4) and (6*b*)
$g$ = gravitational acceleration
$h_{fg}$ = latent heat of vaporization
$q, q_{max}$ = heat flux; peak, or "burnout" heat flux
$r$ = $\rho_f/\rho_g$
Re = Reynolds number, $ud/\nu$
$u$ = the incoming jet velocity
$u_g$ = $q/\rho_g h_{fg}$, average vapor velocity normal to the disk
We = Weber number, $\rho_f u^2 D/\sigma$
$\alpha$ = fraction of liquid jet converted to droplet spray
$\beta$ = $D/d$
$\delta$ = local thicknesses of the liquid sheet on the disk
$\eta$ = an appropriate mean spray-droplet diameter
$\nu$ = kinematic viscosity
$\rho_f, \rho_g$ = saturated liquid and vapor densities, respectively
$\sigma$ = surface tension
$\phi$ = dimensionless peak heat flux, $q_{max}/\rho_g h_{fg} u$

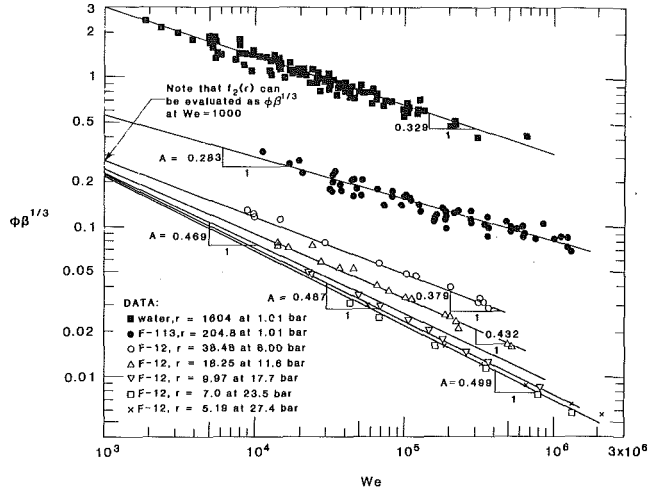


Fig. 3 Experimental determination of values of $f_2(r)$ and $A(r)$

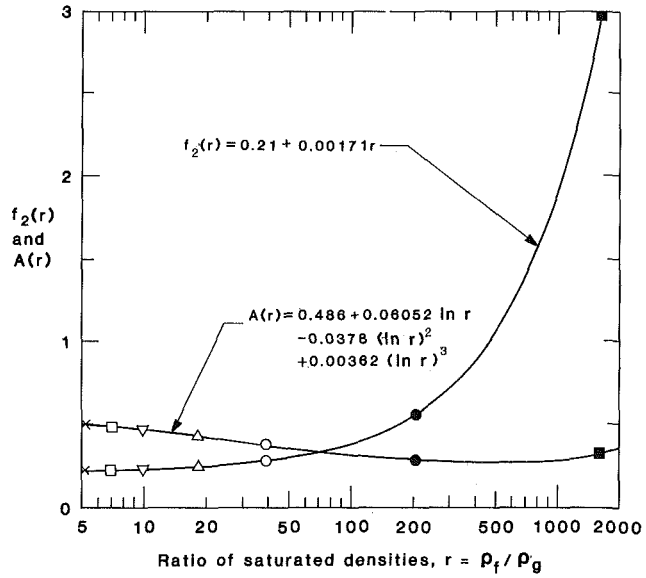


Fig. 4 The functions: $f_2(r)$ and $A(r)$

$$q_{\max} \equiv (\rho_f, \rho_g, h_{fg}, D, d, \sigma, \nu, u, g) \tag{9}$$

Ten variables in four dimensions require six Π-groups

$$\phi = f(r, \mathrm{We}, \beta, \mathrm{Re}, \mathrm{Fr}) \tag{10}$$

where Fr is the Froude number, $u/\sqrt{gD}$. (Equation (6*b*) should account for the roles of $\phi$, $r$, We, and $\beta$, without Fr and Re.)

Normally, an appropriately defined Fr that is less than ten is small enough to signal significant gravity effects. We choose $D$ (instead of $d$) as the characteristic dimension of Fr because we expect gravity to create disturbances whose sizes are on the order of the disk diameter. If this is the case, then the predicted correlating equation (6) will fail for some Fr < 10.

The only data that might permit us to test for the critical value of Fr directly, are those of Monde and Katto [1] who observed $q_{\max}$ on both upward- and downward-facing plates. Two sets of burnout data are plotted against absolute values of Fr in Fig. 2. They appear to superpose down to Fr ≃ 10. Matched upward and downward $q_{max}$ data are not available at lower Fr's.

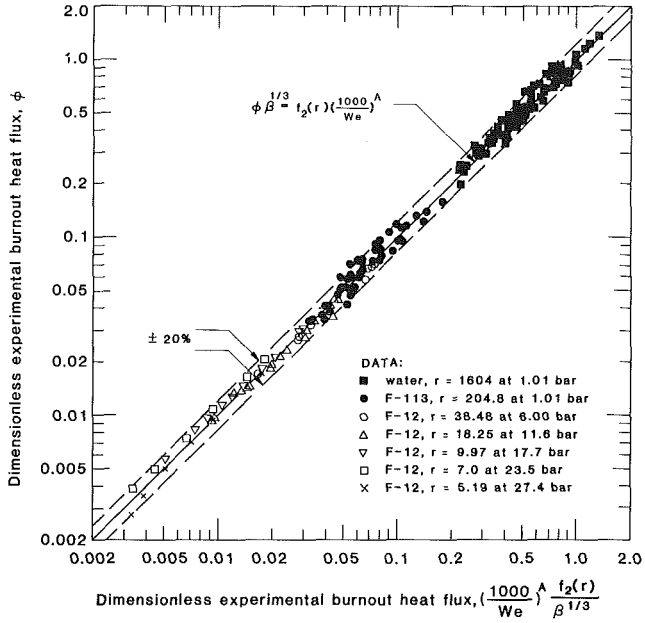


Fig. 5 Comparison of the correlation with data

## Recorrelation

The data of Monde and Katto [1], Katto and Monde [2], Katto and Shimizu [4], and Monde [5] are plotted on $\ln(\phi\beta^{1/3})$ versus ln(We) coordinates in Fig. 3, in conformity with equation (6*b*). A different symbol is alloted to each value of $r$—to each fluid at each pressure. Thus the slopes of faired straight lines through the data for each $r$, and their ordinate intercepts at We = 1000, are $A(r)$ and $f_2(r)$, respectively. We have eliminated those data from Fig. 3 that might be influenced by viscosity or by gravity. We defer explanation of how these points were identified, for the moment.

The measured values of $A(r)$ and $f_2(r)$ are plotted in Fig. 4. They form very regular curves that are given by the functions

$$f_2(r) = 0.00171\, r + 0.21 \tag{11}$$

$$A(r) = 0.486 + 0.06052(\ln r) - 0.0378(\ln r)^2 + 0.00362(\ln r)^3 \tag{12}$$

We finally return to equation (6*b*) with equations (11) and (12) to get our prediction of the peak heat flux. The predicted $\phi$ is plotted against data in Fig. 5. It is accurate within 8.66 percent for $\beta/\mathrm{Re}^{1/3} < 0.40$ and $\mathrm{Fr} \geq 8$.

## Discussion and Conclusions

The viscosity limit, $\beta/\mathrm{Re}^{1/3} = 0.4$, corresponds (see equation (8*a*)) with a 71 percent thickening of $\delta$. This limit and the gravitational limit on Fr are somewhat arbitrary and are set where the available data—and additional unpublished data [9]—cease to correlate well. These limits are presented tentatively; however, the available data do suggest that $q_{\max}$ generally tends below the correlation when $\beta/\mathrm{Re}^{1/3} > 0.40$ or where Fr < 8 for downward facing heaters.

Subject to these limitations, equation (6*b*) with equations (11) and (12) provides excellent correlation of the existing data.

It is interesting to note that Katto and his co-workers [4, 6] identified several regimes of burnout. The primary two were the velocity-independent (or I) regime and the velocity-dependent (or V) regime. Equation (6*b*) reflects these regimes. It shows that $q_{max}$ varies as $u^{1/3}$ at low pressure (where $r$ is large.) But as the pressure is increased and $r$ decreases, the

influence of velocity on $q_{max}$ decreases and vanishes entirely at $r = 5$.

## Acknowledgments

We are grateful to the department of Energy for supporting this work under Contract DE-AC03-815F11557, and to Prof. M. Monde who has been most helpful in sharing his expertise in this problem with us.

## References

1 Monde, M., and Katto, Y., "Burnout in High Heat-Flux Boiling System with an Impinging Jet," *International Journal of Heat and Mass Transfer*, Vol. 21, 1978, pp. 295–305.

2 Katto, Y., and Monde, M., "Study of Mechanisms of Burnout in High Heat-Flux Boiling System with an Impinging Jet," *Proc. 5th Int. Heat Transfer Conf.*, Tokyo, Vol. 4, B6.2, 1974.

3 Katto, Y., and Ishii, K., "Burnout in a High Heat Flux Boiling System with a Forced Supply of Liquid Through a Plane Jet," *Proc. 6th Int. Heat Transfer Conf.*, Toronto, 1978.

4 Katto, Y., and Shimizu, M., "Upper Limit of the CHF in the Forced Convection Boiling on a Heated Disc with a Small Impinging Jet," ASME JOURNAL OF HEAT TRANSFER, Vol. 101, No. 2, 1979, pp. 265–269.

5 Monde, M., "Burnout Heat Flux in Saturated Forced Convection Boiling with an Impinging Jet," *Heat Transfer Japanese Research*, Vol. 9, No. 1, 1980, pp. 31–41.

6 Lienhard, J. H., and Eichhorn, R., "On Predicting Boiling Burnout for Heaters Cooled by Liquid Jets," *International Journal of Heat and Mass Transfer*, Vol. 22, 1979, pp. 774–776.

7 Chemical Engineer's Handbook, 5th ed., edited by R. H. Perry and C. H. Chilton, Section 18, McGraw-Hill, New York, 1973.

8 Lienhard, J. H., and Hasan, M. Z., "Correlation of Burnout Data for Disk Heaters Cooled by Liquid Jets," ASME JOURNAL OF HEAT TRANSFER, Vol. 101, No. 2, 1979, pp. 383–384.

9 Monde, M., private communications, Mar., July 1983.

10 Watson, J. E., "The Radial Spread of a Liquid Jet over a Horizontal Plane," *J. Fluid Mech.*, Vol. 20, 1964, pp. 481–499.

**L. Y. Cheng**
Courant Institute of Mathematical Sciences,
New York University

**D. A. Drew**
Department of Mathematical Sciences.

**R. T. Lahey, Jr.**
Department of Nuclear Engineering.
Fellow ASME

Rensselaer Polytechnic Institute,
Troy, N.Y. 12181

# An Analysis of Wave Propagation in Bubbly Two-Component, Two-Phase Flow

*Wave propagation in bubbly two-phase, two-component flow was analyzed to assess the validity of some interfacial transfer laws for two-fluid models of two-phase flow. A dispersion relation was derived from the linearized conservation equations and the Rayleigh equation. The phase velocity and wave attenuation calculated from the dispersion relation, compared well with existing high- and low-frequency data. The virtual mass term was found to have a significant effect on wave dispersion in the bubbly flow regime. Thermal effects were found to be important in determining the resonance phenomenon and wave scattering was a major source of damping at frequencies higher than the resonance frequency.*

## Introduction

In order to derive tractable mathematical expressions for two-phase mixtures, space/time averaging methods have been applied to the conservation equations for each phase. In two-fluid models [1, 2], the space/time averaged conservation laws for each phase must be coupled with constitutive equations relating the interfacial transfer of mass, momentum, and energy. The postulated forms of these constitutive equations, and the corresponding coefficients which invariably arise in these equations, must be determined empirically. Intuition and empiricism are strong components of the two-fluid approach, nevertheless, there exists a logical framework within which the relevant physical phenomena can be introduced [3].

The two-fluid model explicitly allows for mass, momentum, and energy transfers at the interfaces. Of these interfacial transfers, the most important, from the point of view of system classification and numerical stability, are the nonequilibrium momentum transfer laws, since they basically determine the characteristics of the mathematical system under consideration [4]. A bubble imbedded in a flowing liquid is influenced by a number of mechanisms, such as the drag force, virtual mass force, and Basset force, all of which act on it through the momentum transfer taking place at the gas/liquid interface.

An examination of virtual mass effects for bubbly flows shows [5] that such nonsteady effects in the interaction terms can be bigger than the inertial terms in the bubble's momentum equation. The virtual mass force is normally assumed to be proportional to an appropriate relative acceleration; however, the proportionality factor must be determined experimentally. It is the purpose of this study to show how the proportionality factor can be determined, and that the inclusion of the virtual mass force yields a system of conservation equations which are able to model accelerating two-phase flow phenomena.

The propagation of infinitesimal disturbances (e.g., sound waves) represents one important way to verify and quantify some of the nonsteady aspects of the interactions between phases. Specifically, the importance of virtual mass can be assessed through its effect on the wave dispersion properties of the system of conservation equations that represent the dynamics of the two-phase mixture.

When an oscillatory pressure is imposed on a two-phase mixture, the dispersed gaseous phase reacts by expanding and contracting periodically. The radial motion of the liquid subsequently modifies the response of the two-phase mixture to the forcing function, and hence leads to a frequency-dependent pressure wave propagation speed. Wave propagation in a bubbly flow becomes more complicated when the effects of bubble pulsations become important. Since under the influence of a sinusoidal pressure perturbation, the gas bubbles imbedded in the liquid constitute a potentially resonant system, the phase velocity and attenuation of a pressure wave shows a resonance.

Previous two-fluid dispersion relations derived by Mecredy and Hamilton [6], and by Ardron and Duffey [7], did not take into account the dynamics of the dispersed phase (i.e., the gas bubbles). Hence, their models are unable to predict resonant phenomena. Drumheller and Bedford's [8] model on wave dispersion in a bubbly liquid did consider the effect of the pressure perturbations on bubble response. However, wave scattering by the bubbles was not considered in their model, and thus it could not be applied to frequencies near and beyond resonance. In another study, Van Wijngaarden [11] considered a model for two-phase flows that uses a two-fluid model plus a bubble dynamics equation. However, that model considered neither the relative motion nor the heat transfer effects at the interface.

In order to study the nature of the frequency-dependent wave propagation speed in a two-phase mixture, a wave dispersion relation for a two-component (air/water), two-phase flow was derived from a two-fluid, two-pressure model. A modified Rayleigh bubble dynamics equation was used as the constitutive law which related the two phasic pressures. Both the phase velocity and attenuation were calculated as a function of frequency and were compared with existing low and high frequency data (including resonance).

The two-phase flow equations used in the present wave dispersion model were those of the one-dimensional space/time averaged phasic conservation equations of mass, momentum, and energy with nonequilibrium momentum and energy transfer at the interface. An objective form of the relative acceleration [5] was used in the modeling of the virtual mass force. The liquid and vapor phases were assumed to be compressible, and the vapor phase (air) was assumed to behave like an ideal gas.

## Analysis

**Conservation Equations.** The conservation laws that govern the dynamic behavior of a two-component, two-phase mixture are those of mass, momentum, and energy. For phase-$k$ ($k=g, l$), they are [1, 2]

Contributed by the Heat Transfer Division for publication in the JOURNAL OF HEAT TRANSFER. Manuscript received by the Heat Transfer Division June 1, 1983.

Conservation of Mass

$$\frac{\partial}{\partial t}(\alpha_k \rho_k) + \frac{\partial}{\partial z}(\alpha_k \rho_k u_k) = 0 \tag{1}$$

Conservation of Momentum

$$\frac{\partial}{\partial t}(\alpha_k \rho_k u_k) + \frac{\partial}{\partial z}(\alpha_k \rho_k u_k^2) = -\alpha_k \frac{\partial p_k}{\partial z} + \alpha_k \rho_k g_k \cos\theta + M_k - \tau_k \tag{2}$$

Conservation of Thermal Energy

$$\frac{\partial}{\partial t}(\alpha_k \rho_k h_k) + \frac{\partial}{\partial z}(\alpha_k \rho_k u_k h_k) = \alpha_k \left(\frac{\partial p_k}{\partial t} + u_k \frac{\partial p_k}{\partial z}\right) - u_k \tau_k + \frac{q''_{ki}}{L_s} \tag{3}$$

The dependent variables in equations (1), (2) and (3), (i.e., $\alpha_k$, $\rho_k$, $u_k$, $h_k$, $p_k$), are space/time averaged variables, where for convenience, we have dropped the averaging notion. The time scale used in the averaging process is large compared to microscale fluctuations (e.g., turbulence) but is small compared to the macroscopic scales of interest; specifically the wave period. On the other hand, the length scale is large compared to microscopic scales (e.g., the bubble radius and the inter-bubble distance) but is small compared to the wave length. The continuum approximation further requires that the bubble size be much smaller than the wavelength.

**Constitutive Equations.** The system of equations (1-3) expressed above is insufficient to describe two-phase flows. They must be supplemented with constitutive equations expressing the interfacial transfer laws in terms of the dependent variables

As mentioned previously, for two-component, two-phase flows, the most important transfer law is that due to interfacial momentum transfer. This law has at least three components and can be written in the form

$$M_l = -M_g = \alpha[F_D + F_{VM} + F_R] \tag{4}$$

where (per unit bubble volume), $F_D$ is the drag force, $F_{VM}$ is the virtual mass force, $F_R$ is the reaction force due to the change in radius of the dispersed phase, and $\alpha \triangleq \alpha_g$.

In this study, Hench's [12] model for drag force was used in the form

$$\mathbf{F}_D = \frac{3}{8}\rho_l \frac{C_D}{R_b}(\mathbf{u}_g - \mathbf{u}_l)\,|(\mathbf{u}_g - \mathbf{u}_l)| \tag{5}$$

where, for churn-turbulent and bubbly flows, $(0 < \alpha \leq 0.3)$, the ratio of the drag coefficient, $C_D$, to the bubble radius, $R_b$, is given by [12]

$$\frac{C_D}{R_b} = 110(1-\alpha)^3 \qquad (\mathrm{m}^{-1}) \tag{6}$$

This simple interfacial drag law has been found [15] to be sufficient for our purposes here. Moreover, when the so-called Basset force was included in the analysis it was found [15] that the effect was quite small, and thus it could be neglected.

The virtual mass force ($F_{VM}$) is written as a product of the virtual mass of the liquid displaced by a bubble and the relative acceleration between the two phases. That is

$$\mathbf{F}_{VM} = \rho_l C_{VM} \mathbf{a}_{VM} \tag{7}$$

where, $C_{VM}$ is the so-called virtual volume coefficient. This coefficient is, in general, a second-order tensor. However, we

## Nomenclature

$a$ = thermal diffusivity
$a_{VM}$ = virtual mass acceleration
$C$ = speed of sound
$C_{VM}$ = virtual volume coefficient
$C_{ph}$ = phase velocity
$C_D$ = drag coefficient
$c_p$ = constant pressure specific heat capacity
$c_v$ = constant volume specific heat capacity
$D_H$ = hydraulic diameter
$F$ = force
$F_{VM}$ = virtual mass force
$F_D$ = drag force
$F_R$ = virtual mass reaction force due to the change in radius of the dispersed phase
$F_W$ = wall frictional force
$f$ = Darcy-Weisbach friction factor
$g$ = gravitational acceleration
$H_i$ = interfacial heat transfer coefficient
$h$ = enthalpy
$i$ = imaginary number, $\sqrt{-1}$
$k$ = wave number
$1/L_s$ = interfacial area density
$M_k$ = interfacial momentum transfer of phase-$k$
$p$ = pressure
$q''_{ki}$ = interfacial heat flux
$R$ = radius
$r$ = radial coordinate
$T$ = temperature
$t$ = time
$u$ = velocity
$\hat{u}$ = gas velocity perturbation in the radial direction
$V$ = volume
ZPV = parameter defined in equation (33)
ZTR = parameter defined in equation (34)
$z$ = axial coordinate

### Greek Symbols

$\alpha$ = void fraction
$\beta_k$ = parameter defined by equation (20)
$\eta$ = attenuation coefficient
$\kappa$ = thermal conductivity
K = polytropic exponent of a gas
$\lambda$ = parameter in the objective form of the virtual mass acceleration
$\lambda_g$ = thermal diffusion length of a gas bubble
$\mu$ = dynamic viscosity
$\omega$ = angular frequency
$\phi$ = velocity potential
$\phi_k$ = parameter defined by equation (21)
$\rho$ = density
$\sigma$ = surface tension
$\theta$ = an angle
$\tau$ = wall shear
$\xi$ = eigenvector

### Subscripts

$b$ = bubble
$D$ = drag
fri = friction
$g$ = gas phase
$\infty$ = bulk
$I$ = imaginary
$i$ = interface
$k$ = phase-$k$
$ki$ = interface of phase-$k$
$l$ = liquid phase
$n$ = natural or resonant
$n$ = $n$th mode
$ph$ = phase
$r$ = radial component
$R$ = real
$VM$ = virtual mass
$o$ = equilibrium value

### Other Symbols

$\dot{(\ )}$ = time derivative
$\delta(\ )$ = perturbation
$\hat{(\ )}$ = perturbation in the form of a function of the radial coordinate

have assumed that the two-phase flow is locally isotropic, and thus $C_{VM}$ can be regarded as a scalar. The most general objective virtual mass acceleration is given as [5].

$$\mathbf{a}_{VM} = \frac{D_g}{Dt}(\mathbf{u}_g - u_l) + (\mathbf{u}_g - \mathbf{u}_l)\cdot\{(\lambda-2)\nabla\mathbf{u}_g + (1-\lambda)\nabla\mathbf{u}_l\} \tag{8}$$

Both $C_{VM}$ and $\lambda$ are expected to be a function of the local void fraction $\alpha$.

Another virtual mass type effect is due to the change of radius of the bubble. This additional reaction force is a consequence of the pressure distribution around a sphere of variable radius, and is given by [13]

$$\mathbf{F}_R = \frac{3}{R_b} C_{VM}\rho_l(\mathbf{u}_g - \mathbf{u}_l)\frac{D_g R_b}{Dt} \tag{9}$$

For gaseous bubble undergoing unsteady motion, the virtual mass forces and the bubble inertia are important in the short-lived initial transient period.

Since, in this study, only the liquid phase was assumed to be in contact with the wall, the shear stress at the wall is

$$\tau_g = 0 \tag{10}$$

and,

$$\tau_l = F_W = \frac{1}{2}\frac{f}{D_H}\rho_l u_l |u_l| \tag{11}$$

The task of relating the interfacial pressures $p_{ki}$ to the average pressures $p_k$ will now be considered. For pulsating bubbles, it is a good approximation to assume

$$p_{gi} = p_g(r)|_{r=R_b} \tag{12}$$

It is, however, necessary to account for the scattering of pressure waves in the fluid by the bubbles. For this purpose, we shall assume that scattering effects occur on a scale smaller than the inter-bubble distance. That is, we assume that pressure fluctuations in the neighborhood of the bubble are spherically symmetric and we can treat each bubble as being isolated from the others, thus the motion of the liquid can be related to the pressure difference through the Bernoulli equation

$$\frac{p_{li}(t)}{\rho_l} + \frac{1}{2}[\nabla\phi(R_b)]^2 + \frac{\partial\phi(R_b)}{\partial t} = \frac{p_{l\infty}(t)}{\rho_l} \tag{13}$$

The continuity of normal stress at the bubble wall requires that

$$p_g(R_b,t) - p_{li}(t) = \frac{2\sigma}{R_b} - 2\mu_l\frac{\partial u_l}{\partial r}\bigg|_{r=R_b} \tag{14}$$

where $\sigma$ is the surface tension. By assuming spherical symmetry, the appropriate velocity potential $\phi(r)$ is given by [14]

$$\phi(r) = -\frac{R_b^2\dot{R}_b e^{ik_b(r-R_b)}}{r(1-ik_bR_b)} \tag{15}$$

where

$$k_b \triangleq \omega/C_l \tag{16}$$

is the wave number of the periodic disturbance generated in the surrounding liquid, and $C_l$ is the speed of sound in the liquid phase. By using equations (14) and (15) in equation (13), the bubble dynamics equation can be expressed in the form

$$p_g(R_b,t) - p_{l\infty} = \frac{\rho_l R_b\ddot{R}_b}{(1-ik_bR_b)} + \rho_l\dot{R}_b{}^2\left[\frac{2}{(1-ik_bR_b)} - \frac{1}{2} - \left(\frac{k_bR_b}{ik_bR_b-1}\right)^2\right] + \frac{4\mu_l}{R_b}\dot{R}_b\left[1 - \frac{(k_bR_b)^2/2}{(1-ik_bR_b)}\right] + \frac{2\sigma}{R_b} \tag{17}$$

It is interesting to note that if terms of order $k_bR_b$, or higher, are neglected in equation (17), the classical Rayleigh's equation (including viscous shear) is recovered

$$p_g(R_b,t) - p_{l\infty} = \rho_l R_b\ddot{R}_b + \frac{3}{2}\rho_l(\dot{R}_b)^2 + \frac{4\mu_l\dot{R}_b}{R_b} + \frac{2\sigma}{R_b} \tag{18}$$

In the linearized form of equation (17) terms of order $k_bR_b$ and higher represent the acoustic effects on a forced pulsating bubble.

For the thermodynamic aspect of the problem, the equation of state valid for the local variables is assumed also to be applicable for the averaged variables. The equation of state for phase-$k$ is taken to have the form

$$\rho_k = \rho_k(p_k, h_k) \tag{19}$$

If we define the following partial derivations

$$\beta_k \triangleq \left(\frac{\partial\rho_k}{\partial p_k}\right)_{h_k} \tag{20}$$

and

$$\phi_k \triangleq \left(\frac{\partial\rho_k}{\partial h_k}\right)_{p_k} \tag{21}$$

Then the isentropic speed of sound in phase-$k$ is given by,

$$\frac{1}{C_k^2} = \beta_k + \frac{1}{\rho_k}\phi_k \tag{22}$$

In this analysis, the gas (air) is assumed to behave as an ideal gas. Thus it is possible to replace the gas thermal energy equation by an appropriate gas equation of state which takes into account the thermal energy exchange at the interface.

The volumetric interfacial heat transfer rate, $q''_{ki}/L_s$, is given by

$$\frac{q''_{ki}}{L_s} = \frac{H_i}{L_s}(T_{ki} - T_k) \tag{23}$$

where $H_i$ is the interfacial heat transfer coefficient; $T_{ki}$ is the interfacial temperature, of phase-$k$ and $1/L_s$ is the interfacial area density (i.e., the interfacial area per unit volume of the two-phase mixture). For $N$ uniform spherical bubbles suspended in the liquid

$$\frac{1}{L_s} = \frac{4\pi R_b^2 N}{4/3\pi R_b^3 N}\alpha = \frac{3\alpha}{R_b} \tag{24}$$

The interfacial heat transfer coefficient $H_i$ depends on the geometry of the interface and the thermodynamic properties of the two phases. For low frequencies, equation (23) works well when a standard Nusselt-type correlation for the coefficient $H_i$ is used. For high frequencies (near bubble resonance), however, it was found necessary to derive a new model from microscopic considerations. Since that analysis relates directly to the kinds of constitutive assumptions needed for an adequate description of two-phase media, it will be summarized here.

The harmonically oscillating linearized (radial) continuity, momentum, and energy equations in the gas bubble were solved [15] subject to the following temperature and heat flux boundary conditions

$$\hat{T}_l(R_{bo},t) = \hat{T}_g(R_{bo},t) \tag{25}$$

$$-\kappa_l\frac{\partial\hat{T}_l(R_{bo},t)}{\partial r} = -\kappa_g\frac{\partial\hat{T}_g(R_{bo},t)}{\partial r} \tag{26}$$

and the kinematic condition

$$\hat{u}(R_{bo},t) = \frac{dr}{dt} \tag{27}$$

where $R_{bo}$ is the undisturbed bubble radius, and $\kappa_g$ and $\kappa_l$ are the thermal conductivities of the gas and liquid, respectively. Note that $\hat{T}_k$ and $\hat{u}$ represent the perturbed temperatures and interfacial velocity, respectively. This analysis is similar to,

but extends, the work of Plesset and Hsieh [10] and Prosperetti [9].

The resulting heat transfer coefficient $H_i$ was complex, and frequency dependent [15]. The real part of $H_i$ represents the rate of interfacial heat transfer, while the imaginary part represents the dissipative effect of the interfacial heat transfer process. When the gas bubble behaves isothermally, there is substantial interfacial heat transfer and dissipation. However, for an adiabatic gas bubble there is no interfacial heat transfer and thus no dissipation due to heat transport processes.

Prosperetti [9], and Chapman and Plesset [18] have studied the thermal behavior of a gas bubble in a liquid medium. The polytropic exponent $K$ of the gas was shown to be a function of the ratio between the radius of the bubble ($R_b$) and the thermal diffusion length of the gas ($\lambda_g$)

$$K = K(R_b/\lambda_g) \tag{28}$$

where

$$\lambda_g = \left(\frac{a_g}{2\omega}\right)^{1/2} \tag{29}$$

and,

$$a_g = \frac{\kappa_g}{\rho_g c_{v,g}} \tag{30}$$

An approximate expression for $K$ has been given recently by Prosperetti [19], and it agrees well with measurements reported by Crum [20]. In general, when $R_b/\lambda_g << 1$ the gas behaves isothermally (i.e., $K \simeq 1$), and when $R_b/\lambda_g >> 1$, the gas behaves adiabatically (i.e., $K \simeq 1.4$, for air).

By satisfying the kinematic condition at the bubble interface, it can be shown that [15]

$$\hat{p}_g(R_{bo}) = \frac{[\rho_{go}\omega^2 R_{bo}]}{p_{lo}}\,\eta_{th}\,\hat{R}_b \tag{31}$$

and

$$\delta p_g(R_{bo},t) = \rho_{go}\omega^2 R_{bo}\eta_{th}\delta R_b \tag{32}$$

where, $\eta_{th}$ is a factor that represents the thermal dissipative effect due to heat transfer at the bubble surface [15]. When equation (32) is used in conjunction with the bubble dynamics equation, equation (17), $\eta_{th}$ can be intepreted as an additional "viscosity" due to interfacial heat transfer effects.

Equation (32) gives the pressure perturbation at the surface of the bubble. For use in the linearized conservation laws of mass and momentum, we need the average pressure perturbation inside a gas bubble. This is given by [15]

$$\delta p_g = (\rho_{go}\omega^2 R_{bo})\ \mathrm{ZPV}\ \delta R_b \tag{33}$$

Similarly, the average temperature perturbation of the gas is given by [15],

$$\delta T_g = T_{go}\left(\frac{\rho_{go}\omega^2 R_{bo}}{p_{lo}}\right)\mathrm{ZTR}\ \delta R_b \tag{34}$$

Thus

$$\delta h_g = c_{p_{go}}\,T_{go}\left(\frac{\rho_{go}\omega^2 R_{bo}}{p_{lo}}\right)\mathrm{ZTR}\ \delta R_b \tag{35}$$

where ZPV and ZTR are complex transfer functions. Equation (35) can be used to replace the linearized thermal energy equation of the gas phase. It was obtained from the linearized equation of state for a pulsating gas bubble which has heat transfer occurring at the interface.

**Wave Propagation.** The previously derived conservation laws for mass, momentum, and energy, and the bubble dynamics equation, describe a two-phase mixture as a two-fluid medium with different pressures in each phase (gas/liquid). These equations can be written as a system of nonlinear, first-order partial differential equations. After linearization, these equations can be written in matrix form as ]15]

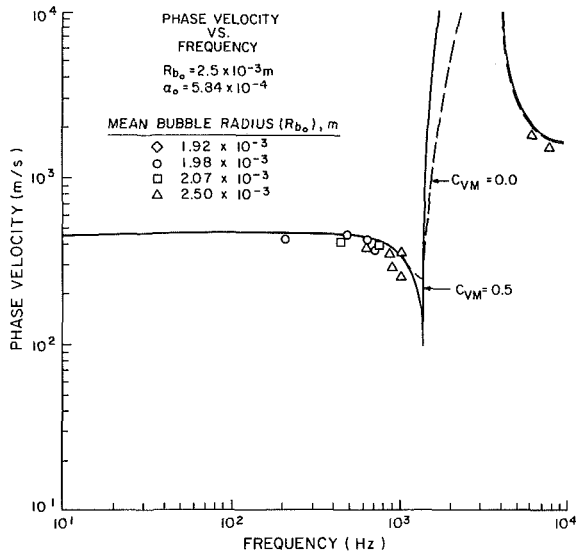


**Fig. 1 Phase velocity versus frequency, $R_{b_o} = 2.5 \times 10^{-3}$m, $\alpha_o = 5.84 \times 10^{-4}$**

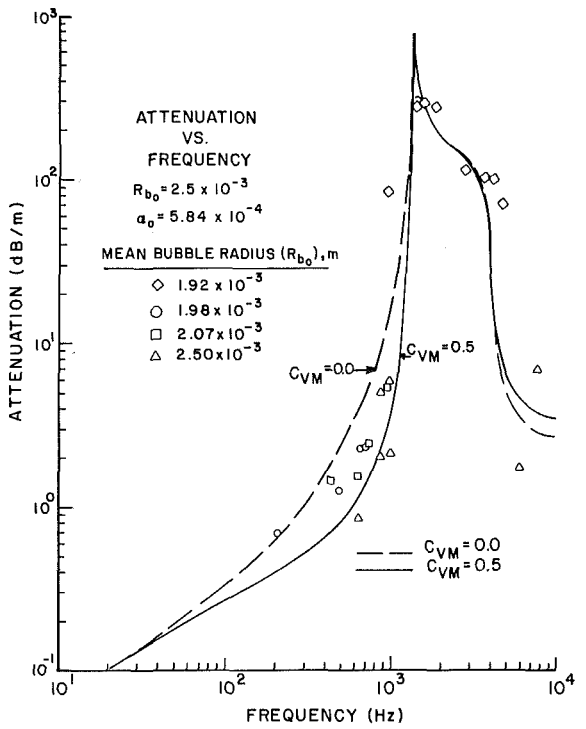


**Fig. 2 Attenuation versus frequency, $R_{b_o} = 2.5 \times 10^{-3}$m, $\alpha_o = 5.84 \times 10^{-4}$**

$$\underline{\underline{A}}(\phi)\frac{\partial \delta\phi}{\partial t} + \underline{\underline{B}}(\phi)\frac{\partial \delta\phi}{\partial t} = \underline{\underline{C}}(\phi)\delta\phi \tag{36}$$

where $\phi$ is the vector of the seven dependent variables: $\alpha$, $p_l$, $u_g$, $u_l$, $h_l$, $R_b$, $\dot{R}_b$. The perturbations in gas pressure and gas enthalpy $\delta p_g$ and $\delta h_g$ are not taken as state variables since they are related to $\delta R_b$ by equations (33) and (35), respectively.

The final set of linearized equations used are from equations (1), (2), (3), and (17) those for gas/liquid mass conservation, gas/liquid momentum conservation, liquid phase thermal energy conservation, and the bubble dynamics equation, which is written in the form of two first-order equations (one for $R_b$ and the other for $\dot{R}_b$).

If we assume a traveling wave perturbation of the form

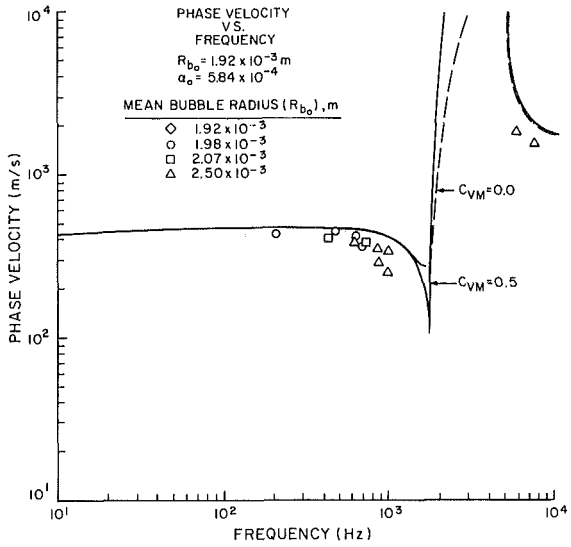


**Fig. 3 Phase velocity versus frequency, $R_{b_o} = 1.92 \times 10^{-3}$m, $\alpha_o = 5.84 \times 10^{-4}$**

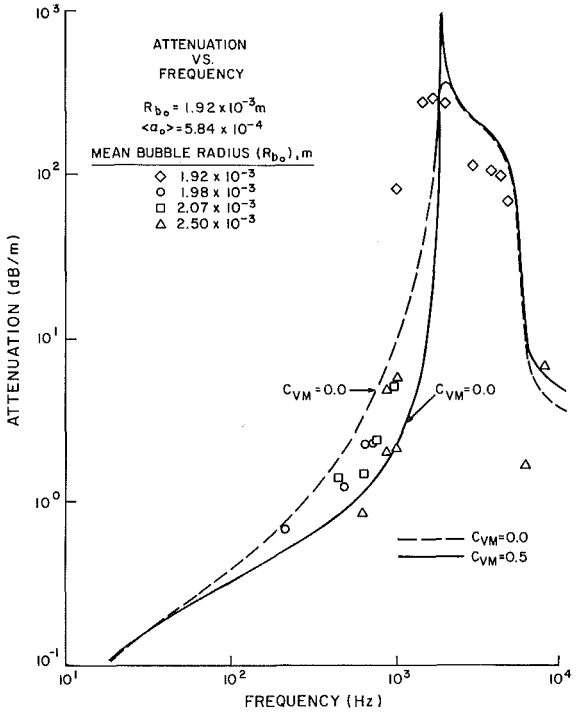


**Fig. 4 Attenuation versus frequency, $R_{b_o} = 1.92 \times 10^{-3}$m, $\alpha_o = 5.84 \times 10^{-4}$**

$$\delta\phi = \hat{\phi} e^{i(kz-\omega t)} \tag{37}$$

Equation (36) becomes

$$\{\underline{\underline{A}}((\phi)[-i\omega] + \underline{\underline{B}}(\phi)[ik] - \underline{\underline{C}}(\phi)\}\hat{\phi} = 0 \tag{38}$$

In order for the $\hat{\phi}$ to be finite, we must have

$$\det[(\omega\underline{\underline{A}} - i\underline{\underline{C}} - k\underline{\underline{B}}] = 0 \tag{39}$$

Equation (39) is one form of the required dispersion relation, since, for a given $\omega$, we can solve for the $k$'s. That is, the dispersion relation is given by

$$k = k(\omega) \tag{40}$$

One physical problem of interest is the boundary value problem modeling the situation where an input transducer is located at the bottom of the flow, and sound is propagated upward through the bubbly mixture. If the transducer is driven sinusoidally, the resulting pressure disturbances should reach an equilibrium situation where the only frequency observed is the driving frequency. This continuous wave (CW) problem can be expressed as a boundary value problem in the following way

$$\delta p_l(0,t) = a\cos\omega t \tag{41}$$

$$\delta p_l(L,t) = 0 \tag{42}$$

All other perturbations at $z = 0$ are zero except $\delta\alpha$. Equation (41) expresses the action of the pressure transducer, while equation (42) states that the top ($z = L$) of the conduit is open to the atmosphere.

Since the channel is assumed to be long, we can approximate the solutions with $L \to \infty$. This removes the possibility of a resonance within the channel and allows us to ignore modes which have $\mathrm{Im}(k) < 0$.

The solutions for $\delta\phi$ have the form

$$\delta\phi = \sum_n C_n \xi_n e^{ik_n z} e^{-i\omega t} + \begin{bmatrix}\text{Complex}\\ \text{Conjugate}\end{bmatrix} \tag{43}$$

where $k_n$ is the (complex) wave number of the $n$th mode and $\xi_n$ the corresponding eigenvector for equation (38). Because of the boundary conditions discussed above, $C_n = 0$ for all $k_n$'s having negative imaginary parts. The relative importance of each harmonic (corresponding to each eigenvalue, $k$) in the solution of equation (43) is based upon the relative magnitude of $C_n$; the greater the value, the more the importance. Using equations (41-43), we can solve for the $C_n$'s. The mode which dominates will be the one which is normally measured in standing-wave experiments.

The complex wave number

$$k = k_R + ik_I \tag{44}$$

can be written as,

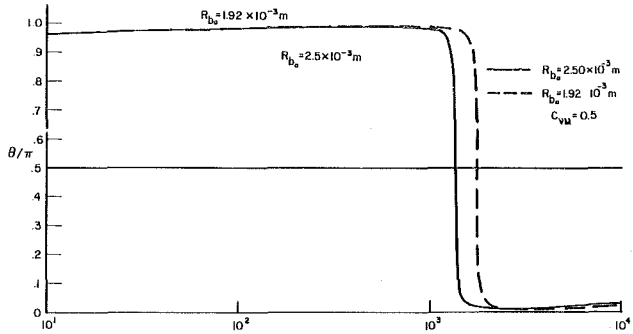


**Fig. 5 Normalized phase angle of $\delta R_b$ versus frequency ($C_{vm} = 0.5$)**

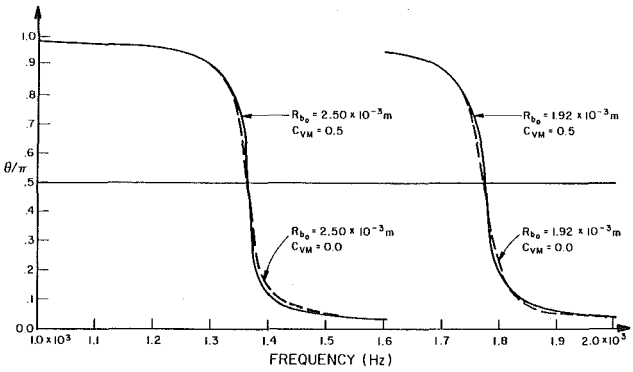


**Fig. 6 Normalized phase angle of $\delta R_b$ versus frequency with and without virtual mass**

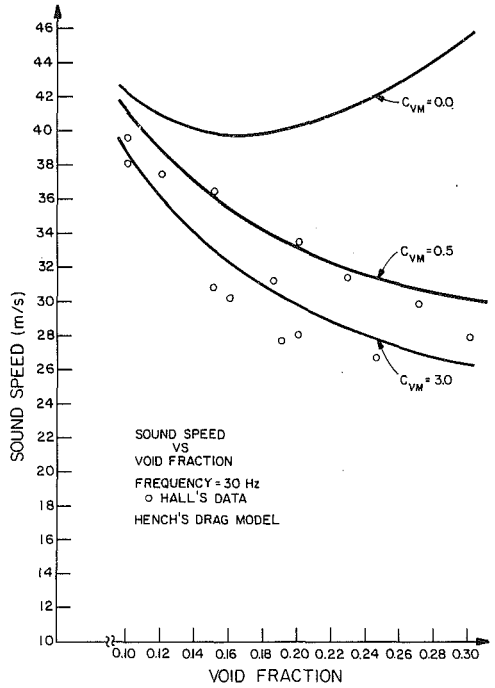


**Fig. 7 Sound speed versus void fraction, driving frequency = 30 Hz**

$$k = \omega / C_{ph} + i\eta \tag{45}$$

where

$$C_{ph} = \omega / k_R \tag{46}$$

is the phase velocity of the propagating wave and

$$\eta \triangleq k_I \tag{47}$$

is the spatial attenuation coefficient. Thus the mode having the smallest $\eta$ will dominate.

## Verification of the Dispersion Model

In order to verify the dispersion model given in equation (39), the predicted phase velocities and attenuations of the wave were compared with experimental standing wave data taken at both high and low frequencies.

The high-frequency data we used for comparison are those due to Silberman [16]. As can be seen in Figs. 1–4, the dispersion model appears to predict the phase velocity and attenuation quite well for frequencies both above and below bubble resonance. In Figs. 1 and 3 virtual mass is observed to have a noticeable effect on the phase velocity at frequencies around the resonance. At lower frequencies, where the resonant effect on phase velocity is negligible, the present model shows a phase velocity increasing with frequency. This can be explained by our heat transfer model which dictates the thermal behavior of the gas bubble. At low frequencies the gas bubble behaves isothermally. As the forcing frequency is increased, the gas bubble becomes increasingly adiabatic, and thus the phase velocity increases.

Although there are not enough data to be conclusive, it can be noted in Figs. 2 and 4, that the predicted attenuation (which is due to a combination of effects) at the resonance point appears to be closer to the data when virtual mass is absent. The higher attenuation when $C_{vm} > 0$ is due to the increased coupling in the relative motion between the two phases. It is also interesting to note in the plots of the phase angle ($\theta$) of $\delta R_b$ versus frequency, Figs. 5 and 6, that the radial motion of the bubble shows greater damping when $C_{vm} = 0$ than when $C_{vm} > 0$. However, there are likely other important dissipation mechanisms at resonance that we have not modeled (e.g., finite amplitude effects, thermal relaxation

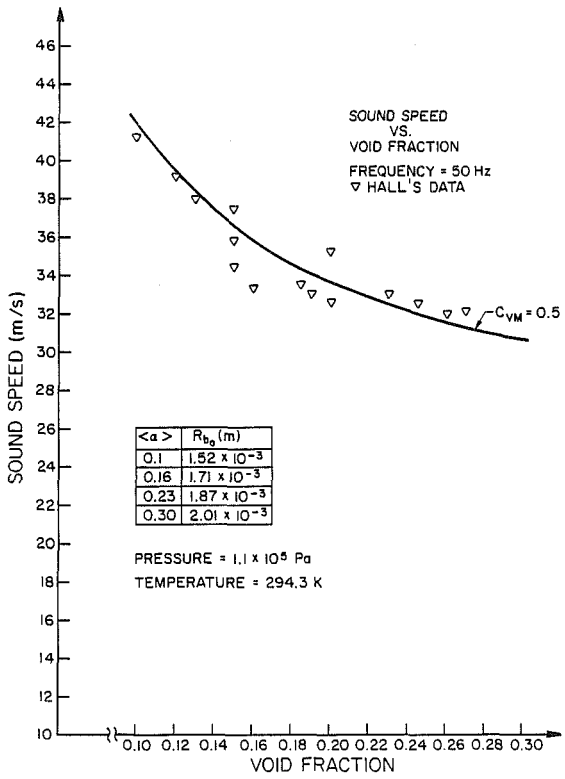


**Fig. 8 Sound speed versus void fraction, driving frequency = 50 Hz**

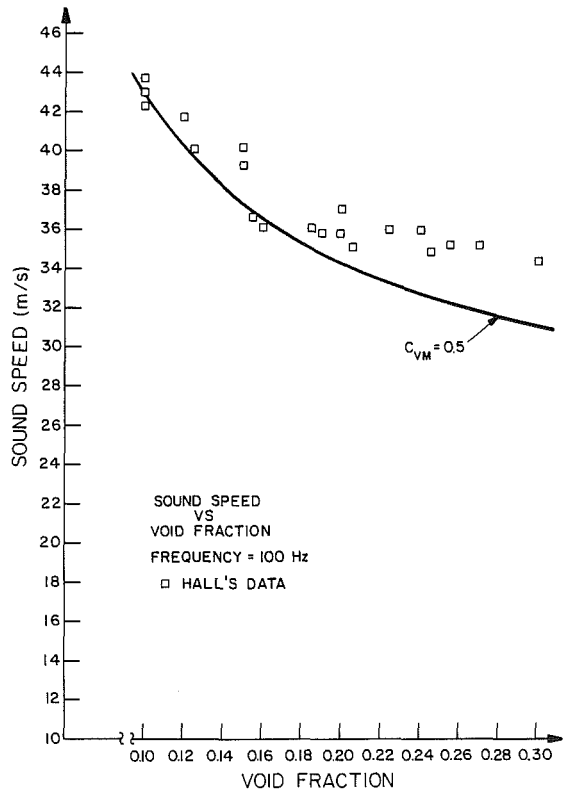


**Fig. 9 Sound speed versus void fraction, driving frequency = 100 Hz**

effects, etc.), thus some caution must be used in interpreting the analytical results around the resonance frequency.

It should be noted that in Silberman's experiment the air bubbles were not of uniform size throughout the test section. Thus in Figs. 1 and 2 the theoretical results were obtained by assuming a mean bubble radius corresponding to the upper

limit of the measured value, while in Figs. 3 and 4 the lower limit of the measured mean bubble radius was used in the calculations. It is obvious from Figs. 5 and 6 that a higher bubble radius yields a lower bubble resonant frequency. The agreement in phase velocity and attenuation between data and calculation are better when the higher mean bubble radius was used (see Figs. 1 and 2).

As the forcing frequency approaches the resonant frequency $\omega_n$ of the pulsating bubbles from the lower end of the frequency spectrum, the response of the bubbles becomes stronger, resulting in higher compressibility in the two-phase mixture, and thus a reduction in the apparent phase velocity. Just above the resonant frequency, the phase velocity increases markedly, since, as can be seen in Figs. 5 and 6, the perturbations in the bubble radius ($\delta R_b$) and the forcing function ($\delta p_l$) are now in-phase. Hence, when the pressure in the liquid is raised the volume of the bubble increases. This implies that the compressibility of the mixture is negative, which leads to a substantial increase in the celerity (and thus phase velocity) at frequencies just beyond $\omega_n$. At higher frequencies, the compressibility of the two-phase medium is predominantly determined by that of the liquid phase. Thus the two-phase celerity approaches the speed of sound in the liquid phase at high frequencies.

Low-frequency data were taken by Hall [17]. As can be noted in Fig. 7, the effect of virtual mass is more significant in Hall's data than in Silberman's data. This is apparently because the void fraction in Hall's experiments is about 200 times higher than in Silberman's data. Note in Fig. 7 that if virtual mass is not included (i.e., $C_{VM} = 0.0$) the agreement is very poor. As can be seen in Figs. 8 and 9, $C_{VM} = 0.5$ appears to agree with these data. It is significant to note that the forcing frequency in Hall's experiment was well below the resonant frequency of the bubbly mixture and hence the dominant factors that affected the phase velocity were those of nonequilibrium momentum and heat transfer between the phases.

A sensitivity study was performed by parametrically varying the interfacial drag coefficient ($C_D/R_b$) and wall friction factor ($f$). Both interfacial drag and wall shear were found [15] to have negligible effect on the results reported herein.

Unfortunately, there is too much scatter in the data to be able to deduce a good functional form for $C_{VM}(\alpha)$. However, $C_{VM} = 0.5$ agrees with our expectations for spherical bubbles [13]. Finally, it is found that the analysis was insensitive to different values of the virtual mass parameter $\lambda$. This is presumably due to the fact that the relative velocity becomes small as the virtual mass forces increases, thus as can be seen in equation (8), the terms involving $\lambda$ become small.

## Conclusion

The wave dispersion relation, which was derived from a two-fluid formulation, is seen to predict phase velocity and wave attenuation in good agreement with data taken in bubbly flows over a wide range of frequencies and void fractions. The range of applicability of the present model is a marked improvement over previous models. Furthermore, the importance of nonequilibrium momentum and heat tranfser on wave dispersion has been demonstrated. The importance of acoustic effects (i.e., wave scattering) on wave dispersion is exemplified by the ability of the present model to predict phase velocity and the attenuation coefficient at frequencies higher than the resonant frequency.

It appears that the wave dispersion relation presented herein accurately captures the data trends, and can be used to determine important parameters in virtual mass models (i.e., $C_{VM}$). This approach provides a valuable method to determine this parameter. However, more and better controlled data are needed before its functional form can be quantified.

## Acknowledgments

The authors wish to acknowledge the financial support given to this work by Dr. Y. Y. Hsu, formerly of the United States Nuclear Regulatory Commission (USNRC).

## References

1 Ishii, M., "Thermo-Fluid Dynamic Theory of Two-Phase Flow," *Eyrolles*, 1975.

2 Delhaye, J. M., and Achard, J. L., "On the Use of Averaging Operators in Two-Phase Flow Modelling," *Thermal and Hydraulic Aspects of Nuclear Reactor Safety*, Vol. 1, edited by O. C. Jones, Jr., and S. G. Bankoff, Light Water Reactors, ASME, New York, 1977.

3 Drew, D. A., and Lahey, R. T., Jr., "Applications of General Constitutive Principles of the Derivation of Multi-Dimensional Two-Phase Flow Equations," *Int. J. Multiphase Flow*, Vol. 5, 1979, pp. 243–264.

4 Lahey, R. T., Jr., Cheng, L., Drew, D., and Flaherty, J., "The Effect of Virtual Mass on the Numerical Stability of Accelerating Two-Phase Flow," *Int. J. Multiphase Flow*, Vol. 6, 1980.

5 Drew, D., Cheng, L., and Lahey, R., Jr., "The Analysis of Virtual Mass Effects in Two-Phase Flow," *Int. J. Multiphase Flow*, Vol. 5, 1979, pp. 233–242.

6 Mecredy, R. C., and Hamilton, L. J., "The Effects of Nonequilibrium Heat, Mass and Momentum Transfer on Two-Phase Sound Speed," *International Journal of Heat and Mass Transfer*, Vol. 15, 1972, pp. 61–72.

7 Ardron, K. H., and Duffey, R. B., "Acoustic Wave Propagation in a Flowing Liquid-Vapor Mixture," *Int. J. Multiphase Flow*, Vol. 4, No. 3, 1978.

8 Drumheller, D. S., and Bedford, A., "A Theory of Bubbly Liquid," *J. Acoust. Soc. Am.*, Vol. 66, 1979, pp. 197–208.

9 Prosperetti, A., "Thermal Effects and Damping Mechanisms in the Forced Radial Oscillations of Gas Bubbles in Liquids," *J. Acoust. Soc. Am.*, Vol. 61, 1977, pp. 17–27.

10 Plesset, M. S., and Hsieh, D. Y., "Theory of Gas Bubble Dynamics in Oscillating Pressure Fields," *The Physics of Fluids*, Vol. 3, No. 6, 1960, pp. 882–892.

11 Wijngaarden, L. Van, "One Dimensional Flow of Liquids Containing Small Gas Bubbles," *Ann. Review Fluid Mech.*, Vol. 4, 1972, p. 369.

12 Hench, J. E., and Johnston, J. P., "Two-Dimensional Diffuser Performance with Subsonic, Two-Phase, Air-Water Flow," *J. of Basic Engineering*, 1972.

13 Milne-Thomson, L. M., *Theoretical Hydrodynamics* (5th Ed.) Macmillan, New York, 1968.

14 Landau, L. D., and Lifshitz, E. M., *Fluid Mechanics*, Pergamon Press, New York, 1959.

15 Cheng, L. Y., Drew, D. A., and Lahey, R. T., Jr., "An Analysis of Wave Dispersion, Sonic Velocity and Critical Flow in Two-Phase Mixtures," NUREG/CR-3372, 1983.

16 Silberman, E., "Sound Velocity and Attenuation in Bubbly Mixtures Measured in Standing Wave Tubes," *J. Acoust. Soc. Am.*, Vol. 29, 1957, pp. 925–933.

17 Hall, P., "The Propagation of Pressure Waves and Critical Flow in Two-Phase Mixtures," Ph.D. thesis, Heriot-Watt University, Edinburgh, U.K., 1971.

18 Chapman, R. B., and Plesset, M. S., "Thermal Effects in the Free Occillation of Gas Bubbles," *J. of Basic Engineering*, 1971.

19 Prosperetti, A., "Bubble Phenomena in Sound Fields: Part One," *Ultrasonics*, Vol. 22, Mar. 1984.

20 Crum, L. A., "The Polytropic Exponent of Gas Contained within Air Bubbles Pulsating in a Liquid," *J. Acoust. Soc. Am.*, Vol. 73(1), 1983, pp. 116–120.

# Heat and Mass Transfer Associated With Condensation on a Moving Drop: Solutions for Intermediate Reynolds Numbers by a Boundary Layer Formulation

**T. Sundararajan**

**P. S. Ayyaswamy**

Mem. ASME

Department of Mechanical Engineering and Applied Mechanics, University of Pennsylvania, Philadelphia, Pa. 19104

*Condensation heat and mass transfer to a liquid drop moving in a mixture of saturated vapor and a noncondensable have been evaluated. The Reynolds number of the drop motion is 0(100). The quasi-steady, coupled, boundary layer equations for the flow field and the transport in the gaseous phase are simultaneously solved. The heat transport inside the drop is treated as a transient process. Results are presented for the heat and mass transport rates to the drop, the surface shear stress, the velocity profiles across the boundary layer, and the temperature-time history of the drop. The comparisons of results with experimental data, where available, show excellent agreement. Tables summarizing results appropriate to a wide range of condensation rates have been included. Local heat and mass transfer rates have also been presented. These features will make the paper useful to the designer of direct contact heat transfer equipment.*

## 1 Introduction

Direct contact heat and mass transfer to a drop experiencing condensation, occurs in a wide variety of applications. For instance, the emergency cooling sprays of nuclear reactors, air conditioning humidifiers, direct contact condensers in thermal power plants, atmospheric studies of raindrop growth, etc., involve condensation on moving drops. Although the analysis of these situations demands the consideration of a spectrum of moving drops of various sizes, there is still a great need for a fundamental understanding of the single-drop problem. The intent of the present paper is to analyze the hydrodynamics and transport phenomena associated with condensation on a single moving drop for a wide range of condensation rates. The Reynolds number of drop motion (hereinafter referred to as $\mathrm{Re}_g\,(=2U_\infty R/\nu_g)$) is in the range 0(100). The drop environment consists of saturated vapor and a noncondensable.

There are several studies in published literature that involve heat and mass transfer and/or hydrodynamics of drop motion [1]. Specifically, with regard to condensation on drops, [2] and [3] have studied stationary drops. Slowly moving drops experiencing condensation have been examined in [4–6]. Condensation heat and mass transfer in the vicinity of the forward stagnation point of a translating drop has been studied in [7–9]. The condensation of pure vapor on a moving drop has been examined in [10] by the Karman-Pohlhausen technique. However, in [10], the radial field induced by condensation has not been taken into account at the outer edge of the boundary layer. Such a neglect cannot be justified for regions away from the front stagnation point. Recently, in [11–13] the authors have solved for the condensation on the entire surface of a moving drop. There the formulation entails a simultaneous solution of the governing elliptic partial differential equations. The growth rate of a water drop in pure steam flow has been experimentally investigated in [14]. Kulic et al. [15–17] have predicted the heat transfer rates for drops moving in air–steam mixtures using standard heat transfer correlations. They have also experimentally recorded the temperature–time history of a water drop experiencing condensation in a forced flow of steam and air.

Here, a boundary layer approach is used to predict the transport rates to the drop. The gaseous phase has been treated as quasi-steady. A similarity solution valid for the vicinity of the forward stagnation point, and a series solution that is applicable for the entire boundary layer region are obtained. In the series solution, the fluid flow and thermodynamic variables are expanded in terms of Legendre Polynomials and associated functions. The resulting nonlinear, ordinary differential equations are solved by the series truncation technique. For the drop-inside, since there is a high degree of liquid circulation ($\mathrm{Re}_l$ = 0(100)), the diffusion of heat across the stream surfaces in the drop is taken to solely govern the transient heat up of the drop. Useful results for the heat/mass transport to the drop and the rate of heat-up of the drop are obtained in terms of the drop size and the temperature differential.

## 2 Physical Description

A drop of radius $R$, moving at a constant terminal velocity $U_\infty$ in a saturated mixture of vapor and noncondensable is considered (Fig. 1). The total pressure $p_\infty$ and temperature $T_\infty$ of the saturated mixture are prescribed. The drop is colder than its environment and condensation occurs on the drop surface. We consider a coordinate frame that coincides with the drop center and moves with the drop velocity $U_\infty$. The Reynolds number of translation is taken to be 0(100) but less than 500. For $\mathrm{Re}_g > 500$, flow instabilities such as drop oscillations and vortex shedding may occur, and the deformation from the spherical shape of the drop may be large [1]. This analysis is restricted to a spherical drop in a laminar flow. The shear stress at the interface due to drop translation causes liquid circulation within the drop. The maximum surface velocity of circulation $U_s$ is an order smaller than the far-stream velocity ($U_s \sim 0(10^{-1})U_\infty$) for a liquid drop translating in a gaseous environment [11]. But the circulation Reynolds number $\mathrm{Re}_l$ based on $U_s$ is also 0(100) in the range

Contributed by the Heat Transfer Division for publication in the JOURNAL OF HEAT TRANSFER. Manuscript received by the Heat Transfer Division November 16, 1983.

of $Re_g$ considered. The flow pattern inside the drop resembles a Hill's spherical vortex [11]. Condensation causes a radially inward flow towards the drop surface. The nonzero mass flux at the interface alters the flow field. As a consequence, the pressure and shear stress profiles on the drop surface are modified. Also, the momentum transfer across the interface due to the radial flow gives rise to an additional drag force. However, this drag contribution is small compared to pressure and shear stress contributions for $Re_g$ and $Re_l = 0(100)$ [12]. The total drag on the drop varies with condensation rate. In turn, the translational velocity continuously changes with time [12]. In this paper, the condensation problem has been solved for a wide range of forced flow conditions ($U_\infty$ prescribed). The radial flow also leads to a buildup of the noncondensable concentration near the drop-surface above that in the far-stream [7]. The accumulation results in a mass transfer resistance and a consequent reduction in the transport rates. For $Re_g = 0(100)$, flow separates in the rear of the drop. With condensation, for a given $Re_g$, the boundary layer covers more of the drop surface compared to a noncondensing situation.

## 3 Theoretical Formulation

For a short period of time, after the drop is introduced into the vapor-gas atmosphere, rapid transients in velocity, temperature, and concentration occur. During this period, thin boundary layers for the various transport variables develop over the drop surface. The time taken for the establishment of these boundary layers is $0(R/U_\infty)$ [18]. For typical values, such as R ~ 1 mm and $U_\infty$ ~ 1 m/sec, the boundary layers are established within a few milliseconds after the introduction of the drop. The established boundary layer thicknesses may be shown to be $0(Re^{-1/2})$ or $0(Pe^{-1/2})$. After this initial period, the condensation phenomenon changes at a slower rate and is mainly controlled by the slow heat up of the drop interior. This latter period, during which the bulk of the condensation occurs, typically lasts a few seconds and is the subject of the present study. The transport to the drop during this stage is quasi-steady [11].

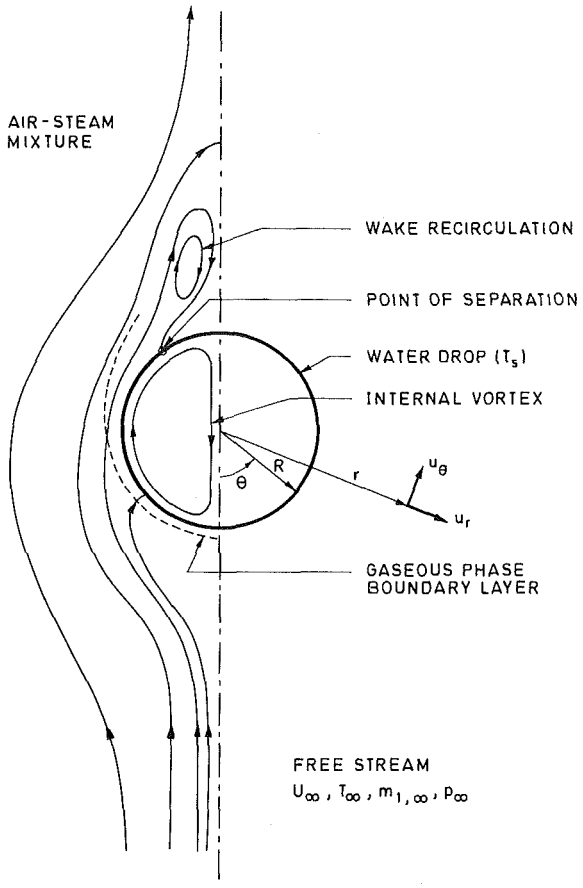


**Fig. 1 Geometry of the problem**

The quasi-steady behavior is demonstrated by comparing the time scales of the various convective and diffusive transport processes in both the phases. First, we note that the

## Nomenclature

$A$ = liquid circulation vortex strength
$C_p$ = specific heat
$D_{12}$ = binary diffusion coefficient
$F$ = a function related to vorticity ($= \zeta/r\sin\theta$)
$h$ = heat transfer coefficient
$Ja_g$ = Jakob number ($= C_{pg}(T_\infty - T_s)/\lambda$)
$k$ = thermal conductivity
$m_1$ = noncondensable mass fraction
$\dot{M}$ = mass transfer rate to the drop
$p_\infty$ = far-stream pressure
$P_i, Q_i$ = Legendre polynomial of $i$th order, integral of $P_i(\mu)$
Pe = Peclet number
Pr = Prandtl number ($= \nu/\alpha$)
$q$ = heat flux
$r$ = radial coordinate
$R$ = radius of the drop
$Re_g$ = Reynolds number for the gas phase $\left(= \frac{2RU_\infty}{\nu_g}\right)$
$Re_l$ = Reynolds number for the liquid phase $\left(= \frac{2RU_s}{\nu_l}\right)$
Sc = Schmidt number ($= \nu_g/D_{12}$)
$t$ = time
$T$ = temperature
$T_{b,l}$ = instantaneous bulk temperature of the drop
$T_s$ = surface temperature of the drop
$u_c$ = condensation velocity at the drop surface
$U_\infty$ = far-stream translational velocity
$U_s$ = maximum tangential velocity at the drop surface
$w_1$ = normalized mass fraction
$W$ = condensation parameter ($= 1 - m_{1,\infty}/m_{1,s}$)
$x_1$ = volume fraction of the noncondensable

**Greek symbols**

$\alpha$ = thermal diffusivity
$\delta$ = boundary layer thickness
$\zeta$ = vorticity
$\eta$ = similarity variable
$\theta$ = polar angle
$\lambda$ = latent heat of condensation
$\mu$ = dynamic viscosity; $\cos\theta$
$\nu$ = kinematic viscosity
$\rho$ = density
$\sigma$ = shear stress
$\psi$ = stream function

**Subscripts**

$av$ = average
$bl$ = boundary layer
$c$ = condensation
$g$ = gas phase
$l$ = liquid phase
pot = potential flow
$s$ = drop surface
0 = at initial time; stagnant drop
1 = noncondensable
$\infty$ = far stream

**Superscripts**

$-$ = average
$*$ = dimensional quantity

gaseous phase diffusivities are typically two orders of magnitude larger than the liquid thermal diffusivity. Also at intermediate Reynolds numbers, the gradients of vorticity, temperature and concentration in the gaseous phase are confined to thin boundary layers (except in the wake). The response times for the gaseous phase are, therefore, much smaller compared to that of the drop heat up. In the time scale of the drop heating, the gaseous phase transport may be treated as quasi-steady.

With regard to the liquid phase, due to the relatively slow diffusion of heat in the liquid, the drop heat-up must be treated as a transient process. However, since the degree of circulation inside the drop is very high ($\mathrm{Re}_l = 0(100)$), faster equalization of temperature occurs in the streamwise direction than in the cross-stream direction. As a result, the liquid stream surfaces may be regarded as isothermal in the time scale of drop heating [19]. Furthermore, the surface temperature of the drop $T_s$ may be considered to be uniform over the entire drop surface [11, 20].

Some assumptions made in the analysis are: (*i*) surface tension is large and constant on the interface; (*ii*) the liquid–vapor interface is at thermodynamic equilibrium. The partial pressure of the vapor at the interface is equal to the vapor-pressure corresponding to $T_s$; (*iii*) a one-third rule [21] is applied for the gaseous phase boundary layers for property evaluation. The liquid phase properties are evaluated at the instantaneous bulk temperature of the drop; (*iv*) the momentum transport associated with phase-change is neglected in both the phases [11]; (*v*) the liquid and gaseous phases are taken to be pure systems and the accommodation coefficient for condensation is assumed to be large. The interfacial resistance is neglected [21].

**Gaseous-Phase Equations.** We define gas-phase stream function $\psi$ and vorticity $\zeta$ as

$$\nabla \times \left\{ -\frac{\psi}{r \sin\theta} \mathbf{e}_\phi \right\} = \mathbf{u} \text{ and } \zeta \mathbf{e}_\phi = \nabla \times \mathbf{u} \tag{1}$$

where $\mathbf{u}$ is the gas-phase velocity vector and $\mathbf{e}_\phi$ is the unit vector in the $\phi$-direction (Fig. 1). The dimensionless quasi-steady gaseous phase equations are

$$E^2 \psi = Fr^2 (1-\mu^2) \tag{2}$$

$$\frac{\mathrm{Re}_g}{2}\left[\frac{\partial\psi}{\partial\mu}\frac{\partial F}{\partial r} - \frac{\partial\psi}{\partial r}\frac{\partial F}{\partial\mu}\right] = \frac{1}{(1-\mu^2)} E^2[Fr^2(1-\mu^2)] \tag{3}$$

$$\frac{\mathrm{Pe}_{g,m}}{2}\left[\frac{\partial\psi}{\partial\mu}\frac{\partial w_1}{\partial r} - \frac{\partial\psi}{\partial r}\frac{\partial w_1}{\partial\mu}\right] = r^2 \nabla^2 w_1 \tag{4}$$

$$\frac{\mathrm{Pe}_{g,t}}{2}\left[\frac{\partial\psi}{\partial\mu}\frac{\partial T}{\partial r} - \frac{\partial\psi}{\partial r}\frac{\partial T}{\partial\mu}\right] = r^2 \nabla^2 T \tag{5}$$

where: $\mu = \cos\theta$, $F = \zeta / r \sin\theta$,

$$\nabla^2 = \frac{1}{r^2}\frac{\partial}{\partial r}\left(r^2 \frac{\partial}{\partial r}\right) + \frac{1}{r^2}\frac{\partial}{\partial\mu}\left[(1-\mu^2)\frac{\partial}{\partial\mu}\right],$$

$$E^2 = \frac{\partial^2}{\partial r^2} + \frac{1-\mu^2}{r^2}\frac{\partial^2}{\partial\mu^2}$$

and

$\psi = \psi^*/U_\infty R^2$, $\zeta = \zeta^*/(U_\infty/R)$, $r = r^*/\mathrm{R}$, $T = (T^* - T_\infty)/(T_s - T_\infty)$, $w_1 = (m_1 - m_{1,\infty})/(m_{1,s} - m_{1,\infty})$. The starred quantities are dimensional.

The boundary conditions are, at $r = 1$ (drop-surface)

$$T = w_1 = 1 \tag{6a}$$

The interface is impermeable to the noncondensable. At each instant of time, the convective and diffusive fluxes of noncondensable balance. With $u_c$, the condensation-induced radial velocity at the interface, the balance yields

$$\frac{u_c}{U_\infty} = \hat{u}_c = \frac{\partial\psi}{\partial\mu} = \frac{2W}{\mathrm{Pe}_{g,m}}\frac{\partial w_1}{\partial r} \tag{6b}$$

where the condensation parameter $W = 1 - m_{1,\infty}/m_{1,s}$. In the quasi-steady formulation of the gaseous phase, time does not enter explicitly. It only enters implicitly through the specification of instantaneous boundary conditions at the drop surface. For a prescribed instantaneous surface temperature $T_s$, the corresponding instantaneous values for the mass transfer and heat transfer may be calculated using the quasi-steady condensation model. We note that the parameter $W$ is only a function of the thermodynamic variables of the problem, viz., $p_\infty$, $T_\infty$, and $T_s$, and hence can be considered as a parametric constant in the context of a quasi-steady model. This feature has been recognized earlier [23]. The parameter $W$ varies in the range 0 to 1 with zero representing a no-condensation situation, and one representing the maximum possible condensation in a pure steam environment. Thus it should be recognized that by solving the condensation problem for various instantaneous values for $W$ in the range 0 to 1, universal results may be obtained for several far-stream and drop-surface conditions. The quasi-steady formulation permits a complete decoupling of the gaseous phase equations from those of the liquid phase. This is achieved by prescribing the instantaneous values for $W$ and $u_\theta$. In the present study, as indicated earlier, the entire range of $W$ variations is included. The prescription of $u_\theta$ depends on three separate considerations: (*i*) $u_\theta$ is an order smaller than $U_\infty$ [8]; (*ii*) the predominant variation of $u_\theta$ with $\theta$ is sinusoidal [4]; and (*iii*) $u_\theta$ has only a weak influence on both the flow and transport in the gaseous phase [1], [20]. Taking into account these considerations, we let

$$u_\theta = \frac{\partial\psi}{\partial r}\frac{1}{(1-\mu^2)^{1/2}} = 0.05\,(1+0.1\mu)\,(1-\mu^2)^{1/2} \tag{6c}$$

At $\theta = 0$ and $\pi$

$$\left|\frac{\partial T}{\partial\mu}\right| < \infty, \quad \left|\frac{\partial w_1}{\partial\mu}\right| < \infty \text{ and } \left|\frac{\partial F}{\partial\mu}\right| < \infty \tag{6d}$$

$$\psi = 0 \quad \text{on } \theta = 0 (\mu = 1) \tag{6e}$$

$$\frac{\partial\psi}{\partial r} = 0 \quad \text{on } \theta = \pi (\mu = -1) \tag{6f}$$

In the far-stream as $r \to \infty$:

$$\psi \to \frac{1}{2} r^2 (1-\mu^2), \quad T \to 0, \; w_1 \to 0 \text{ and } F \to 0 \tag{6g}$$

**Reduction to the Boundary Layer Form.** The potential flow outside the boundary layer is uniform in temperature and concentration. As a consequence, for the potential flow

$$T = w_1 = F = 0 \tag{7}$$

Then, equation (1) reduces to

$$E^2 \psi = 0 \tag{8}$$

and the boundary conditions are:

$$\psi = 0 \text{ on } \mu = 1, \; \frac{\partial\psi}{\partial r} = 0 \text{ on } \mu = -1 \tag{9a,b}$$

and

$$\hat{u}_c = \frac{\partial\psi}{\partial\mu} = \phi(\mu) \text{ at } r = 1, \; \psi \to \frac{1}{2} r^2 (1-\mu^2) \text{ as } r \to \infty \tag{9c,d}$$

Condition (9*c*) represents the nonzero normal flux at the interface. The function $\phi(\mu)$ that appears in the normal flux condition is to be evaluated from matching with the boundary layer solution.

Since the boundary layer thickness is of $0(\mathrm{Re}_g^{-1/2})$, we define a stretched boundary layer coordinate $y$ as

$$y = (r-1)\mathrm{Re}_g^{1/2} \tag{10}$$

Now, for the boundary layer region, we note that, $\psi = 0(\mathrm{Re}_g^{-1/2})$, $F = 0(\mathrm{Re}_g^{1/2})$, $w_1 = 0(1)$ and $T = 0(1)$. Consider expanding these variables in the boundary layer region as follows

$$\psi(y,\mu) = \mathrm{Re}_g^{-1/2}\psi^{(1)}(y,\mu) + \mathrm{Re}_g^{-1}\psi^{(2)}(y,\mu) + \ldots$$
$$F(y,\mu) = \mathrm{Re}_g^{1/2}F^{(1)}(y,\mu) + F^{(2)}(y,\mu) + \ldots$$
$$w_1(y,\mu) = w_1^{(1)}(y,\mu) + \mathrm{Re}_g^{-1/2}w_1^{(2)}(y,\mu) + \ldots$$
$$T(y,\mu) = T^{(1)}(y,\mu) + \mathrm{Re}_g^{-1/2}T^{(2)}(y,\mu) + \ldots \quad (11)$$

We retain only terms of the dominant order for $\mathrm{Re}_g = 0(100)$. As a result, the following set of parabolic partial differential equations are obtained (dropping superscripts)

$$\frac{\partial^2\psi}{\partial y^2} = -2FQ_1(\mu) \quad (12)$$

$$\left[\frac{\partial\psi}{\partial\mu}\frac{\partial F}{\partial y} - \frac{\partial\psi}{\partial y}\frac{\partial F}{\partial\mu}\right] = 2\frac{\partial^2 F}{\partial y^2} \quad (13)$$

$$\left[\frac{\partial\psi}{\partial\mu}\frac{\partial w_1}{\partial y} - \frac{\partial\psi}{\partial y}\frac{\partial w_1}{\partial\mu}\right] = \frac{2}{\mathrm{Sc}}\frac{\partial^2 w_1}{\partial y^2} \quad (14)$$

$$\left[\frac{\partial\psi}{\partial\mu}\frac{\partial T}{\partial y} - \frac{\partial\psi}{\partial y}\frac{\partial T}{\partial\mu}\right] = \frac{2}{\mathrm{Pr}_g}\frac{\partial^2 T}{\partial y^2} \quad (15)$$

The boundary conditions are:
At $y = 0$

$$\frac{\partial\psi}{\partial y} = -0.1(1+0.1\mu)Q_1(\mu), \quad \frac{\partial\psi}{\partial\mu} = \frac{2W}{\mathrm{Sc}}\frac{\partial w_1}{\partial y}, \quad w_1 = T = 1 \quad (16a)$$

At $\mu = 1$

$$\psi = 0, \quad \left|\frac{\partial F}{\partial\mu}\right| < \infty, \quad \left|\frac{\partial T}{\partial\mu}\right| < \infty, \quad \left|\frac{\partial w_1}{\partial\mu}\right| < \infty \quad (16b)$$

In the matching region, with $\psi_{bl}$ and $\psi_{\mathrm{pot}}$ representing the boundary layer and potential flow solutions

$$\psi_{bl}\Big|_{y\to\infty} \to \psi_{\mathrm{pot}}\Big|_{r\to 1}, \; T\to 0, \; w_1 \to 0, \text{ and } F\to 0 \quad (16c)$$

The boundary layer equations (12–15) are a set of nonlinear, coupled, partial differential equations that cannot be solved analytically in closed form. In later sections, a similarity analysis for the front stagnation region and a series truncation analysis for the entire boundary layer region, are developed.

**Liquid-Phase Equations.** The Reynolds number for liquid circulation is of 0(100). In view of this, the internal flow field can be shown [9] to be described by the stream function

$$\psi_l = -\frac{1}{2}\mathrm{Ar}^2(1-r^2)\sin^2\theta \quad (17)$$

were $A$ is the vortex strength. Letting $\mathbf{u}_l$ to represent the corresponding velocity field, the liquid-phase energy equation becomes

$$\frac{\partial T_l}{\partial t} + \frac{\mathrm{Pe}_l}{2}[\mathbf{u}_l \cdot \nabla T_l] = \nabla^2 T_l \quad (18)$$

where

$$T_l = (T_l^* - T_o)/(T_\infty - T_o), \; t = \int\frac{\alpha_l dt^*}{R^2}, \; \mathrm{Pe}_l = U_\infty 2R/\alpha_l$$

and $T_o$ is the initial bulk temperature of the drop. Since the stream surfaces inside the drop are isothermal, the energy equation (18) may be suitably recast in terms of the stream-function coordinate. Following Brignell [19], we employ a normalized stream function coordinate $m$ and an orthogonal streamwise coordinate $\xi$, which are given by

$$m = 4r^2(1-r^2)\sin^2\theta \quad \text{and} \quad \xi = \frac{r^4\cos^4\theta}{2r^2-1} \quad (19)$$

The metric coefficients $h_m$, $h_\xi$, and $h_\phi$ in $(m,\xi,\phi)$ coordinate system are

$$h_m = \frac{1}{8r\Delta\sin\theta}, \; h_\xi = \frac{(2r^2-1)^2}{4r^3\Delta\cos^3\theta} \text{ and } h_\phi = r\sin\theta \quad (20)$$

where $\Delta^2 = (1-2r^2)^2\sin^2\theta + (1-r^2)^2\cos^2\theta$. Defining the streamwise average liquid temperature $\bar{T}_l$ as

$$\bar{T}_l = \frac{\oint T_l h_m h_\xi h_\phi d\xi}{\oint h_m h_\xi h_\phi d\xi} \quad (21)$$

the energy equation (18) may be written in the form

$$H(m)\frac{\partial\bar{T}_l}{\partial t} = \frac{\partial}{\partial m}\left[J(m)\frac{\partial\bar{T}_l}{\partial m}\right] \quad (22)$$

where

$$H(m) = -\frac{1}{2}\oint h_m h_\xi h_\phi d\xi$$

and

$$J(m) = -\frac{1}{2}\oint\frac{h_\xi h_\phi}{h_m}d\xi$$

The liquid-phase boundary conditions are:
At the drop-surface ($m = 0$), continuity of heat flux gives

$$(q_s^*)_{av} = -\frac{k_l(T_\infty - T_o)}{R}\frac{\partial T_l}{\partial r}\Big|_{av} = \frac{16}{3}\frac{k_l(T_\infty - T_o)}{R}\frac{\partial\bar{T}_l}{\partial m}\Big|_o \quad (23a)$$

At the center of the vortex ($m = 1$), $\bar{T}_l$ and its derivatives should be finite. This leads to:

$$\frac{\partial\bar{T}_l}{\partial t} = -\frac{1}{H(m)}\frac{\partial\bar{T}_l}{\partial m}\Big|_1 \quad (23b)$$

The initial condition is

$$\bar{T}_l = 0 \quad \text{at} \quad t = 0 \quad (23c)$$

The transient heat up of the drop interior may now be evaluated subject to the surface heat flux obtained from the gas phase analysis.

## 4 Solution Procedure

**Potential Flow.** We solve equation (8) subject to conditions (9*a–d*) to produce

$$\psi = \psi_{\mathrm{pot}} = -\left(r^2 - \frac{1}{r}\right)Q_1(\mu) + \sum_{n=0}^{\infty} a_n r^{-n}Q_n(\mu) \quad (24)$$

where $Q_n$ are the integrals of Legendre polynomials ($P_n$) and are obtained as

$$Q_n(\mu) = \int_1^\mu P_n(\mu')d\mu'$$

The coefficients $a_n$ are given by

$$a_n = \frac{\int_{-1}^{+1}\phi(\mu)P_n(\mu)\,d\mu}{\int_{-1}^{+1}P_n^2(\mu)\,d\mu} \quad (25)$$

**Boundary Layer Solutions.** The boundary layer equations (12–15) subject to conditions (16*a–c*) will now be considered.

We expand the stream function in the boundary layer $\psi_{bl}$ in terms of $Q_n(\mu)$ as follows

$$\psi = \psi_{bl} = \sum_{n=0}^{N}\xi_n(y)Q_n(\mu) \quad (26)$$

This expansion series is capable of satisfying all the boundary conditions for $\psi_{bl}$. $N$ is a finite number.

**A Similarity Solution for the Front Stagnation Region.** For small values of $\theta$, the functions $Q_n$ may be approximated as

$$Q_n \simeq -\theta^2/2 \quad \text{for} \quad n=0, \ldots \infty \tag{27}$$

Hence, in the front stagnation region, $\psi_{bl}$ may be represented as

$$\psi_{bl} = \theta^2 \xi(y) \tag{28}$$

Using equation (28) in equation (12), it is found that $F$ is only a function of $y$ in the front stagnation region. An examination of the species transport equation (14) and the boundary conditions given by (16*a*), reveals that the normalized concentration $w_1$ may also be represented as a pure function of $y$ alone for small values of $\theta$. Thus, we have

$$\eta = y, \ \psi_{bl} = \theta^2 \xi(\eta), \ F = f(\eta), \ w_1 = g(\eta), \ T = t(\eta) \tag{29}$$

where $\eta$ is the similarity variable. With $d\mu = -\theta \, d\theta$, equations (12–15) may be reduced to the form

$$\xi'' = f \tag{30}$$

$$f'' + \xi f' = 0 \tag{31}$$

$$g'' + \mathrm{Sc}\, \xi g' = 0 \tag{32}$$

$$t'' + \mathrm{Pr}_g \xi t' = 0 \tag{33}$$

Here primes denote differentiation with respect to the similarity variable $\eta$. The boundary conditions are
At $\eta = 0$,

$$\xi'(0) = 0.055, \ \xi(0) = -\frac{W}{\mathrm{Sc}} g'(0), \ g(0) = 1, \ t(0) = 1 \tag{34a}$$

At $\eta \to \infty$,

$$\xi(\infty) = \xi(0) + \frac{3\eta}{2}, \ g(\infty) = 0,$$

$$\xi''(\infty) = f(\infty) = 0, \ t(\infty) = 0 \tag{34b}$$

The equations set (30–33) subject to conditions (34*a*,*b*) are solved by a standard numerical procedure.

**Truncated Series Solution for the Entire Boundary Layer Region.** In addition to the expansion series for $\psi_{bl}$, we let

$$F = \sum_{n=0}^{N} f_n(y) P_n(\mu), \ T = \sum_{n=0}^{N} t_n(y) P_n(\mu), \text{ and,}$$

$$w_1 = \sum_{n=0}^{N} \hat{w}_n(y) P(\mu) \tag{35}$$

Substitution of the expansion series into the equations (12–15) and using a compact notation, we obtain the following nonlinear ordinary differential equations

$$\frac{\xi_i''}{i(i+1)} = -\frac{f_{i-1}}{2i-1} + \frac{f_{i+1}}{2i+1}, \quad i = 1, N \quad \text{and} \quad \xi_0'' = 0$$

(vorticity) (36)

$$\frac{\mathrm{Sc}}{2} \sum_{i=0}^{N+1} \sum_{k=0}^{N} \{\xi_j \hat{w}_k' - (2k+1)\phi_i \hat{W}_k\} a_{ijk} = w_j'', \ j = 1, N$$

(mass transfer) (37)

where

$$\phi_i = \frac{\xi_{i-1}'}{2i-1} - \frac{\xi_{i+1}'}{2i+1}, \ \hat{W}_k = \hat{w}_{k+1} + \hat{w}_{k+3} + \ \ldots \ + \hat{w}_N, \text{ and,}$$

$$a_{ijk} = \frac{\int_{-1}^{+1} P_i P_j P_k \, d\mu}{\int_{-1}^{+1} P_j P_j \, d\mu}$$

The momentum equation (13) and the energy equation (15) will have similar representations to the above equation (37). For the momentum equation, replace Sc by unity and $\hat{w}$ by $f$; for the energy equation replace Sc by $\mathrm{Pr}_g$ and $\hat{w}$ by $t$.
The boundary conditions are:
At $y = 0$:

$$\xi_1'(0) = -0.1, \ \xi_2'(0) = -0.01, \ \xi_i'(0) = 0, \ i \neq 1 \text{ or } 2.$$

$$\xi_i(0) = \frac{2W}{\mathrm{Sc}} \hat{w}_1'(0), \ i = 0,1, \ \ldots N, \ \hat{w}_o(0) = t_o(0) = 1,$$

$$\hat{w}_i(0) = t_i(0) = 0 \quad \text{for } i = 1, \ \ldots N \tag{38a}$$

As $y \to \infty$:

$$\xi_1'(\infty) = -3, \ \xi_i'(\infty) = 0, (i \neq 1), f_i(\infty) = \hat{w}_i(\infty) = t_i(\infty) = 0,$$

$$i = 1, \ \ldots N \tag{38b}$$

The differential equations subject to the boundary conditions are solved by a central difference numerical procedure.

**Liquid-Phase Solution.** A Crank–Nicolson procedure is used to evaluate the transient heat-up of the drop interior. The spatial derivatives are also central differenced. The difference equations are arranged in a tridiagonal matrix form, and a computationally inexpensive tridiagonal matrix solver algorithm is employed. From known initial conditions, computations are made until the drop temperature approaches that of the far-stream. A complete temperature–time history is developed in this manner.

## 5 Results and Discussion

The transport and flow results are presented for various combinations of $\mathrm{Re}_g$, $W$, and Sc. Transient results for the drop heat-up are presented for prescribed initial conditions. The predictions have been compared with experimental results where available.

Figure 2 is a plot of the dimensionless, local mass transport to the drop due to condensation. The nondimensional mass flux $\dot{M}$ is given by $\dot{M} = \dot{M}^* \cdot 2R/\rho_g D_{12}$, where $\dot{M}^*$ is the mass flux, $\rho_g u_c$. In this sense, the plot is also a measure of the strength of the condensation field at various locations on the drop surface. The mass flux is maximum at the front stagnation and decreases with increasing angle $\theta$ due to the thickening of the gaseous-phase boundary layers. The concentration gradient becomes smaller with increasing boundary layer thickness. For fixed $W$ and Sc, $\dot{M}$ increases with $\mathrm{Re}_g$. This reflects the effect of translation on condensation. With increasing $\mathrm{Re}_g$, the forced convection flow field becomes stronger. All the gaseous-phase boundary layers (hydrodynamic, thermal, and species concentration) are thinner, and the gradients are steeper at higher $\mathrm{Re}_g$. For fixed $\mathrm{Re}_g$ and Sc, $\dot{M}$ increases with $W$. Higher $W$ corresponds to a greater thermal driving force, $\Delta T (= T_\infty - T_s)$ and/or to a smaller noncondensable mass fraction in the bulk. A greater $\Delta T$ is accompanied by a higher gradient in the partial pressure of the condensable species between the far stream and the drop surface. A smaller $m_{1,\infty}$ offers decreased resistance to mass transfer. For a fixed $\mathrm{Re}_g$ and $W$, $\dot{M}$ increases with Sc. At higher Sc, the mass transfer boundary layer becomes thinner and the concentration gradient is steeper.

In addition to the local variation of mass transfer, the average rate of condensation on the drop is of interest in engineering. In Fig. 3, the average mass transport rate $\bar{\dot{M}}$ is presented for various values of $\mathrm{Re}_g$ and $W$ (Sc = 0.6). We choose to present the results in terms of a dimensionless quantity $(\bar{\dot{M}}/\dot{M}_0)$, where $\dot{M}_0$ is the transport to a stationary drop experiencing radially symmetric condensation under similar thermodynamic conditions. The $\dot{M}_0$ serves as a reference mass flux and is given in [12] as, $\dot{M}_0 = (\rho_g D_{12}/R) \ln(1 - W)$. The average condensation rate for a moving drop may be expressed as, $\bar{\dot{M}} = \rho_g \bar{u}_c$, where $\bar{u}_c$ is the average

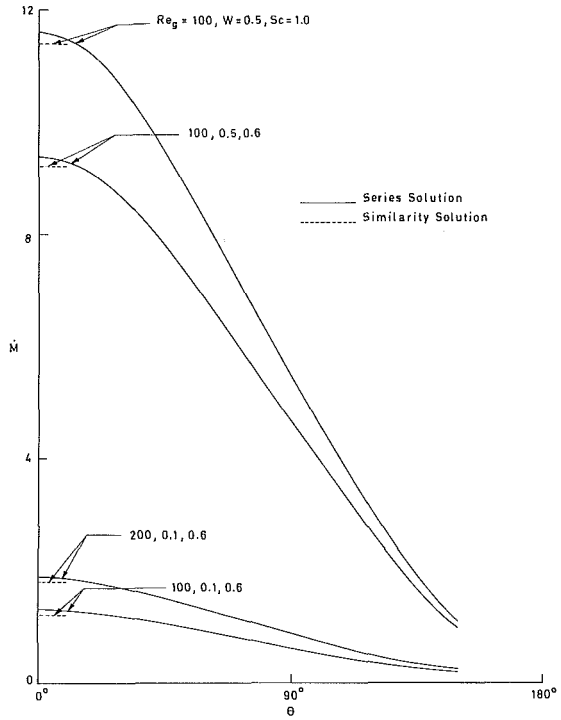


Fig. 2 Variation of dimensionless mass flux $\dot{M}$ with angle $\theta$

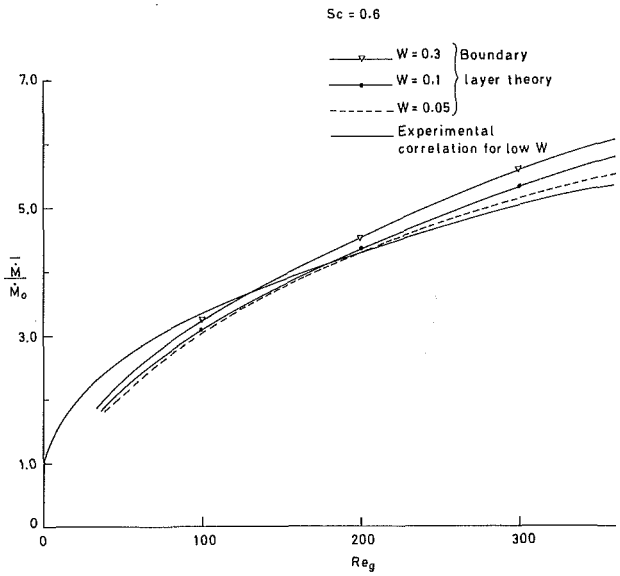


Fig. 3 The variation of $(\bar{\dot{M}}/\dot{M}_0)$ with $Re_g$ and $W$

condensation velocity. The average condensation velocity may in turn be related to the first expansion function $\xi_0$ (see equations 6*b* and 26) to yield

$$\bar{u}_c = (D_{12}/2R)\,\mathrm{Re}_g^{1/2}\,\mathrm{Sc}\,\xi_o$$

The interfacial values of the first four expansion functions for various values of $W$ are tabulated below for convenience (Sc = 0.6)

**Table 1 Interfacial values of expansion functions for the series solution (equation (26))**

| $W$ | $-\xi_0$ | $-\xi_1(0)$ | $-\xi_2(0)$ | $-\xi_3(0)$ |
|---|---|---|---|---|
| 0.1 | 0.1073 | 0.0984 | 0.0071 | 0.0010 |
| 0.3 | 0.3794 | 0.3519 | 0.0205 | 0.0081 |
| 0.5 | 0.7853 | 0.7319 | 0.0185 | 0.0264 |
| 0.7 | 1.5193 | 1.3944 | −0.0852 | 0.0292 |
| 0.9 | 3.7683 | 3.4812 | −0.2942 | 0.1440 |

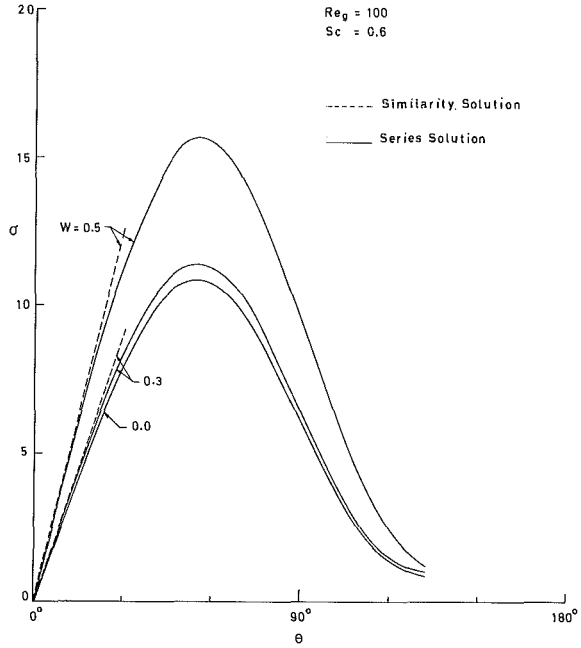


Fig. 4 The effect of condensation on the dimensionless shear stress profile $\sigma$

It is clear from the Fig. 3 that the average condensation rate increases with $Re_g$ and $W$. The figure also shows a comparison of the results obtained here with an experimental correlation (appropriate for low $W$ situations) published in the literature [15, 22]. The agreement between the theory and experiment must be noted to be very good.

The variation of dimensionless shear stress $\sigma(=\sigma^* R/\mu_g U_\infty)$ with angle $\theta$, for various levels of condensation, has been plotted in Fig. 4. The results from the series truncation analysis (solid line) agree well with those of the similarity analysis (dotted line) in the overlap region (vicinity of the front stagnation point). The shear stress maximum occurs approximately around 55 deg. This feature has been observed earlier [1] in the absence of condensation ($W = 0$). The shear stress increases with $W$. In the presence of condensation, fluid particles with a higher tangential momentum are drawn towards the drop surface (note that condensation acts like suction). Thereby a transfer of tangential momentum between fluid particles occurs. As a consequence, the momentum boundary layer gets thinner and the radial gradient of tangential velocity is higher. The shear stress which depends on the velocity gradient at the drop surface increases considerably.

The dimensionless tangential and radial velocity components ($u_\theta$ and $u_r$) across the gas-phase boundary layer are plotted in Fig. 5, for a particular angular location, $\theta = 45$ deg. The choice of the angular location is not significant as long as $\theta < \theta$ at separation. We recall that $r = 1$ refers to the drop surface. The tangential velocity profile attains a maximum in the matching region between the boundary layer and the potential flow. The velocity increases within the boundary layer from a very small surface value to a large value of the edge of the boundary layer. It continuously decreases in the potential flow region and merges with the far stream value. The velocity is higher in the matching region relative to its far stream value due to the deflection of the stream surfaces around the drop. Fluid elements are caused to accelerate along the tangential direction as they negotiate the drop. The radial location of the velocity maximum may be taken to define the thickness of the boundary layer. At higher $W$, there is increased tangential momentum transfer due to higher level of condensation and the boundary layer is

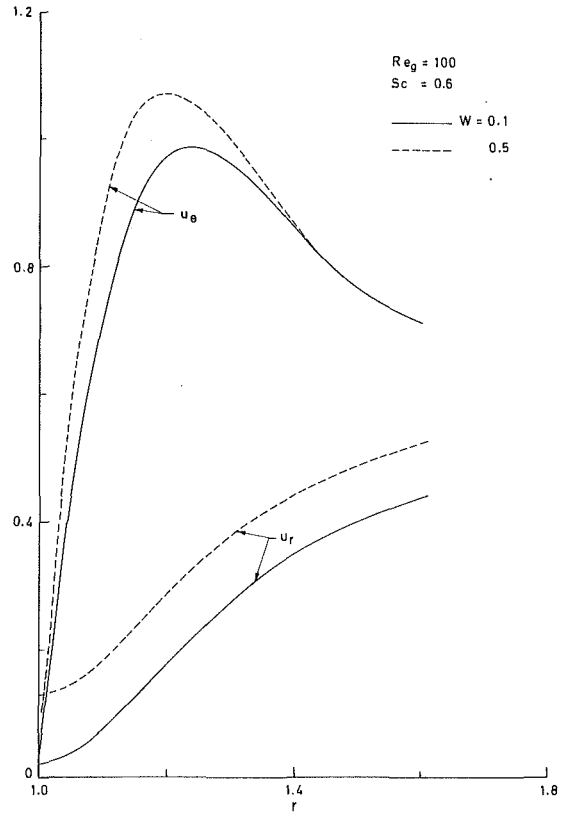


**Fig. 5 The effect of condensation on the velocity profiles across the boundary layer**

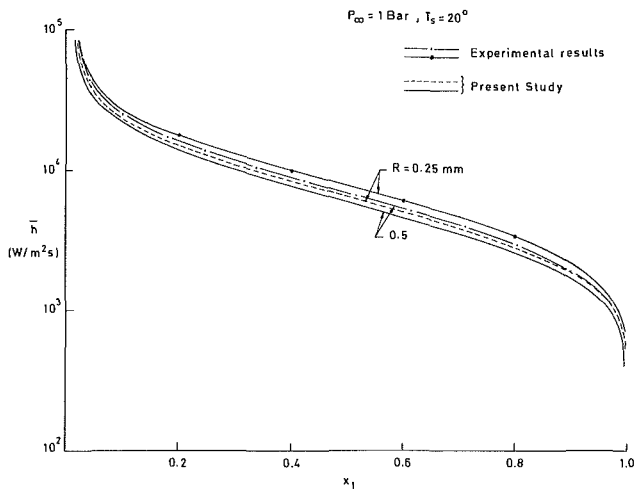


**Fig. 6 The variation of the average heat transfer coefficient $\bar{h}$ with noncondensable volume fraction $x_1$ and $R$**

thinner. The figure also provides the variation in the radial component of velocity, $u_r$. It is interesting to contrast the behavior of $u_\theta$ and $u_r$ in the potential flow region. With an increasing $W$, $u_\theta$ remains essentially unaffected in the potential flow region, while $u_r$ significantly changes. Indeed, $u_\theta$ would also change with $W$, but by substantially smaller amounts. A higher order expansion procedure in Reynolds number will reveal this. We note that $u_r$ continuously increases from the surface value to that in the far stream where it is a maximum. Also, with higher $W$, $u_r$ is obviously higher.

In Fig. 6, the average heat transfer coefficient $\bar{h}$ at the drop surface is plotted against the noncondensable volume fraction $x_1$. The comparison with the experimental results of Kulic et al. [15, 17] are also shown, and there is excellent agreement.

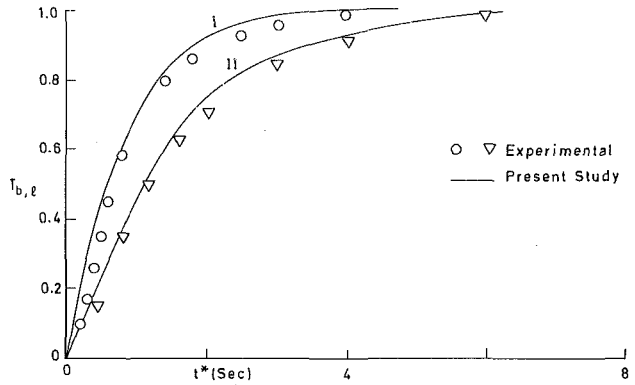


**Fig. 7 The variation of drop bulk temperature $T_{b,l}$ with time: $p_\infty$ = 1 Bar; I-$R_0$ = 1.45mm, $U_\infty$ = 1.91m/s, $T_\infty$ = 80°C, $T_o$ = 16°C; II-$R_0$ = 1.40mm, $U_\infty$ = 1.68m/s, $T_\infty$ = 72.5°C, $T_o$ = 18°C**

**Table 2 Interfacial values of $t_i'$ for the series solution (equation 35)**

| $Pr_g/Sc$ | $-t_0'(0)$ | $-t_1'(0)$ | $-t_2'(0)$ | $-t_3'(0)$ |
|---|---|---|---|---|
| 1.0 | 0.4712 | 0.4391 | 0.0111 | 0.0158 |
| 1.2 | 0.5300 | 0.5008 | 0.0148 | 0.0173 |
| 1.4 | 0.5814 | 0.5509 | 0.0187 | 0.0207 |
| 1.6 | 0.6312 | 0.6012 | 0.0229 | 0.0247 |
| 1.8 | 0.6818 | 0.6527 | 0.0275 | 0.0291 |

The $\bar{h}$ may be shown to be given by

$$\bar{h} = -(k_g/R)(t_0' + Pr_g\, \xi_0/2\, Ja_g)\, Re_g^{1/2}$$

Table 2 provides the interfacial values of $t_i'$ for Sc = 0.6, $W$ = 0.5, and various $Pr_g$.

With an increase in $x_1$, $\bar{h}$ decreases. This is due to the increase in mass transfer resistance.

The comparison between our results and experimental data [16] for the temperature-time history of a water drop experiencing condensation in a forced flow of air-steam mixture is shown in Fig. 7 for two situations: (*i*) $R_o$ = 1.45 mm, $U_\infty$ = 1.91 m/s, $T_\infty$ = 80°C, $p_\infty$ = 1 Bar, and, $T_0$ = 16°C ($Re_g$ ≃ 265); and (*ii*) $R_o$ = 1.4 mm, $U_\infty$ = 1.68 m/s, $T_\infty$ = 72.5°C, $p_\infty$ = 1 Bar (or $x_s$, the far stream volume fraction of steam = 35 percent), and $T_0$ = 18°C ($Re_g$ ≃ 225. The Reynolds numbers here have been shown as approximate, in view of the change in the radius of the drop with time. The change in radius occurs due to the added mass accompanying condensation). The agreement is excellent and lends strong support for the boundary layer formulation. The figure also shows that for larger noncondensable fraction in the bulk, the drop heat-up rate is slower. This illustrates the effect of the gas-phase resistance.

## Acknowledgment

Sponsorship of this work by the National Science Foundation Grant MEA 82-17097 is gratefully acknoweldged.

## References

1 Clift, R., Grace, J. R., and Weber, M. E., *Bubbles, Drops and Particles*, Academic Press, New York, 1978.

2 Jacobs, H. R., and Cook, D. S., "Direct Contact Condensation on a Non-Circulating Drop," *Int. Heat Transfer Conf., 6th*, Vol. 2, 1978, Toronto, Ontario, pp. 389-393.

3 Rakhmatulina, I. Kh., "Nonsteady Evaporation and Growth of Drops in Gas(eous) Medium," *Int. J. Engrg. Sci.*, Vol. 19, 1981, pp. 1114-1122.

4 Sadhal, S. S., and Ayyaswamy, P. S., "Flow Past a Liquid Drop With a Large Non-Uniform Radial Velocity," *J. Fluid Mech.*, Vol. 133, 1983, pp. 65-81.

5 Chung, J. N., Ayyaswamy, P. S., and Sadhal, S. S., "Laminar Condensation on a Moving Drop. Part 1. Singular Perturbation Technique," *J. Fluid Mech.*, Vol. 139, 1984, pp. 105-130.

6 Chung, J. N., Ayyaswamy, P. S., and Sadhal, S. S., "Laminar Condensa-

tion on a Moving Drop. Part 2. Numerical Solutions," *J. Fluid Mech.*, Vol. 139, 1984, pp. 131–144.

7 Chung. J. N., and Ayyaswamy, P. S., "Laminar Condensation Heat and Mass Transfer in the Vicinity of the Forward Stagnation Point of a Spherical Droplet Translating in a Ternary Mixture," *International Journal of Heat and Mass Transfer*, Vol. 21, 1978, pp. 1309–1324.

8 Chung, J. N., and Ayyaswamy, P. S., "Laminar Condensation Heat and Mass Transfer of a Moving Drop," *AIChE Journal*, Vol. 27, 1981, pp. 372–377.

9 Chung, J. N., and Ayyaswamy, P. S., "Material Removal Associated With Condensation on a Droplet in Motion," *Int. J. Multiphase Flow*, Vol. 7, 1981, pp. 329–342.

10 Chung, J. N., and Chang, T-H., "A Mathematical Model of Condensation Heat and Mass Transfer to a Moving Droplet in its Own Vapor," ASME JOURNAL OF HEAT TRANSFER, Vol. 106, 1984, pp. 417–424.

11 Sundararajan, T., and Ayyaswamy, P. S., "Hydrodynamics and Heat Transfer Associated With Condensation on a Moving Drop: Solutions for Intermediate Reynolds Numbers," *J. Fluid Mech*, Vol. 149, 1984, pp. 33–58.

12 Sundararajan, T., and Ayyaswamy, P. S., "Condensation on a Moving Drop: Transient Evolution of the Drop Interior," under review.

13 Sundararajan, T., and Ayyaswamy, P. S., "Numerical Evaluation of Heat and Mass Transfer to a Moving Liquid Drop Experiencing Condensation," in press, *Numerical Heat Transfer*.

14 Ford, J. D., and Lekic, A., "Rate of Growth of Drops During Condensation," *International Journal of Heat and Mass Transfer*, Vol. 16, 1973, pp. 61–64.

15 Kulic, E., Rhodes, E., and Sullivan, G., "Heat Transfer Rate Predictions in Condensation on Droplets From Air-Steam Mixtures," *Can. J. Chem. Engrg.*, Vol. 53, 1975, pp. 252–258.

16 Kulic, E., and Rhodes, E., "Direct Contact Condensation From Air-Steam Mixtures on a Single Droplet," *Can. J. Chem. Engrg.*, Vol. 55, 1977, pp. 131–137.

17 Kulic, E., and Rhodes, E., "Heat Transfer Rates to Moving Droplets in Air/Steam Mixtures," *Int. Heat Transfer Conf., 6th*, 1978, Toronto, Ontario, pp. 464–474.

18 Chao, B. T., "Transient Heat and Mass Transfer to a Translating Droplet," ASME JOURNAL OF HEAT TRANSFER, Vol. 91, 1969, pp. 273–281.

19 Brignell, A. S., "Solute Extraction From an Internally Circulating Spherical Liquid Drop," *International Journal of Heat and Mass Transfer*, Vol. 18, 1975, pp. 61–68.

20 Harpole, G. M., "Droplet Evaporation in High Temperature Environments," ASME JOURNAL OF HEAT TRANSFER, Vol. 103, 1981, pp. 86–91.

21 Minkowycz, W. J., and Sparrow, E. M., "Condensation Heat Transfer in the Presence of Noncondensables, Interfacial Resistance, Superheating, Variable Properties and Diffusion," *International Journal of Heat and Mass Transfer*, Vol. 9, 1966, pp. 1125–1144.

22 Frossling, N., "Uber die verdunstung fallenden tropfen," *Gerlands Beitrage zur Geophysik*, Vol. 52, 1938, pp. 170–216.

23 Sparrow, E. M., Minkowycz, W. J., and Saddy, M., "Forced Convection Condensation in the Presence of Noncondensables and Interfacial Resistance," *International Journal of Heat and Mass Transfer*, Vol. 10, 1967, pp. 1829–1845.

# An Integral Treatment of Laminar and Turbulent Film Condensation on Bodies of Arbitrary Geometrical Configuration

**A. Nakayama**
Associate Professor.

**H. Koyama**
Professor.

Department of Mechanical Engineering,
Shizuoka University,
Hamamatsu, 432 Japan

*A general solution procedure has been developed for laminar and turbulent film condensation problems. The procedure is designed to deal with both plane and axisymmetric isothermal bodies of arbitrary geometrical configuration. Inertia effects are fully considered by introducing a new parameter associated with the flow acceleration. A closed-form expression for the local Nusselt number is obtained for both laminar and turbulent flows. Calculations are carried out for laminar and turbulent condensate layers developed on flat plates, horizontal circular cylinders, and spheres. The results are compared with available predictions and measurements.*

## Introduction

Nusselt [1] solved the problem of laminar film condensation on a vertical flat surface by neglecting the acceleration terms in the momentum equation. Later, Rohsenow [2] improved Nusselt's analysis and showed that the temperature, in fact, varies almost linearly across the film for moderate rates of liquid subcooling. Upon performing a similarity transformation, Sparrow and Gregg treated the full boundary layer equations and obtained solutions for the flat plate [3] and the horizontal circular cylinder [4].

While a number of theoretical works on laminar film condensation are available, only a few analyses of turbulent film condensation problems have been attempted. Colburn [5] suggested a correlation for the vertical flat surface on the basis of the momentum-heat transfer analogy. The Prandtl-Karman analogy was used by Seban [6] to analyze laminar and turbulent film condensation. This method was later modified by Rohsenow et al. [7] to consider the nonvanishing shear stress at the liquid-vapor interface.

Some workers (e.g., [1, 4, 8]) later extended laminar film condensation theories to the nonuniform gravitational field. In 1971, Dhir and Lienhard [9] proposed a general integral method for solving laminar film condensation problems for arbitrary geometrical configurations. Following a procedure similar to the original work by Nusselt [1], they obtained a general expression for the local Nusselt number that is identical to Nusselt's expression except for the use of a modified gravity force. Since the acceleration terms are neglected, as in Nusselt's analysis, their analysis is not valid when the streamwise component of the gravity force changes rapidly. Their analysis also cannot be applied when the Prandtl number of the condensate is much less than unity, as it is for liquid metals.

The present paper introduces a general integral solution procedure for problems of laminar and turbulent film condensation on an isothermal wall. The analysis may be regarded as an extended version of the analysis proposed by Dhir and Lienhard [9] for laminar film condensation, in the sense that it is also designed to deal with both plane and axisymmetric bodies of arbitrary geometrical configuration. In the present effort, however, the inertia terms and convection terms in the momentum and energy equations are retained, in order to describe Prandtl number effects as well as the effects of strong flow acceleration on the local heat transfer process. Special attention is directed toward application to turbulent films developed over curved surfaces, since no such general scheme seems to have been reported elsewhere.

## Physical Model and Governing Equations

The physical model under consideration is shown schematically in Fig. 1, where the boundary layer coordinates $(x, y)$ are aligned along the wall surface and its normal. The model may be either a plane or an axisymmetric body of local radius $r(x)$. It is supposed that the body is situated in a quiescent, pure vapor that is at its saturation temperature $T_e$. The wall temperature $T_w$ is uniform and below the saturation temperature. Thus condensation occurs on the wall and a continuous film of liquid runs downward under the influence of the component of gravity parallel to the wall.

A control volume analysis within the condensate layer of thickness $\delta$ leads to the following momentum and energy conservation equations under the assumption of negligible shear and heat conduction at the liquid-vapor interface:

$$\frac{d}{dx}\int_0^\delta \rho\, r^*\, u^2 dy - u_e \frac{d}{dx}\int_0^\delta \rho\, r^*\, u\, dy = r^*(\Delta\rho\, g_x \delta - \tau_w) \qquad (1a)$$

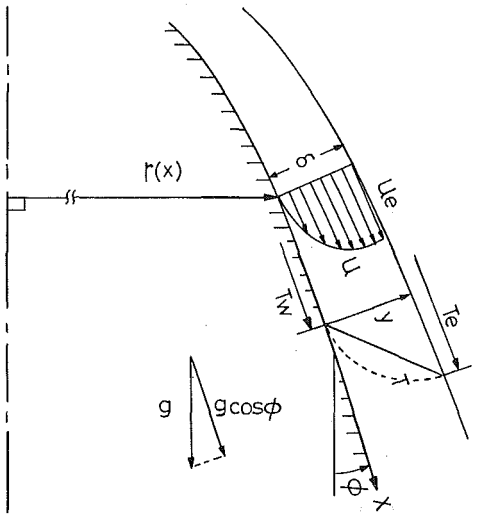


Fig. 1 Physical model and coordinate system

Contributed by the Heat Transfer Division for publication in the JOURNAL OF HEAT TRANSFER. Manuscript received by the Heat Transfer Division August 9, 1983.

$$\frac{d}{dx}\int_0^\delta \rho\, r^*\, u\, C_p(T-T_e)\,dy - h_{fg}\frac{d}{dx}\int_0^\delta \rho\, r^*\, u\, dy = r^*\, q_w \quad (1b)$$

where

$$r^* = \begin{cases} 1 & : \text{plane flow} \\ r(x) & : \text{axisymmetric flow} \end{cases} \quad (1c)$$

and

$$g_x = g\cos\phi = g\left[1-\left(\frac{dr}{dx}\right)^2\right]^{1/2} \quad (1d)$$

In the foregoing equations, $\tau_w$ and $q_w$ are the local wall shear stress and heat flux while $\rho$, $C_p$, and $h_{fg}$ are the density, specific heat, and latent heat of vaporization. The density difference between the liquid and vapor is denoted by $\Delta\rho$ ($\cong \rho$). The tangential component of the acceleration of gravity is indicated by $g_x$, which is related to the local surface orientation $\phi$ through equation (1*d*). The streamwise velocity and the local temperature are denoted by $u$ and $T$, and the subscript $e$ denotes the liquid–vapor interface.

Through a series of the studies on the laminar heat transfer problems, free convection [10], forced convection [11] and film condensation [12], we have demonstrated that it is quite effective to utilize the auxiliary relationship at the wall that is obtainable from the Couette flow consideration near the wall. The same principle can be extended to the case of the laminar and turbulent film condensation as follows.

Since the advection terms must vanish near the wall, the original differential form of the momentum equation implies the following auxiliary relationship, which defines the parameter $\xi$

$$\xi \equiv -\frac{\delta}{\tau_w}\frac{d\tau}{dy}\bigg|_{y=0} = \Delta\rho\, g_x \delta/\tau_w \quad (2)$$

$\xi$ is used as a parameter common to both laminar and turbulent film layers.

Upon introducing the velocity profile function $f$ and the dimensionless temperature profile function $\theta$ as

$$f(\eta) = u/u_e \quad \text{and} \quad \theta(\eta) = (T-T_e)/\Delta T \quad (3a,b)$$

where

$$\Delta T \equiv T_w - T_e \quad \text{and} \quad \eta \equiv y/\delta \quad (3c,d)$$

we may rewrite the governing equations (1*a*, *b*), in terms of $\xi$, as

$$\frac{d}{dx}B\, r^*\, u_e^2\delta - u_e\frac{d}{dx}A\, r^*\, u_e\delta = \left(1-\frac{1}{\xi}\right) r^*\, g_x'\delta \quad (4a)$$

$$\frac{d}{dx}\left(D+\frac{A}{\mathrm{Ja}}\right)^* r u_e\delta = f_R\, r^* g_x'\delta/\xi u_e \quad (4b)$$

where

$$A=\int_0^1 f\,d\eta, \quad B=\int_0^1 f^2 d\eta, \quad D=\int_0^1 f\,\theta\,d\eta \quad (4c,d,e)$$

$$\mathrm{Ja} = -C_p\Delta T/h_{fg}, \quad g_x' = \Delta\rho\, g_x/\rho \quad \text{and} \quad f_R = u_e q_w/C_p\Delta T\,\tau_w \quad (4f,g,h)$$

The right-hand side of the momentum equation (4*a*) clearly indicates that the parameter $\xi$ directly governs the flow acceleration. It should be noted that the solutions of Nusselt [1] and Dhir and Lienhard [9] correspond to the special case, $\xi(x) = 1$, where the inertial effects are negligible and the shear force balances the gravitational force. In any case, the condition $\xi(x) \geqq 1$ must be satisfied throughout the wall surface for a continuous condensate layer to run downward.

## General Solutions Common to Both Laminar and Turbulent Condensate Layers

The solution of the problem is reduced to the determination of the three unknown variables: the film thickness $\delta$, the film velocity at the liquid–vapor interface $u_e$, and the acceleration parameter $\xi$. To solve the governing equations for both laminar and turbulent flows, one may introduce the following expressions for the wall shear and heat flux common to both laminar and turbulent flows

$$\tau_w/\rho\, u_e^2 = C(\nu/u_e\delta)^{2/n_1} \quad (5a)$$

$$q_w/\rho\, C_p\Delta T\, u_e = f_R(\tau_w/\rho\, u_e^2) \quad (5b)$$

where

## Nomenclature

$A,B,D,E$ = shape factors
$C_p$ = specific heat of the liquid
$d$ = diameter of cylinder (sphere)
$f$ = function for velocity profile
$f_R$ = Reynolds analogy factor
$g$ = acceleration of gravity
$g_x$ = tangential component of $g$
$g_x'$ = $\Delta\rho\, g_x/\rho$
$\mathrm{Gr}_d$ = $\Delta\rho\, g\, d^3/\rho\,\nu^2$
$\mathrm{Gr}_x$ = $g_x' x^3/\nu^2$ local Grashof number
$h$ = local heat transfer coefficient
$h_{fg}$ = latent heat of vaporization
$i$ = integer associated with the coordinate system
$I,I_t$ = functions associated with a deviation from unity
$j$ = integer associated with the body shape at stagnation
Ja = $-C_P\Delta T/h_{fg}$ sensible-latent heat ratio (Jakob number)
Ja′ = $\mathrm{Ja}/(1+\frac{D}{A}\mathrm{Ja})$
$k$ = thermal conductivity of the liquid
$n$ = value associated with the power law
$\mathrm{Nu}_f$ = $\bar{h}(\nu^2/g_x')^{1/3}/k$ film Nusselt number
$\mathrm{Nu}_x$ = $h\,x/k$ local Nusselt number
Pr = Prandtl number
$q$ = heat flux
$r$ = function representing wall geometry
$r^*$ = 1 for plane flow and $r$ for axisymmetric flow
$\mathrm{Re}_f$ = $4\int_0^\delta u\,dy/\nu$ film Reynolds number
$\mathrm{Re}_{ftr}$ = transition Reynolds number, equation (22)
$T$ = temperature
$u$ = streamwise velocity component
$x,y$ = boundary layer coordinates
$\delta$ = condensate film thickness
$\Delta T$ = $T_w - T_e$
$\Delta\rho$ = density difference between liquid and vapor
$\eta$ = $y/\delta$
$\theta$ = dimensionless temperature profile
$\Lambda$ = shape factor for laminar velocity profile
$\nu$ = kinematic viscosity
$\xi$ = $\Delta\rho\, g_x\delta/\tau_w$, acceleration parameter
$\rho$ = density
$\tau$ = shear stress
$\phi$ = surface orientation angle

**Subscripts and Superscripts**

$d$ = based on $d$ and $g$
$e$ = liquid–vapor interface
$w$ = wall
$x$ = based on $x$ and $g_x$
$\bar{}$ = average over the surface

$$C = \begin{cases} \left.\dfrac{\partial f}{\partial \eta}\right|_{\eta=0} & : \text{laminar} \\ 0.0225 & : \text{turbulent} \end{cases} \quad (5c,d)$$

$$f_R = \begin{cases} -\left.\dfrac{\partial \theta}{\partial \eta}\right|_{\eta=0} \Big/ \left.\dfrac{\partial f}{\partial \eta}\right|_{\eta=0} \mathrm{Pr} & : \text{laminar} \\ \mathrm{Pr}^{-2/3} & : \text{turbulent} \end{cases} \quad (5e,f)$$

$$n = \begin{cases} 1 & : \text{laminar} \\ 7 & : \text{turbulent} \end{cases} \quad (5g,h)$$

and

$$n_i \equiv n + i \quad (5i)$$

In the foregoing expressions, the kinematic viscosity and Prandtl number are denoted by $\nu$ and Pr, respectively. The wall shear is given by equation (5*a*) in the form of a power law using the short-hand notation $n_1 = n + 1$. Equation (5*a*) along with (5*d*, *h*) gives Blasius' friction law which corresponds to a $1/n$ ($= 1/7$) power law velocity profile, while equation (5*b*) with (5*f*, *h*) for the wall heat flux reduces to the well-known Colburn analogy. (Although equations (5*d*, *h*) for turbulent flow are specifically written following Blasius' friction law, the present analysis is, by no means, restricted to $n = 7$ as long as the empirical coefficient $C$ is adjusted for a given value of $n$ as suggested by Wieghardt [13].) For laminar flow, on the other hand, equations (5*a*, *b*) along with (5*c*, *e*, *g*) automatically reduce to the gradient diffusion expressions, namely, $\tau_w = \rho\,\nu\,(\partial u/\partial y)|_{y=0}$ and $q_w = -k\,(\partial T/\partial y)|_{y=0}$ where $k$ is the thermal conductivity.

Equations (5*a*) and (2) may be combined to give

$$u_e = (g_x'/C\,\xi)^{n_1/2n}\,\delta^{n_3/2n}/\nu^{1/n} \quad (6)$$

The foregoing equation is substituted into equations (4*a*, *b*) to eliminate $u_e$ in favor of $\xi$. After some manipulation, the governing equations (4*a*, *b*) reduce to the following pair of differential equations for $\delta^{n_3/n}$

$$\frac{d}{dx}\delta^{n_3/n} + \delta^{n_3/n}\frac{d}{dx}\ln[r^{*B-A}(g_x'/\xi)^{(2B-A)n_1/2n}]^E = E(\xi-1)(C^{n_1}\nu^2\xi/g_x')^{1/n} \quad (7a)$$

$$\frac{d}{dx}\delta^{n_3/n} + \delta^{n_3/n}\frac{d}{dx}\ln[r^*(g_x'/\xi)^{n_1/2n}]^{2n_3/3n_1} = \frac{2n_3}{3n_1A}\mathrm{Ja}'f_R(C^{n_1}\nu^2\xi/g_x')^{1/n} \quad (7b)$$

where

$$E = \left[\frac{2B-A}{2} - \frac{n}{n_3}(A-B)\right]^{-1} \quad (7c)$$

and

$$\mathrm{Ja}' = \mathrm{Ja}/\left(1 + \frac{D}{A}\mathrm{Ja}\right) \quad (7d)$$

In the foregoing manipulation, the shape factors $A$, $B$, and $D$ are assumed to be constant. The assumption of constant shape factors is consistent with the power law adopted for the turbulent film. For nonsimilar laminar films, the shape factors do vary, yet, the rate of the streamwise change of these shape factors is usually small enough for "quasi-local similarity" to hold. Thus the first derivatives of the shape factors have been neglected to obtain equations (7*a*, *b*).

The integration of equations (7*a*, *b*) yields two distinct closed-form expressions for $\delta^{n_3/n}$ as follows

$$(\delta/x)^{n_3/n}\mathrm{Gr}_x^{1/n} = E(C^{n_1}\xi)^{1/n}(\xi-1)I \quad (8a)$$

and

$$(\delta/x)^{n_3/n}\mathrm{Gr}_x^{1/n} = \frac{2n_3}{3n_1A}(C^{n_1}\xi)^{1/n}\mathrm{Ja}'f_R I_t \quad (8b)$$

where

$$I = \frac{\int_{x_{tr}}^{z}(\xi-1)\left[r^{*B-A}(g_x/\xi)^{\frac{2B-A}{2}+\frac{A-B}{n_3}}\right]^E dx + \text{const.}}{(\xi-1)\left[r^{*B-A}(g_x/\xi)^{\frac{2B-A}{2}+\frac{A-B}{n_3}}\right]^E x} \quad (8c)$$

$$I_t = \frac{\int_{x_{tr}}^{x}(r^{*2n_3/n_1}g_x/\xi)^{1/3}dx + \text{const.}}{(r^{*2n_3/n_1}g_x/\xi)^{1/3}x} \quad (8d)$$

and

$$\mathrm{Gr}_x = g_x'x^3/\nu^2 \quad (8e)$$

$x_{tr}$ is the location where the flow changes from laminar to turbulent. For the laminar flow, $x_{tr}$ and the integration constants should be simply set equal to zero. The functions $I$ and $I_t$ represent the deviations from the flat plate case, and naturally become unity when $r^*$ and $g_x$ are constant. Upon combining equations (8*a*) and (8*b*), one obtains the following characteristic equation for the acceleration parameter $\xi$

$$\xi = 1 + \left(\frac{2n_3}{3n_1AE}\right)(I_t/I)\mathrm{Ja}'f_R \quad (9)$$

The foregoing equation can be used to determine $\xi(x)$ for a given Pr and the geometrical configuration $g_x(x)$. Once $\xi(x)$ is obtained from equation (9), the streamwise variations of all quantities associated with the boundary layer development can be determined.

Some manipulation using equations (5*a*), (5*b*), (6), and (8*b*) finally leads to the following Nusselt number expression of primary interest

$$\mathrm{Nu}_x/\mathrm{Gr}_x^{n_1/2n_3} = \left(\frac{2n_3}{3n_1A}I_t\mathrm{Ja}'\right)^{\frac{n-3}{2n_3}}(f_R^3C^2/\xi)^{n_1/2n_3}\mathrm{Pr} \quad (10)$$

## Solutions for Laminar Condensate Layers

The temperature profiles obtained by Rohsenow [2] and Sparrow and Gregg [3] deviate very little from a linear distribution for moderate values of liquid subcooling. Therefore, the assumption of linearity of the temperature profile may still be a good approximation in the laminar condensate layer. For the velocity profile, on the other hand, a third-order polynomial expression may be adequate. Thus the velocity and temperature profiles across the laminar film are taken to be

$$f(\eta;\Lambda) = \frac{\Lambda+3}{2}\eta - \Lambda\eta^2 + \frac{\Lambda-1}{2}\eta^3 \quad (11a)$$

$$\theta(\eta) = 1 - \eta \quad (11b)$$

The velocity profile automatically satisfies $f = 0$ at $\eta = 0$, while $f = 1$ and $\partial f/\partial\eta = 0$ at $\eta = 1$. On the other hand, the temperature profile $\theta$ satisfies the obvious conditions $\theta = 1$ at $\eta = 0$ and $\theta = 0$ at $\eta = 1$.

All the shape factors and $f_R$ may readily be calculated from equations (11). The shape factor $\Lambda$ associated with the curvature of the velocity profile is directly related to the acceleration parameter $\xi$ by equation (2) as

$$\xi = \frac{4\Lambda}{\Lambda+3} \quad (12)$$

Therefore, $\xi$ and $\Lambda$ may be used interchangeably. Upon substituting the resulting shape factors into equation (10), one obtains the local Nusselt number for the laminar film as

$$\mathrm{Nu}_x/\mathrm{Gr}_x^{1/4} = \left(\frac{\Lambda+15}{64\Lambda}\frac{\mathrm{Pr}}{I_t\mathrm{Ja}'}\right)^{1/4} \quad (13a)$$

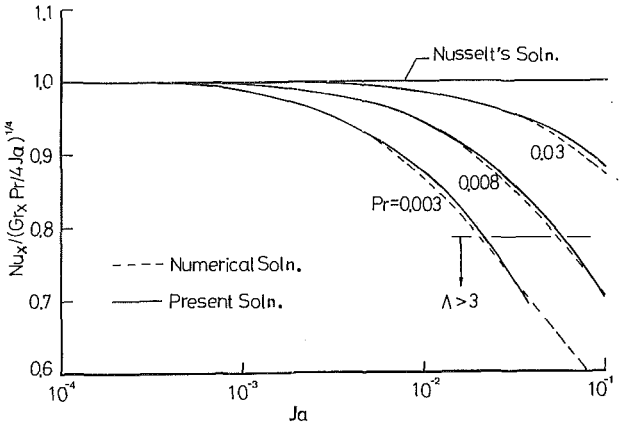


**Fig. 2 Local Nusselt number for laminar film on a flat plate**

where

$$Ja' = Ja/\left(1+\frac{3\Lambda+27}{5\Lambda+75}Ja\right) \tag{13b}$$

$$I = \frac{\int_0^x (\xi-1)[r^{*4(B-A)}(g_x/\xi)^{3B-A}]^{\frac{1}{5B-3A}}dx}{(\xi-1)[r^{*4(B-A)}(g_x/\xi)^{3B-A}]^{\frac{1}{5B-3A}}x} \tag{13c}$$

$$I_t = \frac{\int_0^x (r^{*4}g_x/\xi)^{1/3}dx}{(r^{*4}g_x/\xi)^{1/3}x} \tag{13d}$$

and

$$A=(\Lambda+15)/24, \quad B=(\Lambda^2+19\Lambda+204)/420 \tag{13e,f}$$

It is interesting to note that in the limiting case of no-inertia, namely, $\xi = 1$ ($\Lambda = 1$), equation (13*a*) along with (13*d*) reduces to the expression obtained by Dhir and Lienhard [9]. (The function $I_t$ corresponds to $g/g_{eff}$ in their notation.)

The parameter $\Lambda$ (or $\xi$) may be determined according to equation (9), which can be reduced to the following form

$$Pr = \frac{2}{63}\frac{2\Lambda^2+17\Lambda+93}{(\Lambda-1)(\Lambda+15)}(I_t/I)\,Ja' \tag{14}$$

Upon locally evaluating $I(x)$ and $I_t(x)$ for given geometrical configuration $g_x(x)$, one can solve the implicit equation (14) for $\Lambda(x)$. The solution requires an iterative procedure at each integration step. The integrations appearing in the equations (13*c*, *d*) should be carried out with an estimated value for $\Lambda$ at each end of the integration step, then, the results are substituted back into the equation (14) to check if the estimated $\Lambda$ satisfies the relation. The sequence is repeated to determine $\Lambda$ within any desired accuracy.

The initial value $\Lambda|_{x=0}$, however, must be determined before marching downstream. The consideration of the stagnation flows near $x = 0$ [12] reveals that the functions $I$ and $I_t$ in this region become

$$I = \left[1+\frac{4(B-A)i+(3B-A)j}{5B-3A}\right]^{-1} \tag{15a}$$

and

$$I_t = \left[1+\frac{4i+j}{3}\right]^{-1} \tag{15b}$$

where the integer $i$ is 0 for plane flow and 1 for axisymmetric flow, while $j$ is 0 for a pointed body, and 1 for a blunt body. For example, the integers $(i, j)$ are (0, 0) for a flat plate (or a wedge), (1, 0) for a cone, (0, 1) for the stagnation flow over a horizontal cylinder, and (1, 1) for the stagnation flow over a sphere. The substitution of equations (15) into the characteristic equation (14) yields an algebraic equation for $\Lambda|_{x=0}$, which can easily be solved when Pr and Ja are specified. Upon using this initial value, the aforementioned stepwise iterative calculation can be followed downstream to find $\Lambda(x)$.

## Laminar Calculation Results

Figure 2 shows the local heat transfer results along flat plates for Pr = 0.003, 0.008, and 0.03. The ordinate variable is chosen to provide a direct comparison of results of Nusselt [1] and the numerical solution of Sparrow and Gregg [3]. As the sensible-latent heat ratio Ja becomes sufficiently small, both the present solution and the numerical solution approach the Nusselt solution. Inertia effects on the heat transfer rate are found to be significant, especially for small Prandtl numbers as manifested by an appreciable departure from Nusselt's solution. Equation (8*b*) shows that an increase in Ja thickens the film, thus the effects of both convection and inertia become significant as it increases. The agreement of the present solution with the Sparrow and Gregg solution appears to be excellent. However, equation (11*a*) requires $\Lambda$ to be less than 3 for the velocity to increase monotonically within $0 \le \eta \le 1$. The region below the horizontal line indicated in the lower right of Fig. 2 corresponds to the region where $\Lambda > 3$ where the present solution is expected to be in error.

As a general example of a nonsimilar flow, calculations have been performed for the horizontal circular cylinder. The circumferential variation of the shape factors $\Lambda$ and $\xi$ and the local heat transfer coefficient are illustrated in Figs. 3(*a*) and 3(*b*) for Pr = 0.03. The parameter $\xi$ decreases downstream and becomes unity upstream of the rear stagnation point, implying failure of the boundary layer approximation near the stagnation region. The calculations thereafter proceed up to the stagnation point using equation (13*d*) with $\xi$ being fixed at unity. The inertia effect appears to diminish with decreasing Ja. The curve for Ja = 0 naturally falls on the horizontal line, $\xi = 1$, which corresponds to the Nusselt [1] and Dhir and Lienhard [9] solutions.

The local heat transfer coefficient $Nu_d/(Gr_d Pr/2Ja)^{1/4}$ (where $Nu_d = h\,d/k$ and $Gr_d = \Delta\rho\, g\, d^3/\rho\,\nu^2$) approaches zero at the rear stagnation point as seen in Fig. 3(*b*). The comparison of the present result with Nusselt's (Dhir and Lienhard) solution (obtained by a straightforward numerical integration of equation (13*d*) with $\xi = 1$) reveals that, for the case of small Pr, the inertia force tends to lower the heat transfer rate. The effect of Ja on local heat transfer is more significant upstream than downstream. As a result, the heat flux distribution over the upper half of the cylinder becomes flatter with increasing Ja.

In Fig. 4(*a*), results for various Pr and Ja are compared with Nusselt's solution and the numerial solution by Sparrow and Gregg [4] in terms of the overall heat transfer coefficient averaged over the entire circumference of the cylinder. The agreement of the present solution with that of Sparrow and Gregg is excellent. The curves for small Pr have been extended only to Ja = 0.1 because higher values are normally unattainable in liquid metals. Results obtained for a sphere are plotted in Fig. 4(*b*) in a similar fashion. With decreasing Ja, the curves asymptotically approach the Dhir and Lienhard solution [9].[1]

[1] Dhir and Lienhard [9] miscalculated $\bar{h}$ for a sphere using $\bar{h} = \int_0^\pi h\, d(2x/d)/\pi$ instead of $\bar{h} = \int_0^\pi h\, r\, d(2x/d)/\int_0^\pi r\, d(2x/d)$. A numerical integration reveals that the correct result for the no-inertia limit is $\bar{Nu}_d = 0.828\,(Gr_d Pr/Ja)^{1/4}$.

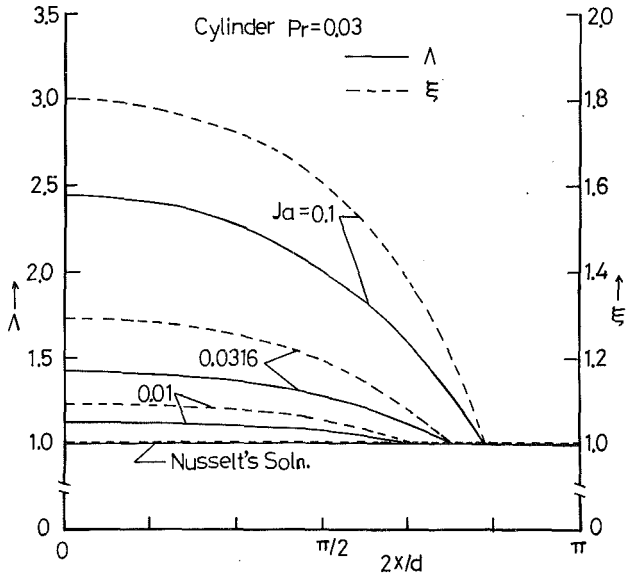


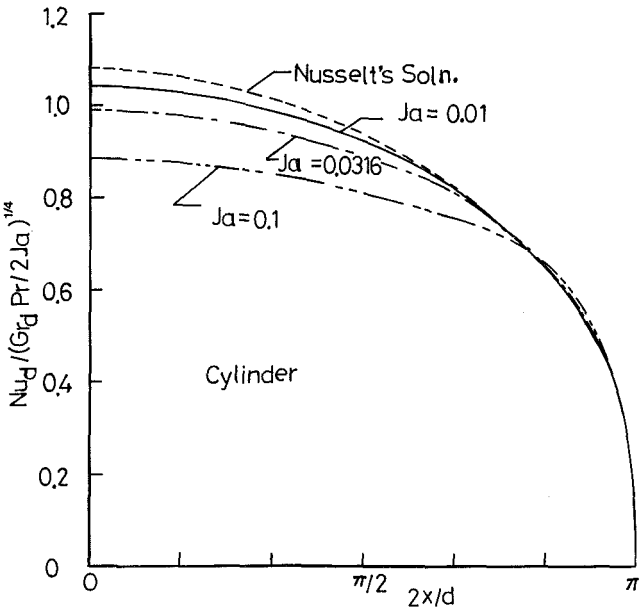


**Fig. 3 Circumferential variations of laminar film on a horizontal circular cylinder: (*a*) acceleration parameter; (*b*) local heat transfer coefficient**

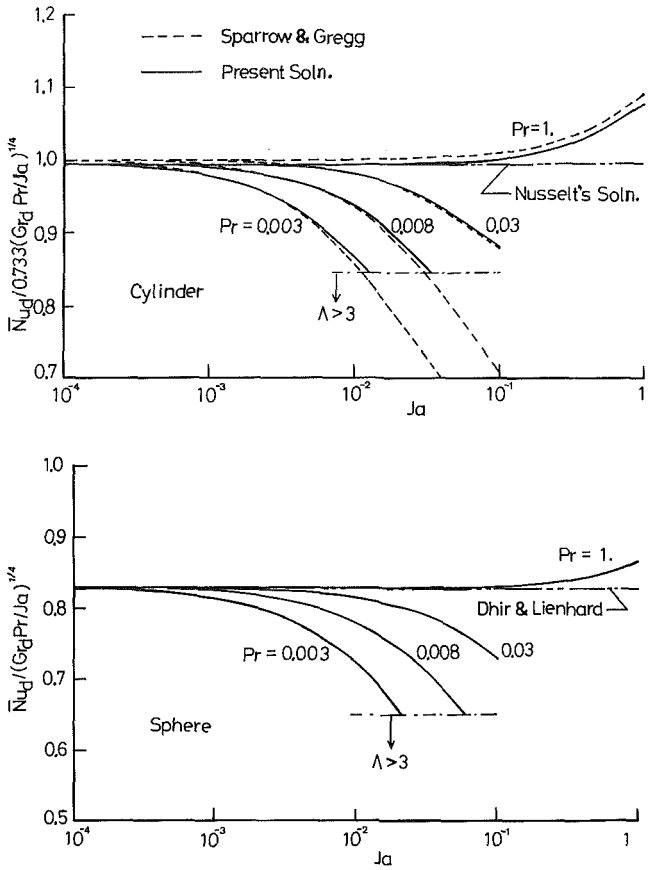


**Fig. 4 Overall heat transfer coefficient for laminar films: (*a*) horizontal circular cylinder; (*b*) sphere**

## Solutions for Turbulent Condensate Layers

We now extend the considerations to turbulent film condensation in which the velocity and temperature profiles follow the power laws such that

$$f(\eta)=\eta^{1/7} \quad \text{and} \quad \theta(\eta)=1-\eta^{1/7} \tag{16a,b}$$

Integrations, using the foregoing profiles, give the shape factors $A$, $B$, and $D$. Thus equation (10) reduces to the local Nusselt number correlation for the turbulent film layer:

$$\mathrm{Nu}_x/\mathrm{Gr}_x^{2/5}=0.0476(I_t\,\mathrm{Ja}'\,\mathrm{Pr}/\xi^2)^{1/5} \tag{17a}$$

where

$$\mathrm{Ja}'=\mathrm{Ja}/\left(1+\frac{1}{9}\,\mathrm{Ja}\right) \tag{17b}$$

$$I=\frac{\int_{x_{tr}}^{x}(\xi-1)\bar{r}^{*\,-5/14}(g_x/\xi)^{9/7}dx+\text{const.}}{(\xi-1)\bar{r}^{*\,-5/14}(g_x/\xi)^{9/7}x} \tag{17c}$$

and

$$I_t=\frac{\int_{x_{tr}}^{x}\bar{r}^{*\,5/6}(g_x/\xi)^{1/3}dx+\text{const.}}{\bar{r}^{*\,5/6}(g_x/\xi)^{1/3}x} \tag{17d}$$

The acceleration parameter $\xi(x)$ is determined from equation (9) which reduces to the following expression for turbulent films

$$\xi=1+\frac{7}{27}\,(I_t/I)(\mathrm{Ja}'/\mathrm{Pr}^{2/3}) \tag{18}$$

It it interesting to note that the solution of the turbulent flow requires only a single lumped parameter $\mathrm{Ja}'/\mathrm{Pr}^{2/3}$ to be specified.

For a given $x_{tr}$, the matching of the laminar and turbulent solutions provides the integration constants. A good estimate of turbulent heat transfer can still be made by simply setting $x_{tr}=0$ if the turbulent region is large.

Stepwise iterative calculations can be followed downstream using the procedure described for laminar flow. Since equations (17*c*, *d*) readily give for stagnation flows $I=(1-5i/14+9j/7)^{-1}$ and $I_t=(1+5i/6+j/3)^{-1}$, the initial value $\xi|_{x=0}$ needed for the integrations associated with equations (17*c*, *d*) can be obtained from the following explicit equation

$$\xi|_{x=0}=1+\frac{7}{27}\,\frac{1-\frac{5}{14}i+\frac{9}{7}j}{1+\frac{5}{6}i+\frac{1}{3}j}\,(\mathrm{Ja}'/\mathrm{Pr}^{2/3}) \tag{19}$$

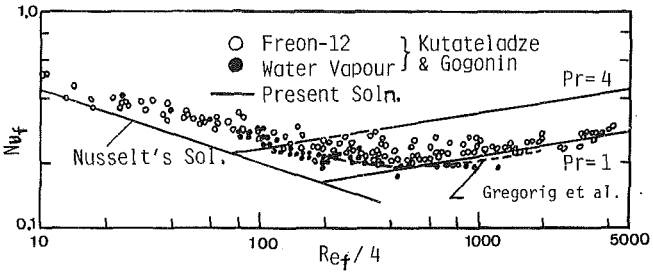


Fig. 5 Film Nusselt number for laminar and turbulent films on a flat plate

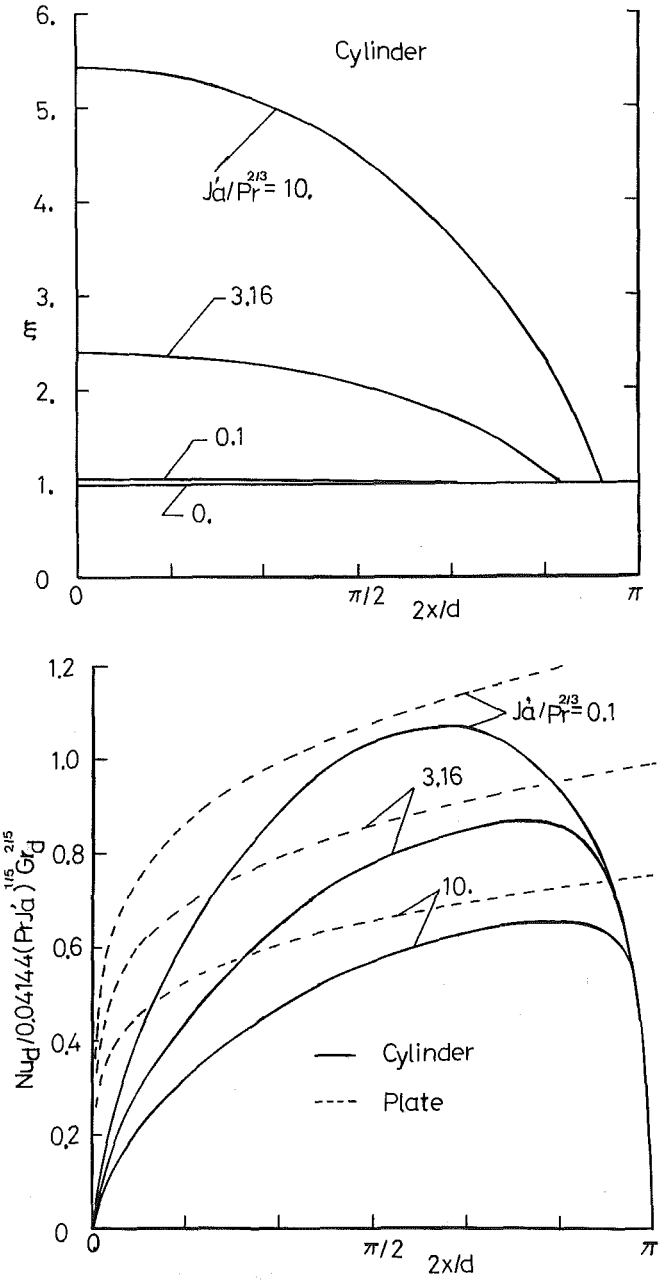


Fig. 6 Circumferential variations of turbulent film on a horizontal circular cylinder: (*a*) acceleration parameter; (*b*) local heat transfer coefficient

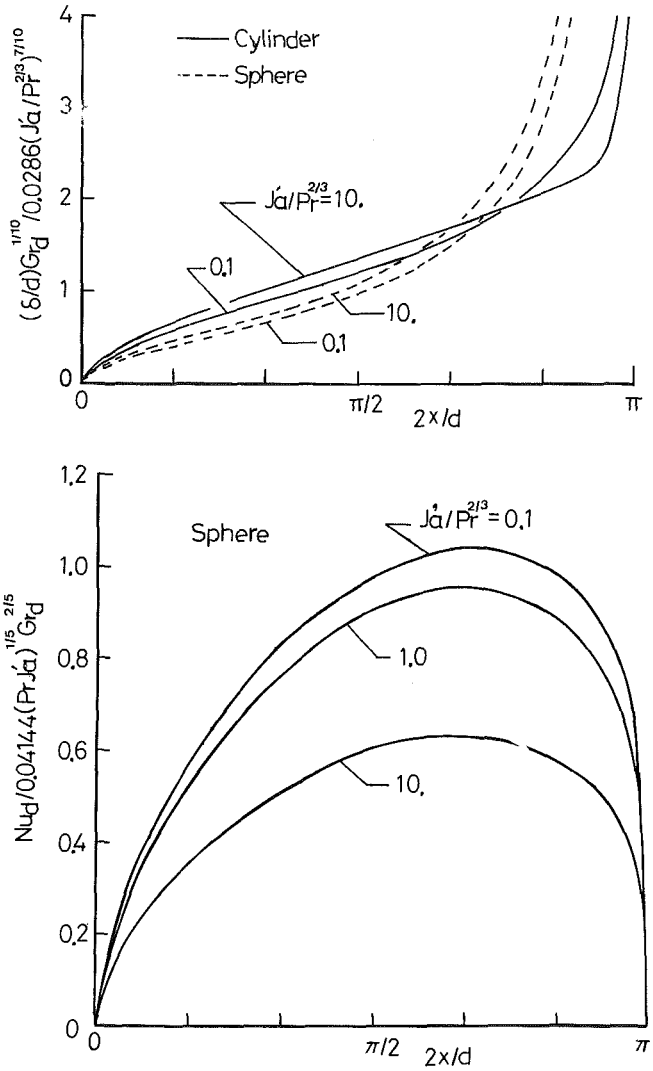


Fig. 7 Circumferential variations of turbulent film on a sphere: (*a*) film thickness; (*b*) local heat transfer coefficient

## Turbulent Calculation Results

It is customary to use the film Nusselt number $Nu_f$ and the film Reynolds number $Re_f$ in place of $Nu_x$ and $Gr_x$ for a vertical flat plate. Using $I = I_t = 1$ for the flat surface, equation (17*a*) can readily be integrated to obtain $Nu_f$

$$Nu_f = 0.0539\ Re_f^{1/6} Pr^{1/3} / \left[1 + \frac{7}{27}(Ja'/Pr^{2/3})\right]^{1/3} \qquad (20a)$$

where

$$Nu_f \equiv \frac{\bar{h}}{k}\left(\frac{\nu^2}{g_x'}\right)^{1/3} = (\bar{h}\,x/k)/Gr_x^{1/3} \qquad (20b)$$

and

$$Re_f \equiv 4\int_0^\delta u\,dy/\nu = (\bar{h}\,x/k)\,(4Ja'/Pr) \qquad (20c)$$

For comparison, the corresponding laminar flow equation is also obtained from equation (13*a*) as

$$Nu_f = (4/3)^{4/3}\left(\frac{\Lambda + 15}{16\Lambda}\right)^{1/3} Re_f^{-1/3} \qquad (21)$$

where $\Lambda$ is determined from equation (14) with $I = I_t = 1$. Equation (21) with $\Lambda = 1$ reduces to Nusselt's solution which is a good approximation for $Pr > 1$. By equating equations (20*a*) and (21), one may roughly estimate a critical film Reynolds number $Re_{ftr}$ for the flow transition as

$$Re_{ftr} \cong 741/Pr^{2/3} \qquad (22)$$

Equation (22) implies that the critical film Reynolds number

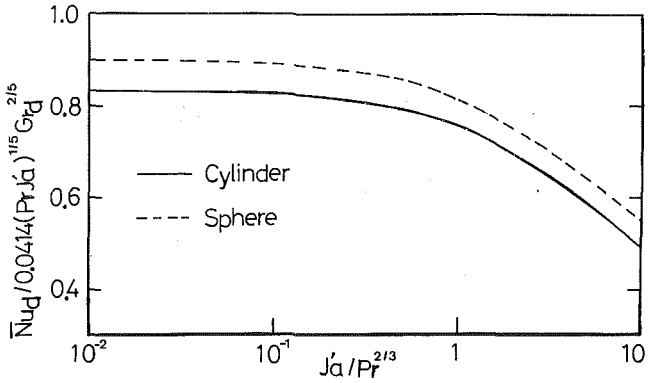


**Fig. 8 Overall heat transfer coefficient for turbulent films on a sphere and a horizontal circular cylinder**

may depend on Prandtl number in contrast with the constant critical film Reynolds numbers suggested by Colburn [5], McAdams [14], and Kutateladze [15]. The trend suggested by equation (22), namely, the decrease of $Re_{ftr}$ with Pr, is consistent with the experimental evidence reported by Uehara et al. [16]. Equations (20*a*) and (21) are compared in Fig. 5 with measurements obtained by Kutateladze and Gogonin [17] for water (Pr $\simeq$ 1.75) and Freon 21 (Pr $\simeq$ 3.3 to 3.5). The experimental data of Gregorig et al. [18] for water with $Tw$ = 50°C and 70°C are also presented by a dashed line. The present predictions appear to be in a fair agreement with the measurements.

Calculations were also carried out for turbulent films on horizontal circular cylinders using various values of $Ja'/Pr^{2/3}$. The circumferential variation of the acceleration parameter $\xi$ is illustrated in Fig. 6(*a*), where the inertia effect is seen to be significant for large values of the lumped parameter $Ja'/Pr^{2/3}$. The variation of the local heat transfer rate is shown in Fig. 6(*b*). Our use of $x_{tr} = 0$, gives the heat transfer rate at the front stagnation point as zero when it should remain finite there.

The local heat transfer rate increases downstream and reaches a maximum within the lower half of the cylinder, before decreasing to zero at the rear stagnation point. The local heat transfer rate consistently decreases with $Ja'/Pr^{2/3}$. The corresponding local heat transfer variation on the vertical flat plate is also shown in Fig. 6 for comparison. The local heat transfer rate of the flat plate is everywhere higher than that of the circular cylinder.

Turbulent condensation heat transfer has also been predicted for a sphere. The circumferential variation of the film thickness is plotted in Fig. 7(*a*) along with results for a cylinder. As expected, the film thickens as $Ja'/Pr^{2/3}$ is increased. This increase in the film thickness is consistent with reduced local heat transfer rates seen in Fig. 7(*b*). Predictions for the cylinder and sphere, with $10^{-2} \leq Ja'/Pr^{2/3} \leq 10$, are plotted together in Fig. 8 in terms of the Nusselt number $\bar{Nu}_d$ averaged over the entire surface.

## Concluding Remarks

The present integral method accounts for inertia in laminar and turbulent film condensation. During actual film condensation, however, the formation of waves, ignored here, is usually observed as the film Reynolds number becomes large. The effects of the wave action on the condensate flow rate should be taken into account during subsequent development of the present analysis. As pointed out by the elegant analyses [7, 19], the shear force at the liquid–vapor interface, which is neglected in the present analysis, may also play an important role in the heat transfer process in some cases. Our effort is now directed toward considering the effects of nonvanishing vapor drag on local heat transfer rates and flow transition.

## References


1 Nusselt, W., "Die Oberflächen Kondensation des Wasserdampfes," *Zeitschrift des Vereines Deutscher Ingenieure*, Vol. 60, 1916, pp. 541–569; 569–575.

2 Rohsenow, W. M., "Heat Transfer and Temperature Distribution in Laminar Film Condensation," ASME *Transactions*, Vol. 78, 1956, pp. 1645–1648.

3 Sparrow, E. M., and Gregg, J. L., "A Boundary-Layer Treatment of Laminar-Film Condensation," ASME JOURNAL OF HEAT TRANSFER, Vol. 81, 1959, pp. 13–18.

4 Sparrow, E. M., and Gregg, J. L., "Laminar Condensation Heat Transfer on a Horizontal Cylinder," ASME JOURNAL OF HEAT TRANSFER, Vol. 81, 1959, pp. 291–296.

5 Colburn, A. P., "Note on the Calculation of Condensation when a Portion of Condensate Layer is in Turbulent Motion," AIChE *Transactions*, Vol. 30, 1933–1944, pp. 187–193.

6 Seban, R. A., "Remarks on Film Condensation with Turbulent Flow," ASME *Transactions*, Vol. 76, 1954, pp. 299–303.

7 Rohsenow, W. M., Webber, J. H., and Ling, A. T., "Effect of Vapor Velocity on Laminar and Turbulent Film Condensation," ASME *Transactions*, Vol. 78, 1956, pp. 1637–1644.

8 Chen, M. M., "An Analytical Study of Laminar Film Condensation: Part 2—Single and Multiple Horizontal Tubes," ASME JOURNAL OF HEAT TRANSFER, Vol. 9, 1961, pp. 55–60.

9 Dhir, V., and Lienhard, J., "Laminar Film Condandation on Plane and Axisymmetric Bodies in Nonuniform Gravity," ASME JOURNAL OF HEAT TRANSFER, Vol. 19, 1971, pp. 97–100.

10 Koyama, H., and Nakayama, A., "An Integral Method in Free Convection Flows under Non-Uniform Gravity," *Letters in Heat and Mass Transfer*, Vol. 9, 1982, pp. 151–158.

11 Nakayama, A., Koyama, H., and Ohsawa, S., "An Approximate Solution Procedure for Laminar Free and Forced Convection Heat Transfer Problems," *International Journal of Heat and Mass Transfer*, Vol. 26, No. 11, 1983, pp. 1721–1726.

12 Nakayama, A., Koyama, H., and Ohsawa, S., "An Integral Method in Laminar Film Condensation on Plane and Axisymmetric Bodies," *Letters in Heat and Mass Transfer*, Vol. 9, 1982, pp. 443–453.

13 Wieghardt, K., "Turbulente Grenzschichten, Göttinger Monographie," Part B5, 1946; also H. Schlichting, *Boundary Layer Theory*, McGraw-Hill (6th ed.), 1968, p. 565.

14 McAdams, W. H., *Heat Transmission*, McGraw-Hill (3rd ed.), 1954, p. 334.

15 Kutateladze, S. S., *Fundamentals of Heat Transfer*, Arnold Press, London, 1963, p. 298.

16 Uehara, H., Kusuda, H., Nakaoka, T., and Yamada, M., "Turbulent Film Condensation on a Vertical Surface," *Transactions JSME*, Vol. 48-435, 1982, pp. 2278–2283.

17 Kutateladze, S. S., and Gogonin, I. I., "Heat Transfer in Film Condensation of Slowly Moving Vapour," *International Journal of Heat and Mass Transfer*, Vol. 22, 1979, pp. 1953–1599.

18 Gregorig, R., Kern, J., and Turek, T., "Improved Correlation of Film Condensation Data Based on a More Rigorous Application of Similarity Parameter," *Wärme- und Stoffübertragung*, Vol. 7, No. 1, 1974, pp. 1–13.

19 Chen, M. M., "An Analytical Study of Laminar Film Condensation: Part 1—Flat Plate," ASME JOURNAL OF HEAT TRANSFER, Vol. 9, 1961, pp. 48–54.

# Prediction of Flow Patterns During Condensation of Binary Mixtures in a Horizontal Tube

T. N. Tandon

H. K. Varma

C. P. Gupta

Department of Mechanical and Industrial Engineering, University of Roorkee, Roorkee, 247667 India

*In the present paper, experimental flow pattern data during forced convection condensation of binary mixtures of R-22 and R-12 inside a horizontal tube are reported for the first time. These visually observed flow patterns were plotted on existing condensing flow as well as on Baker's adiabatic flow map. The mixture flow pattern data were found to best correlate on a flow regimes map suggested earlier by the present authors [8] with dimensionless gas velocity $J_g^*$ and $(1-\alpha)/\alpha$ coordinates ($\alpha$ is the void fraction). The criteria to delineate different flow regimes for mixtures have also been found to be the same as those proposed earlier for pure refrigerants.*

## Introduction

Multicomponent condensation is frequently encountered in process industries. Experimental studies [1–4] have also indicated that use of binary mixtures in refrigeration systems may offer several direct and indirect advantages, namely, better COP, lower power consumption, reduced thermodynamic irreversibility, increased chemical stability, improved oil miscibility, condensation of boiling through a range of temperatures, and variable capacity of refrigeration systems. These merits offer attractive prospects for the use of mixed refrigerants in refrigeration system. It is widely accepted that for economical and efficient operation of the condenser, the prediction of flow pattern that would exist for given operating conditions is essential. This not only helps in proper prediction of the condensing heat transfer coefficient but also leads to a better understanding of the physical phenomena that occur in condensers.

While a number of flow pattern studies of condensing pure vapors inside horizontal tubes have been conducted [5–12], no such effort has been devoted to the study of condensation of binary mixtures.

The purpose of this paper is to report, for the first time the visual observation of flow patterns during condensation of binary mixtures of R-22 and R-12 inside a horizontal tube and to suggest a flow regimes map for prediction of flow patterns. Mixtures of R-22 and R-12 were chosen because of the wide use of these refrigerants in refrigeration and airconditioning systems. Similar studies carried out by the authors using pure R-12 and R-22 have already been reported [9].

## Flow Pattern Identification

The flow patterns were classified into five categories, viz., (*i*) annular, (*ii*) semiannular, (*iii*) wavy, (*iv*) slug, and (*v*) plug, as shown in Fig. 1.

1 Annular flow: The liquid is almost symmetrically distributed as a film over the tube wall inside, and the high velocity vapor flows as a central core.

2 Semiannular flow: The condensate is asymmetrically distributed as a very thin film around the top and sides of the tube wall and as a relatively thick layer at the bottom of the tube.

3 Wavy flow: Vapor and liquid phases are separated by a wavy interface with the liquid flowing at the bottom of the tube.

4 Slug flow: The vapor flowing in the upper part of the tube with relatively high velocity causes the liquid flowing at the bottom of the tube to periodically wet the top of the tube wall.

5 Plug flow: The flow essentially represents continuous liquid phase with large plugs of vapor appearing intermittently in the upper portion of the tube.

These descriptions of major flow patterns conform to most common usage.

## Experimental Test Facility and Data Reduction

During the condensation process, vapor quality progressively decreases along the tube and, hence, different flow patterns may occur at different locations. In order to view the various flow patterns, the test condenser was made of three sections of length 1m each and sight glasses were provided at each tube junction. The schematic diagram of the test facility is shown in Fig. 2. The test sections were horizontally mounted annular coaxial double copper tubes with refrigerant flowing inside the inner tube and the coolant water flowing countercurrently in the outer annulus. The inner tube was of 10 mm i.d. and 12.7 mm o.d., while the outer tube was of 50 mm i.d. The three test sections were joined smoothly in series by four sight glasses, which were of the same i.d. as that of the inner copper tube so as not to disturb the flow pattern.

The test setup included a precondenser, an after condenser, and refrigerant bypass line to enable controlled variation of

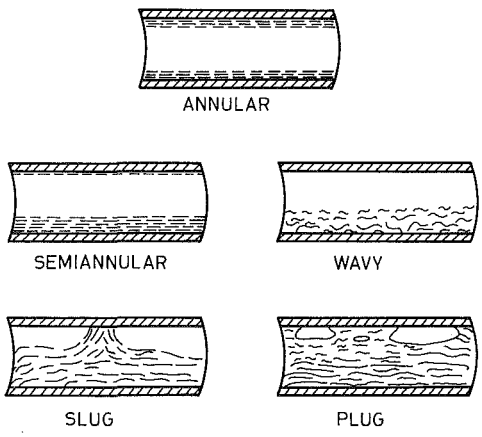


**Fig. 1 Flow patterns description**

Contributed by the Heat Transfer Division for publication in the JOURNAL OF HEAT TRANSFER. Manuscript received by the Heat Transfer Division May 4, 1983.

**Table 1 Details of test runs and range of operating conditions**

| Test fluid | Number of runs | Number of flow patterns observed | Average condensing temp. °C | Refrigerant mass velocity kg/s − m$^2$ | Vapor quality at visual section | Average cooling heat flux in test sections, W/m$^2$ |
|---|---|---|---|---|---|---|
| 25% R-22 mixture (by mass) | 42 | 168 | 24–39 | 174.6–506.2 | 0.001–0.980 | 4780–25000 |
| 50% R-22 mixture | 34 | 136 | 21–37 | 172.3–499.8– | 0.025–0.981 | 5360–24150 |
| 75% R-22 mixture | 33 | 131 | 25–37 | 176.5–529.4 | 0.001–0.994 | 900–26600 |

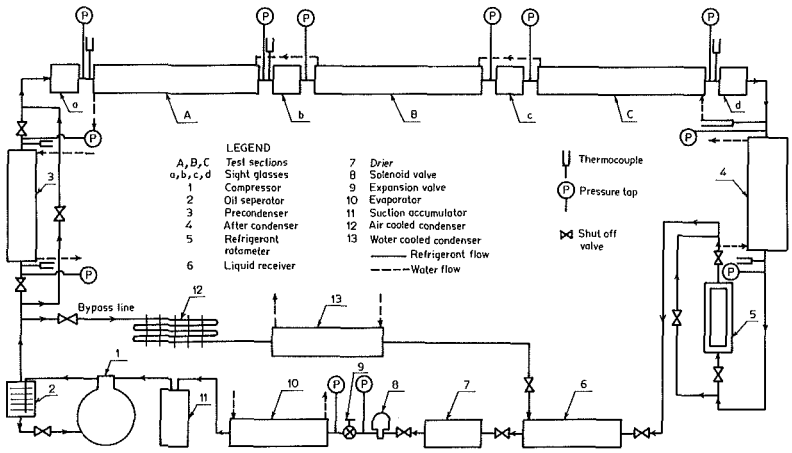


**Fig. 2 Schematic diagram of experimental setup**

the operating conditions over a wide range. The partially condensed refrigerant from the test condenser was completely condensed in the aftercondenser and then returned to the liquid receiver. Note that the condenser tube did not drain into a header as is usually the case of practice.

The test condenser was instrumented to measure refrigerant temperatures at the inlet and exit of first test section, at the exit of the last test section, static pressures at the inlet and exit of each test section, and coolant water temperatures. Refrigerant flow rate was measured by a variable area rotameter at the downstream end of the aftercondenser. Provision was also made to measure refrigerant and water side temperatures, and static pressures across the precondenser and aftercondenser. Coolant flow rates through the test condenser, precondenser and aftercondenser were recorded using water rotameters. All temperatures were measured by copper-constantan thermocouples, the outputs of which were measured by a multichannel automatic data logger. During each steady-state run, the flow patterns were observed at the four visual sections according to the classification described earlier.

In this investigation three different compositions of binary mixtures of R-22 and R-12 with 25, 50 and 75 mass percent of R-22 were charged into the system. In all, 109 steady-state runs with these mixtures were conducted, which yielded 435 flow pattern data. The details of the test runs and the range of operating conditions covered with each mixture are given in Table 1.

The thermodynamic and thermophysical properties of the mixtures were computed by the equations and combining rules suggested by Kandlikar [14]. The raw data were reduced to desired useful form using computer program in Fortran IV

## Nomenclature

$D$ = tube diameter, m
$g$ = acceleration due to gravity, m/s$^2$
$G$ = total mass flux, kg/s•m$^2$
$j_g^*$ = Wallis dimensionless gas velocity; $xG/[gD\rho_V(\rho_L - \rho_V)]^{1/2}$
$V_L$ = average liquid velocity, m/s, [6]
$x$ = vapor quality
$X$ = Martinelli parameter;

$$\left(\frac{1-x}{x}\right)^{0.9}(\rho_V/\rho_L)^{0.5}(\mu_L/\mu_V)^{0.1}$$

### Greek Letters

$\rho$ = density, kg/m$^3$
$\mu$ = dynamic viscosity, kg/m − s
$\sigma$ = liquid surface tension, N/m
$\lambda$ = Baker's parameters; $[(\rho_V/\rho_A)(\rho_L/\rho_W)]^{1/2}$
$\psi$ = Baker's parameter; $(\sigma_w/\sigma)[\mu_L/\mu_W)(\rho_W/\rho_L)^2]^{1/3}$
$\alpha$ = Void fraction;

$$\left\{1+(\rho_V/\rho_L)\left(\frac{1-x}{x}\right)\left[0.4+0.6\sqrt{\frac{(\rho_L/\rho_V)+0.4\left(\frac{1-x}{x}\right)}{1+0.4\left(\frac{1-x}{x}\right)}}\right]\right\}^{-1}$$

Smith's [16] void fraction correlation

### Subscripts

$A$ = air
$L$ = liquid
$V$ = vapor
$W$ = water

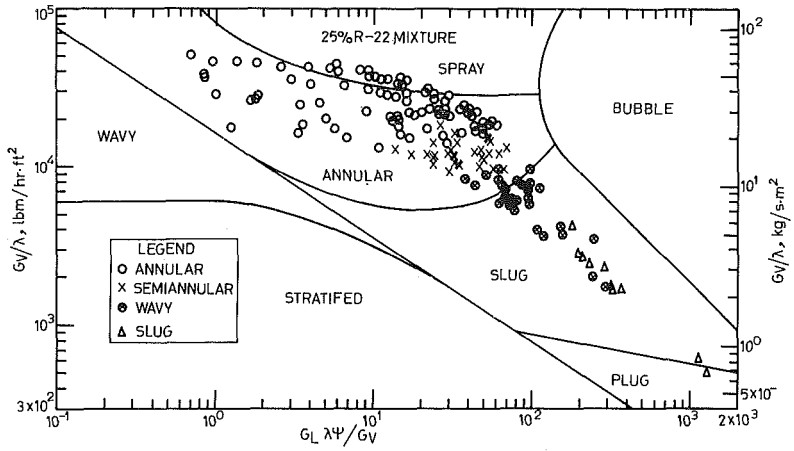


**Fig. 3 Observed flow patterns for 25 percent R-22 mixture plotted on Baker's [5] map**

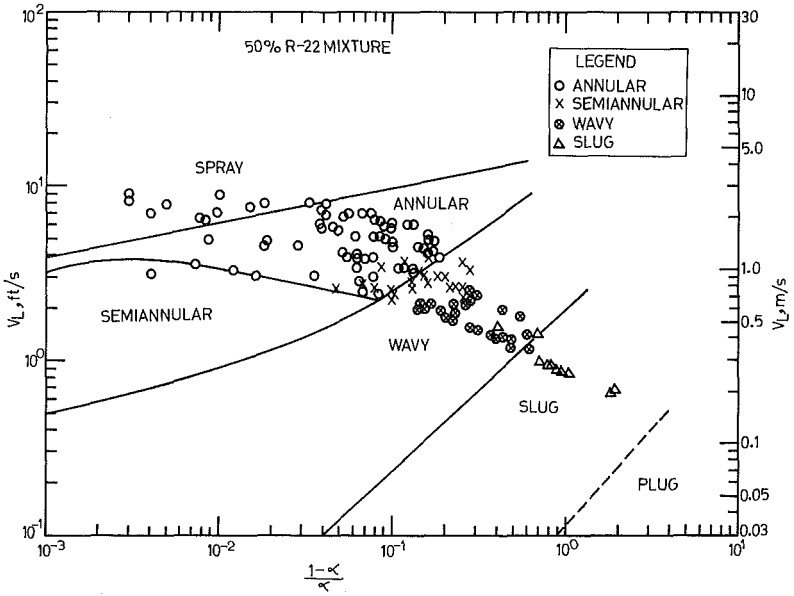


**Fig. 4 Observed flow patterns for 50 percent R-22 mixture plotted on Soliman and Azer's [6] map**

and run on DEC SYSTEM 20. The heat balance error from the inlet of precondenser to the outlet of the aftercondenser was within ±7 percent for 92 percent of the runs and less than ±10 percent for the remaining runs.

## Analysis of Flow Pattern Data

The flow pattern data for binary mixtures of R-12 and R-22 were tested on various flow maps suggested for condensation inside horizontal tubes, viz., those of Baker [5], Soliman and Azer [6], Breber [7], and that of the present authors [8].

It may be recalled that Baker's [5] adiabatic flow map was recommended by Traviss and Rohsenow [10] for prediction of flow patterns during condensation inside horizontal tubes. Soliman and Azer's [6] map was developed using data from [11, 12]. The flow map of Breber et al. [7] is essentially Taitel and Dukler's [13] map with modified flow pattern boundaries based on condensation flow pattern data for pure refrigerants. While representing the flow pattern data on various maps, the plug flow data have not been shown, except on Soliman and Azer's map, as it would have increased the size of the figures very much. However, inferences have been drawn on the basis of numerical values of the mapping coordinates for this flow pattern data for the three mixture compositions on Baker's [5] map. Figure 3 represents a typical plot of observed data for binary mixtures, with 25 percent R-22, on Baker's map. Similar plots were prepared for the other two compositions and the following general conclusions are drawn:

(*i*) The agreement of annular flow data was good.

(*ii*) None of the wavy flow pattern data fell in the specified region of the map. Wavy flow data occupied annular and slug regions, with the majority of the data lying in the latter regime. This behavior refers to the most serious deficiency of Baker's map for the case of condensation inside horizontal tubes, as wavy flow is one of the important flow patterns.

(*iii*) Slug flow data were in agreement with the assigned region on the map; so was the case with plug flow data (not shown in the figures).

Semiannular flow data occupied the annular flow region on the Baker's map. It may be noted here that Baker's map does not identify semiannular flow.

The comparison of the observed flow patterns on the map of Soliman and Azer [6] was also done, and Fig. 4 is for a mixture with 50 percent R-22. An inspection of entire flow pattern data for the three mixture compositions disclosed that:

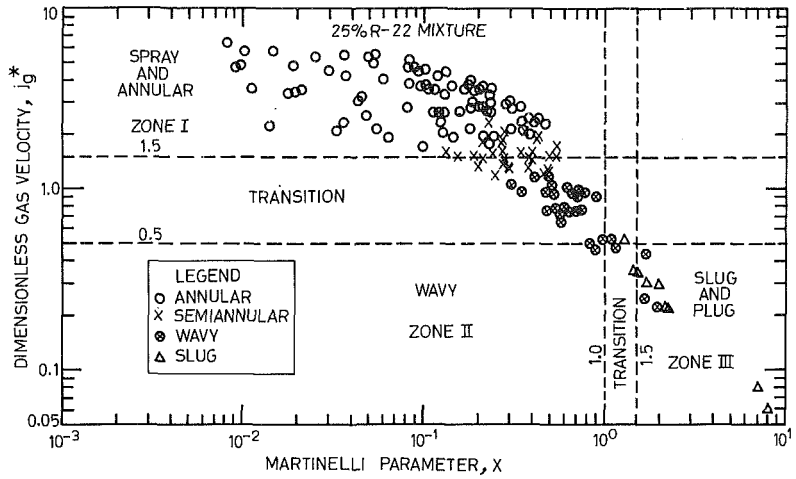


**Fig. 5 Observed flow patterns for 25 percent R-22 mixture plotted on Breber et al. [7] map**

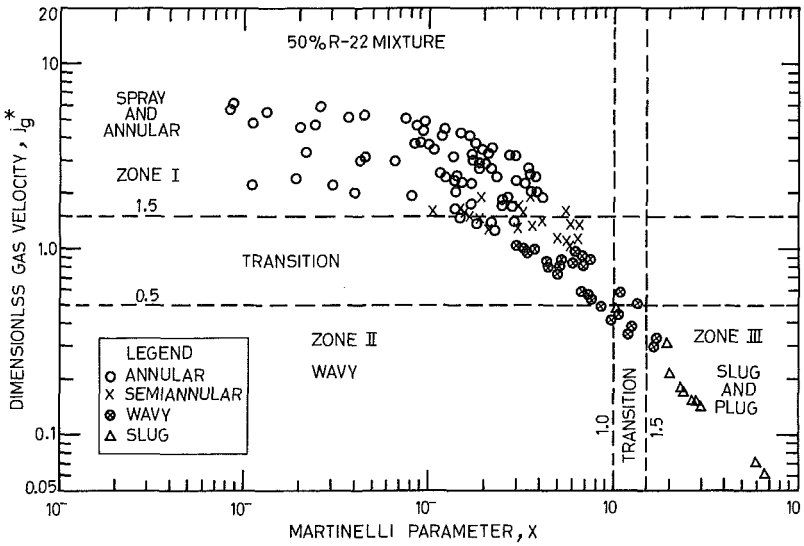


**Fig. 6 Observed flow patterns for 50 percent R-22 mixture plotted on *Breber et al. [7] map***

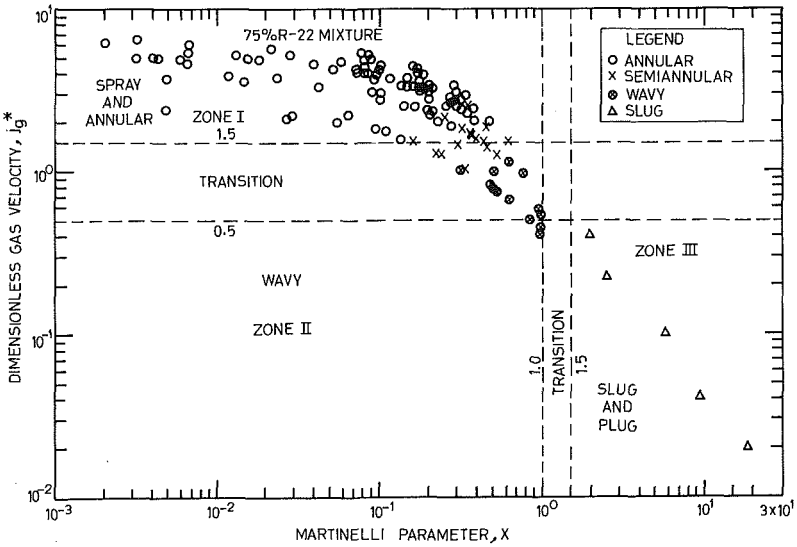


**Fig. 7 Observed flow patterns for 75 percent R-22 mixture plotted on Breber et al. [7] map**

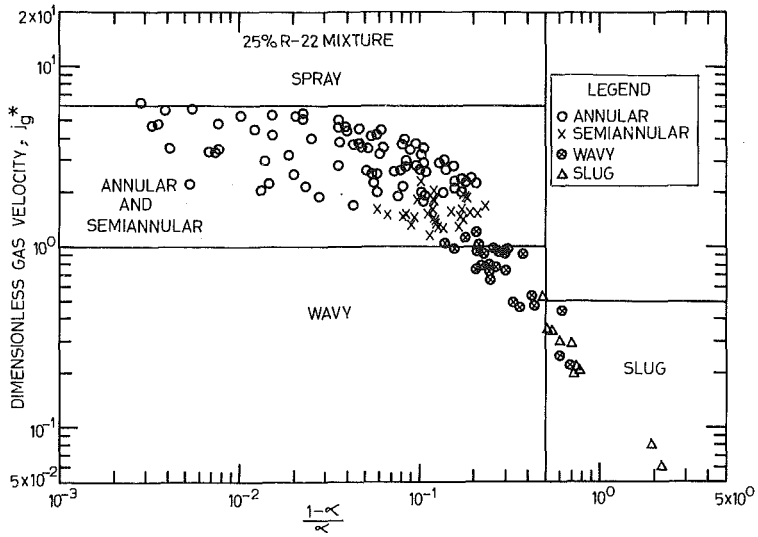


**Fig. 8 Observed flow patterns for 25 percent R-22 mixture plotted on authors' [8] map**

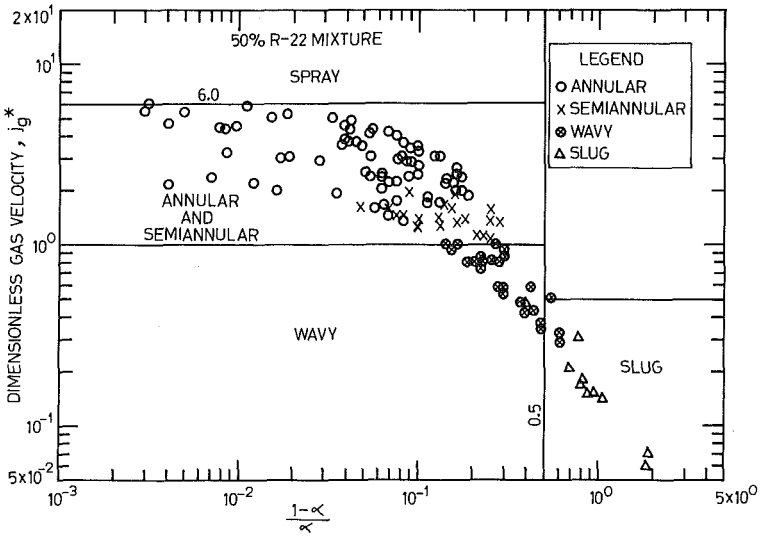


**Fig. 9 Observed flow patterns for 50 percent R-22 mixture plotted on authors' [8] map**

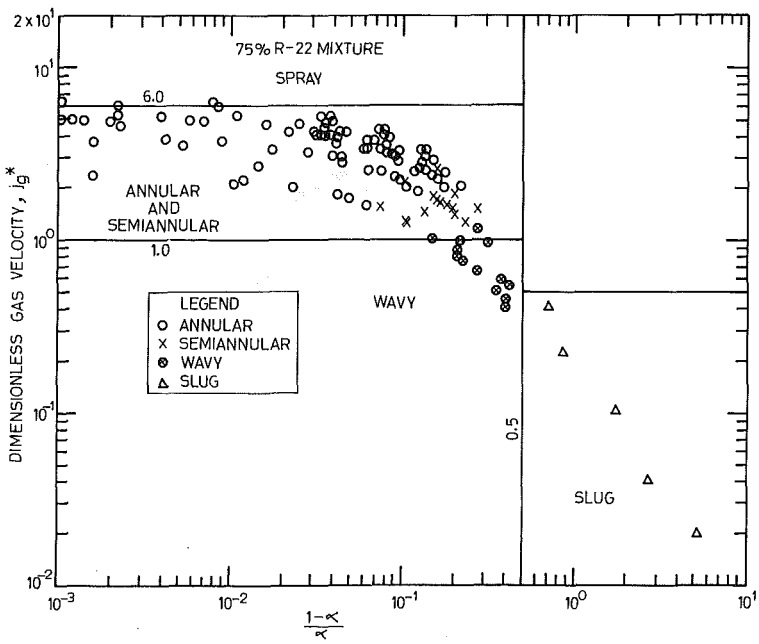


**Fig. 10 Observed flow patterns for 75 percent R-22 mixture plotted on authors' [8] map**

**Table 2 Distribution of observed flow patterns for mixtures of R-22 and R-12 expressed as percentage on authors' [8] earlier map**

| Observed flow pattern \ Predicted flow pattern | Spray | Annular and semi-annular | Wavy | Slug | Plug | Number of data points |
|---|---|---|---|---|---|---|
| Annular and semiannular | 1 | 99 | – | – | – | 330 |
| Wavy | – | 12 | 80 | 8 | – | 73 |
| Slug | – | – | 8 | 92 | – | 25 |
| Plug | – | – | – | – | 100 | 7 |

Total points: 435

**Table 3 Distribution of observed flow patterns for mixtures on R-22 and R-12 expressed as percentage on Baker's [5] map**

| Observed flow pattern \ Predicted flow patterns | Spray | Annular | Wavy | Slug | Plug | Number of data points |
|---|---|---|---|---|---|---|
| Annular | 14 | 84 | 2 | – | – | 255 |
| Wavy | – | 27 | 0 | 73 | – | 73 |
| Slug | – | – | – | 80 | 20 | 25 |
| Plug | – | – | – | – | 100 | 7 |

Total points: 360

Note: Baker's map does not identify semiannular flow, hence these data are not included in Table 3.

**Table 4 Distribution of observed flow pattern for mixture of R-22 and R-12 expressed as percentage on Soliman and Azer's [6] map**

| Observed flow pattern \ Predicted flow pattern | Spray | Annular | Semi-annular | Wavy | Slug | Plug | Number of data points |
|---|---|---|---|---|---|---|---|
| Annular | 17 | 80 | 3 | – | – | – | 255 |
| Semiannular | – | 41 | 0 | 59 | – | – | 75 |
| Wavy | – | – | – | 96 | 4 | – | 73 |
| Slug | – | – | – | 28 | 68 | 4 | 25 |
| Plug | – | – | – | – | – | 100 | 7 |

Total points: 435

**Table 5 Distribution of observed flow patterns for mixtures of R-22 and R-22 expressed as percentage of Breber et al. [7] map**

| Observed flow pattern \ Predicted flow pattern | Spray and Annular Zone I | Transition between Zones I and II (semi-annular flow) | Wavy Zone II | Transition between zones II and III | Slug and plug Zone II | Number of data points |
|---|---|---|---|---|---|---|
| Spray and Annular | 99 | 1 | – | – | – | 255 |
| Semiannular | 45 | 55 | – | – | – | 75 |
| Wavy | – | 75 | 10 | 8 | 7 | 73 |
| Slug and Plug | – | – | – | 6 | 94 | 32 |

Total Points: 435

(*i*) Agreement for annular flow is moderate.

(*ii*) None of the semiannular flow data fell in the specified region. These data occupied the annular and wavy regions on the map.

(*iii*) The agreement with slug flow data is fair.

(*iv*) Wavy and plug flow data occupied their specified regime on the map.

Since the map of Breber et al. has been found to be very successful, flow pattern data for all the three mixture compositions are shown on the map of Breber et al. [7] in Figs. 5–7. These figures reveal that:

(*i*) The agreement of the semiannular flow data is unsatisfactory. It may be noted that Breber et al. have shown semiannular flow pattern in the transition band between zones I and II.

(*ii*) The wavy flow data were poorly correlated on the map. These data virtually occupied the transition zones.

(*iii*) Annular and slug flow data fell in appropriate zones on the map. The plug flow data also occupied the specified region (not shown).

Figures 8–10 exhibit the mixture flow pattern data representd on the authors' [8] flow regimes map with dimensionless gas velocity $j_g^*$ and $(1-\alpha)/\alpha$ as map coordinates, where void fraction $\alpha$ was evaluated from Smith's [16] correlation. Although Smith's void fraction model was derived for annular flow, he found it to be in excellent

agreement with the experimental data of several investigators irrespective of flow pattern. Use of this correlation also yielded more accurate prediction of two-phase pressure drop (see discussion of [16]). Soliman and Azer also used Smith's correlation for evaluating void fraction. It is evident from Figs. 12–14 that:

(*i*) Annular, semiannular, and slug flow data are in excellent agreement with the predictions of the map. This was also the case with plug flow data (not shown).

(*ii*) For wavy flow also, the agreement is good, with 80 percent of the data occupying the assigned region.

## Comparison of Flow Regime Maps

Table 2–5 show the accuracy of prediction of the four flow pattern maps discussed in the previous sections. A comparison of Tables 2 and 3, shows that the flow regimes map suggested by the authors [8] yields significantly improved predictions as compared to Baker's [5] map for annular, wavy, and slug flow patterns. The agreement of both maps with plug flow data is equally good.

Tables 2 and 4 reveal that as compared to predictions of Soliman and Azer's [6] flow map, the authors' map [8] is in substantially better agreement with semiannular and slug flow data. Predictions for annular flow are also considerably better than that of Soliman and Azer. Even if annular and semiannular regions on their map are taken together, the authors' map still shows much better agreement with the data. For wavy flow, Soliman and Azer's map has an edge over the predictions of the authors' map. The agreement of both maps with plug flow data is nearly the same.

The distribution of observed flow patterns on the authors' map [8] and that of Breber et al. [7] flow map is given in Table 2 and 5, respectively. It is evident from these Tables and Figs. 5–10 that the former map gives significantly improved predictions for wavy flow. While only 10 percent of wavy flow data occupied the assigned region on the Breber et al. map, the agreement with the authors' map was 80 percent, a remarkable improvement. For semiannular flow data also, the predictions of authors' map are substantially better than those given in the Breber et al. map. For annular, slug and plug flows, the agreement of both maps with the data is nearly equally good.

From the foregoing discussion, it is clear that the flow regimes map of Baker [5], Soliman and Azer [6], and Breber et al. [7] did show reasonable agreement with mixture flow pattern data only in certain flow regimes. But all of them had some deficiencies, in one or more flow regimes. In contrast to this, as is apparent from Table 2, the authors' [8] map is more consistent and reliable.

## Conclusions

The following inferences may be drawn from the experimental investigation of the flow patterns of the binary mixtures of R-22 and R-12 inside a horizontal tube:

1 Baker's [5] map failed to correlate the wavy flow pattern data, which is an important flow pattern. Thus this map does not satisfactorily characterize the flow patterns during condensation inside a horizontal tube.

2 The agreement of the map of Soliman and Azer [6] with semiannular flow data was unsatisfactory. Also, for annular flow, the agreement was only moderate.

3 The Breber et al. [7] flow map did not represent the wavy flow pattern data well. Agreement of this map with semiannular flow data was also unsatisfactory.

4 The flow pattern data for mixtures of R-22 and R-12 was best correlated on the authors' [8] map with dimensionless gas velocity $j_g^*$ and $(1-\alpha)/\alpha$ as its coordinates. The criteria to delineate different flow regimes for mixtures were also found to be the same as proposed for pure refrigerants [8].

## Acknowledgment

The authors express their gratitude for the financial assistance provided for this work by the Department of Science and Technology, Government of India.

## References

1 Haselden, G. G., and Klimek, K., "An Experimental Study of the Use of Mixed Refrigerants for Non-Isothermal Refrigeration," *Proc. Institution of Refrigeration*, London, 1957–58, p. 129.

2 Mcharness, R. C., and Chapman, D. D., "Refrigerating Capacity and Performance Data," *ASHRAE Journal*, 1962, pp. 49–58.

3 Arora, C. P., "Power Savings in Refrigerating Machines Using Mixed Refrigerants," *Proc. of XII International Congress of Refrigeration*, Madrid, 1967.

4 Arora, C. P., Bhalla, B. K., and Gassab, Addai, "A Study on the Performance of Window Type Air Conditioner Using R22/R12 Azeotrope," Paper No. B2-24, *Progress in Refrigeration Science and Technology; Proceedings of the XV International Congress on Refrigeration*, Venezia, Vol. II, 1979, pp. 905–912.

5 Baker, O., "Simultaneous Flow of Oil and Gas," *The Oil and Gas Journal*, Vol. 53, 1954, pp. 185–195.

6 Soliman, H. M., and Azer, N. Z., "Visual Studies of Flow Patterns During Condensation Inside Horizontal Tubes," *Heat Transfer*, Vol. 3, 1974, pp. 241–245.

7 Breber, G., Palen, J. W., and Taborek, J., "Prediction of Horizontal Tubeside Condensation of Pure Components Using Flow Regime Criteria," ASME JOURNAL OF HEAT TRANSFER, Vol. 102, 1980, pp. 471–476.

8 Tandon, T. N., Varma, H. K., and Gupta, C. P., "A New Flow Regimes Map for Condensation Inside Horizontal Tubes," ASME JOURNAL OF HEAT TRANSFER, Vol. 104, No. 4, Nov. 1982, pp. 763–768.

9 Tandon, T. N., Varma, H. K., and Gupta, C. P., "An Experimental Study of Flow Patterns During Condensation Inside a Horizontal Tube," paper accepted for presentation in ASHRAE meeting to be held at Washington, D.C. in June 1983.

10 Traviss, D. P., and Rohsenow, W. M., "Flow Regimes in Horizontal Two-phase Flow with Condensation (Part II)," *Transactions* ASHRAE, 1973, pp. 31–39.

11 Soliman, H. M., and Azer, N. Z., "Flow Patterns During Condensation Inside a Horizontal Tube (Part 1)," ASHRAE *Transactions*, Vol. 77, 1977, pp. 210–224.

12 Soliman, H. M., "Experimental and Analytical Studies of Flow Patterns During Condensation Inside Horizontal Tubes," Ph.D. dissertation, Kansas State University, 1974.

13 Taitel, Y., and Dukler, A. E., "A Model for Predicting Flow Regime Transitions in Horizontal and Near Horizontal Gas Liquid Flow," *AIChE Journal*, Vol. 22, No. 1, 1976, pp. 47–55.

14 Kandlikar, S. G., "Properties of R22-R12 Mixtures and Their Application to the Study of Binary Annular Two-phase Flow with Heat Transfer, Ph.D. thesis, I.I.T., Bombay, India, 1975.

15 *ASHRAE Handbook of Fundamentals*, ASHRAE, New York, 1977.

16 Smith, S. L., "Void Fraction in Two-phase Flow: A Correlation Based Upon an Equal Velocity Head Model," *Proc. Instn. of Mech. Engrs.*, London, Vol. 184, Pt. 1, No. 36, 1969–1970, pp. 647–657.

# Mixed Convective Flows Around a Slowly Rotating Isothermal Sphere

**B. Farouk**
Assistant Professor,
Department of Mechanical Engineering
and Mechanics,
Drexel University,
Philadelphia, Pa. 19104

*The mixed convective flows generated by a heated rotating sphere have been investigated theoretically. The solutions are obtained by considering the full Navier-Stokes and energy equations along with the Boussinesq approximation. The governing equations are expressed in the R-θ-φ coordinates and due to the nature of the flow field generated, all three velocity components appear in the formulation. Due to the symmetry of the problem studied, $\partial\xi/\partial\phi = 0$, where $\xi$ is any dependent variable considered. The R and θ momentum equations are expressed in the stream function–vorticity formulation. The resulting four coupled elliptic equations (for stream function, vorticity, $v_\phi$, and temperature) are solved numerically. Results have been obtained over a large range of Grashof and Reynolds (based on the rotational velocity of the sphere surface) numbers. The study reveals interesting flow patterns for the mixed convective problems. The gravitationally induced free convection is significant for the slowly rotating sphere where the Grashof number is of the order of or more than the square of the Reynolds number. The results are compared with previously published experimental observations and theoretical predictions based on the boundary layer theory.*

## Introduction

Free-convection heat transfer from stationary spheres has been the subject of several investigations [1–4]. Theoretical investigations of free-convection flows have mainly centered upon approximate solutions based on similarity considerations. Possible similarity solutions, however, depend on body geometry, and the sphere and the horizontal cylinder do not allow such solutions for the free-convection problems. The sphere possesses curvature in two planes, and this feature poses special problems in the two-dimensional analysis of such flows. Chiang, Ossin, and Tien [5] employed the perturbation method in which the trigonometric buoyancy term, the velocity, and the temperature profiles are expanded in power series to determine the temperature and velocity profiles for angular positions around a sphere. Double curvature of the boundary layer about a sphere also introduces some special experimental problems. A modified Abel integral approach needs to be employed when interferometric measurements are made to obtain the axisymmetric temperature field around a sphere [6].

In this paper the flows generated by and the mixed convective heat transfer from a rotating isothermal sphere have been investigated theoretically. The flow and mixed convective heat transfer characteristics of a heated sphere rotating about a diameter in an otherwise quiescent medium are of interest in geophysical and meteorological problems, formation of the earth's weather patterns, and the design of special purpose heat exchangers. The interaction of the buoyancy and centrifugal effects provides many interesting flow situations ranging from natural to forced convection.

The flow induced by a rotating sphere (not considering the buoyancy effects) was first studied by Sir George Stokes in 1845 [7]. Stokes described the sphere to be acting like a centrifugal fan, the motion at a distance from the sphere consisting of a flow outwards from the equator and inwards towards the poles, superimposed on a motion of rotation. Using boundary layer approximations, the foregoing problem was studied about a hundred years later by Howarth [8] and Nigam [9], and the forced convection problem involving the temperature field in the vicinity of a heated sphere has been studied by Singh [10] in the laminar flow regime. In the laminar flow regime the solution of the boundary layer equations for a rotating sphere proposed by Howarth predicts the velocity field closely despite its failure to predict outflow near the equator. Experimental measurements of velocity profiles for the flow problem have been reported by Kobashi [11]. The heat transfer by convection from a heated sphere rotating in air has been investigated experimentally by Nordlie and Krieth [12]. Kreith et al. [13] corrected and extended Singh's [10] analysis to permit theoretical calculations of the average heat transfer coefficients over wide ranges of Reynolds and Prandtl numbers and presented some additional measurements of boundary layer velocity profiles, including the extent of a turbulent separation zone, which was observed in the vicinity of the equator. Gravitationally induced free convection was neglected in the Kreith's study owing to the high rotational speeds considered, and hence Nusselt, Reynolds, and Prandtl numbers were the only variable parameters in the above study.

Most of the previous studies on heat transfer from rotating spheres are for the forced convection case where $(\mathrm{Re})^2 >> \mathrm{Gr}$. Interaction of the centrifugal and buoyancy effects for the rotating sphere has received little attention, both theoretically and experimentally. In this paper an integrated finite difference numerical scheme is used to obtain the temperature and flow field solutions as well as the heat transfer characteristics for the mixed convective flows around an isothermal rotating sphere submerged in an infinite Boussinesq fluid. The axially symmetric nature of the problem enables the $R$ and $\theta$ momentum equations to be combined with the continuity equation and expressed as a vorticity transport and a stream function equations. The $\phi$ momentum and the temperature equations along with the foregoing two equations were solved simultaneously. Results were obtained over a wide range of $\mathrm{Gr}/\mathrm{Re}^2$, varying from forced to natural convection. The effects of rotation were studied in detail for the Grashof number range of $1.39\times10^2$ to $1.39\times10^5$. The interaction of the buoyancy and centrifugal effects on the flow field and heat transfer characteristics are presented and the physics of the mixed convection flows are explained.

## Analysis

The geometry considered consists of a heated solid sphere

Contributed by the Heat Transfer Division for publication in the JOURNAL OF HEAT TRANSFER. Manuscript received by the Heat Transfer Division June 19, 1984.

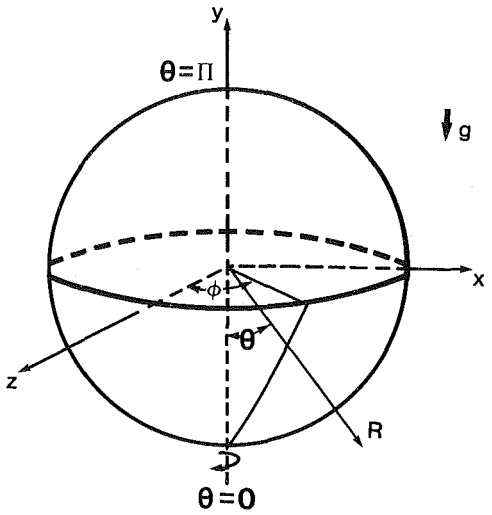


**Fig. 1 Spherical polar coordinate system**

rotating in an infinite Boussinesq fluid. To obtain the flow and temperature distributions, the Navier-Stokes, continuity, and energy equations were expressed in spherical polar coordinates ($R$-$\theta$-$\phi$) as shown in Fig. 1. The coordinate $R$ is normal to the surface of the sphere and is measured radially outwards from the center of the sphere, $\theta$ is measured from the downward vertical axis of rotation, and $\phi$ is the azimuth. For the particular case of an isothermal sphere with rotation around the vertical axis, the mixed flow is symmetric and all variables are independent of $\phi$.

The stream function and the vorticity transport equations are given as follows [14]

$$-\frac{\partial}{\partial R^*}\left[\frac{1}{\mathrm{Sin}\theta}\frac{\partial\psi^*}{\partial R^*}\right]-\frac{\partial}{\partial\theta}\left[\frac{1}{R^*\mathrm{Sin}\theta}\frac{\partial\psi^*}{\partial\theta}\right]=\omega^*R^* \tag{1}$$

$$R^{*2}\mathrm{Sin}^2\theta\left\{\frac{\partial}{\partial R^*}\left(\frac{\omega^*}{R^*\mathrm{Sin}\theta}\frac{\partial\psi^*}{\partial\theta}\right)-\frac{\partial}{\partial\theta}\left(\frac{\omega^*}{R^*\mathrm{Sin}\theta}\frac{\partial\psi}{\partial R^*}\right)\right\}$$

$$-\frac{\partial}{\partial R^*}\left[R^{*4}\mathrm{Sin}^3\theta\frac{\partial\left(\frac{\omega^*}{R^*\mathrm{Sin}\theta}\right)}{\partial R}\right]$$

$$-\frac{\partial}{\partial\theta}\left[R^{*4}\mathrm{Sin}^3\theta\frac{\partial\left(\frac{\omega^*}{R^*\mathrm{Sin}\theta}\right)}{\partial\theta}\right]=\mathrm{Re}^2\left\{\mathrm{Cos}\theta\frac{\partial}{\partial R^*}(v_\phi^{*2})\right.$$

$$\left.-\frac{\mathrm{Sin}\theta}{R^*}\frac{\partial}{\partial\theta}(v_\phi^{*2})\right\}\cdot R^{*2}\mathrm{Sin}\theta+\mathrm{Gr}\cdot R^{*2}\mathrm{Sin}\theta\left[\frac{\mathrm{Cos}\theta}{R^*}\frac{\partial T^*}{\partial\theta}\right.$$

$$\left.+\mathrm{Sin}\theta\frac{\partial T^*}{\partial R^*}\right] \tag{2}$$

where

$$v_R^*=\frac{1}{R^{*2}\mathrm{Sin}\theta}\frac{\partial\psi^*}{\partial\theta};v_\theta^*=-\frac{1}{R^*\mathrm{Sin}\theta}\frac{\partial\psi^*}{\partial R^*} \tag{3a,3b}$$

and

$$\omega^*=\frac{1}{R^*}\left[\frac{\partial(R^*v_\theta^*)}{\partial R^*}-\frac{\partial v_R^*}{\partial\theta}\right] \tag{4}$$

The $\phi$ momentum equation is given by

$$\left\{\frac{\partial}{\partial R^*}\left(R^*\mathrm{Sin}\theta v_\phi^*\cdot\frac{\partial\psi^*}{\partial\theta}\right)-\frac{\partial}{\partial\theta}\left(R^*\mathrm{Sin}\theta v_\phi^*\cdot\frac{\partial\psi^*}{\partial R^*}\right)\right\}$$

$$-\frac{\partial}{\partial R^*}\left[R^{*4}\mathrm{Sin}^3\theta\frac{\partial}{\partial R^*}\left(\frac{v_\phi^*}{R^*\mathrm{Sin}\theta}\right)\right]$$

$$-\frac{\partial}{\partial\theta}\left[R^{*2}\mathrm{Sin}^3\theta\frac{\partial}{\partial\theta}\left(\frac{v_\phi^*}{R^*\mathrm{Sin}\theta}\right)\right]=0 \tag{5}$$

and the energy equation is given by

$$\left\{\frac{\partial}{\partial R^*}\left(T^*\frac{\partial\psi^*}{\partial\theta}\right)-\frac{\partial}{\partial\theta}\left(T^*\frac{\partial\psi^*}{\partial R^*}\right)\right\}$$

$$-\frac{\partial}{\partial R^*}\left[\frac{1}{\mathrm{Pr}}R^{*2}\mathrm{Sin}\theta\frac{\partial T^*}{\partial R^*}\right]-\frac{\partial}{\partial\theta}\left[\frac{1}{\mathrm{Pr}}\mathrm{Sin}\theta\frac{\partial T^*}{\partial\theta}\right]=0 \tag{6}$$

The variables were nondimensionalized with reference to the diameter of the sphere, the kinematic viscosity of the fluid, the rotational speed of the sphere, and the temperature difference between the sphere surface and the ambient.

$$R^*=\frac{R}{D},v_R^*=\frac{v_RD\rho}{\mu},v_\theta^*=\frac{v_\theta D\rho}{\mu}, \tag{7}$$

$$v_\phi^*=\frac{v_\phi}{D\Omega},T^*=\frac{T-T_\infty}{T_w-T_\infty}$$

## Nomenclature

$c_p$ = specific heat at constant pressure
$D$ = sphere diameter
$g$ = acceleration of gravity
Gr = Grashof number based on sphere diameter, $D^3\beta g(T_w-T_\infty)/\nu^2$
$k$ = thermal conductivity
Nu = Nusselt number
$\mathrm{Nu}_N$ = Nusselt number for natural convection
$\mathrm{Nu}_F$ = Nusselt number for forced convection
Pr = Prandtl number $\mu c_p/k$
$R$ = radial coordinate
$R_\infty$ = radius of pseudoboundary
$R^*$ = nondimensional radial coordinate
Ra = Rayleigh number (Gr.Pr)
Re = rotational Reynolds number, $D^2\Omega\rho/\mu$
$T$ = temperature
$T^*$ = nondimensional temperature
$T_w$ = sphere wall temperature
$T_\infty$ = reference temperature
$v_R$ = radial velocity component
$v_R^*$ = nondimensional radial velocity component
$v_\theta$ = angular velocity component
$v_\theta^*$ = nondimensional angular velocity component
$v_\phi$ = azimuthal velocity component
$v_\phi^*$ = nondimensional azimuthal velocity component

### Greek Letters

$\beta$ = thermal coefficient of volume expansion
$\delta$ = hydrodynamic boundary layer thickness
$\theta$ = angular coordinate
$\nu$ = fluid kinematic viscosity ($\nu=\mu/\rho$)
$\rho$ = density
$\phi$ = coordinate representing the angle of rotation about the axis of symmetry of the flow
$\xi$ = a dependent variable
$\psi$ = stream function
$\psi^*$ = nondimensional stream function
$\omega$ = vorticity component in the $\phi$-direction
$\omega^*$ = nondimensional vorticity component in the $\phi$-direction
$\Omega$ = characteristic angular velocity of the sphere, radian/s

$$\psi^* = \frac{\psi}{D\mu}$$

and

$$\omega^* = \frac{\omega D^2}{\nu}$$

It is noted that the source terms in the vorticity transport equation have the coefficients as $Re^2$ and Gr and the terms represent the rotational and buoyancy effects, respectively. The ratio $Gr/Re^2$ is thus considered to be the key parameter of the analysis.

The governing equations are dependent upon the assumption that the temperature variations within the fluid are not large, so that the Boussinesq approximation can be applied. The foregoing equations (1, 2) and (5, 6), along with conditions specified over the entire flow domain, are solved numerically. A symmetry plane is considered along the vertical line and the solutions are obtained for the hemispherical region.

**Boundary Conditions.** The dependent variables in the above formulation are $\psi^*$, $\omega^*/R^*\mathrm{Sin}\theta$, $v_\phi^* R^*\mathrm{Sin}\theta$, and $T^*$. Conditions need to be specified for the foregoing variables along all boundaries before a solution can be attempted.

**Sphere Surface.** Temperature is considered uniform over the boundary section. Since the sphere surface is assumed to be nonpermeable, it follows that for the stream function

$$\psi^* = 0 \text{ for } 0 \le \theta \le \pi \tag{8}$$

The rotational velocity at the sphere wall is given by $v_\phi{}^* = 0.5\ \mathrm{Sin}\theta$
Hence

$$v_\phi{}^* \cdot R^*\mathrm{Sin}\theta = 0.5 R^* \mathrm{Sin}^2\theta \tag{9}$$

The boundary condition for $\omega^*/R^*\mathrm{Sin}\theta$ is not quite so easy to specify on sphere surface, since it requires information on the gradients of velocities which are not known a priori. An expression for the $\omega^*/R^*\mathrm{Sin}\theta$ can be obtained by expanding the stream function near the wall using a three term Taylor series and making use of the continuity and no-slip conditions.

For $\psi^* = 0$ at the wall

$$\frac{\omega^*}{R^*\mathrm{Sin}\theta} = \frac{-2\psi^*}{(R^{*2}\mathrm{Sin}^2\theta)(\Delta R^*)^2} \tag{10}$$

where $\psi^*$ is the value of the stream function at a small distance $\Delta R^*$ into the fluid from the sphere wall.

**Symmetry Plane.** Since an isothermal sphere is considered, the flow along a vertical axis is symmetric and a symmetry plane is considered along a vertical line passing through the center of the sphere. Along the symmetry plane the stream function must have a constant value to satisfy the mass continuity. This constant is taken as zero over the spherical surface. Hence along the symmetry plane $\psi^* = 0$. For the temperature variable the gradient in $\theta$-direction becomes zero. Thus $\partial T^*/\partial\theta = 0$ for $\theta = 0$, $\theta = \pi$. The rotational velocity at the symmetry axis is zero

$$v_\phi^* R^*\mathrm{Sin}\theta = 0$$

Implied in the equation for vorticity is that the vorticity at the symmetry axis must be zero. $\omega^*/R^*\mathrm{Sin}\theta$ on the other hand, may be finite. The axis of the pipe containing parallel flow is a familiar example. The shear stress, which is proportional to the vorticity, is proportional to the distance from the axis [14].

At the symmetry axis, we assume a quadratic expression for the vorticity [14]

$$\omega^* = A(R^*\mathrm{Sin}\theta) + B(R^*\mathrm{Sin}\theta)^2 \tag{11}$$

where $A$ and $B$ are functions of $R^*$ and $\theta$. Using the values of the nearest two nodes of the symmetry axis, the following expression is obtained for the $\omega^*/R^*\mathrm{Sin}\theta$ variable along the symmetry axis

$$\frac{\omega^*}{R^*\mathrm{Sin}\theta} = \frac{\omega^*}{R^*\mathrm{Sin}\theta}\bigg|_2 + \left\{ \frac{\dfrac{\omega^*}{R^*\mathrm{Sin}\theta}\bigg|_2 - \dfrac{\omega^*}{R^*\mathrm{Sin}\theta}\bigg|_3}{R^*\mathrm{Sin}\theta|_3 - R^*\mathrm{Sin}\theta|_2} \right\} R^*\mathrm{Sin}\theta|_2 \tag{12}$$

where the subscripts 2 and 3 represent the nodes nearest the symmetry axis for any $R^*$ value.

**The Far Field.** The necessity to limit the size of the solution domain requires that a pseudoboundary be defined at a finite distance from the sphere surface. In this regard, a concentric spherical far field boundary is considered for the analysis. Any realistic model must allow for fluid to cross the pseudoboundary. It is assumed that the velocity component in the angular direction $v_\phi^*$, along the pseudoboundary is negligible, implying that in the far field

$$\frac{\partial \psi^*}{\partial R^*} = \frac{\partial \omega^*}{\partial R^*} = 0 \tag{13}$$

For the rotational components of the velocity, $\partial v_\phi^*/\partial R^* = 0$ can be assumed if the pseudoboundary is sufficiently far away from the sphere surface. The temperature of the fluid drawn into the flow field is the same as that of the ambient fluid. However a generalization along an entire outer boundary cannot be made since the temperature distribution along the section of the boundary where the plume crosses is not known a priori. It is assumed that the temperature gradient normal to the pseudoboundary is zero, implying that the heat carrying action of the fluid is done purely by convection rather than by conduction in the far field, i.e.,

$$\frac{\partial T^*}{\partial R^*} = 0 \tag{14}$$

From the foregoing expressions, the appropriate boundary conditions for the $\omega^*/R^*\mathrm{Sin}\theta$ and $v_\phi^* R^*\mathrm{Sin}\theta$ variables can be easily derived. The ratio $R_\infty/D$ was varied between 1 and 15 for the cases studied, smaller values of the ratio were used for increasing values of the Grashof and/or Reynolds numbers.

From the distribution of the temperature, the heat transfer characteristics can be calculated. The local Nusselt number at the sphere surface is given by

$$\mathrm{Nu}_\theta = -\frac{\partial T^*}{\partial R^*}\bigg|_{R^* = .5} \tag{15}$$

and the average Nusselt number is given by

$$\overline{\mathrm{Nu}} = \frac{1}{2}\int_0^\pi \mathrm{Nu}_\theta \mathrm{Sin}\theta d\theta \tag{16}$$

## Numerical Solution

The governing equations (1, 2) and (5, 6) can be expressed in a generalized form following Gosman et al. [14]. The above equations are transformed into difference equations by using a finite difference method. Instead of using standard Taylor series expressions, the finite difference equations are obtained by integration over finite cells. For the convective terms, the upwind difference scheme is introduced. The resulting difference equations are solved by a point iteration method. The iteration process is terminated when values of the dependent variables at each grid point satisfy the following convergence criterion

$$\max\left| \frac{\xi^n - \xi^{n-1}}{\xi^n_{\max}} \right| \le 0.0001$$

where $\xi$ stands for any dependent variable $\psi^*$, $\omega^*$, $v_\phi^*$, or $T^*$.

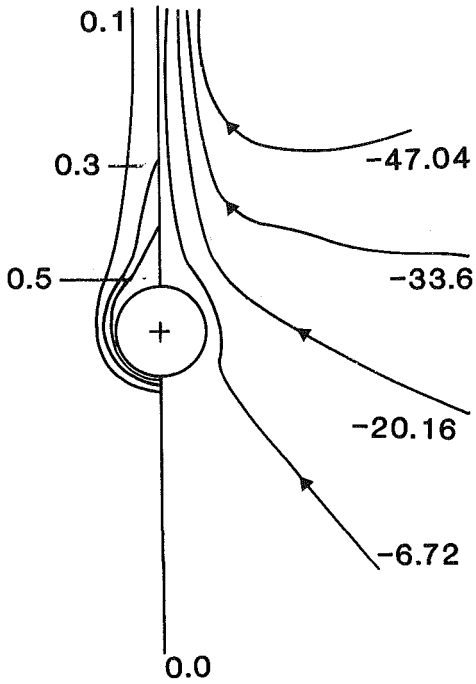


Fig. 2 Streamlines ($\psi^*$) and isotherms ($T^*$) for Gr = 1.39 × $10^4$, Re = 0.0 and Pr = 0.721

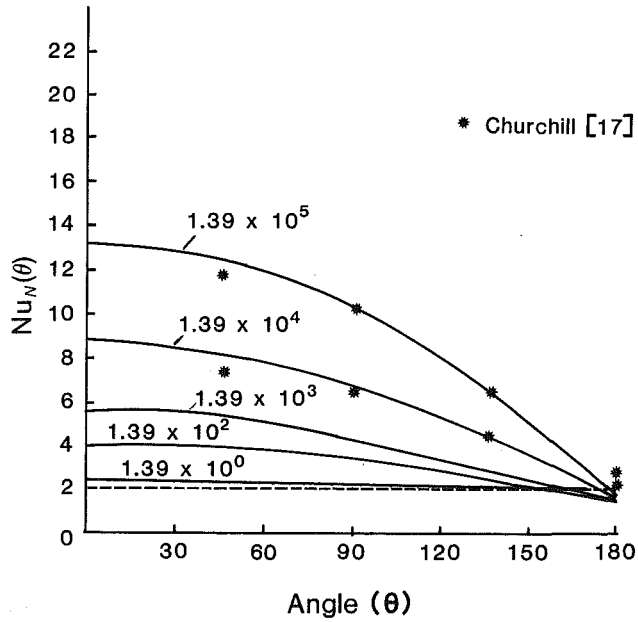


Fig. 3 Local Nusselt number distribution for various Grashof numbers (Re = 0.0)

Also an energy balance was performed before the iteration scheme is terminated. For all cases reported here, the energy balance was satisfied within 5 percent or better between the sphere wall and the outside boundary.

A 41 × 51 (R × $\theta$) grid was found adequate for the computations. Both uniform and variable spacing grid was considered in the $R$-direction. Only uniform grid was employed in the $\theta$-direction. For the higher Grashof and Reynolds number flows, denser grid spacing was used near the sphere wall due to the sharp gradients of the dependent variables at that region. The maximum ratio of the maximum to minimum grid spacing used, in the computational domain was equal to 8. Since smaller computational domains were considered at higher Grashof and/or Reynolds numbers, the same grid size (41 × 51) was sufficient to provide desired grid densities.

## Results and Discussion

Solutions were first obtained for a stationary (Re = 0) sphere for Grashof number ranging from 1.39 to $1.39 \times 10^5$. The properties of air (Pr = 0.721) were used for all the results presented. Constant property values were used, though the numerical method can also handle variable thermophysical properties. For low Grashof numbers ($< 1.39 \times 10^3$) the boundary layer is thick and the ratio of the pseudoboundary radius to the sphere diameter was set to $\geq$ 7.5. With increasing Grashof numbers, as the boundary layer thins, smaller ratios were used for the calculations.

Figure 2 represents the streamlines and isotherms for the natural convection flows around a sphere, the Grashof number being $1.39 \times 10^4$. At this moderately large Grashof number, a boundary layer forms around the sphere. The assumptions of negligible curvature effect is not valid at this Grashof number, so the solution to the boundary layer equations only, does not give valid results here. The majority of the flow approaches the sphere from the side as opposed to the bottom at moderate and high Grashof numbers. Similar observations were also made for flows around heated cylinders by Kuehn and Goldstein [15] and Farouk and Guceri [16]. The ratio of the pseudoboundary radius to the sphere diameter for the aforementioned Grashof number of $1.39 \times 10^4$ was considered to be 3.75. This allowed for denser grids near the sphere surface. The variation of the local Nusselt numbers with the angle $\theta$ for different Grashof numbers is shown in Fig. 3. It is seen that as the Grashof number increases, the Nusselt number of the upstream region increases, while the Nusselt number over the downstream (plume) region remains about the same. The local heat transfer rates are found to decrease rapidly past the angular location of $\theta = 110$ deg, especially for the larger Grashof numbers. In the past, theoretical investigation on natural convection around spheres was mainly centered upon the boundary layer equations and approximate solutions based on integral method [5, 6]. Chiang et al. [5] pointed out that their solution is of questionable validity beyond this region ($\theta > 110°$), because the thin boundary layer assumption is no longer valid. For very low Grashof numbers, the local heat transfer characteristics are fairly uniform and tend towards the pure conduction solution (shown by the dashed line in Fig. 3).

Recently Churchill [17] has developed correlating equations for the local and mean Nusselt number for free convection from an isothermal sphere as a function of the Grashof and Prandtl numbers. These expressions are based primarily on theoretical solutions for limiting cases, and hence are presumed to be more reliable than purely empirical correlations. For the boundary layer regime, taking the curvature and finite thickness of boundary layer, Churchill [17] proposed

$$\mathrm{Nu}_N(\theta) = 2 + \frac{0.765[1 - 0.072\theta]\mathrm{Gr}^{1/4}\mathrm{Pr}^{1/4}}{\left[1 + \left[\frac{0.43}{\mathrm{Pr}}\right]^{9/16}\right]^{4/9}} \tag{17}$$

Local Nusselt number values from the aforementioned correlations for Grashof numbers of $1.39 \times 10^5$ and $1.39 \times 10^4$ are also shown in Fig. 3. The agreement of the present results with those given by [17] is good.

Figure 4 shows the variation of the computed average Nusselt number with Grashof number. In this figure, the correlation presented by Yuge [3] is also shown, which is given by

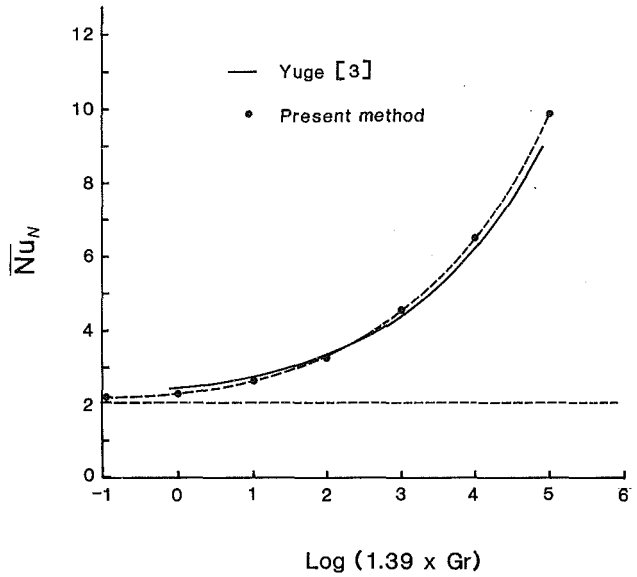


Fig. 4 Mean Nusselt number as a function of the Grashof number (Re = 0.0)

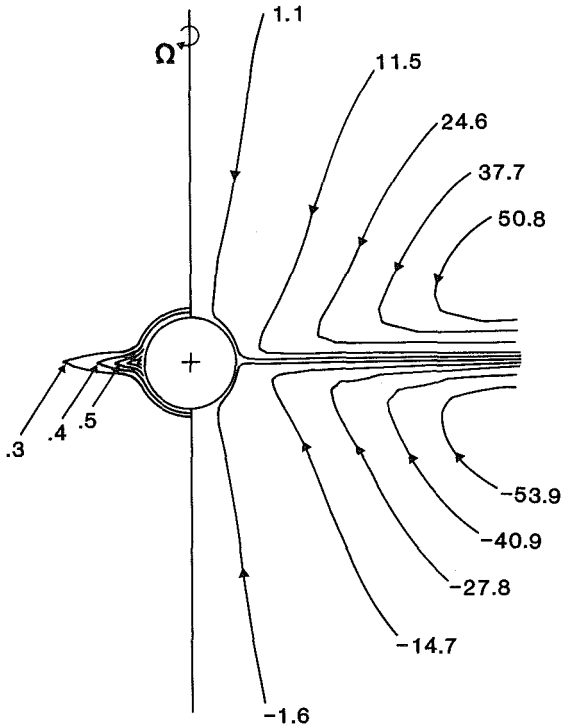


Fig. 5 Streamline ($\psi^*$) and isotherms ($T^*$) for Re = 1173, Gr = 0.0, and Pr = 0.721

$$\overline{Nu}_N = 2 + 0.392\,Gr^{0.25} \text{ for } 1 < Gr < 10^5 \quad (18)$$

The agreement seems to be excellent at the midrange of the Grashof numbers considered, and reasonably good at the lower and upper ends. An attempt to develop a correlating equation with the present results produced an expression very similar to this equation.

Solutions were then obtained for an isothermal rotating sphere immersed in an infinite medium. Buoyancy effects were not considered initially and the Grashof number was set equal to zero ($Gr/Re^2 = 0$). Solutions were obtained for the rotational Reynolds number varying from 10 to 9508. As for the natural convection case, the ratio of the pseudoboundary radius to the sphere diameter was decreased gradually with

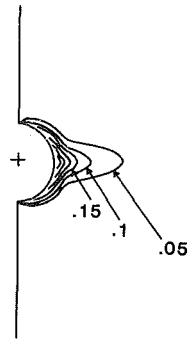


Fig. 6(*a*) Azimuthal velocity ($v_\phi^*$) distribution for Re = 360, Gr = 0.0, and Pr = 0.721

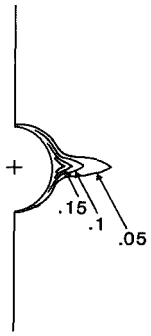


Fig. 6(*b*) Azimuthal velocity ($v_\phi^*$) distribution for Re = 1173, Gr = 0.0, and Pr = 0.721

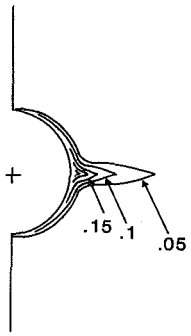


Fig. 6(*c*) Azimuthal velocity ($v_\phi^*$) distribution for Re = 3138, Gr = 0.0, and Pr = 0.721

increasing Reynolds numbers due to the formation of thin boundary layers.

Figure 5 shows the isotherms and streamlines for Re = 1173. The streamline patterns clearly show that the rotating sphere acts like a centrifugal fan. The inward flow near the two poles is carried by the fanlike motion of the upper and lower halves of the sphere toward the equator, where the two streams meet head on and then discharge into the ambient. Howarth [8] has shown in detail that the boundary layer equations for a rotating sphere degenerate in the vicinity of the poles. The streamlines shown in Fig. 5 only give information about $v_\theta^*$ and $v_R^*$ components of velocity. The azimuthal velocity $v_\phi^*$ distributions for the rotating sphere problem are shown in Figs. 6(*a*), 6(*b*), and 6(*c*). The rotational Reynolds numbers are 360, 1173, and 3138, respectively, in the figures. In each case $Gr/Re^2$ was set equal to zero. The results of these flow studies serve to explain the overall convection characteristics of rotating spheres.

Figure 7 shows the azimuthal velocity ($v_\phi/0.5D\Omega Sin\theta$) as a function of distance from the surface of the sphere at 30 deg latitude at a Reynolds number of 5250 and Gr = 0.0. To

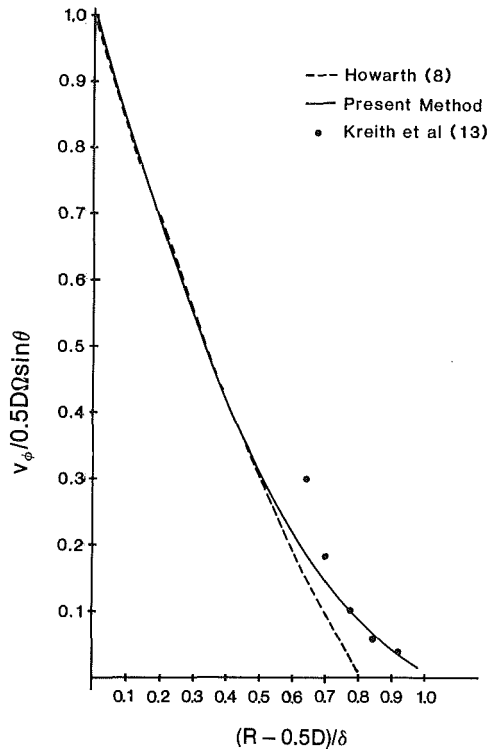


Fig. 7 Comparison of experimental, theoretical, and numerical azimuthal velocity distribution for a rotating sphere at latitude of 30 deg, Re = 5250, Gr = 0.0, and Pr = 0.721

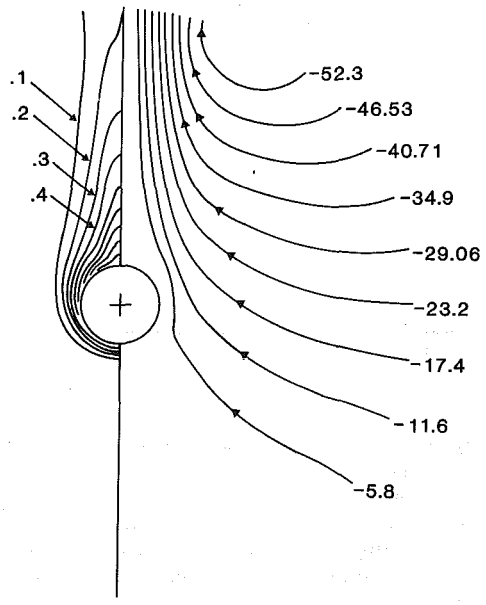


Fig. 8 Streamlines ($\psi^*$) and isotherms ($T^*$) for the mixed convective flow, $Gr/Re^2$ = 0.01, Gr = 1.39 × $10^4$, Re = 363, Pr = 0.721

construct this figure, it was necessary to determine first the boundary layer thickness along a meridian $\delta(\theta)$. This was done by defining the boundary layer thickness as that distance from the surface of the sphere at which the velocity component $v_\phi$ decrease to 2 percent of the rotational speed ($0.5D\Omega\sin\theta$) of the sphere surface and measuring the distance at which this condition obtained. Also shown in Fig. 7 are profiles predicted by Howarth [8] and experimental values obtained by Kreith et al. [13]. There is closed agreement between the numerical results and the velocity profile predicted by Howarth's solution near the sphere surface, which was obtained by an expansion about the pole. Howarth's solution breaks down near $\theta = 90$ deg and needs an estimate of the boundary layer thickness for comparisons. The numerical results agree well with the experimental values of Kreith et al. [17] near the edges of the boundary layer.

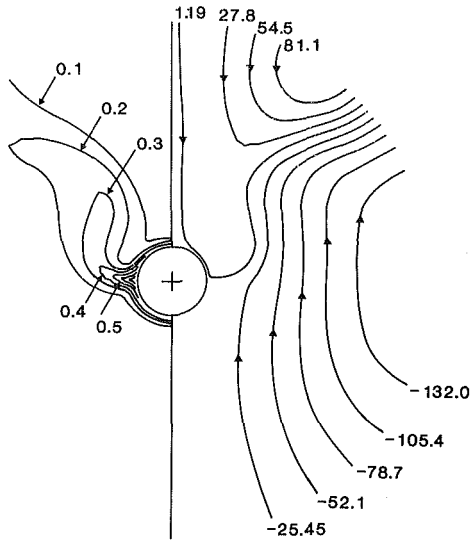


Fig. 9 Streamlines ($\psi^*$) and isotherms ($T^*$) for the mixed convective flow, $Gr/Re^2$ = 0.01, Gr = 1.39 × $10^4$, Re = 1173, Pr = 0.721

As is evident from Fig. 5, the local heat transfer is highest near the two poles for the forced convection case and reaches a minimum near the equator. The mean Nusselt number predictions agreed well with the correlation suggested by Kreith et al. [13], though the experiments performed by the above authors were for a higher Reynolds number range (for Pr = 0.721). The empirical relations obtained in [13] are given as

$$\overline{Nu}_F = 0.43\,Re^{0.5}\,Pr^{0.4} \quad \begin{matrix} Gr < 0.1Re^2 \\ Re < 5\times10^4 \\ 0.7 < Pr < 217 \end{matrix} \tag{19}$$

(The lower limit of Reynolds number for the above expression, however is not specified in [13]).

$$\text{and } \overline{Nu}_F = 0.066\,Re^{0.67}\,Pr^{0.4} \quad \begin{matrix} Gr < 0.1Re^2 \\ 5\times10^4 < Re < 7\times10^5 \\ 0.7 < Pr < 7 \end{matrix} \tag{20}$$

It is to be noted that the foregoing correlations are only valid for $Gr/Re^2 < 0.1$, and the Grashof number does not appear in the correlations. At Reynolds number below $5\times10^4$ the flow induced by a sphere rotating in infinite environment is laminar except for a small region in the vicinity of the equator where the boundary layers from the two halves of the sphere meet [13].

The mean Nusselt number predictions obtained in this study for forced convection agreed well with the expression given by equation (19). For smaller Reynolds numbers, the present results deviate from the given correlation (as shown later). The following correlation was developed for mean Nusselt number predictions for the present calculations:

$$\overline{Nu}_F = 2 + 0.175\,Re^{0.583} \quad \begin{matrix} Gr = 0.0 \\ 10 < Re < 10^4 \\ Pr = 0.721 \end{matrix} \tag{21}$$

Results are next presented for the mixed convection problems where the interaction of the buoyancy and centrifugal forces are studied. $Gr/Re^2$ was varied from $\infty$ to 0.01 and the Grashof number range studied in this case was from

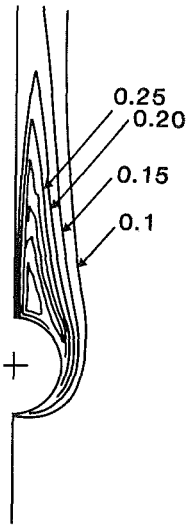


Fig. 10(*a*) Azimuthal velocity ($v_\phi^*$) distribution for the mixed convective flow, $Gr/Re^2 = 0.1$, $Gr = 1.39 \times 10^4$, $Re = 363$, $Pr = 0.721$

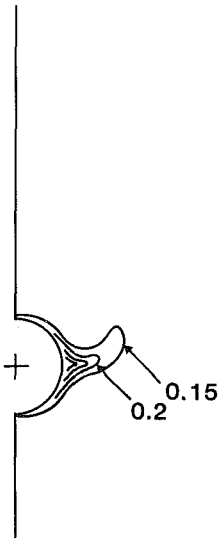


Fig. 10(*b*) Azimuthal velocity ($v_\phi^*$) distribution for the mixed convective flow, $Gr/Re^2 = 0.01$, $Gr = 1.39 \times 10^4$, $Re = 1173$, $Pr = 0.721$

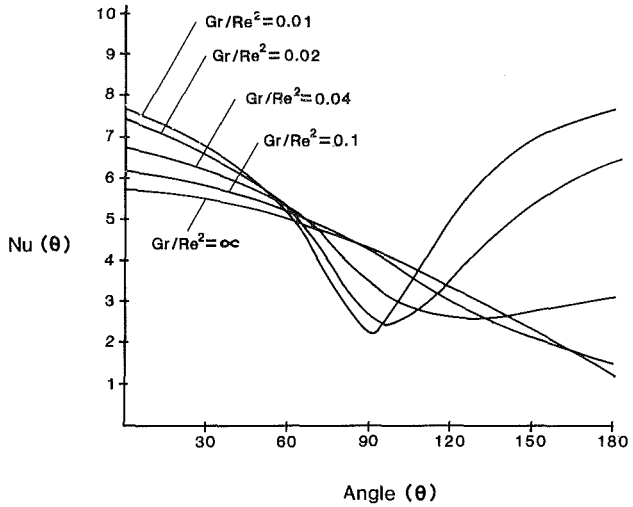


Fig. 11 Local Nusselt number distribution for mixed convection flows: $Gr = 1.39 \times 10^3$, $Pr = 0.721$

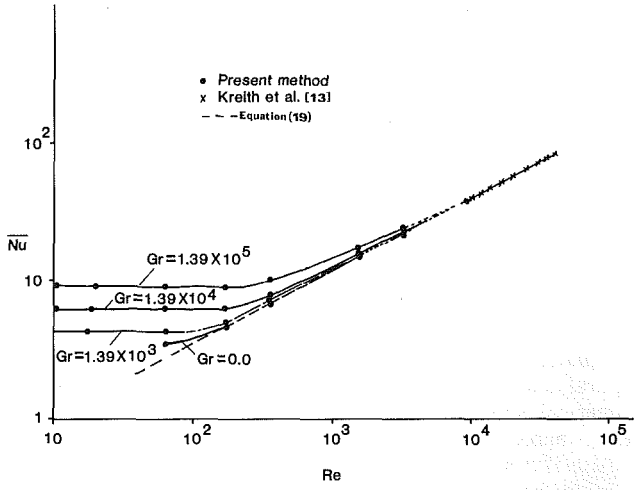


Fig. 12 Mean Nusselt number distribution for mixed flows as a function of rotational Reynolds number

$1.39 \times 10^3$ to $1.39 \times 10^5$. Figure 8 displays the streamlines and isotherms for the mixed convection flow where $Gr = 1.39 \times 10^4$ and $Gr/Re^2 = 0.1$. The effect of buoyancy is prominent as can be seen by the streamline and isotherm patterns. Comparing with Fig. 2, the thermal plume is slightly wider in the mixed convection case, compared to the pure natural convection case. Figure 9 shows the streamlines and isotherms for the mixed convective flow where $Gr = 1.39 \times 10^4$ and $Gr/Re^2 = 0.01$. The flow patterns and the temperature field undergo a remarkable change from the earlier cases and the effect of rotation and buoyancy are both evident. Due to the high rotational Reynolds number, the near field is strongly dominated by the centrifugal effects. However, buoyancy effects dominate, away from the sphere, where an upward plume forms and the flow field becomes distorted. Though the changes in the far field for temperature and velocity are remarkable, the heat transfer characteristics are not affected as much in this case.

Figures 10(*a*) and 10(*b*) show the azimuthal velocity distributions for the cases presented in Figs. 8 and 9, respectively. For high $Gr/Re^2$, the upward diffusion of $v_\phi^*$ component is significant. As can be seen in Fig. 10(*b*), the rotation dominates at $Gr/Re^2 = 0.01$, and there is slight upward diffusion of $v_\phi^*$ at the far field only.

Figure 11 gives the local Nusselt number predictions for the mixed convective flows where $Gr = 1.39 \times 10^3$. At $Gr/Re^2 = 0.1$, the local Nusselt number distribution is similar to that for the pure natural convection ($Gr/Re^2 = \infty$). The local heat transfer, however, increases at the poles and decreases near the equator due to rotation as compard to the pure natural convection case. For higher rotational Reynolds numbers, the local Nusselt number distribution significantly deviates from the pure natural convection case. The heat transfer peaks at the poles and reaches a minima near the equator – typical of the forced flow characteristics around a sphere. Several cases with varying $Gr/Re^2$ are presented in the Fig. 11 to show the transition between the forced- and free-convection limits.

The mean Nusselt numbers of all the cases studied are presented in Fig. 12. Experimental results of Kreith et al. [13] are also shown in the this figure, albeit for higher Reynolds numbers. No cases above $Gr = 1.39 \times 10^5$ were studied as the flow is known to become turbulent beyond that value [6], even when there is no rotation. For $Gr/Re^2 \geq 0.5$, it was observed that the effect of rotation has almost no effect on the heat transfer and flow characteristics for all Grashof numbers studied. The effect of the buoyancy is insignificant when $Gr/Re^2 \leq 0.01$ as far as the overall heat transfer characteristics are concerned. As has been shown in the study the

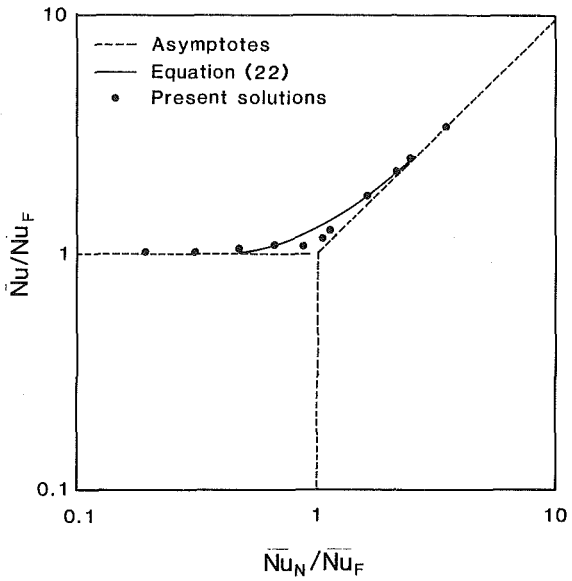


**Fig. 13 Comparison of computed mixed convective flow Nusselt number with correlation given by Churchill [18]**

flow and temperature field away from the sphere surface is still affected by buoyancy at the low $Gr/Re^2$ ratios.

Finally, an asymptotic formulation for correlating the mixed convection heat transfer results, following Churchill [18], is applied for the results obtained. Following Churchill, for the mixed convective flows, the overall Nusselt number can be represented by

$$\overline{Nu}^n = \overline{Nu}_N^n + \overline{Nu}_F^n \tag{22}$$

with $n = 3$.

Equations (18) and (21) are used as the asymptotes for natural and forced convection for the present range of the numerical solutions. As illustrated in Fig. 13, the present results agree reasonably well with equation (22) and justifies the use of $n = 3$ as a good first-order correlation for most cases of mixed convection.

## Conclusions

Solutions to the Navier-Stokes and energy equations have been obtained for mixed convection heat transfer from an isothermal sphere over a large range of $Gr/Re^2$ ratio. Results were obtained in the laminar range where Grashof number varied from 1.39 to $1.39 \times 10^5$ and Reynolds number range covered was from zero to approximately $10^4$. The results give interesting details of the heat transfer characteristics and the flow patterns for a wide range of $Gr/Re^2$. Solutions to the laminar boundary-layer equations will not give acceptable results even at moderate values of either the Grashof or the Reynolds number because curvature effects are always present and boundary layer approximations become invalid near the poles.

The shortcoming of the present method is the approximate boundary conditions at the far field and consideration of a finite outer boundary. A sensitivity study was undertaken to determine the sensitivity of the results on the choice of the outer boundary radius to sphere diameter ratio. In particular, for the results presented in Fig. 8, the ratio was varied by ±20 percent from the chosen value of 3.75. Slight variations of the results in the far field were observed, whereas heat transfer predictions were essentially unchanged.

## Acknowledgments

For bringing to his attention, [17] and [18], the author wishes to thank Professor Stuart W. Churchill.

## References

1 Geola, F., and Cornish, A. R. H., "Numerical Solution of Steady State Free Convective Heat Transfer from a Solid Sphere," *International Journal of Heat and Mass Transfer*, Vol. 24, 1981, pp. 1369–1378.

2 Farouk, B., "Natural Convection Heat Transfer from an Isothermal Sphere," *Proceedings, 16th Southeastern Seminar on Thermal Sciences*, Miami, Fla., Vol. 16, 1982, pp. 347–364.

3 Yuge, T., "Experiments on Heat Transfer from Spheres Including Combined, Natural and Forced Convection," ASME *Transactions*, Series C, Vol. 82, No. 3, 1960, pp. 214–220.

4 Hossain, M. A., and Gebhart, B., "Natural Convection about a Sphere at Low Grashof Number," *Proceedings, 4th International Heat Transfer Conference*, Paris, Vol. 4, No. 1.6, 1970.

5 Chiang, T., Ossin, A., and Tien, C. L., "Laminar Free Convection from a Sphere," ASME JOURNAL OF HEAT TRANSFER, Vol. 86, No. 4, 1964, pp. 537–542.

6 Cremers, C. J., and Finely, D. L., "Natural Convection about Isothermal Spheres," *Proceedings, 4th International Heat Transfer Conference*, Paris, Vol. 4, 1970.

7 Stokes, G. G., "On the Theories of the Internal Friction of Fluids in Motion," *Camb. Trans.* viii, 1845, p. 287.

8 Howarth, L., "Note on the Boundary Layer on a Rotating Sphere," *Phil. Mag.*, Series 7, 42, 1951, pp. 1308–1315.

9 Nigam, S. D., "Note on the Boundary Layer on a Rotating Sphere," Z. *Agnew, Math. Phys.*, Vol. 5, 1954, pp. 151–154.

10 Singh, S. N., "Heat Transfer by Laminar Flow from a Rotating Sphere," *Applied Sci. Res.*, A9, 1960, pp. 197–205.

11 Kobashi, Y., "Measurements of Boundary Layer of a Rotating Sphere," *J. Sci. Hiroshima Univ.*, A20, 1957, pp. 149–156.

12 Nordlie, R., and Kreith, F., "Convection Heat Transfer from a Rotating Sphere," *International Developments in Heat Transfer*, ASME, New York, 1961, pp. 461–467.

13 Kreith, F., Roberts, L. G., Sullivan, J. A., and Sinha, S. N., "Convection Heat Transfer and Flow Phenomena of Rotating Spheres," *International Journal of Heat and Mass Transfer*, Vol. 6, 1963, pp. 881–895.

14 Gosman, A. D., Pun, W. M., Runchal, A. K., Spalding, D. B., and Wolfshtein, M. W., *Heat and Mass Transfer in Recirculating Flows*, Academic Press, London, 1969.

15 Kuehn, T. H., and Goldstein, R. J., "Numerical Solution to the Navier-Stokes Equations for Laminar Natural Convection about a Horizontal Isothermal Circular Cylinder," *International Journal Heat and Mass Transfer*, Vol. 23, 1980, pp. 971–979.

16 Farouk, B., and Guceri, S. I., "Natural Convection from Horizontal Circular Cylinders—Laminar Regime," ASME JOURNAL OF HEAT TRANSFER, Vol. 103, 1981, pp. 522–527.

17 Churchill, S. W., "Comprehensive, Theoretically Based Correlating Equations for Free Convection from Isothermal Spheres," *Chemical Engineering Communications*, Vol. 24, 1983, pp. 339–352.

18 Churchill, S. W., "The Development of Theoretically Based Correlations for Heat and Mass Transfer," *Proceedings, First Latin-American Conference on Heat and Mass Transfer*, LaPlata, Argentina, Nov. 2, 1982.

# Transient Heat Flux Measurements in a Divided-Chamber Diesel Engine

**A. C. Alkidas**
Mem. ASME

**R. M. Cole**

Engine Research Department,
General Motors Research Laboratories,
Warren, Mich. 48090

*Transient surface heat flux measurements were performed at several locations on the cylinder head of a divided-chamber diesel engine. The local heat flux histories were found to be significantly different. These differences are attributed to the spatial nonuniformity of the fluid motion and combustion. Both local time-averaged and local peak heat fluxes decreased with decreasing speed and load. Retarding the combustion timing beyond TDC decreased the peak heat flux in the antechamber but increased the peak heat flux in the main chamber. This is attributed to the relative increase in the portion of fuel that burns in the main chamber with retarded combustion timing.*

## Introduction

Despite a relatively large number of studies dealing with transient heat transfer in open-chamber diesel engines [1–7], corresponding investigations in divided-chamber diesel engines have been very few [8–10]. Of these, Knight [8] presented very limited data, and Hassan [9] investigated only motored conditions in an experimental, low-compression ratio, divided-chamber engine with spherical antechamber geometry. Kamel [10] (see also Kamel and Watson [11]), on the other hand, performed a detailed study of transient heat transfer in a high-swirl, divided-chamber engine. Heat flux measurements were made at a location in the antechamber (hot plug) and at a location in the main chamber. The engine variables examined were engine speed (1320 to 2800 r/min), load (100 and 40 percent) and injection timing (2°, 7°, and 12° BTDC).

The objectives of this investigation were twofold: first, to obtain time-resolved, surface heat flux measurements at several locations on the cylinder head of a divided-chamber diesel engine, and second, to examine the influence of the principal operational parameters of the engine on the local heat flux histories.

## Apparatus and Procedure

**Engine.** The heat flux measurements were performed in a 0.72-L experimental, single-cylinder, divided-chamber diesel engine. The characteristic dimensions of the engine are given in Table 1. The cylinder head was specially designed to allow the introduction of four heat flux probes and two pressure transducers. Two of the probes, designated as TM1 and TM2, were located in the main chamber, and the other two probes, designated as TS1 and TS2, were located in the antechamber. The locations of the probes relative to the valves, cylinder, and antechamber are shown in Fig. 1. Of the two main-chamber probes, TM1 was located between the valves and in line with the antechamber passage, and TM2 was located near the periphery of the cylinder and to the side of the throat. Both of the antechamber probes, TS1 and TS2, were located in the upper half of the antechamber. Probe TS1 was in the plane containing the fuel injector and the centerline of the connecting passage (see section AA, Fig. 1). The location TS2 was used for limited tests only.

**Heat Flux Probes.** The heat flux probes were fast-response, surface thermocouples of the Bendersky type [12] with a second thermocouple placed at a nominal distance of 13 mm from the tip of the probe. The probe bodies were manufactured from the same material used in making the

**Table 1 Engine description**

| | |
|---|---|
| Bore, mm | 103.0 |
| Stroke, mm | 85.6 |
| Connecting rod length, mm | 223.5 |
| Displacement, L | 0.718 |
| Antechamber volume, L | 0.0147 |
| Compression ratio | 19.2:1 |
| Intake valve opens, CA deg | 6 BTC |
| Intake valve closes, CA deg | 38 ABC |
| Exhaust valve opens, CA deg | 64 BBC |
| Exhaust valve closes, CA deg | 17 ATC |

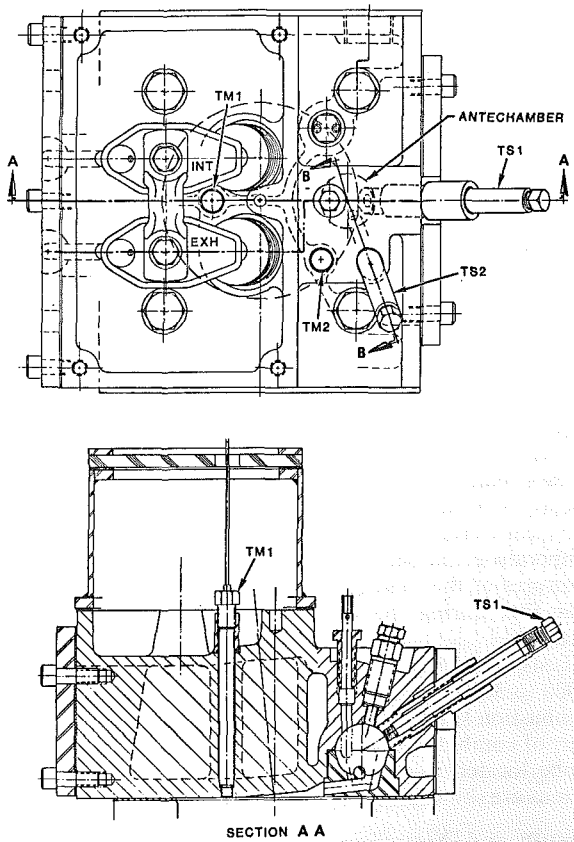


Fig. 1 Locations of heat flux probes on the cylinder head

Contributed by the Heat Transfer Division for publication in the JOURNAL OF HEAT TRANSFER. Manuscript received by the Heat Transfer Division April 6, 1984.

**Table 2 Baseline conditions**

| | |
|---|---|
| Engine speed, r/min | 1000 |
| Fuel-air ratio | 0.022 |
| Start of combustion | TDC |
| Intake-air temperature, °C | 35 |
| Coolant temperature, °C | 82 |
| Intake-air manifold pressure | ambient |
| Oil temperature, °C | 82 |
| Fuel temperature at pump, °C | 35 |

cylinder head. The diameter of the tip of the probe was 6.4 mm. The surface thermocouples have a response time of the order of 1 to 10 $\mu$s. The second thermocouple ("in-depth" thermocouple) was used to measure the time-averaged component of heat flux $q_w$ which is given by the following expression

$$q_w = \frac{K}{\delta}[T(0) - T(\delta)] \quad (1)$$

where $K$ is the thermal conductivity of the probe material, $\delta$ is the distance of the "in-depth" thermocouple from the surface of the probe, and $T(0)$ and $T(\delta)$ are the time-averaged temperatures at the surface ($x = 0$) and at a distance $x = \delta$ from the surface.

The heat flux probes were calibrated in a separate calibration rig which consisted of a water-cooled, high-intensity radiation source (36 kW), a reference heat flux sensor (Hy-Cal asymptotic water-cooled calorimeter), and a holder where the heat flux probe to be calibrated is mounted. The mounting of the heat flux probes in the holder was identical to the mounting of the probes in the cylinder head. The magnitude of the incident radiant heat flux to the probe was measured by the calorimeter. The surface absorptivity of the calorimeter ($\alpha = 0.89$) was assumed to be approximately equal to the surface absorptivity of the heat flux probes whose surfaces were blackened by exposing them to the combustion gases of the engine chamber. Based on this assumption, no corrections for reradiation and reflection of radiation were made.

The calibration procedure consisted of exposing the heat flux probes to known, steady-state levels of radiant heat flux and measuring the corresponding temperature difference $[T(0) - T(\delta)]$. With this procedure the quotient $K/\delta$ is evaluated, since neither the thermal conductivity of the probe material $K$ nor the distance of the "in-depth" thermocouple is precisely known.

**Measurements.** At each operating condition, after the engine was completely warmed and operating at steady state, the temporal variations of pressure in the main chamber and surface temperatures at three locations on the cylinder head (mostly at locations TM1, TM2 and TS1) were recorded for 100 consecutive cycles. From the transient surface-temperature measurements and the corresponding temperatures of the "in-depth" thermocouples, the variation of heat flux during the engine cycle was calculated at each location.

Tests were performed for a wide range of engine speed (1000 to 3000 r/min), fuel-air ratio (0 to 0.040), and start of combustion (TDC to 10° ATDC) using No. 2 diesel fuel. The start of combustion was determined using a flame-luminosity probe located in the glow-plug position. The baseline conditions are shown in Table 2.

## Results and Discussion

**Surface-Temperature Measurements.** Figures 2 and 3 show the temporal variations of the surface temperatures at TM1[1] and TS1, respectively, for different fuel-air ratios and an engine speed of 1000 r/min during the time interval in the compression and expansion strokes of 60° BTDC (300° CA) to 100° ATDC (460° CA). As demonstrated in both figures, increasing the fuel-air ratio increased the overall surface temperature level and increased the temperature swing. At full load, the temperature swing during the engine cycle was about 10°C. An interesting point shown in Figs. 2 and 3 is that the peaks in the surface temperatures at locations TM1 and TS1 occurred later in the cycle as the fuel-air ratio was increased. This indicates that the combustion schedule of the fuel is retarded with increasing fueling rate. One should be reminded that the start of combustion (combustion timing), unless otherwise stated, was kept fixed at TDC.

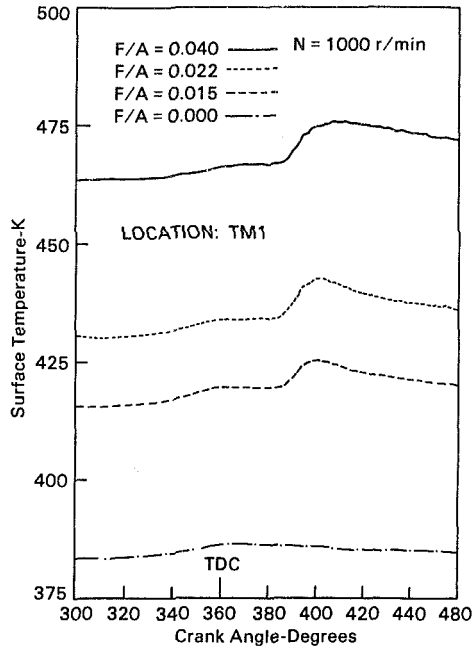


**Fig. 2 Temporal variations of the surface temperature at TM1 for various loads and an engine speed of 1000 r/min**

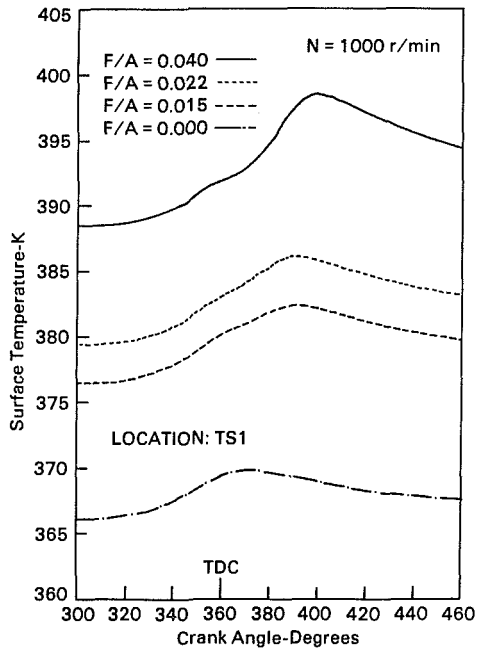


**Fig. 3 Temporal variations of the surface temperature at TS1 for various loads and an engine speed of 1000 r/min**

[1] The designations of the location of the probe, the probe itself, and the temperature at that location are identical.

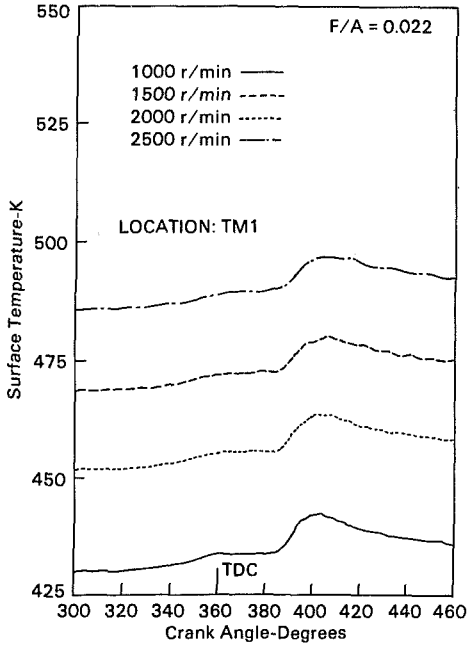


Fig. 4 Temporal variations of the surface temperature at TM1 for various engine speeds and a fuel-air ratio of 0.022

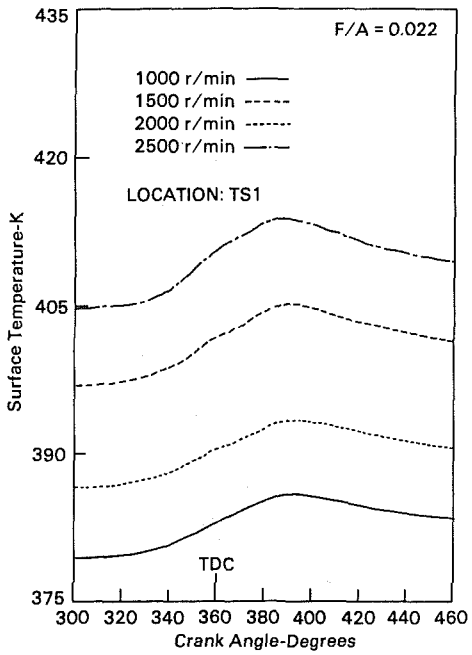


Fig. 5. Temporal variations of the surface temperature at TS1 for various engine speeds and a fuel-air ratio of 0.022

The temporal variations of surface temperatures at TM1 and TS1 for different engine speeds and a fuel-air ratio of 0.022 are shown in Figs. 4 and 5, respectively. Increasing engine speed increased the surface-temperature level. The temperature swing appears to be weakly influenced by engine speed.

**Surface Heat Flux Measurements.** In reciprocating internal combustion engines the combustion-chamber surface heat flux may be represented by two components: the steady-state or time-averaged component, which can be evaluated from time-averaged temperature measurements at two known positions within the walls of the combustion chamber (e.g., see equation (1)), and the unsteady component, which can be

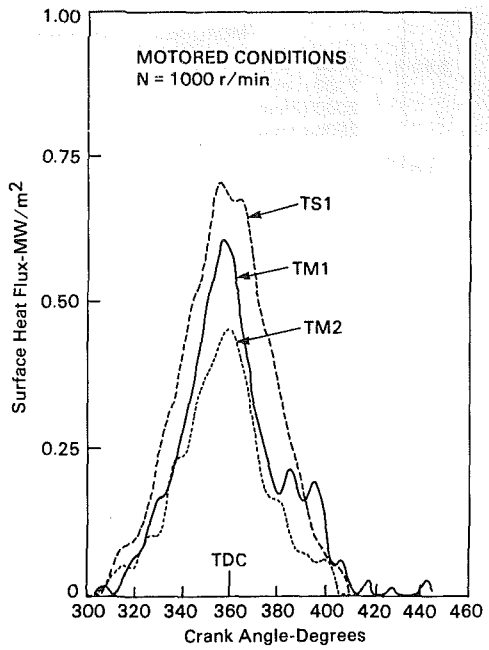


Fig. 6 Comparison of heat flux histories at TM1, TM2 and TS1 at motored conditions and an engine speed of 1000 r/min

evaluated from the measured cyclic surface-temperature variation.

The method of calculating the unsteady heat flux from transient surface-temperature measurements has been described in several studies [13–15]. Briefly, the measured cyclic surface-temperature variation is represented by a Fourier series of sine and cosine terms. The surface heat flux is then derived from the solution of the one-dimensional, unsteady heat-conduction problem with a time-varying surface temperature described by the foregoing harmonic analysis.

The method of calculating heat flux from temperature measurements (this includes the steady and unsteady components) assumes that the flow of heat in the combustion-chamber walls is one-dimensional. In general, this is not true in engines [16]. However, the use of air gaps around the heat flux probes causes the flow of heat through the probes to be approximately one dimensional. Other errors associated with the measurement of heat flux in engines were discussed in [17].

A comparison of the temporal variations of the local heat fluxes at TM1, TM2, and TS1 for motored conditions and for an engine speed of 1000 r/min is shown in Fig. 6. The local heat fluxes peaked near TDC. Because of the high swirl flows present in the antechamber, the highest peak heat flux was measured at TS1, followed by the heat fluxes at TM1 and TM2. The observed spatial variations of the surface heat flux are primarily attributed to differences in the flow field in the vicinity of the measurements.

The influence of engine speed on the local heat flux history of TS1 is shown in Fig. 7 for motored conditions. Increasing the engine speed increased the characteristic velocity in the cylinder, which increased the convective coefficient and consequently the surface heat flux.

Comparison of the heat flux data for motored conditions obtained in this study with the corresponding data obtained by Kamel and Watson [11] showed that their magnitudes of the peak heat fluxes were higher by a factor of 2 to 4. This large difference in the measured heat flux level is primarily due to the difference in the magnitudes of the air velocities in the two combustion chambers and the difference in the locations of measurement of the two studies. The engine used by Kamel and Watson [11] had a Ricardo-Comet an-

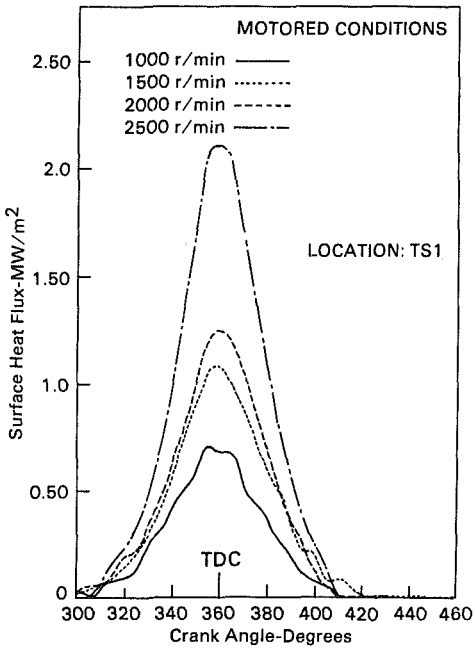


Fig. 7 The influence of engine speed on the heat flux history at TS1 (motored conditions)

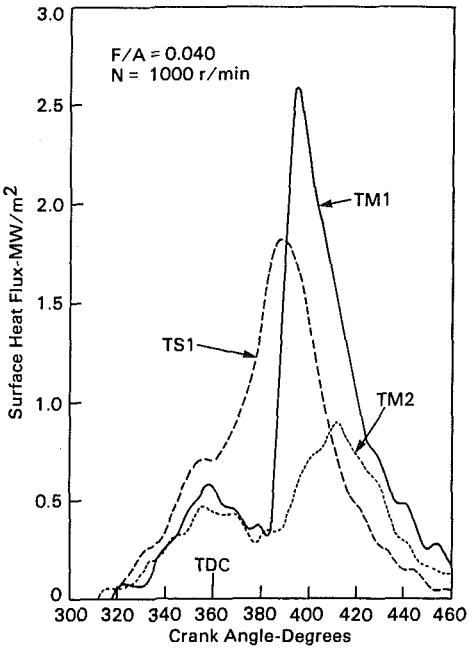


Fig. 8 Comparison of the heat flux histories at TM1, TM2 and TS1 for fuel-air ratio of 0.040 and an engine speed of 1000 r/min

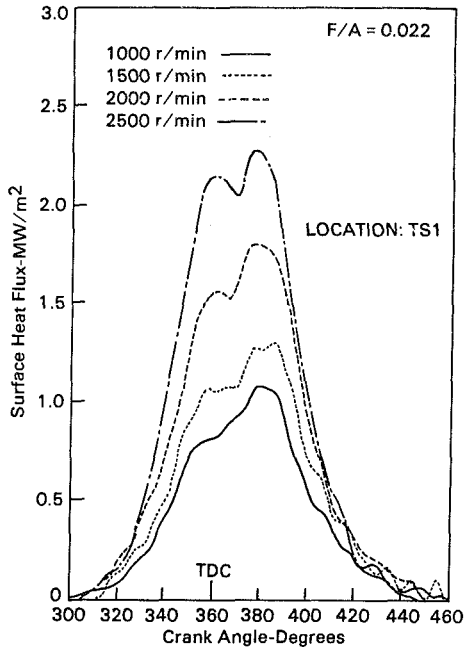


Fig. 9 Heat flux histories at TS1 for various engine speeds and a fuel-air ratio of 0.022

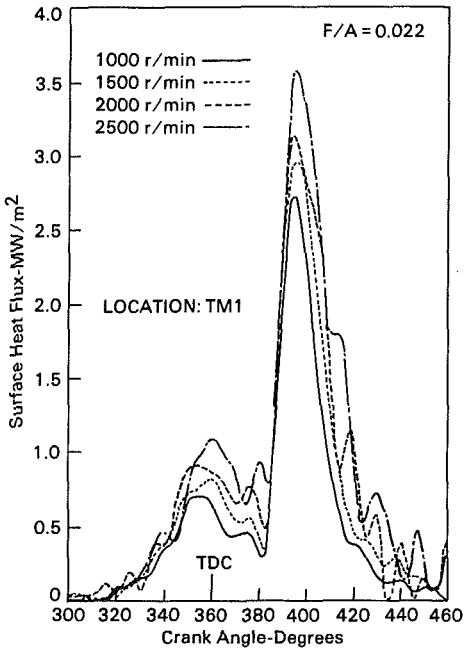


Fig. 10 Heat flux histories at TM1 for various engine speeds and a fuel-air ratio of 0.022

techamber that has a reported swirl ratio (angular velocity of air/angular speed of the engine crankshaft) of 20 to 70 [18, 19] with a more typical value of 40. In contrast, the engine used in the present study had a low-to-moderate swirl antechamber with swirl ratio of 10 to 20 [20, 21].

Comparison of the heat flux histories at TM1, TM2, and TS1 for an engine speed of 1000 r/min and fuel-air ratio of 0.040 is shown in Fig. 8, respectively. As is apparent, the heat flux histories at fired conditions are characterized by double-peak variations. The first peak, which in general is lower in magnitude, occurs near TDC (360° CA) and is due to compression (compression peak). The second peak, which occurs later in the cycle and is strongly dependent on location, is caused by combustion. In agreement with the heat flux measurements for motored conditions (e.g., see Fig. 6), the peak heat flux due to compression was highest at TS1, followed by TM1 and TM2. On the other hand, in the case of the peak heat flux due to combustion, the highest heat flux was at TM1, followed by TS1 and TM2. Furthermore, in contrast to locations TS1 and TM2, the peak heat flux due to combustion at TM1 is several times larger than the corresponding peak heat flux due to compression.

It is apparent from Fig. 8 that combustion affects the local surface heat flux histories significantly. The greatest influence of combustion is exhibited at TM1 because this location experiences the convective heating action of the hot combustion gases entering the main chamber from the antechamber during expansion. In relation to this, it is very interesting that the start of the second peak at location TM1 is

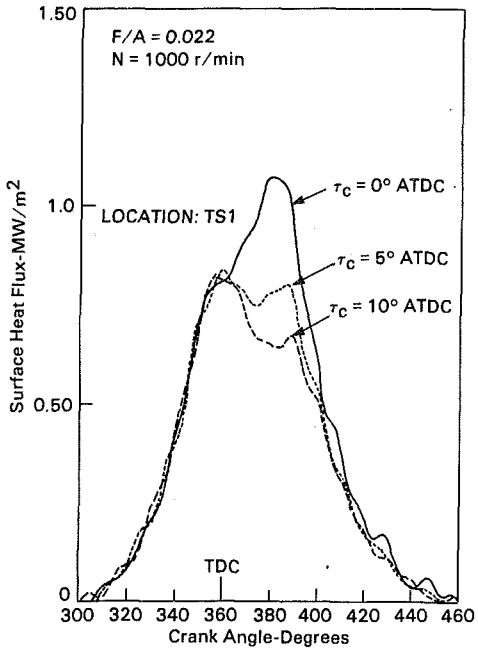


**Fig. 11 The influence of combustion timing on the heat flux histories at TS1 ($F/A$ = 0.022, $N$ = 1000 r/min)**

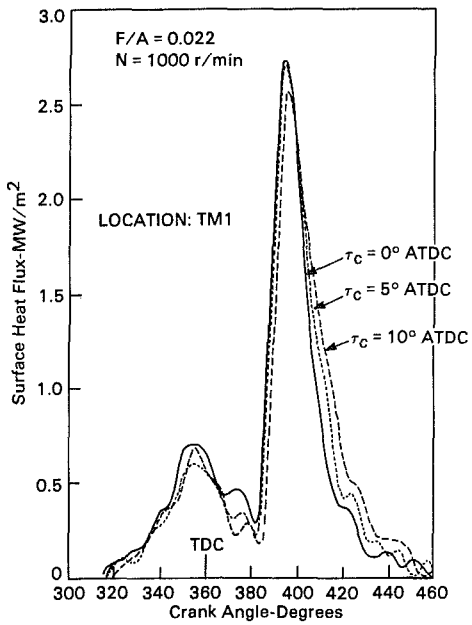


**Fig. 12 The influence of combustion timing on the heat flux histories at TM1 ($F/A$ = 0.022, $N$ = 1000 r/min)**

well defined and occurs at about 20° CA ATDC. Thus one may conclude that TM1 senses the combustion gases entering the main chamber at about 20° CA ATDC. This has also been verified by luminosity measurements at the same location.

The effects of engine speed on the heat flux histories at locations TS1 and TM1 are shown in Figs. 9 and 10, respectively. All tests were run at a fuel-air ratio of 0.022 and the start of combustion at TDC. Increasing the engine speed significantly increased the heat flux levels at the two locations. However, the interval of high heat flux, expressed in crank-angle degrees, appears to remain roughly constant. This suggests that the duration of combustion scales roughly inversely with engine speed.

A most interesting feature exhibited by the heat flux histories at TM1 is that the start of the second heat-flux peak

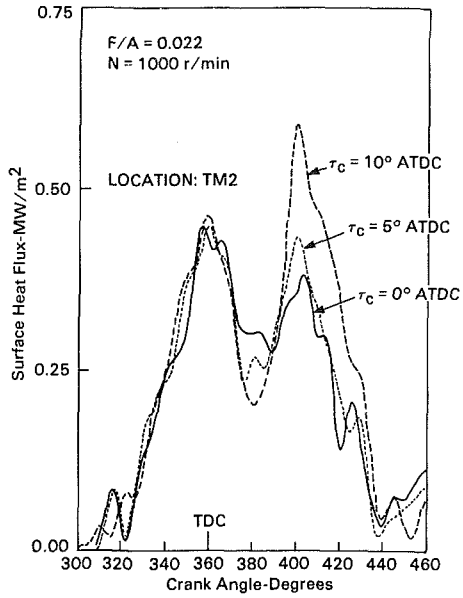


**Fig. 13 The influence of combustion timing on the heat flux histories at TM2 ($F/A$ = 0.022, $N$ = 1000 r/min)**

and the initial stage of the rise in the heat flux due to combustion is independent of engine speed. This may suggest that the initial stage of outflow of gases from the antechamber is not significantly affected by engine speed.

Figures 11–13 show the influence of combustion timing on the heat flux histories at locations TS1, TM1, and TM2. All tests were performed at an engine speed of 1000 r/min and a fuel–air ratio of 0.022. Retarding the combustion timing ATDC significantly decreased the peak heat flux due to combustion at location TS1. Retarding the combustion timing after TDC causes reductions in gas pressure and combustion temperature, which reduce the rate of heat transfer. The heat flux history at location TM1 in the main chamber is not significantly affected by combustion timing, even though retarding the combustion timing decreased the peak heat flux due to combustion and retarded the heat-flux history due to combustion experienced by TM1.

In contrast to the results at TM1, the peak heat flux due to combustion at TM2, the other main-chamber location, increased significantly with retarded combustion timing. The observed different behaviors of the heat flux histories at locations TS1 and TM2 with combustion timing suggest that as the combustion timing is retarded, a proportionally larger amount of unburned fuel enters the main chamber, where it mixes and burns. The increase in the amount of fuel that burns in the main chamber causes the observed increase in the surface heat flux with retarded combustion timing.

## Conclusions

Transient surface heat flux measurements were performed at several locations on the cylinder head of a single-cylinder, divided-chamber diesel engine. The operational parameters of the engine examined and their ranges were: engine speed (1000 to 3000 r/min), fuel/air ratio (0 to 0.040), and combustion timing (TDC to 10° ATDC). Based on the results of this investigation, the following conclusions were reached:

1 The time histories of the local heat fluxes were significantly different at the three locations of measurement. These differences are attributed to the spatial nonuniformity of the fluid motion and combustion.

2 For motored conditions, due to the high swirl flows present, the highest heat flux was measured in the antechamber.

3 For fired conditions, the highest heat flux levels were

measured at the location in the main chamber between the valves and in line with the throat of the antechamber. These high heat fluxes were attributed to the convective action of the high-temperature combustion gases exiting the antechamber during the early stages of the expansion stroke.

4 Both local time-averaged and local peak heat fluxes decreased with decreasing speed and load. Retarding the combustion timing beyond TDC decreased the peak heat flux in the antechamber but increased the peak heat flux in the main chamber. This is attributed to the relative increase in the portion of fuel that burns in the main chamber with retarded combustion timing.

In closing, one should be cautioned that, because of the extreme difficulties associated with the estimation of errors in the measurement of surface heat flux in the combustion chamber of a diesel engine, no error analysis of the heat flux measurements presented in this study was performed.

## Acknowledgment

The authors would like to acknowledge the efforts of L. E. Robb, who provided the main technical support to the experimental program.

## References

1 Sitkei, G., "Beitrag zur Theorie des Warmeuberganges im Motor," *Konstruction*, Vol. 15, 1962, pp. 67–71.

2 Annand, W. J. D., and Ma, T. H., "Instantaneous Heat Transfer Rates to the Cylinder Head Surface of a Small Compression-Ignition Engine," *Proc. Instn. Mech. Engrs.*, Vol. 185, 1971, pp. 976–987.

3 LeFeuvre, T., Myers, P. S., and Uyehara, A. O., "Experimental Instantaneous Heat Fluxes in a Diesel Engine and Their Correlation," SAE Paper 690464, 1969.

4 Whitehouse, N. D., "Heat Transfer in a Quiescent Chamber Diesel Engine," *Proc. Instn. Mech. Engrs.*, Vol. 185, 1971, pp. 963–975.

5 Oguri, T., and Inaba, S., "Radiant Heat Transfer in Diesel Engines," *SAE Transactions*, Vol. 81, 1972, pp. 127–148.

6 Dent, J. C., and Suliaman, S. L., "Convective and Radiative Heat Transfer in a High Swirl Direct Injection Diesel Engine," SAE Paper 770407, 1977.

7 Sihling, K., and Woschni, G., "Experimental Investigation of the Instantaneous Heat Transfer in the Cylinder of a High Speed Diesel Engine," Paper 790833, *Diesel Engine Thermal Loading*, SAE SP-449, 1979, pp. 95–103.

8 Knight, B. E., "The Problem of Predicting Heat Transfer in Diesel Engines," *Proc. Instn. Mech. Engrs.*, Vol. 179, 1965, pp. 99–112.

9 Hassan, H., "Unsteady Heat Transfer in a Motored I.C. Engine Cylinder," *Proc. Instn. Mech. Engrs.*, Vol. 185, 1971, pp. 1139–1148.

10 Kamel, M., "Thermodynamic Analysis of Indirect Injection Diesel Engine Operation," Ph.D. thesis, Imperial College of Science and Technology, University of London, 1977.

11 Kamel, M., and Watson, N., "Heat Transfer in the Indirect Injection Diesel Engine," Paper 790826, *Diesel Engine Thermal Loading*, SAE SP-449, 1979, pp. 81–94.

12 Bendersky, D., "A Special Thermocouple for Measuring Transient Temperatures," *Mechanical Engineering*, Vol. 75, No. 2, 1953, pp. 117–121.

13 Overbye, V. D., Bennethum, J. E., Uyehara, O. A., and Myers, P. S., "Unsteady Heat Transfer in Engines," *SAE Transactions*, Vol. 69, 1961, pp. 461–494.

14 Wendland, D. W., "The Effect of Periodic Pressure and Temperature Fluctuations on Unsteady Heat Transfer in a Closed System," NASA Report CR-72323, Mar. 1968.

15 Alkidas, A. C., "Heat Transfer Characteristics of a Spark-Ignition Engine," ASME JOURNAL OF HEAT TRANSFER, Vol. 102, 1980, pp. 189–193.

16 Hohenberg, G. F., "Advanced Approaches for Heat Transfer Calculations," *Diesel Engine Thermal Loading*, SAE SP-449, 1979, pp. 61–79.

17 Alkidas, A. C., and Myers, J. P., "Transient-Heat-Flux Measurements in the Combustion Chamber of a Spark-Ignition Engine," ASME JOURNAL OF HEAT TRANSFER, Vol. 104, 1982, pp. 62–67.

18 Alcock, J. F., and Watts, R., "The Combustion Process in High-Speed Diesel Engines," Paper A7, CIMAC Colloquium, Wiesbaden, 1959.

19 Alcock, J. F., and Scott, W. M., "Some More Light on Diesel Combustion," *Proc. Instn. Mech. Engrs. (A.D.)*, No. 5, 1962, pp. 179–197.

20 Zimmerman, D. R., "Laser Anemometer Measurements of the Air Motion in the Prechamber of an Automotive Diesel Engine," SAE Paper 830452, 1983.

21 Ahmad, T., Myers, J. P., and Groff, E. G., "Velocity Measurements in a Diesel Prechamber Using a Spark-Discharge Velocity Probe," submitted for presentation at the ASME Winter Annual Meeting, New Orleans, La., 1984.

# Application of the Total Transmittance Nonhomogeneous Radiation Model to Methane Combustion

**W. L. Grosshandler**
Associate Professor.
Mem. ASME

**H. D. Nguyen**
Research Assistant.

Department of Mechanical Engineering,
Washington State University,
Pullman, Wash. 99164-2920

*The total transmittance nonhomogeneous model (TTNH) is about 500 times faster than narrow-band models, and it is usually within 10 percent of the more accurate computation. The purpose of this article is to extend the TTNH model to include $CH_4$ and CO as well as $CO_2$ and $H_2O$, and to include interaction with a black boundary where previously the model had been limited to transparent boundaries. Several realistic combustion examples are presented in which the radiant intensity from a hot, black wall interacts with a nonisothermal volume containing variable concentrations of $CO_2$, $H_2O$, $CH_4$, CO, and soot. The calculations indicate that the TTNH model can be reliably applied to nonhomogeneous combustion environments containing methane and that the presence of a radiating boundary poses no computational difficulty.*

## Introduction

Almost all engineering heat transfer problems possess to a certain extent the effect of thermal radiation, and for many cases this effect may introduce a significant error if it is not taken into account properly. This is particularly true under the high-temperature conditions that usually occur in systems such as furnaces, fires, and gas turbine combustors where radiation can be the dominant mode of heat transfer.

Most of the solution techniques dealing with radiation require simplifying assumptions. The most common assumptions are grayness, homogeneity, or both. The grayness assumption is unrealistic in methane combustion where, under equilibrium adiabatic conditions, the concentrations of $H_2O$, $CO_2$, and CO in a stoichiometric mixture may be as much as 25, 10, and 10 mole percent, respectively. The radiation from these species, as well as from $CH_4$ and fuel fragments if incomplete burning occurs, is known to exhibit a strong spectral dependence. Only in heavy soot environments does it appear that the gases can be treated as gray [1, 2], in which case a closed form solution of the energy equation is attainable [3].

Homogeneity in temperature and composition characterize the well-stirred furnace model. This model yields satisfactory results for industrial furnaces [4] in which there is sufficient movement of the oxidizer and the fuel so that the temperature and concentration distributions can be approximated by single values. The usefulness of the model lies in the allowance of the application of the total emittance charts introduced by Hottel [5]; this is convenient in engineering calculations. The satisfactoriness of this assumption is also indicated in some fire situations, as discussed by Modak [6].

It is clear that solutions involving such restrictions can only cover a narrow range of the whole spectrum of practical situations. The desirability of a more general treatment is apparent in solving more realistic thermal radiation problems. To accomplish this goal, a complete specification of the spectral-dependent properties is necessary, such as through narrow-band radiation models. When this information is available, these models are most useful as a basis for comparison with other simplified models.

The problem of radiative transfer to real gases has been studied in detail, and various simplified models have been developed by numerous authors [e.g., 7–10]. One of these is the total transmittance nonhomogeneous model of Grosshandler, TTNH. He has demonstrated the applicability of the model to nonisothermal combustion gases containing $H_2O$, $CO_2$, and soot; the results from his work compared well to the narrow-band model [9, 10].

While the TTNH model has proven useful in a wide variety of combustion situations, it needs to be expanded to gas mixtures other than $CO_2$ and $H_2O$. In this paper, $CH_4$ and CO are added to the model. The required total transmittance data are generated through the program ABSORB [11], which has been expanded to include CO and $CH_4$ using the narrow-band computer code, RADCAL [10]. Additionally, the narrow-band program has been extended to encompass the 10 and 15 $\mu$m bands of $CO_2$ and the 20 $\mu$m band of $H_2O$. It is shown here that with these additions, general agreement can be achieved with published values of total transmittance for $CO_2$ and $H_2O$.

The combustion configurations analyzed with the TTNH model in previous papers [2, 10, 12] were confined to nonradiating boundaries (free jets, cold nonreflecting walls). The effect of a hot, black wall transmitting through nonisothermal mixtures of $CO_2$, $H_2O$, CO, $CH_4$, and soot is examined here under a variety of operating conditions.

## Background on Narrow-Band Model

The following discussion is restricted to the major combustion products formed from the burning of methane. These gaseous species ($H_2O$, $CO_2$, CO, and $CH_4$) have strong absorption regions as a result of vibrational transitions simultaneously occurring with thousands of rotational transitions, forming vibration-rotation bands in the infrared spectrum [13]. Those bands considered here are 1.1, 1.4, 1.9, 2.7, 6.3, and 20 $\mu$m ($H_2O$); 2.0, 2.7, 4.3, 10, and 15 $\mu$m ($CO_2$); 3.3 and 7.6 $\mu$m ($CH_4$); and 4.7 $\mu$m (CO).

The spectral absorption coefficient $k_\lambda$ quantitatively describes the interaction of the radiation field with matter. It is a simple function of the mean line intensity to spacing ratio $\bar{S}/d$ and the inverse of mean line spacing $\bar{1}/d$, both of which are complicated function of spectral wavelength, $\lambda$.

Many theoretical studies have investigated these two parameters for a number of molecules, including CO [14] and the 4.3- and 2.7-$\mu$m bands of $CO_2$ [15, 16]. For the 15-$\mu$m

Contributed by the Heat Transfer Division for publication in the JOURNAL OF HEAT TRANSFER. Manuscript received by the Heat Transfer Division October 19, 1983. Paper No. 83-HT-54.

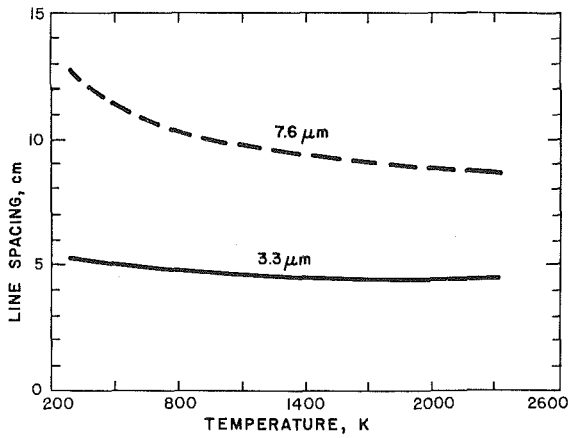


Fig. 1 Spectral line spacing for the methane molecule

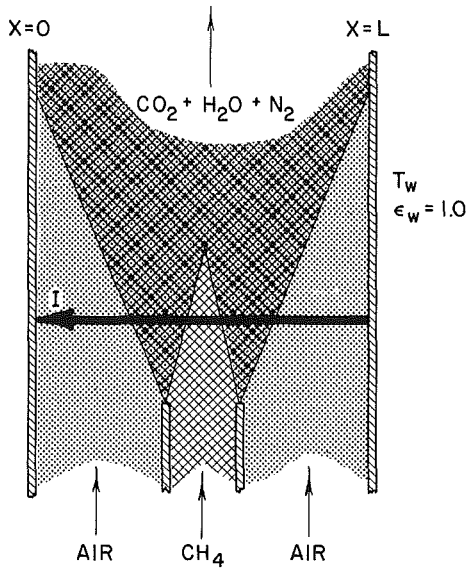


Fig. 2 Example of methane/air burner configuration

band of $CO_2$, the values of $S/d$ are available in the *Handbook of Infrared Radiation from Combustion Gases* [17]. By fitting the statistical band model to the measured total band absorptance of Edwards [18, 19], Leckner [20] obtained some approximated values for $1/d$. Much less attention has been given to the 10-$\mu$m and 2-$\mu$m bands because these combination bands are generally considered to be weak; but it is shown by Leckner that these two bands accounted for more than 10 percent of the total emission at large path length.

Much experimental work has been done on water vapor, but none has led to an adequate model. Extensive measurements made at General Dynamics [21] have been reported in the form of tables for temperature from 300 to 3000 K, and wavelengths between 1 and 22 $\mu$m, which essentially covers the whole thermal radiation spectrum. Their data are used in the narrow band RADCAL model [10].

Not many investigations have been carried out to study the nature of the line parameters of methane, probably because of the complexity of the structure of the molecule. Gray and Penner [22] applied the just-overlapping line model to derive an expression for the 3.3- and 7.6-$\mu$m bands, in which the total band absorptances of Edwards [18] were used. The values of line spacing can be calculated from the measured effective band widths published in the paper of Lee and Happel [23]. These are plotted in Fig. 1.

The line parameters discussed above vary significantly with temperature and composition, so that along a nonhomogeneous path a suitable averaging method is required. The standard method for evaluating the spectral absorption coefficient for a variable $S/d$ and $1/d$ is with the Curtis–Godson approximation [24], the application of which to RADCAL is described in [9].

The absorption coefficient of soot within the combustion volume must be handled separately, and then added to the absorption coefficient of the gas mixture. In RADCAL, it is assumed that the soot particles are small compared to the wavelength of radiation, and that the complex refractive index of soot is independent of wavelength. Under these conditions, electromagnetic theory predicts the spectral absorption coefficient to be inversely proportional to wavelength, and scattering to be negligible [13].

The change in spectral intensity of radiation along a given direction through a cloud of combustion products, such as that sketched in Fig. 2, is given by the equation of transfer. Its solution can be shown to be of the following form [13]:

$$I_\lambda(0) = I_\lambda(L)\exp\left(-\int_0^L \sum_i \rho_i k_{\lambda,i} dx^*\right) + \int_0^L \sum_i \rho_i k_{\lambda,i} I_{b\lambda}\left[\exp\left(-\int_{x^*}^L \sum_i \rho_i k_{\lambda,i} dx^{**}\right)\right] dx \quad (1)$$

where $I_{b\lambda}$ is Planck's function, $\rho$ is the density of $i$th radiating gas or soot cloud, and scattering has been assumed to be negligible.

Generally, the radiance from the boundary $I(L)$ includes the emitted energy of the wall itself and the reflected incoming energy from the gases to the wall. To simplify the analysis, the boundary will be assumed black so that all the incoming energy to the wall is absorbed; none of it is reflected. Many of the refractory materials do not satisfy this assumption, but the emissivity of a furnace interior is not usually known, mainly due to the effects of surface contamination. Dark

## Nomenclature

$C$ = temperature gradient correction factor
$d$ = spectral line spacing, cm
$\overline{1/d}$ = mean strong-line parameter, $cm^{-1}$
$I$ = intensity, $kW/m^2$-sr
$I_{b\lambda}$ = Planck's blackbody intensity, $kW/m^2$-sr-$\mu$m
$k_\lambda$ = spectral absorption coefficient, $m^2/kg$
$L$ = total path length, m
$l_j$ = path length of element 1 up to and including element $j$, m
$M$ = number of spectral intervals
$N$ = number of homogeneous elements
$\bar{P}$ = effective pressure, atm
$\overline{S/d}$ = mean line-strength-to-spacing parameter, $m^2/kg$
$T$ = temperature, K
$\bar{T}$ = effective temperature, K
$x$ = local pathlength, m
$\lambda$ = wavelength, $\mu$m
$\rho$ = density, $kg/m^3$
$\sigma$ = Stefan–Boltzmann constant
$\tau$ = transmittance

**Subscripts**

$i$ = pertaining to species $i$
$j$ = summation index for homogeneous elements
$k$ = summation index for spectral interval
$s$ = pertaining to soot
$w$ = pertaining to the wall
$\lambda$ = spectral quantity

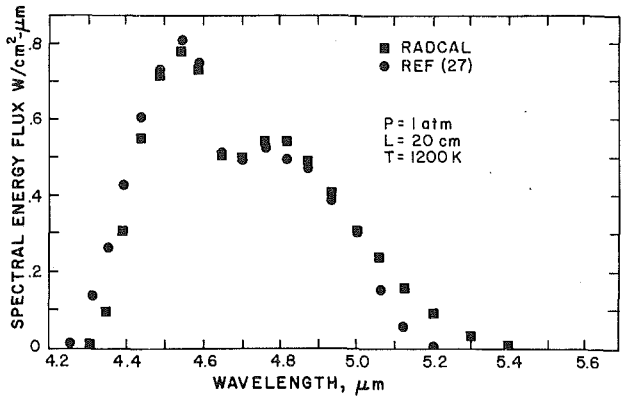


Fig. 3 Spectral energy flux of the 4.7 $\mu$m of carbon monoxide, comparing the narrow-band model to the results of Abu-Romia and Tien [27]

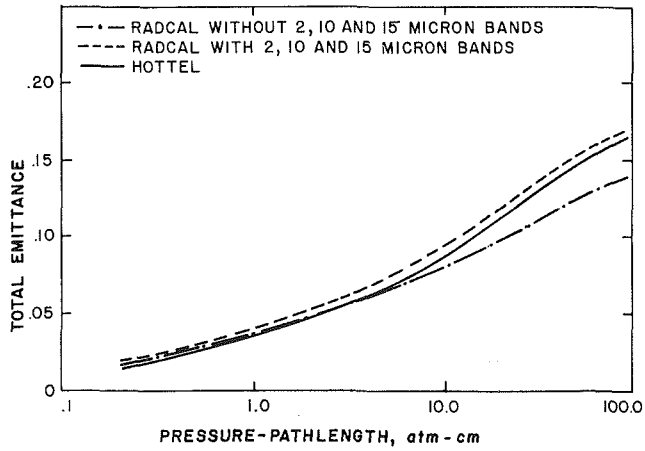


Fig. 4 Total emittance of carbon dioxide at 1500 K and a partial pressure of 0.2 atm, showing the effect of the 2-, 10-, and 15-$\mu$m bands on the narrow-band result. Comparison is to the curve-fit of Hottel's data [5].

chrome refractory brick has very high emissivity even at high temperatures [25], and therefore the results from this study can be applied directly to such material. With this assumption, the emerging intensity is

$$I_\lambda(0) = I_{b\lambda,w}\tau_\lambda(L) - \int_0^{\tau_{y(L)}} I_{b\lambda}(\tau,\lambda)d\tau_\lambda \tag{2}$$

where the spectral transmittance $\tau_\lambda$ is defined by the equation

$$\tau_\lambda(x) = \exp\left(-\int_0^x \sum_i \rho_i k_{\lambda,i} dx^*\right) \tag{3}$$

and the $w$ subscript refers to the wall condition.

In nonhomogeneous systems, the path along $x$ can be approximated by a series of discrete homogeneous elements, so that each element can be characterized by a single temperature and a single concentration for each species; hence the integration over the path can be broken down to a summation over $N$ homogeneous elements:

$$I_\lambda(0) = I_{b\lambda,w}\tau_{\lambda,N} + \sum_{j=1}^{N} I_{b\lambda,j-1}(\tau_{\lambda,j-1} - \tau_{\lambda,j}) \tag{4}$$

where $\tau_{\lambda,j}$ is the spectral transmissivity of the participating medium in element 1 up to and including element $j$, and $I_{b\lambda,j}$ is the blackbody intensity function evaluated at the temperature of the $j$th element.

If a sensor is placed opposite to the wall at $x=0$, the total radiant flux reaching the sensor can be found by integrating

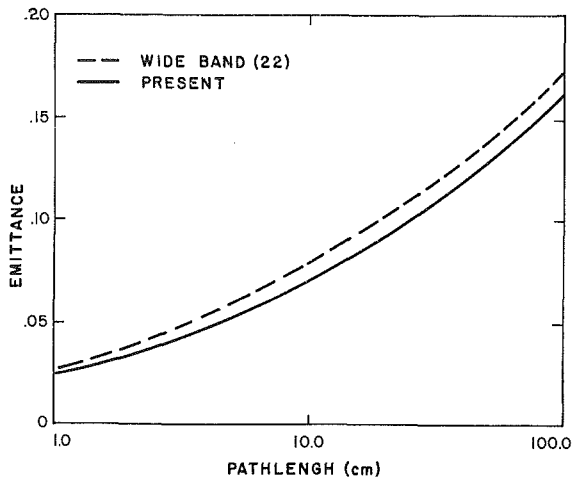


Fig. 5 Total emittance of methane at 500 K, 1 atm, comparing the present narrow-band model to the wide-band model of Lee and Happel [23]

equation (4) over the wavelength from zero to infinity. This integration can also be represented by a summation:

$$I(0) = \sum_{k=1}^{M} \tau_{k,N} I_{b\lambda}(T_w,\lambda_k)\Delta_k - \sum_{k=1}^{M}\sum_{j=1}^{N} I_{b\lambda,j}(\tau_{k,j-1} - \tau_{k,j})\Delta\lambda_k \tag{5}$$

Each of the $M$ spectral intervals $\Delta\lambda_k$ is chosen such that it is small enough to insure the Planck function does not vary significantly within it. The program RADCAL has been written to perform this numerical integration. (A listing can be found in [26]).

Validation of the narrow-band numerical model has been done previously for $CO_2$ and $H_2O$ up to a wavelength of 10 $\mu$m [9, 10]. Figure 3 is an example of a recent calculation made for CO, comparing RADCAL to the work of Abu-Romia and Tien [27]. Additional calculations for the 20-$\mu$m band of water, the 10- and 15-$\mu$m bands of $CO_2$, and the 3.3- and 7.6-$\mu$m bands of methane are discussed elsewhere [26]. Comparisons between the numerical calculations and published experimental measurements indicate that the narrow-band model can be trusted to predict the correct spectral intensity from arbitrary mixtures of CO, $CH_4$, $CO_2$, and $H_2O$.

An additional test for the narrow-band model is the prediction of total emittance from the numerical integration of monochromatic results. The addition of the 2.0, 10, and 15-$\mu$m wavelength bands to the carbon dioxide model improves the accuracy to an acceptable level when compared to the emittance results of Hottel [5], as seen in Fig. 4. Figure 5 shows the total emittance for atmospheric pressure methane and the results from the wide-band model based on experimental measurements [23]. The results for carbon monoxide, based solely on the fundamental band, slightly under predict the published results of Ludwig et al. [17], as shown in the report of Nguyen [26]. A comparison of the total emittance of water vapor calculated by RADCAL, including the 20-$\mu$m rotational band, to the experimental results of others is also given in [26].

## Formulation of TTNH Model

Following the development of Grosshandler [9], equation (4) can be integrated over wavelength to obtain the total intensity. Then, using the fact that the integral of the sum is the

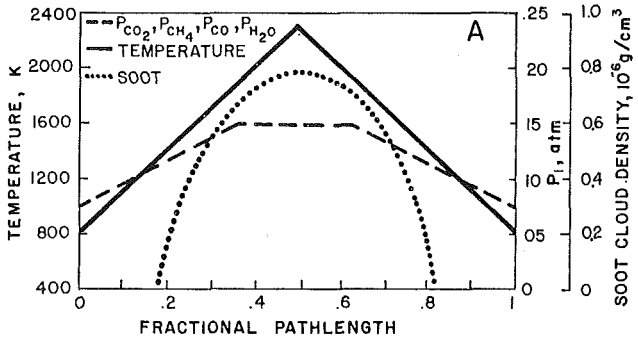


Fig. 6 Temperature, soot, and composition profiles in configuration A

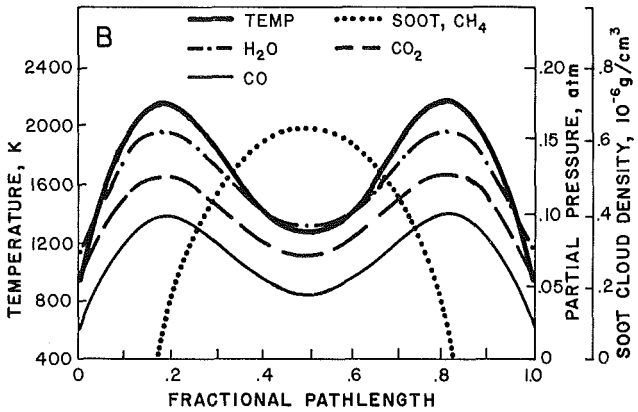


Fig. 7 Temperature, soot, and composition profiles in configuration B

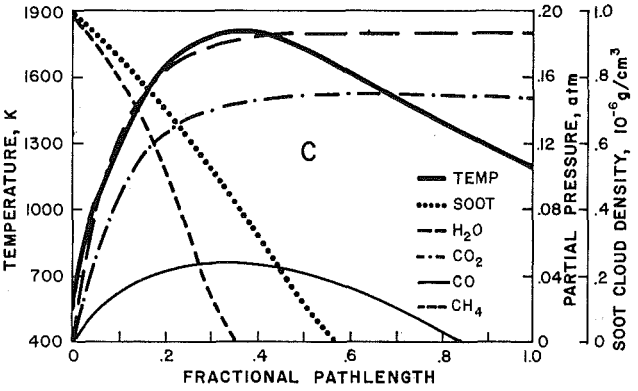


Fig. 8 Temperature, soot, and composition profiles in configuration C

sum of the integrals, an expression equivalent to equation (5) can be written.

$$I_\lambda(0) = \int_0^\infty I_{b\lambda,w}\tau_{\lambda,N}d\lambda + \sum_{j=1}^{N}\int_0^\infty I_{b\lambda,j}(\tau_{\lambda,j-1} - \tau_{\lambda,j})d\lambda \qquad (6)$$

For a homogeneous path, the temperature and pressure are constant, and the total transmittance can be defined as the spectral transmittance weighted with Planck's function. Such a definition is not suitable, however, for a nonhomogeneous path because of the variations of temperature and pressure along the path. Even if the temperature and density of the participating species are known and can be approximated by a simple function, general analytical forms for the transmittance are not possible. Grosshandler [9] has shown that with some appropriately averaged temperature and partial pressures of active gases along a nonhomogeneous path, equation (6) can be rewritten as follows:

$$I(0) = \frac{\sigma T_w^4}{\pi}\tau_N(\bar{T}_N,\bar{P}_N,L)C_N + \sum_{j=1}^{N}\frac{\sigma T_j^4}{\pi}[C_{j-1}\tau_{j-1}(\bar{T}_{j-1},\bar{P}_{j-1},l_{j-1}) - C_j\tau_j(\bar{T}_j,\bar{P}_j,l_j)] \qquad (7)$$

where $C_j$ is a correction factor dependent upon the temperature gradient and the pressure path length of radiating species. $\bar{T}$ and $\bar{P}$ denote the effective temperature and pressure, which are nothing more than the actual properties averaged over the total number density of the radiating molecules [9].

To account for the presence of soot, equation (7) is modified to

$$I(0) = \frac{\sigma T_w^4}{\pi}\tau_{s,N}\tau_N(\bar{T}_N,\bar{P}_N,L)C_N + \sum_{j=1}^{N}\frac{\sigma T_j^4}{\pi}[\tau_{s,j-1}C_{j-1}\tau_{j-1}(\bar{T}_{j-1},\bar{P}_{j-1},l_{j-1}) - \tau_{s,j}C_j\tau_j(\bar{T}_j,\bar{P}_j,l_j)] \qquad (8)$$

The total soot transmittance $\tau_s$ is separated out from the total gas transmittance, since the former is a function of local conditions only.

TTNH is a computer code written to solve equation (8). It is necessary to specify the local values of temperature, partial pressure, and soot density as a function of path length. A data base giving the total transmittance of the various combustion gases is required. The program ABSORB, written by Modak [11] and extended in this work, is the most convenient form for this data base. It is applicable to atmospheric pressure systems containing $CO_2$, $H_2O$, CO, $CH_4$, and soot for pressure-path lengths of radiating species up to 1 atm-m, and has been used for nonhomogeneous computations in the past [2].

## Performance of the TTNH Model

To gain confidence in the model's soundness, TTNH has been tested against the narrow-band model. Three typical combustion systems were brought into the investigation in which symmetric and asymmetric temperature and concentration profiles were assumed. These systems are shown in Figs. 6-8. For computational purposes, the path length in each case is divided into 20 discrete homogeneous elements, and the representative parameters are selected at the midpoint of the elements. The total path length is varied over a factor of 25 for each given profile. In all three configurations, a black wall is located at the extreme right of the figure and its temperature is the same as that of the gas at that point. Table 1 gives the specific values of temperature and partial pressures for the calculations done here.

Figures 6 and 7 represent a two-dimensional flow situation where methane gas is injected along the centerline below a duct as air is axially blown through, such as is depicted in Fig. 2. The temperature and concentration profiles are symmetrically distributed about the center, single-peaked in configuration A (Fig. 6) and double-peaked in configuration B (Fig. 7). In configuration A, the temperature peak coincides with the maximum soot level.

Configuration C in Fig. 8 is an example of a methane fire impinging on a hot surface viewed from below. Methane is at the base, and the combustion products are convected upward. The temperature increases sharply within the flame, but then decreases due to entrainment of a cool environment.

The narrow-band model applied to configuration A over a one meter path length yields a radiance of 144.7 kW/m$^2$-sr.

**Table 1 Temperature and partial pressure profiles through simulated combustion clouds**

| Fractional path length | $T,K$ | Partial pressures, atm $CO_2$ | $H_2O$ | CO | $CH_4$ | Soot cloud density $\times 10^6$ |
|---|---|---|---|---|---|---|
| | | | (Configuration A) | | | |
| 0 –.05 | 875 | .08 | .08 | .08 | .08 | 0 |
| .05–.10 | 1025 | .09 | .09 | .09 | .09 | 0 |
| .10–.15 | 1175 | .10 | .10 | .10 | .10 | 0 |
| .15–.20 | 1325 | .11 | .11 | .11 | .11 | .05 |
| .20–.25 | 1475 | .12 | .12 | .12 | .12 | .30 |
| .25–.30 | 1625 | .13 | .13 | .13 | .13 | .50 |
| .30–.35 | 1775 | .14 | .14 | .14 | .14 | .60 |
| .35–.40 | 1925 | .15 | .15 | .15 | .15 | .70 |
| .40–.45 | 2075 | .15 | .15 | .15 | .15 | .75 |
| .45–.50 | 2225 | .15 | .15 | .15 | .15 | .78 |
| wall | 800 | – | – | – | – | – |
| | | | (Configuration B) | | | |
| 0 –.05 | 1300 | .07 | .08 | .04 | 0 | 0 |
| .05–.10 | 1750 | .10 | .12 | .07 | 0 | 0 |
| .10–.15 | 2000 | .12 | .14 | .09 | 0 | 0 |
| .15–.20 | 2200 | .125 | .15 | .10 | .01 | .05 |
| .20–.25 | 2100 | .12 | .15 | .09 | .07 | .25 |
| .25–.30 | 2000 | .115 | .14 | .08 | .10 | .40 |
| .30–.35 | 1800 | .105 | .13 | .075 | .12 | .47 |
| .35–.40 | 1550 | .09 | .11 | .065 | .14 | .55 |
| .40–.45 | 1400 | .08 | .095 | .05 | .15 | .60 |
| .45–.50 | 1350 | .075 | .09 | .04 | .155 | .63 |
| wall | 900 | – | – | – | – | – |
| | | | (Configuration C) | | | |
| 0 –.05 | 750 | .02 | .05 | .01 | .19 | .95 |
| .05–.10 | 1100 | .07 | .10 | .025 | .17 | .90 |
| .10–.15 | 1450 | .10 | .14 | .035 | .14 | .83 |
| .15–.20 | 1600 | .12 | .16 | .04 | .12 | .75 |
| .20–.25 | 1700 | .13 | .175 | .048 | .08 | .64 |
| .25–.30 | 1770 | .14 | .18 | .05 | .05 | .55 |
| .30–.35 | 1800 | .144 | .184 | .05 | .015 | .46 |
| .35–.40 | 1820 | .148 | .188 | .05 | 0 | .36 |
| .40–.45 | 1800 | .15 | .19 | .048 | 0 | .26 |
| .45–.50 | 1760 | .15 | .19 | .045 | 0 | .15 |
| .50–.55 | 1720 | .15 | .19 | .04 | 0 | .05 |
| .55–.60 | 1640 | .15 | .19 | .035 | 0 | 0 |
| .60–.65 | 1590 | .15 | .19 | .03 | 0 | 0 |
| .65–.70 | 1530 | .15 | .19 | .024 | 0 | 0 |
| .70–.75 | 1460 | .15 | .19 | .018 | 0 | 0 |
| .75–.80 | 1420 | .15 | .19 | .012 | 0 | 0 |
| .80–.85 | 1380 | .15 | .19 | .004 | 0 | 0 |
| .85–.90 | 1320 | .15 | .19 | 0 | 0 | 0 |
| .90–.95 | 1270 | .15 | .19 | 0 | 0 | 0 |
| .95–1.00 | 1230 | .15 | .19 | 0 | 0 | 0 |
| wall | 1200 | – | – | – | – | – |

**Table 2 Comparison of total radiance calculations**

| Configuration | Path length, m | Total radiance, kW/m$^2$-sr TTNH | narrow-band | Deviation % |
|---|---|---|---|---|
| A | 0.2 | 52.6 | 52.5 | +0.2 |
| | 1.0 | 137.6 | 144.7 | −4.9 |
| | 5.0 | 162.9 | 170.2 | −4.3 |
| B | 0.2 | 39.9 | 38.6 | +3.4 |
| | 1.0 | 94.6 | 94.6 | 0.0 |
| | 2.0 | 128.9 | 131.5 | −2.0 |
| | 5.0 | 185.1 | 190.1 | −2.6 |
| C | 0.2 | 50.0 | 57.3 | −12.7 |
| | 1.0 | 68.5 | 70.9 | −3.4 |
| | 5.0 | 53.9 | 54.0 | −0.2 |

By comparison, the TTNH model predicts 137.6 kW/m$^2$-sr, which is less than 5 percent low. To ensure that the grid size chosen (0.05 m) is sufficiently accurate, the TTNH calculation was repeated using 10 homogeneous elements (0.10 m each) and five homogeneous elements (0.20 m each). In the former case, the radiance was less than 2 percent below the base line calculation using 20 homogeneous elements. With only five divisions of the path length, the discrepancy increased to almost 6 percent. All additional calculations with either the narrow-band model or TTNH have been made with 20 elements, regardless of path length.

The one meter path length of configuration A was multiplied by a factor of five and divided by a factor of five to determine if the total transmittance model could properly scale the radiation. With $L = 0.20$ m, the predicted intensity droped to 52.6 kW/m$^2$-sr, or 0.2 percent below the narrow-band calculation. For the 5.0-m path, the intensity increased about 18 percent over the 1.0-m path, which is 4.3 percent below the prediction of the narrow-band model.

The comparison between the two models is equally accurate for configuration B, the double-peaked profile. Table 2 summarizes the results of these calculations for $L$ equal to .20, 1.0, 2.0, and 5.0 m for configuration B (as well as for A and C). The maximum disagreement occurs for the shortest path length, in which the simplified model overpredicts the intensity by 3.4 percent.

The simulated fire, configuration C, is the most revealing case. The TTNH model has difficulty with the .20-m path length, missing the narrow-band prediction by 12.7 percent. However, the total transmittance model shows its worth by accurately predicting the downturn in radiant intensity when the scale of the fire is increased from 2.0 to 5.0 m. This type of scaling cannot be done when the combustion system is approximated as gray or isothermal, since the temperature and composition profiles are unchanged over the 25-fold increase in path length. It is apparent from the behavior of the radiance with path length that two factors influence the magnitude which is fed back to the base of the fire: the shielding effect of the soot and methane and the increased optical depth of the high temperature region. The first acts to reduce the intensity while the second effect enhances it. The importance of accounting for nonhomogeneities effects is obvious here.

The calculations in Table 2 show that the TTNH model performs satisfactorily for mixtures which contain $CH_4$ and CO along with soot, $CO_2$, and $H_2O$. The model can also handle the presence of a hot black wall. In fact, it is evident that the wall will improve the model because of the lessened importance of banded radiation. The accuracy to be expected in general situations is 10 percent or better. This is adequate for most engineering calculations since the convected heat must also be considered in a complete energy balance.

What is equally important with accuracy is the speed at which the simplified model can compute the radiant intensity. The TTNH computation was between 400 and 600 times faster than the narrow-band model, RADCAL, in all of the cases tested. A typical calculation took less than 1.2 s of central processor time on a PRIME 400 minicomputer, or about 60 ms of CPU per homogeneous element. Thus the TTNH model gives the heat transfer designer the ability to quantitatively predict the effect of scaling-up a combustion facility without an undue computational time devoted to radiation, leaving more room for the complexities associated with reacting turbulent flows.

## Summary and Conclusions

Radiation in combustion systems containing methane gas has been analyzed by the total transmittance nonhomogeneous model. The following limitations are suggested to maximize accuracy: (*a*) the ratio of temperatures in adjacent regions should not exceed 3 to 1; (*b*) the total pressure of the system should not exceed 10 atm; and (*c*) the temperature should be higher than 300 K and less than 2500 K. Comparison of the predictions of the simple TTNH model and the narrowband model indicates good agreement for all of the cases examined in this study. The success of these calculations reveals two important features:

1 Besides $CO_2$, $H_2O$, and soot, which previous studies have investigated, the TTNH model is able to handle CO and $CH_4$ together with the presence of a hot black wall.

2 Complex combustion problems in which nongray and nonhomogeneous assumptions are relaxed can be analyzed by a simple method with less computation. Results are reliable for realistic combustion environments.

## Acknowledgment

This research has been performed with the support of the National Science Foundation, grant number MEA 8101953. The significant contribution of Mr. Paul Lebovitz to the revising of the computer code is acknowledged. The Mechanical Engineering Department of Washington State University has provided the use of its computer facilities and staff.

## References

1 Buckius, R. O., and Tien, C. L., "Infrared Flame Radiation," *International Journal of Heat and Mass Transfer*, Vol. 20, 1977, pp. 93–106.

2 Grosshandler, W. L., and Modak, A. T., "Radiation From Nonhomogeneous Combustion Products," *18th Symposium (Int'l) on Combustion*, The Combustion Institute, 1981, pp. 601–609.

3 Felske, J. D., and Tien, C. L., "Calculation of the Emissivity of Luminous Flame," *Comb. Sci. and Tech.*, Vol. 17, 1973, pp. 25–31.

4 Beer, J. M., *Combustion Technology—Some Modern Developments*, ch. VII, edited by H. B. Palmer and J. M. Beer, Academic Press, 1974.

5 Hottel, H. C., *Heat Transmission*, edited by W. M. McAdams (3d ed.), McGraw-Hill, New York, 1954.

6 Modak, A. T., "The Burning of Large Pool Fires," Western States Section/The Combustion Institute, Oct. 1979.

7 Edwards, D. K., Glassen, L. K., Hauser, W. C., and Tuchscher, J. S., "Radiation Heat Transfer in Nonisothermal Nongray Gases," JOURNAL OF HEAT TRANSFER, Vol. 86, 1967, pp. 219–229.

8 Felske, J. D., and Tien, C. L., "Infrared Radiation From Nonhomogeneous Gas Mixtures Having Overlapping Bands," *J. Quant. Spec. Rad. Transfer*, Vol. 14, 1974, pp. 35–48.

9 Grosshandler, W. L., "Radiative Heat Transfer in Nonhomogeneous Gases: A Simplified Approach," *International Journal of Heat and Mass Transfer*, Vol. 23, 1980, pp. 1147–1459.

10 Grosshandler, W. L., "Radiation From Nonhomogeneous Fires," FMRC J. I. OAOE6. BU-4, RC 79-BT-9, Factory Mutual Research Corp., Norwood, Ma., Sept. 1979.

11 Modak, A. T., "Radiation from Products of Combustion," *Fire Research*, Vol. 1, 1979, pp. 339–361.

12 Grosshandler, W. L., "Radiation From Non-Homogeneous Mixtures in Planar and Cylindrical Combustion Systems," Paper No. 80-HT-43, ASME/AIChE National Heat Transfer Conference, Orlando, Fla., July 1980.

13 Siegel, R., and Howell, J. R., *Thermal Radiation Heat Transfer*, McGraw-Hill, 1981.

14 Malkmus, W., and Thomson, A., "Infrared Emissivity of Diatomic Gases for the Anharmonic Vibrating-Rotator Model," *J. Quant. Spectrosc. Radiat. Transfer*, Vol. 2, 1961, pp. 17–39.

15 Malkmus, W., "Infrared Emissivity of Carbon Dioxide (4.3-micron band)," *J. Optical Soc. America*, Vol. 53, 1963, pp. 951–961.

16 Malkmus, W., "Infrared Emissivity of Carbon Dioxide (2.7-micron band)," General Dynamics/Astronautics AE63-0047, 1963.

17 Ludwig, C. B., Malkmus, W., Reardon, J. E., and Thompson, J. A., *Handbook of Infrared Radiation From Combustion Gases*, NASA SP-3080, 1973.

18 Edwards, D. K., and Menard, W. A., "Correlation For Absorption By Methane and Carbon Dioxide Gases," *Applied Optics*, Vol. 3, 1964, pp. 847–852.

19 Edwards, D. K., "Absorption by Infrared Bands of Carbon Dioxide Gas At Elevated Pressure and Temperature," *J. Optical Soc. America*, Vol. 50, 1960, pp. 617–626.

20 Leckner, B., "The Spectral and Total Emissivity of Carbon Dioxide," *Combustion and Flame*, Vol. 17, 1971, pp. 37–44.

21 Ferriso, C. C., Ludwig, C. B., and Thomson, A. L., "Empirically Determined Infrared Absorption Coefficients of $H_2O$ from 300 to 3000K," *J. Quant. Spectros. Radiat. Transfer*, Vol. 6, 1966, pp. 241–273.

22 Gray, L. D., and Penner, S. S., "Approximate Band Absorption Calculations for Methane," *J. Quant. Spectrosc. Radiat. Transfer*, Vol. 5, 1965, p. 611.

23 Lee, R. H. C., and Happel, J., "Thermal Radiation of Methane Gas," *Ind. Eng. Chem. Fundamentals*, Vol. 3, 1964, pp. 167–176.

24 Goody, R. M., *Atmospheric Radiation I, Theoretical Basis*, Oxford University Press, 1964.

25 Singham, J. R., "Tables of Emissivity of Surfaces," *International Journal of Heat and Mass Transfer*, Vol. 5, 1962, pp. 67–76.

26 Nguyen, H., "Application of the Total Transmittance Radiation Model to Methane Combustion," special project report, Master of Science, Department of Mechanical Engineering, Washington State University, Pullman, Wa., 1983.

27 Abu-Romia, M. M., and Tien, C. L., "Measurements and Correlations of Infrared Radiation of Carbon Monoxide at Elevated Temperatures," *J. Quant. Spect. Radiat. Trans.* No. 6, 1966, pp. 143–167.

# Melting Around a Migrating Heat Source

**M. K. Moallemi**

**R. Viskanta**
Fellow ASME

Heat Transfer Laboratory,
School of Mechanical Engineering,
Purdue University,
West Lafayette, Ind. 47907

*The problem of melting around a moving heat source arises in many different situations such as nuclear reactor technology (i.e., "self-burial" process of nuclear waste materials and reactor core "melt-down"), process metallurgy, and geophysics. Experiments were undertaken with a horizontal cylindrical heat source that melted its way through a phase-change material (n-octadecane) under its own weight. The heat source velocity and solid–liquid interface motion for a constant surface temperature source were measured. Effects of heat source density and surface temperature as well as the effects of the initial subcooling of the solid were investigated and are reported. The flow structure in the melt was visualized using a dye. Timewise variation of temperature distribution in the solid and the melt were also measured and are discussed. Results for the heat source migration velocity and the volume of the material melted are correlated in terms of the relevant problem parameters.*

## 1 Introduction

The problem of melting in the vicinity of a moving heat source arises in many different situations in the areas of materials processing [1], spacecraft and nuclear technology [2], and geophysics [3, 4]. Particularly, in the field of nuclear technology, this problem has two important applications: (*i*) "self-burial" process in a nuclear waste disposal scheme [5], and (*ii*) reactor core "melt-down" problem [6].

If a source releases heat in excess of a certain minimum than its surroundings can conduct, the surroundings will eventually melt and the heat source will start moving in the liquid melt in the direction of the net force (gravitational, buoyancy, shear forces, etc.) exerted on it. The problem considered here is a combination of two important classes of heat transfer problems, those involving phase change and those with a moving heat source. The combination of these two phenomena introduce processes that do not exist in either case, such as: (*i*) development of a film flow field between the heat source and the solid due to motion of the heat source; (*ii*) development of a mixed convection field in the melt; and (*iii*) resolidification of the melt after passage of the heat source.

None of these processes have received attention in the limited number of studies reported in the literature. Regardless of the fact that the published analytical works are approximate, they are not based on realistic physical models of the processes involved. Important processes such as phase change [7, 8] and natural and forced convection [9–11] have been neglected. Less important processes such as resolidification of the melt have also been ignored. A more realistic model has been recently suggested [12]. The migration velocity of a hot rigid sphere that melts its way through a solid was calculated. The processes that occur in the molten wake behind the sphere are ignored and solution is only valid as long as the hot sphere and the solid are separated by a very thin melt layer. Experimental work is even more scarce [8, 13, 14] and can be viewed as feasibility or assessment rather than phenomenological or parametric studies.

The objective of this investigation is to report on the heat transfer processes during melting around a moving heat source and the extent and range of their effects. Experiments have been performed by employing a horizontal cylindrical heat source with constant surface temperature which melted its way through the phase-change material and descended under its own weight. The phase-change material used in the experiments was research grade (99.9 percent pure) n-octadecane paraffin as its liquid phase is transparent and permits flow visualization. Its properties are well documented, and its fusion temperature is close to room temperature (27.5°C), which is conducive to experimentation.

The work included two groups of experiments. In the first group the heat source was initially placed on top of the solid. A supplementary set of experiments was performed in which the heat source was initially embedded in the solid matrix. In addition to this, three other parameters were varied during the course of the study: namely, the surface temperature of the heat source, the initial temperature of the solid, and the apparent weight of the heat source. The paper includes measurements and/or observations of the heat source velocity, the shape and motion of the solid–liquid interface and the characteristics of the temperature and the flow fields in the melt.

## 2 Experiments

**2.1 Apparatus and Instrumentation.** The experiments were performed in a container having a rectangular cross section of 35.5 × 7.5 cm and 25.5 cm depth. The test cell consisted of a main U-shaped aluminum frame, 7.4 cm thick (Figs. 1(*a*) and 1(*b*)). The front and back sides of the cell were made of 0.6-cm-thick glass plate to allow flow visualization and photographing. To insure two dimensionality, a second glass plate was installed on each side, parallel to the first one, to reduce the natural convection and overall heat transfer between the test cell and the ambient environment. The top of the test cell was closed before and during the experiments with a plexiglass cover plate. Two parallel bushings fixed to the plexiglass cover plate guided the heat source support tubes (6.5 mm OD and 254 mm long) in the vertical direction and prevented the heat source from tilting or rotating during its migration (Fig. 1).

The apparent weight of the heat source (the net force exerted by the heat source to the melt and/or solid) is one of the governing parameters of the problem and provisions were made to change and control it. The apparent weight was increased by adding weight to the support tubes and was decreased by adding counter balance weight (by using a pair of pulleys).

In order to control the solid temperature, a U-shaped multipass heat exchanger was placed inside the test cell before pouring in the liquid phase change material (Fig. 1). The heat

Contributed by the Heat Transfer Division for publication in the JOURNAL OF HEAT TRANSFER. Manuscript received by the Heat Transfer Division March 28, 1984. Paper No. 84-HT-11.

exchanger was connected to a constant temperature bath for several hours before and also during the experiments. To obtain the temperature distribution in the solid before and during the test (for experiments with a subcooled solid), a total of 16 thermocouples were placed at fixed positions in the test cell before pouring the liquid into the cell. The temperature distribution in the melt is measured by 5 thermocouples installed on a T-shaped probe, which was placed in the melt after passage of the heat source.

A cylindrical ($L/R = 6$) heat source made from copper was designed and built to provide constant surface temperature (Fig. 2). It consisted of a central cylinder on which a double spiral (3.8 × 3.8 mm cross section) was cut and was tightly fitted in a 4.55 mm thick cylindrical shell (25.4 mm OD). Two groves machined on the end faces of the central cylinder connected the two spiral channels formed between the outer shell and the central cylinder. Two end caps (1.5 mm thick and 25.4 mm diameter) were used to complete the fluid path. Thermostated fluid entered the heat source via one of the support tubes and left from the other one after going through the two spiral channels which are connected at the ends.

A total of seven thermocouples were installed on the source surface (at $L/4$ and $\phi = 0$, 90, 180, and 270 deg and at $L/2$ and $\phi = 0$, 90, and 270 deg) to check for the temperature uniformity. The thermocouple wires that pass through small holes drilled in the outer shell were passed through one of the support tubes to prevent their interference with the flow field in the melt.

The heat source was tested under homogeneous external thermal conditions and proved to provide constant surface temperature in range of 30°C to 60°C with ±0.2°C maximum fluctuations (measured uncertainty was also ± 0.2°C). Thus, the 4.55 mm thick copper wall of the outer shell was enough to provide for a constant surface temperature under uniform external conditions. However, under actual test conditions, some temperature drop is expected in the region where heat transfer is highly nonuniform (i.e., around the lower stagnation point where most of the melting takes place). Careful attention was paid to the design of the heat source, and tests reported in the paper are limited to those which do not exceed a maximum temperature difference of more than 2°C on the heat source surface.

The copper-constantan thermocouples on the heat source throughout the solid, and the ones placed in the melt pool were connected to an Esterline Angus (Model PD-2064) programmable data acquisition system for temperature measurement. The data acquisition system is equipped with printer and option to provide for thermocouple linearization and cold junction compensation. The system has an overall accuracy of ± 0.5°C, which was improved to ± 0.2°C (with 90 percent confidence) by calibration. The relative position of the center of the heat source was measured (at the same times that temperatures were being measured) with a cathetometer with 0.05 mm resolution.

**2.2 Experimental Procedure.** The preparation for an experiment always began with the degasification of the paraffin, to prevent void formation during freezing. The paraffin was first heated in a vacuum flask well above its fusion temperature (to about 150°C). The flask was then connected to a vacuum pump while being cooled very slowly to about 30°C (2°C above the fusion temperature). The paraffin was then syphoned into the test cell. A constant temperature bath set at 10°C was then connected to the U-shaped heat exchanger to facilitate the freezing process.

During the freezing process, formation of internal voids, associated with the contraction which accompanies freezing, was avoided by preventing the formation of a frozen crust at the upper surface of the paraffin while the liquid phase still existed underneath. This was accomplished by a freezing pattern that proceeded from the bottom up. Degasified liquid was added several times during the freezing process to compensate for the contraction and the top surface was also leveled at the end.

Three different heat source surface temperatures (32°C, 36°C, and 40°C) were employed by circulating water in the heat source from a second constant temperature bath. The thermostat for this bath was set at 0.5 to 1.0°C above the desired temperature to compensate for the temperature drop across the heat source wall and also in the supply tubes. A colored wax, commercially used for making colored candles, was used to visualize the flow structure in the melt pool above the heat source. The wax was introduced very slowly and carefully in small quantities by a syringe about midway between the front glass wall and the first support tube. The composition of the wax was not known, but was slightly denser than n-octadecane, thus it was diluted at a ratio of 1 to 5.

## 3 Analysis

An approximate analytical solution for the temperature and the flow field under the heat source is presented here, and steady-state velocity of the heat source is determined. The intent of the analysis is only to determine the relevant problem parameters that could be used to scale the data, particularly

## Nomenclature

$c_p$ = specific heat
Fo = Fourier number, $\alpha t/R^2$
$g$ = gravitational acceleration
$h_m$ = latent heat of fusion
$h_m^*$ = reduced latent heat of fusion, $h_m^* = h_m + c_p\,(T_m - T_\infty)$
$k$ = thermal conductivity
$L$ = length of the heat source
$M$ = mass of the heat source
$P$ = pressure
$P_0$ = reference pressure
$q''$ = heat flux of the heat source
$Q$ = heat loss from the lower half of the heat source
Re = Reynolds number, $\rho_f U_0 R/\mu$
$R$ = radius of the heat source
Ste = Stefan number, $c_p(T_w - T_m)/h_m^*$
$t$ = time
$T$ = temperature
$T_\infty$ = initial solid temperature
$u$ = tangential velocity
$U_0$ = velocity of the heat source
$U_0^*$ = dimensionless heat source velocity, $U_0 R/\alpha$
$v$ = normal velocity
$V_0$ = volume of the heat source, $\pi R^2 L$
$V_D$ = volume of the directly melted solid
$V_T$ = total (net) volume
$x$ = distance tangential to the heat source, see Fig. 3
$y$ = distance normal to the heat source, see Fig. 3
$\alpha$ = thermal diffusivity of melt
$\delta$ = molten layer thickness
$\Delta$ = dimensionless molten layer thickness, $\delta/R$
$\Delta\rho$ = density difference between the heat source and melt
$\mu$ = dynamic viscosity of melt
$\nu$ = kinematic viscosity of melt
$\rho_f$ = density of melt
$\rho_H$ = density of the heat source
$\tau$ = shear stress
$\phi$ = angular position, see Fig. 3

**Subscripts**

$f$ = liquid state
$m$ = fusion point of PCM
$s$ = solid state
$w$ = heat source surface

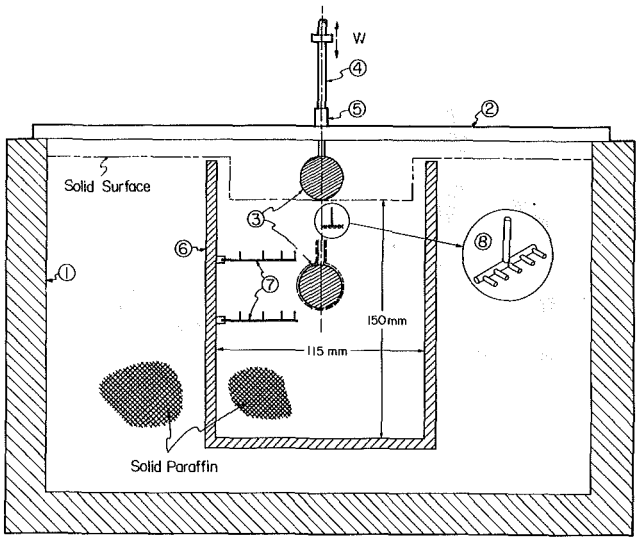


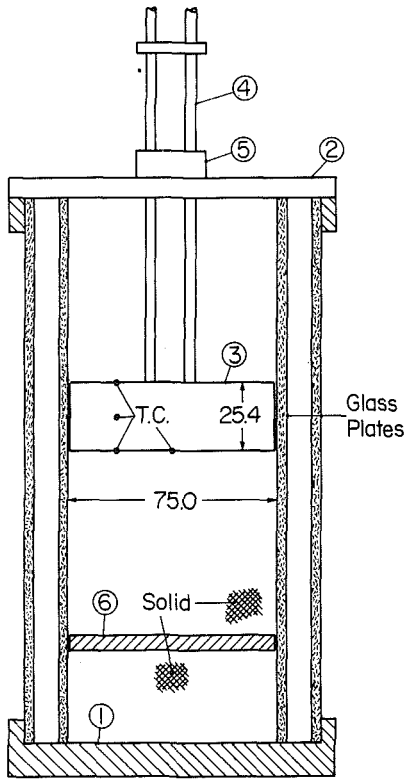


**Fig. 1 Schematic diagram of the setup: (a) front view and (b) side view; (1) main frame of the test cell, (2) plexiglass cover, (3) heat source, (4) support tubes; (5) guide bushings, (6) U-shaped heat exchanger, (7) thermocouples positioned in solid, (8) thermocouples positioned in melt**

the heat source velocity. In the model, it is assumed that the long cylindrical heat source of radius $R$ is fixed and the solid moves towards it at a constant velocity of $U_0$ (Fig. 3). It is also assumed that melt layer separating the source and the solid in front of it is very thin (i.e., $\delta/R \ll 1$.). This assumption, which is well justified by experimental observations, permits using the lubrication approximations [15]. That is, as long as $\delta/R \ll 1$, and $(\delta/R)\mathrm{Re} \ll 1$, the inertial terms can be neglected and also $\partial^2/\partial x^2 \ll \partial^2/\partial y^2$.

With application of the stated assumptions, the momentum and the energy equations simplify to

$$\mu \frac{\partial^2 u}{\partial y^2} = \frac{dP}{dx} \tag{1}$$

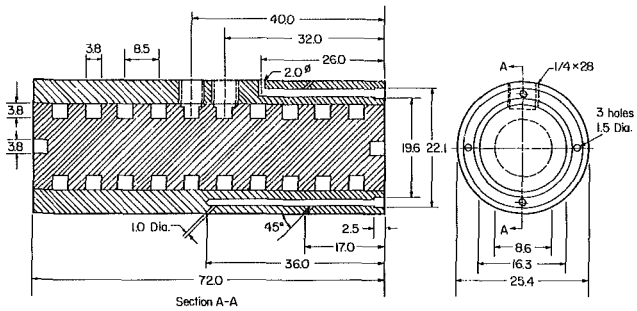


**Fig. 2 Schematic diagram of the constant surface temperature heat source**

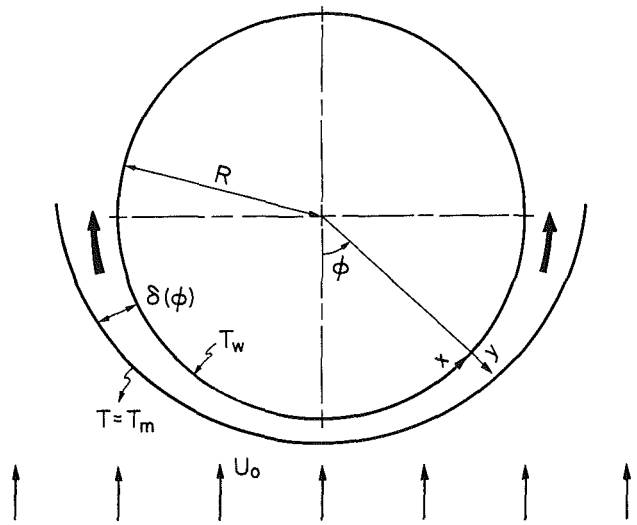


**Fig. 3 Physical model and coordinates**

and

$$u \frac{\partial T}{\partial x} + v \frac{\partial T}{\partial y} = \alpha \frac{\partial^2 T}{\partial y^2} \tag{2}$$

respectively. The boundary conditions on the heat source ($y = 0$) are:

$$u = v = 0, \quad T = T_w \tag{3}$$

and at the solid–liquid interface [$y = \delta(\phi)$] they are

$$u = 0\,,\ v = -U_0 \cos\phi \quad ,\quad T = T_m \tag{4}$$

(It should be noted that these velocity boundary conditions imply that $\rho_f = \rho_s$ and $d\delta/Rd\phi \ll 1$ are assumed) and

$$\left.\frac{\partial T}{\partial y}\right|_{y=\delta} = -\frac{\rho_f U_o}{k_f}\,[h_m + c_p(T_m - T_\infty)]\cos\phi \tag{5}$$

The solution of equation (1) with the boundary conditions (3) and (4) is

$$u = \frac{1}{2\mu}\frac{dP}{dx}\, y(y-\delta) \tag{6}$$

Upon substituting equation (6) into the continuity equation and integrating the resulting equation with respect to $y$, the pressure gradient is found to be

$$\frac{dP}{dx} = -12\mu R U_0 \sin\phi/\delta^3 \tag{7}$$

Combining equations (7) and (6) yields

$$u = -6U_0 R y\,(y-\delta)\sin\phi/\delta^3 \tag{8}$$

The energy equation is integrated over the film layer, after combining it first with the continuity equation, to yield

$$\int_0^\delta \left[\frac{\partial}{\partial x}(uT) + \frac{\partial}{\partial y}(vT)\right] dy = \alpha \int_0^\delta \frac{\partial^2 T}{\partial y^2}\, dy \tag{9}$$

After employing the boundary conditions, this equation reduces to

$$\frac{d}{dx}\int_0^\delta uTdy - U_0 T_m \cos\phi = \alpha\left[\frac{\partial T}{\partial y}(y=\delta) - \frac{\partial T}{\partial y}(y=0)\right] \quad (10)$$

To simplify the solution of equation (10), the temperature profile is approximated by a quadratic polynomial in $y$. The boundary condition, equations (3) and (4), and the energy balance at the interface, equation (5), are satisfied by

$$T = T_w + y\left[-\frac{2(T_w - T_m)}{\delta} + \frac{\rho_f U_0 h_m^*}{k_f}\cos\phi\right] + y^2\left[\frac{(T_w - T_m)}{\delta^2} - \frac{\rho_f U_0 h_m^*}{k_f \delta}\cos\phi\right] \quad (11)$$

where $h_m^* = h_m + c_p(T_m - T_\infty)$.

Substitution of equations (5), (8), and (11) into equation (10), yields

$$\frac{d}{d\phi}(\Delta \sin 2\phi) + \frac{20 + 3\text{Ste}}{U_0^*}\cos\phi - \frac{20\text{Ste}}{U_0^{*2}\Delta} = 0 \quad (12)$$

where $\Delta = \delta/R$, $\text{Ste} = c_p(T_w - T_m)/h_m^*$ and $U_0^* = U_0 R/\alpha$. Equation (12) with the boundary condition $d\Delta/d\phi = 0$ at $\phi = 0$ has a solution of the form

$$\Delta\cos\phi = \text{constant} \quad (13)$$

Inserting equation (13) into (12), yields

$$\Delta = \frac{f(\text{Ste})}{U_0^*\cos\phi} \quad (14)$$

where

$$f(\text{Ste}) = \frac{1}{4}\left[(400 + 280\text{Ste} + 9\text{Ste}^2)^{1/2} - 20 - 3\text{Ste}\right] \quad (15)$$

For small Ste, $f(\text{Ste}) \simeq \text{Ste}$(4.7 percent error for Ste = 0.2).

The heat source velocity can be determined from a force balance acting on it

$$Mg = \pi R^2 L\rho_f g + 2L\int_0^\pi (p\cos\phi + \tau_{yx}\sin\phi)Rd\phi \quad (16)$$

where $M$ is mass of the heat source, $\pi R^2 L\rho_H$. The shear stress is negligible compared to the pressure for $\delta/R \ll 1$. In order to simplify equation (16), it is assumed that for $\pi/2 \leq \phi \leq 3\pi/2$, the pressure is constant and equal to $P_0$. Substituting equation (14) into equation (7) and integrating results in

$$P - P_0 = \frac{3\mu R^2 U_0^4}{\alpha^3 f^3(\text{Ste})}\cos^4\phi \quad (17)$$

Substitution of equation (17) into (16) and integration, the heat source velocity is found to be

$$U_0^* \equiv \frac{U_0 R}{\alpha} = \left[\frac{5\pi g\Delta\rho R^3 f^3(\text{Ste})}{16\rho_f \nu\alpha}\right]^{0.25} \quad (18)$$

For $\text{Ste} \leq 0.2$ the source velocity simplifies to

$$U_0^* = \left(\frac{5\pi g R^3}{16\nu\alpha}\right)^{0.25}\left(\frac{\Delta\rho}{\rho_f}\right)^{0.25}(\text{Ste})^{0.75} \quad (19)$$

These dimensionless groups are employed in presentation of the experimental results and in the comparison with the analytical predictions. The properties of the liquid used in the calculations are determined at the melt mean film temperature $[(T_w + T_m)/2]$.

## 4 Results and Discussion

**4.1 General Observations Phenomenology.** The following generalizations are true for both starting positions of the heat source (i.e., at the top of the solid or initially embedded in the solid), and the exceptions will be clearly identified. Figure 4 presents typical photographs of the instantaneous heat source and the solid–liquid interface

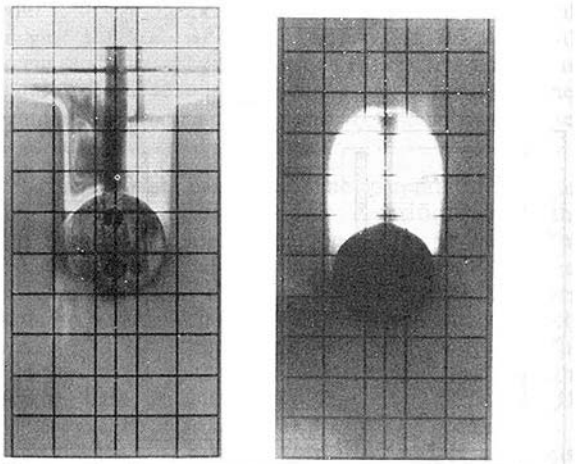

**Fig. 4 Photographs illustrating the heat source and the solid liquid interface position**

positions. The source is almost in contact with the solid in the vicinity of its lower stagnation point ($\phi = 0$ deg). The thickness of this thin melt film increases, and eventually the solid and the heat source become distinguishable at $\phi < 90$ deg. Careful examination of the photographs revealed that the angular extent of this film separation is decreased with increasing surface temperature of the source and also with a decrease in the subcooling of the solid.

Thin film separation at the stagnation point and the fact that this film widens with $\phi$ suggests that the motion of the heat source is essentially defined by the motion of the solid–liquid interface at $\phi = 0$ deg. Moreover, conduction is the dominant mode of heat transfer between the source and the solid in this region. As $\phi$ increases, the mass flux of the melt as well as its bulk temperature increase, which suggests that a transition from conduction melting to convection melting occurs along the film channel. For $\phi > 90$ deg, convective heat transfer between the melt and the solid is the dominant (if not the only) mechanism that dictates the motion and the shape of the solid–liquid interface.

Figures 5 and 6(*a*) illustrate the flow patterns around the heat source inferred from the dye visualization experiments. The newly melted material is squeezed between the solid and the heat source due to the motion of the heat source and moves along the heat source surface as the film channel widens. The motion of the source generates a region of low pressure behind it and causes the newly melted material to maintain its direction and move parallel to the heat source surface. The two streams of the melt, coming from either side of the cylinder, meet at about the centerline, and there is no way for the fluid to flow but upward. At the same time, the melt close to the heat source is heated and buoyancy also aids in the upward motion. After reaching the free surface [or the solid ceiling in the case of the heat source initially embedded in solid (Fig. 6(*a*)], the melt stream is divided into two equal currents and moves along the free surface (or along the solid ceiling). The melt loses some of the heat to the air above it and/or to the solid while flowing sideways. Depending on the solid temperature and also on the melt temperature (which is obviously a function of the surface heat flux), some melting and/or resolidification takes place at the solid–liquid interface (compare Figs. 5(*a*) and 5(*b*)). The melt also loses momentum due to the shear action at the solid surface while being cooled and becoming denser. This causes a downward motion of the melt along the vertical solid–liquid interface.

The descending melt stream eventually meets the newly formed melt being squeezed out of the gap between the solid and the falling heat source and is forced to turn parallel to it in an inner path. Little mixing occurs here again due to the large difference in the temperature and momentum of the two

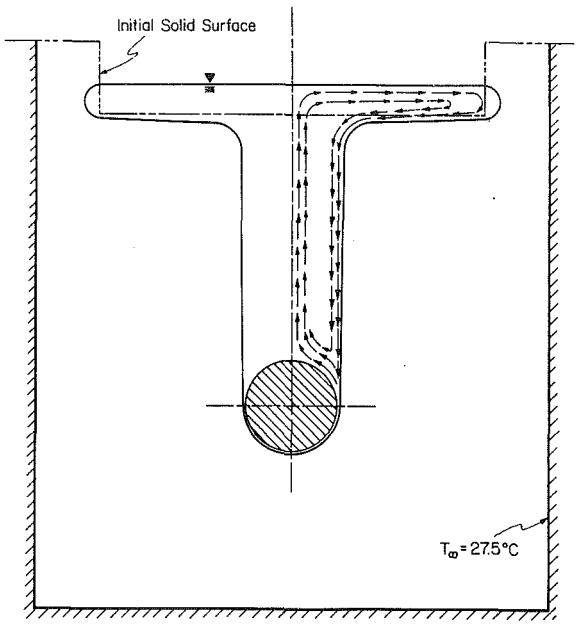


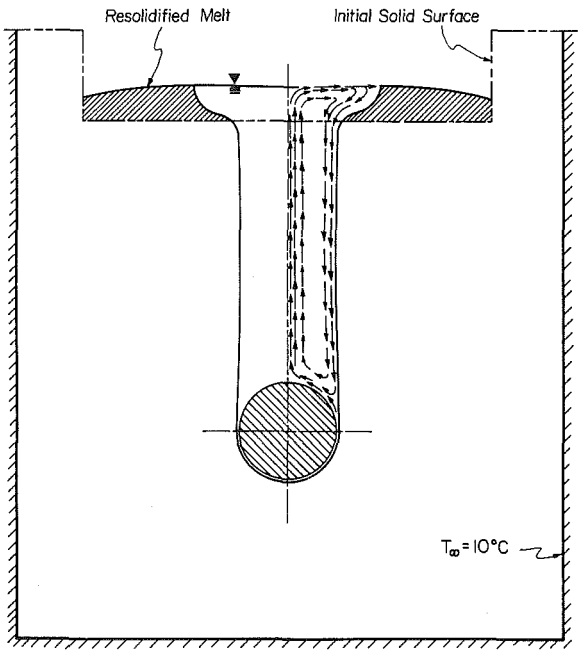


**Fig. 5 The interface shape and melt flow pattern: (*a*) $T_m - T_\infty = 0.5°C$, (*b*) $T_m - T_\infty = 18.0°C$**

streams. The newly melted material follows the path already explained, while the cooler, slower melt moves around a similar but smaller inner loop. The melt in the inner loop is gradually slowed down and creates a region of nearly stagnant melt. The two similar and independent melt cells on the sides of the centerline only elongate as the heat source descends further and as new melt is introduced. The melt cells are essentially two dimensional. The dye that was introduced at quarter way between the glass walls did not move along the axis of the cylinder. Viewed from the top, the dyed melt was like a narrow strip which was diffusing very slowly in the direction of the axis of the source.

Figure 6(*b*) presents the instantaneous position of the solid–liquid interface from the moving heat source standpoint. For $\phi < 90$ deg, the source "sees" a fixed interface shortly after the experiment started ($t \geq 3.5$ min.), and it may be concluded that a quasi-steady state has been reached for this portion of the interface. But for $\phi > 90$ deg, such a conclusion is not valid as the interface is still moving with

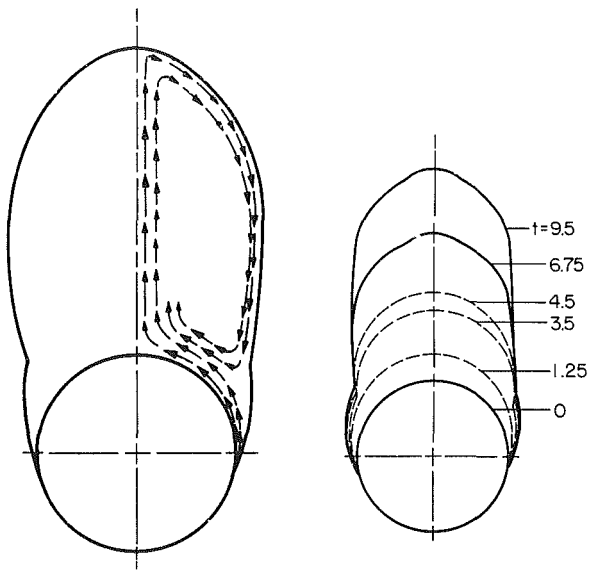


**Fig. 6 The interface shape and melt flow pattern for embedded heat source case (*a*), and interface motion with respect to fixed heat source (*b*)**

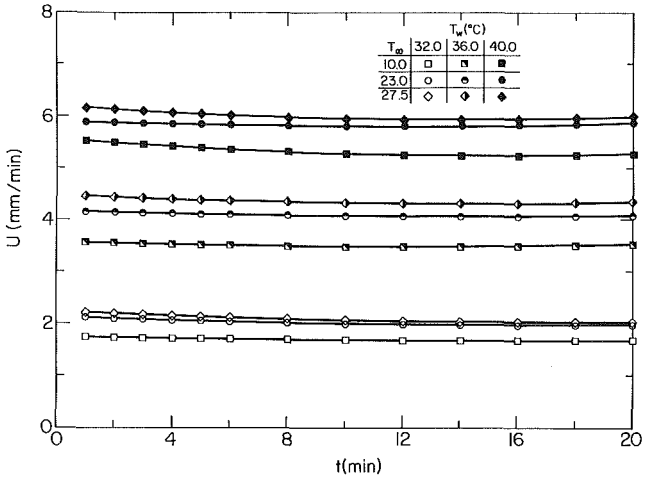


**Fig. 7 Variation of the heat source velocity with time**

respect to the heat source. The length scale of the melt pool above the source is indeed a function of the surface temperature of the source and also the initial temperature of the solid. The experimental setup permitted a maximum travel distance of 15 cm for the heat source. This was not enough for the interface to attain its quasi-steady state shape with respect to the heat source in any of the experiments studied [$(T_w - T_m)_{\min} = 4.5°C$ and $(T_m - T_\infty)_{\max} = 18°C$].

**4.2 Heat Source Velocity.** In order to determine the velocity of the heat source, the instantaneous position of its center was first plotted against time and smoothed by curve fitting. The curve was then differentiated graphically to determine the heat source velocity. Figure 7 illustrates the variation with time of the source velocity for different source surface temperatures and solid subcoolings. The heat source velocity reached its final constant value after a small decrease at the beginning of the experiments.

Figure 8 illustrates the effects of initial surface temperature and position of the heat source on its migration velocity. This figure shows that the terminal source velocity is indeed independent of the initial position and also the initial surface temperature of the source. The solid symbols represent times when the heat source is fully covered by the melt in those cases when it was initially positioned on the top of the solid. The short duration of the effects resulting from the initial heat

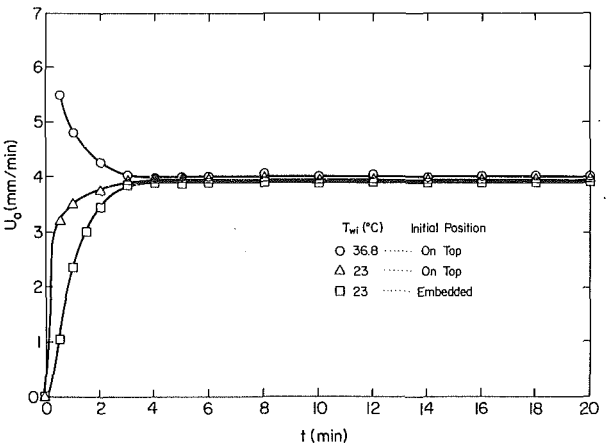


**Fig. 8 Variation of the heat source velocity with time for different heat source initial temperature and position: $T_w$ = 36°C and $T_\infty$ = 23°C**

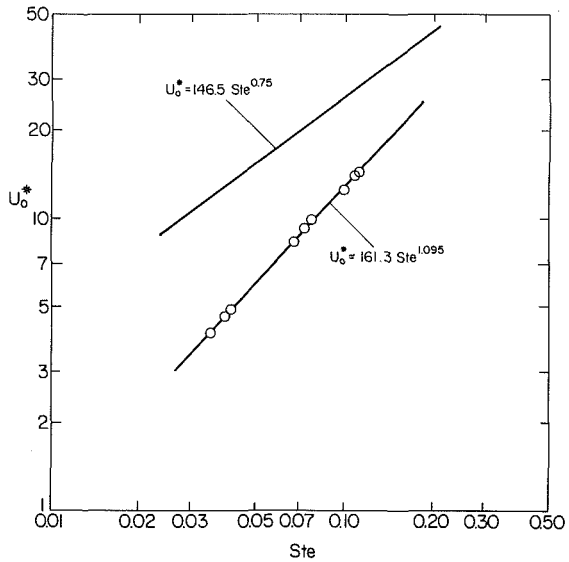


**Fig. 9 Variation of dimensionless heat source velocity with Stefan number**

source conditions (its position or its surface temperature) and also the fact that the terminal velocity is attained before the source is fully covered by the melt suggests that the migration velocity is indeed defined by the heat transfer characteristics under the heat source. In other words, the terminal velocity is attained as soon as the heat source and the solid in front of it have reached a quasi-steady state. The processes taking place away from the lower stagnation point do not have any effect on the terminal velocity of the source.

The variation of the dimensionless heat source velocity with the Stefan number is presented in Fig. 9. The data can be correlated by an empirical equation.

$$U_0^* \simeq 161.3\mathrm{Ste}^{1.095} \tag{20}$$

This result does not agree well with the analytical model [equation (19)] that suggested

$$U_0^* = 146.5\mathrm{Ste}^{0.75} \tag{21}$$

The measured dimensionless velocities are between 64 percent to 47 percent lower than those predicted by the analysis. The discrepancy between the analysis and experiment may be attributed (in order of significance) to:

1 Nonuniform melting along the axis of the source in the vicinity of its lower stagnation point due to the heat losses from the ends of the source to the glass walls of the test cell and also to melting of the thin layer of solid separating the source and the glass walls (1.0 mm on each side)

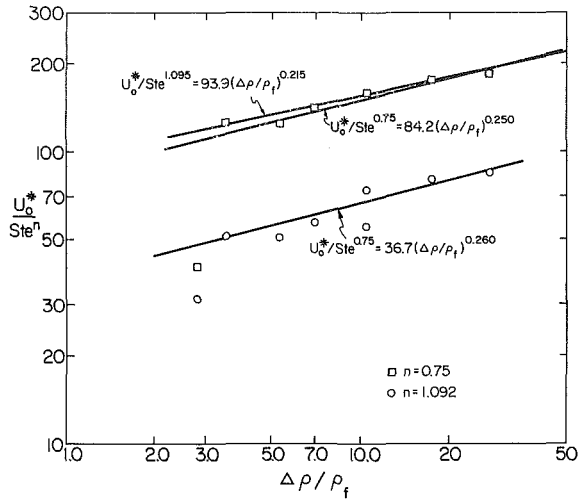


**Fig. 10 Dependence of dimensionless heat source velocity with relative density**

2 Nonuniform surface temperature due to nonhomogeneous heat extraction from the source

3 Neglect of the shear force at the ends of the heat source

4 Neglect of the effect of change in density of the material due to phase transformation. The fact that the discrepancy between the analysis and experiment decreases with an increase in the surface temperature (i.e., Ste) suggests that heat losses from the ends of the heat source are the most significant contributing factor.

Figure 10 illustrates the variation of the dimensionless terminal velocity with the effective density of the heat source. The heat source velocity is scaled with $Ste^{0.75}$ as the analysis suggests. The data are also scaled with $Ste^{1.095}$ according to equation (20) and Fig. 9. In either case, the form of the dependence on the effective density is in agreement with the expectation, equation (19), as the slope of the curves (exponents of $\Delta\rho/\rho_f$) are quite close. The data point at $\Delta\rho/\rho$ = 2.8 is not considered in calculating the correlations as it is far off the trend. Further reduction of $\Delta\rho/\rho_f$ may also invalidate the assumption that $\delta/R$ should be much less than unity.

**4.3 Temperatures in the Solid and Liquid.** The temperature distribution in the melt was measured by placing a probe consisting of five thermocouples above the heat source. Figure 11 (on the right) shows temperature profiles in the melt at different vertical positions with respect to the heat source. The temperature profile is flat in the middle portion of the melt pool. Away from the source, this flatness extends towards the centerline while it remains steep close to the solid-liquid interface. This is in agreement with the flow visualization observations which suggested a region of stagnant melt in the middle of the melt pool on either side of the heat source. The extension of the flatness of the profiles towards the centerline also suggests a reduction of the buoyancy in the melt near the centerline as the melt moves away from the source. Regardless of the fact that (for subcooled solid case) cooling of the melt eventually causes resolidification of the melt on the vertical solid walls (and the solid ceiling in the embedded case), this process is so slow that an observer on the heat source (and moving with it) will see a quasi-steady temperature field in the melt pool. This finding was checked and discussed earlier on motion and quasi-steady shape of the interface. It was also examined by changing the position of the thermocouples probe. The conclusion was that the thermocouple readings were not a function of the position of the probe but a function of the distance between the probe and the source. This finding permitted plotting the temperature profiles in the melt by connecting points of equal temperature (Fig. 11, on the left). The temperature profiles

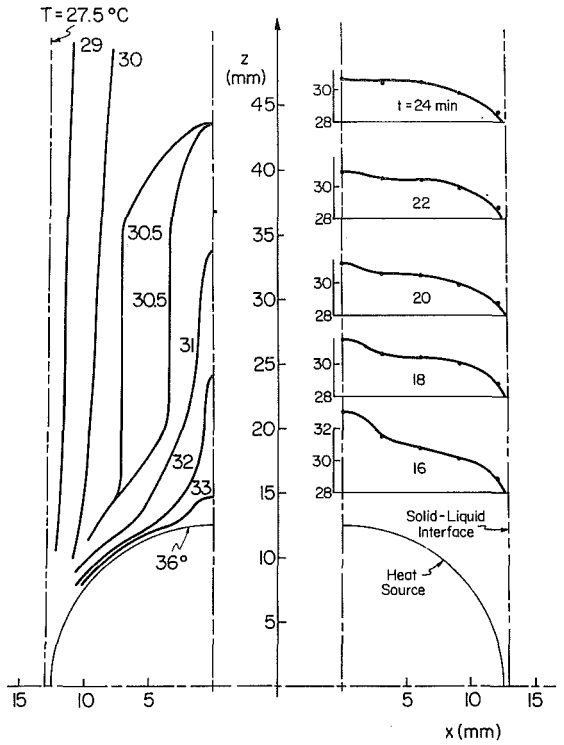


**Fig. 11 Temperature distribution in the melt: $T_W$ = 36°C and $T_\infty$ = 10.0°C**

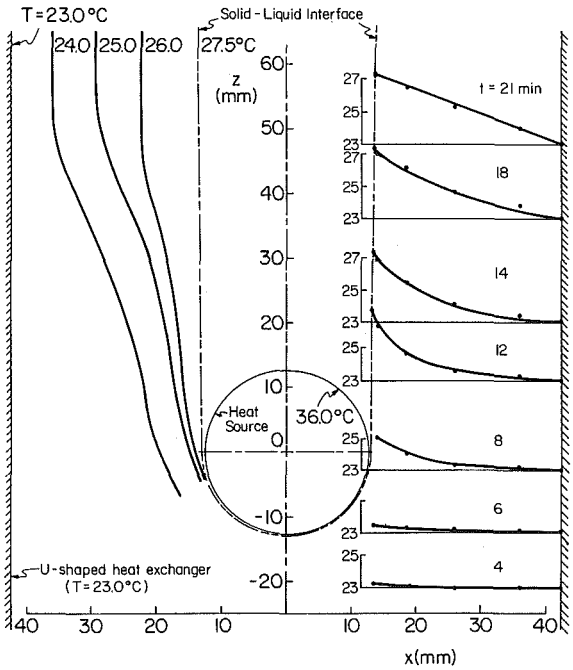


**Fig. 12 Temperature distribution in the solid: $T_W$ = 36°C and $T_\infty$ = 23°C**

also show a region of constant temperature (and stagnant) in the melt pool. The closely spaced isotherms near the heat source indicates a region of a large temperature gradient near the source surface. This is in agreement with the flow visualization observations which showed that the newly melted material forms a boundary layer on the heat source when squeezed out between the source and the solid-liquid interface.

Figure 12 (on the right) shows the temperature profiles in the solid at different times and vertical positions with respect to the source. Two racks of thermocouples positioned 30 mm apart in the vertical direction in the solid recorded the same

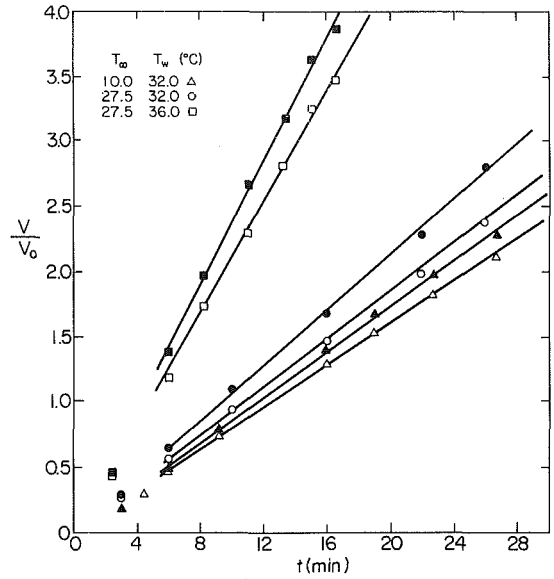


**Fig. 13 Variation of volume of solid melted with time: open symbols, directly melted solid; closed symbols, total melted solid**

temperatures when they were at the same distance from the heat source. This confirmed that the solid too, just like the melt, has reached the quasi-steady state with respect to the heat source. The finding is at least true for the solid ahead of the source and in its vicinity where the solid-liquid interface has already reached the quasi-steady state shape. The temperature contours in the solid are plotted by connecting points of equal temperature and are also presented in Fig. 12 (on the left). The isotherms are most closely spaced in front of the source where heat transfer to the solid is most intense (the liquid film is the thinnest here). Above and away from the heat source the isotherms start to become parallel and more evenly spaced. When the solid-liquid interface reaches its quasi-steady state, the isotherms will become nonparallel and unevenly spaced again while turning around the top of the melt pool.

**4.4 Volume of the Melted Solid.** From sequence of photographs taken during the experiments, the volume of the solid directly melted ($V_D$) by the heat source was measured with a planimeter and is presented in Fig. 13. Also presented in the figure is the total volume (net) of the solid melted ($V_T$) either directly by the heat source or indirectly by the hot melt minus the volume of the resolidified melt. At early times, the melting rate is small as the contact area between the source and the solid is small. As melting proceeds and the heat source penetrates more into the solid (i.e., the contact area increases), the melting rate increases and eventually reaches a constant value at about the time that half of the source is in the solid. During this stage, $V_T$ and $V_D$ are almost equal, mostly because the interaction between the melt and the source is limited (in the thin film channel). Thus the bulk temperature of the melt is close to the fusion temperature, and hence the volume of the indirectly melted solid is very small. The rate of increase of $V_T/V_o$ approaches a constant value after the source is fully covered by the melt, and a quasi-steady state is established in the vicinity of the heat source. This trend can be justified for the cases when the solid was not subcooled; however, for an initially subcooled solid it is expected that $V_T/V_o$ approach a constant value. Hence, the constant rate of increase of $V_T/V_o$ for $T_\infty$ = 10°C (18° subcooled solid) case only suggests that the melt pool and the solid-liquid interface are far from their quasi-steady state.

In order to relate the melt volume and the heat transfer from the source, from equations (11) and (14) the heat transfer at the surface of the source is found to be

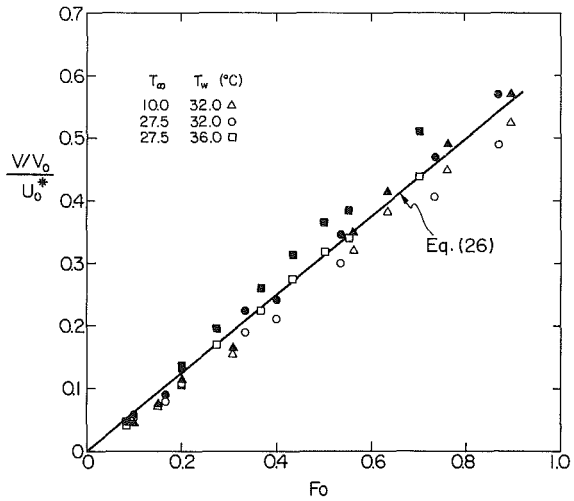


**Fig. 14 Variation of volume of solid melted (scaled with dimensionless velocity) with dimensionless time: open symbols, directly melted solid; closed symbols, total melted solid**

$$q'' \equiv -k_f \frac{\partial T}{\partial y}\bigg|_{y=0} = \rho_f U_0 h_m^* \left[\frac{2\text{Ste}}{f(\text{Ste})} - 1\right]\cos\phi \tag{22}$$

The total heat transfer rate to the phase-change material from the lower half of the heat source is

$$Q = 2LR\rho_f U_0 h_m^* \left[\frac{2\text{Ste}}{f(\text{Ste})} - 1\right] \tag{23}$$

Upon equating the heat loss from the lower half of the source during time $t$ to the energy added to the phase-change material that resulted in melt volume $V_D$ of the solid, we obtain

$$\int_0^t Q dt = \rho_f V_D h_m^* \tag{24}$$

Under quasi-steady state condition, $U_0$ is constant and integration may be carried out to yield

$$\frac{V_D/V_0}{U_0^*} = \frac{2}{\pi}\,\text{Fo}\left[\frac{2\text{Ste}}{f(\text{Ste})} - 1\right] \tag{25}$$

For small Ste, this expression reduces to

$$\frac{V_D/V_0}{U_0^*} = \frac{2}{\pi}\,\text{Fo} \tag{26}$$

Figure 14 illustrates the variation of the dimensionless melt volumes (scaled with $U_0^*$) with dimensionless time Fo. The directly melted volume data agree quite well with equation (26), except for the early times when only part of the lower half of the heat source is involved in the melting of the solid. This also confirms that the melt leaves the film channel at a temperature close to the fusion temperature, and it is indeed heated outside the film channel while passing over the upper half of the heat source. The total melt volume data do not follow the trend of equation (26) and start to deviate from it with increasing time and also the Stefan number. This is because the total melt volume is not only function of the motion and velocity of the heat source but also of other processes (i.e., indirect melting of the solid, resolidification of the melt, and development of natural convection in the melt pool). For larger Stefan numbers, the melt attains higher temperatures while moving over the heat source and this causes higher rate of indirect melting. However, comparison of the total (net) melt volume and the direct melt volume for cases when the solid was initially at the fusion temperature reveals that the heat transfer from the upper half of the source is far less than the heat extracted from the lower half. For the experiment with $T_w = 36°C$ and $T_\infty = 27.5°C$ (square symbols, in Figs. 13 and 14) the heat transfer from the upper half is only 19 percent of the heat transfer from the lower half of the source (compare slope of the lines connecting the hollow and solid squares in Fig. 14).

## 5 Conclusions

The experiments performed have provided phenomenological understanding and also quantitative data on heat transfer during melting around a moving horizontal cylindrical heat source. Important heat transfer mechanisms were identified, and the domain, extent, and duration of their influence were investigated.

Conduction was found to be the dominant heat transfer mechanism around the lower stagnation point of the source where the heat source and the solid are in permanent contact. From this, it was concluded that the velocity of the heat source is essentially defined in this region. The melt motion in the melt pool above the heat source was mainly induced by the descent of the source, and natural convection played a small role in this motion under the thermal conditions studied.

The heat source and the solid-liquid interface in its immediate vicinity reached their quasi-steady state conditions at the same time. This also coincided with the completion of the boundary layer formation of the nearly melted material on and over the heat source. However, the solid-liquid interface away from the heat source and also the melt pool above the source (out of the boundary layer) needed much more time to reach their quasi-steady state with respect to the heat source. This was concluded to be the result of a weak interaction between the heat source and the melt pool due to the formation of the boundary layer over the heat source.

## Acknowlegments

This work was supported in part by the Heat Transfer Program of the National Science Foundation under Grant No MEA-8313573.

## References

1 Jackson, F., "Moving Heat Sources with Change of Phase," ASME JOURNAL OF HEAT TRANSFER, Vol. 87, 1965, pp. 329-332.

2 Tong, L. S., "Core Cooling in a Hypothetical Loss of Coolant Accident. Estimate of Heat Transfer in Core Meltdown," *Nuclear Engineering and Design*, Vol. 8, 1968, pp. 309-312.

3 Marsh, B. D., and Charmichael, I. S. E., "Benioff Zone Magnetism," *Journal of Geophysical Research*, Vol. 79, 1974, pp. 1196-1206.

4 Birth, F. S., "Conduction Heat Flow Anomalies Over a Hot Spot in a Moving Medium," *Journal of Geophysical Research*, Vol. 80, 1975, pp. 4825-4827.

5 Cohen, J. J., Schwartz, L. L., and Tewes, H. A., "Economic and Environmental Evaluation of Nuclear Waste Disposal by Underground in Situ Melting," *Transactions of the American Nuclear Society*, Vol. 18, 1974, pp. 194-195.

6 Jansen, G., and Stepnewksi, D. D., "Fast Reactor Fuel Interactions with Floor Material after a Hypothetical Core Meltdown," *Nuclear Technology*, Vol. 17, 1973, pp. 85-96.

7 Easton, C. R., "Conduction from a Finite-Size Moving Heat Source Applied to Radioisotope Capsule Self-Burial," NBS Special Publication 302, 1968, pp. 209-218.

8 Donea, J., "Operation Hot Mole," *Euro-Spectra*, Vol. 11, 1972, pp. 102-109.

9 Hardee, H. C., and Sullivan, W. N., "Waste Heat Melt Problem," Sandia Laboratories, Technical Report No. SLA-73-0575, 1973.

10 Hardee, H. C., and Sullivan, W. N., "An Approximate Solution for Self-Burial Rates of Radioactive Waste Containers," Sandia Laboratories, Technical Report No. SL-73-0931, 1974.

11 Logan, S. E., "Deep Self-Burial of Radiactive Wastes by Rock-Melting Capsules," *Nuclear Technology*, Vol. 21, 1974, pp. 111-124.

12 Emerman, S. H., and Turcotte, D. L., "Stokes' Problem with Melting," *International Journal of Heat and Mass Transfer*, Vol. 26, 1983, pp. 1625-1630.

13 Armstrong, D. E., Coleman, J. S., McInteer, B. B., Potter, R. M., and Robinson, E. S., "Rock Melting as A Drilling Technique," Los Alamos Scientific Laboratory, Technical Report No. LA-3243, 1965.

14 Robinson, E. S., Potter, R. M., McInteer, B. B., Rowley, J. C., Armstrong, D. E., Mills, R. L., and Smith, M. C., "A Preliminary Study of the Nuclear Subterrene," Los Alamos Scientific Laboratory, Technical Report No. LA-4547, 1971.

15 Schlichting, H., *Boundary Layer Theory* (7th ed.), McGraw-Hill, New York, 1979, pp. 108-114.

# Enhanced Heat Conduction in Fluids Subjected to Sinusoidal Oscillations

**U. H. Kurzweg**
Professor.
Department of Engineering Sciences,
University of Florida,
Gainesville, Fla. 32611

*Enhanced conduction heat transfer via sinusoidal oscillatory flow through circular tubes connecting two fluid reservoirs maintained at different temperatures is examined. Using a multiscale expansion technique for the solution of the governing partial differential equation, the spatial and temporal temperature variation within the tubes is determined for low values of $\alpha^2$ Pr, where $\alpha$ is the Womersley number and Pr the fluid Prandtl number. From this result, a calculation of the effective thermal diffusivity is made and used to determine the enhanced conduction heat transfer from the high- to low-temperature reservoir. The enhanced heat transfer produced by the oscillations is shown to be proportional to the square of the oscillation amplitude and a function of the Prandtl number, the frequency, and the tube radius. Values of effective conductivity in liquid metals three orders of magnitude greater than the normal heat conductivity are shown to be readily obtainable under typical experimental conditions.*

## Introduction

It is well known from the studies of Taylor [1], Aris [13], and Gill [14] that a contaminant will spread axially in laminar tube flow (both steady and time-dependent) at rates considerably above those expected by pure molecular diffusion. The mechanism here is one of radial diffusional transfer coupled with an axial convective transport leading to an enhanced diffusion coefficient that is directly proportional to the square of the mean flow velocity and the square of the tube radius and inversely to the molecular diffusion coefficient. Recently, this work has been extended by considering gas component transfer in binary gas mixtures when these are confined to single tubes or branched systems and a sinusoidal pressure variation is applied [2, 3]. The interest in these more recent studies has been the result of gaining a better understanding of an experimentally observed increase in the dispersional gas transport in the pulmonary system when high-frequency pressure oscillations are applied at the trachea. Jaeger and Kurzweg [4] have recently measured the dispersion coefficient in pure oscillatory flow in oxygen–nitrogen mixtures under laminar conditions. The coefficient is found to be proportional to the square of the oscillation amplitude and the first power of frequency in the Womersley number range $3<\alpha<15$. Values of the dispersion coefficient up to four orders in magnitude in excess of the molecular diffusion value were found. After the original submission of this study, a general analytic study on the dispersion of gases under oscillatory conditions for fluids of arbitrary Schmidt number appeared [5].

The foregoing results on enhanced diffusion in tubes and branched systems suggest that a similar phenomenon should occur in heat conduction in view of the mathematical similarity between heat conduction and diffusion. It suggests that a thermally conducting fluid confined to an open-ended tube with thermally insulating side walls and connected to different temperature reservoirs at its ends can be made to conduct heat at rates orders of magnitude greater than by pure conduction, provided the fluid is oscillated sinusoidally in the tube. It is the purpose of this paper to confirm this conjecture analytically and, in particular, to obtain an expression for the enhanced heat flow from the high to the low temperature reservoir when the quiescent fluid in the connecting tube (or tubes) is subjected to oscillations whose amplitude is assumed small compared to the tube length in order to insure there is no direct convection of fluid between the reservoirs. For mathematical simplification, we will only be concerned with frequencies and fluids for which $\alpha^2 \text{Pr}<\pi$.

Although we have not found any references to work in the heat transfer area dealing directly with the present problem, the general area of oscillating and time-dependent heat transfer has received considerable attention in the literature [6, 7, 15]. An excellent discussion of the mathematical formulation for such time-dependent heat transfer problems can be found in the recent book by Arpaci and Larson [8]

## Mathematical Formulation

Consider a single or a series of parallel tubes of radius $r=a$ and of length $L$ (such that $a<<L$) connecting a large reservoir of cold fluid at temperature $T=T_C$ with a second larger reservoir of the same fluid at higher temperature $T=T_H$. The tubes are oriented in such a manner so that the fluid within the tubes connecting the reservoirs will not undergo natural convection. An oscillator is mounted into the walls of one of the reservoirs and a flexible window is installed in the other reservoir to allow a corresponding expansion in the event one is dealing with an incompressible fluid. The oscillator will produce one-dimensional laminar sinusoidal oscillations of the fluid in the tube connecting the reservoirs as long as the maximum Reynolds number associated with the oscillations does not become too high and one neglects end effects. Within these limitations, it can readily be shown [9] that the velocity of the one-dimensional fluid motion in the tube will have the time-dependent form

$$W(\eta,t)=W_o\left\{\frac{J_o(\sqrt{-i}\alpha)-J_o(\sqrt{-i}\alpha\eta)}{J_o(\sqrt{-i}\alpha)-1}\right\}\exp(i\omega t)=W_oF(\eta)\exp(i\omega t) \quad (1)$$

where $\alpha=a\sqrt{\omega/\nu}$ is the Womersley number, $W_o$ the maximum centerline velocity, $\eta=r/a$ the nondimensional radial distance, and $J_o$ the Bessel function of the first kind of order zero. It will be noted that this time-dependent profile (real part of the equation) consists essentially of a slug flow over most of the fluid core with a thin Stokes's boundary layer of thickness $\delta=\sqrt{2\nu/\omega}$ near the tube wall at high frequency. At low frequencies, it has the familiar Poiseuille distribution.

Contributed by the Heat Transfer Division for publication in the JOURNAL OF HEAT TRANSFER. Manuscript received by the Heat Transfer Division July 18, 1983.

The corresponding temperature variation $T(\eta, \zeta, \tau)$ within the tube is governed by the heat conduction equation

$$T_\tau + \mathrm{Pe}F(\eta)e^{i\Omega\tau}T_\zeta = \nabla^2 T + T_{\zeta\zeta} \tag{2}$$

where $\nabla^2 = 1/\eta\ \partial/\partial\eta\ \eta\ \partial/\partial\eta$, $\zeta = z/a$, $\tau = \kappa t/a^2$ is the time expressed in units of the diffusion time $a^2/\kappa$, $\mathrm{Pe} = W_o a/\kappa$ is the Peclet number, and $\Omega = \omega a^2/\kappa$ the nondimensional frequency. Note that the viscous heating term in equation (2) has been neglected. This is justified as long as one does not deal with high Prandtl number fluids such as oils. The solution of this partial differential equation is clearly a formidable task and one accordingly seeks some simplifying approach. We choose to use the multiple time scale expansion technique as discussed in detail by Pismen [10]. Applying the technique here, we first introduce the coordinate transformations

$$Z = \epsilon\left[\zeta - \frac{W_o}{ia\omega}e^{i\Omega\tau}\bar{F}\right] \tag{3}$$

and

$$\psi = \epsilon^2\tau = \epsilon^2\kappa t/a^2 \tag{4}$$

where $\bar{F}$ is the cross-sectional average of the function $F$ defined in equation (1), and $\epsilon$ is a small parameter. The new independent axial variable $Z$ represents a contracted axial coordinate, and $\psi$ is a contracted time. Substituting equations (3) and (4) into equation (2) yields

$$\epsilon\mathrm{Pe}[F(\eta) - \bar{F}\,]e^{i\Omega\tau}T_Z = \nabla^2 T + \epsilon^2(T_{ZZ} - T_\psi) \tag{5}$$

Expanding $T(\eta, Z, \psi)$ in the perturbation series

$$T = T_0 + \epsilon T_1 + \epsilon^2 T_2 + \tag{6}$$

and substituting this expansion into equation (5) and equating the terms for different powers of $\epsilon$ to zero yields the system of equations

$$\nabla^2 T_0 = 0 \tag{7}$$

$$\nabla^2 T_1 = \mathrm{Pe}(F - \bar{F})e^{i\psi}(T_0)_Z \tag{8}$$

$$\nabla^2 T_2 = \mathrm{Pe}(F - \bar{F})e^{i\psi}(T_1)_Z - (T_0)_{ZZ} + (T_0)_\psi \tag{9}$$

Note that to avoid the appearance of the parameter $\epsilon$ in the $\exp(i\Omega\tau)$ term in equation (5), we have set $\epsilon = \Omega^{1/2} = \alpha\sqrt{\mathrm{Pr}}$, where $\mathrm{Pr} = \nu/k$ is the fluid Prandtl number. The convergence of the method thus requires that $\alpha^2$ Pr is small. Physically, this implies that the time for heat to diffuse radially of $a^2/\kappa$ be less than one-half period of the oscillation $\pi/\omega$, or equivalently, that $\alpha^2\mathrm{Pr} < \pi$.

Equation (7) has a simple solution, independent of the radial coordinate $\eta$, of the form

$$T_0 = G(Z, \psi) \tag{10}$$

To find explicit solutions to the remaining functions $T_1$ and $T_2$ in the present small parameter expansion, it is necessary to have the terms on the right side of equations (8) and (9) be orthogonal to $T_0$ over the tube cross section. That is

$$2GG_Z\int_0^1 [\mathrm{Pe}(F - \bar{F}\,)]e^{i\psi}\eta d\eta = 0 \tag{11}$$

and

$$2G\int_0^1 [\mathrm{Pe}(F - \bar{F}\,)e^{i\psi}(T_1)_Z - G_{ZZ} + G_\psi]\eta d\eta = 0 \tag{12}$$

The first of these conditions is satisfied identically by our choice of the transformation given by equation (3). An explicit solution of equation (8) is now possible using the appropriate boundary condition that $\partial T/\partial\eta = 0$ at $\eta = 1$ corresponding to an insulating wall. One integration yields

$$\eta(T_1)_\eta = \mathrm{Pe}G_Z e^{i\psi}\int_1^\eta [F(\eta) - \bar{F}\,]\eta d\eta \tag{13}$$

Integrating a second time produces, after letting $T_1(0, Z, \psi) = 0$, the result

$$T_1 = \mathrm{Pe}G_Z e^{i\psi}\int_0^\eta \frac{d\eta}{\eta}\int_1^\eta [F(\mu) - \bar{F}\,]\mu d\mu = \mathrm{Pe}G_Z e^{i\psi}H(\eta) \tag{14}$$

Taking the $Z$ derivative of this last expression and substituting into the orthogonality condition equation (12) yields

$$\left\{1 - 2\mathrm{Pe}^2\int_0^1 \mathrm{Real}\,[(F - \bar{F}\,)e^{i\psi}]\ \mathrm{Real}\,[He^{i\psi}]\eta d\eta\right\}G_{ZZ} = G_\psi \tag{15}$$

The term within the curly bracket of this last expression is recognized to be the effective enhanced time-dependent diffusivity for heat conduction in the present geometry. On time averaging over one cycle of the oscillation, we find that the total, time-averaged, enhanced thermal diffusivity becomes

$$\kappa_e = \kappa\left\{1 - \frac{1}{2}\mathrm{Pe}^2\int_0^1 [(F - \bar{F}\,)H^* + (F - \bar{F}\,)^*H]\eta d\eta\right\} \tag{16}$$

where the star denotes the complex conjugate.

## Nomenclature

$a$ = tube radius, m
$c$ = specific heat, J/kg °C
$f$ = oscillation frequency, Hz
$F$ = radial variation of axial velocity
$\bar{F}$ = cross-sectional average of $F$
$G$ = functional form of $T_0$
$H$ = radial variation of the temperature term $T_1$
$i$ = $\sqrt{-1}$
$k$ = thermal conductivity, W/m°C
$L$ = tube length, m
Pe = $W_o a/\kappa$, Peclet number
Pr = $\nu/\kappa$, Prandtl number
$\dot{q}$ = axial heat flow, W
$r$ = radial coordinate, m
$t$ = time, s
$T$ = temperature in tube, °C
$T_0, T_1, T_2$ = temperature expansion terms, °C
$T_H, T_C$ = reservoir temperatures, °C
$W$ = axial velocity, m/s
$W_o$ = maximum axial velocity, m/s
$z$ = axial coordinate, m
$\Delta z$ = tidal displacement of fluid, m
$Z$ = multiscale axial expansion variable
$\alpha$ = $a\sqrt{\omega/\nu}$, Womersley number
$\delta$ = $\sqrt{2\nu/\omega}$, Stokes boundary layer thickness, m
$\epsilon$ = small parameter used in multiscale expansion
$\eta$ = $r/a$, nondimensional radial distance
$\zeta$ = $z/a$, nondimensional axial distance
$\kappa$ = $k/\rho c$, thermal diffusivity, $m^2/s$
$\kappa_e$ = enhanced thermal diffusivity, $m^2/s$
$\nu$ = kinematic viscosity, $m^2/s$
$\rho$ = fluid density, $kg/m^3$
$\tau$ = $\kappa t/a^2$, nondimensional time
$\psi$ = $\epsilon^2\tau$ multiscale time variable
$\Omega$ = $\omega a^2/\kappa$, nondimensional angular frequency
$\omega$ = angular frequency, rad/s

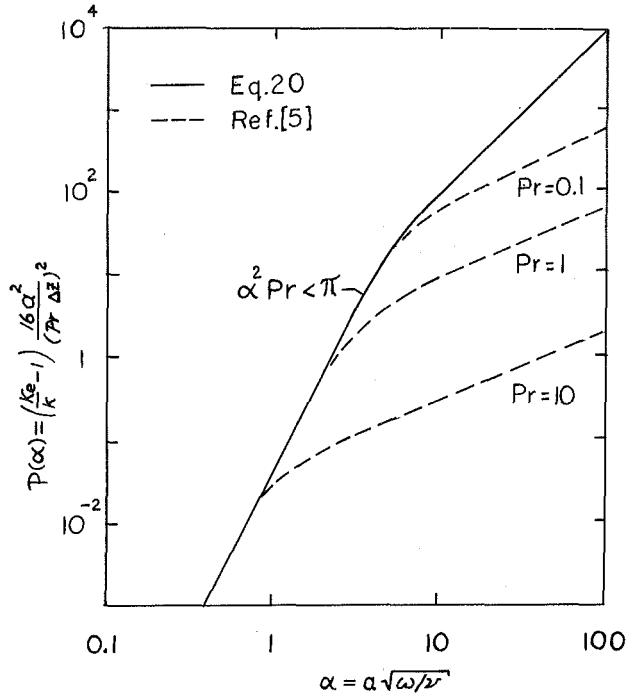


**Fig. 1 Effective thermal diffusivity variations**

## Determination of the Enhanced Thermal Diffusivity

An evaluation of equation (16) can be accomplished by using the velocity profile given by equation (1) and evaluating equation (14). This yields

$$H(\eta)=\frac{i}{\alpha^2}\,\frac{\left[1-J_0(\sqrt{-i}\alpha\eta)-\frac{1}{2}(\eta^2\sqrt{-i}\alpha)J_1(\sqrt{-i}\alpha\right]}{[1-J_0\sqrt{-i}\alpha]} \tag{17}$$

where $J_1$ is the Bessel function of order one. After some further lengthy manipulations, we find that the exact solution of equation (16) becomes

$$\frac{\kappa_e}{\kappa}=1+\frac{\mathrm{Pe}^2}{4\alpha^2}\left\{\frac{[\mathrm{ber}'^2\alpha+\mathrm{bei}'^2\alpha]-(4/\alpha)[\mathrm{ber}'\alpha\mathrm{ber}\alpha+\mathrm{bei}'\alpha\mathrm{bei}\alpha]}{[(\mathrm{ber}\alpha-1)^2+(\mathrm{bei}\alpha)^2]}\right. \tag{18}$$

where $\mathrm{ber}\,\alpha+i\,\mathrm{bei}\,\alpha=J_o(\sqrt{-i}\alpha)$ is the Kelvin function [11] and the primes represent derivatives. A somewhat more convenient form for $\kappa_e/\kappa$ can be obtained by using the tidal displacement $\Delta z$ instead of the maximum axial velocity $W_o$ in the above expression. For the sinusoidal oscillations considered here, we have

$$\Delta z=(4/\omega)W_o\left|\int_0^1 F(\eta)\eta d\eta\right|=(2/\omega)W_o\,|\bar{F}| \tag{19}$$

where $F(\eta)$ is the function defined by equation (1) with the vertical bars representing the absolute value. In terms of $\Delta z$, equation (18) can be rewritten as

$$P(\alpha)=\left(\frac{\kappa_e}{\kappa}-1\right)\frac{16a^2}{(\mathrm{Pr}\Delta z)^2}=\frac{1}{4}\alpha^4 Q(\alpha) \tag{20}$$

where

$$Q(\alpha)=\frac{[(\mathrm{ber}'^2\alpha+\mathrm{bei}'^2\alpha)-\frac{4}{\alpha}(\mathrm{bei}\alpha\mathrm{bei}'\alpha+\mathrm{ber}\alpha\mathrm{ber}'\alpha)]}{[\mathrm{bei}^2\alpha+\mathrm{bei}'^2\alpha)-\alpha(\mathrm{ber}\alpha\mathrm{bei}'\alpha-\mathrm{bei}\alpha\mathrm{ber}'\alpha)+\frac{1}{4}\alpha^2(\mathrm{ber}^2\alpha+\mathrm{bei}^2\alpha)]} \tag{21}$$

The term $P(\alpha)$ represents a measure of the ratio of the enhanced thermal diffusivity $\kappa_e$ to the molecular diffusivity $\kappa$ normalized in such a manner that it is a function of $\alpha$ only. That is, regardless of $\alpha$, $\kappa_e$ will always be proportional to $(\mathrm{Pr}\Delta z)^2/a^2$ provided $\kappa_e >> \kappa$. Using the expansions of the Kelvin functions for both small and large $\alpha$ given in [11], we find the following limiting forms

$$P(\alpha)=\frac{1}{24}\alpha^4, \alpha << 1 \tag{22}$$

and

$$P(\alpha)=\alpha^2\left(1-\frac{1}{\sqrt{2}\alpha}\right), \alpha >> 1 \tag{23}$$

That is, $[(\kappa_e/\kappa)-1]$ is proportional to the square of the tidal displacement for all frequencies, and goes as the square of the frequency ($\alpha^4$) for small $\alpha$ and the first power of frequency for large $\alpha$. A plot of equation (20), using tabulated values of Kelvin functions plus the limiting forms equations (22) and (23), is given in Fig. 1. We have added there the recent results of Watson [5] for $\mathrm{Pr}=0.1$, 1, and 10 when his results for gas dispersion are adjusted to the present heat transfer problem. Note that the results merge at approximately $\alpha^2\,\mathrm{Pr}=\pi$, which is the point where the presently used multiple time scale expansion technique becomes invalid.

## Effective Heat Flow Between Fluid Reservoirs

Having determined the value of the enhanced thermal diffusivity as a function of $\alpha$, Pr, $a$, and $\Delta z$, we are now in a position to calculate the heat flow expected between the fluid reservoirs connecting the tubes. The effective axial heat flow per tube will be

$$\dot{q}=-\pi a^2\rho c\kappa_e\frac{\partial T}{\partial z} \tag{24}$$

which, via equation (20) and the replacement of the temperature gradient $\partial T/\partial z$ by $-(T_H-T_C)/L$, can be written as

$$\dot{q}=k\pi a^2\left[1+P(\alpha)\frac{(\mathrm{Pr}\Delta z)^2}{16a^2}\right]\frac{(T_H-T_C)}{L} \tag{25}$$

Here $k$ is the fluid thermal conductivity related to the diffusivity by $k=\rho c\kappa$, $\rho$ is the fluid density, and $c$ the specific heat. The term within the square bracket of this last equation can be considered to measure the ratio of axial heat flow through the tube under oscillatory conditions to that in the absence of oscillations. This ratio can be quite high. For example, using room temperature mercury as the working fluid where $\mathrm{Pr}=0.025$ and $\nu=10^{-7}\mathrm{m}^2/\mathrm{s}$ and assuming $\Delta z=0.2\mathrm{m}$, $f=8$ Hz in a $10^{-3}$m dia tube, one finds $\alpha=11.2$ which, with aid of Fig. 1, yields $P(\alpha)=10^2$. Therefore, the increase in heat flow, according to equation (25), will be 626 times that in the absence of oscillations for this case. Such an increase suggests that the present method can produce heat flows comparable, if not larger, than those achievable with heat pipes. Heat flows as high as $10^{10}$ W/m$^2$ may possibly be reached, provided turbulence and viscous heating do not become a problem at the high values of $\Delta z$ and $f$ needed to achieve this.

## Discussion and Concluding Remarks

It has been shown that the superposition of sinusoidal oscillations on a fluid in a single tube or a series of parallel tubes connecting two large reservoirs at different temperatures produces a considerable increase in axial heat

transfer between the reservoirs without a net transfer of mass. The physical mechanism for this enhancement is a large time-dependent radial temperature gradient produced by the fluid oscillations. During most of the sinusoidal cycle, the fluid in the wall near region will have a temperature different from the core. As a result, large quantities of heat will be transfered radially and hence transported axially. This enhanced transfer does not require the existence of turbulence or cross-stream fluid motion. It is felt that the present transfer mechanism may find applications in areas where natural convection processes are not present and also in areas requiring very high heat transfer rates without an accompanying mass transfer. In particular, the present heat transfer method may find application in the removal of heat from radioactive fluids without a concomitant mass transfer as required in convection processes.

Extensions of analytical work considered here should include a consideration of the changes in fluid properties with temperature, as these will become important when the temperature difference between the fluid reservoirs becomes large. Also heating effects due to viscous effects should be examined, and a consideration should be given to changes in the heat transfer process when the walls have finite thermal conductivity. Experimentally, the result predicted by equation (25) could be verified by noting the drop in temperature in the hot fluid reservoir as a function of time, provided it is well insulated and the only heat transfer from it is through the connecting tubes. Such an experimental study will be the subject of a forthcoming paper [12].

## Acknowledgment

Discussions with Dr. M. J. Jaeger of the Physiology Department at the University of Florida concerning dispersional gas transfer in high-frequency pulmonary ventilation (HFV) are much appreciated. I also would like to thank G. Howell for discussions concerning the limitations of the multiple time-scale method to the present problem.

## References

1 Taylor, G. I., "Dispersion of Soluable Matter in Solvent Flowing Slowly through a Tube," *Proceedings of the Royal Society of London*, Vol. A 219, 1953, pp. 186-203.

2 Bohn, D. J., Miyasaka, K., Marchak, B. E., Thompson, W. K., Froese, A. B., and Bryan, A. C., "Ventilation by High Frequency Oscillation," *Journal of Applied Physiology*, Vol. 48, 1980, pp. 710-716.

3 Slutsky, A. S., Drazen, J. M., Ingram Jr., R. H., Kamm, R. D., Shapiro, A. H., Fredberg, J. J., Loring, S. H., and Lehr, J., "Effective Pulmonary Ventilation with Small Volume Oscillations at High Frequency," *Science*, Vol. 209, 1980, pp. 609-610.

4 Jaeger, M. J., and Kurzweg, U. H., "Determination of the Longitudinal Dispersion Coefficient in Flows Subjected to High-Frequency Oscillations," *Physics of Fluids*, Vol. 26, 1983, pp. 1380-1382; see also Vol. 27, 1984, pp. 1406-1048.

5 Watson, E. J., "Diffusion in Oscillating Pipe Flows," *Journal of Fluid Mechanics*, Vol. 133, 1983, pp. 233-244.

6 Brocher, E., "Oscillating Flows in Tubes," *Journal of Fluid Mechanics*, Vol. 79, 1977, pp. 113-126.

7 Davidson, B. J., "Heat Transfer from a Vibrating Circular Cylinder," *International Journal of Heat and Mass Transfer*, Vol. 16, 1973, pp. 1703-1727.

8 Arpaci, V. S., and Larsen, P. S., *Convection Heat Transfer*, Prentice Hall, Englewood Cliffs, N.J., 1984, pp. 245-261.

9 Schlichting, H., *Boundary Layer Theory*, McGraw-Hill, New York, 1968, p. 419.

10 Pismen, L. M., "Multiscale Expansions in Nonlinear Stability Theory," *Fourth International Conference on Physiochemical Hydrodynamics, Annals of the New York Academy of Sciences*, Vol. 404, 1983, pp. 135-149.

11 Abramowitz, M., and Stegun, I. A., *Handbook of Mathematical Functions*, Dover, New York, 1972, pp. 379-384.

12 Kurzweg, U. H., and Zhao, L. D., "Heat Transfer by High Frequency Oscillations; a New Hydrodynamic Technique for Achieving Large Effective Thermal Conductivities," *Physics of Fluids*, Vol. 27, 1984, pp. 2624-2627.

13 Aris, R., "The Dispersion of a Solute in Pulsating Flow Through a Tube," *Proceedings of the Royal Society, London*, A 259, 1960, pp. 370-376.

14 Gill, W. N., and Sankarasubramanian, R., "Exact Analysis of Unsteady Convective Diffusion," *Proceedings of the Royal Society, London*, A 316, 1970, pp. 341-350.

15 Hsieh, H. P., Lee, G. Y., and Gill, W. N., "Interfacial Transport of Energy in Laminar Open Channel and Film Flows," *Chemical Engineering Communications*, Vol. 3, 1979, pp. 105-124.

Journal of Heat Transfer

# Technical Notes

This section contains shorter technical papers. These shorter papers will be subjected to the same review process as that for full papers.

## Experimental Natural Convection Heat Transfer From Isothermal Spherical Zones

W. E. Stewart, Jr.[1] and J. C. Johnson[2]

### Introduction

Natural convection heat transfer from segments or zones of a sphere placed upright on a horizontal plane is addressed in this study. Such heat transfer takes place from small geodesic type structures and small spherical storage containers. Natural convection heat transfer from isolated spheres or hemispheres has been investigated by several authors [1-4]. Apparently there has been no work done for laminar natural convective heat transfer from spherical segments or zones other than a hemisphere.

Snoek and Tarasuk [1] experimentally investigated the free convection heat transfer from a 10.2-cm-dia hemisphere for only a very small range of Rayleigh number, $5.36 \times 10^5$ to $6.19 \times 10^5$. Snoek and Tarasuk's reported results were approximately that of McAdams [2] for an isolated sphere, $Nu = 0.53\,(Ra)^{0.25}$.

An extensive experimental study by Jularia and Gebhart [4] consisted, in part, of measuring heat transfer coefficients from an upright hemisphere on a base in water. Their range of Rayleigh number varied from approximately $2 \times 10^8$ to $2 \times 10^9$. Jaluria and Gebhart's [4] data for the hemisphere closely compared to the results of Yuge [3] for an isolated sphere. The data of both Yuge [3] and Jularia and Gebhart [4] were based on a Rayleigh number whose characteristic length $L_c$ is the diameter $d$ of the sphere or hemisphere.

The heat transfer effects due to interaction between the environmental chamber and the spherical zones were considered to be negligible due to the large distances between the zones and the walls of the environmental chamber [5].

An experimental investigation was performed to study the laminar [4, 6] natural convective heat transfer for a 60 deg zone, a 90 deg zone (hemisphere), and a 120 deg zone, all in the upright position. Results are compared to Yuge's [3] experimental results for an isolated sphere, to Jaluria and Gebhart's [4] results for an upright hemisphere in water, and to the data of Lloyd and Moran [7] for a horizontal flat plate.

### Experimental Apparatus and Procedure

**Apparatus.** The experiments were performed on polished copper spherical zones, of 60, 90, and 120 deg as shown schematically in Fig. 1. All of the zones were fabricated from hemispheres 25.4 cm in diameter and 0.064 cm thick. The zones were made of copper to aid in the attainment of isothermal surface temperatures. The surface was heated by locating separate heating elements, wound circumferentially around the inner surface of the zones.

The zones were placed at the center of a 1.2 m × 1.2 m square closed-cell styrofoam insulation sheet, 20.3 cm thick. The insulation board was provided to minimize the extraneous heat loss by conduction from the lower boundary of the zones. The upper plane of the insulation board was located approximately 0.75 m above the floor, at the center of an environmental chamber.

Each of the zones was heated by electrical resistance wires located on the inner surface of the zone, each element covering approximately an equal portion of the inside surface area of the zones. For each of the zones, four of the thermocouples were located at the base, one at the apex, and the remaining thermocouples spaced between the base and apex along the lines separating each of the four quadrants.

Copper-constantan teflon insulated thermocouples (24 gauge) were used to measure the surface temperature of the zones. The constantan wires were soldered into 0.74-mm-dia holes drilled through the surface of the copper zones. This procedure insured the measurement of the actual surface temperature of the zone. The constantan wires were all connected to a single copper thermocouple wire, soldered to the inside surface of the copper zone.

The heating element wires were cemented in place using a heat transfer cement. The cement held the resistance heating wires in place and also provided a heat flow path between the heating elements and the copper shell. The thickness of the cement was approximately 4 mm. The placement of the

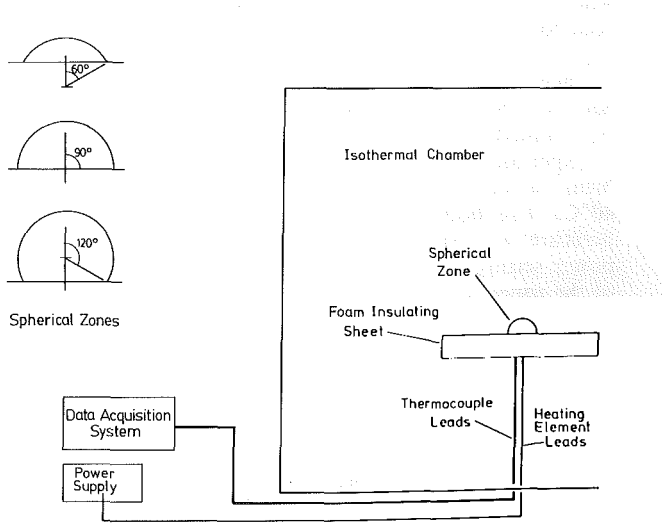


Fig. 1 Spherical zones and experiment schematic

[1]Associate Professor, Mechanical and Aerospace Engineering Department, University of Missouri-Columbia/Kansas City, Truman Campus, Independence, MO 64050, Mem. ASME

[2]Research Assistant, Mechanical and Aerospace Engineering Department, University of Missouri—Columbia/Kansas City, Truman Campus, Independence, MO 64050

Contributed by the Heat Transfer Division for publication in the JOURNAL OF HEAT TRANSFER. Manuscript received by the Heat Transfer Division October 12, 1983.

heating elements was random in relation to the placement of the surface thermocouples, so that the measured surface temperature was near a heating element in one location and approximately halfway between two heating elements in another location. This random arrangement helped verify that the surface temperature measured was indeed isothermal. The interior of the zone was filled with expanding urethane foam insulation to reduce conduction heat loss.

The insulated isothermal environmental test chamber was approximately 2.44 m wide, 2.44 m high, and 4.88 m long. The chamber was constructed of plywood, and insulated with fiberglass approximately 9 cm thick. There were 12 thermocouples located inside the environmental chamber, eight in the eight corners and four on the walls in the center of the chamber to determine whether the ambient air temperature was uniform or stratified. The air temperatures inside the chamber experienced a maximum differential air temperature of less than 1.0°C during any experimental run and showed no stratification.

Additionally three thermocouples were located just above the surface of the insulating board to measure the ambient air temperature near the spherical zone. The measured air temperature at these thermocouples varied less than 2 percent from the other twelve thermocouples measuring the air temperature of the environmental chamber.

Two thermocouples were used to measure the temperature of the insulating foam under the spherical zones. One of the thermocouples was placed in the plane of the zone base and one approximately 8 cm below in the foam sheet. These measured temperatures were used for estimating the heat loss by conduction through the foam insulation.

The temperatures of the zones and the chamber were recorded via a data acquisition system. A schematic of the experimental setup is shown in Fig. 1.

The lead wires from the resistance heating elements were connected to the DC power supply outside the chamber. The experiment required between 2 and 3 hr to reach steady-state conditions. Once steady-state conditions were reached, the resistance and DC current were measured for each heating element.

**Data Reduction.** The average heat transfer coefficient was calculated from the measured average surface temperature of the zone, ambient air temperature, and power input to heat the surface. The definition of average heat transfer coefficient is

$$h = \frac{Q}{A(T_s - T_\infty)} \tag{1}$$

where $Q$ is the net rate of heat transfer from the surface of the zone to the ambient air $T_s$ is the average surface temperature, $T_\infty$ is the average free stream temperature, and $A$ is the surface area. The net heat transfer from the surface of the zone was the net power input to the zone minus the heat losses by conduction and radiation.

Experiments were performed for average surface to ambient temperature differences, $\Delta T = T_s - T_\infty$, of 2°C to 40°C. The boundary condition of uniform surface temperature was easier to obtain experimentally at the lower power settings (the lower values of $\Delta T$). Hence, the surfaces of the zones were nearly uniform in temperature at the lower power settings and more nonuniform in temperature at the higher power settings, due to heat losses to the insulating base and the imperfect distribution of the heating wires on the inside zone surface. The variation of $T_s$ on the surfaces at the lower values of $\Delta T$, 2°C, was less than 1 percent, and increased to about 2.5 percent at the largest values of $\Delta T$, 40°C.

The heat loss by radiation from the spherical zones was estimated by

$$Q_{\text{rad}} = \epsilon\sigma A(T_s^4 - T_\infty^4) \tag{2}$$

where $\epsilon$ is the measured emissivity for the polished copper surfaces, nominally 0.04. The value of $Q_{\text{rad}}$ from equation (2) represented from 5 to 10% of the heat loss from each zone.

The conduction heat losses were estimated by utilizing two thermocouples to measure the temperature variation through the foam insulation base. In equation form, the heat loss by conduction was calculated as

$$Q_{\text{cond}} = -k_i A_b \Delta T/\Delta Z \tag{3}$$

where $k_i$ is the thermal conductivity of the foam insulation, $A_b$ is the cross-sectional area of the base of the zone, and $\Delta T/\Delta Z$ is the measured temperature variation below the spherical zone. This calculated heat loss represented approximately 5 percent of the heat loss from each zone.

## Results and Discussion

The heat transfer configuration considered here is that of a uniform surface temperature spherical zone at $T_s$ whose base is on a plane of a uniform temperature horizontal surface in a uniform temperature air environment, the latter two both at $T_\infty$.

The boundary layer in this free convective geometry continues to grow from the base of the zone to the apex. This results in decreasing amounts of heat transfer per unit area across the boundary layer as the apex is approached. This characteristic was quite apparent in the experiments. During the experiments little or no power input was required to the uppermost resistance heating wire in order to obtain an isothermal surface. Thus, most of the heat loss from the zones occurred on the lower portion of the surface. This was consistent for all three zones studied. These results are contrary to the findings of Jaluria and Gebhart [4] and of Kranse and Schenk [8] where a sudden increase in heat transfer was noted near the apex. The data of both Jaluria and Gebhart [4], and Kranse and Schenk [8] were at Rayleigh numbers ($\text{Ra}_d$) greater than $2.5 \times 10^8$, exceeding the values in this investigation.

The typical correlation for Nusselt number [2] for the case of natural convection is of the form

$$\text{Nu} = C\ \text{Ra}^n \tag{4}$$

where $C$ and $n$ depend on the shape of the object. The value of $n$ is typically found to be about 0.25 for laminar flow.

The characteristic length found to yield the best correlation of the data was defined as $L_c = A/P$, the surface area $A$ divided by the zone perimeter $P$ at the base. The use of $L_c$ defined in this manner may be thought of as pseudo-external hydraulic diameter. The use of $L_c = A/P$ for flat plates was first proposed by Goldstein et al. [9].

For a characteristic length of $L_c = d$, $\text{Ra}_d$ values for the three zones varied from $4.1 \times 10^6$ to $4.7 \times 10^7$, when the characteristic length $L_c = d = 25.4$ cm for all the zones. The use of $L_c = d$ for all zones does not yield a good correlation of the data. For $L_c = d$, the range of $\text{Ra}_d$ for the hemisphere is below that of the results of [4].

When $L_c$ = height of the zone $H$, $\text{Ra}_H$ values vary between approximately $1.8 \times 10^5$ and $1.5 \times 10^7$. As in the case of $L_c = d$ the data do not correlate as well as when $L_c = A/P$.

Hence, the data were correlated using equation (4), with $n = 0.25$, and setting $L_c = A/P = \gamma$,

$$\text{Nu}_\gamma = C(\text{Ra}_\gamma)^{0.25} \tag{5}$$

A least-squares fit of the data for all zones using equation (5) resulted in the following correlation

$$\text{Nu}_\gamma = 0.49(\text{Ra}_\gamma)^{0.25}, \tag{6}$$

for

$$60 \text{ deg} \leq \theta \leq 120 \text{ deg},$$

and

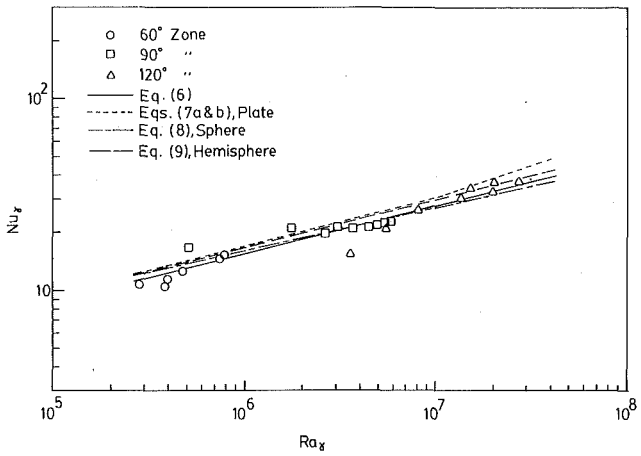


**Fig. 2 Results for 60, 90, and 120 deg zones, in comparison to an isolated sphere [3], an upright Hemisphere on a base [4], and a horizontal flat plate [7]**

$$2.8\times10^5 \le Ra_\gamma \le 2.8\times10^7,\ Pr\sim0.7$$

The data are plotted in Fig. 2 along with equation (6). It should be stressed that the correlation given by equation (6) applies only for $\theta$ between 60 and 120 deg. Since the characteristic length $\gamma$ is the ratio of the surface area $A$ to the base perimeter $P$ the correlation of equation (6) is not applicable to, for example, a sphere where $A/P \to \infty$. Allowing the characteristic length to be equal to the diameter $d$ for a sphere ($\theta$ = 180 deg) would probably result in a reasonable approximation of the case of a sphere sitting on a horizontal plane. The results of [3] for a sphere and the data for the 120 deg zone, shown in Fig. 2, are nearly the same.

As seen in Fig. 2, the data from the 90 deg zone shows a slightly smaller dependence of the Nusselt number on the Rayleigh number. The data from the 60 and 120 deg zones, on the other hand, show a slightly greater dependence of the Nusselt number on the Rayleigh number. There is apparently no physical reason for the variation of Nu dependence between zones, other than experimental error. The experimental results of [4] for the hemisphere show essentially no variation in the slope of the data from $n = 0.25$.

Also shown in Fig. 2 is the correlation for a horizontal flat plate from Lloyd and Moran [7],

$$Nu_L = 0.54\ Ra_L^{0.25} \tag{7a}$$

for

$$10^5 < Ra_L < 10^7,$$

and

$$Nu_\gamma = 0.15\ Ra_\gamma^{0.33} \tag{7b}$$

for

$$10^7 < Ra_\gamma < 10^{10}$$

The correlation of [7] is included here because the characteristic length is defined in the same manner as in this investigation. All three zones show good agreement with the results of Lloyd and Moran [7], for the range of $Ra_\gamma$ investigated, even though the geometrical configurations are quite different.

Also shown in Fig. 2 are the extrapolated results for an isolated sphere (Yuge [3]), and the extrapolated results for a hemisphere in water (Jaluria and Gebhart [4]). The correlations in the investigations of [3] and [4] used diameter as the characteristic length. To compare the results of [4] with the results of this study it was necessary to modify the correlation, using a characteristic length of radius for the hemisphere.

Yuge's [3] experimental results for isolated spheres were given as

$$Nu_d = 2.0 + 0.43(Ra_d)^{0.25}, L_c = d = \gamma \tag{8}$$
$$1 < Ra_d < 10^5.$$

The relationship developed from the data of Jaluria and Gebhart [4] is of the same form as equation (4) and, for the upright hemisphere with a base, is approximately correlated by,

$$Nu_\gamma = 0.53 Ra_\gamma^{0.25},\ L_c = d/2 = \gamma \tag{9}$$
$$2.5\times10^7 < Ra_\gamma < 2.5\times10^8$$

where $n$ was set equal to 0.25, as in [4].

The correlation for the data from this investigation, equation (6), and the extrapolated results of Yuge [3], Jaluria and Gebhart [4], and the correlation of Lloyd and Moran [7] show very similar Nusselt number results.

An estimate of the uncertainty in the experimental data was made. From an estimate of the possible experimental errors in measuring temperatures and power input (and power losses), the uncertainty for $Nu_\gamma$ was estimated as 16 percent and the uncertainty for $Ra_\gamma$ was estimated as 5 percent.

## Concluding Remarks

The new experimental data obtained were used to determine a correlation to predict the laminar flow [4, 6] natural convective heat transfer from isothermal 60, 90, and 120 deg spherical zones placed upright on a horizontal base. The experimental data for all the zones were correlated by the single equation (6) to predict the Nusselt number as a function of the Rayleigh number.

All of the zones investigated showed a slight variation in the dependence of the Nusselt number upon the Rayleigh number from a slope of 0.25. At the relatively large values of $Ra_\gamma$ encountered here the laminar boundary layer should be clearly developed [4, 6] on all the zones. The laminar boundary layer also should not dramatically change in character over the range of $Ra_\gamma$ for each of the zones. Hence, the slight variations from $n = 0.25$ are apparently due to experimental error. Overall, the data obtained through this experiment are in good agreement with the results published for an isolated isothermal sphere [3], an upright hemisphere on an insulated base in water [4], and a flat horizontal plate heated on the upper surface [7].

## References


1 Snoek, C. W., and Tarasuk, J. D., "Heat Transfer from Inflatable Structures," ASME Paper No. 75-WA/HT-97, Nov. 1975.

2 McAdams, W. H., *Heat Transmission*, 3rd ed., McGraw-Hill, New York, 1954.

3 Yuge, T., "Experiments on Heat Transfer From Spheres Including Combined Natural and Forced Convection," ASME JOURNAL OF HEAT TRANSFER, Vol. 82, 1960, pp. 214–220.

4 Jaluria, Y., and Gebhart, B., "On the Buoyancy-Induced Flow Arising From a Heated Hemisphere," *Int. J. Heat Mass Transfer*, Vol. 18, 1975, pp. 415–431.

5 Warrington, R. O., Jr., and Powe, R. E., "Natural Convection Heat Transfer Between Bodies and Their Enclosures," ASME HTD, Vol. 16, 1981, pp. 111–125.

6 Potter, J. M., and Riley, N., "Free Convection from a Heated Sphere at Large Grashof Number," *J. Fluid Mechanics*, Vol. 100, Part 4, 1980, pp. 769–783.

7 Lloyd, J. R., and Moran, W. R., "Natural Convection Adjacent to Horizontal Surfaces of Various Platforms," ASME Paper No. 74-WA/HT-66, 1974.

8 Kranse, A. A., and Schenk, J., "Thermal Free Convection from a Solid Sphere," *Appl. Sci. Res.*, A15, 1965, pp. 397–403.

9 Goldstein, R. J., Sparrow, E. M., and Jones, D. C., "Natural Convection Mass Transfer Adjacent to Horizontal Plates," *Int. J. Heat Mass Transfer*, Vol. 16, No. 5, 1973, pp. 1025–1035.

# Numerical Solution of the Graetz Problem for a Bingham Plastic in Laminar Tube Flow With Constant Wall Temperature

**B. F. Blackwell**[1]

## Nomenclature

$c$ = $\tau_y/\tau_w$, ratio of yield stress to wall shear stress
$C_p$ = specific heat at constant pressure
$C_n$ = constant in series solution
$D$ = pipe diameter
$G_n$ = constant, see equation (9)
$h_x$ = local convective heat transfer coefficient, $h_x = \dot{q}''/(t_b - t_o)$
$k$ = thermal conductivity
$\mathrm{Nu}_x$ = $h_x D/k$, local Nusselt number
$\mathrm{Nu}_m$ = average of $\mathrm{Nu}_x$ between entrance and axial location $x$
$\dot{q}''(x)$ = wall heat flux
Pe = $\bar{u}D/\alpha$, Peclet number
$r$ = radial coordinate
$r_0$ = pipe radius
$r^+$ = $r/r_o$, dimensionless radius
$R_n(r^+)$ = eigenfunction
$t(x,r)$ = temperature
$t_b$ = bulk or mixing cup temperature
$t_e$ = uniform entrance temperature
$t_o$ = uniform wall temperature
$u(r)$ = axial velocity
$u_{\max}$ = maximum axial velocity
$\bar{u}$ = average axial velocity
$u^+$ = $u/\bar{u}$
$x$ = axial coordinate
$x^+$ = $\dfrac{x/r_o}{\mathrm{Pe}}$, dimensionless axial coordinate

## Greek

$\alpha$ = $k/\rho C_p$, thermal diffusivity
$\eta$ = Bingham viscosity
$\theta$ = $\dfrac{t_o - t(x,r)}{t_o - t_e}$, dimensionless temperature
$\theta_b$ = $\dfrac{t_o - t_b}{t_o - t_e}$, dimensionless bulk fluid temperature, see equation (6)
$\lambda$ = eigenvalue
$\rho$ = density
$\tau$ = local shear stress
$\tau_w$ = wall shear stress
$\tau_y$ = yield shear stress

[1]Centrifuge, Climatic and Radiant Heat, Division 7531, Sandia National Laboratories, Albuquerque, N.M. 87185; Mem. ASME

Contributed by the Heat Transfer Division for publication in the JOURNAL OF HEAT TRANSFER. Manuscript received by the Heat Transfer Division August 15, 1983.

## Introduction

Many fluids exhibit a yield stress ($\tau_y$), a stress which must be exceeded before the fluid will flow. Bird et. al. [1] presented an extensive tabulation of materials with yield stresses; some common examples are drilling mud, sewage sludge, grease, paint, and thorium dioxide/methanol. If the local shear stress does not exceed the yield stress, these fluids will not support a velocity gradient. In pipe flow geometries, it is possible that the fluid region near the centerline (low shear stress, $\tau < \tau_y$) may move as a solid (plug flow), while the fluid near the wall (high shear stress, $\tau > \tau_y$) supports a velocity gradient.

This note was motivated by the desire to understand the heat transfer behavior of aqueous foams being used as a drilling fluid in high temperature petroleum and geothermal formations. In some applications, aqueous foams offer several advantages over conventional drilling fluids: (*i*) bottom hole pressure is reduced because aqueous foams have a much lower density than conventional drilling muds, (*ii*) relatively little fall back of cuttings when circulation stops, and (*iii*) low loss of circulation in porous formations. Additional details on the thermal behavior of aqueous foams circulating in geothermal wellbores are presented in Blackwell and Ortega [2]. This article is an extension of the work of Wissler and Schechter [3] concerning the heat transfer behavior of Bingham plastics in developing tube flow.

## Analysis

The constitutive equation for a Bingham plastic in pipe flow is of the form [1, 3, 4]

$$\frac{du}{dr} = 0 \text{ for } \tau < \tau_y$$

$$-\frac{du}{dr} = \frac{1}{\eta}(\tau - \tau_y) \text{ for } \tau > \tau_y \tag{1}$$

where $u$ is the axial velocity component, $r$ is the radial coordinate, $\tau$ is the local shear stress, $\tau_y$ is the yield stress, and $\eta$ is the Bingham viscosity. For constant properties, the results of [1, 3, 4] can be used to express the dimensionless velocity profile as

$$u^+ = \frac{2[1 - r^{+2} - 2c(1 - r^+)]}{1 - \frac{4}{3}c + \frac{c^4}{3}} \qquad c \le r^+ \le 1$$

$$= \frac{2(1-c)^2}{1 - \frac{4}{3}c + \frac{c^4}{3}} \qquad 0 \le r^+ \le c \tag{2}$$

Note that $c = 1$ corresponds to plug flow ($u = u_{\max}$), while $c = 0$ corresponds to laminar Newtonian flow.

If axial conduction is neglected (Pe > 100) and viscous dissipation ignored, the steady flow constant property form of the energy equation and its boundary conditions can be written as

$$\rho C_p u(r)\frac{\partial t}{\partial x} = k\frac{1}{r}\frac{\partial}{\partial r}\left(r\frac{\partial t}{\partial r}\right), t(0,r) = t_e, t(x,r_0) = t_0, \quad \frac{\partial t}{\partial r}(x,0) = 0 \tag{3}$$

For uniform wall temperature $t_o$ and inlet temperature $t_e$, the dimensionless energy equation is

$$\frac{u^+}{2}\frac{\partial \theta}{\partial x^+} = \frac{1}{r^+}\frac{\partial}{\partial r^+}\left(r^+\frac{\partial \theta}{\partial r^+}\right), \theta(0,r^+) = 1, \theta(x^+,1) = 0, \quad \frac{\partial \theta}{\partial r^+}(x^+,0) = 0 \tag{4}$$

**Table 1 Heat transfer results for developing flow of Bingham plastic in a tube with constant wall temperature**

c=1.0 (plug flow)

| $x^+$ | $Nu_x$ | $Nu_m$ | $\theta_b$ |
|---|---|---|---|
| .0001 | 81.352 | 161.146 | .9682847 |
| .0002 | 58.008 | 114.413 | .9552662 |
| .0004 | 41.502 | 81.375 | .9369734 |
| .0010 | 26.876 | 52.074 | .9010919 |
| .0020 | 19.531 | 37.322 | .8613197 |
| .0040 | 14.372 | 26.914 | .8062926 |
| .0100 | 9.844 | 17.731 | .7014360 |
| .0200 | 7.744 | 13.174 | .5904024 |
| .0400 | 6.437 | 10.063 | .4470782 |
| .1000 | 5.817 | 7.620 | .2178524 |
| .2000 | 5.783 | 6.705 | .0684313 |
| .4000 | 5.783 | 6.244 | .0067703 |
| 1.0000 | 5.783 | 5.968 | .0000066 |
| 2.0000 | 5.783 | 5.875 | .0000000 |
| 4.0000 | 5.783 | 5.829 | .0000000 |
| 10.0000 | 5.783 | 5.802 | .0000000 |

c=0.8

| $x^+$ | $Nu_x$ | $Nu_m$ | $\theta_b$ |
|---|---|---|---|
| .0001 | 39.913 | 60.569 | .9879594 |
| .0002 | 31.453 | 47.802 | .9810610 |
| .0004 | 24.774 | 37.701 | .9702898 |
| .0010 | 18.079 | 27.529 | .9464307 |
| .0020 | 14.271 | 21.704 | .9168451 |
| .0040 | 11.299 | 17.129 | .8719433 |
| .0100 | 8.366 | 12.569 | .7777295 |
| .0200 | 6.777 | 10.003 | .6702263 |
| .0400 | 5.703 | 8.069 | .5243750 |
| .1000 | 5.111 | 6.401 | .2779934 |
| .2000 | 5.066 | 5.738 | .1007254 |
| .4000 | 5.066 | 5.402 | .0132775 |
| 1.0000 | 5.066 | 5.200 | .0000304 |
| 2.0000 | 5.066 | 5.133 | .0000000 |
| 4.0000 | 5.066 | 5.099 | .0000000 |
| 10.0000 | 5.066 | 5.079 | .0000000 |

c=0.6

| $x^+$ | $Nu_x$ | $Nu_m$ | $\theta_b$ |
|---|---|---|---|
| .0001 | 33.304 | 50.486 | .9899536 |
| .0002 | 26.265 | 39.866 | .9841801 |
| .0004 | 20.706 | 31.462 | .9751443 |
| .0010 | 15.135 | 22.998 | .9550453 |
| .0020 | 11.972 | 18.153 | .9299621 |
| .0040 | 9.520 | 14.353 | .8915229 |
| .0100 | 7.149 | 10.591 | .8091051 |
| .0200 | 5.892 | 8.503 | .7116963 |

c=0.6

| $x^+$ | $Nu_x$ | $Nu_m$ | $\theta_b$ |
|---|---|---|---|
| .0400 | 5.038 | 6.943 | .5738254 |
| .1000 | 4.539 | 5.593 | .3267612 |
| .2000 | 4.494 | 5.048 | .1327436 |
| .4000 | 4.493 | 4.771 | .0220013 |
| 1.0000 | 4.493 | 4.604 | .0001002 |
| 2.0000 | 4.493 | 4.549 | .0000000 |
| 4.0000 | 4.493 | 4.521 | .0000000 |
| 10.0000 | 4.493 | 4.504 | .0000000 |

c=0.4

| $x^+$ | $Nu_x$ | $Nu_m$ | $\theta_b$ |
|---|---|---|---|
| .0001 | 30.513 | 46.252 | .9907923 |
| .0002 | 24.065 | 36.524 | .9854966 |
| .0004 | 18.970 | 28.825 | .9772039 |
| .0010 | 13.860 | 21.068 | .9587394 |
| .0020 | 10.956 | 16.625 | .9356627 |
| .0040 | 8.703 | 13.139 | .9002269 |
| .0100 | 6.520 | 9.684 | .8239285 |
| .0200 | 5.364 | 7.764 | .7330460 |
| .0400 | 4.585 | 6.332 | .6025852 |
| .1000 | 4.126 | 5.094 | .3610479 |
| .2000 | 4.082 | 4.593 | .1592788 |
| .4000 | 4.081 | 4.337 | .0311343 |
| 1.0000 | 4.081 | 4.183 | .0002326 |
| 2.0000 | 4.081 | 4.132 | .0000001 |
| 4.0000 | 4.081 | 4.106 | .0000000 |
| 10.0000 | 4.081 | 4.091 | .0000000 |

c=0.2

| $x^+$ | $Nu_x$ | $Nu_m$ | $\theta_b$ |
|---|---|---|---|
| .0001 | 29.061 | 44.053 | .9912281 |
| .0002 | 22.921 | 34.788 | .9861812 |
| .0004 | 18.066 | 27.454 | .9782760 |
| .0010 | 13.196 | 20.064 | .9606662 |
| .0020 | 10.426 | 15.830 | .9386436 |
| .0040 | 8.274 | 12.505 | .9047981 |
| .0100 | 6.186 | 9.208 | .8318034 |
| .0200 | 5.075 | 7.372 | .7446142 |
| .0400 | 4.319 | 5.999 | .6188482 |
| .1000 | 3.861 | 4.803 | .3826712 |
| .2000 | 3.814 | 4.314 | .1780752 |
| .4000 | 3.813 | 4.063 | .0387508 |
| 1.0000 | 3.813 | 3.913 | .0003994 |
| 2.0000 | 3.813 | 3.863 | .0000002 |
| 4.0000 | 3.813 | 3.838 | .0000000 |
| 10.0000 | 3.813 | 3.823 | .0000000 |

c=0.0 (Laminar Newtonian)

| $x^+$ | $Nu_x$ | $Nu_m$ | $\theta_b$ |
|---|---|---|---|
| .0001 | 28.244 | 42.814 | .9914737 |
| .0002 | 22.278 | 33.810 | .9865668 |
| .0004 | 17.559 | 26.683 | .9788795 |
| .0010 | 12.824 | 19.501 | .9617496 |
| .0020 | 10.130 | 15.384 | .9403183 |
| .0040 | 8.036 | 12.152 | .9073635 |
| .0100 | 6.002 | 8.943 | .8362189 |
| .0200 | 4.916 | 7.155 | .7511056 |
| .0400 | 4.172 | 5.815 | .6280276 |
| .1000 | 3.710 | 4.641 | .3952988 |
| .2000 | 3.658 | 4.156 | .1897101 |
| .4000 | 3.657 | 3.906 | .0439350 |
| 1.0000 | 3.657 | 3.757 | .0005458 |
| 2.0000 | 3.657 | 3.707 | .0000004 |
| 4.0000 | 3.657 | 3.682 | .0000000 |
| 10.0000 | 3.657 | 3.667 | .0000000 |

Equation (4) can be solved by the classical separation of variables technique which leads to the Sturm–Liouville eigenvalue problem. The details of this are available in Kays and Crawford [5], and only pertinent results will be presented here.

$$\theta(x^+,r^+) = \sum_{n=0}^{\infty} C_n R_n(r^+)\exp(-\lambda_n^2 x^+) \tag{5}$$

where $C_n$ is a constant to be determined form the boundary conditions and $R_n(r^+)$ and $\lambda_n$ are eigenfunctions and eigenvalues, respectively. The bulk fluid temperature $\theta_b$ and local and average Nusselt numbers are determined by

$$\theta_b(x^+) = \frac{t_o - t_b}{t_o - t_e} = 2\int_0^1 u^+ \theta r^+ dr^+$$

$$= 8\sum_{n=0}^{\infty} \frac{G_n}{\lambda_n^2}\exp(-\lambda_n^2 x^+) \tag{6}$$

$$\mathrm{Nu}_x = \frac{h_x D}{k} = \frac{-2}{\theta_b}\left.\frac{\partial\theta}{\partial r^+}\right|_{(x,1)} = \frac{4}{\theta_b}\sum_{n=0}^{\infty} G_n \exp(-\lambda_n^2 x^+) \tag{7}$$

$$\mathrm{Nu}_m(x^+) = \frac{1}{x^+}\int_0^{x^+} \mathrm{Nu}_x dx^+ = \frac{1}{2x^+}\ln(1/\theta_b) \tag{8}$$

where the more convenient constant $G_n$ is defined by

$$G_n = -\frac{C_n}{2}\frac{dR_n(1)}{dr^+} = \frac{[dR_n(1)/dr^+]^2/2}{\lambda^2\int_0^1 \frac{u^+}{2} r^+ R_n^2 dr^+} \tag{9}$$

The development of equation (8) is given in Burmeister [6].

The eigenfunctions $R_n(r^+)$ and eigenvalues $\lambda_n$ of equation (5) are determined from the Sturm–Liouville problem. A closed-form analytical solution exists for plug flow ($c = 1$, see Burmeister [6] for a discussion); Sellars, Tribus, and Klein [7] developed an approximate solution for laminar Newtonian flow ($c = 0$); and Wissler and Schechter [3] numerically determined the first seven eigenvalues and eigenfunctions for $c = 0.0, 0.25, 0.5, 0.75$, and 1.0. Additional works are referenced in [1]. The number of eigenvalues and eigenfunctions reported by Wissler and Schechter [3] was found to be inadequate for small values of $x^+$ and the calculations were extended to include the first 60 eigenvalues for $c = 0.0$, 0.2, 0.4, 0.6, 0.8, 1.0. The numerical results presented here were obtained from a general purpose Sturm–Liousille computer code, SLEIGN, developed by Bailey [8].

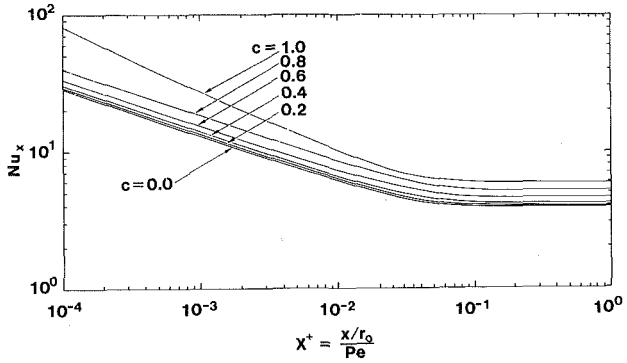


Fig. 1 Variation of local Nusselt number ($Nu_x$) with dimensionless axial distance ($x/r_o$)/Pe for $c$ = 0.0, 0.2, 0.4, 0.6, 0.8, and 1.0

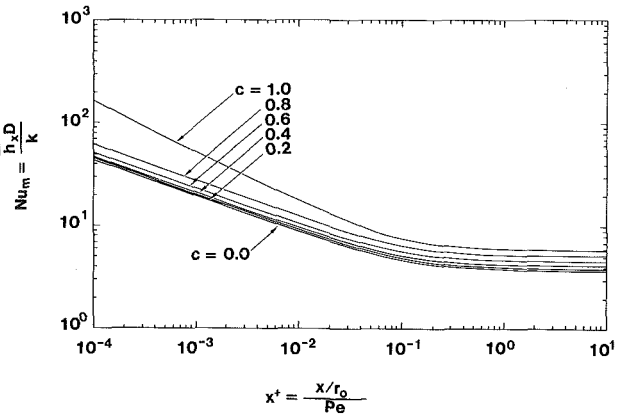


Fig. 2 Variation of mean Nusselt number ($Nu_m$) with dimensionless axial distance ($x/r_o$)/Pe for $c$ = 0.0, 0.2, 0.4, 0.6, 0.8, and 1.0

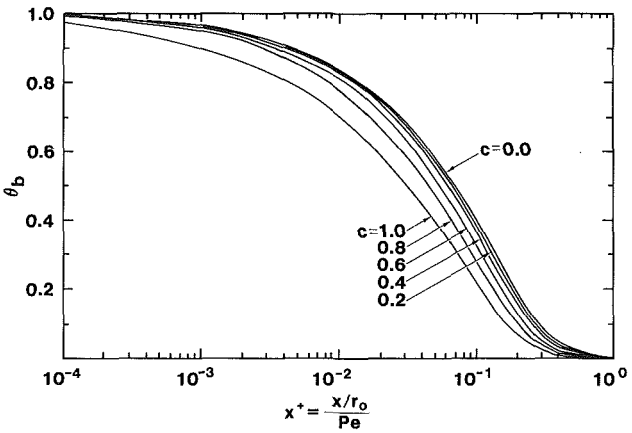


Fig. 3 Variation of dimensionless bulk fluid temperature ($\theta_b$) with dimensionless axial distance ($x/r_o$)/Pe for $c$ = 0.0, 0.2, 0.4, 0.6, 0.8, and 1.0

## Results

Table 1 presents numerical results for the local Nusselt number ($Nu_x$), average Nusselt number $Nu_m$, and bulk fluid temperature as a function of the dimensionless entry length $x^+$. All calculations were performed on a CDC Cyber 170/Model 855 computer using single precision arithmetic (nominally 14 1/2 digits). The series for $Nu_x$ converges more slowly than that for $\theta_m$. A relative convergence criteria of $10^{-6}$ on the last term (normalized by the partial sum) was used. Sixty eigenvalues were adequate for convergence for all values of $x^+$ except 0.0001; for this $x^+$, the relative error was typically less than $7 \times 10^{-5}$ for all values of $c$. The numerical results for $c$ = 1.0 were compared with the analytical solution; for this case, the eigenvalues are the roots of $J_o(\lambda_n/\sqrt{2}) = 0$ and the eigenfunctions are $R_n(r^+) = J_o(\lambda_n/\sqrt{2}\, r^+)$. The results from SLEIGN were identical to the analytical solution for the number of significant digits printed, except for $x^+ = 0.0001$. For example, the analytical result was $Nu_x = 81.352$, while the numerical result was 81.365. The $c$ = 1 (plug flow) results were also compared with those presented in Burmeister [5]; exact agreement was obtained for large $x^+$ but it appears that the results of [4] are not accurate at small $x^+$.

The results of Sellars, Tribus, and Klein [6] for laminar Newtonian flow ($c$ = 0) and presented in Kays and Crawford [5] and Burmeister [6] do not appear to be accurate at small $x^+$. The results of Table 1 are also presented graphically in Figs. 1-3. For $c$ near zero, the results are insensitive to $c$; however, this is not the case for $c$ near unity.

## Acknowledgment

This work was supported by the Department of Energy under Contract DE-AC0476DP00789.

## References

1 Bird, R. B., Dai, G. C., and Yarusso, B. J., "The Rheology and Flow of Viscoplastic Materials," *Reviews in Chemical Engineering*, Vol. 1, No. 1, 1982, pp. 1-70.

2 Blackwell, B. F., and Ortega, A., "A Quasi-Steady Model for Predicting Temperature of Aqueous Foams Circulating in Geothermal Wellbores," *Proceedings ASME/JSME Thermal Engineering Joint Conference*, Vol. II, 1983, pp. 101-111.

3 Wissler, E. H., and Schechter, R. S., "The Graetz-Nusselt Problem (with Extension) for a Bingham Plastic," *Chemical Engineering Progress Symposium Series No. 29*, Vol. 55, 1959, pp. 203-208.

4 Bird, R. B., Stewart, W. E., and Lightfoot, E. N., *Transport Phenomena*, Wiley & Sons, New York, 1960.

5 Kays, W. M., and Crawford, M. E., *Convective Heat and Mass Transfer*, (2d ed.), McGraw-Hill, New York, 1980.

6 Burmeister, L. C., *Convective Heat Transfer*, John Wiley & Sons, New York, 1983.

7 Sellars, J. R., Tribus, M., and Klein, J. S., "Heat Transfer to Laminar Flow in a Round Tube or Flat Conduit—The Graetz Problem Extended," ASME *Transactions*, Vol. 78, Feb. 1956, pp. 441-448.

8 Bailey, P. B., "SLEIGN An Eigenvalue-Eigenfunction Code for Sturm-Liouville Problems," Sandia National Laboratories, SAND77-2044, Mar. 1978.

# Effects of Liquid Level on Boiling Heat Transfer in Potassium Layers on a Horizontal Plane Heater

**I. Michiyoshi,[1] N. Takenaka,[1] T. Murata,[2] T. Shiokawa,[1] and O. Takahashi[1]**

## Nomenclature

$c_l$ = specific heat of liquid
$E(\beta)$ = value defined in [6]
$h$ = empirical constant in equation (1)
$k_l$ = thermal conductivity of liquid
LL = liquid level above heating surface
$q$ = heat flux
SP = system pressure
$T_{sat}$ = saturation temperature corresponding to SP
$T_v$ = vapor temperature

[1]Department of Nuclear Engineering, Kyoto University, Kyoto, 606, Japan.
[2]Nuclear Fuel Industries, Kumatori, Osaka 590-04, Japan.

Contributed by the Heat Transfer Division for publication in the JOURNAL OF HEAT TRANSFER. Manuscript received by the Heat Transfer Division July 23, 1983.

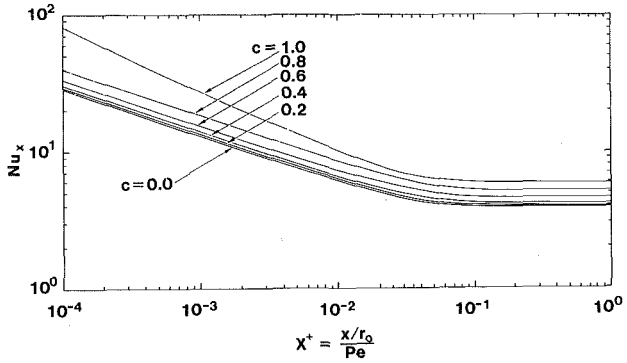


Fig. 1 Variation of local Nusselt number ($Nu_x$) with dimensionless axial distance ($x/r_o$)/Pe for $c$ = 0.0, 0.2, 0.4, 0.6, 0.8, and 1.0

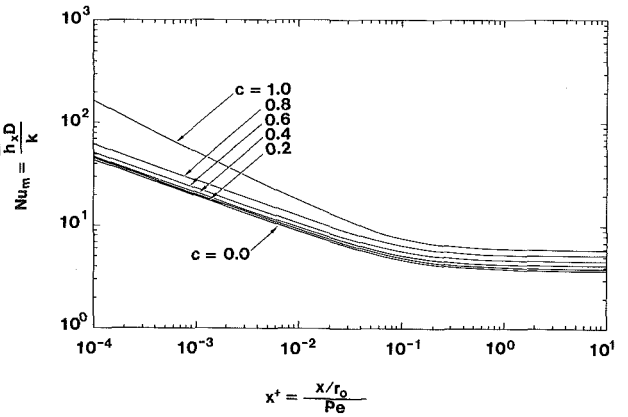


Fig. 2 Variation of mean Nusselt number ($Nu_m$) with dimensionless axial distance ($x/r_o$)/Pe for $c$ = 0.0, 0.2, 0.4, 0.6, 0.8, and 1.0

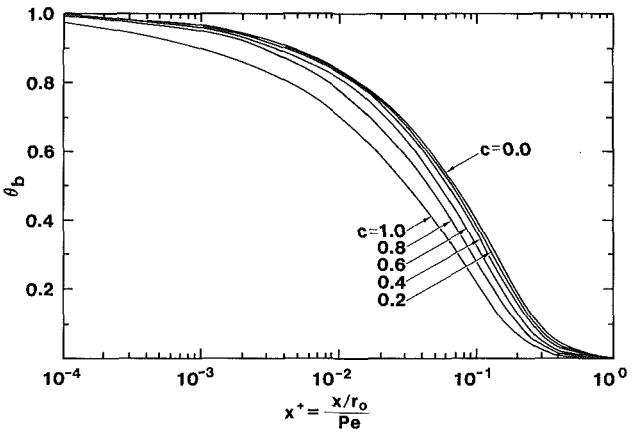


Fig. 3 Variation of dimensionless bulk fluid temperature ($\theta_b$) with dimensionless axial distance ($x/r_o$)/Pe for $c$ = 0.0, 0.2, 0.4, 0.6, 0.8, and 1.0

## Results

Table 1 presents numerical results for the local Nusselt number ($Nu_x$), average Nusselt number $Nu_m$, and bulk fluid temperature as a function of the dimensionless entry length $x^+$. All calculations were performed on a CDC Cyber 170/Model 855 computer using single precision arithmetic (nominally 14 1/2 digits). The series for $Nu_x$ converges more slowly than that for $\theta_m$. A relative convergence criteria of $10^{-6}$ on the last term (normalized by the partial sum) was used. Sixty eigenvalues were adequate for convergence for all values of $x^+$ except 0.0001; for this $x^+$, the relative error was typically less than $7 \times 10^{-5}$ for all values of $c$. The numerical results for $c$ = 1.0 were compared with the analytical solution; for this case, the eigenvalues are the roots of $J_o(\lambda_n/\sqrt{2}) = 0$ and the eigenfunctions are $R_n(r^+) = J_o(\lambda_n/\sqrt{2}\, r^+)$. The results from SLEIGN were identical to the analytical solution for the number of significant digits printed, except for $x^+ = 0.0001$. For example, the analytical result was $Nu_x = 81.352$, while the numerical result was 81.365. The $c$ = 1 (plug flow) results were also compared with those presented in Burmeister [5]; exact agreement was obtained for large $x^+$ but it appears that the results of [4] are not accurate at small $x^+$.

The results of Sellars, Tribus, and Klein [6] for laminar Newtonian flow ($c$ = 0) and presented in Kays and Crawford [5] and Burmeister [6] do not appear to be accurate at small $x^+$. The results of Table 1 are also presented graphically in Figs. 1-3. For $c$ near zero, the results are insensitive to $c$; however, this is not the case for $c$ near unity.

## Acknowledgment

This work was supported by the Department of Energy under Contract DE-AC0476DP00789.

## References

1 Bird, R. B., Dai, G. C., and Yarusso, B. J., "The Rheology and Flow of Viscoplastic Materials," *Reviews in Chemical Engineering*, Vol. 1, No. 1, 1982, pp. 1-70.

2 Blackwell, B. F., and Ortega, A., "A Quasi-Steady Model for Predicting Temperature of Aqueous Foams Circulating in Geothermal Wellbores," *Proceedings ASME/JSME Thermal Engineering Joint Conference*, Vol. II, 1983, pp. 101-111.

3 Wissler, E. H., and Schechter, R. S., "The Graetz-Nusselt Problem (with Extension) for a Bingham Plastic," *Chemical Engineering Progress Symposium Series No. 29*, Vol. 55, 1959, pp. 203-208.

4 Bird, R. B., Stewart, W. E., and Lightfoot, E. N., *Transport Phenomena*, Wiley & Sons, New York, 1960.

5 Kays, W. M., and Crawford, M. E., *Convective Heat and Mass Transfer*, (2d ed.), McGraw-Hill, New York, 1980.

6 Burmeister, L. C., *Convective Heat Transfer*, John Wiley & Sons, New York, 1983.

7 Sellars, J. R., Tribus, M., and Klein, J. S., "Heat Transfer to Laminar Flow in a Round Tube or Flat Conduit—The Graetz Problem Extended," ASME *Transactions*, Vol. 78, Feb. 1956, pp. 441-448.

8 Bailey, P. B., "SLEIGN An Eigenvalue-Eigenfunction Code for Sturm-Liouville Problems," Sandia National Laboratories, SAND77-2044, Mar. 1978.

# Effects of Liquid Level on Boiling Heat Transfer in Potassium Layers on a Horizontal Plane Heater

**I. Michiyoshi,[1] N. Takenaka,[1] T. Murata,[2] T. Shiokawa,[1] and O. Takahashi[1]**

## Nomenclature

$c_l$ = specific heat of liquid
$E(\beta)$ = value defined in [6]
$h$ = empirical constant in equation (1)
$k_l$ = thermal conductivity of liquid
LL = liquid level above heating surface
$q$ = heat flux
SP = system pressure
$T_{sat}$ = saturation temperature corresponding to SP
$T_v$ = vapor temperature

[1]Department of Nuclear Engineering, Kyoto University, Kyoto, 606, Japan.
[2]Nuclear Fuel Industries, Kumatori, Osaka 590-04, Japan.

Contributed by the Heat Transfer Division for publication in the JOURNAL OF HEAT TRANSFER. Manuscript received by the Heat Transfer Division July 23, 1983.

$T_{wH}, T_{wL}$ = heating surface temperature in nucleate boiling shown in Fig. 2(*b*)
$\alpha$ = nucleate boiling heat transfer coefficient
$\theta_w(0, 0)$ = $T_{wH} - T_{sat}$
$\rho_l$ = density of liquid
$\tau$ = ebullition period

## Introduction

Boiling heat transfer in a thin layer of water and organic liquids was studied by Nishikawa et al. [1], Patten and Turmeau [2] and Tolubinski et al. [3]. They reported that the boiling heat transfer coefficients in layers thinner than 3 mm were larger than in pool. This was caused by large bubbles growing over the liquid layer.

On the other hand, boiling heat transfer in thin layers of liquid metal has been studied only in our laboratory. This is an attractive problem not only in an academic sense but also because of safety considerations of the utilization of liquid metal for future heat transfer systems. Takahashi et al. [4] dealt with experiments of boiling heat transfer in a thin mercury layer, and they observed large bubbles growing over the liquid surface, beneath which dry patches were formed. Boiling heat transfer in a thin potassium layer was first studied by Takenaka et al. [5]. The boiling was entirely intermittent and the boiling heat transfer coefficient was not affected by the liquid level LL $\geqq$ 6 mm for system pressures 30 and 50 torr.

Another aspect of the effect of liquid level on the boiling heat transfer is related to the subcooling effect due to the difference of the saturation temperature between the heating surface and the liquid free surface by the hydrostatic liquid head. This effect is important for studying the boiling heat transfer for low system pressure and high liquid level.

To predict nucleate boiling heat transfer, the bubble cycle period, the bubble departure diameter and the number of active sites are important factors, as stated by Mikic and Rohsenow [9]. Bubble cycle period of liquid alkali metal was studied theoretically and experimentally with sodium by Shai and Rohsenow [6]. Experiments results with sodium showed good agreement with theoretical results. But the experimental data of bubble cycle period in thin layer of liquid alkali metal have never been obtained.

This paper deals with the boiling of potassium on a horizontal plane heater when the subcooling-effect previously mentioned is negligibly small (less than a few degrees), and presents the experimental data of nucleate boiling heat transfer coefficient and bubble cycle period for various liquid levels less than 50 mm under system pressures between 30 torr (4.0kPa) and 300 torr (40.0kPa).

## Experimental Apparatus

The boiling vessel is a type 600 Inconnel cylinder of 80 mm in inner diameter and 218 mm high. A horizontal heating wall of nickel disk of 40 mm in effective heating diameter and 6 mm thick is situated near the center of the cylinder. This wall is heated by a tantalum element, to which a direct current is supplied. The wall temperature is measured at four points in the heating wall by 0.3-mm-o.d. sheathed chromel-alumel thermocouples, and the liquid and vapor temperatures are measured by the similar type thermocouples, which can be traversed vertically. Figure 1 shows the test section of the experimental apparatus, the details of which were described in [7].

## Experimental Results and Discussion

The effect of liquid level on natural convection heat transfer before the initiation of boiling was observed when the thickness of the liquid layer was decreased to the same order as that of the boundary layer [5, 7]. The thinner the liquid layer was, the smaller was the temperature difference between the heating surface and the vapor at fixed heat flux, and hence higher heat flux was needed to provide the thinner liquid layer with sufficient superheat for the inception of boiling.

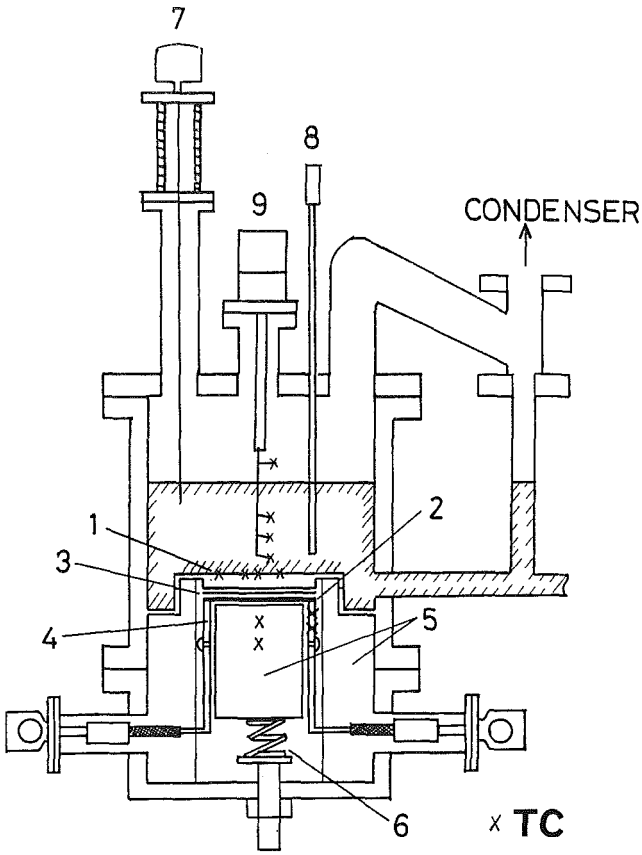


Fig. 1 Test section:
1 Nickel heating wall
2 Tantalum heating element
3 Boron nitride insulator
4 Nickel electrode
5 Ceramic insulator
6 Spring
7 Liquid level sensor
8 Piezo microphone
9 Thermocouple slider.

Experiments of boiling heat transfer were conducted when the vapor temperature $T_v$ was kept near the saturation temperature corresponding to the system pressure.

Boiling state in the present experimental condition is classified into four regions: namely, (1) nonboiling region, (2) intermittent boiling region, (3) stable boiling region, and (4) the region where dry patch formation and rewetting are alternatively repeated in intermittent boiling. Boiling state in region (4) was discussed in [7]. Typical pen-recorder chart traces of heating surface, liquid and vapor temperatures are shown in Fig. 2 (*a*, *b*). The experimental conditions are shown in the captions. The heating surface temperatures $T_w$ was measured at the center of the wall, the liquid temperature $T_l$ at the positions of 0.5 and 20 mm above the center, and the vapor temperature $T_v$ at about 70 mm above the heating surface. In the nonboiling region (1), the heating surface and the liquid temperatures are superheated above the saturation temperature $T_{sat}$ and $T_v$ is kept near $T_{sat}$. Figure 2(*a*) also shows those in the intermittent boiling region (2). When the boiling occurs first at $q = 4.3 \times 10^5$ W/m$^2$, the heating surface and the liquid temperatures drop and the liquid temperature at 20 mm comes down to near $T_{sat}$. After the nucleate boiling continues for a few seconds, it ceases and then it is followed by nonboiling stage. Stable boiling region

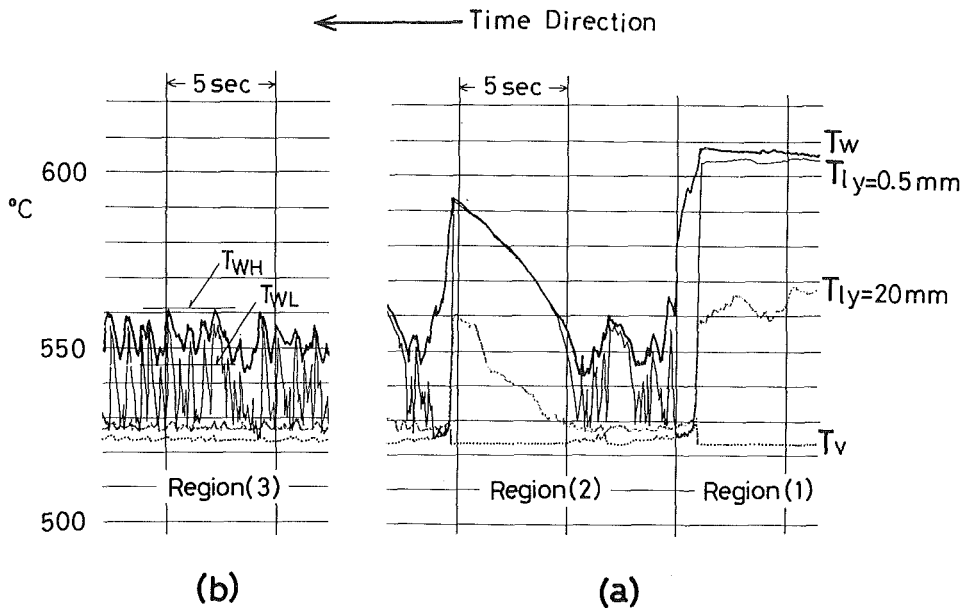


**Fig. 2 Recorder chart traces of temperatures, LL = 31 mm, SP ≃ 50 torr, $T_{sat}$ = 532 °C (50 torr): (*a*) intermittent boiling, $q$ = 4.3 × $10^5$ W/$m^2$; (*b*) stable boiling, $q$ = 6.4 × $10^5$ W/$m^2$**

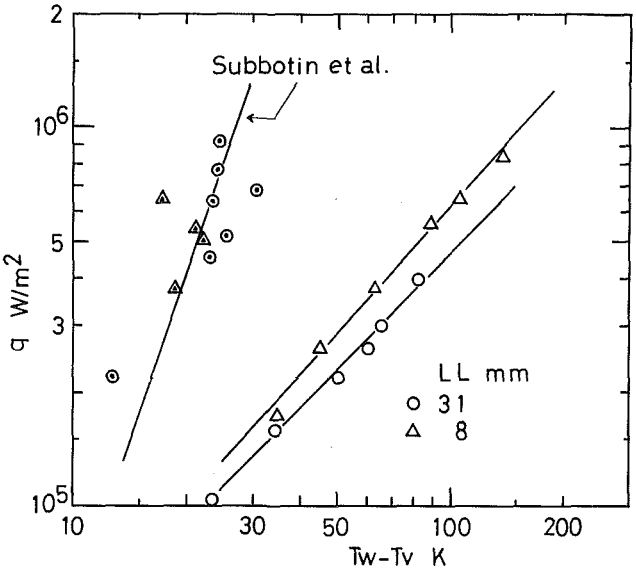


**Fig. 3 Boiling curve, SP = 50 torr**

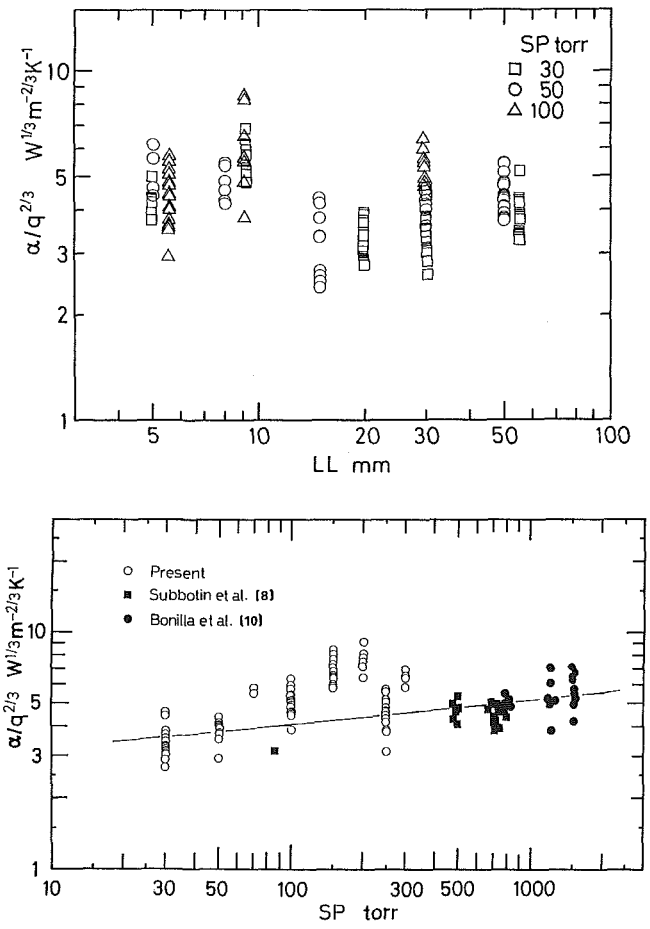


**Fig. 4 Nucleate boiling heat transfer; (*a*) effect of liquid level LL, SP = 30, 50, 100 torr; (*b*) effect of system pressure SP, LL = 30 mm**

(3) at $q$ = 6.4 × $10^5$ W/$m^2$ is shown in Fig. 2(*b*). The heating surface temperature as well as the liquid temperature at 0.5 mm fluctuates periodically. This period represents the ebullition period, which can be measured more sensibly with the fluctuations of the liquid temperature at 0.5 mm. The liquid temperature at 20 mm and the vapor temperature fluctuate a little near the satuartion temperature. The averaged heating surface temperature during nucleate boiling is defined as the arithmetical average of $T_{wH}$ and $T_{wL}$ shown in the figure. This definition is also used in the nucleate boiling stages in the regions (2) and (4) to discuss the nucleate boiling heat transfer.

The averaged ebullition period in the nucleate boiling stage is determined as an average over a hundred cycles of the liquid temperature fluctuations at 0.5 mm.

Figure 3 shows examples of boiling curves to indicate the heat transfer for 8 and 31 mm liquid levels under 50 torr system pressure. Temperature difference is defined as $T_w - T_v$. The straight line 1 in the nucleate boiling stage is calculated with an empirical correlation by Subbotin et al. [8], and the lines 2 correspond to the natural convection region for each liquid level. In the intermittent boiling region (2), $T_w - T_v$ fluctuates between the stage in the natural convection and in the nucleate boiling at fixed heat flux. In the natural

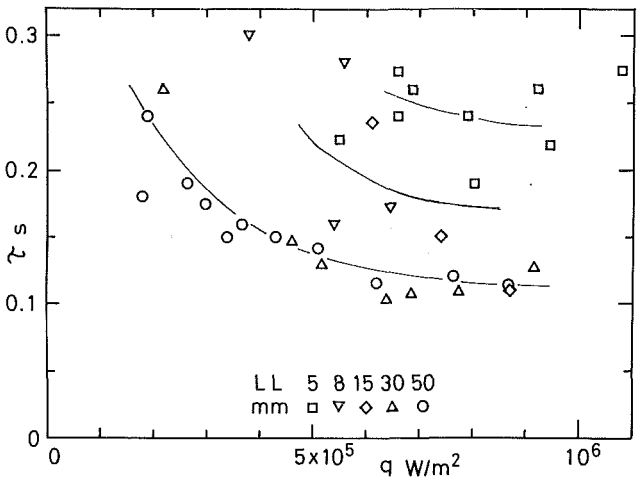


Fig. 5 Ebullition periods for various liquid levels, SP = 50 torr

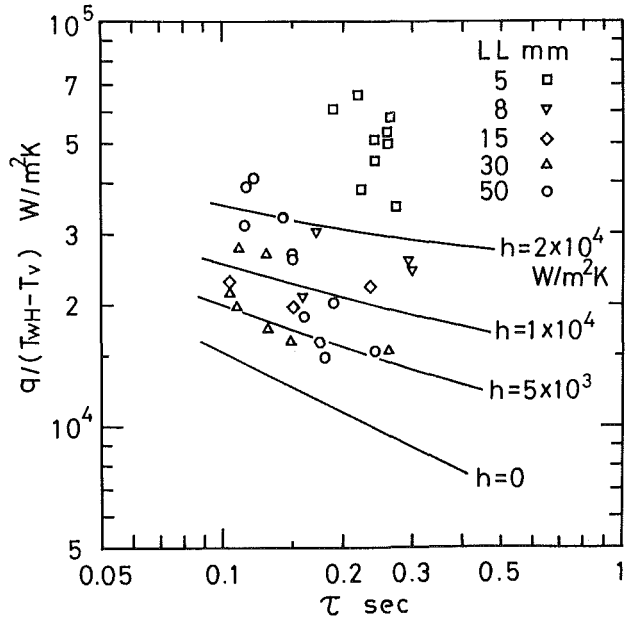


Fig. 6 Ebullition periods $\tau$ versus $q/(T_{wH} - T_v)$, SP = 50 torr

convection stage, $T_w - T_v$ is smaller for lower liquid level, and in the nucleate boiling stage, no apparent effect of liquid level is seen.

Nucleate boiling heat transfer is discussed on the stable region (3) as well as the nucleate boiling stages in the regions (2) and (4). Since the heat flux shows a tendency to be proportional to about third power of the temperature difference, $\alpha/q^{2/3}$ is plotted against both system pressure and liquid level, where the heat transfer coefficient $\alpha$ is defined as $q/(T_w - T_v)$. Figure 4(*a*) shows dependencies of nucleate boiling heat transfer on the liquid level for system pressures of 30, 50 and 100 torr. No apparent effect of the liquid level on the nucleate boiling heat transfer is observed when LL $\geqq$ 5 mm. For LL $<$ 5 mm, the boiling was initiated only at high heat flux and the dry patches were frequently formed and thus the nucleate boiling stage was seldom observed. Figure 4(*b*) shows a dependency of nucleate boiling heat transfer on the system pressure for 30 mm liquid level. Experimental data of nucleate boiling heat transfer from a horizontal plate to potassium by Subbotin et al. [8] and Bonilla et al. [10] are also plotted. The straight line in the figure is the empirical correlation by Subbotin et al. [8], which was based on few data obtained for subatmospheric pressure. The present experimental results show a slightly larger dependency on system pressure than that by the correlation of Subbotin et al.

Figure 5 shows the ebullition periods for 50 torr system pressure and various liquid levels. It is indicated that the period is longer when the liquid level is lower. The same tendency is obtained for 30 and 100 torrr system pressures. Shai and Rohsenow [6] proposed an equation for the bubble cycle period $\tau$

$$\sqrt{\tau} = \frac{\sqrt{k_l c_l \rho_l}}{q/\theta_w(0,0) - h} E(\beta) \tag{1}$$

where $\theta_w(0,0)$ is equal to $T_{wH} - T_v$ (see Fig. 2(*b*)), $E(\beta)$ is a value determined by thermal properties of the wall and the liquid, and $h$ is an empirical constant to account for the convection effect, which is related to the natural convection heat transfer coefficient. For the sodium pool boiling, $h$ was taken as constant at $h = 6.8 \times 10^3$ W/m$^2$K [6]. To make a comparison between the present experimental data and equation (1), $\tau$ versus $q/(T_{wH} - T_v)$ is plotted in Fig. 6. The dependency of $q/(T_{wH} - T_v)$ on $\tau$ in the present experimental data is similar to that in equation (1) though the experimental data are scattered, and larger empirical constant $h$ is required for lower liquid level. Equation (1) may be translated into

$$\sqrt{\tau} \propto \frac{1}{\alpha - h} \tag{2}$$

because $q/\theta_w(0,0)$ is not so much different from the boiling heat transfer coefficient $\alpha = q/(T_w - T_v)$. Since $\alpha$ is not affected by liquid level when LL $\geqq$ 5 mm, as described above, and natural convection heat transfer coefficient is larger in lower liquid level as discussed in Fig. 3, the right-hand side of equation (2) is larger in lower liquid level. Therefore, the dependency of ebullition period on the liquid level is explained qualitatively by equation (1).

## Conclusion

Experimental data are presented on boiling heat transfer from a horizontal plane nickel wall to potassium layers of various liquid levels under subatmospheric system pressures. Concluding remarks are as follows:

1 Nucleate boiling heat transfer is not affected by the liquid level when LL $\geqq$ 5 mm. The dependency of $\alpha/q^{2/3}$ on system pressure is slightly larger than the correlation of Subbotin et al. For LL $<$ 5 mm, the nucleate boiling stage is seldom observed.

2 Ebullition period is longer for lower liquid level, and it is qualitatively explained by Shai and Rohsenow's equation applying a large value of $h$ for lower liquid level.

## Acknowledgment

This research was supported through the Grant-in-Aid for Special Projects by the Ministry of Education of Japanese Government.

## References

1 Nishikawa, N., Kusuda, H., Yamasaki, K., and Tanaka, K., "Nucleate Boiling at Low Liquid Levels," *Transactions JSME*, Vol. 32, 1966, pp. 944-949.

2 Patten, T. D., and Turmeau, T. A., "Some Characteristics of Nucleate Boiling in Thin Liquid Layers," *Heat Transfer 1970*, Paris, Vol. V, B2.10 Elsevier, 1970.

3 Tolubinsky, V. I., Antoneko, V. A., and Ostrovsky, Ju. N., "Heat Transfer at Liquid Boiling Thin Films," Seminar International Center for Heat Mass Transfer 1978, Yugoslavia, 1978.

4 Takahashi, O., Nishida, M., Takenaka, N., and Michiyoshi, I., "Pool Boiling Heat Transfer from Horizontal Plane Heater to Mercury under Magnetic Field," *International Journal of Heat and Mass Transfer*, Vol. 23, 1980, pp. 27-36.

5 Takenaka, N., Murata, T., Takahashi, O., and Michiyoshi, I., "Boiling

Heat Transfer from Horizontal Plane Heater to Potassium," *International Journal of Heat and Mass Transfer*, Vol. 26, 1983, pp. 154–156.

6 Shai, I., and Rohsenow, W., "The Mechanism of and Stability Criterion for Nucleate Pool Boiling of Sodium," ASME JOURNAL OF HEAT TRANSFER, Vol. 91, 1969, pp. 315–329.

7 Michiyoshi, I., Takenaka, N., Murata, T., Shiokawa, T., and Takahashi, O., "Boiling Heat Transfer in Potassium Layers on a Horizontal Plane Heater," *Proceedings of the ASME-JSME Thermal Engineering Joint Conference*, Vol. 1, Honolulu, 1983, pp. 207–214.

8 Subbotin, V. I., Sorokin, D. N., Ovechkin, D. M., and Kudryavtsev, A. P., "Heat Transfer in Boiling Metals by Natural Convection," Israel Program for Scientific Translation, Jerusalem, 1972.

9 Mikic, B. B., and Rohsenow, W. M., "A New Correlation of Pool-Boiling Data Including the Effect of Heating Surface Condition," ASME JOURNAL OF HEAT TRANSFER, Vol. 91, 1969, pp. 205–211.

10 Bonilla, C. F., Wiener, M., and Bilfinger, H., "Pool Boiling Heat Transfer of Potassium," *Proc. High-Temp. Liquid Metal Heat Transfer Technology Meeting*, Vol. 1, O.R.N.L.-3605, 1963, pp. 286–309.

## Heat Transfer in an Annular Two-Phase Flow

**F. Dobran**[1]

### Nomenclature

$A$ = flow cross-sectional area, $\pi D^2/4$
Bo = buoyancy number, $1-\rho_g/\rho_l$
Ca = capillary number, $\mu_l^2/(\rho_l D\sigma)$
$C_E$ = entrainment parameter, $\dot{m}_d/A\rho_l u_c$
$C_p$ = specific heat at constant pressure
$D;D^+$ = tube internal diameter, $\rho_l D u^*/\mu_l$
$E$ = fraction of the total liquid flow which is entrained
$f$ = friction factor
$g$ = gravitational constant
$G$ = mass flux
$h$ = heat transfer coefficient
$k$ = thermal conductivity
$\dot{m}$ = mass flow rate
$N_l$ = two-phase Grashof number, $(gD^3\rho_l(\rho_l-\rho_g)/\mu_l^2)^{1/2}$
$\mathrm{Nu}_\delta$ = Nusselt number, $h\delta/k_l$
$P$ = pressure
Pr = Prandtl number, $\mu C_p/k$
$\mathrm{Pr}_{\mathrm{eff}}$ = effective Prandtl number for the wavy layer region of the film, $\mu_{\mathrm{eff}}/\rho_l\epsilon_{\mathrm{eff}}$
$\mathrm{Pr}_{lt}$ = turbulent Prandtl number for the continuous layer region of the liquid film, $\epsilon_m/\epsilon_h$
$q$ = heat flux
$\mathrm{Re}_c$ = Reynolds number, $u_c\rho_c D/\mu_g$
$\mathrm{Re}_l$ = film Reynolds number, $4W^+$
$S$ = entrainment parameter, $\tau_i\delta/\sigma$
$T;T^+$ = temperature; $C_{pl}\rho_l u^*(T_w-T)/q_w$
$u;u_c$ = axial film velocity; superficial gas velocity, $A_c u_g/A$
$u^*$ = shear velocity, $(|\tau_w|/\rho_l)^{1/2}$
$u^+$ = dimensionless film velocity, $u/u^*$
$W^+$ = dimensionless film flow-rate, $\int_0^{\delta^+} u^+ dy^+ = \mathrm{Re}_l/4$
We = Weber number, $\frac{\rho_G u_c^2 D}{\sigma}\left(\frac{\mathrm{Bo}}{1-\mathrm{Bo}}\right)^{1/3}$
$x$ = quality
$y;y^+$ = distance from the tube wall; $\rho_l u^* y/\mu_l$
$z$ = distance along the tube

### Greek Symbols

$\alpha_c$ = core void fraction, $A_g/(A_g+A_d)$
$\beta$ = interfacial shear stress parameter, defined by equation (2)
$\epsilon$ = fraction of total flow flowing as entrained liquid
$\delta;\delta^+$ = film thickness; $\rho_l\delta u^*/\mu_l$
$\delta_c;\delta_c^+$ = wave crests thickness, $\rho_l\delta_c u^*/\mu_l$
$\delta_l;\delta_l^+$ = continuous liquid layer thickness; $\rho_l\delta_l u^*/\mu_l$
$\epsilon_m;\epsilon_h$ = turbulent diffusivities for momentum and heat
$\mu;\nu$ = viscosity, $\mu/\rho$
$\rho$ = density
$\sigma$ = surface tension
$\tau$ = shear stress

### Subscripts

$c$ = pertains to the core
$d$ = pertains to liquid droplets in the core
eff = effective
$g$ = pertains to the gas phase
$i$ = liquid film–gas core interface
$l$ = pertains to the liquid phase
sat = saturation value
$w$ = wall
$wl$ = pertains to the wavy layer

## 1 Introduction

The two-phase vertical annular flow pattern occurs in many situations of practical interest and consists of a liquid film adjacent to the channel wall and a core which consists of liquid droplets entrained in the gas phase. The interface between the liquid film and the dispersed core region is covered by a complex system of waves, and the wave structure depends on the volumetric fluxes of the two phases [1–3]. This rather complex flow pattern has been under investigation for many years and little progress has been achieved in its analytical modeling.

In modeling of the liquid film, it has been a common practice to assume that the turbulence structure in the film is identical to the structure of a single-phase turbulent pipe flow at the equivalent distances from the pipe wall; and the effects of waves on the hydrodynamic and heat transfer processes are neglected [4]. It is possible that this assumption in turbulence modeling of the liquid film is responsible for considerable overprediction of heat transfer rate across the liquid film [4, 5]. The experimental data in [2, 3, 6] show that the liquid film consists of a continuous liquid layer region close to the tube wall and of a wavy layer region close to the liquid film–dispersed core interface. Based on the experimental data of Ueda and Tanaka [2], Ueda and Nose [3], and Chien and Ibele [6], Dobran [7] has deduced an effective wavy layer region diffusivity and integrated the two-layer liquid film structure into an annular flow model for the prediction of hydrodynamics and heat transfer rate. The resulting two-layer liquid film hydrodynamic and heat transfer model gives lower rates of heat transfer than the single-layer model in which the turbulence is assumed to be identical to the single-phase turbulent pipe flow. At equivalent distances from the channel wall, the new model also gives lower values for effective turbulence diffusivities than the single liquid layer model.

In this paper, the results from the further development of the annular two-phase flow model with heat transfer are presented by accounting in the model for the entrainment of liquid droplets in the gas phase. It is shown that the effect of entrainment on the hydrodynamics and heat transfer can be significant and that the entrainment correlations should be used with caution, especially if they were developed on a basis of particular annular flow model.

## 2 Hydrodynamic and Heat Transfer Model

**2.1 Hydrodynamics.** An annular-dispersed two-phase

[1]Department of Mechanical Engineering, Stevens Institute of Technology, Hoboken, N.J. 07030, Assoc. Mem. ASME

Contributed by the Heat Transfer Division for publication in the JOURNAL OF HEAT TRANSFER. Manuscript received by the Heat Transfer Division August 25, 1983.

Heat Transfer from Horizontal Plane Heater to Potassium," *International Journal of Heat and Mass Transfer*, Vol. 26, 1983, pp. 154–156.

6 Shai, I., and Rohsenow, W., "The Mechanism of and Stability Criterion for Nucleate Pool Boiling of Sodium," ASME JOURNAL OF HEAT TRANSFER, Vol. 91, 1969, pp. 315–329.

7 Michiyoshi, I., Takenaka, N., Murata, T., Shiokawa, T., and Takahashi, O., "Boiling Heat Transfer in Potassium Layers on a Horizontal Plane Heater," *Proceedings of the ASME-JSME Thermal Engineering Joint Conference*, Vol. 1, Honolulu, 1983, pp. 207–214.

8 Subbotin, V. I., Sorokin, D. N., Ovechkin, D. M., and Kudryavtsev, A. P., "Heat Transfer in Boiling Metals by Natural Convection," Israel Program for Scientific Translation, Jerusalem, 1972.

9 Mikic, B. B., and Rohsenow, W. M., "A New Correlation of Pool-Boiling Data Including the Effect of Heating Surface Condition," ASME JOURNAL OF HEAT TRANSFER, Vol. 91, 1969, pp. 205–211.

10 Bonilla, C. F., Wiener, M., and Bilfinger, H., "Pool Boiling Heat Transfer of Potassium," *Proc. High-Temp. Liquid Metal Heat Transfer Technology Meeting*, Vol. 1, O.R.N.L.-3605, 1963, pp. 286–309.

## Heat Transfer in an Annular Two-Phase Flow

**F. Dobran**[1]

### Nomenclature

$A$ = flow cross-sectional area, $\pi D^2/4$
Bo = buoyancy number, $1-\rho_g/\rho_l$
Ca = capillary number, $\mu_l^2/(\rho_l D\sigma)$
$C_E$ = entrainment parameter, $\dot{m}_d/A\rho_l u_c$
$C_p$ = specific heat at constant pressure
$D;D^+$ = tube internal diameter, $\rho_l D u^*/\mu_l$
$E$ = fraction of the total liquid flow which is entrained
$f$ = friction factor
$g$ = gravitational constant
$G$ = mass flux
$h$ = heat transfer coefficient
$k$ = thermal conductivity
$\dot{m}$ = mass flow rate
$N_l$ = two-phase Grashof number, $(gD^3\rho_l(\rho_l-\rho_g)/\mu_l^2)^{1/2}$
$\mathrm{Nu}_\delta$ = Nusselt number, $h\delta/k_l$
$P$ = pressure
Pr = Prandtl number, $\mu C_p/k$
$\mathrm{Pr}_{\mathrm{eff}}$ = effective Prandtl number for the wavy layer region of the film, $\mu_{\mathrm{eff}}/\rho_l\epsilon_{\mathrm{eff}}$
$\mathrm{Pr}_{lt}$ = turbulent Prandtl number for the continuous layer region of the liquid film, $\epsilon_m/\epsilon_h$
$q$ = heat flux
$\mathrm{Re}_c$ = Reynolds number, $u_c\rho_c D/\mu_g$
$\mathrm{Re}_l$ = film Reynolds number, $4W^+$
$S$ = entrainment parameter, $\tau_i\delta/\sigma$
$T;T^+$ = temperature; $C_{pl}\rho_l u^*(T_w-T)/q_w$
$u;u_c$ = axial film velocity; superficial gas velocity, $A_c u_g/A$
$u^*$ = shear velocity, $(|\tau_w|/\rho_l)^{1/2}$
$u^+$ = dimensionless film velocity, $u/u^*$
$W^+$ = dimensionless film flow-rate, $\int_0^{\delta^+} u^+ dy^+ = \mathrm{Re}_l/4$
We = Weber number, $\frac{\rho_G u_c^2 D}{\sigma}\left(\frac{\mathrm{Bo}}{1-\mathrm{Bo}}\right)^{1/3}$
$x$ = quality
$y;y^+$ = distance from the tube wall; $\rho_l u^* y/\mu_l$
$z$ = distance along the tube

### Greek Symbols

$\alpha_c$ = core void fraction, $A_g/(A_g+A_d)$
$\beta$ = interfacial shear stress parameter, defined by equation (2)
$\epsilon$ = fraction of total flow flowing as entrained liquid
$\delta;\delta^+$ = film thickness; $\rho_l\delta u^*/\mu_l$
$\delta_c;\delta_c^+$ = wave crests thickness, $\rho_l\delta_c u^*/\mu_l$
$\delta_l;\delta_l^+$ = continuous liquid layer thickness; $\rho_l\delta_l u^*/\mu_l$
$\epsilon_m;\epsilon_h$ = turbulent diffusivities for momentum and heat
$\mu;\nu$ = viscosity, $\mu/\rho$
$\rho$ = density
$\sigma$ = surface tension
$\tau$ = shear stress

### Subscripts

$c$ = pertains to the core
$d$ = pertains to liquid droplets in the core
eff = effective
$g$ = pertains to the gas phase
$i$ = liquid film–gas core interface
$l$ = pertains to the liquid phase
sat = saturation value
$w$ = wall
$wl$ = pertains to the wavy layer

## 1 Introduction

The two-phase vertical annular flow pattern occurs in many situations of practical interest and consists of a liquid film adjacent to the channel wall and a core which consists of liquid droplets entrained in the gas phase. The interface between the liquid film and the dispersed core region is covered by a complex system of waves, and the wave structure depends on the volumetric fluxes of the two phases [1–3]. This rather complex flow pattern has been under investigation for many years and little progress has been achieved in its analytical modeling.

In modeling of the liquid film, it has been a common practice to assume that the turbulence structure in the film is identical to the structure of a single-phase turbulent pipe flow at the equivalent distances from the pipe wall; and the effects of waves on the hydrodynamic and heat transfer processes are neglected [4]. It is possible that this assumption in turbulence modeling of the liquid film is responsible for considerable overprediction of heat transfer rate across the liquid film [4, 5]. The experimental data in [2, 3, 6] show that the liquid film consists of a continuous liquid layer region close to the tube wall and of a wavy layer region close to the liquid film–dispersed core interface. Based on the experimental data of Ueda and Tanaka [2], Ueda and Nose [3], and Chien and Ibele [6], Dobran [7] has deduced an effective wavy layer region diffusivity and integrated the two-layer liquid film structure into an annular flow model for the prediction of hydrodynamics and heat transfer rate. The resulting two-layer liquid film hydrodynamic and heat transfer model gives lower rates of heat transfer than the single-layer model in which the turbulence is assumed to be identical to the single-phase turbulent pipe flow. At equivalent distances from the channel wall, the new model also gives lower values for effective turbulence diffusivities than the single liquid layer model.

In this paper, the results from the further development of the annular two-phase flow model with heat transfer are presented by accounting in the model for the entrainment of liquid droplets in the gas phase. It is shown that the effect of entrainment on the hydrodynamics and heat transfer can be significant and that the entrainment correlations should be used with caution, especially if they were developed on a basis of particular annular flow model.

## 2 Hydrodynamic and Heat Transfer Model

**2.1 Hydrodynamics.** An annular-dispersed two-phase

[1]Department of Mechanical Engineering, Stevens Institute of Technology, Hoboken, N.J. 07030, Assoc. Mem. ASME

Contributed by the Heat Transfer Division for publication in the JOURNAL OF HEAT TRANSFER. Manuscript received by the Heat Transfer Division August 25, 1983.

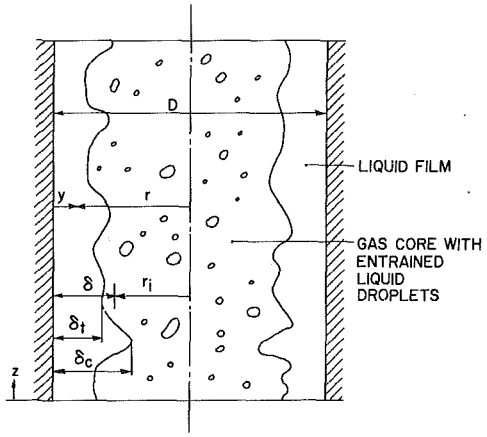


**Fig. 1 An annular-dispersed, two-phase flow pattern**

flow pattern in a vertical tube in upflow is illustrated in Fig. 1. It consists of a liquid film adjacent to the tube wall and of a gas core with entrained liquid droplets. The average film thickness is represented by $\delta$; $\delta_t$ is the continuous liquid layer thickness; and $\delta_c - \delta_t$ is the wavy layer thickness. By eliminating the pressure gradient between the one-dimensional form of momentum equations for a two-phase mixture and for the liquid film, assuming that the liquid film momentum equation adequately represents the state of the film in the entire (continuous and wavy layer) thickness $\delta$, neglecting the liquid and gas core inertia effects and momentum transport through the liquid film-core interface, and by assuming that the core consists of a homogeneous mixture of gas and liquid droplets, it is possible to derive the following equation [7, 8]

$$-\alpha_c\left(1-\frac{\delta^+}{D^+}\right)\frac{N_l^2}{D^{+3}}\delta^+ + \beta\frac{N_l^{4/3}}{\mathrm{Bo}^{1/3}(D^+)^2\left(1-\frac{2\delta^+}{D^+}\right)} - 1 = 0 \tag{1}$$

where the interfacial shear parameter $\beta$ is defined as follows

$$\beta \equiv \frac{|\tau_i|}{[g^2(\rho_l-\rho_g)\mu_l^2]^{1/3}} = \frac{\tau_i}{\tau_w}\left(\frac{D^{+2}}{N_l^{4/3}}\right)\mathrm{Bo}^{1/3} \tag{2}$$

The two-layer liquid film structure enters into the hydrodynamic model through a correlation for the continuous liquid layer thickness

$$\frac{\delta_t^+}{D^+} = 140\, N_l^{0.433}\, \mathrm{Re}_c^{-1.35} \tag{3}$$

an effective momentum diffusivity for the wavy layer

$$\left(\frac{\mu_{\mathrm{eff}}}{\mu_l}\right)_{wl} = 1 + 1.6\times 10^{-3}(\delta^+ - \delta_t^+)^{1.8} \tag{4}$$

and the assumption that in the continuous layer region the turbulent velocity profile (or turbulence structure) is identical to the universal velocity profile of single phase flow [7]. For thin liquid films, the turbulent momentum equation may be written as

$$\frac{\tau}{\tau_w} = 1 - \left(1-\frac{r_i}{\tau_w}\right)\frac{y^+}{\delta^+} \tag{5}$$

and utilizing

$$\tau = \mu_{\mathrm{eff}}\frac{\partial u}{\partial y} \tag{6}$$

it is possible to combine these equations with the universal velocity profile in the continuous liquid layer region of the film to yield the liquid film flow rate, i.e.,

$$W^+ = \frac{\mathrm{Re}_l}{4} = \int_0^{\delta^+} u^+ dy^+ = W^+(\delta_t^+) + (\delta^+ - \delta_t^+)\left\{u^+(\delta_t^+) + \frac{(\delta^+ - \delta_t^+)}{2\left(\frac{\mu_{\mathrm{eff}}}{\mu_l}\right)_{wl}}\left[1-\left(1-\frac{\tau_i}{\tau_w}\right)\frac{\delta^+ + 2\delta_t^+}{3\delta^+}\right]\right\} \tag{7}$$

where $\mathrm{Re}_l$ is the liquid film Reynolds number and $u^+(\delta_t^+)$ and $W^+(\delta_t^+)$ are given in [7].

**2.2 Heat Transfer.** The heat flux rate in the film can be expressed by the usual equation

$$q = -(k_l + \rho_l C_{pl}\epsilon_h)\frac{\partial T}{\partial y} \tag{8}$$

and can be nondimensionalized as follows:

$$\frac{\partial T^+}{\partial y^+}\left(\frac{1}{\mathrm{Pr}_l} + \frac{1}{\mathrm{Pr}_{lt}}\frac{\epsilon_m}{\nu_l}\right) = \frac{\partial T^+}{\partial y^+}\left(\frac{\mu_{\mathrm{eff}}}{\mu_l}\right)\frac{1}{\mathrm{Pr}_{\mathrm{eff}}} = \frac{q}{q_w} \tag{9}$$

where $\mathrm{Pr}_l = \mu_l C_{pl}/k_l$ is the molecular Prandtl number, $\mathrm{Pr}_{lt} = \epsilon_m/\epsilon_h$ is the turbulent Prandtl number, $\mathrm{Pr}_{\mathrm{eff}} = \mu_{\mathrm{eff}}/\rho_l\epsilon_{\mathrm{eff}}$ is the effective Prandtl number and $\epsilon_m$ and $\epsilon_h$ are turbulent momentum and heat diffusivities, respectively. The turbulent momentum diffusivities follow from the development in section 2.1 and are given in [9]. Also, by neglecting the convective energy transport along the liquid film, it is possible to set $q/q_w = 1$ in equation (9) and integrate this equation from $y^+ = 0$ to $y^+ < \delta^+$ to obtain the temperature distribution in the liquid film [9].

Using equation (13) in the definition of Nusselt number, we thus obtain

$$\mathrm{Nu}_\delta \equiv \frac{q_w\delta}{(T_w - T(\delta))k_l} = \frac{\mathrm{Pr}_l\delta^+}{T^+(\delta^+)} \tag{10}$$

Notice that in the wavy layer region of the liquid film, the heat transfer process is represented by an effective diffusivity and is not split into viscous and turbulent parts as in the continuous liquid layer region. The reason for this is that the diffusivity represented by equation (4) represents the turbulent state of a *two-phase* mixture, and a split into viscous and turbulent parts as in a single phase flow situation does not appear to be physically realistic.

The hydrodynamic and heat transfer models described above are not complete until specifications for $\mathrm{Re}_c$, $\alpha_c$, and $\beta$ are made. These specifications are, therefore, considered next.

**2.3 Closure of the Hydrodynamic and Heat Transfer Model.** The core void fraction $\alpha_c$ of a homogeneous annular-dispersed flow can be expressed as follows [10]

$$\alpha_c = \frac{1}{1+(1-\mathrm{Bo})\frac{\epsilon}{x}} \tag{11}$$

whereas the core Reynolds number $\mathrm{Re}_c$ follows from the definition, i.e.,

$$\mathrm{Re}_c \equiv \frac{u_c\rho_c D}{\mu_g} = \frac{x\,GD\left(1+\frac{\epsilon}{x}\right)}{\mu_g} \tag{12}$$

where $G$ is the total mass flux and $\rho_c$ is the homogeneous density in the core, i.e.,

$$\rho_c = \alpha_c\rho_g + (1-\alpha_c)\rho_l \tag{13}$$

The interfacial friction parameter $\beta$ can be expressed in terms of the pressure gradient, or if this is not available, in terms of the interfacial roughness correlation [4, 11]. Neglecting the inertia effect in the core and the momentum transfer through the liquid film-core interface, the pressure gradient becomes

$$-\frac{dP}{dz}=\frac{2\tau_i}{\frac{D}{2}-\delta}+g\rho_c \tag{14}$$

Combining equations (2), (13), and (14) yields

$$\beta=\frac{\left(1-\frac{2\delta^+}{D^+}\right)N_l^{2/3}}{4\ \mathrm{Bo}^{2/3}}\left\{\frac{-\frac{dP}{dz}}{\rho_l g}-[(1-\alpha_c)+\alpha_c(1-\mathrm{Bo})]\right\} \tag{15}$$

When the pressure gradient is not available, the parameter $\beta$ can be expressed in terms of an interfacial roughness correlation [4, 11]. This correlation supplies the interfacial friction factor $f_i$ in the equation

$$\tau_i\equiv\frac{1}{2}f_i\rho_c u_c^2 \tag{16}$$

in terms of the core Reynolds number $\mathrm{Re}_c$ and film thickness $\delta$, i.e.,

$$f_i=0.079\ \mathrm{Re}_c^{-0.25}\left(1+\frac{24}{(1-\mathrm{Bo})^{1/3}}\frac{\delta^+}{D^+}\right) \tag{17}$$

Combining equations (2), (12), (13), (16), and (17), we obtain

$$\beta=0.079\ \mathrm{Re}_c^{1.75}\left(1+\frac{24}{(1-\mathrm{Bo})^{1/3}}\frac{\delta^+}{D^+}\right)\left(\frac{\mu_g}{\mu_l}\right)^2 \frac{\mathrm{Bo}^{1/3}}{2N_l^{4/3}[\alpha_c(1-\mathrm{Bo})+(1-\alpha_c)]} \tag{18}$$

For the entrainment correlation, three models will be considered. The simplest model assumes no entrainment and corresponds to $\alpha_c=1$, the second model is due to Whalley and Hewitt [11], and the third model is due to Ishii and Mishima [12].

The entrainment correlation of Whalley and Hewitt [11] is expressed in terms of the parameter $C_E$ as a function of the independent parameter $S$, and when use is made of the definitions of $\dot{m}_d=\rho_l u_d A_d$, $u_c=A_c u_d/A$ and $\alpha_c=(A_c-A_d)/A_c$, these parameters can be transformed into the following form

$$\frac{C_E}{\rho_l}=1-\alpha_c \tag{19}$$

$$S=\beta\frac{N_l^{4/3}}{\mathrm{Bo}^{1/3}}\frac{\delta^+}{D^+}\mathrm{Ca} \tag{20}$$

The parameter Ca is the capillary number and represents a ratio of viscous to surface tension forces. It is important to note that Whalley's and Hewitt's entrainment correlation was determined from Hewitt's [13] annular flow model and experimental data. This model assumes that the turbulent velocity profile in the film is identical to the single-phase turbulent velocity profile in a tube. The data used to obtain the correlation pertain to air-water and stream-water mixtures, and the correlation is valid under a hydrodynamic equilibrium condition in which the local entrainment is balanced by the local droplets deposition onto the liquid film.

The entrainment correlation of Ishii and Mishima [12] is based on the low-pressure air-water data and for a hydrodynamic equilibrium condition. This correlation is expressed by

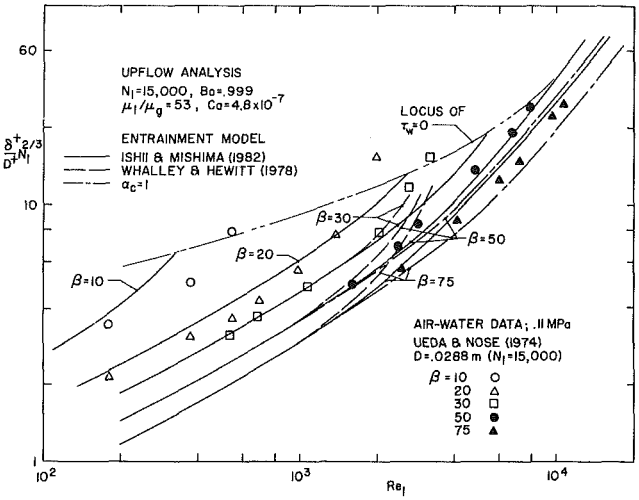


**Fig. 2 Relationship between the predicted and experimental values of the liquid film thickness in upflow**

$$E=\tanh\left[7.25\times10^{-7}\mathrm{We}^{1.25}\left(\frac{4W^+}{1-E}\right)^{0.25}\right] \tag{21}$$

where $E$ is the fraction of the total liquid flow that is entrained, and We is the Weber number. Using equations (12), (13) and the definition of capillary number, it follows that

$$\mathrm{We}=\mathrm{Re}_c^2\mathrm{Bo}^{1/3}(1-\mathrm{Bo})^{2/3}\left(\frac{\mu_g}{\mu_l}\right)^2\frac{\mathrm{Ca}}{[1-\alpha_c\mathrm{Bo}]^2} \tag{22}$$

whereas by utilizing the definitions of $E$, $\epsilon$, $\dot{m}_{lf}=\pi D\mu_l W^+$, and equation (12), it can be shown that

$$\frac{\epsilon}{x}=\frac{E}{(1-E)\frac{\mathrm{Re}_c}{4W^+}\frac{\mu_g}{\mu_l}-E} \tag{23}$$

and thus from equation (11), the core void fraction $\alpha_c$ can be determined.

The entrainment correlations expressed by equations (19) and (20), or by (21), (22) and (23) are similar in the sense that they both depend on the same parameters although this dependence is functionally very different. It is important to note that the entrainment correlation in [12] assumes that the mechanism of entrainment is the shearing of roll waves by the streaming gas velocity and that it is not produced from any specific model of the liquid film.

Equations (1-4), (7), (11-13), (15) or (18), (19) and (20) or (21), (22) and (23) yield a closed system of equations for the conditions of no phase change and in hydrodynamic equilibrium. The latter condition is assumed only in the entrainment correlations. The independent parameters of the model are buoyancy number Bo; viscosity ratio $\mu_g/\mu_l$; two-phase Grashof number $N_l$; capillary number Ca; molecular Prandtl number $\mathrm{Pr}_l$; turbulent Prandtl number in the continuous layer region of the liquid film $\mathrm{Pr}_{ll}$; and the effective Prandtl number in the wavy layer region of the film, $\mathrm{Pr}_{\mathrm{eff}}$.

## 3 Results and Discussion

The hydrodynamic and heat transfer model presented in the previous section for the case without accounting in the model for entrainment is compared with the experimental data by Dobran [7]. This comparison is shown to be very reasonable for vertical upflow, vertical downflow, and horizontal flow. It is also shown that the two-layer liquid film model of turbulence gives lower rates of heat transfer than the single-layer model with single-phase flow turbulent velocity profile.

Figure 2 illustrates the relationship between film thickness

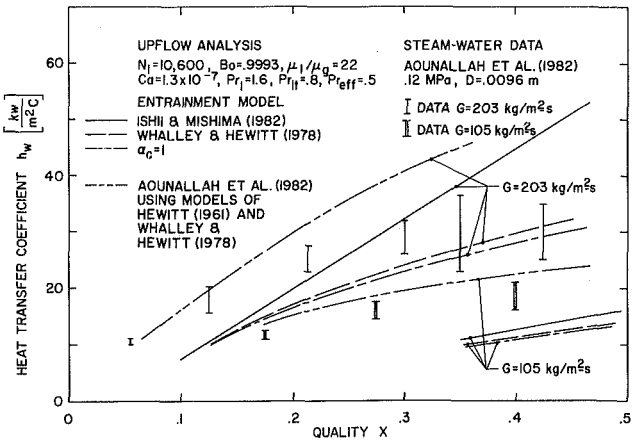


**Fig. 3 Comparison between experimental and predicted heat transfer coefficients using *dP/dz* from experiment**

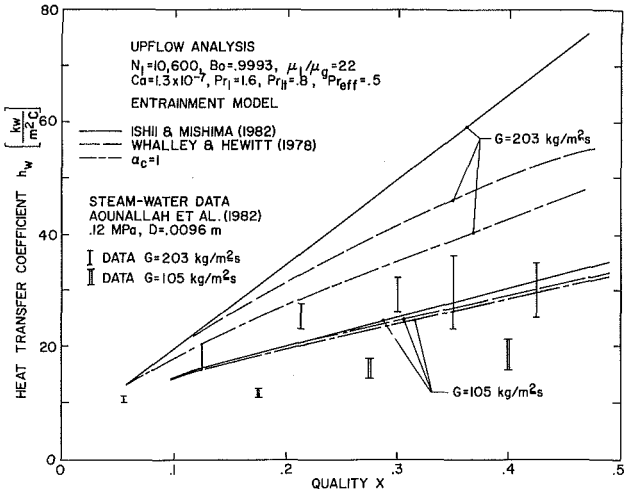


**Fig. 4 Comparison between experimental and predicted heat transfer coefficients**

and film Reynolds number as a function of the interfacial parameter $\beta$ for vertical upflow. Also shown in this figure are the air–water data of Ueda and Nose [3] and the analytical predictions using three different entrainment models discussed in the previous section. At low $\beta$ and film Reynolds numbers, all entrainment models do not affect the film thickness–Reynolds number distribution, and the accord with data is very reasonable except close to the locus of zero value of the wall shear stress ($\tau_w = 0$) where the assumed turbulence model in the film is not expected to apply. At high $\beta$ and $Re_l$, however, the assumption that there is no entrainment in the core is not very reasonable, and a better comparison between the analysis and experiment is achieved when an account is taken in the analysis for entrainment. Note that an increase in the mean film thickness with an increase of the entrainment for fixed values of $\beta$ results from the decrease of the continuous liquid layer thickness as seen from equations (3), (4), (7), and (12). As can be also seen in Fig. 2, the use of Ishii's and Mishima's entrainment correlation in the present analysis gives superior results than that due to Whalley and Hewitt. The latter entrainment correlation is found very reasonable when used in conjunction with the annual flow model of Hewitt [13].

Figures 3 and 4 illustrate the comparison between predicted and experimental values of local heat transfer coefficients as a function of quality for steam–water upflow close to the hydrodynamic equilibrium condition for two different mass fluxes. In Fig. 3, the analysis is based on the experimental value of pressure gradient, and $\beta$ was, therefore, computed from equation (15), whereas in Fig. 4, $\beta$ was computed from equation (18). Both of these figures also illustrate the predictions utilizing different entrainment correlations.

The accord between analysis and experiment in Fig. 3 is superior to that of Fig. 4 only at a high value of mass flux, and Whalley's and Hewitt's entrainment correlation gives slightly better heat transfer results than that of Ishii and Mishima. Lower qualities correspond to higher film Reynolds numbers, and at higher qualities that correspond to $Re_l < 2000$, the predicted heat transfer coefficients are overestimated. A possible reason for this overprediction is that the heat transfer analysis presented in section 2.2 neglects the convective energy transport along the film and thus underestimates the liquid film thermal resistance. An annular flow model in which no account is taken for entrainment leads to lower heat transfer coefficients than the one with the entrainment. This is physically realistic, since the entrainment in the analysis leads to thinner liquid films and, therefore, to lower resistance of heat transfer.

Using the annular flow model of Hewitt [13] and the entrainment correlation of Whalley and Hewitt [11], Aounallah et al. [14] carried out the analytical prediction of their experimental data, and their results are also illustrated in Fig. 3. Their prediction of heat transfer coefficient is higher than in the present analysis, and at higher Reynolds numbers (lower qualities) it is somewhat better than the prediction of the present model. At lower Reynolds numbers or higher qualities, the present model compares more favorably with the experimental data.

A better comparison of the present model with the experimental data of steam–water can be achieved by modifying the values of the turbulent Prandtl number $Pr_{lt}$ in the continuous liquid layer region of the film and the value of effective Prandtl number $Pr_{eff}$ in the wavy layer region of the film. In the results shown in Figs. 3 and 4, the former value is set at 0.8 and the latter at 0.5, since these values were found to be most reasonable in [7]. The value of $Pr_{eff} = 0.5$ signifies that the interfacial waves transfer their heat energy over a distance which is larger than the thickness of the wavy layer.

The disparities between analytical predictions and experimental data in Figs. 3 and 4 reflect (*i*) the uncertainty of the interfacial roughness correlation expressed by equation (17), (*ii*) the uncertainty of turbulence modeling in the film, (*iii*) the uncertainty of entrainment models, and (*iv*) the neglect of convective energy transport in the film.

## 4 Conclusions

An analytic model was presented for modeling annular-dispersed two-phase flows with heat transfer in a vertical upflow. The analysis incorporated a two-layer liquid film turbulence structure and was supplemented by using two recent developments for the entrainment of liquid droplets in the core. It is shown that the prediction of hydrodynamics and heat transfer from the model depends on the model for entrainment, and that the best prediction is achieved with an entrainment correlation that was not developed from any specific model of the liquid film. The two-layer liquid film turbulence structure also yielded the predicted heat transfer coefficients that are in better agreement with the experiments that those predicted by utilizing the single-layer model and turbulent velocity profile of single-phase flow.

## References

1 Dukler, A. E., "Characterization, Effects and Modeling of the Wavy Gas-Liquid Interface," *Progress in Heat and Mass Transfer*, Vol. 6, Pergamon Press, New York, 1972, pp. 207–234.

2 Ueda, T., and Tanaka, T., "Studies of Liquid Film Flow in Two-Phase Annular and Annular-Mist Flow Regions; Part 1, Downflow in a Vertical Tube," *Bulletin JSME*, Vol. 17, 1974, pp. 603–613.

3 Ueda, T., and Nose, S., "Studies of Liquid Film Flow in Two-Phase

Annular and Annular-Mist Flow Regions; Part 2, Upflow in a Vertical Tube," *Bulletin JSME*, Vol. 17, 1974, pp. 614-624.

4 Bergles, A. E., Collier, J. G., Delhaye, J. M., Hewitt, G. F., and Mayinger, F., *Two-Phase Flow and Heat Transfer in Power and Process Industries*, Hemisphere, New York, 1981.

5 Butterworth, D., and Hewitt, G. F., *Two-Phase Flow and Heat Transfer*, Oxford University Press, 1977.

6 Chien, S., and Ibele, W., "Pressure Drop and Liquid Film Thickness of Two-Phase Annular and Annular-Mist Flows," ASME JOURNAL OF HEAT TRANSFER, 1964, pp. 80-96.

7 Dobran, F., "Hydrodynamic and Heat Transfer Analysis of Two-Phase Annular Flow with a New Liquid Film Model of Turbulence," *International Journal of Heat and Mass Transfer*, Vol. 26, 1983, pp. 1159-1171.

8 Dobran, F., "Condensation Heat Transfer and Flooding in a Counter-Current Subcooled Liquid and Saturated Vapor Flow," *Thermal Hydraulics in Nuclear Power Technology*, edited by K. H. Sun and S. C. Yao, ASME, New York, 1981, pp. 9-19.

9 Dobran, F., "Heat Transfer in an Upflowing Annular-Dispersed Flow," *Interfacial Transport Phenomena*, edited by J. C. Chen and S. G. Bankoff, ASME, New York, 1983, pp. 93-99.

10 Wallis, G. B., *One-Dimensional Two-Phase Flow*, McGraw-Hill, New York, 1969.

11 Whalley, P. B., and Hewitt, G. F., "The Correlation of Liquid Entrainment Fraction and Entrainment Rate in Annular Two-Phase Flow," AERE-R9187 Report, July, 1978.

12 Ishii, M., and Mishima, K., "Liquid Transfer and Entrainment Correlation for Droplet-Annular Flow," *Seventh International Heat Transfer Conference*, Vol. 5, 1982, pp. 307-312.

13 Hewitt, G. F., "Analysis of Annular Two-Phase Flow: Application of the Dukler Analysis to Vertical Upward Flow in a Tube," UKAEA Report No. AERE-R-3680, 1961.

14 Aounallah, Y., Kenning, D. B. R., Whalley, P. B., and Hewitt, G. F., "Boiling Heat Transfer in Annular Flow," *Seventh International Heat Transfer Conference*, Vol. 4, 1982, pp. 193-199.

## Combined Free and Forced Convection on Vertical Slender Cylinders

**M. N. Bui[1] and T. Cebeci[2]**

### Introduction

Flows over cylinders are usually considered to be two dimensional as long as the body radius is large compared to the boundary layer thickness. With the slender cylinders considered in this paper, the boundary layer thickness may be of the same order as the cylinder radius and the governing conservation equations must be solved for axisymmetric flows. In this case, the equations contain the transverse curvature term, which strongly influences velocity and temperature profiles, and the corresponding skin-friction and wall heat transfer as the ratio of cylinder radius to boundary layer thickness becomes smaller.

The magnitude of the transverse-curvature effect has been investigated for isothermal, laminar flows by, for example, Seban and Bond [1], Kelly [2], Stewartson [3] and Cebeci [4], and the results show, for example, that the local skin friction can be altered by an order of magnitude by a similar change in the ratio of boundary layer thickness to cylinder radius. It is evident, therefore, that the calculation of momentum and heat transfer on slender cylinders should consider the transverse curvature effect, especially in applications such as wire and fiber drawing, where accurate predictions are required and thick boundary layers can exist on slender, near-cylindrical bodies.

The results of [1-3], and of related heat transfer investigations such as that of Sparrow and Gregg [5] made use of similarity methods and power series to obtain these solutions. Reference [4], in contrast, solved the boundary layer equations in their differential form by a finite difference procedure that has been extensively tested and shown to be accurate and precise. A version of this solution procedure has been used to obtain the results presented in this paper and is described in [6]. The equations that have been solved are presented in the following section and represent conservation of mass, momentum, and energy. The buoyancy term is included in the momentum equations and the solutions correspond to the laminar forced-convection flow upwards along a vertical, slender cylinder with heat-flux boundary conditions that correspond to wall heating and cooling. The combination of free and forced convection, with the two acting both together and in opposite directions, represents an extension of free-convection solutions of Cebeci [4], which, like the present results, quantify the influence of transverse curvature in which the boundary forces aid and oppose the development of the boundary layer.

### Basic Equations

We consider a steady laminar incompressible flow over a vertical cylinder of radius $r_o$. The boundary layer equations and their boundary conditions are well known and can be written as

$$\frac{\partial}{\partial x}(ru) + \frac{\partial}{\partial y}(rv) = 0 \tag{1}$$

$$u\frac{\partial u}{\partial x} + v\frac{\partial u}{\partial y} = g_c\beta(T - T_e) + \frac{\nu}{r}\frac{\partial}{\partial y}\left(r\frac{\partial u}{\partial y}\right) \tag{2}$$

$$u\frac{\partial T}{\partial x} + v\frac{\partial T}{\partial y} = \frac{\nu}{\mathrm{Pr}}\frac{1}{r}\frac{\partial}{\partial y}\left(r\frac{\partial T}{\partial y}\right) \tag{3}$$

$$y=0,\ u=v=0,\ T=T_w;\ y=\delta,\ u=u_e,\ T=T_e \tag{4}$$

Equations (1-4) can be put into a more convenient form for solution by using the following transformation and dimensionless variables

$$d\eta = \sqrt{\frac{\bar{u}_e}{\nu x}}\frac{r}{r_o}dy,\ z = x/r_o,\ g = \frac{T - T_e}{T_w - T_e} \tag{5}$$

together with a dimensionless stream function defined by

$$\psi = (u_e \nu x)^{1/2} r_o f(z,\eta) \tag{6}$$

Introducing the above relations into equations (1-4), and with primes denoting differentiation with respect to $\eta$, we get

$$[(1+\Lambda\eta)f'']' + \frac{1}{2}ff'' = \pm \mathrm{Ri} z g + z\left(f'\frac{\partial f'}{\partial z} - f''\frac{\partial f}{\partial z}\right) \tag{7}$$

$$\left[\frac{(1+\Lambda\eta)}{\mathrm{Pr}}g'\right]' + \frac{1}{2}fg' = z\left(f'\frac{\partial g}{\partial z} - g'\frac{\partial f}{\partial z}\right) \tag{8}$$

$$\eta = 0;\ f = f' = 0,\ g = 1;\ \eta = \eta_e;\ f' = 1,\ g = 0 \tag{9}$$

Here $\Lambda$ defines the transverse curvature parameter and Ri, the Richardson number,

$$\Lambda = 2(z/R)^{1/2},\quad \mathrm{Ri} = \frac{\mathrm{Gr}}{R^2},\quad R = \frac{u_e r_o}{\nu},$$

$$\mathrm{Gr} = \frac{g_c\beta}{\nu^2}(T_w - T_e)r_o^3 \tag{10}$$

### Results and Discussion

Results have been obtained for Prandtl numbers of 0.1, 1.0, and 10, for positive and negative heat transfer through the wall (i.e., heating and cooling) and as a function of the curvature parameter $\Lambda$ defined in equation (10). A sample of the results is presented in Figs. 1 to 3 and the reader is referred to reference 6 for the complete set of results.

The velocity and temperature profiles of Figs. 1(*a*) and 1(*b*) correspond to wall heating and wall cooling, respectively, so

[1] Graduate student, Mechanical Engineering Department, California State University, Long Beach, Calif., Student Mem. ASME

[2] Professor, Mechanical Engineering Department, California State University, Long Beach, Calif., Mem. ASME

Contributed by the Heat Transfer Division for publication in the JOURNAL OF HEAT TRANSFER. Manuscript received by the Heat Transfer Division December 7, 1983.

Annular and Annular-Mist Flow Regions; Part 2, Upflow in a Vertical Tube," *Bulletin JSME*, Vol. 17, 1974, pp. 614-624.

4 Bergles, A. E., Collier, J. G., Delhaye, J. M., Hewitt, G. F., and Mayinger, F., *Two-Phase Flow and Heat Transfer in Power and Process Industries*, Hemisphere, New York, 1981.

5 Butterworth, D., and Hewitt, G. F., *Two-Phase Flow and Heat Transfer*, Oxford University Press, 1977.

6 Chien, S., and Ibele, W., "Pressure Drop and Liquid Film Thickness of Two-Phase Annular and Annular-Mist Flows," ASME JOURNAL OF HEAT TRANSFER, 1964, pp. 80-96.

7 Dobran, F., "Hydrodynamic and Heat Transfer Analysis of Two-Phase Annular Flow with a New Liquid Film Model of Turbulence," *International Journal of Heat and Mass Transfer*, Vol. 26, 1983, pp. 1159-1171.

8 Dobran, F., "Condensation Heat Transfer and Flooding in a Counter-Current Subcooled Liquid and Saturated Vapor Flow," *Thermal Hydraulics in Nuclear Power Technology*, edited by K. H. Sun and S. C. Yao, ASME, New York, 1981, pp. 9-19.

9 Dobran, F., "Heat Transfer in an Upflowing Annular-Dispersed Flow," *Interfacial Transport Phenomena*, edited by J. C. Chen and S. G. Bankoff, ASME, New York, 1983, pp. 93-99.

10 Wallis, G. B., *One-Dimensional Two-Phase Flow*, McGraw-Hill, New York, 1969.

11 Whalley, P. B., and Hewitt, G. F., "The Correlation of Liquid Entrainment Fraction and Entrainment Rate in Annular Two-Phase Flow," AERE-R9187 Report, July, 1978.

12 Ishii, M., and Mishima, K., "Liquid Transfer and Entrainment Correlation for Droplet-Annular Flow," *Seventh International Heat Transfer Conference*, Vol. 5, 1982, pp. 307-312.

13 Hewitt, G. F., "Analysis of Annular Two-Phase Flow: Application of the Dukler Analysis to Vertical Upward Flow in a Tube," UKAEA Report No. AERE-R-3680, 1961.

14 Aounallah, Y., Kenning, D. B. R., Whalley, P. B., and Hewitt, G. F., "Boiling Heat Transfer in Annular Flow," *Seventh International Heat Transfer Conference*, Vol. 4, 1982, pp. 193-199.

## Combined Free and Forced Convection on Vertical Slender Cylinders

**M. N. Bui[1] and T. Cebeci[2]**

### Introduction

Flows over cylinders are usually considered to be two dimensional as long as the body radius is large compared to the boundary layer thickness. With the slender cylinders considered in this paper, the boundary layer thickness may be of the same order as the cylinder radius and the governing conservation equations must be solved for axisymmetric flows. In this case, the equations contain the transverse curvature term, which strongly influences velocity and temperature profiles, and the corresponding skin-friction and wall heat transfer as the ratio of cylinder radius to boundary layer thickness becomes smaller.

The magnitude of the transverse-curvature effect has been investigated for isothermal, laminar flows by, for example, Seban and Bond [1], Kelly [2], Stewartson [3] and Cebeci [4], and the results show, for example, that the local skin friction can be altered by an order of magnitude by a similar change in the ratio of boundary layer thickness to cylinder radius. It is evident, therefore, that the calculation of momentum and heat transfer on slender cylinders should consider the transverse curvature effect, especially in applications such as wire and fiber drawing, where accurate predictions are required and thick boundary layers can exist on slender, near-cylindrical bodies.

The results of [1-3], and of related heat transfer investigations such as that of Sparrow and Gregg [5] made use of similarity methods and power series to obtain these solutions. Reference [4], in contrast, solved the boundary layer equations in their differential form by a finite difference procedure that has been extensively tested and shown to be accurate and precise. A version of this solution procedure has been used to obtain the results presented in this paper and is described in [6]. The equations that have been solved are presented in the following section and represent conservation of mass, momentum, and energy. The buoyancy term is included in the momentum equations and the solutions correspond to the laminar forced-convection flow upwards along a vertical, slender cylinder with heat-flux boundary conditions that correspond to wall heating and cooling. The combination of free and forced convection, with the two acting both together and in opposite directions, represents an extension of free-convection solutions of Cebeci [4], which, like the present results, quantify the influence of transverse curvature in which the boundary forces aid and oppose the development of the boundary layer.

### Basic Equations

We consider a steady laminar incompressible flow over a vertical cylinder of radius $r_o$. The boundary layer equations and their boundary conditions are well known and can be written as

$$\frac{\partial}{\partial x}(ru)+\frac{\partial}{\partial y}(rv)=0 \tag{1}$$

$$u\frac{\partial u}{\partial x}+v\frac{\partial u}{\partial y}=g_c\beta(T-T_e)+\frac{\nu}{r}\frac{\partial}{\partial y}\left(r\frac{\partial u}{\partial y}\right) \tag{2}$$

$$u\frac{\partial T}{\partial x}+v\frac{\partial T}{\partial y}=\frac{\nu}{\mathrm{Pr}}\frac{1}{r}\frac{\partial}{\partial y}\left(r\frac{\partial T}{\partial y}\right) \tag{3}$$

$$y=0,\ u=v=0,\ T=T_w;\ y=\delta,\ u=u_e,\ T=T_e \tag{4}$$

Equations (1-4) can be put into a more convenient form for solution by using the following transformation and dimensionless variables

$$d\eta=\sqrt{\frac{\bar{u}_e}{\nu x}}\frac{r}{r_o}dy,\ z=x/r_o,\ g=\frac{T-T_e}{T_w-T_e} \tag{5}$$

together with a dimensionless stream function defined by

$$\psi=(u_e\nu x)^{1/2}r_o f(z,\eta) \tag{6}$$

Introducing the above relations into equations (1-4), and with primes denoting differentiation with respect to $\eta$, we get

$$[(1+\Lambda\eta)f'']'+\frac{1}{2}ff''=\pm\mathrm{Ri}zg+z\left(f'\frac{\partial f'}{\partial z}-f''\frac{\partial f}{\partial z}\right) \tag{7}$$

$$\left[\frac{(1+\Lambda\eta)}{\mathrm{Pr}}g'\right]'+\frac{1}{2}fg'=z\left(f'\frac{\partial g}{\partial z}-g'\frac{\partial f}{\partial z}\right) \tag{8}$$

$$\eta=0;\ f=f'=0,\ g=1;\ \eta=\eta_e;\ f'=1,\ g=0 \tag{9}$$

Here $\Lambda$ defines the transverse curvature parameter and Ri, the Richardson number,

$$\Lambda=2(z/R)^{1/2},\quad \mathrm{Ri}=\frac{\mathrm{Gr}}{R^2},\quad R=\frac{u_e r_o}{\nu},$$

$$\mathrm{Gr}=\frac{g_c\beta}{\nu^2}(T_w-T_e)r_o^3 \tag{10}$$

### Results and Discussion

Results have been obtained for Prandtl numbers of 0.1, 1.0, and 10, for positive and negative heat transfer through the wall (i.e., heating and cooling) and as a function of the curvature parameter $\Lambda$ defined in equation (10). A sample of the results is presented in Figs. 1 to 3 and the reader is referred to reference 6 for the complete set of results.

The velocity and temperature profiles of Figs. 1(*a*) and 1(*b*) correspond to wall heating and wall cooling, respectively, so

[1] Graduate student, Mechanical Engineering Department, California State University, Long Beach, Calif., Student Mem. ASME

[2] Professor, Mechanical Engineering Department, California State University, Long Beach, Calif., Mem. ASME

Contributed by the Heat Transfer Division for publication in the JOURNAL OF HEAT TRANSFER. Manuscript received by the Heat Transfer Division December 7, 1983.

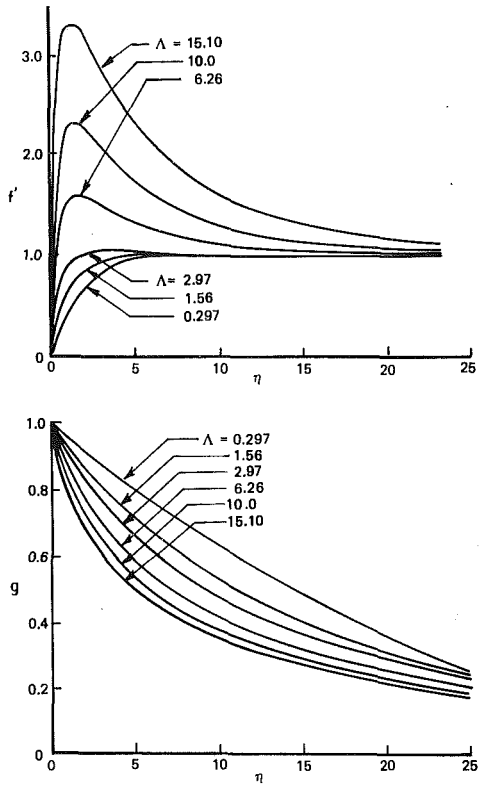


Fig. 1(*a*) The effect of transverse curvature on velocity and temperature profiles on uniformly heated cylinders with $\lambda = 1.0$ and $Pr = 1$

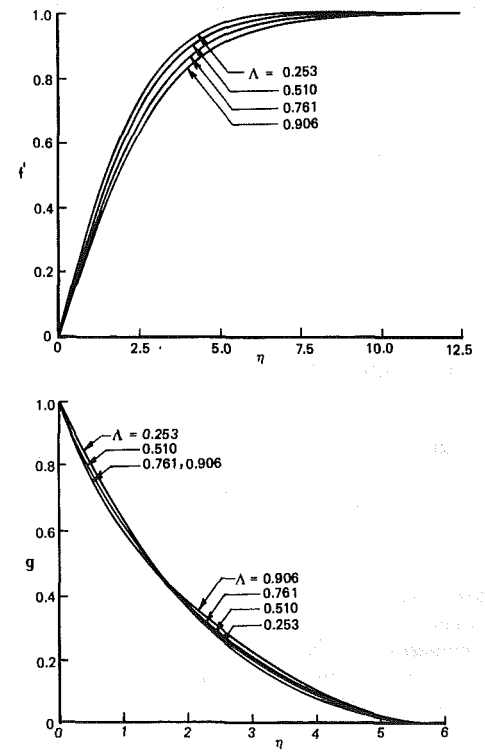


Fig. 1(*b*) The effect of transverse curvature on velocity and temperature profiles on uniformly cooled cylinders with $\lambda = -1.0$ and $Pr = 1$

that, in the former the forced convection flow is aided by the natural convection flow and in the latter it is opposed. The results correspond to equal Grashof and Reynolds number and to a Prandtl number of unity and, as expected, the velocity and temperature boundary layers are of similar

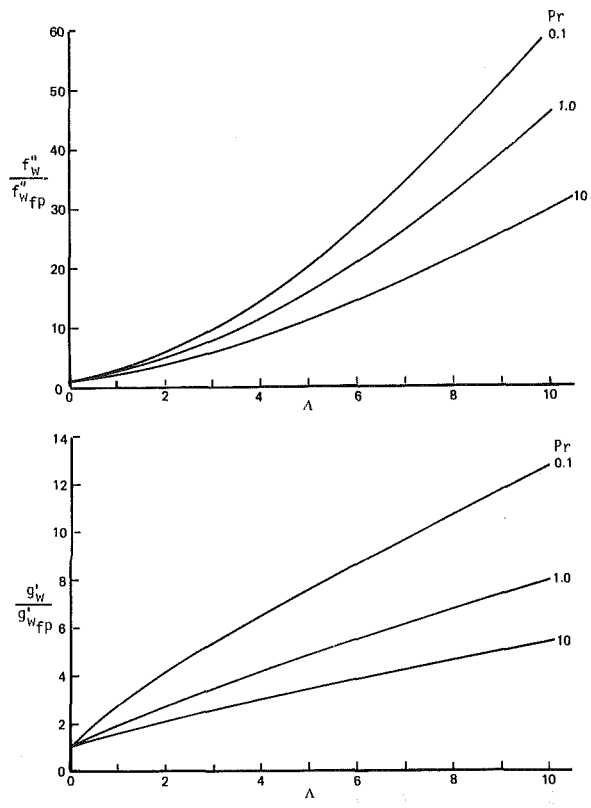


Fig. 2(*a*) The effect of transverse curvature on the dimensionless wall shear parameter $f''_w/(f''_w)_{fp}$ and on the dimensionless wall heat flux $g'_w/(g'_w)_{fp}$ on uniformly heated cylinders with $\lambda = 1.0$ at three Prandtl numbers

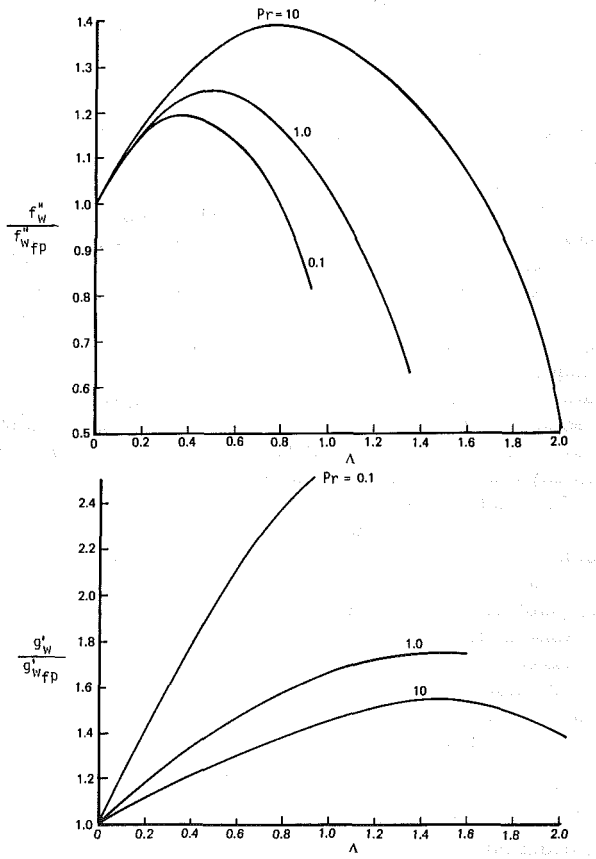


Fig. 2(*b*) The effect of transverse curvature on the dimensionless wall shear parameter $f''_w/(f''_w)_{fp}$ and on the dimensionless wall heat flux $g'_w/(g'_w)_{fp}$ on uniformly cooled cylinders with $\lambda = -1.0$ at three Prandtl numbers

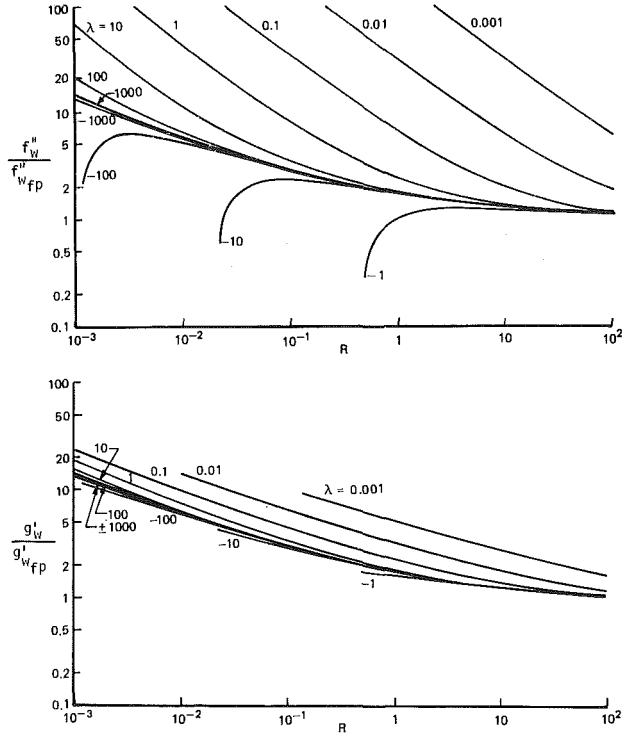


**Fig. 3 The effect of transverse curvature on the dimensionless (*a*) wall shear parameter $f''_w/(f''_w)_{fp}$ and on the dimensionless (*b*) wall heat flux $g'_w/(g'_w)_{fp}$ at different values of λ: Pr = 1**

thickness. The influence of the curvature parameter Λ may be interpreted in two ways: first, for constant values of free-stream velocity and cylinder radius; and secondly, for constant values of free-stream velocity and distance. From the first interpretation, it is clear that the effect of buoyancy increases with distance for the wall heating case of Fig. 1(*a*); with a larger ratio of $\mathrm{Gr}_L$ to $R_L$, a larger effect would occur. The second interpretation, of greater importance here, shows that an increase in Λ, which corresponds to a reduction in the radius $r_o$ results in a rapid change in the shape of the velocity profile and a significant, but smaller change in the temperature profile. The profiles of Fig. 1(*b*) correspond to wall cooling, and for large values of the ratio of $\mathrm{Gr}_L$ to $R_L$ it is to be expected that this arrangement would lead to separated flow. In the present case where λ = 1, the contrast with the profiles of Fig. 1(*a*) is evident with the natural convection tending to retard the forced convection flow. In effect, the natural convection acts as an adverse pressure gradient, whereas an increase Λ acts as a favorable pressure gradient. However, its effect is small so that it does not cause the velocity profiles to have overshoots as in aided flows.

The results obtained with Prandtl numbers of 0.1 and 10 show, for example, that the temperature boundary layer is some five times thicker at the lower value. With wall heating, the velocity boundary layer is of similar thickness to the temperature boundary layer for both values and the velocity maximum decreases with increasing Prandtl number. With wall cooling, the boundary layers have similar thickness at the lower value and the velocity boundary layer is around five times thicker than the temperature boundary layer at a Prandtl number of 10.

The variation of the nondimensional wall shear parameter $f''_w$, divided by the corresponding flat-plate value, are shown in Figs. 2(*a*) and 2(*b*), together with corresponding distributions of wall heat transfer ratios for the three values of Prandtl number and for heating and cooling, respectively. As expected, the ratio of $[f''_w/(f''_w)_{fp}]$ increases with Λ for the case of wall heating and shows the largest effect with the lowest Prandtl number. With wall cooling the tendency to increase is rapidly overcome by the adverse pressure-gradient effect of the natural convection and the tendency toward separation is evident. The difference in the scales of the abscissae of the wall heat flux ratio with heating and cooling should be noted and stems from the limitations imposed by the tendency to separation in the case of cooling. The effect of increasing Λ, in the range shown, is greater in the heating case.

Figure 3 extends the skin-friction and heat-flux results to a wide range of values of the ratio of $R_L$ and $\mathrm{Gr}_L$, namely, λ. The results tend to the flat-plate values as $1/\Lambda$ tends to infinity. High values of λ (low Richardson numbers) imply that forced convection is dominant and for low values that free convection is dominant. Thus, for particular value of $1/\Lambda$, $[f''_w/(f''_w)_{fp}]$ tends towards the natural convection values reported by Cebeci [4] as $|\lambda|$ tends to zero. The conflict between free and forced convection is evident for negative values of λ, and an increase in λ results in an extension in the dominance of the force convection due to the favorable pressure-gradient effect of the increased transverse-curvature effect.


### Acknowledgment

This research was supported under the National Science Foundation Grant MEA-8018565.


### References


1 Seban, R. A., and Bond, R., "Skin-Friction and Heat-Transfer Characteristics of a Laminar Boundary Layer on a Circular Cylinder in Axial Incompressible Flow," *J. Aero. Sci.*, Vol. 18, 1951, pp. 671–675.

2 Kelly, H. R., "A Note on the Laminar Boundary Layer on a Circular Cylinder in Axial Incompressible Flow," *J. Aero. Sci.*, Vol. 21, 1954, p. 634.

3 Stewartson, K., "The Asymptotic Boundary Layer on a Circular Cylinder in Axial Incompressible Flow," *Quart. Appl. Math.*, Vol. 13, 1955, pp. 113–122.

4 Cebeci, T., "Laminar-Free-Convective-Heat Transfer From the Outer Incompressible Boundary Surface of a Vertical Slender Circular Cylinder," *Proceedings of the Fifth Int. Heat Transfer Conf.*, Vol. 3, NC1.4, 1975, pp. 15–19.

5 Sparrow, E. M., and Gregg, J. L., "Laminar-Free-Convection-Heat Transfer from the Outer Surface of a Vertical Circular Cylinder," ASME *Transactions*, Vol. 78, 1956, pp. 1823–1829.

6 Bui, M. N., "Combined Free and Forced Convection on Vertical Slender Cylinders," M.S. thesis, Mechanical Engineering Department, California State University, Long Beach, 1983.


## Differential Approximation to Radiative Transfer in Semitransparent Media


**F. H. Azad**[1]



*Radiative transfer in a semitransparent medium is treated using the differential approximation. Boundary conditions are formulated to accommodate direction-dependent reflection and refraction at a dielectric interfaces. The approximate results are compared to numerical solution of the exact integral equation. Also, a modification based on the exact formulation of the integrated intensity at the interface is presented that significantly improves the accuracy of the differential approximation in the optically thin regimes.*


### Nomenclature

$E_n$ = exponential integral of order $n$
$G_\nu$ = direction-integrated intensity


[1]Corporate Research and Development, General Electric Company, Schenectady, N.Y. 12345, Assoc. Mem. ASME



Contributed by the Heat Transfer Division for publication in the JOURNAL OF HEAT TRANSFER. Manuscript received by the Heat Transfer Division March 20, 1984.

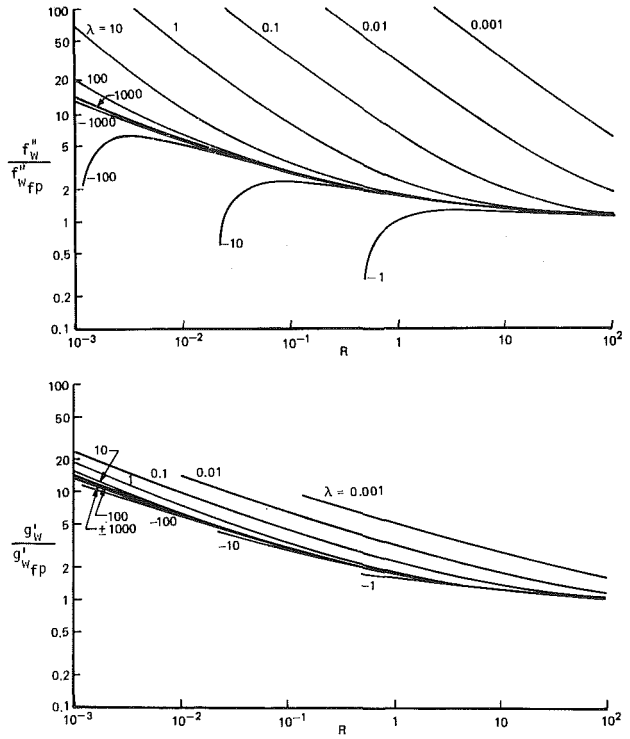


**Fig. 3 The effect of transverse curvature on the dimensionless (*a*) wall shear parameter $f''_w/(f''_w)_{fp}$ and on the dimensionless (*b*) wall heat flux $g'_w/(g'_w)_{fp}$ at different values of λ: Pr = 1**

thickness. The influence of the curvature parameter Λ may be interpreted in two ways: first, for constant values of free-stream velocity and cylinder radius; and secondly, for constant values of free-stream velocity and distance. From the first interpretation, it is clear that the effect of buoyancy increases with distance for the wall heating case of Fig. 1(*a*); with a larger ratio of $\mathrm{Gr}_L$ to $R_L$, a larger effect would occur. The second interpretation, of greater importance here, shows that an increase in Λ, which corresponds to a reduction in the radius $r_o$ results in a rapid change in the shape of the velocity profile and a significant, but smaller change in the temperature profile. The profiles of Fig. 1(*b*) correspond to wall cooling, and for large values of the ratio of $\mathrm{Gr}_L$ to $R_L$ it is to be expected that this arrangement would lead to separated flow. In the present case where λ = 1, the contrast with the profiles of Fig. 1(*a*) is evident with the natural convection tending to retard the forced convection flow. In effect, the natural convection acts as an adverse pressure gradient, whereas an increase Λ acts as a favorable pressure gradient. However, its effect is small so that it does not cause the velocity profiles to have overshoots as in aided flows.

The results obtained with Prandtl numbers of 0.1 and 10 show, for example, that the temperature boundary layer is some five times thicker at the lower value. With wall heating, the velocity boundary layer is of similar thickness to the temperature boundary layer for both values and the velocity maximum decreases with increasing Prandtl number. With wall cooling, the boundary layers have similar thickness at the lower value and the velocity boundary layer is around five times thicker than the temperature boundary layer at a Prandtl number of 10.

The variation of the nondimensional wall shear parameter $f''_w$, divided by the corresponding flat-plate value, are shown in Figs. 2(*a*) and 2(*b*), together with corresponding distributions of wall heat transfer ratios for the three values of Prandtl number and for heating and cooling, respectively. As expected, the ratio of $[f''_w/(f''_w)_{fp}]$ increases with Λ for the case of wall heating and shows the largest effect with the lowest Prandtl number. With wall cooling the tendency to increase is rapidly overcome by the adverse pressure-gradient effect of the natural convection and the tendency toward separation is evident. The difference in the scales of the abscissae of the wall heat flux ratio with heating and cooling should be noted and stems from the limitations imposed by the tendency to separation in the case of cooling. The effect of increasing Λ, in the range shown, is greater in the heating case.

Figure 3 extends the skin-friction and heat-flux results to a wide range of values of the ratio of $R_L$ and $\mathrm{Gr}_L$, namely, λ. The results tend to the flat-plate values as $1/\Lambda$ tends to infinity. High values of λ (low Richardson numbers) imply that forced convection is dominant and for low values that free convection is dominant. Thus, for particular value of $1/\Lambda$, $[f''_w/(f''_w)_{fp}]$ tends towards the natural convection values reported by Cebeci [4] as $|\lambda|$ tends to zero. The conflict between free and forced convection is evident for negative values of λ, and an increase in λ results in an extension in the dominance of the force convection due to the favorable pressure-gradient effect of the increased transverse-curvature effect.


### Acknowledgment

This research was supported under the National Science Foundation Grant MEA-8018565.


### References


1 Seban, R. A., and Bond, R., "Skin-Friction and Heat-Transfer Characteristics of a Laminar Boundary Layer on a Circular Cylinder in Axial Incompressible Flow," *J. Aero. Sci.*, Vol. 18, 1951, pp. 671–675.

2 Kelly, H. R., "A Note on the Laminar Boundary Layer on a Circular Cylinder in Axial Incompressible Flow," *J. Aero. Sci.*, Vol. 21, 1954, p. 634.

3 Stewartson, K., "The Asymptotic Boundary Layer on a Circular Cylinder in Axial Incompressible Flow," *Quart. Appl. Math.*, Vol. 13, 1955, pp. 113–122.

4 Cebeci, T., "Laminar-Free-Convective-Heat Transfer From the Outer Incompressible Boundary Surface of a Vertical Slender Circular Cylinder," *Proceedings of the Fifth Int. Heat Transfer Conf.*, Vol. 3, NC1.4, 1975, pp. 15–19.

5 Sparrow, E. M., and Gregg, J. L., "Laminar-Free-Convection-Heat Transfer from the Outer Surface of a Vertical Circular Cylinder," ASME *Transactions*, Vol. 78, 1956, pp. 1823–1829.

6 Bui, M. N., "Combined Free and Forced Convection on Vertical Slender Cylinders," M.S. thesis, Mechanical Engineering Department, California State University, Long Beach, 1983.


## Differential Approximation to Radiative Transfer in Semitransparent Media


**F. H. Azad**[1]



*Radiative transfer in a semitransparent medium is treated using the differential approximation. Boundary conditions are formulated to accommodate direction-dependent reflection and refraction at a dielectric interfaces. The approximate results are compared to numerical solution of the exact integral equation. Also, a modification based on the exact formulation of the integrated intensity at the interface is presented that significantly improves the accuracy of the differential approximation in the optically thin regimes.*


### Nomenclature

$E_n$ = exponential integral of order $n$
$G_\nu$ = direction-integrated intensity


[1]Corporate Research and Development, General Electric Company, Schenectady, N.Y. 12345, Assoc. Mem. ASME



Contributed by the Heat Transfer Division for publication in the JOURNAL OF HEAT TRANSFER. Manuscript received by the Heat Transfer Division March 20, 1984.

$I_\nu$ = directional intensity
$\mathbf{n}$ = surface normal vector
$n_{o\nu}$ = surrounding refractive index
$n_{m\nu}$ = medium refractive index
$\mathbf{q}$ = radiative flux
$R_n^*$ = function defined by equation (10*b*)
$R_n^k$ = function defined by equation (10*c*)
$\mathbf{s}$ = direction vector
$T_n^*$ = function defined by equation (10*a*)
$t$ = interface transmissivity

**Greek Letters**

$\gamma$ = function defined by equation (8)
$\kappa_\nu$ = spectral absorption coefficient
$\mu$ = direction cosine
$\nu$ = frequency
$\rho$ = interface reflectivity
$\tau$ = optical distance

## Introduction

Heat transfer analysis in semitransparent materials such as glass is complicated by the fact that in addition to internal conduction, treatment of various radiative effects is also required. These effects include absorption, emission, and multiple internal reflections of radiation. The latter phenomenon is particularly significant when dealing with relatively thin material samples. Also most semitransparent materials exhibit strongly wavelength-dependent properties, thus necessitating spectral treatment of the radiative problem.

An excellent review of heat transfer analyses in semitransparent solids is presented by Viskanta and Anderson [1]. Several papers by Gardon [2, 3] represent some of the more comprehensive analyses available in the literature. These treatments have generally employed the integral approach to solution of the equation of radiative transfer and have thus been limited to the simple planar geometry. Moreover, use of the integral formulation in transient problems involving both conduction and radiation results in a partial integrodifferential equation, the numerical solution of which (even in plane-parallel geometry) is quite cumbersome. An alternative approach is to use the differential formulation of radiative transfer.

The differential approximation has been used successfully in a variety of applications (e.g., [4–6]) in radiative transfer. This method results in differential governing equations and is more conveniently extendible to multidimensional geometries and spectral treatment. The major drawback of the standard differential approximation, however, is its limitation to optically thick conditions.

Recently Amlin and Korpela [7] used the differential approximation for analysis of radiative transfer in a two-dimensional semitransparent solid. In extending the standard differential approximation boundary conditions to a semitransparent interface, however, they assumed a direction-independent interface reflectivity. Furthermore, the accuracy of the differential approximation in optically thin regimes was not discussed in this analysis.

Improvements to the differential approximation in the optically thin and intermediate regimes were presented in several papers by Modest [8–10]. This approach involved the evaluation of several geometric factors based on the exact formulation of the radiation intensity in order to accommodate the optically thin limit. Modest's results for gray media bounded by opaque walls were in excellent agreement with Monte Carlo and zone solutions.

In this paper, (*i*) a formulation for the standard differential approximation boundary condition at a semitransparent interface is presented; (*ii*) the exact integral equation for radiative transfer in a semitransparent medium [1] is solved numerically, and the results are used for comparison to the differential approximation; (*iii*) a modification (based on the exact formulation of the integrated intensity at the interface) is presented which significantly improves the accuracy of the differential approximation in optically thin regimes.

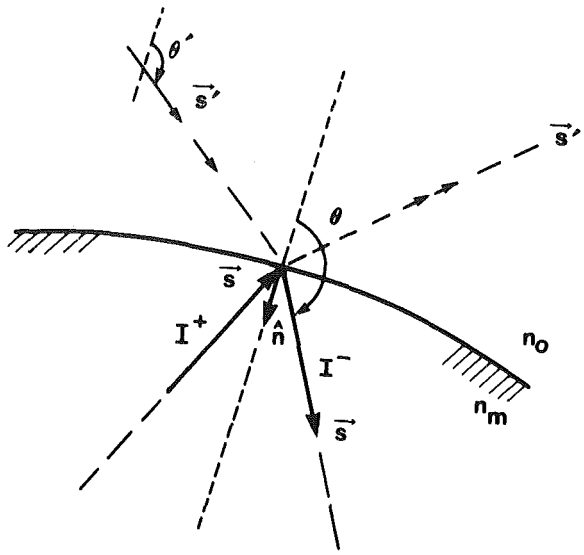

Fig. 1 Dielectric interface

## Analysis

The divergence of the radiative heat flux, which appears as the source term in the overall energy equation, is given by [1]

$$\nabla \cdot \mathbf{q}_{\text{rad}} = \int_0^\infty \nabla \cdot \mathbf{q}_\nu d\nu = \int_0^\infty \kappa_\nu (4\pi n_{m\nu}^2 I_{b\nu} - G_\nu) d\nu \tag{1}$$

where $\mathbf{q}_\nu$ is the radiative flux, $\kappa_\nu$ is the spectral absorption coefficient, $n_{m\nu}$ is the refractive index of the medium, $I_{b\nu}$ is the blackbody intensity, and the subscript $\nu$ denotes frequency dependence. In Equation (1), $G_\nu$ is the direction-integrated intensity. Using the differential approximation [11] and eliminating the radiative flux in favor of the integrated intensity yields

$$\nabla^2 G_\nu - 3\kappa_\nu^2 G_\nu = -12\pi n_{m\nu}^2 \kappa_\nu^2 I_{b\nu} \tag{2}$$

For a given temperature field, $I_{b\nu}$ is known and $G_\nu$ is the only unknown to be determined subject to the appropriate boundary conditions.

Figure 1 depicts a dielectric interface at which boundary conditions for equation (2) are to be evaluated. The intensity arriving at this interface from the optically thick medium can be expressed as [11]

$$I_\nu^+(\mathbf{s}) = \frac{1}{4\pi}(G_\nu + 3\mathbf{q}_\nu \cdot \mathbf{s}): \quad (\mathbf{s}\cdot\mathbf{n} < 0), \tag{3}$$

where $\mathbf{s}$ is the unit direction vector, $\mathbf{n}$ is the unit interface normal pointing into the medium, and $I_\nu^+$ is the intensity traveling towards the interface. The downward traveling intensity $I_\nu^-$ (Fig. 1) is composed of two components: (*i*) the specularly reflected portion of $I_\nu^+$, and (*ii*) partial transmission (refraction) of any externally incident radiation $I_\nu^i$ into the $\mathbf{s}$ direction, namely

$$I_\nu^-(\mathbf{s}) = \rho(\mathbf{s}\cdot\mathbf{n}) I_\nu^+(\mathbf{s} - 2(\mathbf{n}\cdot\mathbf{s})\mathbf{n}) + \left(\frac{n_{m\nu}}{n_{o\nu}}\right)^2 t(\mathbf{s}\cdot\mathbf{n}) I_\nu^i(\mathbf{s}): \quad (\mathbf{s}\cdot\mathbf{n} > 0), \tag{4}$$

where $\rho$ is the internal interface reflectivity, $t$ is the external

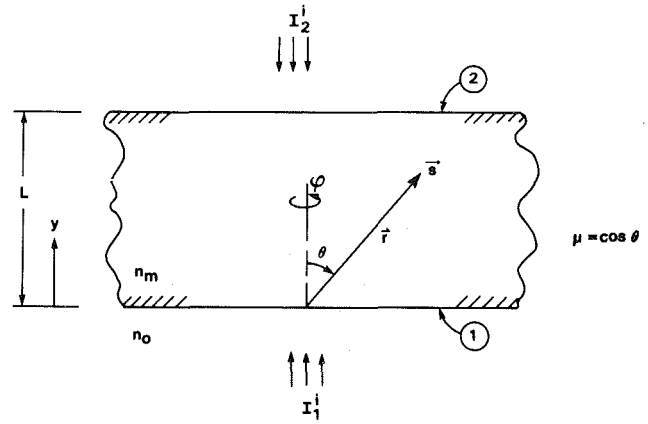


Fig. 2 Slab geometry

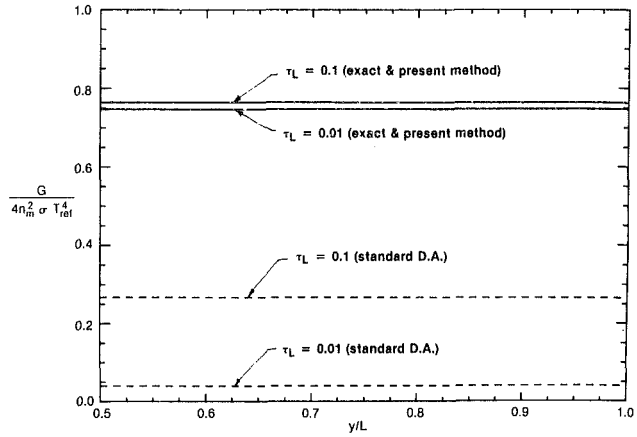


Fig. 3(*a*) Isothermal slab 1100 K, surrounding at 300 K, $T_{ref} = 1100$ K, $n_m = 1.5$

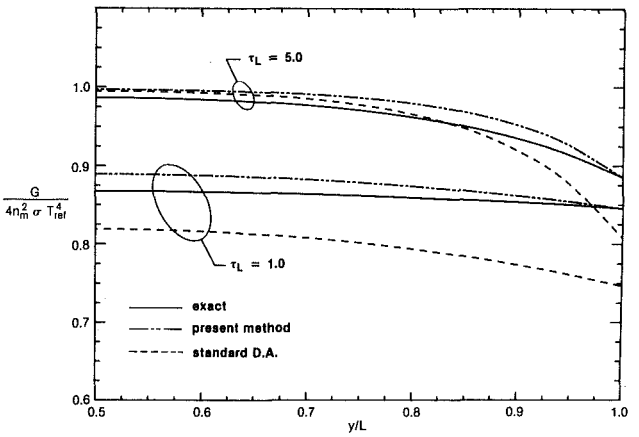


Fig. 3(*b*) Isothermal slab at 1100 K, surrounding at 300 K, $T_{ref} = 1100$ K, $n_m = 1.5$

transmissivity, and $n_{ov}$ is the refractive index of the surrounding. In the present analysis, the directional interface properties are obtained by averaging the two components of polarization [12]. With $\mu \equiv |\mathbf{s}\cdot\mathbf{n}|$ the resulting expressions become

$$0 \le \mu \le \mu_c : \rho(\mu) = 1$$

$$\mu_c \le \mu \le 1 : \rho(\mu) = \frac{1}{2}\left\{\left(\frac{\mu - \sqrt{\mu^2 - \mu_c^2}}{\mu + \sqrt{\mu^2 - \mu_c^2}}\right)^2 + \left(\frac{\mu(1-\mu_c^2) - \sqrt{\mu^2 - \mu_c^2}}{\mu(1-\mu_c^2) + \sqrt{\mu^2 - \mu_c^2}}\right)^2\right\} \tag{5a}$$

where

$$\mu_c \equiv \left\{1 - \left(\frac{n_{ov}}{n_{mv}}\right)^2\right\}^{\frac{1}{2}} \tag{5b}$$

$$t(\mu') = 1 - \rho(\mu') \tag{5c}$$

and

$$\mu' \equiv \left\{1 - \left(\frac{n_{mv}}{n_{ov}}\right)^2 (1-\mu^2)\right\}^{\frac{1}{2}}, \quad \mu \ge \mu_c \tag{5d}$$

The boundary condition to equation (2) can now be obtained from an energy balance at a point just inside the interface

$$\mathbf{n}\cdot\mathbf{q}_v = \mathbf{n}\cdot\int \mathbf{s} I_v^+ \, d\Omega + \mathbf{n}\cdot\int \mathbf{s} I_v^- \, d\Omega \tag{6}$$

where $d\Omega$ denotes integration over solid angles. Using equations (3) and (4) in (6) then yields

$$\mathbf{n}\cdot\nabla G_v - \frac{3}{2}\kappa_v \gamma G_v = -6\pi\kappa_v \gamma \left(\frac{n_{mv}}{n_{ov}}\right)^2 I_{dv}^i \tag{7}$$

where $I_{dv}^i$ is the diffuse externally incident intensity, and

$$\gamma \equiv \frac{1 - 2\int_0^1 \rho(\mu)\mu d\mu}{1 + 3\int_0^1 \rho(\mu)\mu^2 d\mu} \tag{8}$$

In equation (8), the broken integral sign denotes integration in the two separate regions defined by equation (5*a*).

Equations (2) and (7) constitute the differential approximation for a semitransparent medium with direction-dependent interface properties. Note that for given values of the medium and surrounding indices of refraction, $\gamma$ can be evaluated once and for all. For the results presented in this paper, $\gamma$ was computed by Gaussian quadrature and a finite difference scheme was used for the numerical solution of equation (2).

In optically thin situations, the radiation field within a semitransparent medium is governed by the externally incident radiation, refraction at the interfaces, and multiple internal reflections. In such cases, the differential approximation boundary conditions can no longer yield accurate results. On the other hand, because of the low internal attenuation, the integrated intensity does vary significantly within the medium. Therefore, solution of equation (2) with more accurate boundary conditions can be expected to yield acceptable results for the integrated intensity. For a one-dimensional slab, such boundary conditions can be obtained from the exact solution [1]. The resulting expressions for a slab of optical thickness $\tau_{Lv}$ are

$$\begin{aligned} G_v(\tau_v = 0) = {} & 2\pi n_{mv}^2 \Big\{ [1 + R_2^*(0,0)] I_{bv}(0) \\ & - [R_2^*(0,\tau_{Lv}) - E_2(\tau_{Lv})] I_{bv}(\tau_{Lv}) \\ & + ([T_2^0(0) + T_1^2(2\tau_{Lv})] I_{dv}^1 + [T_2^0(\tau_{Lv}) \\ & + T_2^1(\tau_{Lv})] I_{dv}^2)/n_{ov}^2 \\ & + \int_0^{\tau_{Lv}} \left(\frac{dI_{bv}}{d\eta}\right) [R_2^*(0,\eta) + E_2(\eta)] d\eta \Big\}, \end{aligned} \tag{9a}$$

and

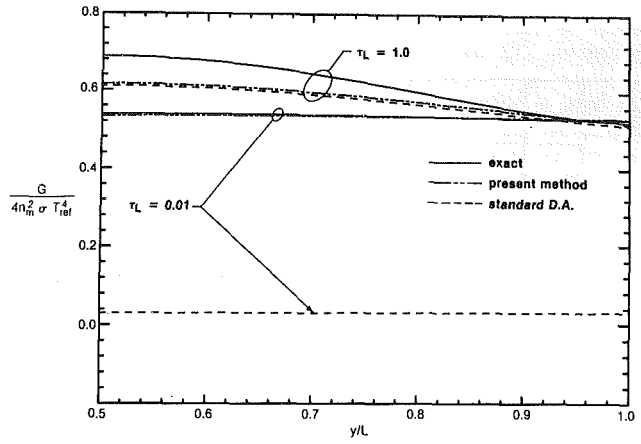


**Fig. 4(a)** $T(y) = 1100 - 300[1 - 2(y/L)]^2$ K, surrounding at 300 K, $T_{ref} = 1100$ K, $n_m = 1.5$

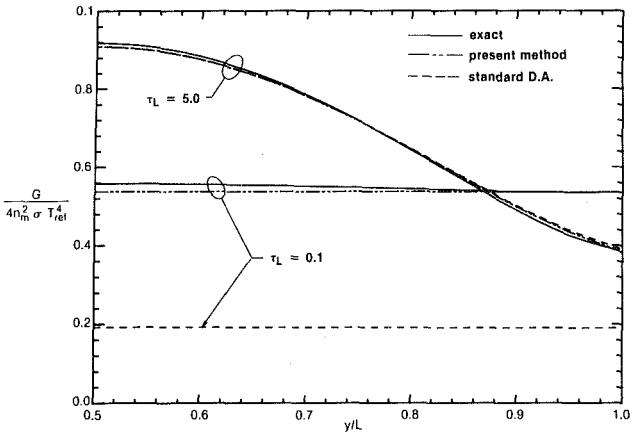


**Fig. 4(b)** $T(y) = 1100 - 300[1 - 2(y/L)]^2$ K, surrounding at 300 K, $T_{ref} = 1100$ K, $n_m = 1.5$

$$G_\nu(\tau_\nu = \tau_{L\nu}) = 2\pi n_{m\nu}^2 \Big\{ [1 + R_2^*(0,0)] I_{b\nu}(\tau_{L\nu}) - [R_2^*(0,\tau_{L\nu}) - E_2(\tau_{L\nu})] I_{b\nu}(0) + ([T_2^0(0) + T_2^1(2\tau_{L\nu})] I_{d\nu}^2 + [T_2^0(\tau_{L\nu}) + T_2^1(\tau_{L\nu})] I_{d\nu}^1)/n_{o\nu}^2 + \int_0^{\tau_{L\nu}} \left(\frac{dI_{b\nu}}{d\eta}\right) [R_2^*(\tau_{L\nu},\eta) - E_2(\tau_{L\nu} - \eta)] d\eta \Big\} \quad (9b)$$

where $I_d$ and $I_{d\nu}^2$ are the diffuse externally incident intensities at the $\tau_\nu = 0$ and $\tau_\nu = \tau_{L\nu}$ boundaries, respectively. In equations (9), $E_2$ is the exponential integral of order two, and the geometric functions $T_n^k$ and $R_n^*$ turn out to be

$$T_n^k(\tau) \equiv \int_{\mu_c}^1 \frac{\rho^k(\mu) t(\mu') \exp(-\tau/\mu)\, \mu^{n-2}}{1 - \rho^2(\mu) \exp(-2\tau_L/\mu)}\, d\mu \quad (10a)$$

$$R_n^*(\tau,\eta) \equiv [R_n^1(\tau + \eta) - R_n^2(2\tau_L + \tau - \eta)] - (-1)^n [R_n^1(2\tau_L - \tau - \eta) - R_n^2(2\tau_L - \tau + \eta)] \quad (10b)$$

$$R_n^k(\tau) \equiv \int_0^1 \frac{\rho^k(\mu) \exp(-\tau/\mu) \mu^{n-2}}{1 - \rho^2(\mu) \exp(-2\tau_L/\mu)}\, d\mu \quad (10c)$$

Equations (2) and (9) constitute the modified differential approximation. While the new boundary conditions are more complex than those of the standard differential approximation, the computation time they require is substantially lower than that for the full exact solution.

## Results and Discussion

In order to demonstrate the validity range of the standard differential approximation, and increased accuracy obtained through the modified formulation, a slab geometry (Fig. 2) with a number of temperature profiles is considered. Figures 3(*a*) and 3(*b*) depict a comparison of the two approximate models to the exact solution in an isothermal slab. At low values of the optical thickness the standard differential approximation underpredicts the results for the integrated intensity. The modified solution, however, is coincident with exact results. With increased optical thickness, the accuracy of the standard differential approximation improves at the interior points. At the boundaries, however, the sudden temperature jump is not satisfactorily accommodated by the standard differential approximation. The modified formulation, on the other hand, yields good results in both regimes.

The effect of a quadratic temperature distribution is demonstrated in Figs. 4(*a*) and 4(*b*). Under this condition, the accuracy of the standard differential approximation improves near the boundaries and both approximate methods yield good results in optically thick conditions. In the optically thin regime, however, the modified formulation is again superior.

## Summary and Conclusion

The differential approximation for a semitransparent medium bounded by dielectric interfaces was formulated. The approximate results were compared to the exact integral solutions for a semitransparent slab. Also, a modification based on accurate evaluation of the integrated intensity at the boundaries was presented that significantly improved the performance of the differential approximation in optically thin regimes. The modified formulation in its present form is applicable to planar and high-aspect-ratio geometries. Extension to more complex shapes would require the evaluation of appropriate geometric integrals.

## References

1 Viskanta, R., and Anderson, E. E., "Heat Transfer in Semitransparent Solids," *Advances in Heat Transfer*, Vol. 11, 1975, pp. 317–441.

2 Gardon, R., "Calculation of Temperature Distributions in Glass Plates Undergoing Heat-Treatment," *J. Amer. Ceramic Soc.*, Vol. 41, No. 6, 1958, pp. 200–209.

3 Gardon, R., "A Review of Radiant Heat Transfer in Glass," *J. Amer. Ceramic Soc.*, Vol. 44, No. 7, 1961, pp. 305–312.

4 Modest, M. F., and F. H. Azad, "The Differential Approximation for Radiative Transfer in an Emitting, Absorbing, and Anisotropically Scattering Medium," *J. Quant. Spectrosc. Radiat. Transfer*, Vol. 23, 1980, pp. 117–120.

5 Azad, F. H., and Modest, M. F., "Evaluation of the Radiative Heat Flux in Absorbing, Emitting and Linear-Anisotropically Scattering Cylindrical Media," ASME JOURNAL OF HEAT TRANSFER, Vol. 103, No. 2, 1981.

6 Ratzel, A. C., and Howell, J. R., "Two-Dimensional Radiation in Absorbing-Emitting-Scattering Media Using the P-N Approximation," ASME Paper No. 82-HT-19, 1982.

7 Amlin, D. W., and Korpela, S. A., "Influence of Thermal Radiation on the Temperature Distribution in a Semi-Transparent Solid," ASME JOURNAL OF HEAT TRANSFER, Vol. 101, No. 76-80, 1979.

8 Modest, M. F., "Two-Dimensional Radiative Equilibrium of a Gray Medium in a Plane Layer Bounded by Gray Nonisothermal Walls," ASME JOURNAL OF HEAT TRANSFER, 1974, pp. 483–458.

9 Modest, M. F., "Radiative Equilibrium in a Rectangular Enclosure Bounded by Gray Walls," *J. Quant. Spectrosc. Radiat. Transfer*, Vol. 15, 1975, pp. 445–461.

10 Modest, M. F., and Stevens, D. S., "Two-Dimensional Radiative Equilibrium of a Gray Medium Between Concentric Cylinders," *J. Quant. Spectros. Radiat. Transfer*, Vol. 19, 1978, pp. 353–365.

11 Modest, M. F., "Photon-Gas Formulation of the Differential Approximation in Radiative Transfer," *Lett. Heat and Mass Transfer*, Vol. 3, 1976, pp. 111–116.

12 Siegel, R., and Howell, J. R., *Thermal Radiation Heat Transfer*, McGraw-Hill, New York, 1981.

# Radiative and Convective Transfer in a Cylindrical Enclosure for a Real Gas[1]

T. F. Smith[2], Z. F. Shen[3], and A. M. Alturki[4]

## Introduction

Analysis of convective and radiative transfer in fossil-fueled energy units represented by a cylindrical system may be based on solution of the governing integro-differential equations utilizing band models [1], flux methods [2], spherical harmonics methods [3], or zone methods [4]. The zone method has a wide range of application to energy generation systems, exhibits the ability to predict real gas behavior in multidimensional systems, and has been successfully employed to examine temperature distributions and heat transfer rates in furnaces and circular enclosures [5–12]. Therefore, the zone method is adopted for this investigation. Although several previous investigations using the zone method, as well as other methods, have been performed, a systematic approach is lacking for the study of laminar and turbulent flow of a real gas in straight ducts where multidimensional radiation effects are included. Important factors such as the flow conditions (namely, laminar or turbulent), boundary conditions, and entrance effects are of interest.

The purpose of this study is to examine the interaction of gaseous radiative transfer with conductive and convective transfer for flow in a black wall circular duct. Results of interest consist of axial and radial gas temperature profiles along with wall heat flux distributions or wall temperatures for various values of the system parameters.

## Analysis

**System Description.** The system consists of a gas flowing through a circular duct of length $L$ and diameter $D$ as depicted in Fig. 1. The gas enters the duct with steady-state, fully developed and laminar or turbulent conditions, and specified temperature profile. Furthermore, the gas exhibits constant properties with the exception of those for radiative transport. The gas absorbs and emits thermal radiation with temperature and pressure-path length-dependent radiative properties described by the weighted sum of gray gases model. Axial conduction is negligible within the gas and duct wall [11, 13]. Radial conduction in the duct wall is neglected but is accounted for in the gas by introducing molecular and turbulent transport quantities. The duct wall is black, and a prescribed heat flux based on the duct wall area or temperature distribution exists. A volumetric heat source may be distributed within the gas in order to simulate a combustion process. The inlet and outlet surfaces are porous to gas flow but are black surfaces for radiative transfer. The inlet surface is assigned the inlet gas temperature distribution and the outlet surface assumes the outlet gas bulk temperature.

**Governing Equations.** The zone method consists of dividing the enclosure into a number of volume and surface zones where each zone is taken to be isothermal with uniform properties. The gas is divided into volume zones with radial width $B=D/2N$ and axial length $H=L/M$ where $N$ and $M$ denote the number of radial and axial zones, respectively. Gas

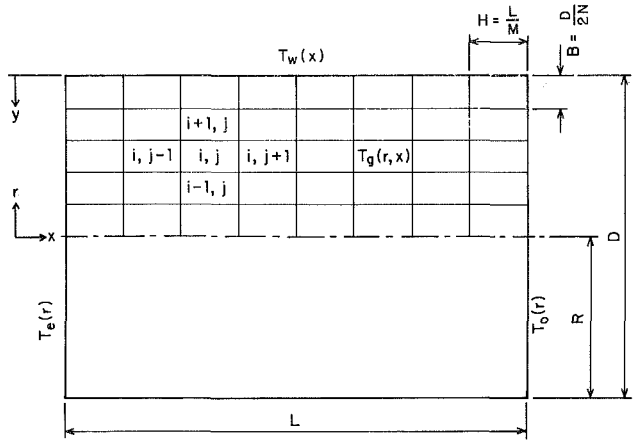


Fig. 1 Schematic diagram of system

volume zone $V_{i,j}$ is considered first, where the first and second subscripts denote, respectively, radial and axial zone locations. By using the finite difference technique and introducing dimensionless variables and parameters the energy balance for this zone is written as

$$\frac{M}{\xi}u_i^*(\theta_{i,j-1}-\theta_{i,j}) + \frac{8N^2(i-1)}{2i-1}\left[\frac{1}{\mathrm{Pe}}+\frac{E_{i-1,j}+E_{i,j}}{4}(\theta_{i-1,j}-\theta_{i,j})\right] + \frac{8N^2 i}{2i-1}\left[\frac{1}{\mathrm{Pe}}+\frac{E_{i+1,j}+E_{i,j}}{4}(\theta_{i+1,j}-\theta_{i,j})\right] + \frac{1}{\mathrm{Pe}\bar{N}}(\tau_r Q^R_{i,j}+\dot{Q}_{i,j})=0 \quad (1)$$

The first term in equation (1) represents the change in enthalpy of the gas flowing through the zone, the next two terms are the net radial conduction and turbulent transport with respect to the inner and outer radial surfaces of the considered zone, the fourth term is the net radiant energy gained by the volume zone as stated later, and the last term is the heat generation within the volume zone. $u^*$ is the gas velocity $u$ normalized with the gas mean velocity $u_m$. The temperatures are made dimensionless with a reference temperature of $T_r$. Pe is the Peclet number describing the ratio of enthalpy flow of energy to gas molecular conduction and is the product of the Reynolds number Re and gas molecular Prandtl number Pr. The importance of gas molecular conduction to blackbody radiation at the reference temperature is described by $\bar{N}$ $(=k/4D\sigma T_r{}^3)$, with $k$ denoting the gas thermal conductivity and $\sigma$ the Stefan-Boltzmann constant. $E$ is the ratio of eddy diffusivity for heat transfer $\epsilon_H$ to the product of gas mean velocity and duct radius $R$ and is evaluated at the midpoints between two zones. $\tau_r = \kappa_{T,r}D$ and is the reference optical depth defined in terms of the total absorption coefficient $\kappa_T$ at the reference temperature and the duct diameter. When $i=1$, 2, or $N$, and $j=1$ to $M$, the thermal diffusivity terms in equation (1) are expressed in a similar manner, and [13] should be consulted for specific expressions.

Using the finite difference technique for a wall area zone $A_{w,j}$, where $j$ denotes axial wall zone location, introducing dimensionless variables and parameters, and assuming a second degree polynomial for the gas temperature to evaluate the gas temperature gradient at the wall [13], the energy balance for a wall zone is

$$Q^R_{w,j}+Q_{w,j}=4\bar{N}(A_1\theta_{N-1,j}+B_1\theta_{N,j}+C_1\theta_{w,j}) \quad (2)$$

where specific expressions for the polynomial coefficients of $A_1$, $B_1$, and $C_1$ are furnished in [13]. $Q_{w,j}$ is the imposed wall

[1]Based on ASME Paper No. 83-HT-53 presented at the 1983 ASME/AIChE National Heat Transfer Conference.

[2]Professor, Mem. ASME
[3]Post Dr., Assoc. Mem. ASME
[4]Graduate Student, Student Mem. ASME
Department of Mechanical Engineering, The University of Iowa, Iowa City, Iowa 52242

heat flux when the wall temperature $T_w$ is sought or is the resulting wall heat flux when $T_w$ is prescribed. $Q^R_{w,j}$ is the net radiant energy gained by the wall.

The fully developed parabolic velocity profile is used for laminar flow conditions. Expressions for the fully developed turbulent profile are present next followed by those for the radiant energy terms of $Q^R_{i,j}$ and $Q^R_{w,j}$.

**Eddy Diffusivity.** In order to describe the velocity distribution for turbulent flow, the dimensionless velocity and wall coordinates are introduced as follows

$$u^+ \doteq \frac{u}{\sqrt{\tau_w/\rho}}; \quad y^+ = \frac{y\sqrt{\tau_w/\rho}}{\nu} \tag{3}$$

where $\rho$ and $\nu$ are the gas density and kinematic viscosity, respectively. The wall shear stress $\tau_w$ is expressed as [14]

$$\tau_w = 0.039\rho u_m^2 \,\mathrm{Re}^{-0.25} \tag{4}$$

and $y = R - r$. Within the viscous sublayer, the velocity profile for $0 < y^+ \leq 8$ varies linearly with $y^+$ and for $8 < y^+ \leq 20$, Spalding's law of the wall [15] is used. For the outer region where $y^+ > 20$, the one-seventh power law [14] is used. By using the Prandtl mixing length theory, the dimensionless eddy diffusivity for heat transfer is represented by [14, 16]

$$E = 0.1749(y^*)^{-6/7}\{0.14 - 0.08(1-y^*)^2 - 0.06(1-y^*)^4\}^2/\mathrm{Pr}_t \tag{5}$$

where $\mathrm{Pr}_t$ is the turbulent Prandtl number which varies with $y^+$ according to the expression provided in [14] and $y^* = y/R$. The eddy diffusivity for heat transfer is taken to be zero within the viscous sublayer [14].

**Nusselt Numbers.** The Nusselt number is expressed as the sum of the convective and radiative Nusselt numbers given, respectively, by

$$\mathrm{Nu}^C_x = \frac{Q^C_{w,x}}{(\theta_{w,x} - \theta_{b,x})} \tag{6}$$

$$\mathrm{Nu}^R_x = -\frac{1}{4\bar{N}} \frac{Q^R_{w,x}}{(\theta_{w,x} - \theta_{b,x})} \tag{7}$$

and $\theta_{b,x}$ is the local bulk gas temperature obtained by integrating the product of gas temperature and velocity profiles over the duct cross section. $Q^C_{w,x}$ and $Q^R_{w,x}$ are the wall conductive and radiative heat transfer at location $x$. It should be noted that $\mathrm{Nu}^C_x$ depends on the radiant exchange process.

**Gas Radiative Properties.** The zone method of analysis utilizes total radiative properties as represented by the weighted sum of gray gases model [17]. The total absorption coefficient is evaluated from [18]

$$\kappa_T(T) = \sum_{n=1}^{N_g} \kappa_n a_{\epsilon,n}(T) \tag{8}$$

where $\kappa_n$ are the gray gas absorption coefficients with $N_g$ denoting the number of gray gases. $a_{\epsilon,n}$ are the temperature weighting factors which are described in terms of polynomials in temperatures. Values for the absorption and polynomial coefficients for carbon dioxide, water vapor, and mixtures of these gases are available for a total pressure 1 atm, a temperature range of 600 to 2400 K, and a partial pressure-path length range of 0.001 to 10 atm-m [17].

**Direct Exchange Areas.** Direct exchange areas represent fundamental factors for evaluation of radiative transfer in participating gases utilizing the zone method of analysis. Direct exchange area expressions reported by Smith et al. [19, 20] are utilized in this study. Directed flux areas [4, 10, 13, 20] were evaluated from weighting factors and direct exchange areas.

**Radiant Energy.** The dimensionless net radiant energy gained per unit volume for a volume zone can be represented as

$$Q^R_{i,j} = \frac{M}{4\tau_r(2i-1)\xi}\left\{\sum_{k=1}^{N}(\mathbf{E}_{e,k}\mathbf{G}_{i,j}\theta^4_{e,k} + \mathbf{E}_{o,k}\mathbf{G}_{i,j}\theta^4_{o,k}) + \sum_{l=1}^{M}\mathbf{W}_l\mathbf{G}_{i,j}\theta^4_w + \sum_{k=1}^{N}\sum_{l=1}^{M}\mathbf{G}_{k,l}\mathbf{G}_{i,j}\theta^4_{k,l}\right\} - \frac{\tau_{i,j}}{\tau_r}\theta^4_{i,j} \tag{9}$$

The first three terms account for radiant energy emitted by the inlet and outlet end and wall surface zones and absorbed by the volume zone, respectively, the fourth term represents the absorption of radiant energy from all volume zones, and the fifth term is the emission by the volume zone itself. $\tau_{i,j}$ is the optical thickness given by the product of the total absorption coefficient evaluated at $T_{i,j}$ and $D$. The surface to gas and gas to gas directed flux areas of EG, WG, and GG are normalized by the factor $\pi B^2$ as found convenient [19].

The radiant energy term for a wall zone after dividing by the wall zone area and employing dimensionless variables can be written as

$$Q^R_{w,j} = \frac{M}{4N^2\xi}\left\{\sum_{k=1}^{N}(\mathbf{E}_{e,k}\mathbf{W}_j\theta^4_{e,k} + \mathbf{E}_{o,k}\mathbf{W}_j\theta^4_{o,k}) + \sum_{l=1}^{M}\mathbf{W}_l\mathbf{W}_j\theta^4_{w,l} + \sum_{k=1}^{N}\sum_{l=1}^{M}\mathbf{G}_{k,l}\mathbf{W}_j\theta^4_{k,l}\right\} - \theta^4_{w,j} \tag{10}$$

where the first three terms represent the radiant energy emitted by the end and wall zones and absorbed by the wall zone, respectively, the fourth term is the absorbed radiant energy from all volume zones, and the last term is the emission by the wall zone itself. Surface to surface and gas to surface directed flux areas are designated by EW, WW, and GW.

Radiant exchange for a gray gas is characterized by the optical depth $\tau_o$, which is expressed in terms of a gray gas absorption coefficient and duct diameter. Furthermore, the directed flux areas in the radiant expressions are replaced with the direct exchange areas.

**Solution Scheme.** An iteration solution scheme was employed to solve for the gas temperatures. Within this scheme, the radiant emission term for each iteration was linearized [21] by $\theta \approx \theta_p^3\theta$, where $\theta_p$ is the previous iteration temperatures. This linearization helped maintain stability and improved convergence. It should be noted that this linearization does not restrict the applicability of the results to small temperature differences.

## Results and Discussion

The analysis yields the parameters of the Peclet and molecular Prandtl numbers, gas conduction to radiation parameter, gas radiative properties, volumetric heat generation, length to tube diameter ratio, and duct diameter. The molecular Prandtl number was taken as 0.71 to be typical of a gas. The Peclet number was assigned values of 2000 and 10,000 for laminar and turbulent flows, respectively. The cylindrical system was chosen with a length to diameter ratio of 5. The characteristic length of the system was selected as the tube diameter which was assigned a value of 1 m to satisfy the partial pressure-path length product of the gas properties. Unless otherwise noted, reference to a real gas (RC) implies a radiatively participating gas at a total pressure of 1 atm and an equimolal mixture of carbon dioxide and water vapor each existing at a partial pressure of 0.1 atm. In addition, certain parameters appear in the solution scheme. For the results,

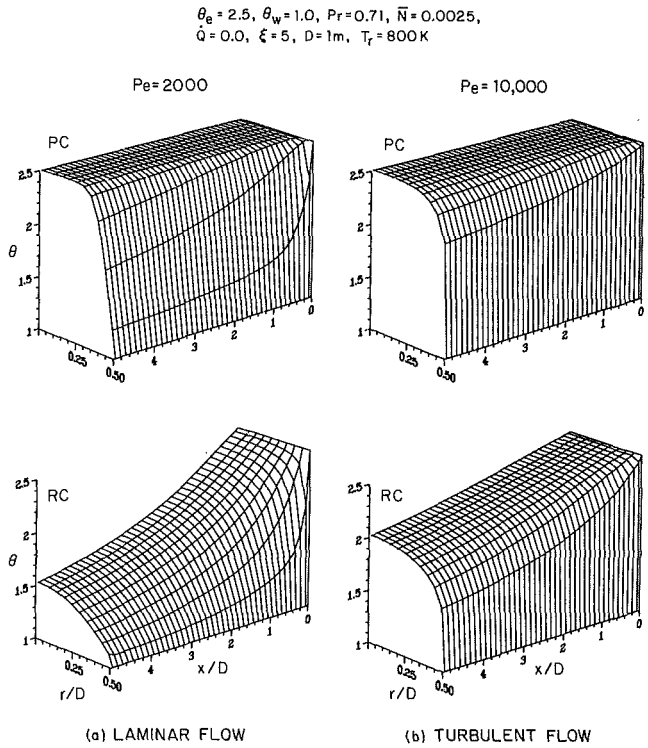


**Fig. 2 Effects of flow conditions and gas radiative properties**

presented, $N = 10$ and $M = 40$, which yield an axial to radial zone with ratio of 2.5. Results are presented for an inlet gas temperature of 2000 K and a reference temperature of 800 K to satisfy the temperature range of the gas properties.

**Gas Temperature.** Representative results for gas temperature distributions for pure convection (PC) and RC cases are illustrated in Fig. 2 for gas cooling where the wall temperature is specified at 1.0, inlet gas temperature at 2.5, $\bar{N} = 0.0025$, and $\dot{Q} = 0$. Laminar and turbulent flow results are presented in the left- and right-hand columns of Fig. 2. The intersection of the grid lines represent the gas temperature at the zone center. The inlet is at $x/D = 0$ and the wall is along $r/D = 0.5$. The gas temperature profiles are more uniform and the gas exiting temperatures are higher for turbulent flow than for laminar flow. Gas radiation is seen to reduce the centerline gas exiting temperature from near 2.5 to 1.5 for laminar flow and to 2.0 for turbulent flow.

**Wall Heat Flux.** Wall heat flux distributions for a uniform wall temperature are displayed in Fig. 3 for turbulent flow and several cases where the degree of radiant energy participation in the heat transfer processes is varied. The values of $Q_w$ for gas cooling are negative, signifying that energy must be removed from the wall to maintain its temperature. To simplify the discussion, the absolute value of the wall heat flux is signified and denoted by $Q_w$. Molecular and turbulent transfer and enthalpy flow are included in the PC case and gas and surface radiation is absent. In the CC case, the gas is radiatively transparent but surface radiant exchange occurs. The gray gas cases are characterized by $\tau_o$. Finally, the RC case includes all modes of heat transfer along with a real gas. Except for the PC results, $Q_w$ is highly nonuniform with high values near the high-temperature inlet, decreases with $x/D$, and may increase near the outlet due to the radiant exchange with the high temperature outlet surface where this is particularly noticeable for the CC case. Near the inlet, values of $Q_w$ are ordered according to the participation of the radiant exchange process. Note that the gray gas result for $\tau_o = 10$ are lower than those for $\tau_o = 1.0$ for $x/D > 0.4$. For a very large value of $\tau_o$, $Q_w$ would approach the PC results [22].

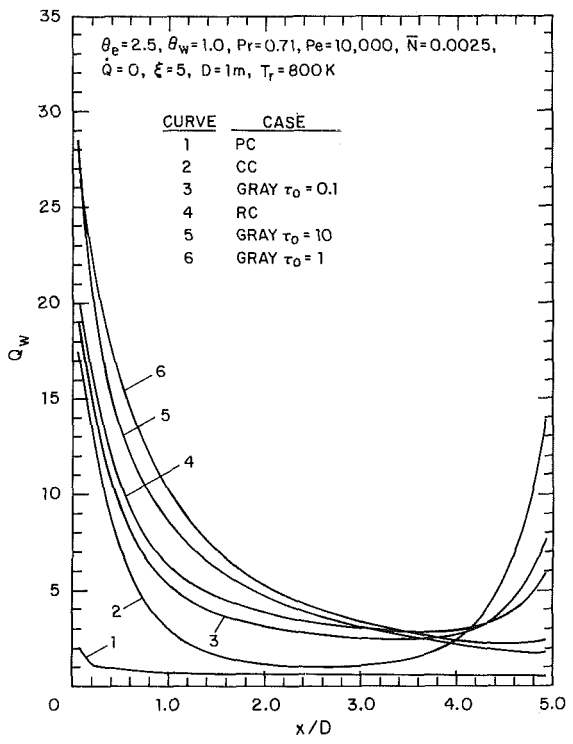


**Fig. 3 Wall heat flux distribution**

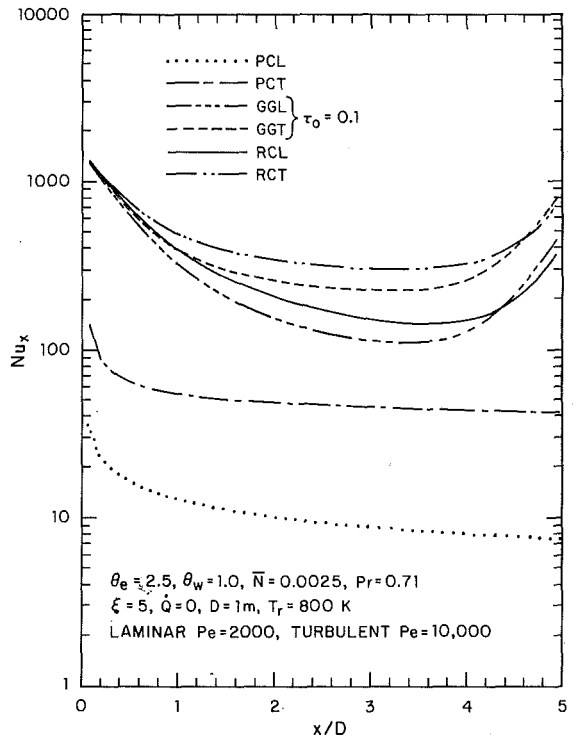


**Fig. 4 Local Nusselt number**

Wall heat flux results for RC are reasonably described by the gray gas results when $\tau_o = 0.1$. This implies that the real gas is not a strong participator in the radiant exchange process. The real gas optical depths range from 3.11 at 800 K to 0.34 at 2400 K. As shown in Fig. 2 gas temperatures are generally within the range of 1500 to 2000 K for turbulent flow. The real gas optical depths for these temperatures is approximately 0.7. Gray gas results for $Q_w$ using these optical depths do not correspond with the real gas results. Thus there does not at present exist a systematic method for predicting real gas results using a gray gas.

**Nusselt Number.** Representative results for the local Nusselt number are presented in Fig. 4 to illustrate the influence of the flow conditions and radiant participation of the gas. These results are for $\theta_e = 2.5$ and a uniform wall temperature distribution with $\theta_w = 1.0$. The degree of participation by the gas in the radiant exchange process is shown by cases for PC, gray gas (GG) with $\tau_o = 0.1$, and RC. A third letter appended to these acronyms designates laminar (L) or turbulent (T) flow. The results for PCL and PCT were computed using a fine zone pattern to account for the steep temperature gradients near the wall, especially for turbulent flow. The local Nusselt numbers decrease with axial distance and, for the radiating gas cases, increase near the duct outlet. As expected, the Nusselt numbers for turbulent flow are higher than those for laminar flow. In comparison with the results for PC, the Nusselt numbers with gaseous radiation accounted for are larger by at least a factor of ten. In addition, the percentage differences between laminar and turbulent flow results are smaller for the cases when gaseous radiation exists. For example, the Nusselt numbers near $x/D = 2.5$ differ by about 400 and 75 percent with and without gaseous radiation, respectively, where both percentages are based on the laminar flow results. The Nusselt numbers for the radiation cases have not approached constant values indicative of fully developed flow conditions. This finding is partially attributed to the influence that the outlet end has on the radiant exchange process.

## Conclusions

The analysis of heat transfer for laminar or turbulent fully developed flow with developing temperature profiles of a radiatively participating gas through a black wall circular tube is presented for prescribed wall temperature and heat flux distributions. The zone method is utilized to obtain axial and radial gas temperature distributions in terms of several parameters. The magnitude of the wall heat flux for specified wall temperatures for a real gas decreases with axial distance but increases near the outlet due to radiant exchange with the outlet surface. Wall heat flux with radiation is larger than that without radiation for the same values of the system parameters. The gas temperature profile is more uniform for turbulent flow than for laminar flow under either specified wall temperature or heat flux distributions. The Nusselt numbers with gaseous radiation are higher by about a factor of ten than those without radiation for the same values of the system parameters. The Nusselt numbers for a gas with an equimolal mixture of carbon dioxide and water vapor are similar to those for a gray gas with an optical depth of 0.1.


## Acknowledgment

The authors gratefully acknowledge the financial assistance of the United States Department of Energy, Grant #DE-AC02-79ER10515.A000 for support of this research.


## References


1 Edwards, D. K., "Molecular Gas Band Radiation," *Advances in Heat Transfer*, Vol. 12, Academic Press, 1976, pp. 115–193.

2 Gosman, A. D., Lockwood, F. C., and Salooja, A. P., "The Prediction of Cylindrical Furnaces Gaseous fueled with Premixed and Diffusion Burners," *Proceedings, 17th Symposium (International) on Combustion*, The Combustion Institute, 1979, pp. 747–760.

3 Selcuk, N., and Siddal, R. G., "Two-Flux Spherical Harmonic Modeling of Two-Dimensional Radiative Transfer in Furnaces," *International Journal of Heat and Mass Transfer*, Vol. 19, 1976, pp. 313–321.

4 Hottel, H. C., and Sarofim, A. F., *Radiative Transfer*, McGraw-Hill, 1967.

5 Hottel, H. C., and Sarofim, A. F., "The Effect of Gas Flow Patterns on Radiative Transfer in Cylindrical Enclosures," *International Journal of Heat and Mass Transfer*, Vol. 8, 1965, pp. 1153–1169.

6 Lowe, A., Wall, T. F., and Stewart, I. McC., "A Zone Heat Transfer Model of a Large Tangentially Fired Pulverized Coal Boiler," *Proceedings, 15th Symposium on Combustion*, Tokyo, Japan, 1974, pp. 1261–1270.

7 Bueters, K. A., Cogoli, J. G., and Habelt, W. W., "Performance Prediction of Tangentially Fired Utility Furnace by Computer Model," *Proceedings, 15th Symposium on Combustion*, Tokyo, Japan, 1974, pp. 1245–1260.

8 Johnson, T. R., "Application of Zone Method of Analysis to the Calculation of Heat Transfer from Luminous Flame," Ph.D. thesis, Sheffield University, 1971.

9 Whitacre, G. R., and McCann, R. A., "Comparison of Methods for the Prediction of Radiant Flux Distribution and Temperature," ASME Paper No. 75-HT-9, 1975.

10 Nakra, N. K., and Smith, T. F., "Combined Radiation-Convection for a Real Gas," ASME JOURNAL OF HEAT TRANSFER, Vol. 99, 1977, pp. 60–65.

11 Clausen, C. W., and Smith, T. F., "Radiative and Convective Transfer for Real Gas Flow Through a Tube with Specified Wall Heat Flux," ASME JOURNAL OF HEAT TRANSFER, Vol. 101, 1979, pp. 376–378.

12 Smith, T. F., and Clausen, C. W., "Radiative and Convective Transfer for Tube Flow of a Real Gas," *Proceedings, 6th Int. Heat Transfer Conf.*, Vol. 3, 1978, pp. 391–396.

13 Shen, Z. F., and Smith, T. F., "Radiative and Convective Transfer in a Cylindrical Enclosure for a Real Gas Utilizing the Zone Method," Technical Report E-TFS-82-002, Division of Energy Engineering, University of Iowa, 1982.

14 Kays, W. M., and Crawford, M. E., *Convective Heat and Mass Transfer*, McGraw-Hill, 1980.

15 White, F. M., *Viscous Fluid Flow*, McGraw-Hill, 1974.

15 Nikuradse, J., "Gesetzmassigkeit Der Turbulenten Stromung in Glatten Rohren," *VDI Forschungsheft*, 1932, p. 356.

17 Smith, T. F., Shen, Z. F., and Friedman, J. N., "Evaluation of Coefficients for the Weighted Sum of Gray Gases Model," ASME JOURNAL OF HEAT TRANSFER, Vol. 104, 1982, pp. 602–608.

18 Smith, T. F., "Radiative Exchange with the Zone Method," Technical Report E-TFS-81-008, Division of Energy Engineering, University of Iowa, 1981.

19 Smith, T. F., Kim, K. T., and Shen, Z. F., "Evaluation of Direct Exchange Areas for a Cylindrical Enclosure," Technical Report E-TFS-81-007, Division of Energy Engineering, University of Iowa, 1981.

20 Smith, T. F., Alturki, A. M., and Kim, T. K., "Improvement of Computational Times for Direct Exchange Areas," Technical Note E-TFS-81-002, Division of Energy Engineering, University of Iowa, 1981.

21 Shen, Z. F., Smith, T. F., and Hix, P., "Linearization of the Radiation Terms for Improved Convergence Using the Zone Method," *Numerical Heat Transfer*, Vol. 6, 1983, pp. 377–382.

22 Einstein, T. H., "Radiant Heat Transfer to Absorbing Gas Enclosed in a Circular Pipe with Conduction, Gas Flow and Internal Heat Generation," NASA TR R-156, 1963.


# The Cubic Spline Integration Technique for Solving Fusion Welding Problems


**Pu Wang[1], Sui Lin[2], and R. Kahawita[3]**


## 1 Introduction

Fusion welding is a process by which two metal sheets are welded together by infusion of molten metal between them. Depending on the welding setup and physical properties of the material, two possibilities may arise in the heat transfer process: solidification of the molten metal, a process akin to common soldering or, solidification following the melting of a very small part of the parent plates. Theoretically, a superior result is obtained in the latter case due to the intimate metallurgical combination formed between the liquid and solid metal. A theoretical analysis of this second case forms the basis of the present paper.

During the welding process, the intense heat required in the molten metal is transferred by radiation, convection, and conduction to the surrounding material. Compared to radiation and convection, conduction is the dominant mode in


[1]Department of Mathematics and Mechanics, Lanzhou University, The People's Republic of China; presently visiting scholar at Ecole Polytechnique Du Montreal and Concordia University in Montreal

[2]Department of Mechanical Engineering, Concordia University, Montreal, Quebec, Canada H3G 1M8

[3]Department of Civil Engineering, Ecole Polytechnique Du Montreal, Montreal, Quebec, Canada H3C 3A7



Contributed by the Heat Transfer Division for publication in the JOURNAL OF HEAT TRANSFER. Manuscript received by the Heat Transfer Division February 24, 1984.

**Nusselt Number.** Representative results for the local Nusselt number are presented in Fig. 4 to illustrate the influence of the flow conditions and radiant participation of the gas. These results are for $\theta_e = 2.5$ and a uniform wall temperature distribution with $\theta_w = 1.0$. The degree of participation by the gas in the radiant exchange process is shown by cases for PC, gray gas (GG) with $\tau_o = 0.1$, and RC. A third letter appended to these acronyms designates laminar (L) or turbulent (T) flow. The results for PCL and PCT were computed using a fine zone pattern to account for the steep temperature gradients near the wall, especially for turbulent flow. The local Nusselt numbers decrease with axial distance and, for the radiating gas cases, increase near the duct outlet. As expected, the Nusselt numbers for turbulent flow are higher than those for laminar flow. In comparison with the results for PC, the Nusselt numbers with gaseous radiation accounted for are larger by at least a factor of ten. In addition, the percentage differences between laminar and turbulent flow results are smaller for the cases when gaseous radiation exists. For example, the Nusselt numbers near $x/D = 2.5$ differ by about 400 and 75 percent with and without gaseous radiation, respectively, where both percentages are based on the laminar flow results. The Nusselt numbers for the radiation cases have not approached constant values indicative of fully developed flow conditions. This finding is partially attributed to the influence that the outlet end has on the radiant exchange process.

## Conclusions

The analysis of heat transfer for laminar or turbulent fully developed flow with developing temperature profiles of a radiatively participating gas through a black wall circular tube is presented for prescribed wall temperature and heat flux distributions. The zone method is utilized to obtain axial and radial gas temperature distributions in terms of several parameters. The magnitude of the wall heat flux for specified wall temperatures for a real gas decreases with axial distance but increases near the outlet due to radiant exchange with the outlet surface. Wall heat flux with radiation is larger than that without radiation for the same values of the system parameters. The gas temperature profile is more uniform for turbulent flow than for laminar flow under either specified wall temperature or heat flux distributions. The Nusselt numbers with gaseous radiation are higher by about a factor of ten than those without radiation for the same values of the system parameters. The Nusselt numbers for a gas with an equimolal mixture of carbon dioxide and water vapor are similar to those for a gray gas with an optical depth of 0.1.


## Acknowledgment

The authors gratefully acknowledge the financial assistance of the United States Department of Energy, Grant #DE-AC02-79ER10515.A000 for support of this research.


## References


1 Edwards, D. K., "Molecular Gas Band Radiation," *Advances in Heat Transfer*, Vol. 12, Academic Press, 1976, pp. 115–193.

2 Gosman, A. D., Lockwood, F. C., and Salooja, A. P., "The Prediction of Cylindrical Furnaces Gaseous fueled with Premixed and Diffusion Burners," *Proceedings, 17th Symposium (International) on Combustion*, The Combustion Institute, 1979, pp. 747–760.

3 Selcuk, N., and Siddal, R. G., "Two-Flux Spherical Harmonic Modeling of Two-Dimensional Radiative Transfer in Furnaces," *International Journal of Heat and Mass Transfer*, Vol. 19, 1976, pp. 313–321.

4 Hottel, H. C., and Sarofim, A. F., *Radiative Transfer*, McGraw-Hill, 1967.

5 Hottel, H. C., and Sarofim, A. F., "The Effect of Gas Flow Patterns on Radiative Transfer in Cylindrical Enclosures," *International Journal of Heat and Mass Transfer*, Vol. 8, 1965, pp. 1153–1169.

6 Lowe, A., Wall, T. F., and Stewart, I. McC., "A Zone Heat Transfer Model of a Large Tangentially Fired Pulverized Coal Boiler," *Proceedings, 15th Symposium on Combustion*, Tokyo, Japan, 1974, pp. 1261–1270.

7 Bueters, K. A., Cogoli, J. G., and Habelt, W. W., "Performance Prediction of Tangentially Fired Utility Furnace by Computer Model," *Proceedings, 15th Symposium on Combustion*, Tokyo, Japan, 1974, pp. 1245–1260.

8 Johnson, T. R., "Application of Zone Method of Analysis to the Calculation of Heat Transfer from Luminous Flame," Ph.D. thesis, Sheffield University, 1971.

9 Whitacre, G. R., and McCann, R. A., "Comparison of Methods for the Prediction of Radiant Flux Distribution and Temperature," ASME Paper No. 75-HT-9, 1975.

10 Nakra, N. K., and Smith, T. F., "Combined Radiation-Convection for a Real Gas," ASME JOURNAL OF HEAT TRANSFER, Vol. 99, 1977, pp. 60–65.

11 Clausen, C. W., and Smith, T. F., "Radiative and Convective Transfer for Real Gas Flow Through a Tube with Specified Wall Heat Flux," ASME JOURNAL OF HEAT TRANSFER, Vol. 101, 1979, pp. 376–378.

12 Smith, T. F., and Clausen, C. W., "Radiative and Convective Transfer for Tube Flow of a Real Gas," *Proceedings, 6th Int. Heat Transfer Conf.*, Vol. 3, 1978, pp. 391–396.

13 Shen, Z. F., and Smith, T. F., "Radiative and Convective Transfer in a Cylindrical Enclosure for a Real Gas Utilizing the Zone Method," Technical Report E-TFS-82-002, Division of Energy Engineering, University of Iowa, 1982.

14 Kays, W. M., and Crawford, M. E., *Convective Heat and Mass Transfer*, McGraw-Hill, 1980.

15 White, F. M., *Viscous Fluid Flow*, McGraw-Hill, 1974.

15 Nikuradse, J., "Gesetzmassigkeit Der Turbulenten Stromung in Glatten Rohren," *VDI Forschungsheft*, 1932, p. 356.

17 Smith, T. F., Shen, Z. F., and Friedman, J. N., "Evaluation of Coefficients for the Weighted Sum of Gray Gases Model," ASME JOURNAL OF HEAT TRANSFER, Vol. 104, 1982, pp. 602–608.

18 Smith, T. F., "Radiative Exchange with the Zone Method," Technical Report E-TFS-81-008, Division of Energy Engineering, University of Iowa, 1981.

19 Smith, T. F., Kim, K. T., and Shen, Z. F., "Evaluation of Direct Exchange Areas for a Cylindrical Enclosure," Technical Report E-TFS-81-007, Division of Energy Engineering, University of Iowa, 1981.

20 Smith, T. F., Alturki, A. M., and Kim, T. K., "Improvement of Computational Times for Direct Exchange Areas," Technical Note E-TFS-81-002, Division of Energy Engineering, University of Iowa, 1981.

21 Shen, Z. F., Smith, T. F., and Hix, P., "Linearization of the Radiation Terms for Improved Convergence Using the Zone Method," *Numerical Heat Transfer*, Vol. 6, 1983, pp. 377–382.

22 Einstein, T. H., "Radiant Heat Transfer to Absorbing Gas Enclosed in a Circular Pipe with Conduction, Gas Flow and Internal Heat Generation," NASA TR R-156, 1963.


# The Cubic Spline Integration Technique for Solving Fusion Welding Problems


**Pu Wang[1], Sui Lin[2], and R. Kahawita[3]**


## 1 Introduction

Fusion welding is a process by which two metal sheets are welded together by infusion of molten metal between them. Depending on the welding setup and physical properties of the material, two possibilities may arise in the heat transfer process: solidification of the molten metal, a process akin to common soldering or, solidification following the melting of a very small part of the parent plates. Theoretically, a superior result is obtained in the latter case due to the intimate metallurgical combination formed between the liquid and solid metal. A theoretical analysis of this second case forms the basis of the present paper.

During the welding process, the intense heat required in the molten metal is transferred by radiation, convection, and conduction to the surrounding material. Compared to radiation and convection, conduction is the dominant mode in


[1]Department of Mathematics and Mechanics, Lanzhou University, The People's Republic of China; presently visiting scholar at Ecole Polytechnique Du Montreal and Concordia University in Montreal

[2]Department of Mechanical Engineering, Concordia University, Montreal, Quebec, Canada H3G 1M8

[3]Department of Civil Engineering, Ecole Polytechnique Du Montreal, Montreal, Quebec, Canada H3C 3A7



Contributed by the Heat Transfer Division for publication in the JOURNAL OF HEAT TRANSFER. Manuscript received by the Heat Transfer Division February 24, 1984.

the heat transfer process [1] and will therefore be the only mode of heat transfer considered here.

The prime characteristic of the melting and solidification process is the existence of a moving boundary between the solid and liquid phases, whose location is unknown and which has to be determined as a part of the solution. The moving boundary problem is nonlinear and solutions involve considerable mathematical difficulties. Exact solutions of such problems are presently restricted to only a few idealized situations [2]. With regard to the nonlinear problem, solutions have been obtained by analytical approximations and numerical methods. In the present work, the fusion welding problem involving both the melting and solidification processes has been solved with a numerical integration technique using cubic splines.

The principal advantages of using a cubic spline procedure are as follows:

1 The requirement of a uniform mesh is not necessary. However for a uniform mesh, the spline approximation is fourth-order accurate for the first derivative, while being third order for a nonuniform grid. The second derivative is approximated to second order for uniform as well as nonuniform grids.

2 Since the value of first or second derivatives may be evaluated directly, boundary conditions containing derivatives may be directly incorporated into the solution procedure.

3 The governing matrix system obtained with the implicit formulation is always tridiagonal, thus facilitating the inversion procedure. The matrix system obtained may be reduced to a scalar set of equations that either contain values of the function itself, its first derivative, or its second derivative at the node points while maintaining a tridiagonal formulation.

4 The governing system of equations obtained with the explicit formulation may be solved directly for the function itself, its first derivative, or its second derivative.

The implicit spline integration technique has been applied to solve problems in fluid mechanics by, for example, Rubin and Graves [3], Rubin and Kholsa [4], Panton and Sallee [5], and Wang and Kahawita [6, 7]. The explicit spline integration technique, due to the restriction of its stability condition [3, 8], has not yet been used for solving practical engineering problems. However, under certain circumstances, the explicit spline method is more adaptable than the explicit finite difference method because a nonuniform grid may be utilized in the cubic spline approximation. In the present paper, a problem in fusion welding has been solved as an illustration of the application of the explicit spline integration technique. Error estimates of the numerical technique have been provided by comparing the results with an exact solution.

## 2 Mathematical Formulation of the Fusion Welding Problem

We consider two large metal sheets formed of the same material of thickness $L_2$, having identical dimensions, and the same initial temperature $T_{20}$. They are separated by a distance $2L_1$ as shown in Fig. 1. These sheets are welded together by infusing molten metal of the same material having a uniform initial temperature $T_{10}$ between them. It is assumed that the edge surfaces of the metal sheets lose heat to the surroundings at a much slower rate than the heat transferred by conduction into the metal sheets, so that the process can be treated as a one-dimensional heat conduction problem with a moving phase boundary. Furthermore, it is assumed that the material properties may be taken as a constant in the solid and liquid phases, respectively, and that density changes across the phase boundary may be neglected. The temperatures and material properties in the liquid and solid phases are denoted by subscripts 1 and 2, respectively.

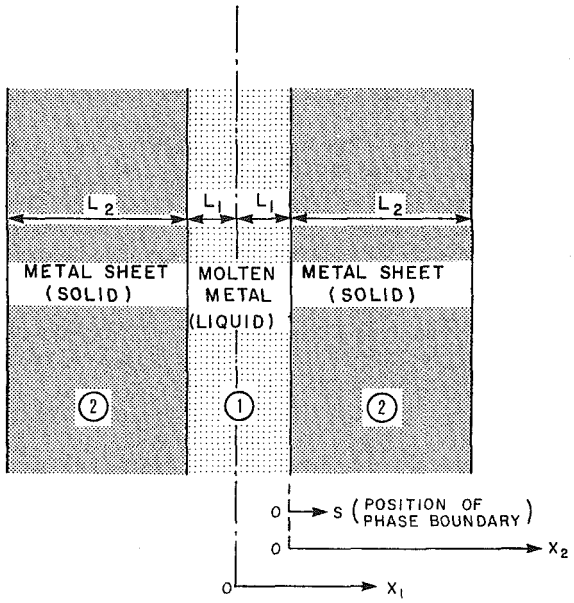


**Fig. 1 Schematic diagram of the fusion welding problem**

To formulate the problem, two space coordinates $x_1$ and $x_2$ are used for the liquid and solid phases, respectively. The $x_1$ coordinate starts from the center of the molten metal and ends at the phase boundary between the liquid and solid. The $x_2$-coordinate starts from the initial phase interface, $x_1 = L_1$ and ends at the outer surface of the metal sheet. The coordinate origin for the phase boundary $s(t)$ is identical to that of the $x_2$-coordinate, at $x_1 = L_1$, as shown in Fig. 1.

In order to make a dimensionless presentation of the problem, the space coordinates $x_1$ and $x_2$ are transformed as follows

$$y_1 = \frac{x_1}{L_1 + s(t)} \tag{1}$$

$$y_2 = \frac{x_2 - s(t)}{L_2 - s(t)} \tag{2}$$

With the foregoing transformation, the coordinates $x_1$ and $x_2$, with the moving boundary $s(t)$ become respectively the fixed coordinates $y_1$ and $y_2$, which vary between 0 and 1. The other dimensionless variables and parameters are introduced as follows

$$\theta_1 = \frac{T_1 - T_s}{T_{10} - T_s} \tag{3}$$

$$\theta_2 = \frac{T_2 - T_s}{T_{20} - T_s} \tag{4}$$

$$\tau = \frac{a_1 t}{l_1^2} \tag{5}$$

$$S = \frac{s}{L_1} \tag{6}$$

$$L = \frac{L_2}{L_1} \tag{7}$$

$$K = \frac{k_2}{k_1} \tag{8}$$

$$a_{21} = \frac{a_2}{a_1} \tag{9}$$

$$\mathrm{Bi} = \frac{hL_1}{k_2} \tag{10}$$

$$\text{Ste} = \frac{k_1(T_{10}-T_s)}{a_1\rho_1 q_L} = \frac{c_1(T_{10}-T_s)}{q_L} \tag{11}$$

$$\theta_0 = \frac{T_{20}-T_s}{T_{10}-T_s} \tag{12}$$

$$\theta_\infty = \frac{T_\infty - T_s}{T_{20}-T_s} \tag{13}$$

where $T$ is the temperature, $t$ the time, $a$ the thermal diffusivity, $k$ the thermal conductivity, $h$ the heat transfer coefficient, $\rho$ the density, and $q_L$ the latent heat of fusion. The subscripts $o$, $s$, and $\infty$ refer to the initial, melting or solidification,and ambient conditions, respectively.

The system of equations formulating the fusion welding problem may be described as follows:

In the liquid phase,

$$\frac{\partial\theta_1(y_1,\tau)}{\partial\tau} = \frac{y_1}{1+S(\tau)}\frac{dS(\tau)}{d\tau}\frac{\partial\theta_1(y_1,\tau)}{\partial y_1} + \frac{1}{[1+S(\tau)]^2}\frac{\partial^2\theta_1(y_1,\tau)}{\partial y_1^2}$$
$$\text{for } \tau>0, \quad 0<y_1<1 \tag{14}$$

$$\theta_1(y_1,0)=1 \quad \text{for} \quad 0\le y_1\le 1 \tag{15}$$

$$\frac{\partial\theta_1(0,\tau)}{\partial y_1}=0 \quad \text{for } \tau>0 \tag{16}$$

$$\theta_1(1,\tau)=0 \quad \text{for } \tau>0 \tag{17}$$

In the solid phase,

$$\frac{\partial\theta_2(y_2,\tau)}{\partial\tau} = \frac{1-y_2}{L-S(\tau)}\frac{dS(\tau)}{d\tau}\frac{\partial\theta_2(y_2,\tau)}{\partial y_2} + \frac{a_{21}}{[L-S(\tau)]}\frac{\partial^2\theta_2(y_2,\tau)}{\partial y_2^2}$$
$$\text{for } \tau>0, \quad 0<y_2<1 \tag{18}$$

$$\theta_2(y_2,0)=-1 \quad \text{for} \quad 0\le y_2\le 1 \tag{19}$$

$$\theta_2(0,\tau)=0 \quad \text{for } \tau>0 \tag{20}$$

$$\frac{\partial\theta_2(1,\tau)}{\partial y_2} = -\text{Bi}[L-S(\tau)][\theta_2(1,\tau)-\theta_\infty] \quad \text{for } \tau>0 \tag{21}$$

The energy balance at the phase boundary may be expressed as

$$\frac{dS(\tau)}{d\tau} = -\text{Ste}\left[\frac{1}{1+S(\tau)}\frac{\partial\theta_1(1,\tau)}{\partial y_1} - \frac{K\theta_o}{L-S(\tau)}\frac{\partial\theta_2(0,\tau)}{\partial y_2}\right] \tag{22}$$

where all variables and parameters are dimensionless.

## 3 The Numerical Solution Using Cubic Spline Integration

In this section, an explicit technique is used for solving the fusion welding problem. In discretised form, the system of equations (14-22) may be expressed as follows [6, 7]:

$$\frac{\theta^{n+1}{}_i-\theta^n_{1i}}{\Delta\tau} = \frac{y_{1i}}{1+S^n}\left(\frac{dS}{d\tau}\right)^n m^n_{1i} + \frac{1}{(1+S^n)^2}\left\{M^n_{1i} + \frac{\Delta_1 i}{6}(M^n_{1(i+1)} - (1+\sigma_{1i})M^n_{1i} + \sigma_{1i}M^n_{1(i-1)}\right\}$$
$$\text{for } i=1, \text{ to } N-1 \tag{23}$$

$$\theta^o_{1i}=1 \quad \text{for } i=0 \text{ to } N \tag{24}$$

$$m^n_{10}=0 \tag{25}$$

$$\theta^n_{1N}=0 \tag{26}$$

$$\frac{\theta^{n+1}_{2i}-\theta^n_{2i}}{\Delta\tau} = \frac{1-y_{2i}}{1-S^n}\left(\frac{dS}{d\tau}\right)^n m^n_{2i} + \frac{1}{(L-S^n)^2}\left\{M^n_{2i} + \frac{\Delta_{2i}}{6}[M^n_{2(i+1)} - (1+\sigma_{1i})M^n_{2i} + \sigma_{1i}M^n_{2(i-1)}]\right\} \quad \text{for } i=1 \text{ to } N-1 \tag{27}$$

$$\theta^o_{2i}=-1 \quad \text{for } i=1 \text{ to } N \tag{28}$$

$$\theta^n_{20}=0 \tag{29}$$

$$m^n_{2N} = -\text{Bi}(L-S^n)(\theta^n_{2N}-\theta_\infty) \tag{30}$$

$$\frac{S^{n+1}-S^n}{\Delta\tau} = \left\{1-\frac{\Delta\tau}{2}\left[\frac{C_1}{(1+S^n)^2} - \frac{C_2}{(L-S^n)^2}\right]\right\}\left[\frac{C_1}{1+S^n} - \frac{C_2}{1-S^n}\right] \tag{31}$$

where

$$m^n_{ji} = \left(\frac{\partial\theta_j}{\partial y_j}\right)^n_i \quad j=1.2 \tag{32}$$

$$M^n_{ji} = \left(\frac{\partial^2\theta_j}{\partial y_j^2}\right)^n_i \quad j=1.2 \tag{33}$$

$$\sigma_{ji} = \frac{h_{j(i+1)}}{h_{ji}} = \frac{y_{j(i+1)}-y_{ji}}{y_{ji}-y_{j(i-1)}} \quad j=1.2 \tag{34}$$

$$\Delta_{ji} = \frac{1+\sigma_{ji}^3}{\sigma_{ji}(1+\sigma_{ji})^2}, \quad j=1.2 \tag{35}$$

$$C_1 = -\text{Ste}\bullet m^n_{1N} \tag{36}$$

$$C_2 = \text{Ste}\bullet K\bullet\theta_o m^n_{20} \tag{37}$$

In equation (31) $S^{n+1} = S(\tau^n + \Delta\tau)$ was obtained by using a Taylor series expansion that included the term containing the second derivative. For a uniform mesh with $\sigma_{ji} = 1$, equations (23) and (27) reduce to the following forms which are of fourth-order accuracy

$$\frac{\theta^{n+1}_{1i}-\theta^n_{1i}}{\Delta\tau} = \frac{y_{1i}}{1+S^n}\left(\frac{dS}{d\tau}\right)^n m^n_{1i} + \frac{1}{(1+S^n)^2}\left[\frac{M^n_{1(i+1)}+10\,M^n_{1i}+M^n_{1(i-1)}}{12}\right] \tag{38}$$

and

$$\frac{\theta^{n+1}_{2i}-\theta^n_{2i}}{\Delta\tau} = \frac{1-y_{2i}}{L-S^n}\left(\frac{dS}{d\tau}\right)^n m^n_{2i} + \frac{1}{(L-S^n)^2}\left[\frac{M^n_{2(i+1)}+10\,M^n_{2i}+M^n_{2(i-1)}}{12}\right] \tag{39}$$

Since the values of $m_{ji}$ and $M_{ji}$ may be extracted from the basic spline relations, equations (23), (27), (38), and (39) may be solved directly.

**Table 1 Comparison of numerical results with exact solution for Ste = 4.06**

| | Exact | | Spline | |
|---|---|---|---|---|
| $\tau$ | $S$ | $\frac{dS}{d\tau}$ | $S$ | $\frac{dS}{d\tau}$ |
| 0.0020 | −0.08944 | −22.361 | −0.08925 | −22.3140 |
| 0.0100 | −0.19999 | −10.000 | −0.19962 | −9.9819 |
| 0.09634 | −0.62078 | −3.2217 | −0.61964 | −3.2158 |
| 0.14883 | −0.77158 | −2.5921 | −0.77014 | −2.5873 |
| 0.19881 | −0.89177 | −2.2427 | −0.89009 | −2.2385 |
| 0.21879 | −0.93550 | −2.1379 | −0.93373 | −2.1338 |

## 4 Example—Aluminum Fusion Welding

As an example, we consider two aluminum plates of 0.05 m thickness that are to be joined by fusion welding. The fusion zone is set at 0.3 m in width. In this case, $L_1 = 0.015$ m and $L_2 = 0.05$ m. The two plates are preheated to 300°C. The initial temperature of the molten aluminum is 1677°C and the ambient temperature is 30°C. The physical properties of aluminum in the liquid and solid phases are given as follows [9]:

| | | |
|---|---|---|
| Density | $\rho_1 = 2310\ \text{Kg/m}^3$ | $\rho_2 = 2700\ \text{Kg/m}^3$ |
| Thermal conductivity | $k_1 = 83.7\ \text{W/m°C}$ | $k_2 = 238.6\ \text{W/m°C}$ |
| Specific heat | $c_1 = 1.084\ \text{KJ/Kg°C}$ | $c_2 = 1.076\ \text{KJ/Kg°C}$ |
| Thermal diffusivity | $a_1 = 3.343 \times 10^{-5}\ \text{m}^2/\text{s}$ | $a_2 = 8.214 \times 10^{-5}\ \text{m}^2/\text{s}$ |
| Latent heat of fusion | $q_L = 387.8\ \text{KJ/Kg}$ | |
| Melting point | $T = 660°\text{C}$ | |

The dimensionless parameters required for numerical calculations are determined as follows:

| | |
|---|---|
| $L = 3.333$ | $\text{Ste} = 2.843$ |
| $K = 2.851$ | $\theta_0 = 0.354$ |
| $a_{21} = 2.457$ | $\theta_\infty = -1.75$ |
| $\text{Bi} = 6.601 \times 10^{-4}$ | |

This example has been solved using the explicit spline technique described in this section, on a nonuniform mesh with six grid points. Figure 2 indicates the location of the dimensionless moving boundary, obtained with two different mesh systems. It is shown that the values obtained from the nonuniform mesh with six grid points are very close to the results obtained with the uniform mesh using twenty one grid points, except at the later stage of the solidification process, in which the value of $S$ approaches $-1$ and the value of $(1 + S)$ approaches 0. Because the factor $(1 + S)$ exists in the denominator of the terms on the right-hand side of equations (14) and (22), it causes large numerical differences. The singularity at $S = -1$ occurs because, as the liquid finally freezes, the essential character of the problem changes, from one involving both liquid and solid phases to one involving only solid phase. This sudden change in the nature of the problem manifests itself as a singularity in the governing equations. The dimensionless temperatures obtained from the nonlinear mesh with six grid points in comparison with those obtained from the uniform mesh with twenty one grid points are given in Fig. 3 for $\tau = 0.60$ and $S = S_{\max} = 0.205$. Again the values obtained with the two computations are very close. In Fig. 2, the slope of the $S$-$\tau$ curve represents the rate of propagation of the phase boundary between the liquid and solid phases. The positive and negative values of $dS/d\tau$ indicate the melting and solidification process, respectively. The changes of the values of $dS/d\tau$ is caused by the change of the temperature gradients in the liquid and solid phases at the phase boundary as shown in equation (22). The phase boundary reaches its maximum value when the melting process stops and the solidification process starts with $dS/d\tau = 0$ as also shown in Fig. 2.

## 5 Error Estimate of the Numerical Result

For an error estimate of the numerical solution, we consider the simple case of solidification of metal which is initially at its melting temperature, $T_1 = T_s$. It is assumed that at a certain time $t = 0$, the temperature at the surface $x_2 = 0$, drops to $T_o$ and remains constant thereafter. The exact solution of this simplified solidification process is given by

$$\theta_2(y_2, \tau) = -1 + \frac{\text{erf}[\lambda(1 - y_2)]}{\text{erf}(\lambda)} \tag{40}$$

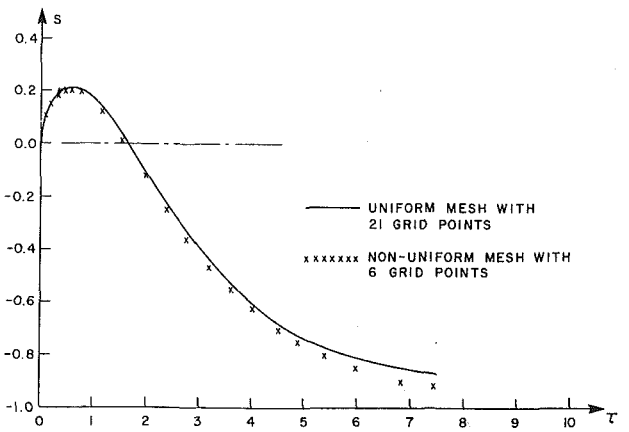


**Fig. 2 Dimensionless location of the moving phase boundary $S$ as a function of dimensionless time $\tau$ for the aluminum fusion welding**

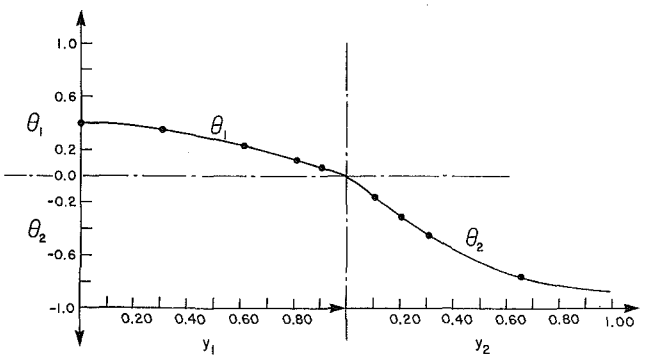


**Fig. 3 Dimensionless temperature distributions in the molten metal $\theta_1$ and in the metal sheet $\theta_2$ for the aluminum fusion welding, at $\tau = 0.60$ and $S = S_{\max} = 0.205$: • nonuniform mesh with six grid points; — uniform mesh with twenty one grid points**

and

$$S = 2\lambda\sqrt{\tau} \tag{41}$$

where $\lambda$ is determined from

$$\sqrt{\pi}\ \lambda\ e^{\lambda^2}\ \text{erf}(\lambda) = \text{Ste} \tag{42}$$

Table 1 shows the comparison of the results obtained with the spline numerical solution on a nonuniform mesh with six grid points for the location and the velocity of the moving phase front with those obtained from the exact solution, for Ste = 4.06. The table indicates a maximum relative error of less than 0.3 percent.

## 6 Conclusions

The differential equations describing a fusion welding problem involving a moving unknown phase boundary have been integrated numerically using a cubic spline technique. Since a nonuniform coarsely spaced grid appears to provide sufficient accuracy, the method appears to be computationally efficient.

## References


1 Udin, H., Funk, E. R., and Wulff, J., *Welding for Engineers*, ch. 10, John Wiley and Sons, New York, 1954.

2 Carslaw, H. S., and Jaeger, J. C., *Conduction of Heat in Solids* (2nd Edition), ch. XI, Oxford University Press, London, 1959.

3 Rubin, S. G., and Graves, R. A., "Viscous Flow Solutions with a Cubic Spline Approximation," *Computers and Fluids*, Vol. 3, 1975, pp. 1-36.

4 Rubin, S. G., and Kholsa, P. K., "Higher-Order Numerical Solutions Using Cubic Splines," *Journal of AIAA*, Vol. 14, No. 7, 1976, pp. 851–858.
5 Panton, R. L., and Sallee, M. B., "Spline Function Representation for Computer Solutions to Fluid Problems," *Computers and Fluids*, Vol. 3, 1975, pp. 257–269.
6 Wang, Pu, and Kahawita, R., "A Two Dimensional Model of Esturine Circulating using Cubic Splines," *International Journal of Civil Engineering*, Vol. 10, 1983, pp. 116–124.
7 Wang, Pu, and Kahawita, R., "Numerical Integration of Partial Differential Equations using Cubic Splines," *International Journal of Computer Mathematics*, Vol. 13, 1983, pp. 271–286.
8 Wang, Pu, and Kahawita, R., "The Numerical Solution of Burger's Equation Using Splines," presented at the *Third Asian Congress of Fluid Mechanics*, Beijing, People's Republic of China, Oct. 1983.
9 Smithells, C. J., *Metal Reference Book* (2d ed.), Vol. II, Butterworths' Scientific Publications, London, 1955, pp. 636–645.

## Unsteady-State Heat Conduction in Semi-Infinite Regions With Mixed-Type Boundary Conditions

**S. C. Huang**[1]

### Nomenclature

erfc = complementary error function
Fo = $\alpha t/L^2$, Fourier number
$i$ = $(-1)^{1/2}$
$J$ = Bessel function of the first kind
$k_{mn}$ = thermal conductivity ($m$, $n=1,2$)
$L$ = length
$q''$ = heat flux
Re = real part of complex variable functions
$s$ = Laplace transform parameter, complex
$t$ = time
$T$ = temperature
$\bar{T}$ = Laplace transform of $T$
$\bar{\bar{T}}$ = generalized Fourier transform of $\bar{T}$
$x,y$ = Cartesian coordinates

### Greek

$\alpha$ = thermal diffusivity based on $k_{22}$
$\beta$ = $(\nu_{11}-\nu_{12}^2)^{1/2}$
$\lambda$ = Fourier transform parameter, complex
$\nu_{mn}$ = $k_{mn}/k_{22}$

### Subscript

o = on the boundary $y=0$
+ = for $\xi \geq 0$
− = for $\xi \leq 0$

### 1 Introduction

Heat conduction problems with mixed-type boundary conditions occur frequently in engineering applications. Such examples include the dip-forming process in metallurgy [1], the surface rewetting during loss-of-coolant accidents [2], the contact resistance between solids [3]. In the two-dimensional analysis of these problems, the conventional integral transform method does not apply. One has to rely on the Weiner-Hopf technique [4] or the dual integral/series equation [5]. Due to the complexity of these techniques, available closed-form solutions are limited [2–7]. They are mostly restricted to either steady-state or long-time approximation.

This note is to report an unsteady-state, closed-form solution in a semi-infinite region with isothermal and isoflux mixed-type boundary conditions.

### 2 Statement of the Problem

Consider the unsteady-state anisotropic heat conduction in the semi-infinite region $-\infty<x<\infty$, $y>0$. The solid is initially at a uniform temperature $T=0$. For time $t>0$, a mixted-type boundary condition is imposed on the surface $y=0$ so that a constant temperature is prescribed on the boundary $x>0$ and a constant heat flux is prescribed on the boundary $x<0$.

Assume that there is no heat generation in the domain, the governing conduction equation takes the following form

$$\nu_{11}\frac{\partial^2 T}{\partial x^2}+2\nu_{12}\frac{\partial^2 T}{\partial x\partial y}+\frac{\partial^2 T}{\partial y^2}-\frac{1}{\alpha}\frac{\partial T}{\partial t}=0 \qquad \begin{matrix}-\infty<x<\infty \\ y>0\end{matrix} \qquad t>0 \tag{1}$$

The corresponding initial and boundary conditions are

$$T=0 \qquad t=0,\ -\infty<x<\infty,\ y>0 \tag{2}$$

$$T=T_o \qquad x>0, y=0, t>0 \tag{3}$$

$$\nu_{12}\frac{\partial T}{\partial x}+\frac{\partial T}{\partial y}=-\frac{q_o''}{k_{22}} \qquad x<0, y=0, t>0 \tag{4}$$

$$T=0 \qquad x\to\infty, y\to\infty, t>0 \tag{5}$$

If the medium is isotropic, one just takes $\nu_{11}=1$ and $\nu_{12}=0$ in equations (1) and (4).

### 3 Analysis

Following Chang [8], one can simplify the anisotropic problem by the nonorthonormal coordinate transformation

$$\xi=(x-\nu_{12}y)/\beta \tag{6}$$

$$\eta=y \tag{7}$$

Substituting equations (6) and (7) into equations (1–5) and then applying Laplace transform with respect to time $t$ and generalized Fourier transform with respect to $\xi$, one obtains

$$\frac{d^2\bar{\bar{T}}}{d\eta^2}-\left(\lambda^2+\frac{s}{\alpha}\right)\bar{\bar{T}}=0 \qquad 0<\eta<\infty \tag{8}$$

$$\bar{\bar{T}}_+=\frac{iT_o}{(2\pi)^{1/2}s\lambda} \qquad \eta=0 \tag{9}$$

$$\frac{d\bar{\bar{T}}_-}{d\eta}=\frac{iq_o''/k_{22}}{(2\pi)^{1/2}s\lambda} \qquad \eta=0 \tag{10}$$

$$\bar{\bar{T}}=0 \qquad \eta\to\infty \tag{11}$$

where $\bar{\bar{T}}(\eta;\lambda,s)=\bar{\bar{T}}_+(\eta;\lambda,s)+\bar{\bar{T}}_-(\eta;\lambda,s)$.

The $\bar{\bar{T}}$ satisfying equations (8) and (11) is simply

$$\bar{\bar{T}}(\eta;\lambda,s)=A(\lambda,s)\exp(-(\lambda^2+s/\alpha)^{1/2}\eta) \tag{12}$$

where $A(\lambda,s)$ is a complex variable function to be determined.

Substituting equation (12) into equations (9) and (10), one gets

$$A(\lambda,s)=\frac{iT_o}{(2\pi)^{1/2}s\lambda}+\bar{\bar{T}}_-\Big|_{\eta=0} \tag{13}$$

$$-\left(\lambda^2+\frac{s}{\alpha}\right)^{1/2}A(\lambda,s)=\frac{d\bar{\bar{T}}_+}{d\eta}\Big|_{\eta=0}+\frac{iq_o''/k_{22}}{(2\pi)^{1/2}s\lambda} \tag{14}$$

In the above, one has three unknowns $A(\lambda,s)$, $\bar{\bar{T}}_-|_{\eta=0}$ and $d\bar{\bar{T}}_+/d\eta|_{\eta=0}$ in two conditions (13) and (14). This makes the problem unsolvable by conventional methods.

[1] Mechanical Technology, Inc., Latham, N.Y. 12110, Assoc. Mem. ASME
Contributed by the Heat Transfer Division for publication in the JOURNAL OF HEAT TRANSFER. Manuscript received by the Heat Transfer Division February 17, 1984.

4 Rubin, S. G., and Kholsa, P. K., "Higher-Order Numerical Solutions Using Cubic Splines," *Journal of AIAA*, Vol. 14, No. 7, 1976, pp. 851–858.
5 Panton, R. L., and Sallee, M. B., "Spline Function Representation for Computer Solutions to Fluid Problems," *Computers and Fluids*, Vol. 3, 1975, pp. 257–269.
6 Wang, Pu, and Kahawita, R., "A Two Dimensional Model of Esturine Circulating using Cubic Splines," *International Journal of Civil Engineering*, Vol. 10, 1983, pp. 116–124.
7 Wang, Pu, and Kahawita, R., "Numerical Integration of Partial Differential Equations using Cubic Splines," *International Journal of Computer Mathematics*, Vol. 13, 1983, pp. 271–286.
8 Wang, Pu, and Kahawita, R., "The Numerical Solution of Burger's Equation Using Splines," presented at the *Third Asian Congress of Fluid Mechanics*, Beijing, People's Republic of China, Oct. 1983.
9 Smithells, C. J., *Metal Reference Book* (2d ed.), Vol. II, Butterworths' Scientific Publications, London, 1955, pp. 636–645.

# Unsteady-State Heat Conduction in Semi-Infinite Regions With Mixed-Type Boundary Conditions

**S. C. Huang**[1]

### Nomenclature

erfc = complementary error function
Fo = $\alpha t/L^2$, Fourier number
$i$ = $(-1)^{1/2}$
$J$ = Bessel function of the first kind
$k_{mn}$ = thermal conductivity ($m$, $n=1,2$)
$L$ = length
$q''$ = heat flux
Re = real part of complex variable functions
$s$ = Laplace transform parameter, complex
$t$ = time
$T$ = temperature
$\bar{T}$ = Laplace transform of $T$
$\bar{\bar{T}}$ = generalized Fourier transform of $\bar{T}$
$x,y$ = Cartesian coordinates

### Greek

$\alpha$ = thermal diffusivity based on $k_{22}$
$\beta$ = $(\nu_{11}-\nu_{12}^2)^{1/2}$
$\lambda$ = Fourier transform parameter, complex
$\nu_{mn}$ = $k_{mn}/k_{22}$

### Subscript

o = on the boundary $y=0$
+ = for $\xi \geq 0$
− = for $\xi \leq 0$

## 1 Introduction

Heat conduction problems with mixed-type boundary conditions occur frequently in engineering applications. Such examples include the dip-forming process in metallurgy [1], the surface rewetting during loss-of-coolant accidents [2], the contact resistance between solids [3]. In the two-dimensional analysis of these problems, the conventional integral transform method does not apply. One has to rely on the Weiner-Hopf technique [4] or the dual integral/series equation [5]. Due to the complexity of these techniques, available closed-form solutions are limited [2–7]. They are mostly restricted to either steady-state or long-time approximation.

This note is to report an unsteady-state, closed-form solution in a semi-infinite region with isothermal and isoflux mixed-type boundary conditions.

## 2 Statement of the Problem

Consider the unsteady-state anisotropic heat conduction in the semi-infinite region $-\infty<x<\infty$, $y>0$. The solid is initially at a uniform temperature $T=0$. For time $t>0$, a mixted-type boundary condition is imposed on the surface $y=0$ so that a constant temperature is prescribed on the boundary $x>0$ and a constant heat flux is prescribed on the boundary $x<0$.

Assume that there is no heat generation in the domain, the governing conduction equation takes the following form

$$\nu_{11}\frac{\partial^2 T}{\partial x^2}+2\nu_{12}\frac{\partial^2 T}{\partial x\partial y}+\frac{\partial^2 T}{\partial y^2}-\frac{1}{\alpha}\frac{\partial T}{\partial t}=0 \qquad \begin{matrix}-\infty<x<\infty \\ y>0\end{matrix} \qquad t>0 \tag{1}$$

The corresponding initial and boundary conditions are

$$T=0 \qquad t=0,\ -\infty<x<\infty,\ y>0 \tag{2}$$

$$T=T_o \qquad x>0, y=0, t>0 \tag{3}$$

$$\nu_{12}\frac{\partial T}{\partial x}+\frac{\partial T}{\partial y}=-\frac{q_o''}{k_{22}} \qquad x<0, y=0, t>0 \tag{4}$$

$$T=0 \qquad x\to\infty, y\to\infty, t>0 \tag{5}$$

If the medium is isotropic, one just takes $\nu_{11}=1$ and $\nu_{12}=0$ in equations (1) and (4).

## 3 Analysis

Following Chang [8], one can simplify the anisotropic problem by the nonorthonormal coordinate transformation

$$\xi=(x-\nu_{12}y)/\beta \tag{6}$$

$$\eta=y \tag{7}$$

Substituting equations (6) and (7) into equations (1–5) and then applying Laplace transform with respect to time $t$ and generalized Fourier transform with respect to $\xi$, one obtains

$$\frac{d^2\bar{\bar{T}}}{d\eta^2}-\left(\lambda^2+\frac{s}{\alpha}\right)\bar{\bar{T}}=0 \qquad 0<\eta<\infty \tag{8}$$

$$\bar{\bar{T}}_+=\frac{iT_o}{(2\pi)^{1/2}s\lambda} \qquad \eta=0 \tag{9}$$

$$\frac{d\bar{\bar{T}}_-}{d\eta}=\frac{iq_o''/k_{22}}{(2\pi)^{1/2}s\lambda} \qquad \eta=0 \tag{10}$$

$$\bar{\bar{T}}=0 \qquad \eta\to\infty \tag{11}$$

where $\bar{\bar{T}}(\eta;\lambda,s)=\bar{\bar{T}}_+(\eta;\lambda,s)+\bar{\bar{T}}_-(\eta;\lambda,s)$.

The $\bar{\bar{T}}$ satisfying equations (8) and (11) is simply

$$\bar{\bar{T}}(\eta;\lambda,s)=A(\lambda,s)\exp(-(\lambda^2+s/\alpha)^{1/2}\eta) \tag{12}$$

where $A(\lambda,s)$ is a complex variable function to be determined.

Substituting equation (12) into equations (9) and (10), one gets

$$A(\lambda,s)=\frac{iT_o}{(2\pi)^{1/2}s\lambda}+\bar{\bar{T}}_-\Big|_{\eta=0} \tag{13}$$

$$-\left(\lambda^2+\frac{s}{\alpha}\right)^{1/2}A(\lambda,s)=\frac{d\bar{\bar{T}}_+}{d\eta}\Big|_{\eta=0}+\frac{iq_o''/k_{22}}{(2\pi)^{1/2}s\lambda} \tag{14}$$

In the above, one has three unknowns $A(\lambda,s)$, $\bar{\bar{T}}_-|_{\eta=0}$ and $d\bar{\bar{T}}_+/d\eta|_{\eta=0}$ in two conditions (13) and (14). This makes the problem unsolvable by conventional methods.

[1] Mechanical Technology, Inc., Latham, N.Y. 12110, Assoc. Mem. ASME
Contributed by the Heat Transfer Division for publication in the JOURNAL OF HEAT TRANSFER. Manuscript received by the Heat Transfer Division February 17, 1984.

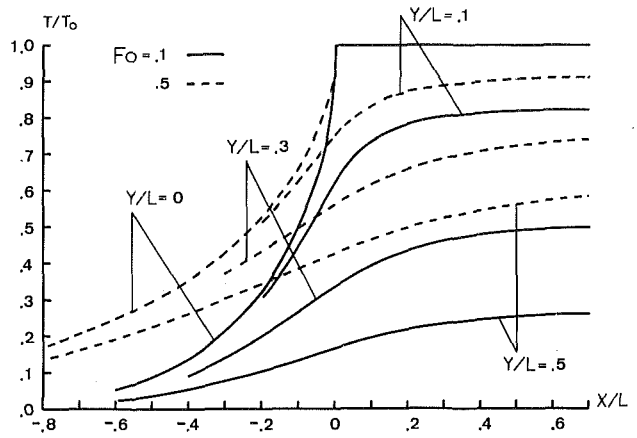


Fig. 1 Temperature distribution for $q_o''=0$ and nonzero $T_o$ at Fo = 0.1 and Fo = 0.5

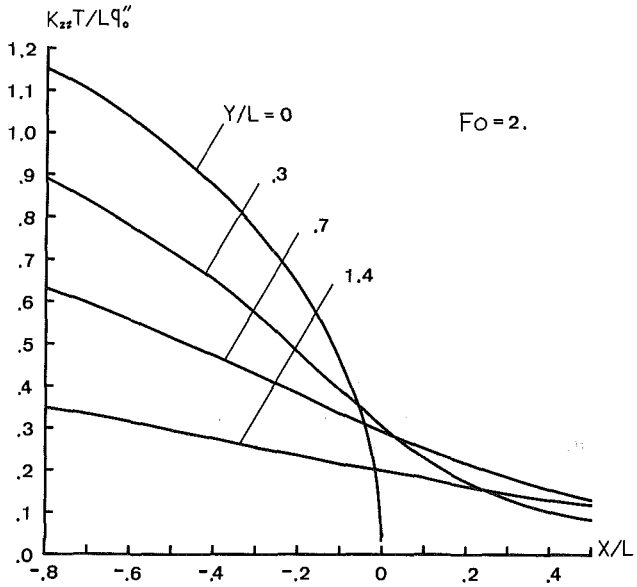


Fig. 2 Temperature distribution for $T_o=0$ and nonzero $q_o''$ at Fo = 2.0

Following the Weiner-Hopf technique [4], one can obtain an additional condition from the theory of complex functions. The result gives

$$\bar{\bar{T}}(y;\lambda,s)=\frac{\exp\left(-\left(\lambda^2+\frac{s}{\alpha}\right)^{1/2}\eta\right)}{(2\pi)^{1/2}s\lambda(\lambda-i(s/\alpha)^{1/2})^{1/2}}\left(T_o(i(s/\alpha)^{1/2})^{1/2}-\frac{iq_o''/k_{22}}{(i(s/\alpha)^{1/2})^{1/2}}\right) \quad (15)$$

The inverse Fourier transform of equation (15) is

$$\bar{T}(\xi,\eta;s)=\frac{T_o}{s}e^{-(s/\alpha)^{1/2}\eta}+\bar{T}_1(\xi,\eta;s) \quad \xi>0 \quad (16)$$

$$=\frac{q_o''/k_{22}}{s(s/\alpha)^{1/2}}e^{-(s/\alpha)^{1/2}\eta}+\bar{T}_1(\xi,\eta;s) \quad \xi<0 \quad (17)$$

where

$$\bar{T}_1(\xi,\eta;s)=-\frac{1}{2^{1/2}\pi s}\int_{-\infty}^{\infty}\frac{\sin\frac{\theta+i\tau}{2}}{\cos(\theta+i\tau)}\left(T_o-\frac{q_o''/k_{22}}{(s/\alpha)^{1/2}}\right)e^{-(s/\alpha)^{1/2}r\cosh\tau}d\tau \quad (18)$$

r and $\theta$ are polar coordinates defined by $\xi=r\cos\theta$, $\eta=r\sin\theta$.

Through the use of Laplace transform table, one obtains the temperature distribution as given below

$$T(x,y,t)=T_o\operatorname{erfc}\left(\frac{\eta}{2(\alpha t)^{1/2}}\right)+T_1(x,y,t) \quad \xi>0 \quad (19)$$

$$=\frac{q_o''}{k_{22}}\left(2\left(\frac{\alpha t}{\pi}\right)^{1/2}\exp\left(-\frac{\eta^2}{4\alpha t}\right)-\eta\operatorname{erfc}\left(\frac{\eta}{2(\alpha t)^{1/2}}\right)\right)+T_1(x,y,t) \quad \xi<0 \quad (20)$$

where

$$T_1(x,y,t)=-\frac{2^{1/2}}{\pi}\int_0^{\infty}\operatorname{Re}\left(\frac{\sin\frac{\theta+i\tau}{2}}{\cos(\theta+i\tau)}\right)\left(\left(T_o+\frac{q_o''}{k_{22}}r\cosh\tau\right)\operatorname{erfc}\left(\frac{r\cosh\tau}{2(\alpha t)^{1/2}}\right)-\frac{2q_o''}{k_{22}}\left(\frac{\alpha t}{\pi}\right)^{1/2}\exp\left(-\frac{r^2\cosh^2\tau}{4\alpha t}\right)\right)d\tau \quad (21)$$

## 4 Results and Discussion

The temperature distribution in equations (19) and (20) consists of two terms. The first term in equation (19) is the unsteady-state, one-dimensional temperature satisfying the Dirichlet boundary condition (3). The first term in equation (20) is the unsteady-state, one-dimensional temperature satisfying the Neumann boundary condition (4). Thus the $T_1(x,y,t)$ in these equations represents the deviation of the solution from the foregoing one-dimensional solutions due to the mixed-type boundary conditions.

Since $T_1(x,y,t)$ approaches to zero for large values of $r$, the temperature distribution at large distances from the origin is given by the one-dimensional solutions in their respective regions. As the temperature is continuous, the function $T_1(x,y,t)$ is not continuous across the line $\xi=0$. This point will be confirmed by numerical calculation.

Because of the linear nature of the problem, the general cases can be obtained by superposition. Thus the case $q_o''=0$ and the case $T_o=0$ are discussed separately in the following.

If the boundary $x<0$ is adiabatic, i.e., $q_o''=0$, the present problem reduces to that in a wedge of angle $2\pi$ with the boundaries $\theta=0$ and $\theta=2\pi$ being at $T_o$. The corresponding temperature can be obtained by conventional transform method and was given by Carslaw and Jaeger [9]

$$\frac{T}{T_o}=1-\frac{2}{\pi}\sum_{n=0}^{\infty}\sin(n+\tfrac{1}{2})\theta\int_0^{\infty}\exp\left(-\frac{\alpha t\tau^2}{r^2}\right)J_{n+1/2}(\tau)\frac{d\tau}{\tau} \quad (22)$$

For $t\to\infty$, both solutions, equations (19–21) and equation (22), yield the same trivial solution of $T(x,y)=T_o$. Comparison shows that the present solution offers reduced computational effort.

For the purpose of numerical demonstration, one assumes isotropic heat condition in the following. Consequently, $\xi=x$ and $\eta=y$. Figure 1 shows the obtained temperature distributions with $q_o''=0$ and nonzero $T_o$. The solid and dashed lines are for Fo = 0.1 and Fo = 0.5, respectively. While one uses equation (19) for the region $x>0$ and equation (20) for the region $x<0$, the calculated results indicate that these solutions are indeed continuous across the line $x=0$.

Along the negative side of the $x$-axis, one sees that the temperature drops rapidly in regions close to the adiabatic boundary. Along the positive side of the $x$-axis, one sees that the temperature distribution is mostly one-dimensional except where $x$ is small. The $x$-dependent variation is due to the function $T_1(x,y,t)$.

Figure 2 shows the obtained temperature distributions with $T_o = 0$ and nonzero $q_o''$ for Fo = 2.0. The calculated temperature is again continuous across the line $x = 0$ as would be expected.

In the positive $x$ region, one sees that the maximum temperature is somewhere away from the boundary. This indicates that the heat flux changes direction along a constant $y$ line. This heat flux reversal actually extends slightly beyond the $x = 0$ line as shown. Since there is no steady-state for this case, the temperature will continue to rise with time.


### Acknowledgments

I am indebted to Professor Y. P. Chang of SUNY at Buffalo for his advice and inspiration.


### References


1 Horvay, G., "The Dip-Forming Process," ASME JOURNAL OF HEAT TRANSFER, Vol. 87, 1965, pp. 1–16.

2 Tien, C. L., and Yao, L. S., "Analysis of Conduction-Controlled Rewetting of a Vertical Surface," ASME Journal of Heat Transfer, Vol. 97, 1975, pp. 161–165.

3 Sadhal, S. S., "Unsteady Heat Flow between Solids with Partially Contacting Interface," ASME JOURNAL OF HEAT TRANSFER, Vol. 103, 1981, pp. 32–35.

4 Noble, B., *Methods Based on the Wiener-Hopf Technique*, Pergamon Press, New York, 1958.

5 Sneddon, I. N., *Mixed Boundary Value Problems in Potential Theory*, North-Holland Publishing Company, Amsterdam, 1966.

6 Horvay, G., "Temperature Distribution in a Slab Moving From a Chamber at One Temperature to a Chamber at Another Temperature," JOURNAL OF HEAT TRANSFER, Vol. 83, 1961, pp. 391–402.

7 Horvay, G., and DaCosta, M., "Temperature Distribution in a Cylindrical Rod Moving From a Chamber at One Temperature to a Chamber at Another Temperature," ASME JOURNAL OF HEAT TRANSFER, Vol. 86, 1964, pp. 265–270.

8 Chang, Y. P., "Analytical Solution for Heat Conduction in Anisotropic Media in Infinite, Semi-Infinite, and Two-Plane-Bounded Regions," *International Journal of Heat Mass Transfer*, Vol. 20, 1977, pp. 1019–1028.

9 Carslaw, H. S., and Jaeger, J. C., *Conduction of Heat in Solids*, Clarendon Press, Oxford, 1959.


## Heat Conduction in a Rectangular Parallelopiped With Multiple Cylindrical Cavities


**A. K. Naghdi**[1]


### Introduction

Employing a new class of functions, the three-dimensional, steady-state heat conduction in a rectangular parallelopiped with four longitudinal circular cylindrical cavities are solved. It is assumed that the holes are symmetrically located with respect to the axes of symmetry of the transverse cross sections. It is also assumed that the outer boundary planes of the rectangular parallelopiped are kept at a uniform temperature and that the material properties are temperature independent. Numerical results are presented.

### Method of Solution

Steady-state plane heat conduction as well as a number of other applied mechanics problems require the solution of two-dimensional Laplace equations. In recent years, many authors have investigated the mentioned problems. Among the authors who obtained solutions for the problems of steady-state heat conduction and torsion of prismatic bars in a circular region with holes are Rowley and Payne [1], Ling [2], and Kuo and Conway [3]. Recently, the solutions for certain two-dimensional heat transfer problems in a rectangular region with circular cutouts was given by the author [4, 5]. The present technique is the extension of the method of [5] to the three-dimensional case of heat conduction.

Consider heat conduction in a rectangular parallelopiped with length $L$, containing four symmetrically located longitudinal circular cylindrical cavities and having the cross section shown in Fig. 1. Choose the origin of the coordinate axes at the middle of the length of the bar. The governing equation for the steady-state heat conduction in a material with constant thermal conductivity is the three-dimensional Laplace equation

$$\nabla^2 T = 0, \qquad \nabla^2 \equiv \frac{\partial^2}{\partial x^2} + \frac{\partial^2}{\partial y^2} + \frac{\partial^2}{\partial z^2}, \tag{1}$$

in which $T$ is the temperature. It is assumed that the outer boundry planes of the rectangular parallelopiped are maintained at a uniform temperature $T_w$ and that the inner boundary temperature $T_i(Z)$ is the same for all of the four cylindrical cavities. Furthermore, without the loss of generality it is assumed that $T_i(Z)$ is an even function of $z$, has the values $T_i(\pm L/2) = T_w$, and possesses a Fourier series representation. Thus it is found

$$\left.\begin{aligned} T_i(Z) &= \sum_{m=1,3,5}^{\infty} T_{im} \cos\frac{m\pi Z}{L}, \\ T_w &= \sum_{m=1,3,5}^{\infty} T_{wm} \cos\frac{m\pi Z}{L}, \quad T_{wm} = \frac{4T_w}{m\pi} \sin\frac{m\pi}{Z} \end{aligned}\right\} \tag{2}$$

Introducing

$$T_g = T - T_w \tag{3}$$

into equation (1) it is obtained

$$\nabla^2 T_g = 0 \tag{4}$$

The function $T_g$ must satisfy a homogeneous outer boundary condition and has to fulfill

$$T_g = T_i(Z) - T_w \tag{5}$$

on the inner cylindrical surfaces.

The solution of equation (4) is now sought in the form

$$T_g = \sum_{m=1,3,5}^{\infty} T_m(x,y) \cos\frac{m\pi Z}{L} \tag{6}$$

which obviously satisfies the boundary conditions $T_g = 0$ at $Z = \pm L/2$. Substituting relation (6) into equation (4) and utilizing nondimensional factors, it is found

$$\left.\begin{aligned} &\bar{\nabla}^2 \bar{T}_m - K_m^2 \bar{T}_m = 0, \quad \bar{\nabla}^2 \equiv \frac{\partial^2}{\partial \xi^2} + \frac{\partial^2}{\partial \eta^2}, \\ &\xi = \frac{x}{a}, \quad \eta = \frac{y}{a}, \quad K_m = \frac{m\pi a}{L}, \\ &\bar{T}_m = \frac{T_m}{T_{im} - T_{wm}}, \quad m = 1,3,5, \ldots \end{aligned}\right\} \tag{7}$$

Thus the solution of the title problem is reduced to obtaining the components $\bar{T}_m(\xi,\eta)$, which must satisfy the conditions

$$\bar{T}_m = 0 \quad \text{on} \quad C_o \tag{8}$$

$$\bar{T}_m = 1 \quad \text{on} \quad C_i \tag{9}$$

Here in relations (8) and (9) $C_o$ and $C_i$ respectively represent the outer rectangular boundary and the inner circular boundaries of the transverse cross section of the bar.


[1]Professor of Aeronautical-Astronautical Engineering and Mathematical Science, Purdue University School of Engineering and Technology, and School of Science at Indianapolis, Ind. 46223.



Contributed by the Heat Transfer Division for publication in the JOURNAL OF HEAT TRANSFER. Manuscript received by the Heat Transfer Division September 12, 1983.

Figure 2 shows the obtained temperature distributions with $T_o = 0$ and nonzero $q_o''$ for Fo = 2.0. The calculated temperature is again continuous across the line $x = 0$ as would be expected.

In the positive $x$ region, one sees that the maximum temperature is somewhere away from the boundary. This indicates that the heat flux changes direction along a constant $y$ line. This heat flux reversal actually extends slightly beyond the $x = 0$ line as shown. Since there is no steady-state for this case, the temperature will continue to rise with time.


### Acknowledgments

I am indebted to Professor Y. P. Chang of SUNY at Buffalo for his advice and inspiration.


### References


1 Horvay, G., "The Dip-Forming Process," ASME JOURNAL OF HEAT TRANSFER, Vol. 87, 1965, pp. 1–16.

2 Tien, C. L., and Yao, L. S., "Analysis of Conduction-Controlled Rewetting of a Vertical Surface," ASME Journal of Heat Transfer, Vol. 97, 1975, pp. 161–165.

3 Sadhal, S. S., "Unsteady Heat Flow between Solids with Partially Contacting Interface," ASME JOURNAL OF HEAT TRANSFER, Vol. 103, 1981, pp. 32–35.

4 Noble, B., *Methods Based on the Wiener-Hopf Technique*, Pergamon Press, New York, 1958.

5 Sneddon, I. N., *Mixed Boundary Value Problems in Potential Theory*, North-Holland Publishing Company, Amsterdam, 1966.

6 Horvay, G., "Temperature Distribution in a Slab Moving From a Chamber at One Temperature to a Chamber at Another Temperature," JOURNAL OF HEAT TRANSFER, Vol. 83, 1961, pp. 391–402.

7 Horvay, G., and DaCosta, M., "Temperature Distribution in a Cylindrical Rod Moving From a Chamber at One Temperature to a Chamber at Another Temperature," ASME JOURNAL OF HEAT TRANSFER, Vol. 86, 1964, pp. 265–270.

8 Chang, Y. P., "Analytical Solution for Heat Conduction in Anisotropic Media in Infinite, Semi-Infinite, and Two-Plane-Bounded Regions," *International Journal of Heat Mass Transfer*, Vol. 20, 1977, pp. 1019–1028.

9 Carslaw, H. S., and Jaeger, J. C., *Conduction of Heat in Solids*, Clarendon Press, Oxford, 1959.


## Heat Conduction in a Rectangular Parallelopiped With Multiple Cylindrical Cavities


**A. K. Naghdi**[1]


### Introduction

Employing a new class of functions, the three-dimensional, steady-state heat conduction in a rectangular parallelopiped with four longitudinal circular cylindrical cavities are solved. It is assumed that the holes are symmetrically located with respect to the axes of symmetry of the transverse cross sections. It is also assumed that the outer boundary planes of the rectangular parallelopiped are kept at a uniform temperature and that the material properties are temperature independent. Numerical results are presented.

### Method of Solution

Steady-state plane heat conduction as well as a number of other applied mechanics problems require the solution of two-dimensional Laplace equations. In recent years, many authors have investigated the mentioned problems. Among the authors who obtained solutions for the problems of steady-state heat conduction and torsion of prismatic bars in a circular region with holes are Rowley and Payne [1], Ling [2], and Kuo and Conway [3]. Recently, the solutions for certain two-dimensional heat transfer problems in a rectangular region with circular cutouts was given by the author [4, 5]. The present technique is the extension of the method of [5] to the three-dimensional case of heat conduction.

Consider heat conduction in a rectangular parallelopiped with length $L$, containing four symmetrically located longitudinal circular cylindrical cavities and having the cross section shown in Fig. 1. Choose the origin of the coordinate axes at the middle of the length of the bar. The governing equation for the steady-state heat conduction in a material with constant thermal conductivity is the three-dimensional Laplace equation

$$\nabla^2 T = 0, \qquad \nabla^2 \equiv \frac{\partial^2}{\partial x^2} + \frac{\partial^2}{\partial y^2} + \frac{\partial^2}{\partial z^2}, \tag{1}$$

in which $T$ is the temperature. It is assumed that the outer boundry planes of the rectangular parallelopiped are maintained at a uniform temperature $T_w$ and that the inner boundary temperature $T_i(Z)$ is the same for all of the four cylindrical cavities. Furthermore, without the loss of generality it is assumed that $T_i(Z)$ is an even function of $z$, has the values $T_i(\pm L/2) = T_w$, and possesses a Fourier series representation. Thus it is found

$$\left.\begin{aligned} T_i(Z) &= \sum_{m=1,3,5}^{\infty} T_{im} \cos\frac{m\pi Z}{L}, \\ T_w &= \sum_{m=1,3,5}^{\infty} T_{wm} \cos\frac{m\pi Z}{L}, \quad T_{wm} = \frac{4T_w}{m\pi} \sin\frac{m\pi}{Z} \end{aligned}\right\} \tag{2}$$

Introducing

$$T_g = T - T_w \tag{3}$$

into equation (1) it is obtained

$$\nabla^2 T_g = 0 \tag{4}$$

The function $T_g$ must satisfy a homogeneous outer boundary condition and has to fulfill

$$T_g = T_i(Z) - T_w \tag{5}$$

on the inner cylindrical surfaces.

The solution of equation (4) is now sought in the form

$$T_g = \sum_{m=1,3,5}^{\infty} T_m(x,y) \cos\frac{m\pi Z}{L} \tag{6}$$

which obviously satisfies the boundary conditions $T_g = 0$ at $Z = \pm L/2$. Substituting relation (6) into equation (4) and utilizing nondimensional factors, it is found

$$\left.\begin{aligned} &\bar{\nabla}^2 \bar{T}_m - K_m^2 \bar{T}_m = 0, \quad \bar{\nabla}^2 \equiv \frac{\partial^2}{\partial \xi^2} + \frac{\partial^2}{\partial \eta^2}, \\ &\xi = \frac{x}{a}, \quad \eta = \frac{y}{a}, \quad K_m = \frac{m\pi a}{L}, \\ &\bar{T}_m = \frac{T_m}{T_{im} - T_{wm}}, \quad m = 1,3,5, \ldots \end{aligned}\right\} \tag{7}$$

Thus the solution of the title problem is reduced to obtaining the components $\bar{T}_m(\xi,\eta)$, which must satisfy the conditions

$$\bar{T}_m = 0 \quad \text{on} \quad C_o \tag{8}$$

$$\bar{T}_m = 1 \quad \text{on} \quad C_i \tag{9}$$

Here in relations (8) and (9) $C_o$ and $C_i$ respectively represent the outer rectangular boundary and the inner circular boundaries of the transverse cross section of the bar.


[1]Professor of Aeronautical-Astronautical Engineering and Mathematical Science, Purdue University School of Engineering and Technology, and School of Science at Indianapolis, Ind. 46223.



Contributed by the Heat Transfer Division for publication in the JOURNAL OF HEAT TRANSFER. Manuscript received by the Heat Transfer Division September 12, 1983.

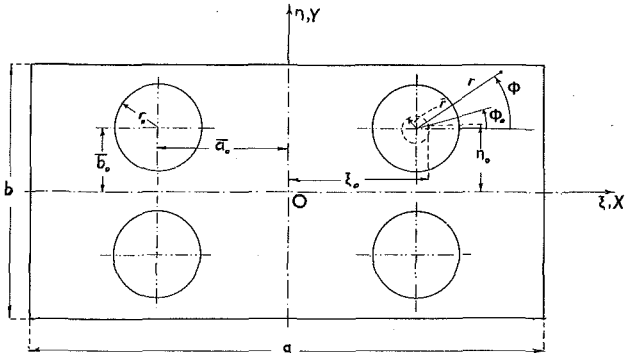


**Fig. 1 The transverse cross section of the rectangular parallelopiped**

The solution of equation (7) subject to boundary conditions (8) are now written in the form

$$\left.\begin{aligned}\bar{T}=&A_0T_0^*+A_1T_1^*+\ldots\ldots\ldots+A_jT_j^*+\ldots.\\&+B_1T_1^0+B_2T_2^0+\text{------}B_jT_j^0+\ldots.\end{aligned}\right\}\quad(10)$$

in which $\bar{T}$ represents any of the functions of $\bar{T}_m$, and $T_j^*$ and $T_j^0$ are certain solutions of equation (7) that automatically satisfy the outer boundary condition (8). The unknown coefficients $A_0, A_1, \ldots B_1, B_2, \ldots$ in relation (10) are to be determined from the inner boundary condition (9). The general solution $T_g(x,y,z)$ is obtained by substituting various components $T_m$ in relation (6).

**Determination of $T_j^*$ and $T_j^0$**

With a technique similar to that pursued in [5], the functions under consideration are sought in the form

$$\left.\begin{aligned}T_j^{**}&=\int_0^{2\pi}\bar{T}_c(\xi,\eta,\xi_o,\eta_o)\cos j\phi_0\bar{\rho}d\phi_o\\&\qquad j=0,1,2,\ldots\\T_j^{00}&=\int_0^{2\pi}\bar{T}_c(\xi,\eta,\xi_o,\eta_o)\sin j\phi_o\bar{\rho}d\phi_o\\&\qquad j=1,2,3,\ldots\end{aligned}\right\}\quad(11)$$

in which the integrations are carried over a small circular path with radius $\bar{r}=\bar{\rho}a$ (see Fig. 1), and $\bar{T}_c$ is the Green's function for four concentrated sources at $\xi=\pm\xi_o$, $\eta=\pm\eta_o$ in the form

$$\left.\begin{aligned}&\bar{T}_c(\xi,\eta,\xi_o,\eta_o)\\&=4\sum_{n=1,3,5}^{\infty}\left[\frac{1}{l}\frac{\cosh(l\eta_o)}{\cosh\left(l\frac{b}{2a}\right)}\sinh l\left(\eta-\frac{b}{2a}\right)\right]\\&\times\cos n\pi\xi\cos n\pi\xi_o\quad\text{for}\quad\eta\geq\eta_o,\\&\bar{T}_c(\xi,\eta,\xi_o,\eta_o)\\&=4\sum_{n=1,3,5}^{\infty}\left[-\frac{1}{l}\frac{\sinh l\left(\frac{b}{2a}-\eta_o\right)}{\cosh\left(l\frac{b}{2a}\right)}\cosh(l\eta)\right]\\&\times\cos n\pi\xi\cos n\pi\xi_o\quad for\quad\eta_o>\eta>-\eta_o,\\&\bar{T}_c(\xi,\eta,\xi_o,\eta_o)\\&=-4\sum_{n=1,3,5}^{\infty}\left[\frac{1}{l}\frac{\cosh(l\eta_o)}{\cosh\left(l\frac{b}{2a}\right)}\sinh l\left(\eta+\frac{b}{2a}\right)\right]\\&\times\cos n\pi\xi\cos n\pi\xi_o\quad for\quad\eta\leq-\eta_o,\\&l=\sqrt{n^2\pi^2+K^2}.\end{aligned}\right\}\quad(12)$$

substituting

$$\left.\begin{aligned}\xi_o&=\bar{a}_c+\bar{\rho}\cos\phi_o,\\\eta_o&=\bar{b}_o+\bar{\rho}\sin\phi_o,\\\bar{a}_o&=\frac{a_o}{a},\quad\bar{b}_o=\frac{b_o}{a}\end{aligned}\right\}\quad(13)$$

into (12) and employing the results in Green's function, the integrations given in (11) are performed analytically. Thus, after a few steps, the functions $T_j^{**}$ and $T_j^{00}$ are obtained for the region $b/2a\geq\eta\geq\bar{b}_o+\bar{\rho}$. for example,

$$\left.\begin{aligned}T_{2j}^{**}&=4\sum_{n=1,3,5}^{\infty}\left[\frac{1}{l}\frac{\sinh l(\eta-b/2a)}{\cosh(lb/2a)}\cos n\pi\xi\right]\\&\times(-1)^j2\pi\bar{\rho}I_{2j}(K\bar{\rho})\cosh(2jb^*)\cos(n\pi\bar{a}_o)\cosh(l\bar{b}_o)\\b/2a\geq\eta\geq\bar{b}_o+\bar{\rho},\ b^*&=\ln\left[\frac{n\pi+\sqrt{n^2\pi^2+K^2}}{K}\right].\end{aligned}\right\}\quad(14)$$

Here in relation (14) $I_{2j}(K\bar{\rho})$ are modified Bessel functions of the first kind. However, for the regions $\|\eta|-\bar{b}_o|<\bar{\rho}$ the procedure does not lead to the determination of the functions in single series as the different forms of the Green's functions given in relations (12) have to be utilized. In order to eliminate this difficulty, the radius of the path of integration $\bar{\rho}$ is shrunk to zero. Considering now that

$$I_{2j}(K\bar{\rho})\sim\frac{(\tfrac{1}{2}K)^{2j}(\bar{\rho})^{2j}}{(2j)!}\quad\text{as}\quad\bar{\rho}\to0\qquad(15)$$

and absorbing the $n$ independent terms in the constants $A_j$ and $B_j$, the relations (14) and similar functions for the region $-\bar{b}_o<\eta<\bar{b}_o$ are simplified to

$$\left.\begin{aligned}T_{2j}^*&=(-1)^j\sum_{n=1,3,5}^{\infty}F_n(\xi,\eta)\cos(n\pi\bar{a}_o)\\&\times\cosh(l\bar{b}_o)\cosh(2jb^*),\\T_{2j-1}^*&=(-1)^j\sum_{n=1,3,5}^{\infty}F_n(\xi,\eta)\sin(n\pi\bar{a}_o)\\&\times\cosh(l\bar{b}_o)\sinh[(2j-1)b^*],\\T_{2j}^0&=(-1)^j\sum_{n=1,3,5}^{\infty}F_n(\xi,\eta)\sin(n\pi\bar{a}_o)\\&\times\sinh(l\bar{b}_o)\sinh(2jb^*),\\T_{2j-1}^0&=(-1)^{j+1}\sum_{n=1,3,5}^{\infty}F_n(\xi,\eta)\cos(n\pi\bar{a}_o)\\&\times\sinh(l\bar{b}_o)\cosh[(2j-1)b^*],\\F_n(\xi,\eta)&=\frac{\sinh[l(\eta-b/2a)]}{l\cosh(lb/2a)}\cos n\pi\xi,\\&\qquad b/2a\geq\eta\geq\bar{b}_o,\\\bar{T}_{2j}^*&=(-1)^j\sum_{n=1,3,5}^{\infty}G_n(\xi,\eta)\cos(n\pi\bar{a}_o)\\&\times\cosh(2jb^*)\sinh\left[l\left(\frac{b}{2a}-\bar{b}_o\right)\right],\end{aligned}\right\}$$

**Table 1 The nondimensional values of temperature $\bar{T}_m$ versus $\phi$ for two values of $\rho$ with $K_m = 1$, $\bar{\rho}_o = 0.0625$, $\bar{a}_o = 0.25$, $\bar{b}_o = 0.125$, $b/a = 0.5$, and $L/a = \pi$**

| $\phi$(rad) | $(1)\pi/24$ | $(9)\pi/24$ | $(17)\pi/24$ | $(25)\pi/24$ | $(33)\pi/24$ | $(41)\pi/24$ |
|---|---|---|---|---|---|---|
| $\bar{T}_m$ for $\rho=0.25/3$ | 0.7826 | 0.6435 | 0.6910 | 0.8615 | 0.9443 | 0.8930 |
| $\bar{T}_m$ for $\rho=0.3125/3$ | 0.6164 | 0.3568 | 0.4483 | 0.7594 | 0.9082 | 0.8117 |

$$\bar{T}^*_{2j-1} = (-1)^{j+1} \sum_{n=1,3,5}^{\infty} G_n(\xi,\eta)\sin(n\pi\bar{a}_o) \times \sinh[(2j-1)b^*]\sinh\left[l\left(\frac{b}{2a}-\bar{b}_o\right)\right],$$

$$\bar{T}^0_{2j} = (-1)^m \sum_{n=1,3,5}^{\infty} G_n(\xi,\eta)\sin(n\pi\bar{a}_o) \times \sinh(2jb^*)\cosh\left[l\left(\frac{b}{2a}-\bar{b}_o\right)\right],$$

$$\bar{T}^0_{2j-1} = (-1)^j \sum_{n=1,3,5}^{\infty} G_n(\xi,\eta)\cos(n\pi\bar{a}_o) \times \cosh[(2j-1)b^*]\cosh\left[l\left(\frac{b}{2a}-\bar{b}_o\right)\right]$$

$$G_n(\xi,\eta) = \frac{\cosh(l\eta)}{l\cosh\left(\frac{lb}{2a}\right)}\cos(n\pi\xi), \quad -\bar{b}_o < \eta < \bar{b}_o \tag{16}$$

Similar to the case of [5], there is, however, convergence problem for these functions at and near the lines $\eta = \pm \bar{b}_o$. To overcome this difficulty another set of functions in the system of coordinate axes $\bar{\xi} = (a/b)\eta$, $\bar{\eta} = (a/b)\xi$ are derived with a similar technique. The new set of functions which have good convergence properties at or near $\eta = \pm \bar{b}_o$ shall not be given here for the sake of brevity.

## Numerical Results

Since the functions $T^*_M$ and $T^0_M$ or $T^{(*)}_M$ and $T^{(0)}_M$ for $M = 0, 1, 2 \ldots$ automatically satisfy the homogeneous outer boundary condition, it is only necessary to satisfy the inner boundary condition (9). Due to the fact that the aforementioned functions are not orthogonal, the satisfaction of (9) is accomplished as follows: retaining $p$ terms in the series solution (10), and satisfying the boundary condition (9) at $P > p$ points on one of the symmetrical inner boundaries, a system of $P$ by $p$ linear algebraic equations is obtained. The system is normalized and solved approximately by the employment of the method of least-square error [6]. For all of the numerical results presented here $P$ and $p$ are chosen as 24 and 16, respectively. These numerical results are for the cases of rectangular bars with $L/a = \pi/2$, $\pi$, and $2\pi$. Other geometrical dimensions are selected as $b/a = 0.5$, $\rho_o = 0.0625$, $\bar{a}_o = 0.25$, and $\bar{b}_o = 0.125$. In Table 1 the nondimensional values of temperature versus $\phi$ (see Fig. 1) are given at $Z = 0$ along $\rho = 0.25/3$ and $\rho = 0.3125/3$ for the case of $T_i(Z) - T_w = T_o \cos \pi Z/L$. In Table 2 dimensionless values of the cross-sectional heat transfer rate components

**Table 2 The dimensionless values of heat transfer $\bar{Q}_m$ versus $K_m$ for $\bar{\rho}_o = 0.0625$, $\bar{a}_o = 0.25$, $\bar{b}_o = 0.125$, $b/a = 0.5$, and $L/a = \pi$**

| $K_m$ | $\bar{Q}_m$ | $K_m$ | $\bar{Q}_m$ | $K_m$ | $\bar{Q}_m$ |
|---|---|---|---|---|---|
| 1 | −17.267 | 15 | −34.556 | 29 | −56.943 |
| 3 | −18.304 | 17 | −37.734 | 31 | −60.137 |
| 5 | −20.172 | 19 | −40.930 | 33 | −63.327 |
| 7 | −22.599 | 21 | −44.134 | 35 | −66.514 |
| 9 | −25.367 | 23 | −47.339 | 37 | −69.697 |
| 11 | −28.333 | 25 | −50.544 | | |
| 13 | −31.412 | 27 | −53.745 | | |

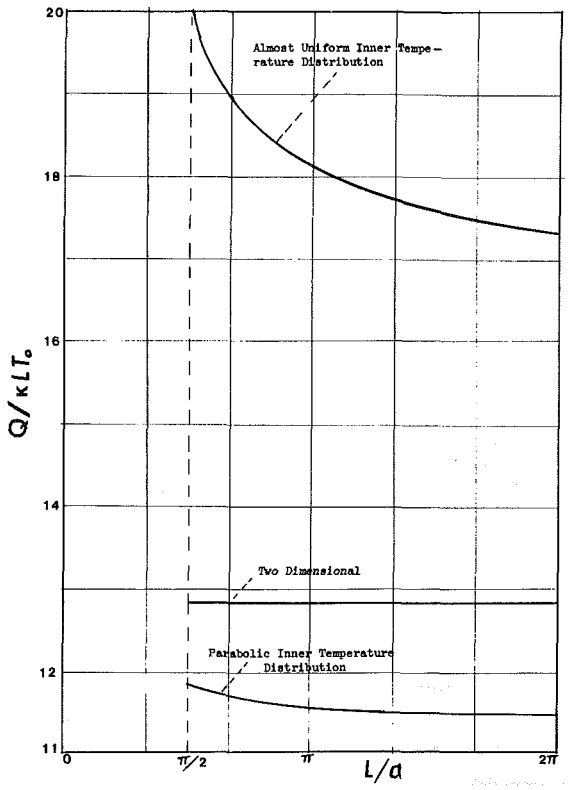


**Fig. 2 Nondimensional rate of heat transfer $Q/(kLT_o)$ versus $L/d$ for various cases**

$$\bar{Q}_m = 4\int_0^{2\pi}\left(\frac{\partial T_m}{\partial \rho}\right)_{\rho=\rho_o}\rho_o d\phi \tag{17}$$

are presented for various $m$ and for $L/a = \pi$. The actual values of heat transfer rate components $Q_m$ are obtained from

$$Q_m = 4\int_0^{2\pi}\int_{-L/2}^{L/2} -K\left(\frac{\partial T_m}{\partial r}\right)_{r=r_o}\cdot\cos\frac{m\pi Z}{L}\, r_o dz d\phi$$

$$= -2kL(T_{im}-T_{wm})\frac{\sin(m\pi/2)}{m\pi}\cdot\bar{Q}_m, \quad m = 1,3,5 \tag{18}$$

in which $k$ is the thermal conductivity of the material of the bar.

Knowing the values of $Q_m$, the total heat transfer per unit time can be calculated easily for a number of inner temperature distribution cases. At this point it should be reminded that according to the previous assumptions, one must have $T_i(z) - T_w = 0$ at $Z = \pm L/2$. For this reason the exact solution for a rectangular parallelopiped subject to two different uniform inner and outer boundary temperatures should not be sought. However, for comparison of the heat transfer rates between the two- and three-dimensional cases, the truncated and almost uniform inner temperature distribution is the most suitable. This temperature distribution is constructed from a finite number of terms in the Fourier series expansion of a uniform temperature. Retaining 19 terms in such a series the relative error in the temperature is about 0.02 or smaller for the span of 80 percent of the length of the bar. Another interesting inner boundary temperature distribution is $T_i(Z) - T_w = T_o\ (L^2/4 - Z^2)$. In Fig. 2, the nondimensional total heat transfer rates $Q/(kLT_o)$ versus $L/a$ are presented for the two-dimensional and the aforementioned three-dimensional cases. It is observed that the heat transfer rates for the case of approximately uniform inner temperature distribution are much higher than that of the two-dimensional case. However, these values decrease as $L/a$ increases, and it is expected that for long bars they approach the two-dimensional heat transfer rate.


### Acknowledgment

The author wishes to thank the Department of Computing Services of IUPUI for providing CDC 6600 computer time for this investigation.


## References


1 Rowley, J. C., and Payne, J. B., "Steady-State Temperature Solution for a Heat Generating Circular Cylinder Cooled by a Ring of Holes," ASME JOURNAL OF HEAT TRANSFER, Vol. 86, pp. 531–536.

2 Ling, C. B., "Torsion of a Circular Tube with Longitudinal Circular Holes," *Quart. Appl. Math.*, Vol. 5, No. 2, July 1947, pp. 168–181.

3 Kuo, Y-M., and Conway, H. D., "The Torsion of Composite Tubes and Cylinders," *International Journal of Solids and Structures*, Vol. 9, 1973, pp. 1553–1566.

4 Naghdi, A. K., "Solution of Poisson's Equation in a Rectangular Region with Multiple Holes," *Proceedings of the Tenth South Eastern Conference on Theoretical and Applied Mechanics*, Vol. 10, April 1980, pp. 151–161.

5 Naghdi, A. K., "Cerain Heat Transfer Problems in a Rectangular Region with Multiple Cutouts," *International Journal of Heat and Mass Transfer*, Vol. 26, No. 8, 1983, pp. 1143–1149.

6 Hildebrand, F. B., *Introduction to Numerical Analysis*, McGraw-Hill, New York, 1956.


# Use of a Boundary-Fitted Coordinate Transformation for Unsteady Heat Conduction Problems in Multiconnected Regions With Arbitrarily Shaped Boundaries


**S. Uchikawa[1] and R. Takeda[1]**


## 1 Introduction

Heat transfer analyses are essential for mechanical design and manufacturing. Various numerical techniques to solve heat conduction equations have been developed; among these the finite difference approach is the most straightforward. However, many real problems involve irregular boundaries which require interpolation between boundaries and interior grid points. Such interpolations are inaccurate and produce large errors at boundary vicinities. Alternatively, the finite element approach is powerful in dealing with geometric complexity. However, one of its more serious problems is division into finite elements. This division cannot always be done automatically, and it requires considerable experience.

Another approach to dealing with geometric complexity is the use of a curvilinear coordinate transformation, where a computational domain of an arbitrarily shape is mapped onto a simply shaped domain in the transformed coordinate system. Thompson et al. [1] have proposed a technique for automatic numerical generation of a general curvilinear coordinate system with coordinate lines coincident with all boundaries of the arbitrarily shaped domains and have successfully applied it to fluid mechanic problems. McWhorter and Sadd [2, 3] applied the method to steady and transient anisotropic heat conduction problems. Goldman and Kao [4] discussed the application of several coordinate transformations to solve a simple unsteady conduction problem. Rieger et al. [5] applied the method to phase-change problems. A large portion of the aforementioned work concerned problems where only one region with irregular boundaries was a direct object of computation.

The present paper deals with the extension of this coordinate transformation technique to unsteady heat conduction problems in two-dimensional, multiconnected, heterogeneous regions with arbitrarily shaped boundaries, and application to a solidification problem in a large steel casting.

## 2 Method

**(a) Boundary-Fitted Coordinate Transformation.** Consider transforming the two-dimensional regions I and II, bounded by two arbitrarily shaped boundaries $\Gamma_1$ and $\Gamma_2$, onto simple rectangular regions, as illustrated in Fig. 1. The basic idea of the transformation is to make all boundaries coincide with coordinate lines in the transformed plane. The transformation from the physical plane $(x, y)$ to the transformed plane $(\xi, \eta)$ is given by $\xi = \xi(x, y)$ and $\eta = \eta(x, y)$, where $\xi$ and $\eta$ are solutions of an elliptic equation with Dirichlet boundary conditions of the form

$$\frac{\partial^2 \xi}{\partial x^2} + \frac{\partial^2 \xi}{\partial y^2} = P(\xi,\eta) \tag{1a}$$

$$\frac{\partial^2 \eta}{\partial x^2} + \frac{\partial^2 \eta}{\partial y^2} = Q(\xi,\eta) \tag{1b}$$

where $P(\xi, \eta)$ and $Q(\xi, \eta)$ are coordinate control functions [6].

Since all numerical computations are performed in the rectangular transformed plane, the dependent $(\xi, \eta)$ and independent $(x, y)$ variables must be interchanged in equation (1). This results in the coupled system

$$\alpha \frac{\partial^2 x}{\partial \xi^2} - 2\beta \frac{\partial^2 x}{\partial \xi \partial \eta} + \gamma \frac{\partial^2 x}{\partial \eta^2} + J^2 P(\xi,\eta) \frac{\partial x}{\partial \xi} + J^2 Q(\xi,\eta) \frac{\partial x}{\partial \eta} = 0 \tag{2a}$$

$$\alpha \frac{\partial^2 y}{\partial \xi^2} - 2\beta \frac{\partial^2 y}{\partial \xi \partial \eta} + \gamma \frac{\partial^2 y}{\partial \eta^2} + J^2 P(\xi,\eta) \frac{\partial y}{\partial \xi} + J^2 Q(\xi,\eta) \frac{\partial y}{\partial \eta} = 0 \tag{2b}$$

where


[1]Energy Research Laboratory, Hitachi Ltd., Ibaragi 316, Japan

Knowing the values of $Q_m$, the total heat transfer per unit time can be calculated easily for a number of inner temperature distribution cases. At this point it should be reminded that according to the previous assumptions, one must have $T_i(z) - T_w = 0$ at $Z = \pm L/2$. For this reason the exact solution for a rectangular parallelopiped subject to two different uniform inner and outer boundary temperatures should not be sought. However, for comparison of the heat transfer rates between the two- and three-dimensional cases, the truncated and almost uniform inner temperature distribution is the most suitable. This temperature distribution is constructed from a finite number of terms in the Fourier series expansion of a uniform temperature. Retaining 19 terms in such a series the relative error in the temperature is about 0.02 or smaller for the span of 80 percent of the length of the bar. Another interesting inner boundary temperature distribution is $T_i(Z) - T_w = T_o\ (L^2/4 - Z^2)$. In Fig. 2, the nondimensional total heat transfer rates $Q/(kLT_o)$ versus $L/a$ are presented for the two-dimensional and the aforementioned three-dimensional cases. It is observed that the heat transfer rates for the case of approximately uniform inner temperature distribution are much higher than that of the two-dimensional case. However, these values decrease as $L/a$ increases, and it is expected that for long bars they approach the two-dimensional heat transfer rate.


### Acknowledgment

The author wishes to thank the Department of Computing Services of IUPUI for providing CDC 6600 computer time for this investigation.


### References


1 Rowley, J. C., and Payne, J. B., "Steady-State Temperature Solution for a Heat Generating Circular Cylinder Cooled by a Ring of Holes," ASME JOURNAL OF HEAT TRANSFER, Vol. 86, pp. 531–536.

2 Ling, C. B., "Torsion of a Circular Tube with Longitudinal Circular Holes," *Quart. Appl. Math.*, Vol. 5, No. 2, July 1947, pp. 168–181.

3 Kuo, Y-M., and Conway, H. D., "The Torsion of Composite Tubes and Cylinders," *International Journal of Solids and Structures*, Vol. 9, 1973, pp. 1553–1566.

4 Naghdi, A. K., "Solution of Poisson's Equation in a Rectangular Region with Multiple Holes," *Proceedings of the Tenth South Eastern Conference on Theoretical and Applied Mechanics*, Vol. 10, April 1980, pp. 151–161.

5 Naghdi, A. K., "Cerain Heat Transfer Problems in a Rectangular Region with Multiple Cutouts," *International Journal of Heat and Mass Transfer*, Vol. 26, No. 8, 1983, pp. 1143–1149.

6 Hildebrand, F. B., *Introduction to Numerical Analysis*, McGraw-Hill, New York, 1956.


## Use of a Boundary-Fitted Coordinate Transformation for Unsteady Heat Conduction Problems in Multiconnected Regions With Arbitrarily Shaped Boundaries


**S. Uchikawa[1] and R. Takeda[1]**


### 1 Introduction

Heat transfer analyses are essential for mechanical design and manufacturing. Various numerical techniques to solve heat conduction equations have been developed; among these the finite difference approach is the most straightforward. However, many real problems involve irregular boundaries which require interpolation between boundaries and interior grid points. Such interpolations are inaccurate and produce large errors at boundary vicinities. Alternatively, the finite element approach is powerful in dealing with geometric complexity. However, one of its more serious problems is division into finite elements. This division cannot always be done automatically, and it requires considerable experience.

Another approach to dealing with geometric complexity is the use of a curvilinear coordinate transformation, where a computational domain of an arbitrarily shape is mapped onto a simply shaped domain in the transformed coordinate system. Thompson et al. [1] have proposed a technique for automatic numerical generation of a general curvilinear coordinate system with coordinate lines coincident with all boundaries of the arbitrarily shaped domains and have successfully applied it to fluid mechanic problems. McWhorter and Sadd [2, 3] applied the method to steady and transient anisotropic heat conduction problems. Goldman and Kao [4] discussed the application of several coordinate transformations to solve a simple unsteady conduction problem. Rieger et al. [5] applied the method to phase-change problems. A large portion of the aforementioned work concerned problems where only one region with irregular boundaries was a direct object of computation.

The present paper deals with the extension of this coordinate transformation technique to unsteady heat conduction problems in two-dimensional, multiconnected, heterogeneous regions with arbitrarily shaped boundaries, and application to a solidification problem in a large steel casting.

### 2 Method

**(a) Boundary-Fitted Coordinate Transformation.** Consider transforming the two-dimensional regions I and II, bounded by two arbitrarily shaped boundaries $\Gamma_1$ and $\Gamma_2$, onto simple rectangular regions, as illustrated in Fig. 1. The basic idea of the transformation is to make all boundaries coincide with coordinate lines in the transformed plane. The transformation from the physical plane $(x, y)$ to the transformed plane $(\xi, \eta)$ is given by $\xi = \xi(x, y)$ and $\eta = \eta(x, y)$, where $\xi$ and $\eta$ are solutions of an elliptic equation with Dirichlet boundary conditions of the form

$$\frac{\partial^2 \xi}{\partial x^2} + \frac{\partial^2 \xi}{\partial y^2} = P(\xi,\eta) \tag{1a}$$

$$\frac{\partial^2 \eta}{\partial x^2} + \frac{\partial^2 \eta}{\partial y^2} = Q(\xi,\eta) \tag{1b}$$

where $P(\xi, \eta)$ and $Q(\xi, \eta)$ are coordinate control functions [6].

Since all numerical computations are performed in the rectangular transformed plane, the dependent $(\xi, \eta)$ and independent $(x, y)$ variables must be interchanged in equation (1). This results in the coupled system

$$\alpha \frac{\partial^2 x}{\partial \xi^2} - 2\beta \frac{\partial^2 x}{\partial \xi \partial \eta} + \gamma \frac{\partial^2 x}{\partial \eta^2} + J^2 P(\xi,\eta) \frac{\partial x}{\partial \xi} + J^2 Q(\xi,\eta) \frac{\partial x}{\partial \eta} = 0 \tag{2a}$$

$$\alpha \frac{\partial^2 y}{\partial \xi^2} - 2\beta \frac{\partial^2 y}{\partial \xi \partial \eta} + \gamma \frac{\partial^2 y}{\partial \eta^2} + J^2 P(\xi,\eta) \frac{\partial y}{\partial \xi} + J^2 Q(\xi,\eta) \frac{\partial y}{\partial \eta} = 0 \tag{2b}$$

where


[1]Energy Research Laboratory, Hitachi Ltd., Ibaragi 316, Japan

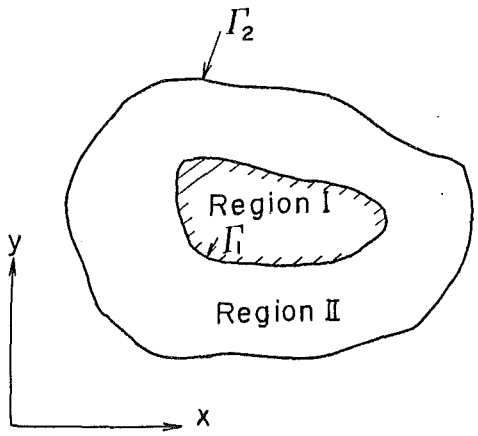


(a) Physical plane

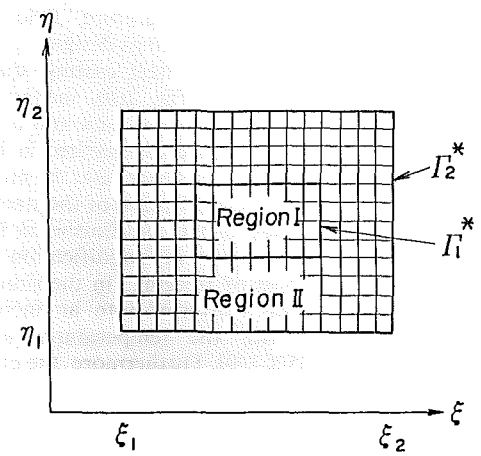


(b) Transformed plane

**Fig. 1 Boundary-fitted coordinate transformation**

$$\alpha = x_\eta^2 + y_\eta^2, \qquad \beta = x_\xi x_\eta + y_\xi y_\eta$$
$$\gamma = x_\xi^2 + y_\xi^2, \qquad J = x_\xi y_\eta - x_\eta y_\xi \tag{2c}$$

The subscripts $\xi$ and $\eta$ in equations (2c) denote first partial derivatives with respect to $\xi$ and $\eta$. The quantity J is the Jacobian of the transformation.

For most heat conduction problems in the field of mechanical design and manufacturing, it is desirable to perform computations in all regions bounded by the outer boundary contour. Thus both regions I and II must be transformed onto the $(\xi, \eta)$ plane. One such transformation, often called the slab form [7], is shown in Fig. 1(*b*). The inner boundary contour $\Gamma_1$ maps onto the rectangular boundary $\Gamma_1^*$ in the transformed plane, and $\Gamma_2$ maps onto $\Gamma_2^*$. In this transformation, one boundary contour is divided into two $\xi$-constant coordinate lines and two $\eta$-constant lines. Thus the transformed boundary conditions of equation (2) become

$$x = x_1(\xi_{b1}, \eta_{b1}), \quad y = y_1(\xi_{b1}, \eta_{b1}) \quad \text{on} \quad \Gamma_1{}^*,$$
$$x = x_2(\xi_{b2}, \eta_{b2}), \quad y = y_2(\xi_{b2}, \eta_{b2}) \quad \text{on} \quad \Gamma_2{}^*$$

where $(\xi_{bi}, \eta_{bi})$ represents points on the transformed boundary $\Gamma_i^*$. This transformation retains the essential feature that all boundaries are coincident with coordinate lines. This transformation has been successfully applied to neutron diffusion problems in nuclear reactors by Uchikawa [8].

**(*b*) Equations of Unsteady Heat Conduction Problem.** The unsteady heat conduction equation in the $(x, y)$ plane is given by

$$\rho c \frac{\partial T}{\partial t} = \frac{\partial}{\partial x}\left(k \frac{\partial T}{\partial x}\right) + \frac{\partial}{\partial y}\left(k \frac{\partial T}{\partial y}\right) + S \tag{3}$$

where $T$ = temperature, $\rho$ = mass density, $c$ = specific heat, $k$ = thermal conductivity, and $S$ = heat generation rate. The boundary condition takes a general form

$$C_1 T(S) + C_2 \mathbf{n} \cdot K \nabla T(S) = C_3 \tag{4}$$

where $c_i$ can be chosen to produce specified temperature, specified heat flux, or convection boundary conditions, $s$ denotes the outer boundary surface, and $\mathbf{n}$ is the unit vector normal to the surface.

In general, the following relations hold for the coordinate transformation

$$\frac{\partial f}{\partial x} = \frac{1}{J} y_\eta \frac{\partial f}{\partial \xi} - \frac{1}{J} y_\xi \frac{\partial f}{\partial \eta}$$
$$\frac{\partial f}{\partial y} = -\frac{1}{J} x_\eta \frac{\partial f}{\partial \xi} + \frac{1}{J} x_\xi \frac{\partial f}{\partial \eta} \tag{5}$$

where $f$ is an arbitrary function. Equation (3) is transformed utilizing the operation of equation (5). The equation applicable in the transformed plane is

$$\rho c J \frac{\partial T}{\partial t} = \frac{\partial}{\partial \xi}\left(\frac{\alpha}{J} k \frac{\partial T}{\partial \xi} - \frac{\beta}{J} k \frac{\partial T}{\partial \eta}\right) + \frac{\partial}{\partial \eta}\left(\frac{\gamma}{J} k \frac{\partial T}{\partial \eta} - \frac{\beta}{J} k \frac{\partial T}{\partial \xi}\right) + JS \tag{6}$$

where $\alpha$, $\beta$, $\gamma$, and J are as stated in equation (2c). All of the coefficients $\alpha$, $\beta$, etc., are calculated as a part of the coordinate transformation and are known quantities. It should be noted here that the form of equation (6) is independent of the methods of coordinate transformation and suitable for obtaining the difference equations. The boundary condition, equation (4) is expressed in the transformed plane as follows

$$c_1 T - c_2 \frac{k}{J\alpha^{1/2}}\left\{\alpha \frac{\partial T}{\partial \xi} - \beta \frac{\partial T}{\partial \eta}\right\} = c_3 \quad \text{at} \quad \xi = \xi_1$$
$$c_1 T + c_2 \frac{k}{J\alpha^{1/2}}\left\{\alpha \frac{\partial T}{\partial \xi} - \beta \frac{\partial T}{\partial \eta}\right\} = c_3 \quad \text{at} \quad \xi = \xi_2$$
$$c_1 T - c_2 \frac{k}{J\gamma^{1/2}}\left\{\gamma \frac{\partial T}{\partial \eta} - \beta \frac{\partial T}{\partial \xi}\right\} = c_3 \quad \text{at} \quad \eta = \eta_1$$
$$c_1 T + c_2 \frac{k}{J\gamma^{1/2}}\left\{\gamma \frac{\partial T}{\partial \eta} - \beta \frac{\partial T}{\partial \xi}\right\} = c_3 \quad \text{at} \quad \eta = \eta_2 \tag{7}$$

The above formulations can be applied to the problems of axisymmetric geometry with minor modifications.

The transformed heat conduction equation (6) with the boundary conditions (equation (7)) is solved numerically in the $(\xi, \eta)$ plane by using a finite difference approximation with a uniform mesh width.

## 3 Applications of the Method

***(a)* Simulation of Solidification in Casting.** In order to demonstrate the actual implementation of the method to solution of engineering problems, the method was applied to a numerical simulation of solidification in a large steel casting.

Solidification in castings is one of heat conduction phenomena in multiconnected regions with irregular shaped boundaries, i.e., between a cast metal region and a mould. In the design of casting, it is necessary to avoid shrinkage cavities in castings. Presently, occurrence of such cavities are predicted in some degree from the temperature gradients at the time of solidification [9, 10]. Therefore a detailed

**Table 1**

1) Property constants

| | Density ($g/cm^3$) | Thermal conductivity ($W/cm \cdot °C$) | Specific heat*1) ($J/g \cdot °C$) | | | | |
|---|---|---|---|---|---|---|---|
| | | | above 1505°C | 1505°C -1499°C | 1499°C -1486°C | 1486°C -1450°C | below 1450°C |
| cast steel | 7.3 | 0.335 | 0.67 | 14.27 | 8.00 | 3.32 | 0.67 |
| mould | 1.5 | 0.0126 | 1.130 | | | | |

*1) The effects of the latent heat are taken into account by the variation of specific heat within the temperature range of solidification (1450–1505°C)

2) Boundary condition

| Boundary | Gap conductance ($W/cm^2 °C$) |
|---|---|
| cast steel – mould | ∞ |
| mould – open air | 0.00209 |

3) Initial condition

| | Temperature (°C) |
|---|---|
| cast steel | 1540 |
| mould | 20 |

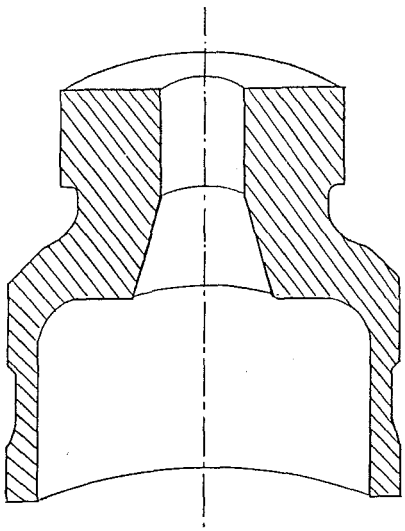

(a) Sketch of casting

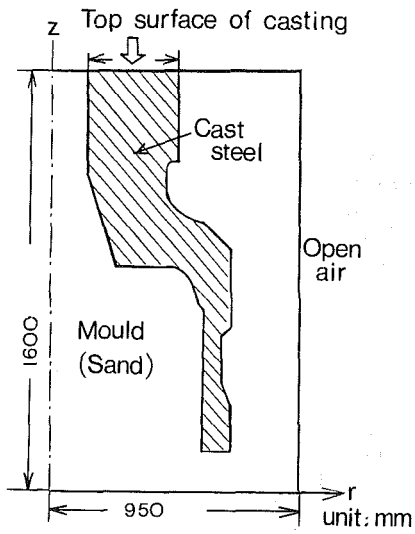


(b) Cross-section of mould

**Fig. 2 The axisymmetric steel casting chosen for the present simulation study**

numerical simulation of the temperature field during solidification is an essential part in castings design.

The shape of the axisymmetric steel casting studied is shown in Fig. 2(*a*). As shown in Fig. 2(*b*), melted steel is poured into a sand mould. The property data and boundary conditions used in the simulation are summarized in Table 1. The initial temperatures of the melted steel and the mould are 1540 and 20°C, respectively. Solidification of the steel begins when the temperature reaches 1505°C and finishes at 1450°C. One of the important features in solidification is the generation of the latent heat of freezing. In the simulation, latent heat of freezing was converted into an increase of apparent specific heat with the temperature range of solidification (1450 ~ 1505°C) [9]. Furthermore, the effects of natural convection were ignored in the study.

The mould is exposed to air at the outer boundary. A thermal convection condition is applied at the outer boundary between the mould and the open air, except at the top surface of the casting, where the adiabatic condition is applied. The temperature of the open air is given as 20°C. At the inner boundary between the cast steel and mould, it is assumed that the perfect contact condition holds, that is, the temperature and heat flux are continuous at the boundary.

**(*b*) Control of Curvilinear Coordinate.** A transformation from the physical $(r, z)$ to the transformed $(\xi, \eta)$ plane used in the simulation is indicated in Figs. 3(*a*) and 3(*b*). The irregular inner boundary between the cast steel and the mould in the physical plane (A-B-C-D-E-F-G) is transformed to the simple boundary. Assignment of the boundary in the transformed plane can be done in an arbitrary manner. In this case, the boundary A-B-C is transformed to the straight boundary, so that $\xi$-constant coordinate lines in the cast steel region lie along the boundary. The resulting curvilinear coordinate grids are plotted in Fig. 3(*c*). In the transformation of Fig. 3(*c*), the coordinate control functions, $P(\xi, \eta)$ and $Q(\xi, \eta)$ appearing in equation (1), are set to zero. As seen in Fig. 3(*c*), the $\xi$-constant coordinate line just outside the boundary A-B-C lies away from the boundary, in particular above a concave portion of the boundary near the point B.

The attraction of coordinate lines to the specified boundaries or points is accomplished by varying the functions $P(\xi, \eta)$ and $Q(\xi, \eta)$. For control of the $\xi$-constant lines, the following form of the function $P(\xi, \eta)$ was used

$$P(\xi,\eta) = -a\,\mathrm{sgn}(\xi-\xi_1)\exp(-C|\xi-\xi_1|) - b\,\mathrm{sgn}(\xi-\xi_B)\exp(-d\sqrt{(\xi-\xi_B)^2+(\eta-\eta_B)^2}) \quad (8)$$

The first term has the effect of attracting $\xi$-constant lines to the boundary A-B-C ($\xi = \xi_1$). The second term causes con-

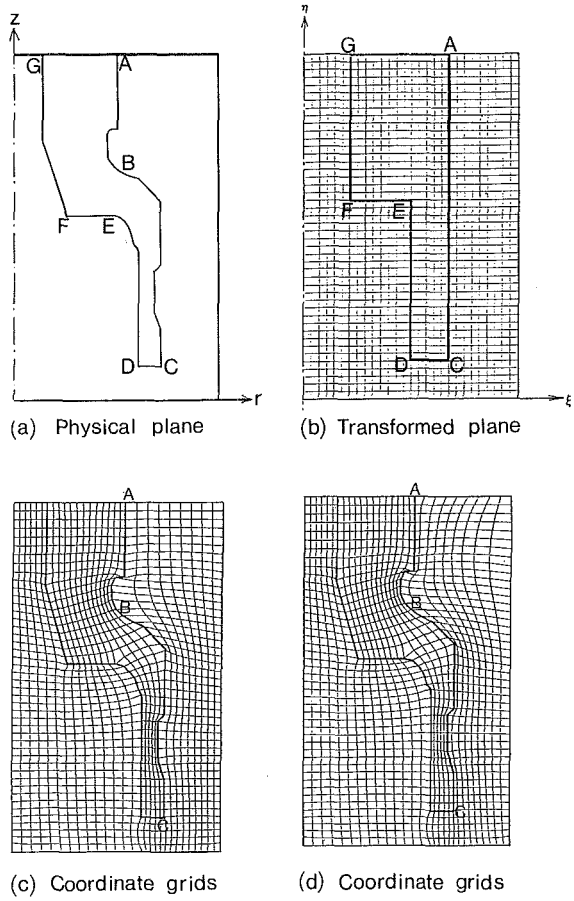


**Fig. 3 Boundary-fitted coordinate transformation of the casting geometry**

stant lines to be attracted to the point B ($\xi_B$, $\eta_B$). The parameters $a$, $b$, $c$, and $d$ were searched and set to 300, 50, 9.0, and 1.0, respectively. The resulting curvilinear coordinate grids are plotted in Fig. 3($d$). In this case, most of the $\xi$-constant lines are attracted to the boundary A-B-C, in constrast to the case shown in Fig. 3($c$).

In the foregoing coordinate transformation, special caution must be paid to the grids near the point E, at which the physical boundary is smooth, but the species of coordinate lines change. In the solution of equation (6), a special procedure was used by defining a local pair of coordinate lines at the point E, as discussed in [7].

**($c$) Results for Temperature Field.** Variation in the temperature field after pouring the melted steel into the mould was simulated using the coordinate transformation shown in Fig. 3($d$). The isothermal lines over the cast steel are presented in Fig. 4, at two different times after pouring.

Solidification begins in the portions facing the boundary with the mould, and one hour after pouring, solidification has proceeded througout the entire region of the cast. However, during solidification, the rate of temperature drop is slow due to the latent heat generation. With respect to the shrinkage cavities, it has been observed that these usually occur in areas where the temperature gradient at the time of solidification is below a certain degree (~2°C/cm) [9]. Figure 4($a$) shows that the temperature field has two peaks, which means that there are two points at which the temperature gradient is zero. The simulation predicts that shrinkage cavities may occur near the region indicated by the dashed circle shown in the figure. To avoid these, materials with high thermal conductivity are buried in the mould region near the boundary to eliminate this area of low temperature gradient.

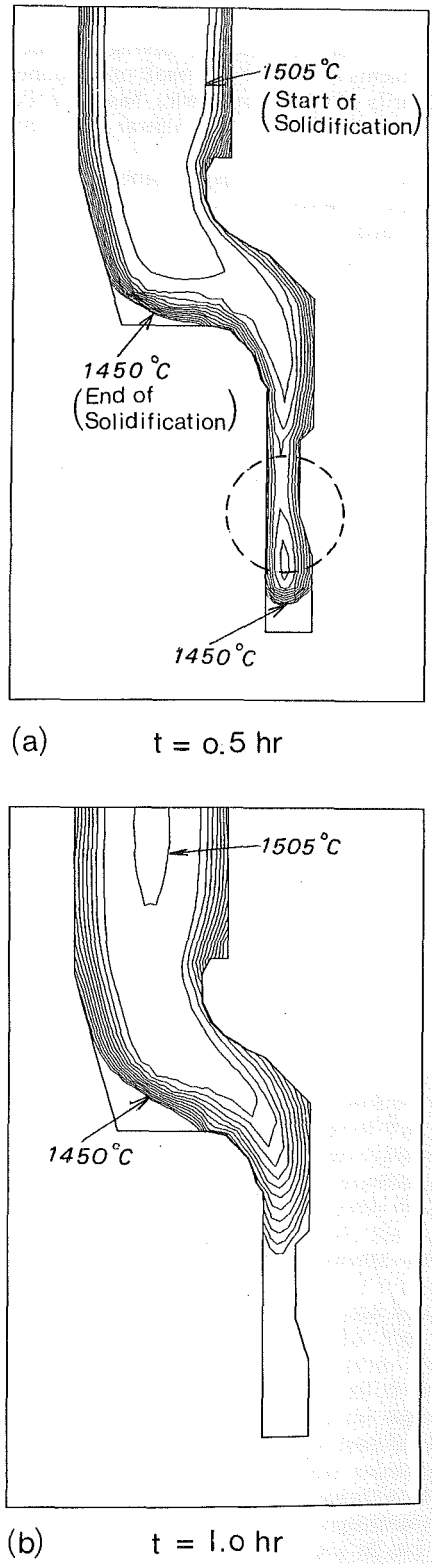


**Fig. 4 Temperature fields during solidification in the casting. The spacing of isothermal lines is 5°C. The dashed line indicates the region where shrinkage cavities may occur.**

One of the features of the present solution is that it can treat the irregular boundaries accurately, and in particular conserve the length or the surface of the boundaries. This feature is desirable in predicting the temperature field in castings where the influx or outflux of heat at the boundary is essential. This application confirms that the present solution is very useful in engineering problems.

## 4 Conclusion

A procedure for numerically solving unsteady heat conduction problems in two-dimensional, multiconnected regions with arbitrarily shaped boundaries has been developed by using a boundary-fitted curvilinear coordinate transformation.

Each region with arbitrarily shaped boundaries in the physical plane is transformed onto a simply shaped region in the transformed plane. The coordinate transformation is given as solutions of an elliptic equation with Dirichlet boundary conditions. The heat conduction equation is also transformed, and solved in the rectangular coordinate system where some of the straight coordinate lines represent the boundaries, to insure accurate representation of the boundary conditions.

The present solution was applied to predicting the temperature fields during solidification in a large steel casting. The results demonstrated that it has good potential applicability to solving various engineering problems. Major advantages of the present method include geometric versatility and automatic generation of coordinate grids, which is suitable for implementation to a CAD system.


## Acknowledgments

The authors' appreciation is expressed to K. Taniguchi, S. Yamada, and S. Kobayashi of Energy Research Laboratory, Hitachi Ltd. for their encouragement during this work. Acknowledgments are also due to E. Niiyama of Hitachi Research Laboratory, Hitachi Ltd. for his valuable discussion.


## References


1 Thompson, J. F., Thames, F. C., and Mastin, C. W., "Automatic Numerical Generation of Body-Fitted Curvilinear Coordinate System for Field Containing Any Number of Arbitrary Two-Dimensional Bodies," *J. Comp. Phys.*, Vol. 15, 1974, pp. 299–319.

2 Mcwhorter, J. C., and Sadd, M. H., "Numerical Anisotropic Heat Conduction Solutions using Boundary-Fitted Coordinate Systems," ASME Paper No. 79-WA/HT-41.

3 Sadd, M. H., and McWhoter, J. C., "Transient Anisotropic Heat Conduction Solutions Using the Boundary-Fitted Coordinate Method," *Proc. 10th Southeastern Conf. Theo. & Appli. Mech.*, Vol. 10, Univ. of Tenn., 1980, pp. 541–545.

4 Goldmann, A., and Kao, Y. C., "Numerical Solution to a Two-Dimensional Conduction Problem Using Rectangular and Cylindrical Body-Fitted Coordinate Systems," ASME JOURNAL OF HEAT TRANSFER, Vol. 103, 1981, pp. 753–756.

5 Rieger, H., Projahn, U., and Beer, H., "Analysis of the Heat Transport Mechanisms during Melting around a Horizontal Circular Cylinder," *Int. Journal of Heat and Mass Transfer*, Vol. 25, 1982, pp. 137–147.

6 Thompson, J. F., Thames, F. C., and Mastin, C. W., "Boundary-Fitted Curvilinear Coordinate System for Solution of Partial Differential Equations on Fields Containing any Number of Arbitrary Two-Dimensional Bodies," NASA CR-2729, 1976.

7 Thompson, J. F., "General Curvilinear Coordinate Systems," *Numerical Grid Generation*, edited by J. F. Thompson, North-Holland, 1982, pp. 1–30.

8 Uchikawa, S., "Use of Boundary-Fitted Coordinate Transformation in Neutron Diffusion Calculations for Arbitrary Two-Dimensional Geometries," *Nucl. Sci. Eng.*, Vol. 85, 1983, pp. 36–44.

9 Niiyama, E., et al., "Predicting Shrinkage in Large Steel Castings (in Japanese)," *Imono*, Vol. 52, 1981, pp. 636–640.

10 Niyama, E., et al., "A Method of Shrinkage Prediction and Its Application to Steel Casting Practice," *AFS International Cast Metal Journal*, Vol. 7, 1982, pp. 52–63.

Journal of Heat Transfer

# Discussion

## The Latent Heat of Vaporization of a Widely Diverse Class of Fluids[1]

**H. Soumerai.**[2] The existence of a universal expression in the entire domain $T_t < T < T_c$ for the scaled latent heat $\lambda = L/L_t$ in terms of a dimensionless temperature $\tau \equiv (T_c - T)/(T_c - T_t) = \{(T_c - T)/T_c\}/\{(T_c - T_t)/T_c\} \equiv t/t_t$ demonstrated in this excellent technical note is particularly remarkable in view of the fact that some polar fluids are also included among the 20 different substances considered in this study. Most earlier generalization methods such as [1] and [2] systematically exclude strongly polar molecules.

It might further strengthen their case for the validity of a *universal expression* such as equation (2) if the authors could clarify the following points:

- What is the estimated accuracy of the data used in this study?
- It is stated that "less than half" of the latent heat values at the triple point, $L_t$, were computed as indicated on p. 253. It would be useful to identify exactly which of the 20 fluids listed in Table 1 were obtained in this manner.
- As the authors of [1] corroborated (footnote p. 3440 of [1]) the results obtained along the saturation curves by Riedel [2] on the basis of a much larger number of substances (more than 100 different fluids are listed in Table 10, p. 263 of [2]), it would be desirable to know how the results obtained from equation (2) compare with those of Riedel's Table 3 on p. 681 of [2].

In many two-phase heat transfer applications such as nucleate and/or forced convection boiling (or condensation) the best correlations proposed to date for the heat transfer coefficient $h_{tp}$ are valid with deviations of over 20 to 50 percent [3–7] or *one order of magnitude larger* than the 2 to 5 percent deviation for $\lambda$ shown on p. 253 of Torquato and Smith's paper for the two fluids bounding the latent heat curve of water. Since the molar latent heat $mL$ (where $m$ is the molar weight) and the molar entropy change $mL/T$ are key parameters in *all* two-phase heat transfer correlations [3–9], the existence of a universal correlation such as equation (2) provides, in spite of insignificant deviations of the order of 2 to 5 percent, additional support for the validity of the extremely simple and effective methods of generalizations based on thermodynamic corresponding states considerations proposed in [3–7].

It should be further noted that in many normal engineering applications, for instance in the case of refrigeration/heat pump evaporator designs, the refrigerant will always operate above the triple point but *significantly* below the critical point, i.e., at reduced pressures $P^+ = P/P_c << 1$ (in order to obtain acceptable cycle coefficients of performance) or at $\tau$ values of $0.5 \lesssim \tau \lesssim 1$ in the upper range of Fig. 1 when the deviations of corresponding states generalizations become insignificant [11]. It is then possible to generalize empirical data obtained with *one reference fluid* simply on the basis of *reduced pressure* $P^+$ [3, 7] because both the molar latent entropy change $mL/T$ and the specific volume ratio $v'/v'' = \rho''/\rho'$ (where $\rho = 1/v \equiv$ density; $'$ and $''$ refer respectively to the liquid and vapor phase at saturation) can be expressed as universal functions of $P^+$ as shown in Figs. 1 and 2, reproduced here from [3]. It is evident from Fig. 2 that a single common curve can be plotted for all the halogenated refrigerants with a negligible error up to the highest reduced pressures of 0.2 to 0.3 normally encountered in refrigeration cycles. Even a most "dissimilar" polar substance such as water deviates only slightly (about 12 percent and less than 5 percent at reduced pressures of respectively 0.2 and $< 0.001$!), compared to the best accuracy of any correlation for $h_{tp}$, from the average universal curve for the halogenated refrigerants. It is also noteworthy that the molar latent heat generalization method recommended by Riedel (Table 3, p. 681 of [2]) yields the same results as shown in Fig. 2.

The significant fact that the molar latent entropy change as well as the ratio $v'/v'' = \rho''/\rho'$ are *universal functions* of $P^+$ provides a more fundamental rationale for the validity of the thermodynamic generalization methods for two-phase forced convection with condensation or evaporation and nucleate boiling, when interpreted in the light of classical and irreversible thermodynamic considerations or, conversely,

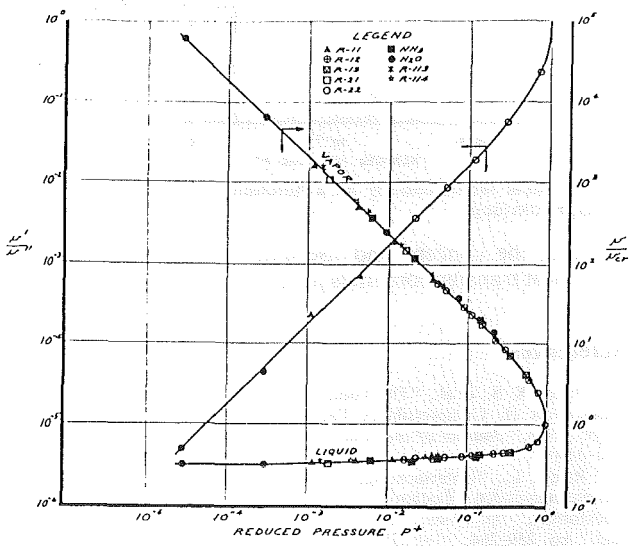


Fig. 1 $v'/v''$ = universal function of reduced pressure $P^+$ (excerpt from [3a])

[1] By S. Torquato and P. Smith, published in the February 1984 issue of JOURNAL OF HEAT TRANSFER, Vol. 106, No. 1, pp. 252–254.

[2] Mem. ASME; Private Consultant, CH-5442 Fislisbach, Switzerland

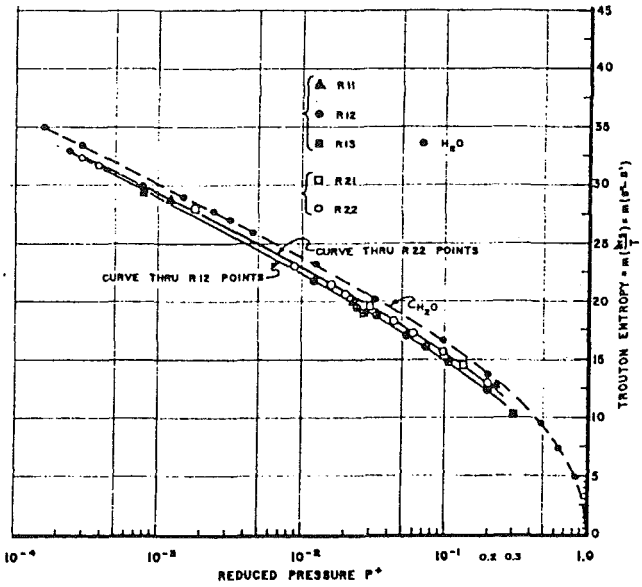


**Fig. 2 Molar latent entropy as a function of reduced pressure $P^+$ (excerpt from [3c])**

validates the concept and usefulness of alternate entropy-based heat transfer potentials proposed in [7–10].

## References


1 Pitzer, K. S., et al., "The Volumetric and Thermodynamic Properties of Fluids. Part II. Compressibility Factor, Vapor Pressure and Entropy of Vaporization," *Journal of the American Chemical Society*, July 5, 1955, pp. 3433–3440.

2 Riedel, L., "Untersuchungen über eine Erweiterung des Theorems der übereinstimmenden Zustände. Teil I. Eine neue universelle Dampfdruckformel," pp. 83–89; "Teil II. Die Flüssigkeitsdichte im Sättigungszustand," pp. 259–264; "Teil III. Kritischer Koeffizient, Dichte des gesättigten Dampfes und Verdampfungswärme," pp. 679–683, *Chemie-Ing.-Techn.*, 26. Jahrg.1954/Nr.2, 5, 12.

3 Soumerai, H., "Application of Thermodynamic Similitude," *ASHRAE Journal*, 3*a*, June 1966: Part I, Pressure Drop; 3*b*, July 1966: Part II, Heat and Mass Transfer; 3*c*, September 1966: Part III, Comments on Applications of Thermodynamic Similitude.

4 Borishansky, W., et al., "Generalization of Experimental Data for the Heat Transfer Coefficient in Nucleate Boiling," *Leningrad Physical Journal*, Dec. 1962.

5 Danilova, G., "Influence of Pressure and Temperature on Heat Exchange in the Boiling of Halogenated Hydrocarbons," *Kholodilnaya Teknika*, No. 2, 1965 (English Abstract: Modern Refrigeration, Dec. 1965).

6 *ASHRAE Handbook, 1981, Fundamentals*, Chap. 2, Boiling, American Society of Heating, Refrigerating and Air-Conditioning Engineers, Inc., pp. 2.16–2.21.

7 Soumerai, H., "A Unified Thermodynamic Theory of Heat, Mass and Momentum Exchange, Part B: Extensions Beyond the Current 'State of the Art'," 16th International Congress of Refrigeration, Paris 1983, Commission B1, Thermodynamics and Transport Processes.

8 Soumerai, H., "Second Law Thermodynamic Treatment of Heat Exchangers," in: *Second Law Aspects of Thermal Design*, ed. A. Bejan and R. L. Reid, ASME, 1984, pp. 11–18.

9 Soumerai, H., "Forced Convection Thermodynamics," submitted for publication Sept. 1984.

10 Soumerai, H., "A Unified Thermodynamic Theory of Heat, Mass and Momentum Exchange," ASHRAE Summer National Meeting, 1984, to be published in *ASHRAE*, Vol. 90, Part 2A, 1984.

11 Doolittle, J. S., and Hale, F. J., *Thermodynamics for Engineers (SI version)*, Chaps. 3–9, Corresponding States and Reduced Properties, Wiley, 1984, pp. 74–80.


## Author's Closure

The authors wish to thank Dr. Soumerai for his interest and comments. We offer the following replies to the questions he raises:

We address the question of the accuracy of Vargaftik's data on p. 252 and again in our conclusions on p. 254. We consider this data source reliable based upon comparison with highly accurate data for specific substances.

The latent heat of vaporization at the triple point, $L_t$, was computed as indicated on p. 253 for the following substances: ethanol, Freon-12, Freon-22, isooctane, methanol, n-nonane, propane, and 1-propanol. The temperature range of engineering (and experimental) interest for these fluids is well above the triple-point temperature, $T_t$, especially for the Freons.

We have compared our latent-heat correlation with that given by Riedel. Riedel's correlation is given in tabular form, which requires tedious double interpolation. Our comparison shows for a sample of ten diverse substances (Ar, Kr, Xe, CO, $CO_2$, $CH_4$, $C_6H_6$, $C_4F_8$, and $O_2$) at a dimensionless temperature of $\tau = 0.5$, a maximum error of $-4.18$ percent for $C_4F_8$ using our correlation. An error of over 20 percent for $C_6H_6$ is obtained using Riedel's correlation, which is highly sensitive to the value of the correlation parameter, $\alpha_k$.

For simplicity and accuracy, we recommend the use of our correlation.

The following errata for Table 1 should be noted: isooctane $- a_6 = +0.91875$; 1-propanol $- a_5 = +8.64866$, $a_6 = -4.26884$.

# ERRATA

Corrections to "The Effect of Coatings on the Steady-State and Short Time Constriction Resistance for an Arbitrary Axisymmetric Flux," by J. R. Dryden, M. M. Yovanovich, and A. S. Deakin, published in the February 1985 issue of the ASME JOURNAL OF HEAT TRANSFER, pp. 33–38.

---

There are seven places where the "0" symbol should be replaced with the "$o$" symbol.

p. 33 $$R = R_{2c} - \frac{1}{\pi a k_1}\,\frac{2K}{1-K}\,\frac{2}{1-K}\,\frac{\delta}{a}[1+o(1)]$$

p. 35 I $$\int_{x=o}^{1} dx f(ax)x \int_{\xi=o}^{\frac{1-K}{\sigma}} d\xi \frac{J_1(\xi)}{\xi} J_o(\xi x)\left(\frac{\sigma\xi}{1-K}\right) = \frac{\sigma}{1-K} I_1 + o\left(\frac{\sigma}{1-K}\right)$$

p. 36 III $$\int_{x=o}^{1} dx f(ax)x \int_{\xi=\left(\frac{1-K}{\sigma}\right)^p}^{\frac{1-K}{\sigma}} d\xi \frac{J_1(\xi)}{\xi} J_o(\xi x) 0\left(\left(\frac{\sigma\xi}{1-K}\right)^2\right)$$

$$= o\left(\frac{\sigma}{1-K}\right)$$

IV $$\int_{x=o}^{1} dx f(ax)x \int_{\xi=\frac{1-K}{\sigma}}^{\infty} d\xi \frac{J_1(\xi)}{\xi} J_o(\xi x)\left[\frac{1-e^{-\sigma\xi}}{1-K_e{}^{-\sigma\xi}}\right]$$

$$= o\left(\frac{\sigma}{1-K}\right)$$

$$\psi(\sigma) = \frac{\sigma}{1-K} I_1 + o\left(\frac{\sigma}{1-K}\right)$$

In equation (29) replace 0(1) with $o(1)$.

p. 37 In equation 38($b$) replace $0\left(\frac{k_1}{k_2}\frac{\delta}{a}\right)$ with $o\left(\frac{k_1}{k_2}\frac{\delta}{a}\right)$.

p. 33 In the second column, second line from the top, for $2/1-K\,\delta/a$ read $2(\delta/a)/(1-K)$

p. 34 Equation (10) should read

$w_1 = Ae^{\eta_1 z} + Be^{-\eta_1 z}\quad \delta > z > o$

p. 36 The $\ln(1-k)$ in the first row of Table 1 should be $\ln(1-K)$

p. 37 In the second column, third line from the bottom, for

$2/1-K\delta/a$ read $2(\delta/a)/(1-K)$